

*The Japan Research and Development  
Center of Metals' National Project on*

**Light for the 21<sup>st</sup> Century:**

**The Development of Compound Semiconductors for  
High Efficiency Optoelectronic Conversion**

**Year 2000 Report of Results<sup>1</sup>**

---

<sup>1</sup> Translation from Japanese to English sponsored by the Optoelectronics Industry Development Association and Sandia National Laboratories, and completed March 29, 2002 by Kirill V Sereda ([kvsereda@worldnet.att.net](mailto:kvsereda@worldnet.att.net)) and Jeff Y Tsao (Sandia National Laboratories -- [jytsao@sandia.gov](mailto:jytsao@sandia.gov)).

## **Background**

According to the international agreement, COP, energy efficiency is becoming an important consideration for consumer products. The electric power consumed for lighting is about 20% of the total electric power consumed in Japan. Appropriate effort is therefore required to develop energy-efficient lighting equipment.

The Japan Research and Development Center of Metals (JRCM) has organized a 5-year R&D project (1998-2002) to develop energy-efficient lighting equipment using light-emitting diodes (LEDs), with the participation of thirteen member companies and universities, as required by the New Energy and Industrial Technology Development Organization (NEDO).

The current project targets an energy efficiency twice that of traditional fluorescent lamps, through the use of long-life, thin, lightweight, GaN-based high-efficiency blue and ultraviolet LEDs.

This lighting equipment would have the following advantages:

1. Less electricity consumption due to high optoelectronic conversion efficiency.
2. Ease of miniaturization due to the small size of the light source -- the lighting equipment would be smaller, thinner and lighter.
3. Long life.
4. Simple structure -- no special devices would be needed to control the lighting equipment, and the number of components in the equipment would be reduced.
5. High reliability due to the use of all-solid-state devices without any gases or filaments -- very reliable against mechanical shock.

# Table of Contents

<b>0 EXECUTIVE SUMMARY .....</b>	<b>10</b>
0.1 FUNDAMENTAL STUDIES ON LIGHT EMISSION MECHANISMS .....	10
0.2 IMPROVEMENTS OF EPITAXIAL GROWTH PROCESSES FOR BLUE AND UV LEDs .....	10
0.3 SUBSTRATES FOR HOMOEPITAXY AND THEIR CHARACTERIZATION.....	11
0.4 TECHNOLOGIES FOR PHOSPHOR-BASED WHITE LEDs AND BASIC PROPERTIES OF LED LIGHTING SOURCES .....	12
<b>1 SUMMARY, PLAN, AND RESEARCH .....</b>	<b>14</b>
1.1 DETAILS OF RESEARCH AND DEVELOPMENT .....	14
1.2 PLANS AND ACTIONS SURROUNDING EACH RESEARCH CHALLENGE .....	14
1.2.1 <i>Research &amp; Development Plans and Objectives; Overseas Trends</i> .....	14
1.2.2 <i>White Diodes and Luminescence Characteristics</i> .....	16
1.3 COOPERATIVE PROJECT .....	19
1.4 PARTICIPATION IN “21 <sup>ST</sup> CENTURY DREAM TECHNOLOGY EXHIBITION” .....	19
1.5 REPORT ON TECHNOLOGY TRENDS FROM MRS 2000 FALL MEETING.....	19
1.5.1 <i>Overview of 2000 Fall Meeting</i> .....	20
1.6 PATENT SEARCH .....	23
1.6.1 <i>New Open Applications and Registrations</i> .....	24
1.7 CONCLUSIONS .....	29
1.8 FUTURE COURSE.....	29
1.9 REFERENCES .....	30
<b>2 BASIC RESEARCH RELATED TO LIGHT EMISSION MECHANISMS.....</b>	<b>31</b>
2.1 ACHIEVEMENTS IN 1998~1999 .....	31
2.2 SUMMARY OF RESEARCH AND DEVELOPMENT IN 2000 .....	32
2.3 EXCITATION SPECTROSCOPY MEASUREMENTS OF TEMPERATURE DEPENDENCE OF ABSORPTION AND EMISSION .....	32
2.3.1 <i>Methods and means</i> .....	32
2.3.2 <i>Results and Discussion</i> .....	33
2.4 GROWTH OF GAN EPITAXIAL THIN FILMS BY MBE METHOD AND THEIR EVALUATION ...	45
2.4.1 <i>Methods for MBE Growth of GaN Epitaxial Thin Films and their Evaluation</i> .....	45
2.4.2 <i>Results and Discussion</i> .....	48
2.5 SUMMARY .....	55
2.6 FUTURE PLANS.....	56
2.7 REFERENCES .....	57
<b>3 CLARIFICATION OF LIGHT EMISSION MECHANISMS AND PHYSICAL PROPERTIES OF GAN-BASED SEMICONDUCTORS .....</b>	<b>58</b>
3.1 ACHIEVEMENTS IN 1998~1999 .....	58
3.2 SUMMARY OF RESEARCH AND DEVELOPMENT IN 2000 .....	59
3.2.1 <i>Examination of light emission mechanism of GaInN/GaN multiple quantum well LEDs with different In compositions</i> .....	59
3.2.2 <i>Examination of emission lifetime characteristics of LEDs of different luminescence efficiencies</i> .....	59
3.2.3 <i>Examination of in-plane distribution of light emission</i> .....	59
3.2.4 <i>Reverse bias PL characteristics of Si-doped quantum well LEDs</i> .....	60

3.3 METHODS AND MEANS .....	60
3.3.1 PL and Time Resolved PL Measurement System .....	60
3.3.2 Reverse Biased PL and Time-Resolved PL Measurements of LED Samples.....	60
3.3.3 High Spatial Resolution PL Mapping System Utilizing a Near-Field Optical Probe .	60
3.3.4 Method of Interference-Free Measurement of Emission Spectra .....	61
3.4 RESULTS AND DISCUSSION .....	64
3.4.1 Investigation of Emission Characteristics of GaInN/GaN Quantum Well Structure LEDs with Different In Compositions .....	64
3.4.2 Investigation of Emission Lifetime Characteristics of LEDs with Different Emission Efficiencies .....	69
3.4.3 Investigation of In-Plane Distribution of Light Emission.....	72
3.4.4 Reverse Bias PL Characteristics of Si-Doped Quantum Well LEDs .....	73
3.5 SUMMARY .....	79
3.6 FUTURE PLANS .....	80
3.7 REFERENCES .....	80
<b>4 BASIC RESEARCH CONCERNING GAN SINGLE CRYSTALS GROWN BY THE SOLUTION GROWTH METHOD.....</b>	<b>82</b>
4.1 ACHIEVEMENTS IN 1998 AND 1999 .....	82
4.2 SUMMARY OF RESEARCH AND DEVELOPMENT IN 2000 .....	83
4.3 METHODS AND MEANS .....	83
4.3.1 Principles of the pressure-controlled solution growth method.....	83
4.3.2 Laboratory equipment.....	84
4.3.3 GaN single crystal growth method.....	87
4.3.4 Crystal evaluation method .....	88
4.4 EXPERIMENTAL RESULTS AND DISCUSSION.....	88
4.4.1 Results of GaN single crystal growth experiments .....	88
4.4.2 Results of crystal evaluation .....	93
4.5 SUMMARY .....	97
4.6 FUTURE PLANS.....	98
4.7 REFERENCES .....	99
<b>5 RESEARCH CONCERNING SUBSTRATE SURFACE MORPHOLOGY .....</b>	<b>101</b>
5.1 ACHIEVEMENTS IN 1998 ~1999 .....	101
5.2 SUMMARY OF RESEARCH AND DEVELOPMENT IN 2000 .....	102
5.3 INTRODUCTION OF HIGH PRECISION PROCESSING TECHNOLOGY FOR SAPPHIRE SUBSTRATES .....	102
5.3.1 Methods and Means .....	102
5.3.2 Results and Discussion.....	103
5.4 INTRODUCTION OF GAN SUBSTRATE PRECISION PROCESSING TECHNOLOGY .....	105
5.4.1 Methods and Means .....	105
5.4.2 Results and discussion.....	105
5.5 SUMMARY .....	106
5.6 PLANS FOR THE FUTURE .....	107
5.7 REFERENCES .....	107
<b>6 RESEARCH AND DEVELOPMENT OF GANASP-BASED MULTICOLORED LIGHT EMITTING MATERIALS USING MOCVD.....</b>	<b>108</b>
6.1 ACHIEVEMENTS IN 1998 – 1999 .....	108
6.2 SUMMARY OF RESEARCH AND DEVELOPMENT OF 2000 .....	109

6.3 DEVELOPMENT OF $\text{GAN}_{1-x}\text{P}_x$ MULTICOLORED LIGHT EMITTING MATERIALS THROUGH LASER-ASSISTED MOCVD .....	109
6.3.1 <i>Methods and Means</i> .....	109
6.3.2 <i>Results and Considerations for Growth of GaNP</i> .....	110
6.4 GANP GROWTH (DMHY/ $\text{PH}_3$ /TMG) THROUGH NONRADIATED MOCVD .....	119
6.4.1 <i>Methods and Means</i> .....	119
6.4.2 <i>Results and Observations</i> .....	119
6.5 GANP LEDs .....	122
6.5.1 <i>Methods and Means</i> .....	122
6.5.2 <i>Results and Observations</i> .....	123
6.6 SUMMARY .....	124
6.7 FUTURE COURSE .....	124
6.8 REFERENCES .....	125
<b>7 DEVELOPMENT OF MOCVD-GROWN LOW-DEFECT GAN THIN FILM EPI-SUBSTRATES .....</b>	<b>126</b>
7.1 ACHIEVEMENTS IN 1998 AND 1999 .....	126
7.2 SUMMARY OF RESEARCH AND DEVELOPMENT IN 2000 .....	127
7.3 INVESTIGATIONS INTO DISLOCATION DEFECT REDUCTION BY ELOG GROWTH .....	127
7.3.1 <i>Methods and Means (Investigation into ELOG Growth for Reduced Dislocation Density)</i> .....	129
7.3.2 <i>Results and discussion (investigation of ELOG growth-based dislocation defect reduction)</i> .....	132
7.4 EVALUATION OF ELOG-GROWN SUBSTRATES .....	140
7.4.1 <i>Methods and Means</i> .....	141
7.4.2 <i>Results and Discussion</i> .....	143
7.5 SUMMARY .....	152
7.6 FUTURE PLANS .....	152
7.7 REFERENCES .....	153
<b>8 DEVELOPMENT OF GAN EPITAXIAL SUBSTRATES BASED ON LOW PRESSURE GAS PHASE TECHNIQUE .....</b>	<b>154</b>
8.1 ACHIEVEMENTS IN 1998 AND 1999 .....	154
8.2 SUMMARY OF RESEARCH & DEVELOPMENT IN 2000 .....	155
8.2.1 <i>Research on GaN-related transport and reaction phenomena</i> .....	155
8.2.2 <i>Research on single crystal growth techniques</i> .....	156
8.3 MICROWAVE-BASED GAN SYNTHESIS EXPERIMENTS .....	156
8.3.1 <i>Methods and means</i> .....	156
8.3.2 <i>Results and Discussion</i> .....	160
8.4 GAN CRYSTAL GROWTH METHOD UTILIZING NOVEL PLASMA GENERATION TECHNIQUE .....	168
8.4.1 <i>Methods and means</i> .....	168
8.4.2 <i>Results and discussion</i> .....	169
8.5 SUMMARY .....	173
8.6 FUTURE PLANS .....	174
<b>9 DEVELOPMENT OF LED EPI PROCESS TECHNOLOGY .....</b>	<b>175</b>
9.1 ACHIEVEMENTS IN 1998 AND 1999 .....	175
9.1.1 <i>Achievements in 1998</i> .....	175
9.1.2 <i>Achievements in 1999</i> .....	175
9.2 SUMMARY OF RESEARCH AND DEVELOPMENT IN 2000 .....	176

9.3 FABRICATION OF ALGaN/GaInN UV MQW STRUCTURES.....	177
9.3.1 <i>Methods and means</i> .....	177
9.3.2 <i>Results and discussion</i> .....	178
9.4 STUDY OF ALGaN CLADDING LAYERS WITH HIGH AlN MOLAR FRACTION.....	181
9.4.1 <i>Methods and means</i> .....	181
9.4.2 <i>Results and discussion</i> .....	182
9.5 FABRICATION OF UV LED STRUCTURES.....	183
9.5.1 <i>Methods and means</i> .....	183
9.5.2 <i>Results and discussion</i> .....	184
9.6 SUMMARY.....	184
9.6.1 <i>Fabrication of AlGaN/GaInN UV MQW structures</i> .....	184
9.6.2 <i>Study of AlGaN cladding layer with high AlN molar fraction</i> .....	185
9.6.3 <i>Fabrication of UV LED element structures</i> .....	185
9.7 FUTURE PLANS.....	185
9.7.1 <i>Non-radiative recombination rate reduction</i> .....	185
9.7.2 <i>AlGaInN emitting layer (high InN molar fraction)</i> .....	185
9.7.3 <i>ELO technique</i> .....	186
9.7.4 <i>Large-size MOCVD apparatus</i> .....	186
9.7.5 <i>Application of SiC substrates</i> .....	186
9.8 REFERENCES.....	186
<b>10 DEVELOPMENT OF HIGH-OUTPUT UV LIGHT-EMITTING COMPONENTS ...</b>	<b>187</b>
10.1 ACHIEVEMENTS IN 1998 AND 1999.....	187
10.1.1 <i>Achievements in 1998</i> .....	187
10.1.2 <i>Achievements in 1999</i> .....	187
10.2 SUMMARY OF RESEARCH AND DEVELOPMENT IN 2000.....	188
10.3 BUILDING OF PROTOTYPES OF UV-EMITTING COMPONENTS.....	188
10.3.1 <i>Experimental method</i> .....	188
10.3.2 <i>Results and discussion</i> .....	189
10.3.3 <i>Building of white LED prototypes</i> .....	191
10.4 INVESTIGATIONS INTO NEW DISLOCATION REDUCTION TECHNIQUES.....	192
10.4.1 <i>LEPS technique</i> .....	193
10.4.2 <i>Experimental (LEPS-GaN growth)</i> .....	193
10.4.3 <i>Results and discussion</i> .....	194
10.5 APPLICATION OF LEPS TECHNIQUE TO LEDS.....	196
10.5.1 <i>Experimental methods</i> .....	196
10.5.2 <i>Results and discussion</i> .....	196
10.6 BUILDING OF WHITE LED PROTOTYPES UTILIZING BLUE LEDS.....	198
10.6.1 <i>Experimental method</i> .....	199
10.6.2 <i>Results and discussion</i> .....	199
10.7 SUMMARY.....	199
10.8 FUTURE PLANS.....	200
10.9 REFERENCES.....	200
<b>11 DEVELOPMENT OF HIGH-EFFICIENCY PHOSPHORS .....</b>	<b>201</b>
11.1 ACHIEVEMENTS IN 1998 AND 1999.....	201
11.1.1 <i>Review of phosphors and selection of model phosphors</i> .....	201
11.1.2 <i>Improvements in characteristics of red phosphors</i> .....	201
11.1.3 <i>Introduction of equipment for phosphor firing</i> .....	201
11.1.4 <i>Precise measurements and evaluation of phosphor emission characteristics</i> .....	201

11.2 SUMMARY OF RESEARCH AND DEVELOPMENT IN 2000 .....	202
11.3 QUANTUM EFFICIENCY MEASUREMENTS .....	202
11.3.1 <i>Methods and means</i> .....	202
11.3.2 <i>Results and discussion</i> .....	204
11.4 EVALUATION OF TEMPERATURE CHARACTERISTICS .....	208
11.4.1 <i>Methods and means</i> .....	208
11.4.2 <i>Results and discussion</i> .....	208
11.5 SUMMARY .....	209
11.6 FUTURE PLANS .....	209
11.6.1 <i>Quantum efficiency improvement</i> .....	209
11.6.2 <i>Methods of synthesis</i> .....	210
11.6.3 <i>Other</i> .....	210
11.7 REFERENCES .....	210
<b>12 ELECTRODE ATTACHMENT, PACKAGING, AND WHITE LED DEVELOPMENT</b>	<b>211</b>
12.1 ACHIEVEMENTS IN 1998~1999 .....	211
12.1.1 <i>Achievements in 1998</i> .....	211
12.1.2 <i>Achievements in 1999</i> .....	211
12.2 SUMMARY OF RESEARCH AND DEVELOPMENT IN 2000 .....	212
12.3 DEVELOPMENT OF ELECTRODE FORMING TECHNIQUES .....	212
12.3.1 <i>Methods and Means</i> .....	212
12.3.2 <i>Results and Discussion</i> .....	213
12.4 INVESTIGATIONS INTO INCREASING LIGHT EXTRACTION EFFICIENCY (EDGE TILTING TECHNOLOGY)	
.....	220
12.4.1 <i>Methods and means</i> .....	220
12.4.2 <i>Results and discussion</i> .....	222
12.5 WHITE LED DEVELOPMENT .....	226
12.5.1 <i>Study of mixed white light production and emission characteristics of RGB model phosphors</i>	
.....	226
12.5.2 <i>Study of phosphor layer forming techniques and transmitted UV light control</i> .....	227
12.5.3 <i>Evaluation of emission characteristics and color rendering of a white LED lamp</i> .....	231
12.6 DEVELOPMENT OF SEALING RESINS FOR UV LEDs .....	236
12.6.1 <i>Methods and means</i> .....	236
12.6.2 <i>Results and discussion</i> .....	237
12.7 SUMMARY .....	240
12.7.1 <i>Electrode forming techniques</i> .....	240
12.7.2 <i>Improvements in light extraction efficiency</i> .....	240
12.7.3 <i>Development of white LEDs</i> .....	241
12.7.4 <i>Development of sealing resins for UV LEDs</i> .....	241
12.8 PLANS FOR THE FUTURE .....	241
12.9 REFERENCES .....	242
<b>13 DEVELOPMENT OF LED-BASED LIGHT-SOURCE DEVICES FOR ILLUMINATION</b>	<b>243</b>
.....	
13.1 ACHIEVEMENTS IN 1998-1999 .....	243
13.2 SUMMARY OF RESEARCH AND DEVELOPMENT IN 2000 .....	243
13.3 STUDY OF PHOSPHOR CONVERSION-BASED LED LIGHT SOURCE DEVICES BY OPTICAL SIMULATION	
.....	244
13.3.1 <i>Methods and means (simulation-based study of light source devices)</i> .....	244
13.3.2 <i>Results and discussion (simulation-based study of light source devices)</i> .....	247

13.4 CORRELATED COLOR TEMPERATURE ALTERATION TECHNIQUES AND COLOR RENDERING PROPERTY EVALUATION OF MIXED LIGHT FROM WHITE, RED, AND GREEN LEDs .....	251
13.4.1 <i>Methods and means (correlated color temperature alteration technique &amp; color rendering property evaluation)</i> .....	252
13.4.2 <i>Results and discussion (correlated color temperature alteration technique &amp; color rendering property evaluation)</i> .....	252
13.5 STUDY OF ENVIRONMENTAL COMPATIBILITY EVALUATION OF LED LIGHT SOURCE DEVICES .....	254
13.5.1 <i>Methods and means (environmental compatibility evaluation study)</i> .....	255
13.5.2 <i>Results and discussion (environmental compatibility evaluation research)</i> .....	256
13.6 SUMMARY .....	260
13.7 FUTURE PLANS .....	260
13.8 REFERENCES .....	260
<b>14 RESEARCH AND DEVELOPMENT OF LIGHT-EMITTING-REGION CONVERSION ILLUMINATION SYSTEMS .....</b>	<b>262</b>
14.1 ACHIEVEMENTS IN 1998~1999 .....	262
14.2 SUMMARY OF RESEARCH AND DEVELOPMENT IN 2000 .....	263
14.3 VERIFICATION OF IMPROVED EFFICIENCY OF COUPLING ELEMENTS .....	264
14.3.1 <i>Methods and means</i> .....	265
14.3.2 <i>Results and discussion</i> .....	266
14.4 CONCEPTUAL DESIGN OF DIRECTIONALITY CONVERSION SYSTEM.....	274
14.4.1 <i>Methods and means (conceptual design of directionality conversion system)</i> .....	274
14.4.2 <i>Results and discussion (conceptual design of directionality conversion system)</i> ....	276
14.5 SUMMARY .....	277
14.6 PLANS FOR THE FUTURE.....	278
14.7 REFERENCES .....	279
<b>15 LIGHTING FIXTURE DEVELOPMENT BASED ON NOVEL LED CONCEPTS....</b>	<b>280</b>
15.1 ACHIEVEMENTS IN 1998~1999 .....	280
15.1.1 <i>Achievements in 1998</i> .....	280
15.1.2 <i>Achievements in 1999</i> .....	280
15.1.3 <i>Discussion of Achievements in 1998~1999</i> .....	280
15.2 SUMMARY OF RESEARCH AND DEVELOPMENT IN 2000 .....	281
15.3 PROTOTYPING AND EVALUATION OF LED TABLE LAMP .....	282
15.3.1 <i>Methods and Means</i> .....	282
15.3.2 <i>Results and Discussion</i> .....	282
15.4 PROTOTYPING AND EVALUATION OF LED CEILING DOWNLIGHT .....	283
15.4.1 <i>Methods and Means</i> .....	283
15.4.2 <i>Results and Discussion</i> .....	284
15.5 CONCLUSIONS .....	286
15.6 AGENDA FOR THE FUTURE.....	286
<b>16 CONCLUSIONS AND FUTURE COURSE .....</b>	<b>289</b>
16.1 PLANNING AND INVESTIGATIONS .....	289
16.2 BASIC RESEARCH ON LIGHT EMISSION MECHANISMS .....	289
16.3 PROPERTIES OF GAN-BASED SEMICONDUCTORS AND DISCOVERY OF LIGHT EMISSION MECHANISMS.....	291
16.4 BASIC RESEARCH ON BULK GAN SINGLE CRYSTALS BY SOLUTION GROWTH METHOD	292
16.5 RESEARCH INTO CRYSTALLINE SUBSTRATE SURFACES .....	294

16.6 RESEARCH AND DEVELOPMENT OF GANASP-BASED MULTICOLORED LIGHT EMITTING MATERIALS BY MOCVD.....	294
16.7 DEVELOPMENT OF LOW DEFECT DENSITY GAN THIN FILM EPITAXIAL SUBSTRATES THROUGH MOCVD .....	295
16.8 DEVELOPMENT OF GAN EPITAXIAL SUBSTRATES THROUGH LOW PRESSURE VAPOR PHASE METHOD .....	296
16.9 DEVELOPMENT OF LED EPITAXIAL PROCESS TECHNOLOGIES .....	297
16.10 DEVELOPMENT OF HIGH OUTPUT ULTRAVIOLET EMITTING ELEMENTS .....	298
16.11 DEVELOPMENT OF HIGHLY EFFICIENT PHOSPHOR SUBSTANCES.....	299
16.11.1 <i>Improving Quantum Efficiency</i> .....	299
16.11.2 <i>Synthesis Method</i> .....	299
16.11.3 <i>Other</i> .....	299
16.12 DEVELOPMENT OF LEAD BONDING METHODS, PACKAGING TECHNOLOGIES, AND WHITE LEDS .....	300
16.12.1 <i>Electrode Formation Technology</i> .....	300
16.12.2 <i>Improvement in Light Extraction Efficiency</i> .....	300
16.12.3 <i>Development of White LEDs</i> .....	300
16.12.4 <i>Development of Resin Sealants for UV LED</i> .....	300
16.13 DEVELOPMENT OF LIGHT EMITTING DIODE LIGHT SOURCE DEVICES FOR ILLUMINATION.....	301
16.14 RESEARCH AND DEVELOPMENT OF ZONE CONVERSION ILLUMINATION SYSTEMS .....	302
16.14.1 <i>Robust Design</i> .....	302
16.14.2 <i>Fundamental Specifications</i> .....	303
16.15 DEVELOPMENT OF ILLUMINATION DEVICES BASED ON NEW LED CONCEPTS.....	303
<b>17 LIST OF RESEARCH PUBLICATIONS AND ARTICLES.....</b>	<b>305</b>

# 0 Executive Summary

This is the summary of the “Light for the 21<sup>st</sup> Century” National Project, based on white light-emitting diodes (LEDs), which has been carried out through a cooperation between universities and industry in the fiscal year 2000. The following results in four research areas have been obtained.

## 0.1 Fundamental Studies on Light Emission Mechanisms

In order to clarify the light emission mechanism in InGaN-based semiconductors, time-resolved photoluminescence (PL) and photoluminescence excitation (PLE) spectroscopy measurements have been carried out. PLE spectroscopy enabled us to observe clear structures associated with the absorption of InGaN ternary alloys up to room temperature for the first time. It was found that the Stokes shift was independent of temperature, and that the two observed emission components derived from states populated by carrier relaxation from the same excited state. The experimental value of the Stokes shift was in good agreement with a theoretical value based on the electron-phonon interaction. It has therefore been proposed that coupled electron/phonon polaron states contribute to the highly efficient radiative recombination processes in this material system. The obtained results seem to be important for understanding high-efficiency recombination mechanisms in ultraviolet (UV) LEDs.

We have studied carrier recombination processes in InGaN/GaN multiple quantum wells (MQWs) through systematic measurements of the luminescence of LED samples under various conditions. From carrier lifetime measurements over a wide range (7-540K) of temperatures, carrier localization and delocalization characteristics were consistently observed for LED samples with varying In composition. Through a comparison with simulations, we found that the localization energy depth increases with increasing In composition, which prevents the transfer of carriers to non-radiative recombination centers. Non-radiative recombination centers, which are probably dominated by point defects in InGaN, also increase with increasing In composition.

Characteristics associated with more deeply localized states were observed for an LED with higher quantum efficiency based on the temperature dependence of the carrier decay time. By using a near-field PL mapping system with high spatial resolution, the luminescence intensity and wavelength distribution in the plane of the QW (quantum well) of a typical blue LED were observed. The spatial scale of this distribution was estimated to be 0.3-0.5  $\mu\text{m}$ .

The piezoelectric field strength in a 2 nm InGaN QW was studied using PL measurements under reverse bias, taking into account the measured depletion length of the diode, and was estimated to be  $E_{\text{piezo}} = 1.48$  MV/cm for  $x=0.23$ , close to the published values. Bias-dependent measurements on LEDs suggest that Si doping is important both for modifying the overall band structure of the device and for free-carrier screening of the internal electric field in the QWs.

## 0.2 Improvements of Epitaxial Growth Processes for Blue and UV LEDs

A MQW structure consisting of AlGaIn barrier and InGaIn well layers for UV LEDs has been studied. By increasing the growth temperature of the AlGaIn barrier layers, the surface morphology of the MQW layers clearly showed steps formed by a step-flow growth mode, and the interface between well and barrier layers was sharp. An AlGaIn/InGaIn MQW LED was then fabricated on a sapphire substrate. The peak

wavelength of the emission spectrum was 390 nm at room temperature. At a forward current of 20 mA, the forward bias voltage and the output power were 3.7 V and about 1 mW, respectively.

We have observed that low-level doping of Si in barrier layers in a MQW increased the output power of the UV LED.

A new GaN growth process called LEPS (Lateral Epitaxy on a Patterned Substrate) was developed. It has been found that the LEPS process is effective in decreasing the dislocation density and for improving the output power of UV LEDs. When the LEPS UV LED die was operated at a forward bias current of 20 mA at room temperature, the emission wavelength, the output power and the external quantum efficiency were measured to be 382 nm, 2.5 mW and 3.7%, respectively.

We have developed a new technique for GaNP growth. A laser-assisted MOCVD method was applied to GaNP growth. It is anticipated that, through ArF laser irradiation, source gases will be decomposed at lower temperatures, resulting in GaNP with a high P composition. Using this method, we obtained GaNP with 10% P composition. This composition is the highest reported value for MOCVD-grown GaNP. A GaN<sub>0.9</sub>P<sub>0.1</sub>/GaN single quantum well (SQW) LED was fabricated and bright blue emission at 425 nm was observed for the first time.

## 0.3 Substrates for Homoepitaxy and their Characterization

We have investigated the effect of nitrogen pressure ramp rate on the size and morphology of GaN bulk single crystals grown by the pressure-controlled solution growth (PC-SG) method. A GaN single crystal with a surface area of 334 mm<sup>2</sup>, which is the largest GaN single crystal ever grown by the solution growth method, was obtained by natural nucleation without any seeds. To characterize the GaN bulk crystals, improvements were first made to the lapping and polishing techniques. Next, the GaN crystals were lapped and polished to achieve flat surfaces. Finally, these high quality flat surfaces were characterized by XRD, AFM, TEM and PL. The resulting data indicated that the crystals with good morphology also had good crystallinity. It was found that reductions in nitrogen pressure ramp rate and temperature fluctuations are necessary to grow larger GaN bulk single crystals with good morphology and good crystallinity. We have also studied the crystal growth of GaN on a hetero seed by the PC-SG method. A GaN crystal with a diameter of 47 mm with a normal axis in the (0001) direction, could be grown on a 2-inch sapphire substrate.

Homoepitaxial growth of GaN thin films on GaN bulk single crystals prepared by pressure-controlled solution growth (PC-SG) method has been carried out using molecular beam epitaxy. A correlation between the lattice-polarity of bulk GaN substrates, the lattice-polarity of homoepitaxial GaN layers, and their optical properties, was determined. The luminescence intensity of homoepitaxial layers has been greatly improved as compared to that of heteroepitaxial layers on sapphire substrates. Relatively lower minimum yields ( $\chi_{\min}$ ) of polarity-controlled GaN epilayers as measured by Rutherford backscattering have indicated a high crystalline quality.

We have succeeded in growing GaN crystals using a new vapor phase growth technology which allows high-yield low-cost substrates for GaN based LEDs. We have constructed an innovative semi-closed system where metal gallium is in a quartz ampoule and nitrogen gas activated by microwaves is introduced to synthesize GaN on a substrate. A high growth rate of 100  $\mu\text{m}/\text{h}$  was achieved by adjusting the growth conditions. We have indications of the possibility of maximum growth rates up to 1 mm/h by using high-frequency-discharge nitrogen plasma. By optimizing the growth conditions (microwave power, nitrogen pressure and growth temperature), we have obtained a thick GaN crystalline film on a sapphire substrate of 10x4 mm<sup>2</sup> area. The surface showed good uniformity. However, our best results were obtained using a GaN substrate. The grown surface showed 6-fold symmetric grain boundaries and the full width at half maximum (FWHM) of the x-ray rocking curve was about 360 arcsec.

By the newly developed FACELO (Facet Controlled ELOG) method, we successfully lowered the etch pit density (EPD) to as low as  $10^4$ - $10^6$  cm<sup>2</sup>, the lowest level in the world as far as we know. On a GaN template with low EPD grown by optimizing the nuclei density, we carried out FACELO growth using a two-step process: ELOG growth of inclined  $\{11\bar{2}2\}$  facets for the first step, followed by growth of vertical  $\{11\bar{2}0\}$  facets for the second step. A trial of growth on 2 inch sapphire was carried out; however, the overgrowth over the masks remained incomplete and only a rough surface morphology was obtained. The effective reduction of the dislocation density was attributed to the following phenomena: (1) bending of the a+c type threading dislocations (TDs) toward the  $\langle 11\bar{2}0 \rangle$  direction due to the inclined facet and termination of the laterally propagating dislocations due to the void surface, (2) bending of the a type TDs parallel to the mask stripe, (3) generation of new dislocations above the coalescence line at the top of voids, and (4) the blocking of the penetration towards the surface due to a SiO<sub>2</sub> mask layer by the second FACELO (vertical facet) process. From  $\mu$ -PL spectroscopic observations, it was suggested that the degree of impurity inclusions into regrown GaN layers in the FACELO process depends on the type of facet, in the order  $\{11\bar{2}0\} > \{11\bar{2}2\} > \{0001\}$ .

From time-resolved PL spectroscopy measurements it was confirmed that in comparison to ELOG GaN films grown with an SiO<sub>2</sub> mask, ELOG-GaN films grown with a W mask exhibit a longer free exciton lifetime.

## 0.4 Technologies for Phosphor-Based White LEDs and Basic Properties of LED Lighting Sources

We have pointed out that it is important to measure precisely the absorption, internal and external quantum efficiency of red, green and blue phosphor materials. It is expected using the best candidate phosphors that the emission efficiency of the red phosphor will be higher than that of the usual one.

In the area of electrode formation technology, 70% reflectivity and  $2 \times 10^{-5}$  ohm-cm<sup>2</sup> contact resistivity in the n-type electrode were obtained by optimizing the conditions for Ti/Al contact formation. For the formation of the p-type electrode, Rh and Pt, which are electrode materials with lower contact resistance compared to Ni/Ag, were explored.

Chip shaping was studied in order to improve light extraction efficiency. It was proposed that etching the end face to produce inclined facets was effective in directing the light, which would otherwise be absorbed internally, through the substrate for extraction. Inclined facets were formed by the dry etching method.

For white LED device development, application technologies for phosphors have been examined. Both basic evaluation of typical RGB phosphors and simulation of mixed RGB white phosphors have been carried out. Transmission of ultraviolet radiation through the phosphor layer can be controlled by the phosphor layer fabrication method. Luminescence and color rendering properties of the white LED lamp have been investigated. The ultraviolet radiation was reflected over a phosphor layer mounted on the UV LED chip, and an optical thin film filter, into which the visible light can penetrate, was formed. It was confirmed that the transmission intensity of ultraviolet radiation was decreased from 31% to 13% and that the luminous flux of all white LED lamps can be improved up to 30% by coating the side edge of the UV LED chip with the phosphor.

We have examined the luminescence properties of reflection type light sources which are composed of blue LEDs and YAG phosphor by using optical computer simulation. It was found that the computer simulation results agree well with the properties of the actual light source. This fact suggests that light sources can in principle be designed by using this simulation method.

Furthermore, we have examined the changes of correlated color temperatures of white LEDs formed from combining red and green LEDs, and evaluated color rendering properties for each condition. We examined light source properties for five correlated color temperatures by controlling the intensities of the three LEDs. In particular, a high color rendering index (Ra=95) was obtained under daylight conditions. We psychophysically measured the effects of visual stress induced by the light sources composed of LEDs using

the method of magnitude estimation. The results indicate that the glare (“mabushisa”) and discomfort (“fukaikan”) sensations are closely correlated to one another and that magnitude estimates exponentially increase as a function of illuminance.

The light efficiency was evaluated in order to design light guides for mass-production. The parameters (the deformation of the pattern, the LED location, etc.) were chosen, and the relationship between each parameter and light efficiency was simulated to evaluate the allowed variability of these parameters. Moreover, in order to reduce the influence of fabrication errors, new methods (the trapezoidal pattern shape, the corner LED setting, etc.) were proposed.

The effect of the directivity conversion method utilizing a prism sheet was evaluated for high-directivity application, for example, a footlight and a spotlight. High directivity was realized by utilizing a prism sheet on a 4 inch light guide. The uniformity of the light intensity was also evaluated. It is confirmed that the uniformity is not affected by using a prism sheet.

We fabricated lighting fixtures using white LEDs which have the highest-level luminous efficacy (15 lm/W) in commercially available devices. We also studied the utility of chip-type LEDs and tried to clarify potential benefits of downsizing while still providing reasonable lighting characteristics. Through the prototyping of LED table lamps and LED down-ceiling lights, it is suggested that a drastic energy saving can be achieved by downsizing. In addition, it is necessary to investigate the flexibility in designing LED light sources and the benefits of utilizing LEDs were discussed from the point of view of installation.

# 1 Summary, Plan, and Research

## 1.1 Details of Research and Development

At the 3rd Session of the Conference of the Parties to the United Nations Framework Convention on Climate Change (COP3) held in 1997 Japan was called upon to reduce emissions of greenhouse effect gases by 6% (compared to 1990 levels). To combat global warming, Japan's promotion of energy-saving measures in commercial, civilian, and transportation sectors has become an urgent task [1]. Development of energy-saving technologies for lighting is especially important since it represents over 20% of the energy consumed by the public. In 1998, the Ministry of International Trade and Industry (presently the Ministry of Economy, Trade and Industry) launched a national project entitled "Development of Compound Semiconductors for High Efficiency Lighting" (commonly referred to as "Light for the 21<sup>st</sup> Century") for the purpose of developing practical applications of white LED light sources that exceed the energy efficiency of conventional incandescent and fluorescent lamps [2, 3].

Over the years since the project started, the term LED (light-emitting diode) "semiconductor lighting" has become firmly established [4]. Most notably, with the practical application of blue LEDs using InGaN nitride semiconductors, white LEDs having a luminous efficiency of better than 20 lm/W have been developed by combining yellow phosphors (YAG:Ce) and high luminance blue LEDs capable of over 10 candela. As such, white LEDs are receiving worldwide attention as a next-generation energy-saving light source [5]. What's more, innovative semiconductor structures have been developed for UV LEDs that emit light via the short-wavelength ultraviolet region, raising expectations for practical uses of white LEDs as an illumination source [6].

This report discusses primary research achievements over the three years of the project. This Chapter outlines objectives and plans of the research, characteristics of white LED light sources, and the project's cooperative arrangement and policies. Chapters 2 through 15 present fourteen research themes, and Chapter 16 sums up the achievements of 2000 and future policy.

## 1.2 Plans and Actions Surrounding Each Research Challenge

### 1.2.1 Research & Development Plans and Objectives; Overseas Trends

By making highly efficient white LEDs practical, the national project "Light for the 21<sup>st</sup> Century" aims to promote energy savings, to aid in the prevention of global warming, and to create new lighting applications and culture. As a result, the effect of energy savings achieved in 2010 through the use of white LED illumination is estimated at a market penetration of 13% with an equivalence of 83,000 kl of crude oil.

At present, the following four R&D programs are underway to make white LEDs practical.

- (1) Discovery of light emitting mechanisms of mixed crystal semiconductors and chemical compounds based on AlN, GaN, InN for UV LEDs.
- (2) Development of substrates for homoepitaxy.
- (3) Improvement of epitaxial growth technologies for blue and UV LEDs and development of UV LEDs of high luminosity.

- (4) Development of highly efficient RGB phosphors and discovery of practical uses of white LEDs as an illumination system.

As shown in figure 1.2.1-(1), a number of high performance products using UV LEDs already exist in 2001, based on growth of high quality semiconductor crystals and development of highly efficient LEDs and evaluation of materials. We hope to achieve white LEDs with an efficiency of 80 – 100 lm/W by about 2003 and then 120 lm/W by 2010, thus paving the way for lighting fixtures that eventually exceed the efficiency of fluorescent lamps.

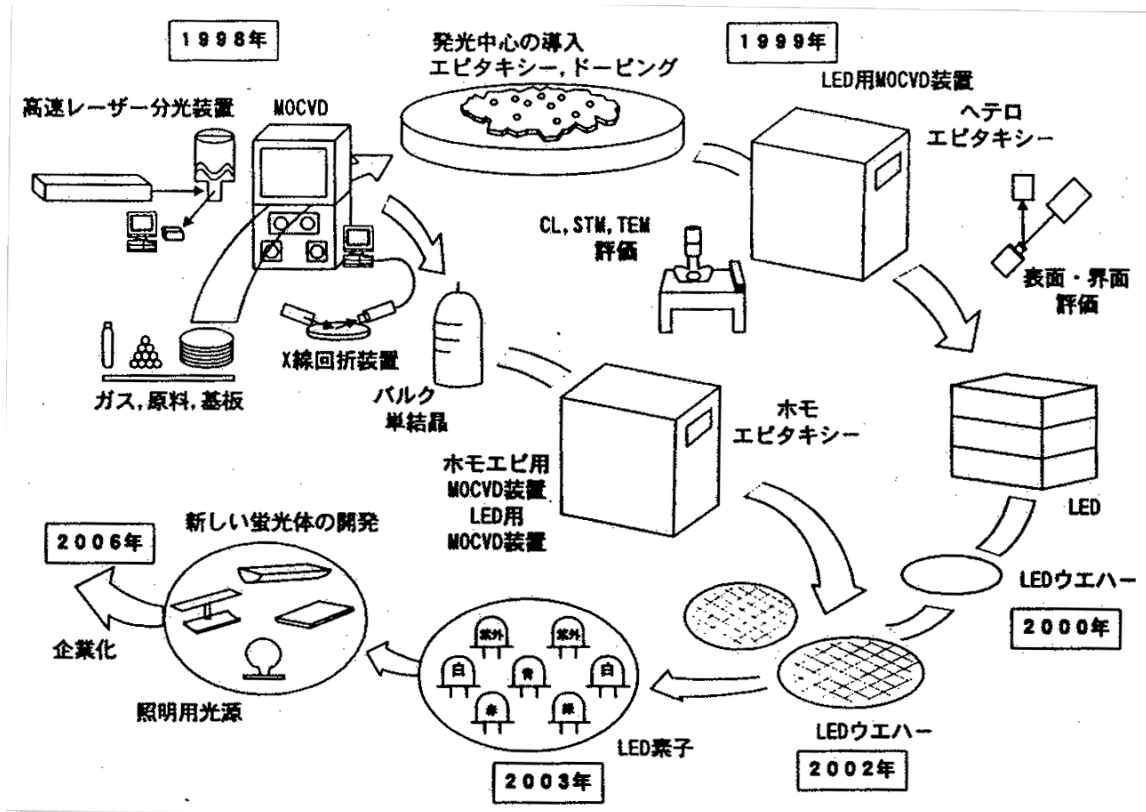


Figure 1.2.1-(1): Research on Semiconductor Lighting under the "Light for the 21<sup>st</sup> Century" Project.

1998: 1) high-speed laser spectrometer; 2) chemical agent (gas), raw materials, substrates; 3) X-ray analysis device; 4) bulk single crystals; 5) introduction of luminescence center - epitaxy, doping; 6) CL, STM, TEM evaluation

1999: 1) MOCVD for LEDs; 2) heteroepitaxy; 3) evaluation of surface and boundary face

2000: 1) LED wafers; 2) MOCVD for homoepitaxy, MOCVD for LEDs; 3) homoepitaxy

2002: 1) LED wafers

2003: (1) LED elements; (2) white, red, blue, green, white, UV, UV

2006: (1) development of new phosphors; (2) lighting sources for illumination; (3) industrialization

At present, semiconductor manufacturers and primary light fixture manufacturers in America and Germany are establishing joint ventures (GELcore, LumiLeds, Osram Opto, Cree Lighting) and aggressively pursuing research and development of white LED lighting technologies and applications. Japan's national project is influencing the overseas lighting industry, starting with the U.S. and its Solid State Lighting Initiative of 2001, followed by Taiwan which is likewise establishing projects to find practical uses for white LEDs.

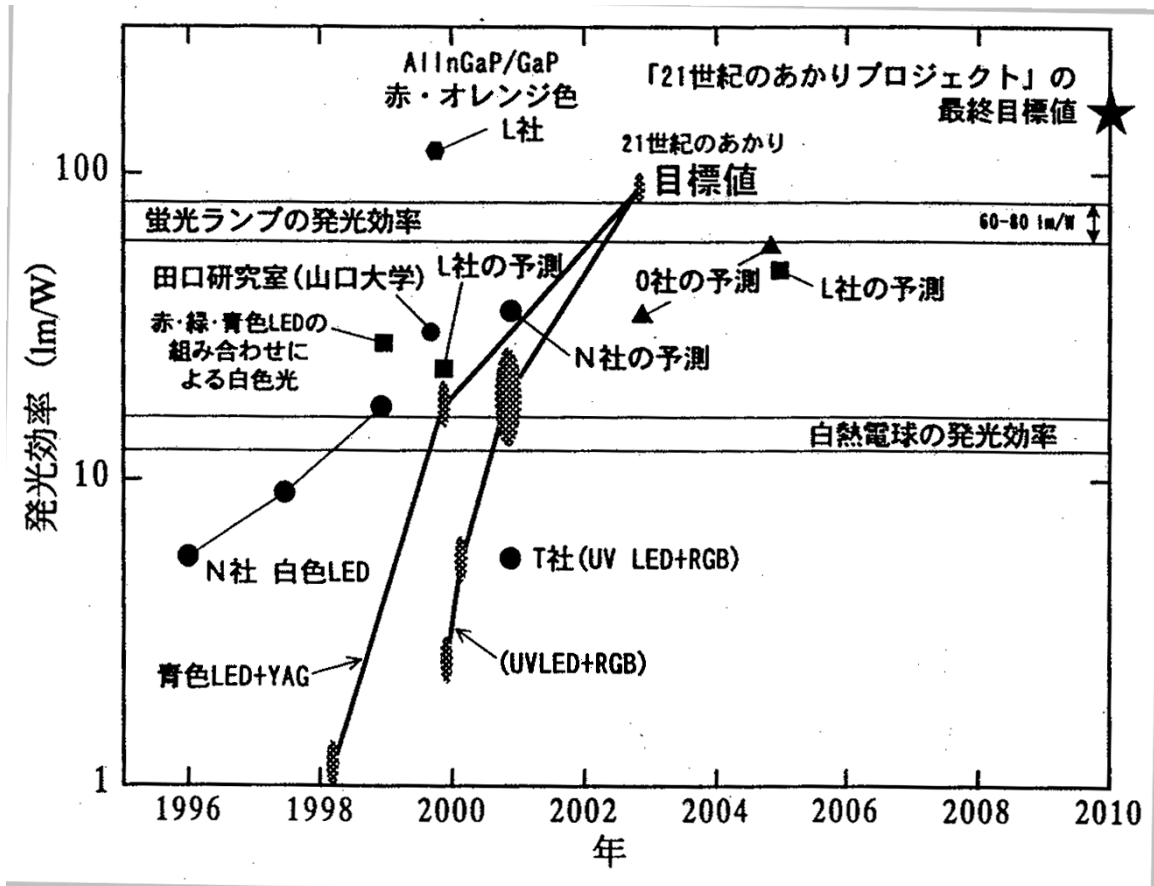


Figure 1.2.1-(2): Evolution by Year of White LED Luminous Efficiency and Future Predictions (bold line(s) represents this project).

Axes: Year; Luminous Efficiency (lm/W).

Labels: Blue LED + YAG; Company N - white LED; Company T (Toyoda Gosei)- UV LED + RGB; luminous efficiency of an incandescent lamp; white illumination by combining red, green, and blue LEDs; Taguchi research lab (Yamaguchi University); Company L (LumiLeds) estimate; Company N estimate; Company O (Osram Opto) estimate; Company L estimate; luminous efficiency of a fluorescent lamp; Goal of Light for 21<sup>st</sup> Century project; Company L - red, orange; \* Ultimate goal of Light for 21<sup>st</sup> Century project.

### 1.2.2 White Diodes and Luminescence Characteristics

A light emitting diode emits light when a current is applied in the forward direction to the p-n junction of a semiconductor, injecting a negative electron and a positive hole into the active layer and causing a radiation recombination process. Usually a double heterojunction or a quantum well structure is used for light and charge confinement.

In general, the luminous efficiency (wallplug efficiency) of an LED is found through the following equation and is based on three independent efficiency factors.

$$(1) \quad \eta_{wp} = \eta_v \cdot \eta_i \cdot \eta_{ext}$$

In this equation,  $\eta_{wp}$  is the input to output wallplug efficiency,  $\eta_v$  is the potential efficiency,  $\eta_i$  is the internal quantum efficiency, and  $\eta_{ext}$  is the light extraction efficiency.

As shown in Figure 1.2.2-(1), using a wavelength  $\lambda_0$  (UV) of a UV LED, the luminous efficiency that can be gained from a white LED by exciting the three primary color phosphors is given in the following equation [3].

$$\eta_{white} = \frac{\int [\lambda_0(UV) / \lambda] \cdot F_{ph}(\lambda) \cdot \kappa(\lambda) d\lambda}{I \cdot V \cdot \int F_{ph}(\lambda) d\lambda} \cdot P \cdot \eta_{uvph} \cdot \eta_{ph} \tag{2}$$

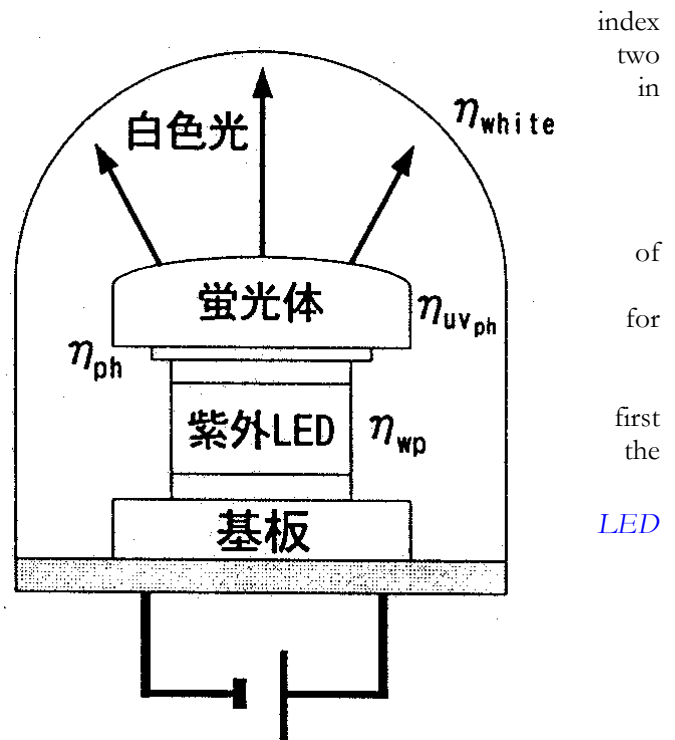
Here, P is the output from the UV LED,  $\eta_{ph}$  the efficiency of the phosphor,  $\eta_{uvph}$  the conversion efficiency,  $F_{ph}(\lambda)$  the phosphor's emission spectrum, and  $\kappa(\lambda)$  the visibility coefficient. Assuming  $\eta_{uvph}$  equals 95% and  $\eta_{ph}$  equals 90%, a 30 mW LED will achieve about 100 lm/W.

Within the Light for the 21<sup>st</sup> Century project, output light of 15.6 mW (at 20 mA) and 38 mW (at 50 mA) has been achieved at 382 nm with an external quantum efficiency of 24% (at 20 mA) [6].

To obtain a whiteness with high color rendering (Ra >= 85) using an LED, there are basically two methods (single chip and multi-chip), as shown in Table 1.2.2. The first (single-chip) method involves exciting phosphors using LEDs radiating blue or UV light as the excitation source. The second (multi-chip) method is to simultaneously use two or three different colors LEDs, such as red, green and blue, or blue and yellow. The second method presents challenges practical use, such as differences in drive voltage, luminous output, element life and thermal characteristics among LEDs. In contrast, the method employs only one type of element and drive circuit design is quite simple.

Figure 1.2.2-(1): Conceptual Diagram of White by Combining UV LED and Phosphors and the Relationship of Efficiency.

Labels: White light; Phosphor; UV LED; Substrate.



Within the first (single-chip) method, there are two approaches [8]. The first approach excites a yellow phosphor using a blue LED. The second approach uses a UV LED to excite RGB phosphors. The second approach was proposed for the first time under the Light for the 21<sup>st</sup> Century project and was developed as a new white LED light source for illumination.

Method	Excitation Source	Light Emitting Material and Fluorescent Characteristics	Principles of Light Emission
Single Chip	Blue LED	InGaN/YAG, ZnS-based	Blue light excites yellow phosphor
	UV LED	InGaN/RGB phosphors	RGB phosphors excited by UV light in same manner as in fluorescent lamps
Multi-Chip	Blue LED Yellow LED	InGaN, GaP, AlInGaP	Two complementary colors placed in a single package.
	Blue LED Green LED Red LED	InGaN, AlInGaP, AlGaAs	Three primary color LEDs placed in a single package.

Figure 1.2.2-2 shows the dependence of the injection current of

Table 1.2.2: Methods for producing white light with LEDs and phosphors.

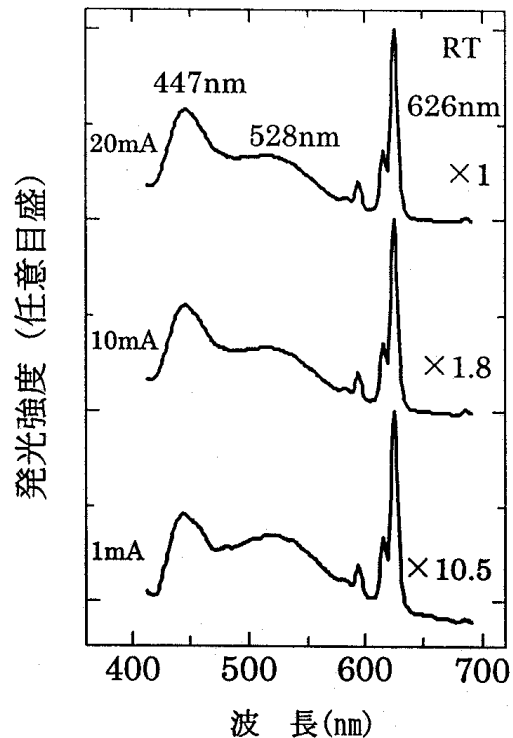
phosphor made by combining red ( $Y_2O_3S: Eu^{3+}$ ), green ( $ZnS: Cu, Al$ ), and blue ( $Sr, Ca, Ba, Mg_{10}(PO_4)_6Cl_2: Eu^{2+}$ ) phosphors using a UV LED (light wavelength of 371 nm, output of 5 mW (at 20 mA), and external quantum efficiency of 5%) as an excitation source.

The peaks are at 447, 528, and 626 nm respectively [9]. Even if the current is increased, no significant change is seen in the emission spectrum. The luminosity of each tends to increase linearly with an increase in current. The average color rendering index is  $R_a = 83$ .

The white LED light source used to excite the RGB phosphors can emit various colors of light according to the particular combination of phosphors, making their range of application for illumination purposes broad. Nonetheless, the luminous flux of each LED is weak (1 lm), making it necessary to arrange multiple LEDs to serve as a source of illumination.

Figure 1.2.2-2: Changes in the emission spectrum with a rise in injection current of RGB white phosphors.

Axes: Luminosity (free scale); Wavelength (nm)



To develop LED-based illumination, optimized design of a device system including light distribution from multiple LED integrated elements is necessary. As such, models to calculate the ideal luminous intensity and illumination distribution of multi-point LED light sources are being studied [10].

## 1.3 Cooperative Project

This project is promoted by a joint research body established by 13 companies and 4 universities (Yamaguchi University, Mie University, Tokyo University, and Chiba University) under the purview of the Japan Research Center for Metal-based Materials (JRCM). In 2001, prototype UV LEDs were developed whose characteristics surpass those exhibited by LEDs of leading manufacturers. In the coming year, it is expected that further research will yield additional improvements in lighting efficiencies.

## 1.4 Participation in “21<sup>st</sup> Century Dream Technology Exhibition”

Nihon Keizai Shimbun hosted “The Exhibition of Dream Technologies for the 21<sup>st</sup> Century” at the Tokyo International Exhibition Center for 17 days from July 21 through August 6, 2001. This project was introduced as part of the NEDO exhibit to show the promise of LED lighting. The exhibit showed the principles of LEDs, the potential of LEDs as illumination sources, and displayed prototype LEDs and LED-based lighting fixtures.



Figure 1.4: Exhibition Booth at the Exhibition of Dream Technologies for the 21<sup>st</sup> Century

## 1.5 Report on Technology Trends from MRS 2000 Fall Meeting

We attended the Material Research Society (MRS) 2000 Fall meeting held in Boston from November 25 through December 1, 2000 to research market trends, primarily from the GaN symposium.

The MRS is a non-profit organization established in 1973 among governmental, academic, and industry participants to share knowledge on new materials and to promote exchange of information through the publication of related books. The Fall meeting was the second major meeting for GaN materials.

### **1.5.1 Overview of 2000 Fall Meeting**

Forty-one symposia - some large, some small - were held at 3 sites: the Hynes Convention Center, the Sheraton Hotel, and the Marriott Hotel. Among these, the symposia on GaN-based and SiC-based materials were of primary interest while other symposiums were of tangential relevance. There were 2,703 talks, 1,556 poster exhibits, and 3,639 research announcements.

Other than a few symposia like that on GaN-based materials, most of the names of the symposia were different than the previous year, making it quite difficult to identify relevance. Based on the limited number of symposia viewed, it appeared that the number of attendees of each lecture was proportional to the number of research announcements. The great success of the symposium on organic optoelectronic materials was especially impressive.

#### **1.5.1.1 GaN-based Materials Symposium**

Similar to last year, the symposium on GaN-based materials was the largest, with a total of 271 announcements, including lectures and poster exhibits. Announcements on GaN-based materials could also be seen here and there at other symposiums.

Announcements involved research bodies from 25 countries comprised of 331 universities, 109 commercial firms, 45 governmental research labs and 10 military research labs, for a total of 495 organizations. The U.S., Japan, Germany, France, and South Korea were at the top.

Announcements on GaN-based materials worthy of attention are listed below.

#### **1.5.1.2 Nanomaterials**

Among the 7 symposiums obviously covering nanomaterials, there were 841 announcements. Still, there were a large number of announcements at other symposiums that could be categorized under nanomaterials. Among the numerous applications of nanomaterials expected to be in semiconductor devices and displays, 9 announcements on hydrogen occlusion via a nanotube gained much attention.

#### **1.5.1.3 Interesting Announcements from Symposium on GaN and Related Alloys**

Among the announcements made on GaN-based compounds and semiconductors, those relevant to this project are listed below, categorized as: substrates, UV light emission, elemental structures and processes, and LEDs.

##### **Substrates**

“Structure and Optical Properties of GaN Bulk Crystals Grown from the Liquid Phase”, M. Albrecht, Erlangen-Nuernberg University (with Ioffe Inst. and TDI)

- While melting GaN, LPE growth at 1000°C, less than 2 barometric pressure on a 50 mm GaN crystal substrate.
- At present, achieved oriented polycrystals. Maximum length 15 mm, diameter 20 mm, dimension of crystal grain  $\leq 3$  mm x 1.5 mm.

“Growth of Self-Seeded Aluminum Nitride by Sublimation-Recondensation and Substrate Preparation”, C. Rojo, Crystal IS (with Rensselaer Polytechnic Inst.)

- AlN single crystals a promising substrate for growth of GaN mixed crystals, especially Al-rich ones.
- Sublimation. Transport by a temperature gradient in Al + N<sub>2</sub> state. 2000°C Growth rate of 0.9 mm/h.

- Diameter of 15 mm, grain size of 10 mm x 6 mm, poly portion also present.
- Yellow or colorless. With CL, strong emission from a deep level which is about 0.8 times the band edge energy.
- AlN film formed on substrate. Various tests and HEMT prototype performed.

“Characteristics of FIELO-GaN Grown by Hydride Vapor Phase Epitaxy”, A. Usui, NEC

- FIELO-GaN grown film by HVPE exhibits a dislocation density of  $10^6 \text{ cm}^{-2}$ , PL decay time of 1.3 ns at its longest, which is significantly longer than that by conventional MOVPE.
- Achieved  $\phi 35 \text{ mm}$  GaN substrate by depositing 60 to 400  $\mu\text{m}$  GaN film on a  $\phi 2''$  sapphire substrate and then cooling it to allow thermal expansion to naturally cause separation between substrate and film.
- Created InGaN MQW blue LD on FIELO-GaN.

Several additional announcements (Air Force Research Lab. + University Massachusetts + Samsung + Wright State University + University of Dayton; Tech. University of Munich; and others.) covered formation of independent GaN film by HVPE, GaN film growth thereon and its characteristics.

### UV Light Emission

“UV Emitter Based on High-Efficiency GaN/Al<sub>x</sub>Ga<sub>1-x</sub>N Multi-Quantum Wells”, M. Iwaya, Meijo University (Meijodai)

- Luminosity distribution is observed at the light emission surface of an LED where the region of high luminosity is found to be at the region of low dislocation density.
- PL luminescence characteristics close to GaN obtained at room temperature via low dislocation density and Si doping.

“Current Injection UV-Emission from InAlGa<sub>N</sub> Multi-Quantum Well Light Emitting Diodes”, A. Kinoshita, Riken (with Waseda University)

- 230 nm PL observed on InAlGa<sub>N</sub> at room temperature.
- Substrate is CREE (0001) SiC.
- MQW, thick luminous layer, add SL layer on top (above and below) the active layer.
- Peak wavelength during current injection found to be 360 nm with MQW and 340 nm with thick light emitting layer.

“Improved Optical Quality of BAIGaN/AlN MQW Structure Grown on 6H-SiC Substrate by Controlling Residual Strain Using Multi-Buffer Layer”, Hideo Kawanishi, Kogakuin.

- B 5-13% possible with BAIGaN on 6H-SiC.
- Light emission wavelength of 248.1 nm with B<sub>0.07</sub>Al<sub>0.52</sub>Ga<sub>0.41</sub>N/AlN MQW
- Growth temperature of 1460 / 1200°C
- Conductivity still unobtainable

### Elemental Structures and Processes

“Transfer of Nitride Device Heterostructures from Sapphire Growth Substrates to Silicon by Metal Bonding and Laser Lift-Off”, T. Sands, UC Berkeley

- GaN element separated from sapphire substrate by irradiating with an excimer laser
- The substrate/nitride boundary area reaches 1000°C, but most of the nitride portion remains at 400°C.
- Grow In film on the electrodes to make a In/Pd/GaN/sapphire substrate, then attach it to a Pd/Si substrate by heating to 200°C, causing it to bond via a Pd-In reaction. Then separate the sapphire substrate via laser irradiation. This leaves a GaN/electrode/inner layer/Si structure.
- No changes in LED characteristics before and after separation (lift off).

“Integration of In<sub>x</sub>Ga<sub>1-x</sub>N Laser Diodes with Dissimilar Substrates by Laser Lift-Off”, W.S. Wong, Xerox

- Apply Si or Cu atop an LD structure (GaN/sapphire substrate), then separate the sapphire substrate using laser lift off. Heat dissipation when using Cu is good.
- Even if the Al<sub>2</sub>O<sub>3</sub>-GaN boundary area reaches 900°C, the GaN beyond 2μm from the boundary area reaches only 200°C.
- By removing the Si or Cu temporarily applied, it is possible to create an “LD film”. It is also good to attach this atop a diamond base.

“Group-III Nitride Quantum Heterostructures Emitting in the Whole Visible Range”, N. Grandjean, CNRS

- Creation of quantum dots by employing island structures produced naturally during MBE.
- Island height (3 nm to 5.5 nm) supported by PL light emission wavelength (2.6 eV to 1.9 eV).
- Unclear whether the wavelength change mechanism is due to quantum size or Stark effects.
- It is possible to achieve white LEDs.

“Drastic Reduction of Threading Dislocation Density of AlGaN on SiC by Using Highly-Si-Incorporated AlGaN Superlattice”, M. Aino, Riken (with Waseda University)

- AlGaN containing  $1.2 \times 10^{20}/\text{cm}^3$  Si
- The thermal dislocation density (TDD) changes from  $10^{10}/\text{cm}^2$  to  $10^8/\text{cm}^2$  with (AlGaN 80 nm + AlGaN:Si 20 nm) x 6.
- Dislocations bend within the Si doping layer.
- Same effects observed with both SiC substrates and sapphire substrates.

“Growth and Characterization of the GaN Underlying Layer Used in Blue-Violet GaN-Based Laser Diodes on Sapphire”, Kenji Funato, Sony

- Dislocation reduced by improving underlayer, life extended (1000 h or more).
- Relaxation of crystals increases dislocation and threshold current rises.
- Growth pressure was 0.9 to 1.6 atm. Raising the pressure tends to restrain relaxation.
- PL strength was reduced remarkably to better than EPD  $1.2 \times 10^7 \text{cm}^{-2}$ .

- With lines of 2  $\mu\text{m}$  and spaces of 10  $\mu\text{m}$ , the dislocation density of the wing equaled mix  $< 10^5\text{cm}^{-2}$  and edge  $< 10^6\text{cm}^{-2}$ .
- LD life: the life of ELO is twice that of sapphire at low output, but the difference grows smaller at higher output.
- The output with ELO is 1.21 W/mA (74mA). With sapphire it is 0.92 W/mA (90mA).
- The minimum dislocation density on sapphire is  $4 \times 10^8\text{cm}^{-2}$ . With ELO it is below  $1 \times 10^6\text{cm}^{-2}$ .

“Gallium Nitride Films on Liquid Precursors”, M. Puchinger, Max-Planck-Inst. (with UCSB)

- GaN crystals obtained by spin coating liquid precursors onto the substrate and then heating within  $\text{N}_2$ .
- At present, only multi crystals are obtained with thick film, but single crystals of GaN film ( $\leq 20$  nm) can be obtained on sapphire even if facet exists.

### LEDs

“Development of High Power Nitride LEDs for Semiconductor Lighting”, S. A. Stockman, Lumileds

- The present maximum levels are 100 lm/W (600 nm yellow) for AlInGaP and 80 lm/W (540 nm yellow green) for InGaN.
- Due to the heat resistance of epoxy resins, an artillery shell shape is thought to limit light output to  $\leq 0.1$  W. (currently 5 to 10 mW). On the other hand, 1 W per element is desired immediately.
- Direct bonding to a copper block holds promise. Concept of 18 LEDs mounted to a square substrate that is 2 to 2.5". Some thinking of enlarging the chip size and then forming into a flipchip or multi-chip module.
- With an increase in chip size, comb-shaped electrodes will be needed. A prototype is being worked on.
- However, there is data suggesting that the efficiency quickly degrades as the chip size grows larger. Therefore, LumiLeds is aiming for a segregated chip plus a multi-chip approach.
- <While demonstrating a blue LED> Compared to a conventional LED, it outputs 20 times the light at 15 times the current. There are also white LEDs. These use red and green phosphors but the efficiency is still low.
- <Application> LCD backlight, indoor lighting, road and tunnel lighting, etc. 10W device is hoped for.
- The most important problem to solve is that of heat.

## 1.6 Patent Search

Registrations and open applications for patents and new uses dealing with GaN-based LEDs from the years 1998 and 1999 have been entered into a database, categorized according to their importance, and then studied. New applications for the year 2000 will be entered into the database. The content of those in dispute has been researched.

## 1.6.1 New Open Applications and Registrations

### 1.6.1.1 New Data Supplement

A patent search was performed to locate patents covering important technological problems pertinent to this project. The contents of these patents have been read from a CD-ROM published by the patent office and added to a database. During the period spanning from December 5, 1999 to November 13, 2000, there were 477 new filings and patent awards relating to this project. This is broken down further as follows:

New patent filings: 402

New patent awards: 79

Among these, as shown in Table 1.6.1-(1), four had already been awarded when filed. While these were new filings, they also constituted new patent awards. Care must be taken because it cannot be determined by checking public disclosure (patent filings) only that they were already awarded.

Public Disclosure Number	Date of Disclosure	Award Number	Date of Award
2000-105321	April 11, 2000	2954203	July 16, 1999
2000-114597	April 21, 2000	3019085	January 7, 2000
2000-114664	April 21, 2000	3031415	February 10, 2000
2000-196196	July 14, 2000	2995187	October 22, 1999

*Table 1.6.1-(1): Patents Already Awarded upon Public Disclosure*

### 1.6.1.2 Grant Classifications

Table 1.6.1-(2) shows the number of registered patents and open filings according to grant classification of the 477 registered patents and open applications.

The number of patents relating to MOCVD-based crystal growth and buffer layers exceeded all others, followed by element isolation and cleavage, substrate materials, active layers, current constriction layers to create lasers and stripes, etching, and dopant-related patents. This study found patents relating to phosphors and combined white light emission, but none had reached the award stage.

Classification Number	Classification Description	New Applications	New Registrations
A01	Substrate Material: Sapphire	11	1
A02	Substrate Material: GaN	8	
A03	Substrate Material: Other	16	4
B01	Layer Structure: Dopant	10	1
B02	Layer Structure: Buffer layer	51	7
B03	Layer Structure: Contact layer	11	
B04	Layer Structure: Clad layer	7	

B05	Layer Structure: Active layer	12	5
B06	Layer Structure: Current constriction layer	10	6
B07	Layer Structure: Barrier layer	3	
B08	Layer Structure: Heterostructure	2	1
B09	Layer Structure: Quantum well structure	9	2
B10	Layer Structure: MIS structure	2	
B11	Layer Structure: Ridge structure	6	
B12	Layer Structure: Carrier concentration	7	1
B13	Layer Structure: Stripe	10	
B14	Layer Structure: Other		
C01	Electrode: Ohmic	9	2
C02	Electrode: P-structure	4	1
C03	Electrode: N-structure	1	2
C04	Electrode: Shape	3	4
C05	Electrode: Material		2
C06	Electrode: Wire bonding		
C07	Electrode: Other	1	
D01	Manufacturing Technology: MOCVD, MOVPE	45	15
D02	Manufacturing Technology: MBE, PVD	4	4
D03	Manufacturing Technology: Heat processing	7	1
D04	Manufacturing Technology: Etching	12	2
D05	Manufacturing Technology: Isolation, Cleavage	25	1
D06	Manufacturing Technology: Sealant	2	
D07	Manufacturing Technology: Bonding	3	2
D08	Manufacturing Technology: Other	4	1
E01	Element Structure: Single		
E02	Element Structure: Multiple	4	1
E03	Element Structure: Direction of light extraction	7	1
E04	Element Structure: Combination with phosphors	12	1
E05	Element Structure: Phosphor material		
E06	Element Structure: Other	1	
F01	Element Morphology: LED	6	
F02	Element Morphology: LD	5	
F03	Element Morphology: Other	6	3
G01	Mount Structure: Package	9	1

G02	Mount Structure: Lead frame	1	
G03	Mount Structure: Flipchip	3	
G04	Mount Structure: Face down	3	
G05	Mount Structure: Other	4	
H01	Characteristics: High		
H02	Characteristics: Blue light, UV light		
H03	Characteristics: White light, multi-colored light	10	
H04	Characteristics: Surface luminescence	2	
H05	Characteristics: Crystallization		
H06	Characteristics: Other (heat resistance, etc.)	6	

*Table 1.6.1-(2) Number of Patents based on Grant Classification.*

### 1.6.1.3 Examples of Important New Patent Registrations and Applications

Tables 1.6.1-(3) through 1.6.1-(6) below show examples of patent registrations and applications pertaining to buffer layer structures.

Number	Claimant	Description
302687	Toyoda Gosei	Low temperature growth (400 – 900 degrees) AlN Wursted-structure buffer layer (film thickness of 10 – 15 nm).
3091593	Nichia Chemical	MOCVD using a GaAlN buffer layer on sapphire + GaN formed substrate.
3036495	Toyoda Gosei	Stripe or lattice AlGaIn buffer layer (on Si substrate).
3028809	Sanken Electric	TiN buffer layer.

*Table 1.6.1-(3): New Patent Registrations on Buffer Layer Structure*

Number	Claimant	Description
2000-261037	Sharp	Super lattice formation on n-type clad layer.
2000-068594	Nichia Chemical	Super lattice buffer layer.
2000-040842	Toyoda Gosei	Multi-crystal buffer layer.
2000-040843	Toyoda Gosei	Two GaN buffer layers on sapphire substrate.

*Table 1.6.1-(4): Open Applications (those relating to growth methods for layer structures).*

Number	Claimant	Description
--------	----------	-------------

2000-077336	Sony	Ion implantation stripe mask usage
2000-164929	Sony	Specific crystal facet growth
2000-021789	Toshiba	SiO <sub>2</sub> stripe mask usage
2000-101194	Sanyo	SiO <sub>2</sub> stripe mask + surface polishing
2000-124500	Toshiba	Growth of crystals on a cyclically irregular surface
2000-058918	Murata Manufacturing	Striping of an N-type electrode
2000-068609	Ricoh	Two stage stripe masking
2000-156348	Nichia Chemical	Growth on substrates with height differences
2000-106348	Matsushita Electric	Growth on porous substrates
2000-174343	Sharp	Cross layer stripe mask usage

*Table 1.6.1-(5): Open Applications Founded on Same Concept as Patent 3036495 (lateral growth by stripe and substrate surface irregularities).*

Number	Claimant	Description
2000-036617	Murata Manufacturing	ZnO buffer layer (on Si substrate)
2000-058451	Showa Denko	Phosphorus boron (BP) buffer layer
2000-133843	Fuji Electric	Fluoride thin film buffer layer
2000-188260	Samsung Electric	Boron nitride (BN) buffer layer
2000-031537	Matsushita Electric	GaN buffer layer containing arsenic
2000-031539	Hewlett-Packard	MgZnCd-doped boundary layer

*Table 1.6.1-(6): Buffer Layers Based on Non-Conventional Materials.*

#### 1.6.1.4 Distribution of Applicants by Technology Classification

Table 1.6.1-(7) shows the distribution of patent applicants and assignees of new published unexamined patent applications (Kokai) and registered patents by technical field.

Classification Number	Classification Description	Number of Applicants	Number of Assignees
A01	Substrate Material: Sapphire	10	1
A02	Substrate Material: GaN	5	
A03	Substrate Material: Other	10	4
B01	Layer Structure: Dopant	6	1
B02	Layer Structure: Buffer layer	25	10

B03	Layer Structure: Contact layer	8	
B04	Layer Structure: Clad layer	4	
B05	Layer Structure: Active layer	11	5
B06	Layer Structure: Current constriction layer	8	5
B07	Layer Structure: Barrier layer	3	
B08	Layer Structure: Heterostructure	2	1
B09	Layer Structure: Quantum well structure	8	2
B10	Layer Structure: MIS structure	4	
B11	Layer Structure: Ridge structure	5	
B12	Layer Structure: Carrier concentration	11	1
B13	Layer Structure: Stripe	8	
B14	Layer Structure: Other		
C01	Electrode: Ohmic	10	2
C02	Electrode: P-structure	4	1
C03	Electrode: N-structure	1	1
C04	Electrode: Shape	3	4
C05	Electrode: Material		2
C06	Electrode: Wire bonding		
C07	Electrode: Other	1	
D01	Manufacturing Technology: MOCVD, MOVPE	20	14
D02	Manufacturing Technology: MBE, PVD	4	4
D03	Manufacturing Technology: Heat processing	5	1
D04	Manufacturing Technology: Etching	13	2
D05	Manufacturing Technology: Isolation, Cleavage	12	1
D06	Manufacturing Technology: Sealant	2	
D07	Manufacturing Technology: Bonding	3	2

D08	Manufacturing Technology: Other		
E01	Element Structure: Single		
E02	Element Structure: Multiple		
E03	Element Structure: Direction of light extraction		
E04	Element Structure: Combination with phosphors		
E05	Element Structure: Phosphor material		
E06	Element Structure: Other		

F01	Element Morphology: LED		
F02	Element Morphology: LD		
F03	Element Morphology: Other		
G01	Mount Structure: Package		
G02	Mount Structure: Lead frame		
G03	Mount Structure: Flipchip		
G04	Mount Structure: Face down		
G05	Mount Structure: Other		
H01	Characteristics: High		
H02	Characteristics: Blue light, UV light		
H03	Characteristics: White light, multi-colored light		
H04	Characteristics: Surface luminescence		
H05	Characteristics: Crystallization		
H06	Characteristics: Other (heat resistance, etc.)		

### Patent Disputes

Blue highlighting indicates missing pages.

*Table 1.6.1-(7): Number of Participants by Technology Classification.*

## 1.7 Conclusions

The 21st Century is certainly the era of technology innovation with semiconductor lighting and this project is playing a leadership role. Differing from conventional visible light LEDs, white LEDs have strong needs as a general lighting source. Nonetheless, since such applications need a high volume of light (several tens to several thousands lm) in future new and innovative technologies by researchers and engineers of semiconductor technology, light emission element technology, and illumination engineering in collaboration with lighting and interior designers is critical to the realization of white LED lighting systems. It is hoped that further technology innovation in white LEDs for illumination will not only create a new lighting culture through LED applications, but will also build a safe societal foundation which produces less environmental waste.

## 1.8 Future Course

Research is progressing as planned according to the flow shown in Figure 1.2.1-(1). The light emission mechanism of the UV LED developed this year has been uncovered and defect densities have been reduced, contributing to improvements in external quantum efficiency. From here, we plan to pursue improvements in the precision of the epitaxial growth process and to strengthen the cooperation among project participants so that the evaluation of film quality in growth layers and end characteristics can lead to improvements in LED structures. Additionally, with regard to white LED lighting, we plan to lead the world in proposing concrete applications and standardization of LED lighting fixtures through lighting system section meetings.

## 1.9 References

- [1] Public Notice by Ministry of International Trade and Industry “Basic Plan for Development of Compound Semiconductors for High-Efficiency Optoelectronic Conversion (Light for the 21<sup>st</sup> Century)”, April 1, 1998 34
- [2] “Development of Compound Semiconductors for High-Efficiency Optoelectronic Conversion, ‘Light for the 21<sup>st</sup> Century’ Project Pamphlet”, New Energy and Industrial Technology Development Organization (NEDO), Published March 1999.
- [3] Proposal “Development of Compound Semiconductors for High-Efficiency Optoelectronic Conversion”, Japan Research and Development Center for Metals (JRCM) [Light for 21<sup>st</sup> Century research book], “Development of Compound Semiconductors for High-Efficiency Optoelectronic Conversion (Light for the 21<sup>st</sup> Century)” 1998 Report of Results and 1999 Report of Results, Japan Research and Development Center for Metals, March 1999 and March 2000.
- [4] T. Taguchi, “White LED and Lighting Systems”, O plus E, No. 8 (2000) 1028.
- [5] T. Taguchi, “Lighting in the 21<sup>st</sup> Century with LEDs”, Nikkan Display March Issue (2000) 1.
- [6] Nikkan Kogyo Newspaper, April 6, 2001.
- [7] T. Whitaker, “Compound Semiconductor”, 4 (2000) 34.
- [8] T. Taguchi, “The 21<sup>st</sup> Century Lighting Project Based on LED”, Proc. of Int. Display Workshop, (2000) 817.
- [9] K. Murakami, T. Taguchi and M. Yoshino, “White Illumination Characteristics of ZnS-based Phosphor Materials Excited by InGaN-based Ultraviolet Light-Emitting Diode”, Proc. of SPIE, Display Tech. III 4079 (2000) 112.
- [10] Uchida, Taguchi, “Evaluating Characteristics of White LED Light Sources with Multipoint Light Source Illumination Calculation Method”, Collection of Papers from 2000 Electric Society Basic Materials Common Department Lecture (2000) 188.

# 2 Basic Research Related to Light Emission Mechanisms

## 2.1 Achievements in 1998~1999

In order to find out more about the peculiar physical properties of GaN-based materials and to obtain knowledge helpful in improving the luminous efficiency of white LEDs, our research in 1998-1999 was done in close cooperation with other Joint Research Groups. Specifically, using high-quality GaN and  $\text{In}_x\text{Ga}_{1-x}\text{N}$  epitaxial films, we conducted basic research related to the elucidation of light emission mechanisms and to hetero/homoepitaxial interface control technology.

As a result, we discovered that InGaN luminescence spectra were made up of two components. Judging by the results of detailed emission spectroscopy measurements, the light emission mechanism of InGaN could not be explained by previously discussed localized excitons and quantum-dot-bound excitons, which was indicative of contribution by free electrons. Time-resolved spectroscopy results confirmed the presence of localized carriers in mixed InGaN crystals, which spurred us to conduct investigations into mechanisms capable of satisfying both results. Based on considerations related to the temperature dependence of the decay time constant of the two components measured by time-resolved spectroscopy, a model involving polarons was introduced and shown to explain the light emission measured from InGaN mixed crystal thin films. It was found that the model, which took into consideration the fact that nitride semiconductors exhibit an extremely strong electron-lattice interaction, could also provide a non-contradictory explanation for previously obtained measurements showing peculiar temperature- and magnetic-field-dependences of the luminescence spectra.

Furthermore, based on the reverse bias dependence of the decay time constant of the two emission components, we discovered that the shielding effect of the piezoelectric field did not contribute to the light emission mechanism of InGaN mixed crystal thin films.

Using homoepitaxially grown high-quality GaN thin films, we carried out time-resolved spectroscopy of light emission due to exciton recombination. By measuring the excitation energy density dependence of time-decay characteristics, we observed that the dominant emission line of the exciton system, which manifests itself at 3.471 eV, undergoes a transition from neutral-donor-bound-exciton emission to exciton molecule emission. The radiative recombination lifetime of the exciton molecules was estimated to be approximately 45 ps, and the radiative recombination lifetime of exciton molecules was estimated to be approximately 940 ps. In addition, based on the spectrum of the exciton molecule emission, the exciton molecule binding energy was estimated to be 6.8 meV.

Growth of GaN crystals was carried out using the RF-MBE method and the  $\text{NH}_3$  gas source MBE method.

In the RF-MBE method, the pre-growth treatment conditions for both sapphire substrates and MOCVD-grown GaN substrates were optimized, and the treatment conditions necessary for obtaining high-quality GaN epitaxial thin films were clarified. Using a sulfuric/phosphoric etchant, we observed atomic steps on the surface of the sapphire substrate at an etchant temperature of 110°C. In addition, it was shown that etching with buffered hydrofluoric acid was an efficient way of cleaning the GaN substrate surface. Optimum treatment conditions and the importance of factors such as substrate selection and substrate surface treatment for obtaining higher quality were demonstrated. In addition, InGaN was grown and, based on the results of X-ray diffraction measurements and Auger electron spectroscopy measurements, it was confirmed that In had been incorporated into the crystal.

In the NH<sub>3</sub> gas source MBE growth method, we obtained a GaN thin film that had a Ga polar face, was flat at the atomic layer level (RMS = 5 Å), and exhibited outstandingly excellent emission characteristics.

## 2.2 Summary of Research and Development in 2000

Various experiments were carried out within the framework of this study for the explanation of the physico-optical properties of GaN compound semiconductors and high-quality GaN compound semiconductor thin film growth.

In order to clarify the light emission mechanism, we investigated the correlation between the excitation spectrum and the two emission components observed in the luminescence spectra of In<sub>x</sub>Ga<sub>1-x</sub>N. Our results were: we observed a distinct absorption peak between low and room temperature in the excitation spectrum of In<sub>x</sub>Ga<sub>1-x</sub>N; and at the same time, the Stokes shift value was practically constant with respect to temperature for the high-energy emission component. Such results could not be explained by an emission model based on excitons localized at the minima of the potential fluctuations in quantum dots caused by In composition inhomogeneity, which had been reported previously. However, they could be accounted for in a non-contradictory manner by a light emission mechanism model including the polaron concept, which we had proposed in our previous research work.

We received substrates from the Bulk Growth Group and conducted basic research concerned with homoepitaxial growth to clarify the correlation between the crystal polarity of GaN bulk single crystals used for the substrates and the crystal polarity of the epitaxial thin films. In addition, it should be noted that emission characteristics were greatly improved by homoepitaxial growth.

Single polarity control of GaN thin films was implemented using the NH<sub>3</sub> GS-MBE method, and the crystalline properties of the resultant GaN epitaxial thin films were evaluated using RBS analysis, which confirmed their extremely high crystalline properties.

## 2.3 Excitation Spectroscopy Measurements of Temperature Dependence of Absorption and Emission

### 2.3.1 Methods and means

In the course of this study, emission mechanism models proposed prior to last year were investigated by carrying out measurements of the physico-optical properties of InGaN thin films using selective excitation spectroscopy.

Excitation spectroscopy is a method in which wavelength-variable lasers, such as dye lasers, are used as light sources to selectively excite carriers having a resonance level at a specific wavelength, and the emission caused by the carriers is observed. By using this method of measurement, it is possible to investigate dependence on various excitation energies of a particular emission.

In general, the method for measuring excitation spectra is called photoluminescence excitation spectroscopy (Photoluminescence Excitation: PLE) and is used to vary the wavelengths of the exciting light. Sources of white light, such as Xe lamps etc., are typically used as excitation light sources for such measurements, during which, after rendering the light monochromatic, specimens are irradiated with the light and the PL spectra of the specimens are observed. However, the intensity of the excited light in this method is extremely low, and, as a result, the emission intensity becomes extremely low, too. This is why in the present study we used a powerful dye laser. The PLE method is characterized by a dramatic increase in the amount of generated information because PL spectra are obtained as two functions of excitation wavelength and emission

wavelength. The use of a high-power dye laser permits measurement of excitation light intensity and temperature dependences as well, which makes the method a powerful means for optical evaluation.

Figure 2.3.1-(1) Excitation Spectroscopy Measurement System.

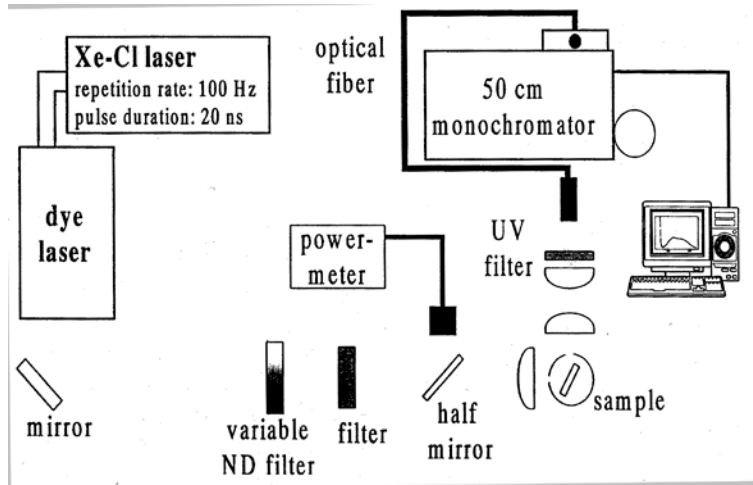


FIG. 2.3.1-(1) shows the excitation spectroscopy measurement system used in the present study. The system is basically the same as a PL measurement system. A dye laser pumped by a Xe-Cl excimer laser (wavelength: 308 nm, pulse 20 ns, repetition rate: 100 Hz) used as an excitation light source. Because the power of the dye laser varied depending on the wavelength, adjustments were carried out using a power meter and a variable ND filter to maintain the excitation power density constant during measurement.

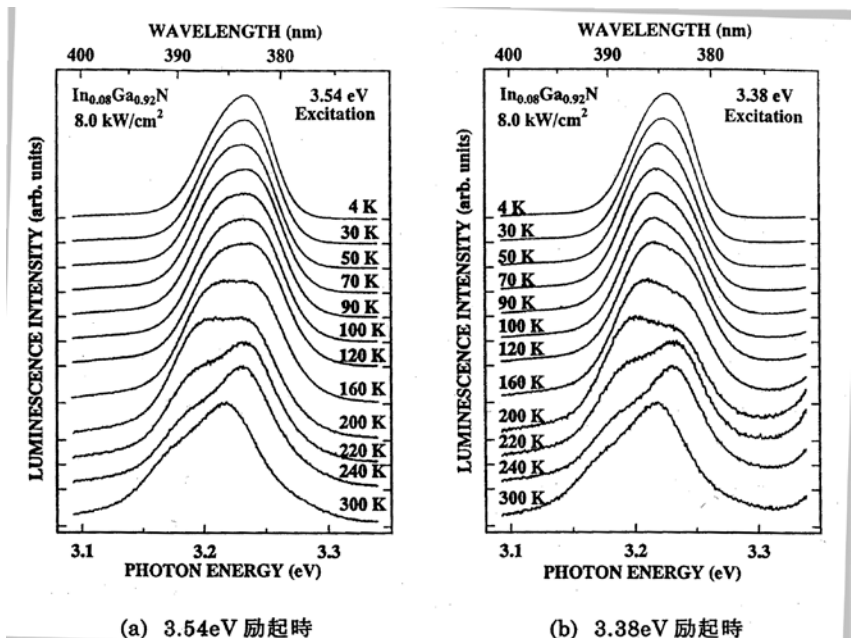
The specimens used for the measurements were undoped InGaN mixed crystal thin films with a thickness of 0.1  $\mu\text{m}$  grown by metal-organic chemical vapor deposition (Metalorganic Chemical Vapor Deposition: MOCVD) on a sapphire (0001) substrate with a 3- $\mu\text{m}$  GaN buffer layer in between, where the In composition ranged from 4 and 14%.

### 2.3.2 Results and Discussion

#### 2.3.2.1 Excitation energy dependence of PL spectra

This section addresses the temperature dependence obtained when varying the excitation energy of a single In<sub>0.08</sub>Ga<sub>0.92</sub>N thin film. These measurements differ from previous measurements in which a He-Cd laser (325 nm) and an Ar laser (257 nm) were used as excitation light sources, and for which the GaN which was used as a buffer layer was excited simultaneously.

Figure 2.3.2-(1) Temperature dependence of PL spectra. (a) Excitation at 3.54 eV. (b) Excitation at 3.38 eV.



(a) 3.54eV 励起時

(b) 3.38eV 励起時

Here, we would like to discuss the difference between the emission for excitation using light of an energy higher than that of the GaN bandgap, and for excitation using light of an energy lower than that of the GaN bandgap.

FIG. 2.3.2-(1) shows the temperature dependence of PL spectra obtained by excitation at an energy of 3.54 eV (above the  $E_g$  of GaN) using a dye laser as the excitation light source. Although using higher power for excitation made it more difficult to detect, we were able to confirm the presence of two components to the emission in all of the spectra. In the same manner as before, we used Gaussian fitting for the two components and plot the temperature dependence of their peak positions in FIG. 2.3.2-(2), together with the overall PL peak position.

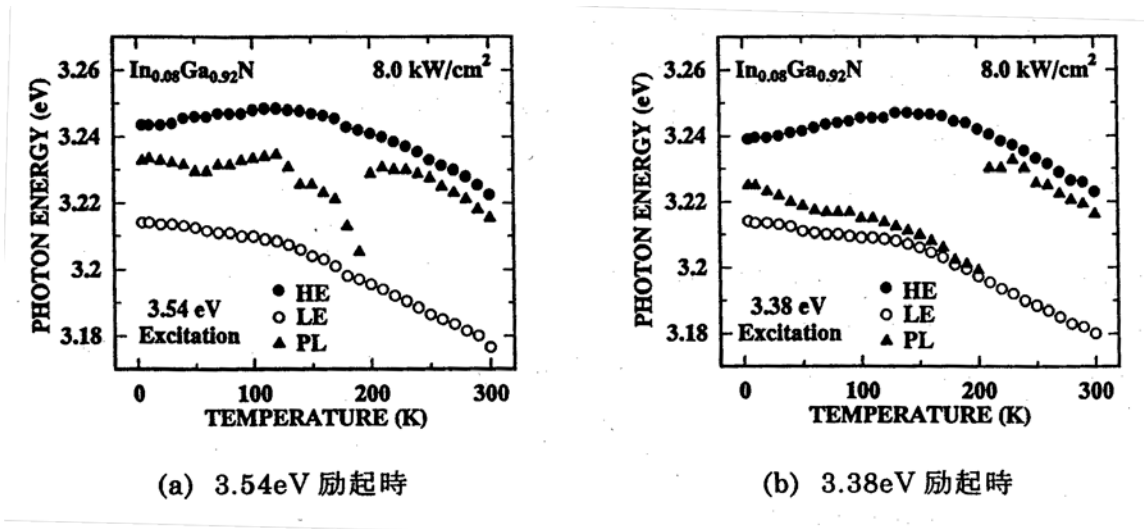


Figure 2.3.2-(2) Temperature dependence of emission peak positions. (a) Excitation at 3.54 eV. (b) Excitation at 3.38 eV.

The principal characteristics apparent from the figures are:

- (1) At temperatures below 200K, the temperature dependence of the PL peak position is different for the two emission components.
- (2) For the two different excitation energies, the peak positions of the two emission components exhibit practically the same temperature dependences, as in the case of measurements conducted previously using a He-Cd laser (325 nm) and an Ar<sup>+</sup> laser (257 nm).

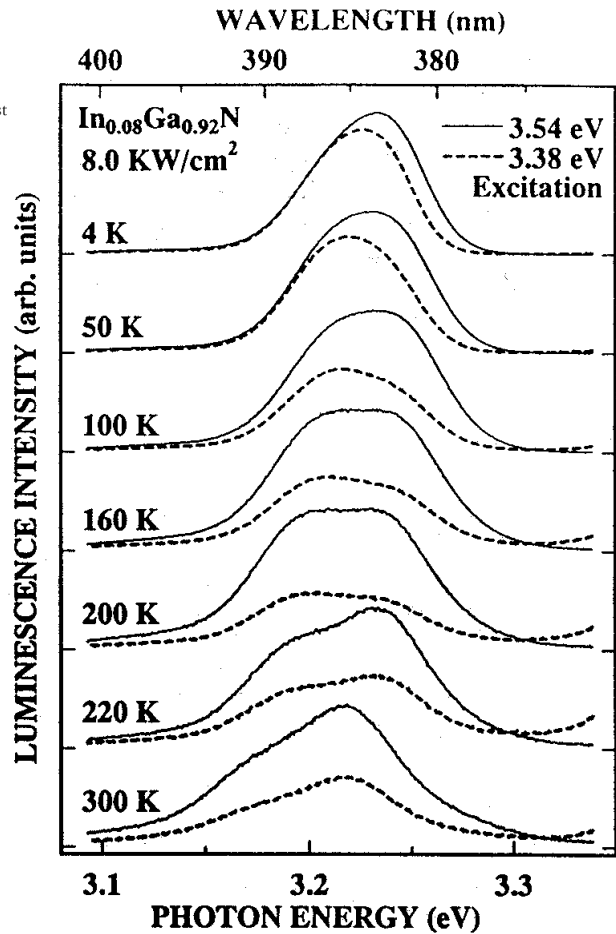


Figure 2.3.2-(3) Comparison of PL spectra.

Next, we would like to examine the difference in emission intensity in the case of varying excitation energy. As far as luminous efficiency is concerned, considerable differences are observed, which is why we plotted PL spectra for the two cases together in FIG. 2.3.2-(3). At each temperature, normalization was carried out at maximum emission intensity during 3.54 eV excitation. Characteristics apparent from the figure are:

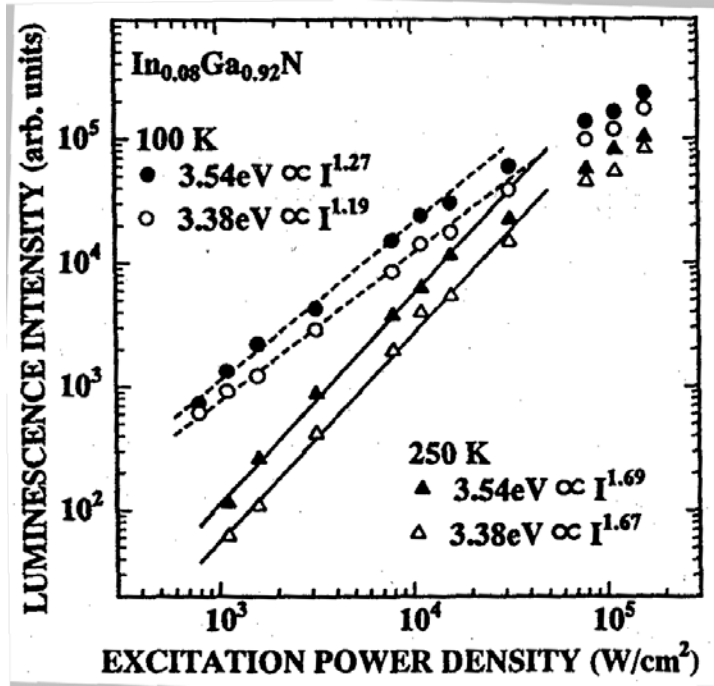
- (3) At low temperatures, varying the excitation energy from 3.54 eV to 3.38 eV resulted in a decrease in the emission intensity of the higher-energy component.
- (4) When the temperature is raised, the emission intensity of both components decreases during 3.38 eV excitation in comparison with 3.54 eV excitation.

(1) and (2) result from the contribution of the two components to emission from  $\text{In}_{0.08}\text{Ga}_{0.92}\text{N}$ . The difference between the intensities of the higher-energy and lower-energy components influences the peak positions of the PL spectra in  $\text{In}_{0.08}\text{Ga}_{0.92}\text{N}$ . These results can also serve as a confirmation of the existence of the two components. In addition, under the conditions used, the difference between the two spectra was the difference between the excitation energy being above the GaN bandgap and below it, and results (3) and (4) show that carriers excited in the vicinity of the GaN band edge contributed to the luminescence of  $\text{In}_{0.08}\text{Ga}_{0.92}\text{N}$ . In addition, it is evident from (4) that the higher the temperature, the higher the amount of contribution of the carriers excited at the GaN band edge to the luminescence of  $\text{In}_{0.08}\text{Ga}_{0.92}\text{N}$ . This is believed to be due to the fact that carriers become prone to diffusion at high temperatures.

In this manner, the contribution of the GaN-excited carriers to the luminescence of  $\text{In}_{0.08}\text{Ga}_{0.92}\text{N}$  is evident from the temperature dependence results. Therefore, next, we will examine the dependence of the luminescence on excitation light intensity. FIG. 2.3.2-(4) shows the excitation power density dependence of the emission intensity at 100K and 250K. First of all, it should be noted that when comparison by excitation energy was carried out at each temperature, with varying excitation energy at both 100K and 250K, there were differences in terms of absolute emission intensity, but the amount of increase in the emission intensity versus the excitation power density was practically the same. Furthermore, when comparison by temperature was carried out, the amount of increase in the emission intensity versus the excitation power density was larger at 250K than at 100K. This result was identical to the temperature variation of the excitation power density dependence of the integrated emission intensity observed in the previous section.

Figure 2.3.2-(4) Excitation power dependence in case of 3.54 eV excitation and 3.38 eV excitation.

From the above results, it is evident that although there were no significant changes in the temperature characteristics of the emission components in  $\text{In}_{0.08}\text{Ga}_{0.92}\text{N}$  no matter whether the of the buffer layer was simultaneously excited during the excitation of  $\text{In}_{0.08}\text{Ga}_{0.92}\text{N}$  or not, considerable changes in emission intensity did occur. In particular, it evident that when the temperature reached approximately room temperature, transition of carriers GaN greatly increased the emission intensity of  $\text{In}_{0.08}\text{Ga}_{0.92}\text{N}$ , with the layer playing an important role as a carrier-supplying source.



density

two

GaN

is

from

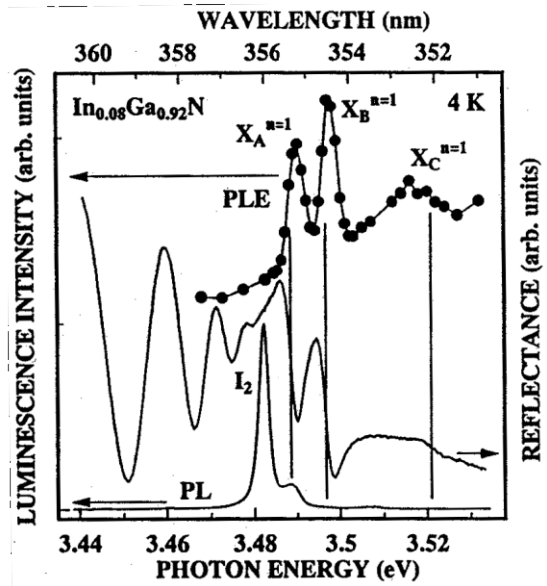
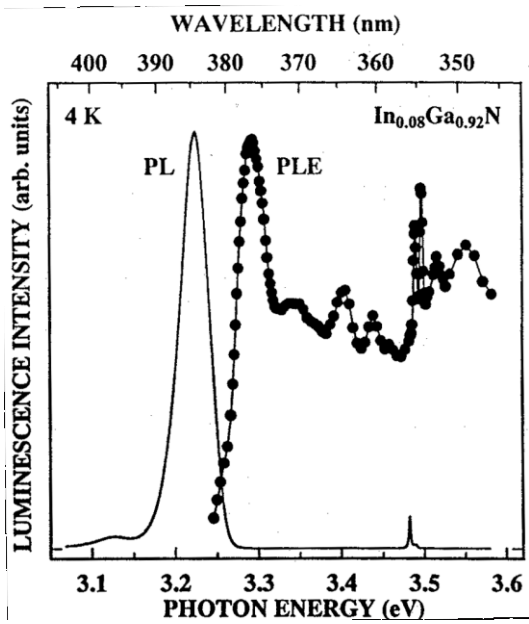
GaN

This fact means that when quantum well structures etc. are actually used as devices, the contribution of carriers from GaN used as a barrier layer can be a means for increasing the emission intensity of  $\text{In}_x\text{Ga}_{1-x}\text{N}$ , which is regarded as an important issue in device fabrication.

**2.3.2.2 Excitation spectra of  $\text{In}_x\text{Ga}_{1-x}\text{N}$  mixed semiconductors**

There is a considerable energy difference (Stokes shift) between absorption and emission in  $\text{In}_x\text{Ga}_{1-x}\text{N}$ . In other words, carriers excited at the absorption edge contribute to radiative recombination after undergoing a considerable energy relaxation from their energy position. The gigantic Stokes shift observed in  $\text{In}_x\text{Ga}_{1-x}\text{N}$  has long been a huge mystery. This is also another reason for the general acceptance of the theory that claims that the origin of  $\text{In}_x\text{Ga}_{1-x}\text{N}$  emission is attributable to localized excitons [1].

Thus, for a more detailed discussion of the characteristic emission of  $\text{In}_x\text{Ga}_{1-x}\text{N}$  [2], which had been discovered prior to last year, we investigated the Stokes shift of  $\text{In}_x\text{Ga}_{1-x}\text{N}$  using selective excitation spectroscopy.

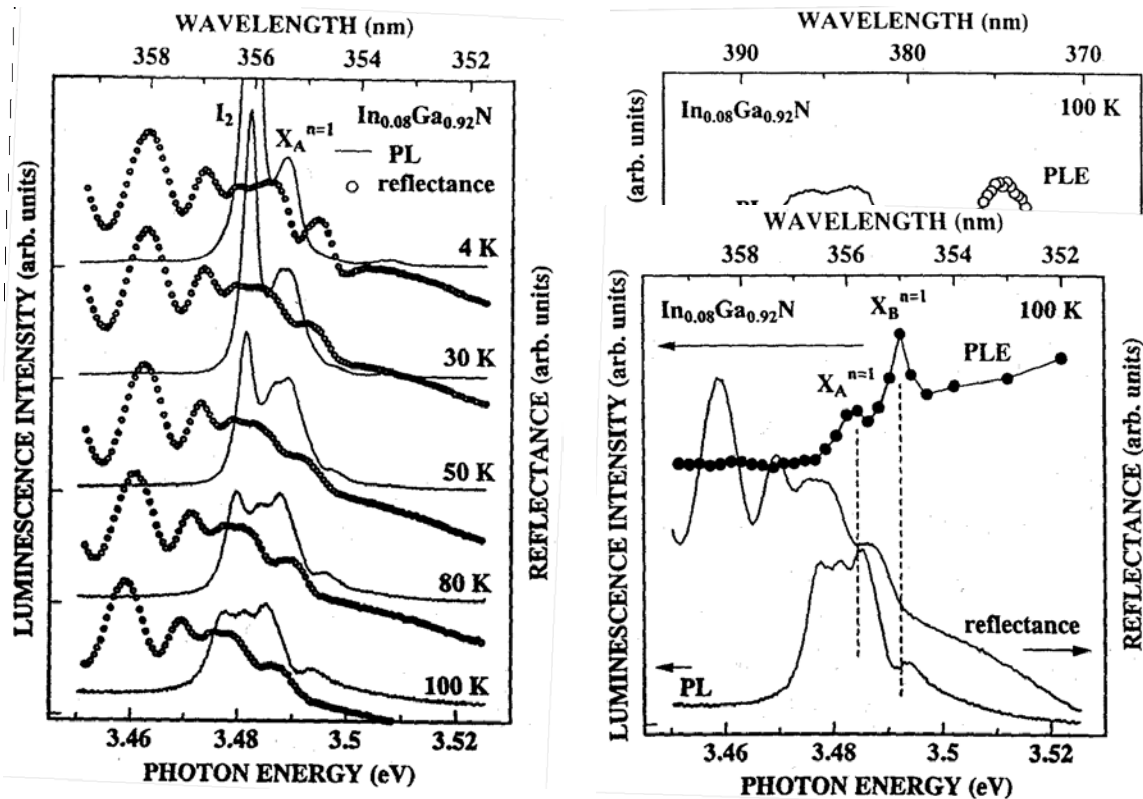


Left: Figure 2.3.2-(5) Excitation spectrum of  $\text{In}_{0.08}\text{Ga}_{0.92}\text{N}$ .

Right: Figure 2.3.2-(6) Enlarged view of the vicinity of GaN band edge in excitation spectrum of  $\text{In}_{0.08}\text{Ga}_{0.92}\text{N}$ .

An excitation spectrum (PLE) of an  $\text{In}_{0.08}\text{Ga}_{0.92}\text{N}$  thin film at 4K is shown in FIG. 2.3.2-(5). The detection position is the peak position of the PL spectrum of  $\text{In}_{0.08}\text{Ga}_{0.92}\text{N}$ .  $\text{In}_{0.08}\text{Ga}_{0.92}\text{N}$  has roughly two main absorption peaks in energy positions in the vicinity of 3.5 eV (GaN) and in the vicinity of 3.3 eV ( $\text{In}_{0.08}\text{Ga}_{0.92}\text{N}$ ).

An enlarged view of the vicinity of 3.5 eV is shown in FIG. 2.3.2-(6). A reflectance spectrum of the specimen is also shown in FIG. 2.3.2-(6). The excitation spectrum correlated with the reflectance spectrum in that the position of the three peaks that can be seen in the vicinity of 3.5 eV in the excitation spectrum was determined by the free excitons A, B, and C of GaN. There is one interesting experimental result, illustrated in FIG. 2.3.2-(7) and FIG. 2.3.2-(8), which is concerned with the issue of whether the GaN was that of the buffer layer or was the GaN present in  $\text{In}_{0.08}\text{Ga}_{0.92}\text{N}$ . FIG. 2.3.2-(7) shows the temperature dependence of reflectance spectrum (Reflectance) and PL spectrum in the vicinity of GaN observed in the  $\text{In}_{0.08}\text{Ga}_{0.92}\text{N}$  thin film, and FIG. 2.3.2-(8) shows the PL spectrum, reflectance spectrum, and excitation spectrum at 100K plotted together.



Left: Figure 2.3.2-(7) Temperature dependence of exciton emission of  $\text{GaN}$  in  $\text{In}_{0.08}\text{Ga}_{0.92}\text{N}$  thin film.

Right: Figure 2.3.2-(8) Enlarged view of the vicinity of  $\text{GaN}$  band edge at 100K.

It can be seen from FIG. 2.3.2-(7) that the emission line of the free exciton A of  $\text{GaN}$  seen at 4K is made up of two emission lines. Of these two emission lines, the one corresponding to the reflectance spectrum is on the lower energy side. Examination of FIG. 2.3.2-(7) also reveals that of these two lines, the one corresponding to PLE is on the higher energy side. If we take into consideration the fact that it is the surface of the  $\text{In}_{0.08}\text{Ga}_{0.92}\text{N}$  thin film that is observed in reflectance spectrum measurements, we can speculate that, out of these two emission lines, the one on the lower energy side is probably the  $\text{GaN}$  of the  $\text{In}_{0.08}\text{Ga}_{0.92}\text{N}$  mixed crystal, and the one on the higher energy side is probably the free exciton A emission line originating from the  $\text{GaN}$  of the buffer layer. Therefore, it can be assumed that the absorption peak observed in the excitation spectrum this time was generated by the  $\text{GaN}$  of the buffer layer. Although at the present moment we still cannot leave the realm of speculation and more detailed measurements are necessary, at least it has been firmly established that free excitons excited in  $\text{GaN}$  contribute to the emission of  $\text{In}_{0.08}\text{Ga}_{0.92}\text{N}$  in one form or another.

Next, let us take a look at the absorption peaks in the vicinity of 3.3 eV. FIG. 2.3.2-(9) is an enlarged view of the vicinity of 3.3 eV in FIG. 2.3.2-(5). Examination of this figure reveals that judging by the drop in the intensity of the excitation spectrum at the boundary of about 3.3 eV, this peak is the absorption peak of  $\text{In}_{0.08}\text{Ga}_{0.92}\text{N}$ . Although there have been reports regarding  $\text{In}_x\text{Ga}_{1-x}\text{N}$  excitation spectra before [3], such a beautiful absorption peak was observed for the first time only in the present study. The fact that a peak was observed in the excitation spectrum means that at this energy position there exists some kind of resonance level. For this reason, in order to investigate the relationship between this resonance level and the two-component emission, we examined the excitation energy dependence at 100K, where the two components are clearly observed.

Left: Figure 2.3.2-(9) Excitation spectrum of  $\text{In}_{0.08}\text{Ga}_{0.92}\text{N}$ .

Right: Figure 2.3.2-(10) Excitation spectrum of two components

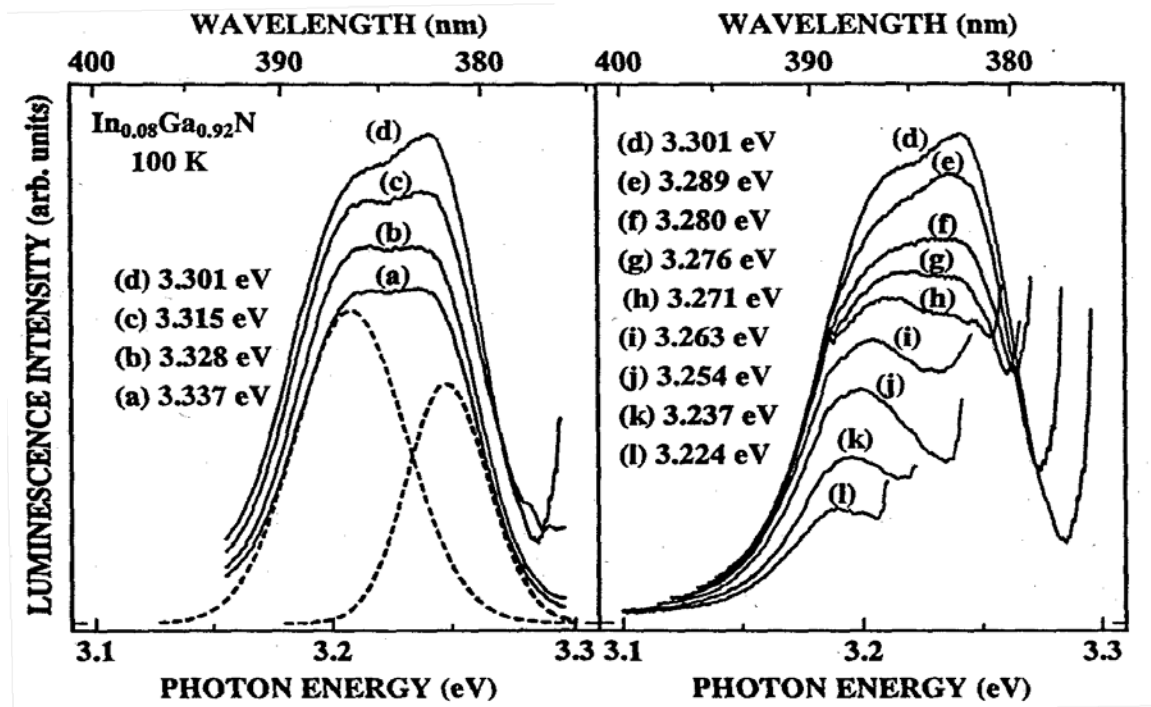


Figure 2.3.2-(11) Excitation energy dependence of PL spectra. (a) Higher-energy side relative to peak position (b) Lower-energy side relative to peak position

The excitation energy dependence of the emission intensity of the two components at such time is plotted in FIG. 2.3.2-(10). From this figure, it is evident that the absorption peaks of the two components are located practically in the same energy position. Changes in the PL spectrum at excitation energy above and below the absorption peak position are shown in FIG. 2.3.2-(11).

Here, (a) is the excitation energy dependence on the higher energy side relative to the absorption peak position, and (b) is the excitation energy dependence on the lower energy side relative to the absorption peak position. For either one of the two emission components, prior to and subsequent to the absorption peak position, the emission intensity first increases and then drops, but on the higher-energy side, the amount of increase is larger, and the amount of decrease is larger, too.

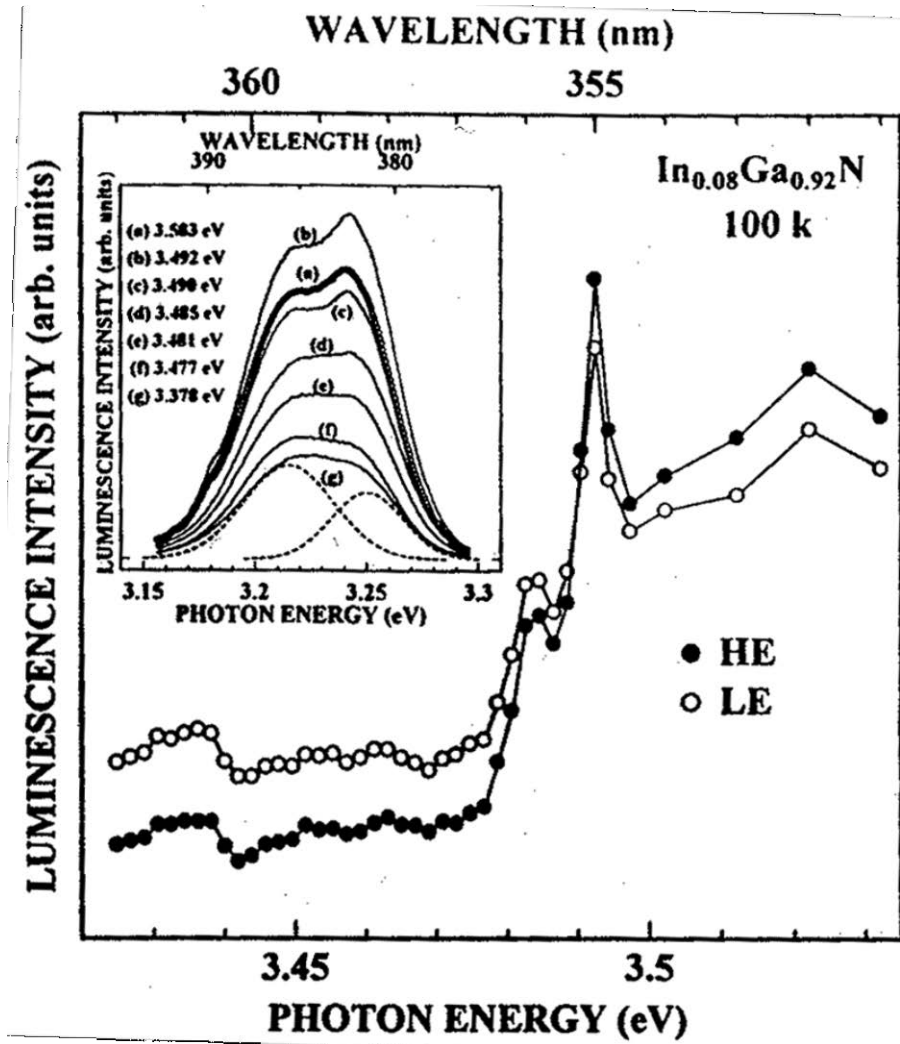


Figure 2.3.2-(12) Excitation energy dependence of spectra in the vicinity of GaN band edge.

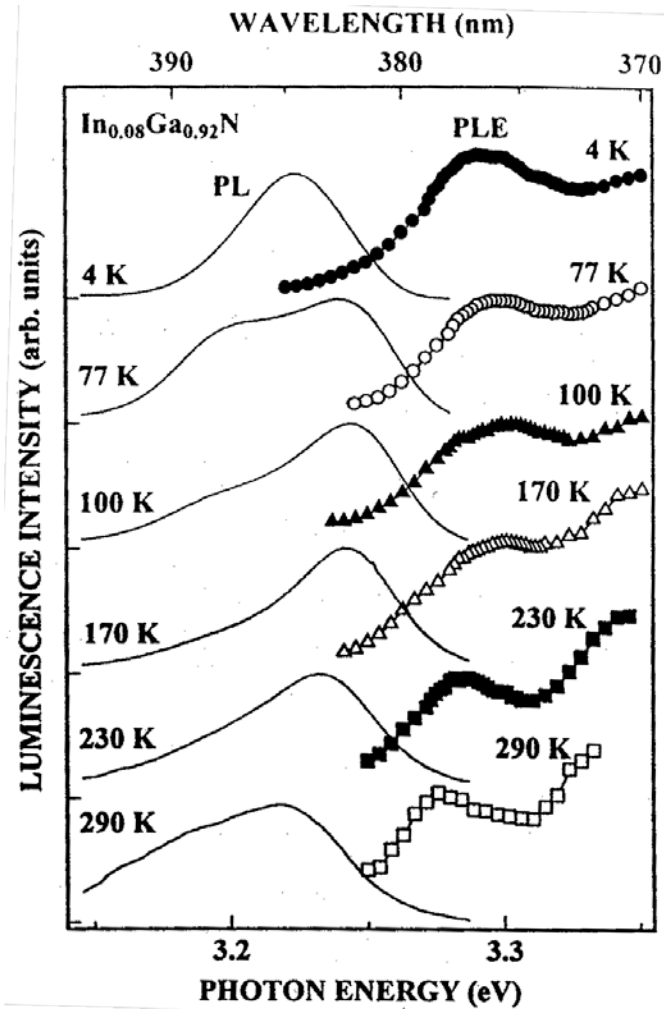
In addition, as shown in FIG. 2.3.2-(12), during absorption in the vicinity of the GaN band edge, the amount of decrease in the emission intensity was larger for the high-energy component when the excitation energy changed from above the band edge to below the band edge. Furthermore, the positions of the absorption peaks at the GaN band edge associated with the two emission components were equal, just as they are for the analogous absorption peaks at the  $\text{In}_{0.08}\text{Ga}_{0.92}\text{N}$  band edge. It is evident from the above results that carriers contributing to the high-energy component and carriers contributing to the low-energy component were generated in the same absorption position. Thus, one may infer that excited carriers first undergo energy relaxation from their excitation energy position to a high energy level, and from there they undergo a transition to a low energy level.

Next, when we carried out measurements of the temperature dependence of  $\text{In}_{0.08}\text{Ga}_{0.92}\text{N}$  excitation spectrum, a distinct absorption peak was observed in the excitation spectrum in the vicinity of room temperature. The peak is shown in FIG. 2.3.2-(13). Inspection of the figure reveals that while no significant

shift is observed in the excitation spectrum in the temperature range from low temperatures to 100K, there is a gradual red shift taking place in the excitation spectrum as soon as the temperature exceeds 100K.

The shift of the excitation spectrum is shown in FIG. 2.3.2-(14). The figure shows that the position of the peak in the excitation spectrum varies with temperature practically in parallel with the position of the emission peak of the high-energy component, and, as a result, the Stokes shift with respect to the high-energy component is a constant value of approximately 50 meV at all temperatures. Based on time-resolved spectroscopy results, it is evident that there are no substantial changes in the emission position of the high-energy component in the temperature range low temperatures to 100K. As is well known for other compound semiconductors, in a system where there is a contribution from localized excitons, when the temperature is increased, the energy difference between the absorption spectrum and PL spectrum (the Stokes shift) becomes smaller due to exciton delocalization. From this point of view, we can say that the large Stokes shift observed in In<sub>0.08</sub>Ga<sub>0.92</sub>N is not caused by localized excitons. Therefore, to understand the origin of high-energy component luminescence, should be taken into account that the Stokes shift is large and that it can be maintained all the way to room temperature.

Figure 2.3.2-(13) Temperature dependence spectra and excitation spectra.



there  
from  
there  
the  
view,  
the  
it  
of PL

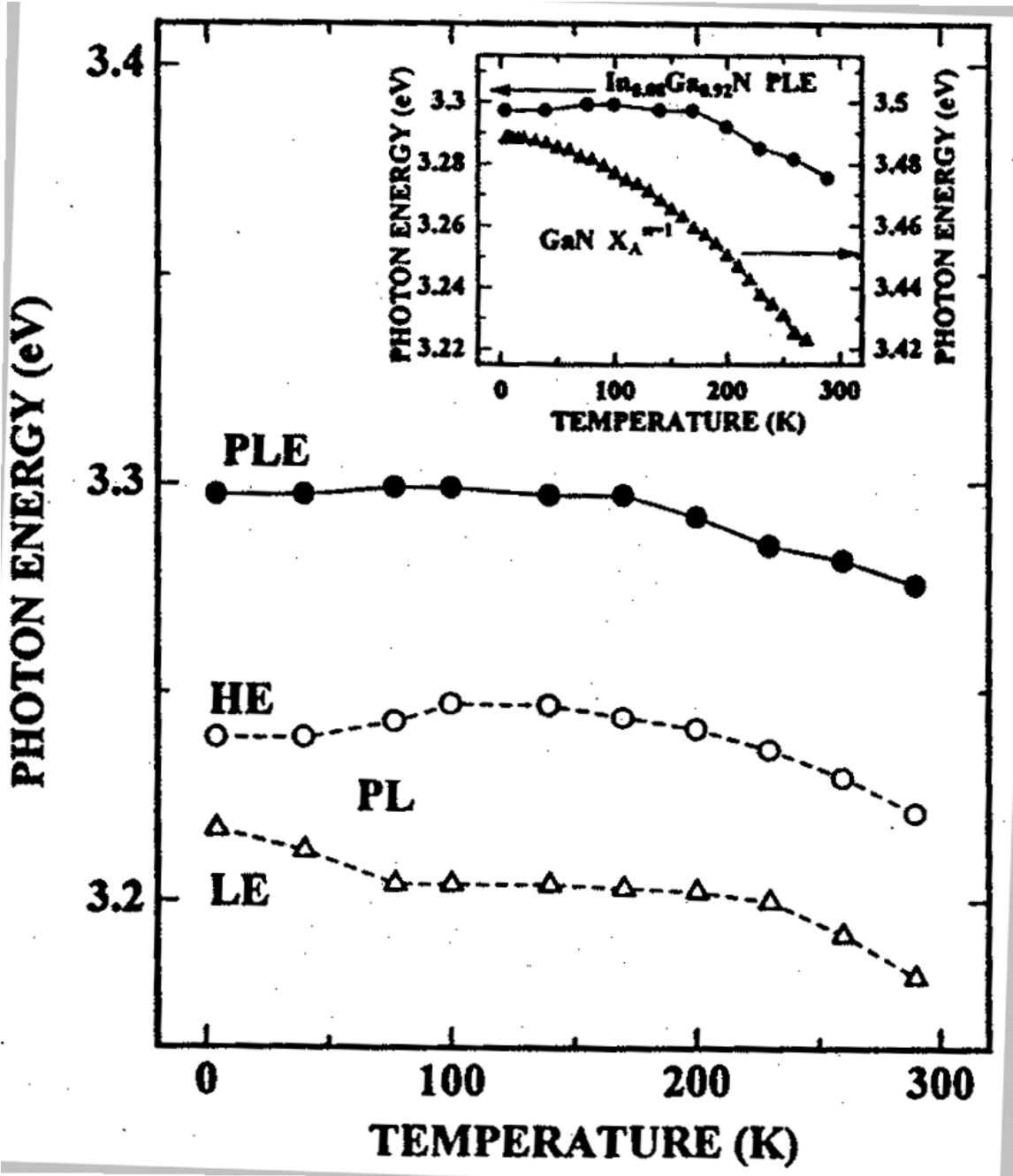


Figure 2.3.2-(14) Temperature dependence of the peak position of PL spectra and excitation spectra.

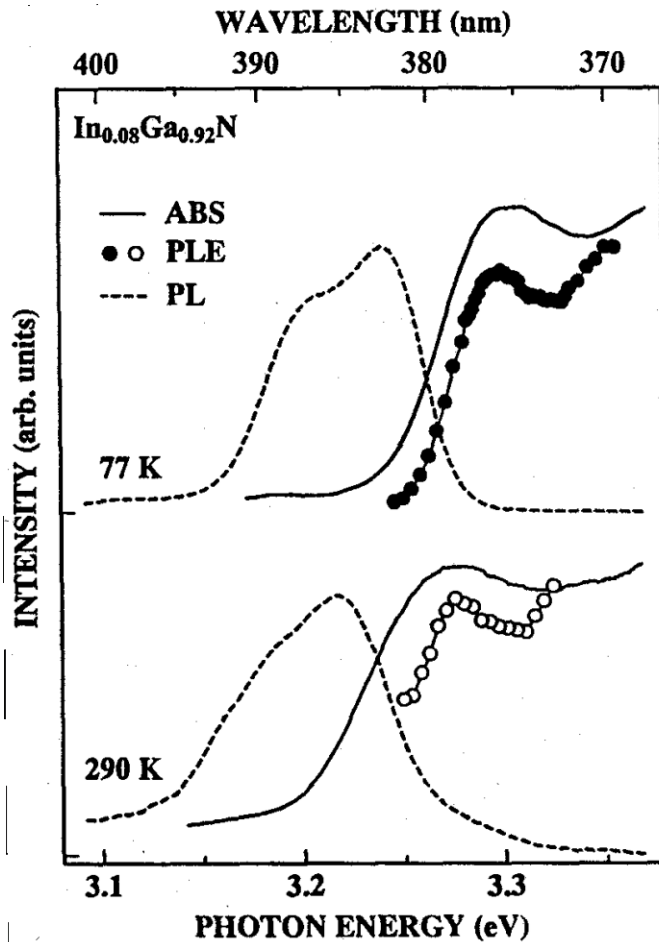
Based on the results of magnetic field dependence and time-resolved spectroscopy measurements of PL spectra conducted prior to last year, and taking into consideration the facts that

- the emission of the high-energy component in In<sub>0.08</sub>Ga<sub>0.92</sub>N is caused by free carriers,
- the high-energy component has an extremely short lifetime (about 30 ps) [4], [5], and
- there is an extremely strong interaction with LO phonons in GaN [6],

it is believed that electrons in a polaron state contribute to emission in the high-energy component, and that the amount of shift expected based on the electron-phonon interaction is  $\alpha_c \eta \omega_1 = 44.2$  meV ( $\alpha_c$ : Fröhlich coupling constant,  $\eta \omega_1$ : LO phonon energy). Thus, there is a very good agreement with 50 meV, the size of the Stokes shift obtained in the present series of experiments, thereby allowing for a non-contradictory explanation of the light emission mechanism model including the concept of the polaron, which has been suggested by us.

Furthermore, there is another fact that is evident from the insert shown in FIG. 2.3.2-(14). Because the excitation spectrum provides information about the excitation state of In<sub>0.08</sub>Ga<sub>0.92</sub>N, we can say that the position of the peak of the excitation spectrum practically represents the bandgap of In<sub>0.08</sub>Ga<sub>0.92</sub>N. Thus, it can be seen that the temperature dependence of the bandgap of In<sub>0.08</sub>Ga<sub>0.92</sub>N is weaker in comparison with GaN.

Figure 2.3.2-(15) Comparison of absorption spectra and excitation spectra at 77K and 290K.



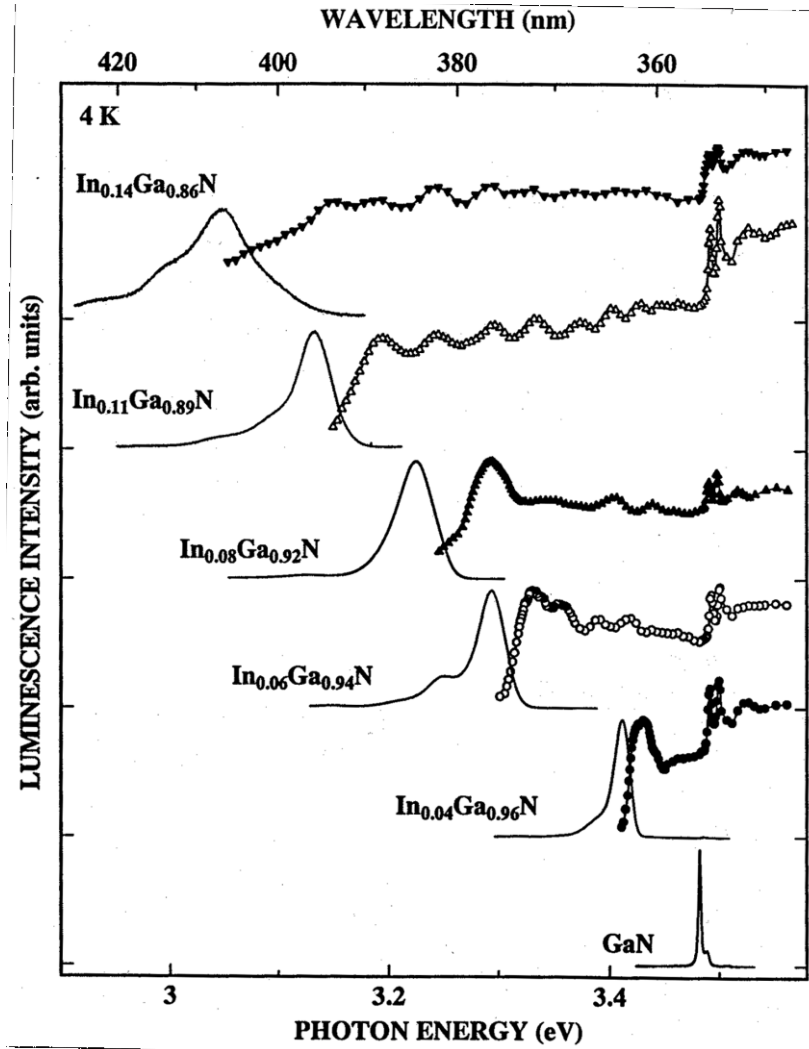
77K

a  
2.3.2-  
and  
290K.  
and  
two  
it is a

So far we have described excitation spectra only, and next, we will examine comparison between absorption spectra and excitation spectra. FIG. (15) shows absorption spectra (ABS) excitation spectra (PLE) at 77K and The positions of the absorption spectra those of the excitation spectra at these temperatures coincide, and, of course, firmly established fact that light absorbed by the In<sub>0.08</sub>Ga<sub>0.92</sub>N sample excites carriers in the crystal and the carriers participate in the radiative recombination of the In<sub>0.08</sub>Ga<sub>0.92</sub>N.

Figure 2.3.2-(16)  
Dependence of PL spectra  
excitation spectra on In  
composition.

The above discussion centered exclusively on samples with an In composition of 8%. Now, will examine changes in the excitation spectra and PL spectra occurring when the composition is different. 2.3.2-(16) shows PL spectra and excitation spectra obtained when the composition is varied from 14%. The temperature at the measurements were carried out was 4K. When content of In is increased pure GaN, the position of peaks of both PL spectra excitation spectra shifts towards lower energies. is due to the change in the bandgap occurring during transition from a GaN to an InN state occurring the increase in the In composition. The position of the peaks of the PL spectra and excitation spectra at various compositions is depicted in FIG. 2.3.2-(17).

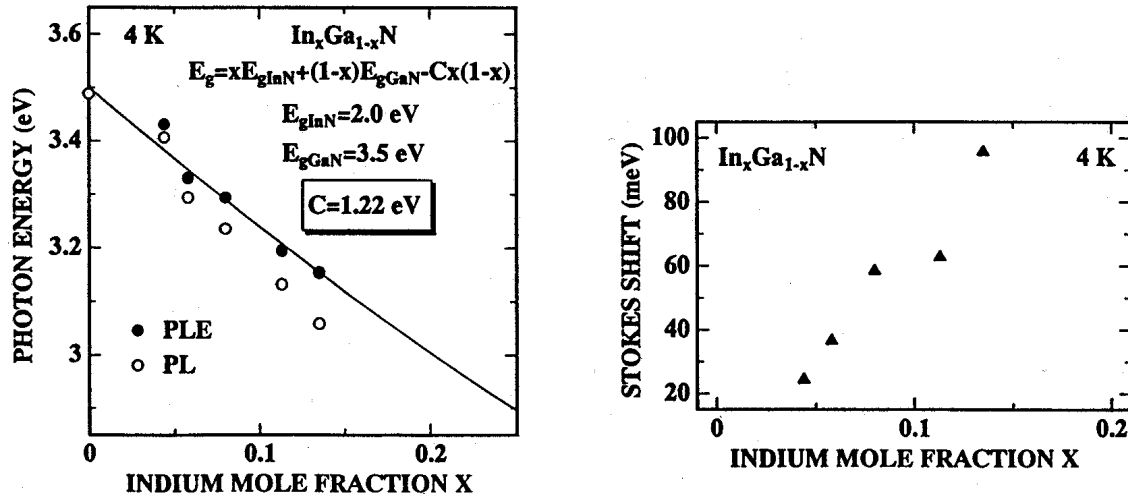


and  
we  
In  
FIG.  
In  
4% to  
which  
the  
from  
the  
and  
This  
state  
with

The bowing parameter C of In<sub>x</sub>Ga<sub>1-x</sub>N, obtained from a formula used to determine the bandgap energy of a mixed crystal semiconductor by the peak position of the excitation spectrum:

$$E_g = xE_{gAC} + (1-x)E_{gBC} - Cx(1-x) \tag{2.3.2-(1)}$$

was approximately 1.22 eV. Here, the bandgap of GaN was assumed to be 3.5 eV and the bandgap of InN was assumed to be 2.0 eV. The bowing parameter turned out to be extremely close to the value of 1.00 eV reported in the past. Now, the dependence of the Stokes shift on the In composition is shown in FIG. 2.3.2-(18). With increase of the In composition the amount of the Stokes shift increased as well. From these results it was evident that as In increased, the state from which there was a high probability of radiative recombination became deeper, and the process of relaxation of carriers from an excited state to an emitting energy state took a longer time.



Left: Figure 2.3.2-(17) Dependence of the peak position of PL spectra and excitation spectra on In composition.

Right: Figure 2.3.2-(18) Dependence of the Stokes shift on In composition.

## 2.4 Growth of GaN Epitaxial Thin Films by MBE Method and Their Evaluation

### 2.4.1 Methods for MBE Growth of GaN Epitaxial Thin Films and their Evaluation

#### 2.4.1.1 RF-MBE Method and Homoepitaxial Growth

Homoepitaxial growth was carried out using the RF-MBE method on bulk GaN single crystal c-face substrates grown by the pressure-controlled solution growth (PC-SG) technique. The GaN bulk single crystal c-face substrates possessed Ga polarity in the [0001] direction and N polarity in the [000-1] direction. The different polarities resulted in different chemical stabilities and crystal growth character, and thus it was necessary to control the polarity of bulk GaN and evaluate the results of crystal growth on the respective faces. Therefore, a substrate was cleaved and crystal growth was carried out on the N-polar face and on the Ga-polar face. The determination of the polar faces of the GaN bulk single crystal substrates was based on the degree of activity with respect to alkali etching [7]. The bulk single crystals had a smooth face and a face with a macro-stepped structure, and it was determined that the smooth face was an N-polar face while the stepped face was a Ga-polar face.

Prior to sending the GaN bulk single crystal substrates to a growth chamber, they were subjected to etching with aqua regia for 10 minutes in order to eliminate impurities adhering to the surface. After increasing the substrate temperature to 870°C in a nitrogen atmosphere and conducting heat treatment for 30 minutes, growth of homoepitaxial GaN thin films was carried out for 4 hours at a growth temperature of 870 °C, with the Knudsen cell temperature set to 970°C, the nitrogen flow rate set to 1.5 sccm, the RF plasma output set to 350W, and the ion polarization voltage set to 500V. Upon termination of growth, the temperature was gradually lowered in a nitrogen atmosphere.

#### 2.4.1.2 $\text{NH}_3$ GS-MBE Method and Heteroepitaxial Growth on Sapphire

A detailed investigation was carried out into the influence exerted on the crystal polarity by the nitriding treatment conducted in the initial stage of heteroepitaxial growth on sapphire substrates by the  $\text{NH}_3$  GS-MBE method. FIG. 2.4.1-(1) shows the sequence of growth steps under the  $\text{NH}_3$  GS-MBE method. A phosphoric/sulfuric etchant was used for surface treatment of the sapphire substrates prior to growth. First

of all, the sapphire substrates were subjected to a heat treatment at a substrate temperature of 1100°C (measured using a thermocouple) for 10 minutes, followed by a nitriding treatment. Experiments were carried out by varying the nitridation time as a parameter.

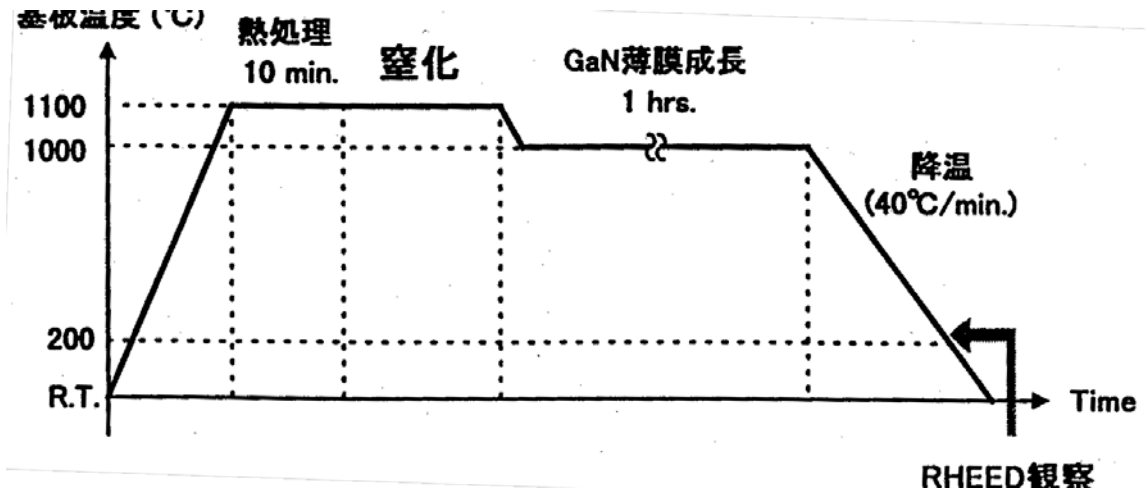


Figure 2.4.1-(1) Growth time graph under  $\text{NH}_3$  GS-MBE method.

Y-axis label: Substrate temperature (°C)

Other labels, left to right: Heat treatment 10 min; Nitridation; GaN thin film growth 1 hrs; Lowering temperature (40°C/min); RHEED observations.

After nitridation, GaN thin film growth was carried out at a substrate temperature of 1000°C. The lowering of the temperature upon termination of growth was carried out in an ammonia atmosphere and in vacuo while observing reflection high-energy electron diffraction (reflection high-energy electron diffraction: RHEED) images at a substrate temperature of about 200~300°C for the purpose of polarity determination. In addition, in order to determine the effects produced by an AlN buffer layer, evaluation was also conducted with respect to samples obtained by depositing an AlN buffer layer at 1000°C after nitridation and then carrying out the deposition of the GaN thin film.

#### 2.4.1.3 Evaluation of Crystalline Properties using Rutherford Back Scattering

A schematic diagram of a Rutherford back scattering analyzer (Rutherford back scattering: RBS) used in the experiments is shown in FIG. 2.4.1-(2). In addition to ordinary RBS measurements utilizing a semiconductor detector and high energy ions of 350~990 keV (in the case of monovalent helium ions) and 0.70~1.98 MeV (in the case of divalent helium ions), the analyzer possesses analytical capabilities, whereby it is capable of performing RBS measurements of the region closest to the surface (approx. 500~800 Å) with an ion beam of 350 keV~450 keV at high resolution (of the order of several Å). Therefore, in regions with extremely thin surfaces, using its resolution of several Å units, the analyzer permits measurement of elemental composition and film thickness in the depth direction while at the same time allowing for obtaining elemental depth profiles extending to deeper regions. Furthermore, because it possesses a micro-beam focusing function allowing it to focus a high energy beam to a size of 5 μm, it permits local analysis of sample surface as well.

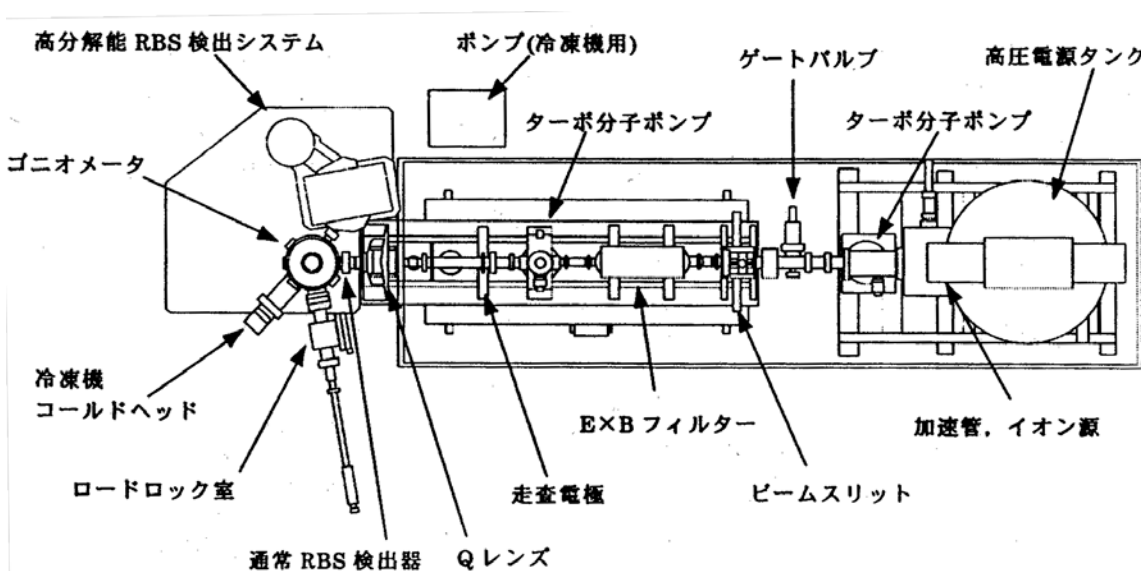


Figure 2.4.1-(2) Schematic diagram of RBS analyzer

Keys:

(Top line, 4 items, left to right) High-resolution RBS detection system; Pump (for cooling system); Gate valve; High-voltage power supply tank

(Line below, 2 items) Molecular turbo-pump; Molecular turbo-pump

(Line below, 1 item) Goniometer

(Line below, 1 item) Cooling system cold head

(Line below, 2 items) E×B filter; Accelerating tube, ion source

(Line below, 3 items) Load lock chamber; scanning electrode; beam slit

(Line below, 2 items) Ordinary RBS detector; Q lens

The analyzer is made up of an ion source/accelerator, beam optics, a sample chamber, and a high-resolution RBS detection system.

The ion source/accelerator is a rotary disk-type high-voltage generator model accelerator, which is made up of an ion source and a high-voltage generator consisting of a drive motor and a laminated disk and is contained inside a sealed tank filled with SF<sub>6</sub> gas. The beam optics are made up of an object slit (beam slit), an E×B type mass separation filter, a microprobe scanning electrode, and a twin microprobe-forming quadrupole magnetic lens (Q lens).

The sample stage consists of a sample chamber, a goniometer used for sample position determination, an ordinary RBS detector, a high-resolution RBS detection system, and a sample-changing apparatus. The goniometer possesses degrees of freedom determined by two translation axes and two rotational axes, which permits measurement in various sample positions. The cooling of samples to 20K is also possible.

He ions from the ion source are accelerated to a high energy of 350 keV~990 keV (for monovalent ions), and, after mass separation by the E×B filter and the Q lens, are directed at the sample. At such time, back-scattered ions are detected by the semiconductor detector or the high-resolution RBS detection system.

If the sample is a single crystal, then the incident ions are scattered only by the atomic nuclei of the region closest to the surface when the ions coincide with a specified crystal axis, and, for this reason, penetrate into the depth of the sample in the manner shown in FIG. 2.4.1-(3). This is called channeling. If measurements

are conducted under channeling conditions, then ion backscattering occurs when there is imperfection in the lattice positions inside the crystal (atom C in the figure), and it is possible to carry out a detailed analysis regarding the lattice positions of impurities and the perfection of the crystal. The minimum ion yield  $\chi_{\min}$ , which is used as an indicator of crystal properties, is defined by the following formula, wherein the RBS signal intensity under channeling conditions is designated as H and the RBS signal under random conditions (an average value of the RBS signal in non-channeling conditions) is designated as  $H_0$ :

$$\chi_{\min} = (H/H_0) \times 100 (\%) \quad (2.4.1-(1))$$

In other words, the smaller  $\chi_{\min}$ , the more regular the arrangement of the crystal. In the present series of experiments, the evaluation of the crystal properties of GaN was carried out by measuring  $\chi_{\min}$ .

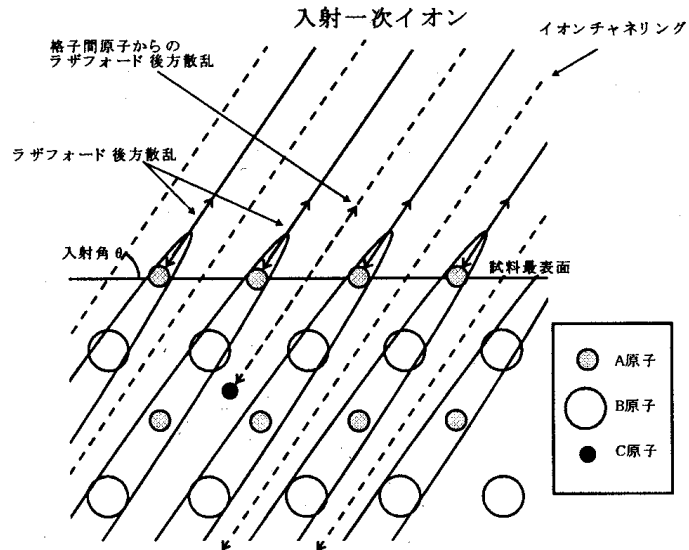
Figure 2.4.1-(3) The principle of channeling.

(Top three items, left to right) Rutherford backscattering from interstitial atoms; incident primary ions; ion channeling

(Below, on the left): Rutherford backscattering

(Below, two items, left to right): Angle of incidence  $\theta$ ; region closest to surface of sample.

(Box, top to bottom): A atoms, B atoms, atoms



## 2.4.2 Results and Discussion

### 2.4.2.1 RF-MBE Method and Homoepitaxial growth

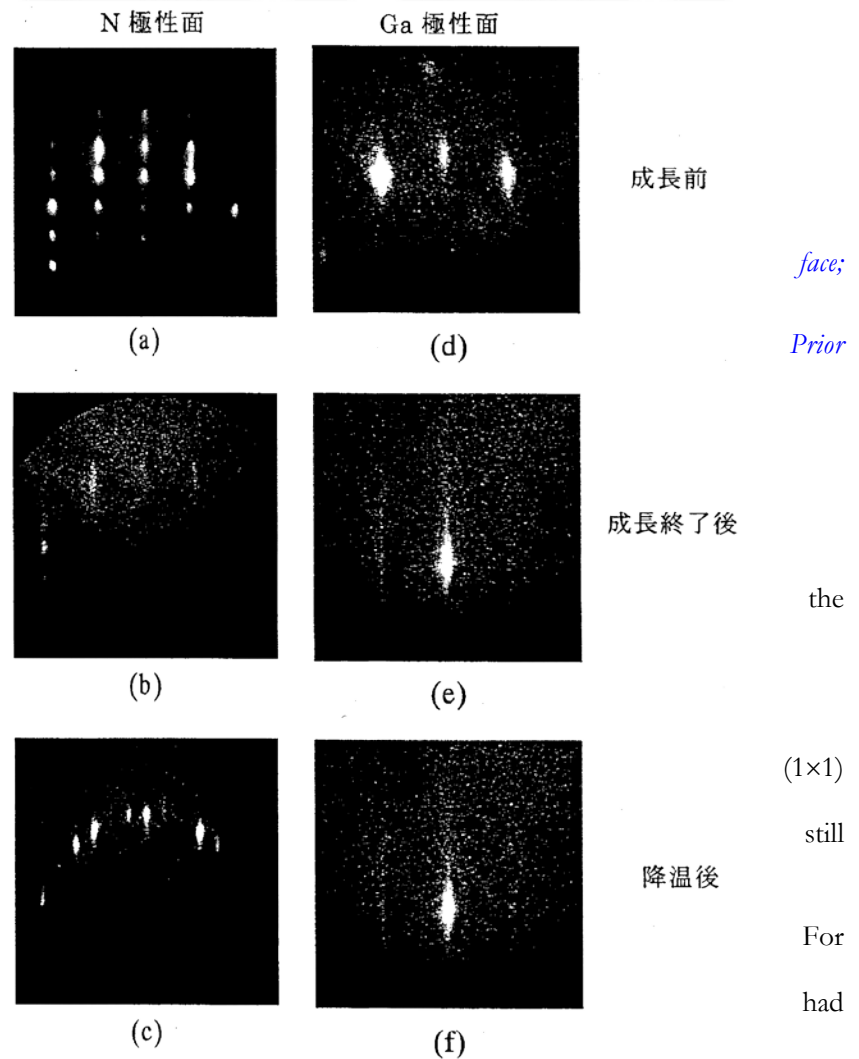
FIG. 2.4.2-(1) shows RHEED patterns, in the  $\langle 11\bar{2}0 \rangle$  direction, of a homoepitaxial GaN thin film grown on the N-polar face and Ga-polar face prior to growth (immediately prior to sending samples to the growth chamber), upon termination of growth, and after lowering the temperature. The fact that the RHEED pattern of the N-polar face prior to growth has a spotty appearance suggests that there are atom-level irregularities on the smooth N-polar face (FIG. 2.4.2-(1) (a)). The fact that the RHEED pattern changed its appearance from spotty to streaky after carrying out homoepitaxial growth on the surface shows that the flatness of the surface was restored (FIG. 2.4.2-(1) (b)). Then, judging by the fact that the RHEED pattern ( $1 \times 1$ ) symmetry upon termination of growth changed to ( $3 \times 3$ ) as a result of surface rearrangement upon lowering the temperature, is believed to be due to the growth of a homoepitaxial GaN thin film with an N-polar face (FIG. 2.4.2-(1) (c)) [7].

*Figure 2.4.2-(1) RHEED patterns in <11-20> direction upon termination of growth of GaN bulk, homoepitaxial thin film and after lowering temperature*

*[Keys, FIG. 2.4.2-(1)]*

*(Across top, left to right): N-polar Ga-polar face*

*(Left hand side, top to bottom): to growth; Upon termination of growth; After lowering temperature.*



In contrast, the fact that the RHEED pattern obtained from Ga-polar face prior to growth is streaky is believed to reflect the flatness of the macro-stepped terrace (FIG. 2.4.2-(1) (d)). The RHEED pattern that exhibited structure upon termination of growth (FIG. 2.4.2-(1) (e)) was unchanged, exhibiting (1×1) structure after lowering the temperature (FIG. 2.4.2-(1) (f)). this reason, it is believed that a homoepitaxial GaN thin film grown with a Ga-polarity.

Furthermore, the crystal polarity of these homoepitaxial GaN thin films was determined using the difference in reaction to an aqueous solution of NaOH [7]. A 1.8M aqueous solution of NaOH was used to conduct etching for 3 minutes, as a result of which the homoepitaxial GaN thin film grown on the N-polar face was etched away by the aqueous solution of NaOH and there was a certain deterioration in surface morphology, while the homoepitaxial GaN thin film grown on the Ga-polar face exhibited no conspicuous differences in the characteristics of its surface prior to and after the etching. This suggests that the homoepitaxial GaN thin film grown on the N-polar face possesses N-polarity while the homoepitaxial GaN thin film grown on the Ga-polar face possesses Ga-polarity. This supports the above-described RHEED observation results, and confirms that the homoepitaxial GaN thin film grows with the same polarity as the GaN bulk single crystal used as the substrate.

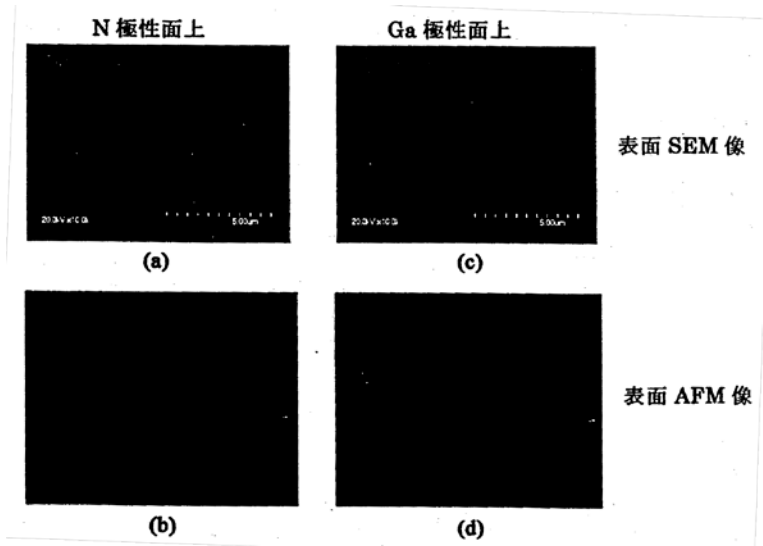
Next, the surface of the homoepitaxial GaN thin film was examined using a scanning electron microscope (SEM) and an atomic force microscope (AFM). SEM images of the surface and AFM images of the surface are shown in FIG. 2.4.2-(2).

Figure 2.4.2-(2) SEM images and AFM images of the surface of a homoepitaxial GaN thin film grown on the N-polar (smooth) face (on the left) and on the Ga-polar (stepped) face (on the right) of a bulk GaN substrate.

[Keys, FIG. 2.4.2-(2)]

(Across top, left to right): N-polar face; Ga-polar face

(Left hand side, top to bottom): SEM images of surface; AFM images of surface



It can be confirmed that in the case of a homoepitaxial GaN thin film grown on the N-polar face, which is the smooth face of the bulk GaN, the surface assumed a stepped shape. Conversely, in the case of the homoepitaxial GaN thin film grown on the Ga-polar face, which had a stepped shape, the surface became practically flat. The height of the stepped structure of the homoepitaxial GaN thin film grown on the N-polar face was about 1.5~10.9 nm, and because this corresponds to a 3~21 monolayers (MLs), it was obvious that the structure was not the same as atomic layer steps observed on MOCVD-grown GaN thin films. Thus, this type of stepped surface morphology is believed to be due to the fact that the GaN thin film was grown three-dimensionally. On the other hand, because in the case of the homoepitaxial GaN thin film grown on the Ga-polar face the stepped surface morphology could not be confirmed, it is believed that the GaN thin film had been grown two-dimensionally. These results suggest that, in the same manner as with epitaxial growth on sapphire substrates, as a result of different polarity, there occur changes in the growth mode, which exert influence on the surface morphology.

FIG. 2.4.2-(3) shows PL spectra obtained at 4.2K for the N-polar face and Ga-polar face of the GaN bulk single crystal and of the homoepitaxial GaN thin films grown thereon. Conspicuous differences are visible in the PL spectra obtained when the N-polar side and Ga-polar side of the GaN bulk single crystal were excited, so that both deep level luminescence and luminescence in the vicinity of the band edge are observed in the PL spectra obtained for the N-polar side while only deep level luminescence is observed and no luminescence in the vicinity of the band edge is visible in the PL spectra obtained for the Ga-polar side. This is believed to be due to the difference in the surface properties of the GaN bulk single crystal. On the other hand, it is evident from the PL spectra obtained for the homoepitaxial thin films grown on the N- and Ga-polar faces of the GaN bulk single crystal substrates that neutral donor-bound exciton edge luminescence with a strong emission intensity and a narrow emission half-width is dominant and deep level luminescence is suppressed.

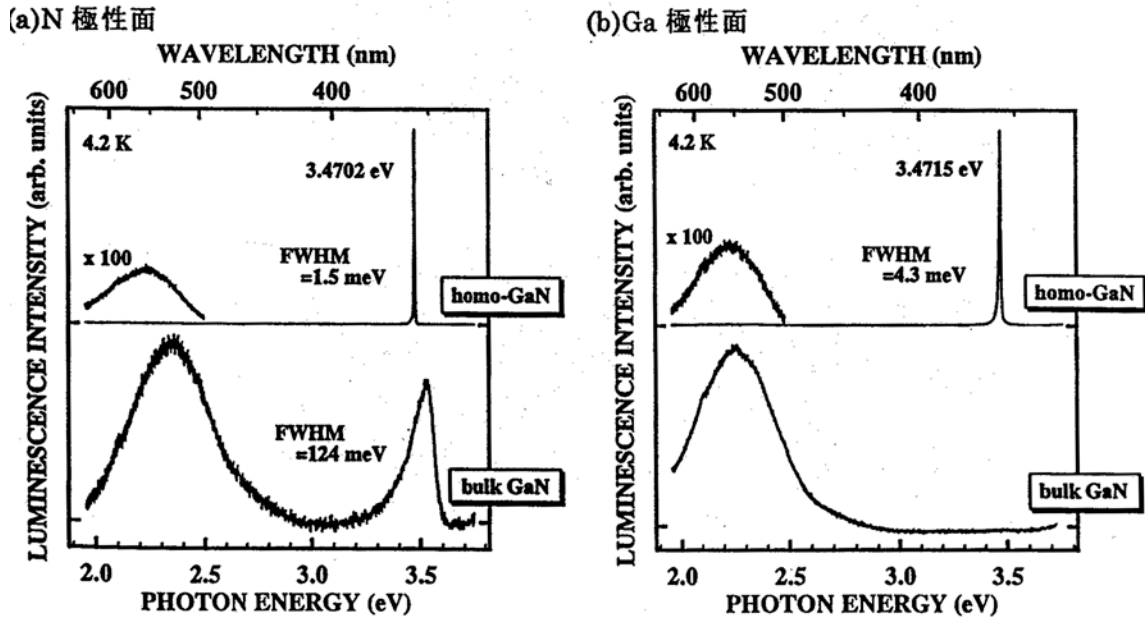


Figure 2.4.2-(3) PL spectra obtained at 4.2K for (a) the N-polar face and (b) Ga-polar face of the GaN bulk single crystal and of the homoepitaxial GaN thin films grown thereon. (a) N-polar face (b) Ga-polar face.

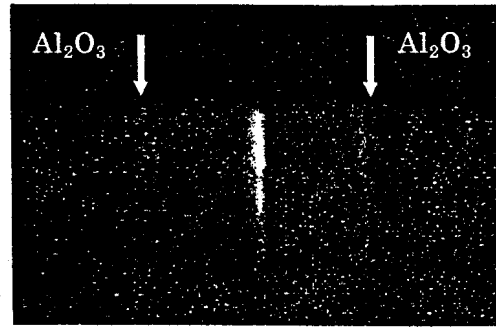
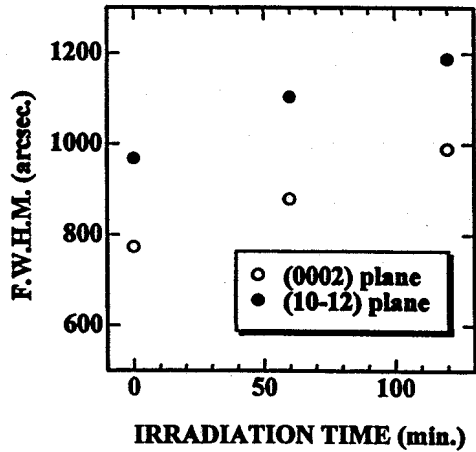
It was found that the emission half-width of neutral donor-bound excitons was 1.5 meV for the film grown on the N-polar face and 4.3 meV for the film grown on the Ga-polar face, which represented a considerable improvement in terms of the emission characteristics of the substrate.

Inspection of the peak positions of the exciton emission of the homoepitaxial GaN thin films reveals that for homoepitaxial GaN thin film on the N-polar face and on the Ga-polar face, the positions were 3.4702 eV and 3.4715 eV, respectively. The position of the emission peak of neutral donor-bound excitons in an unstrained state, in which no strain due to compression or stretching is present, is 3.4706 eV. Therefore, there is practically no strain in the homoepitaxial GaN thin films grown on the N-polar face and on the Ga-polar face. Some emission peak shift is believed to be due to the fact that the thickness of the GaN bulk single crystal is relatively small, at about 20  $\mu\text{m}$ , and some warping occurs during the growth of the single crystal.

In addition, it was found that in comparison with heteroepitaxial growth on a sapphire substrate there were considerable improvements, such as the fact that the emission half-width was reduced by more than 1/2, the emission intensity became stronger by two orders of magnitude, and the emission intensity ratio between band edge emission/deep level emission increased by 1~2 orders of magnitude, etc.

#### 2.4.2.2 NH<sub>3</sub> GS-MBE Method and Heteroepitaxial Growth on Sapphire Substrates

FIG. 2.4.2-(4) shows the dependence of the X-ray rocking curve half-width of the GaN thin film on nitridation time. This dependence suggests that changes definitely occurred on the sapphire surface as a result of nitridation. Next, a RHEED image of the sapphire surface that has been subjected to nitridation with NH<sub>3</sub> is shown in FIG. 2.4.2-(5). In the RHEED image, in addition to a streak pattern originating from the sapphire substrate (Al<sub>2</sub>O<sub>3</sub>), inside it, there appears to be an image with a narrow streak interval. In addition, it was confirmed that when nitridation was carried out over an extended period of time, there was a gradual approach to the streak interval of AlN. This confirms that, in the same manner as when RF nitrogen plasma is used, a process of substitution with AlN took place on the surface of the sapphire substrate as a result of exposure to NH<sub>3</sub> gas.



Left: Figure 2.4.2-(4) Dependence of the X-ray rocking curve half-width of the GaN thin film on nitridation time.

Right: Figure 2.4.2-(5) RHEED pattern of the sapphire substrate obtained by nitridation with  $\text{NH}_3$ .

Next, we investigated the influence exerted by the nitridation of the sapphire substrate by means of exposure to  $\text{NH}_3$  gas on the polarity of the crystalline thin film that grows on it. It is known that when nitridation is carried out using  $\text{NH}_3$  gas under the metal-organic chemical vapor deposition (MOCVD) method, in the same manner as in the case of nitridation using the RF-MBE technique, the epitaxial thin film grown thereafter has an N-polar face. By contrast, under the  $\text{NH}_3$  GS-MBE method, an N-polar face is obtained when direct epitaxial thin film growth is carried out on a sapphire substrate, but there have been reports that a Ga-polar face is obtained when the sapphire substrate surface is nitrided with  $\text{NH}_3$  gas, and a definite conclusion has not yet been reached [9].

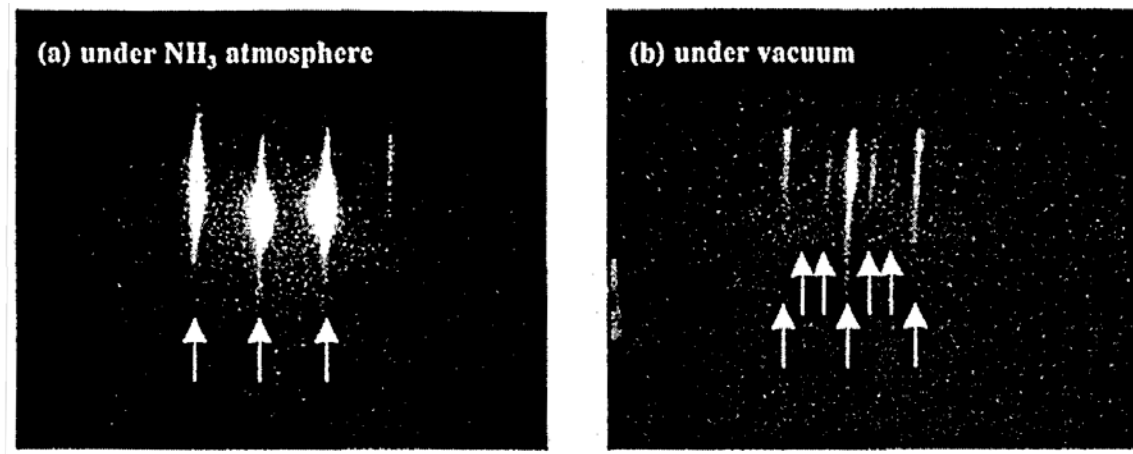
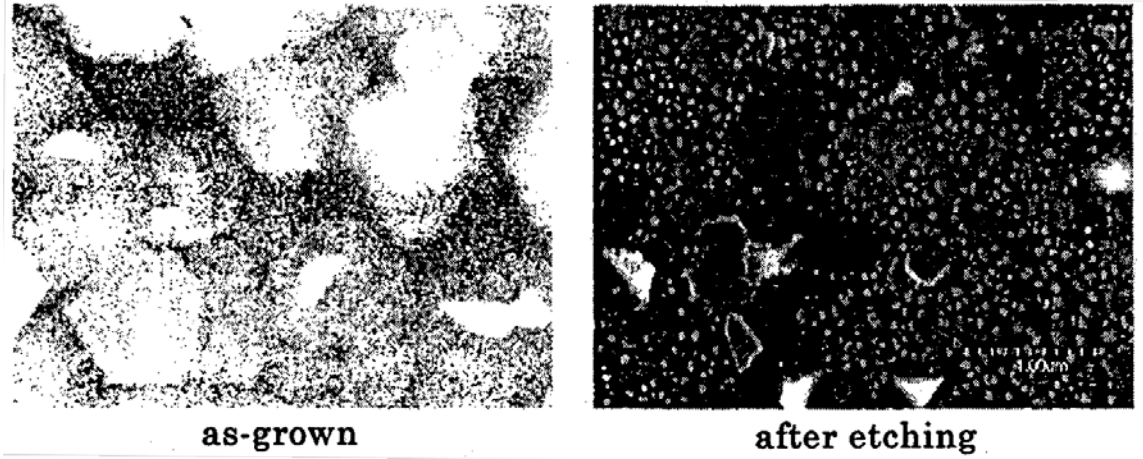


Figure 2.4.2-(6) RHEED patterns obtained upon termination of growth under  $\text{NH}_3$  atmosphere and in vacuo after lowering the temperature to  $300^\circ\text{C}$ .



*Figure 2.4.2-(7) SEM images of the surface prior to and after NaOH etching of a GaN thin film directly grown after nitridation.*

In this series of experiments, it was evident that the sapphire substrate surface had been definitely nitrided, and, for this reason, the polarity of the GaN epitaxial thin film was determined based on the degree of activity with respect to alkali etching and surface reorganization in the RHEED images. FIG. 2.4.2-(6) shows a RHEED pattern obtained after lowering the temperature after growing a GaN epitaxial thin film on top of a nitrided sapphire. The pattern obtained when the temperature was lowered under a  $\text{NH}_3$  gas atmosphere exhibited a  $(1 \times 1)$  structure, whereas the one obtained when it was lowered in vacuum exhibited a  $(3 \times 3)$  structure. Furthermore, FIG. 2.4.2-(7) shows SEM images obtained prior to and after etching the sample with NaOH. As is evident from the SEM images, the GaN epitaxial thin film grown on the nitrided sapphire was extremely active with respect to alkali etching. Based on these results, it is believed that the GaN epitaxial thin film grown on the nitrided sapphire has an N-polar face. The  $(1 \times 1)$  structure exhibited by the RHEED pattern obtained under a  $\text{NH}_3$  atmosphere is believed to be due to the fact that there was no adhered layer of Ga on top of the N-polar face and surface reorganization due to attached Ga atoms did not occur because the temperature was lowered in the presence of active nitrogen. The same phenomenon has been observed in the RF-MBE method when the temperature was lowered while performing irradiation with nitrogen plasma [10].

As a result of the investigation, it was found that regardless of the presence or absence of nitridation and the degree of nitridation, under the growth conditions used in the present series of experiments, GaN epitaxial thin films grown by the  $\text{NH}_3$  GS-MBE method had only an N-polar face.

Furthermore, we examined the polarity of the GaN epitaxial thin films with an AlN buffer layer. FIG. 2.4.2-(8) shows SEM images obtained prior to and after alkali etching of a GaN epitaxial thin film, in which an AlN buffer was used. Both when nitridation was and was not conducted, the etching of the GaN thin film surface did not take place, based on which, it is evident that using an AlN buffer layer makes it possible to exercise polarity control from an N-polar face to a Ga-polar face in a simple manner.

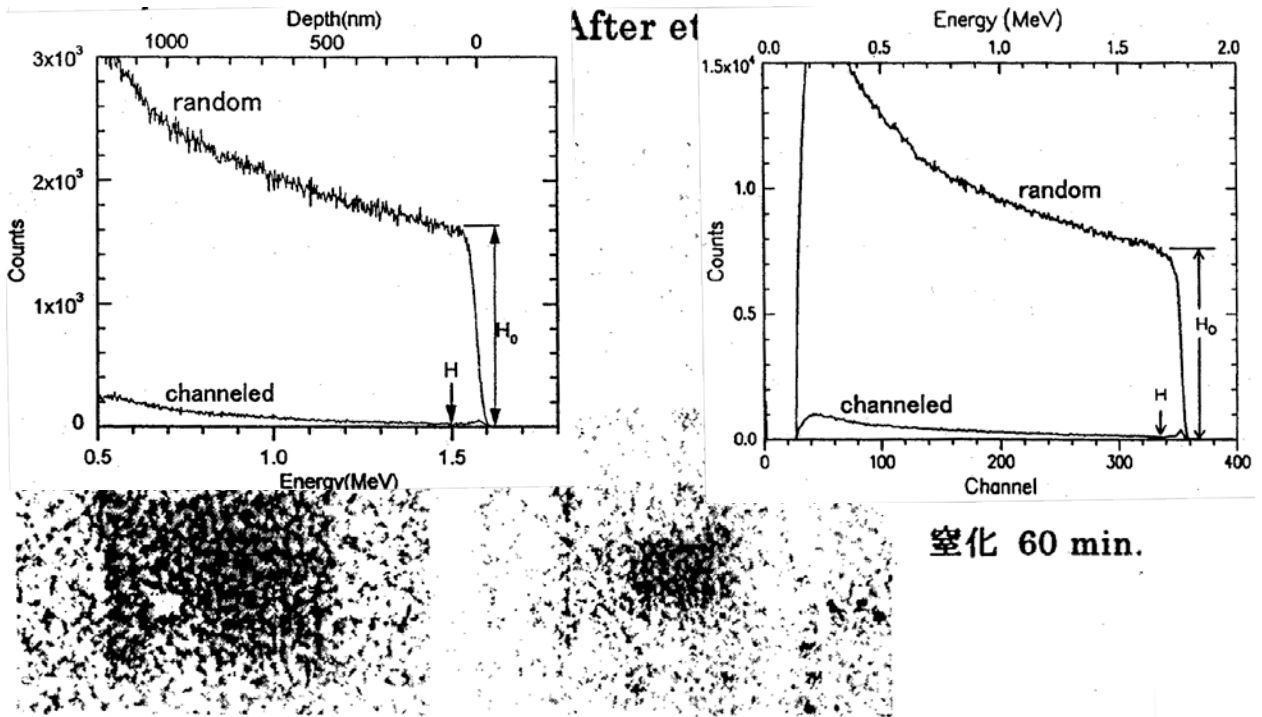


Figure 2.4.2-(8) SEM images of the surface prior to and after NaOH etching of a GaN thin film grown using an AlN buffer layer (top: without nitriding treatment, bottom: with nitriding treatment).

[Keys, FIG. 2.4.2-(8)]

(Right hand side, top to bottom): Nitridation 0 min; Nitridation 60 min.

Finally, evaluation of the crystal properties of GaN epitaxial thin films grown under the  $\text{NH}_3$  GS-MBE method using nitridation and an AlN buffer layer was carried out with the help of RBS analysis. FIG. 2.4.2-(9) shows RBS spectra of a GaN epitaxial thin film grown under the  $\text{NH}_3$  GS-MBE method. In addition, for reference purposes, FIG. 2.4.2-(10) shows RBS spectra of a GaN epitaxial thin film grown using the MOCVD method. The random spectrum is an RBS spectrum measured without channeling, and the channeled spectrum is an RBS spectrum measured under channeling conditions. During measurement, the  $\langle 0001 \rangle$  axis was used as the channeling axis. In the random spectrum, the signal intensity ( $H_0$ ) is high because ions are subjected to backscattering by atoms in the crystal, but in the channeled spectrum, as is also shown in FIG. 2.4.1-(3), ions penetrate into the crystal without being scattered by the atoms and therefore, the signal intensity ( $H$ ) becomes weaker.

Here, we obtained the minimum ion yield  $\chi_{\min}$ , which is used as an indicator of crystal properties, for GaN thin films grown using the  $\text{NH}_3$  GS-MBE method and the MOCVD method. As a result, the  $\chi_{\min}$  of GaN epitaxial thin films grown using nitriding-based and AlN buffer layer-based  $\text{NH}_3$  GS-MBE were 1.5%, and films grown by MOCVD were 1.7%, respectively. Based on this, it was found that the crystal properties of both films, as viewed from the  $\langle 0001 \rangle$  axis direction, were practically identical. In addition, in comparison with Si single crystal wafers, which have a  $\chi_{\min}$  of about 2%, or GaAs single crystal wafers, which have a  $\chi_{\min}$  of several %, the value of  $\chi_{\min}$  of GaN epitaxial thin films is equivalent or lower, which means that in this crystal the crystal defect density is extremely high and the deviation from the crystal lattice positions of the atoms making up the crystal is extremely small.

*Left: Figure 2.4.2-(9) RBS spectrum of GaN grown using NH<sub>3</sub> GS-MBE (channeling axis: [0001]).*

*Right: Figure 2.4.2-(10) RBS spectrum of GaN grown using MOCVD (channeling axis: [0001]).*

## 2.5 Summary

① When PL measurements were carried out using excitation energies higher and lower than the bandgap of GaN for the two emission components obtained for In<sub>0.08</sub>Ga<sub>0.92</sub>N thin films, no significant variations were observed in the emission peak positions of the two components of In<sub>0.08</sub>Ga<sub>0.92</sub>N. However, it was found that when GaN was not excited, the intensity of emission decreased and as the temperature became higher, the role of GaN as a carrier-supplying source became more important.

② Excitation spectrum measurements for In<sub>0.08</sub>Ga<sub>0.92</sub>N were carried out and distinct absorption peaks of In<sub>0.08</sub>Ga<sub>0.92</sub>N were observed in the temperature range from 4K to room temperature. In addition, we discovered that free excitons A, B, and C produced by GaN at 4K contributed to the emission of In<sub>0.08</sub>Ga<sub>0.92</sub>N. This suggested the possibility that the GaN was primarily a buffer layer. The absorption positions of the two emission components emanating from the In<sub>0.08</sub>Ga<sub>0.92</sub>N thin film were identical, from which it was inferred that excited carriers underwent energy relaxation from the excitation energy position first to a higher energy level and from there performed a transition to a lower energy level. Because when the temperature dependence of the excitation spectra was measured, the peak positions did not exhibit significant changes depending on temperature, it was believed that the bandgap of In<sub>0.08</sub>Ga<sub>0.92</sub>N itself did not exhibit a peculiar temperature dependency.

③ Among the two emission components, the emission peak position and the excitation spectrum peak position of the high-energy component shifted practically in parallel in response to temperature changes, and the Stokes shift of the high-energy component exhibited no temperature dependence, its value being approximately 50 meV across all temperatures. It is known that in a system where there is contribution from localized excitons, when the temperature is increased, the energy difference between the absorption spectrum and the PL spectrum (the Stokes shift) becomes smaller due to exciton delocalization, and based on this, the large Stokes shift observed in In<sub>0.08</sub>Ga<sub>0.92</sub>N is not due to localized excitons. Thus, to understand the origin of the high-energy component luminescence, it should be taken into account that the Stokes shift is large and can be maintained all the way to room temperature. Considering the emission mechanism model including the polaron concept, which was proposed by us in research conducted prior to last year, the amount of Stokes shift,  $\alpha_e \eta \omega_1 = 44.2$  meV ( $\alpha_e$ : Fröhlich coupling constant,  $\eta \omega_1$ : LO phonon energy), which is expected based on electron-phonon interaction, is in extremely good agreement with the value obtained in the present series of experiments and can explain it in a non-contradictory fashion.

④ Because the peak positions of the absorption spectrum and the excitation spectrum were located practically in the same energy position, it was evident that, in the same manner as with ordinary semiconductor materials, the light absorbed by the In<sub>0.08</sub>Ga<sub>0.92</sub>N sample excited carriers inside the crystal and the carriers contributed in the radiative recombination of In<sub>0.08</sub>Ga<sub>0.92</sub>N.

⑤ Excitation spectrum measurements were carried out for InGaN with an In composition of 4~14%. The smaller the In composition became, the more distinctly was the absorption peak observed in the excitation spectrum. In addition, the larger the In composition became, the larger the Stokes shift was.

⑥ Homoepitaxial growth by the RF-MBE method on GaN bulk single-crystal substrates grown by the pressure-controlled solution growth technique was investigated. As a result, epitaxial thin films that represented a continuation of the polarity of the GaN bulk single crystals used for the substrates were obtained. In addition, it was confirmed that when the N-polar face of the GaN bulk single crystal was used as the substrate, the GaN epitaxial thin films grown thereon grew three-dimensionally, whereas GaN epitaxial thin films grown on the Ga-polar face grew two-dimensionally. Results of PL measurements of these homoepitaxial thin films showed that an extremely sharp and strong emission line due to neutral donor-bound excitons was dominant, and practically no deep level luminescence was observed. In addition, it was

found that in comparison with heteroepitaxial growth on sapphire substrates, there were considerable improvements, such as the fact that the emission half-width was reduced by more than 1/2, the emission intensity became stronger by two orders of magnitude, and the emission intensity ratio between band edge emission/deep level emission increased by 1~2 orders of magnitude, etc.

⑦ Regarding control over the initial-stage growth process under the  $\text{NH}_3$  GS-MBE method, we clarified the influence exerted by an AlN buffer layer and sapphire substrate surface nitridation using  $\text{NH}_3$  gas on the crystal properties. It was found that for GaN epitaxial thin films grown on sapphire substrates, N-polar face growth was dominant regardless of the presence or absence of nitridation of the sapphire substrate surface. It was confirmed that, by contrast, insertion of an AlN buffer layer prior to GaN epitaxial thin film growth resulted in obtaining a single Ga-polar face regardless of the presence or absence of nitridation. The ability to control single polarity faces is useful in high-quality crystal growth by the  $\text{NH}_3$  GS-MBE method. Furthermore, as a result of RBS analysis-based evaluation of the crystal properties of the GaN epitaxial thin films grown by the  $\text{NH}_3$  GS-MBE method using an AlN buffer layer, it was also found that the crystallinity of the resultant epitaxial films was extremely high.

## 2.6 Future Plans

In research conducted up until now, based on measurement results, we have been able to develop some ideas on the origin of the high-energy component and the mutual transitions of carriers between the two components. The specific tasks and plans for the future are described below.

① No experimental results have been obtained that would allow us to make definite conclusions regarding the low-energy component among the two components. However, based on numerous experimental results, the low-energy component is expected to exert important influence on the emission characteristics of  $\text{In}_x\text{Ga}_{1-x}\text{N}$ . At present, it has not been confirmed yet whether the low-energy component, which is observed at low temperatures, continues to exist at high temperatures. In addition, judging from the fact that the intensity of the LO phonon replica changes when the In composition is varied, the low-energy component is expected to strongly depend on the In composition. In the future, we are preparing to elucidate the origin of the low-energy component by conducting more detailed measurements using samples with different In compositions.

② In comparison with the high-energy component, the low-energy component has a wider linewidth and its dependence on external forces, such as excitation intensity, temperature, etc. is difficult to see. In addition, in samples with a wide linewidth, there is a considerable chance of the localization effect in  $\text{In}_x\text{Ga}_{1-x}\text{N}$  obscuring the authentic emission characteristics of  $\text{In}_x\text{Ga}_{1-x}\text{N}$ . In this connection, we will use crystals of higher quality produced by the Joint Research Organization.

③ When we examined the emission of  $\text{In}_x\text{Ga}_{1-x}\text{N}$ , there was an unmistakable contribution of GaN to the intensity of the emission. In particular, the higher the temperature becomes, the more important the carriers originating from GaN become, and we are planning a more detailed examination of this mechanism. This presents much interest in terms of device fabrication.

④ We are planning to improve the crystal properties of GaN thin films obtained by homoepitaxial growth, in particular, their surface flatness, which was insufficient this time. As for the Ga-polar face, which has step-shaped irregularities on the surface, we will have to try to bury the irregularities of the substrate by increasing the growth time, increasing the diffusion length of the starting material, etc. As for the N-polar face, in order to control the stepped three-dimensional structure formed during homoepitaxial growth, we will examine the possibility of introducing shutter control techniques, etc. In addition, we will simultaneously continue our research regarding homoepitaxial growth based on the  $\text{NH}_3$  GS-MBE method, which allows for easily obtaining films with excellent emission characteristics. We will grow high-quality InGaN mixed crystals on excellent homoepitaxial GaN buffer layers.

⑤ We will conduct a detailed investigation into the structural (defect density, surface properties) and optical characteristics of homoepitaxial thin films. In addition, in order to clarify the relationship between the crystal properties and emission characteristics, in the future we are preparing to conduct more detailed RBS measurements, X-ray diffraction measurements, etc. regarding GaN bulk single crystals and GaN epitaxial thin films. In particular, as far as RBS measurements are concerned, we will conduct more detailed measurements using channeling axes other than the  $\langle 0001 \rangle$  axis evaluated this time.

## 2.7 References

- [1] K. P. O'Donnell, R. W. Martin, and P. G. Middleton: Phys. Rev. Lett. 82 (1999) 237.
- [2] H. Kudo, H. Ishibashi, R. Zheng, Y. Yamada, and T. Taguchi: phys. stat. sol. (b) 216 (1999) 163.
- [3] S. Chichibu, T. Sota, K. Wada, and S. Nakamura: J. Vac. Sci. Technol. B16 (1998) 2204.
- [4] H. Kudo, H. Ishibashi, R. Zheng, Y. Yamada, T. Taguchi, S. Nakamura, and G. Shinomiya: J. Lumin. 87-89 (2000) 1199.
- [5] H. Kudo, T. Tanabe, H. Ishibashi, R. Zheng, Y. Yamada, and T. Taguchi: phys. stat. sol. (a) 180 (2000) 27.
- [6] R. Zheng, T. Taguchi, and M. Matsuura: J. Appl. Phys. 87 (2000) 2526.
- [7] A. R. Smith, R. M. Feenstra, D. W. Greve, M. S. Shin, M. Skowronski, J. Neugebauer, and J. E. Northrup: Appl. Phys. Lett. 72 (1998) 2114.
- [8] S. Kurai, A. Kawabe, T. Sugita, S. Kubo, Y. Yamada, T. Taguchi, and S. Sakai: Jpn. J. Appl. Phys. 38 (1999) L102.
- [9] S. Sonoda, S. Shimizu, X. Q. Shen, S. Hara, and H. Okumura: Jpn. J. Appl. Phys. 39 (2000) L202.
- [10] S. Kurai, S. Kubo, T. Sugita, A. Kawabe, Y. Yamada, T. Taguchi: Technical Report of Institute of Electronics, Information and Communication Engineers 98 (384) (1998) 33.

# 3 Clarification of Light Emission Mechanisms and Physical Properties of GaN-based Semiconductors

## 3.1 Achievements in 1998~1999

Generally speaking, the material used for the active layer of nitride-based light-emitting devices is GaInN, a ternary mixed crystal, and active research has been conducted by numerous researchers in order to establish the origin of its highly efficient luminescence. Roughly three models have been proposed that attempt to explain the highly efficient luminescence of GaInN in spite of a high density of defects [1].

- (1) A model in which carriers are captured into extremely small regions of high In concentration (quantum dots) present in the GaInN active layer [2].
- (2) A model in which carriers are localized at potential fluctuations generated by inhomogeneities in the In composition in the GaInN active layer [3].
- (3) A model in which electrons enter a polaron state as a result of a strong interaction between the electron system and the lattice and are captured into the lattice [4].

In each of these models, capture or spatial localization of carriers contributes to the high-efficiency luminescence. However, up till now no definite conclusions have been reached regarding the details of the process, including its origin, although active discussions have been conducted by scientific societies and other organizations in Japan and overseas. Furthermore, at present, all of the available reports attempt only to understand emission characteristics and do some modeling and none of them suggests ways to practically implement high-efficiency light-emitting elements.

The origin of carrier localization is believed to be the key to the practical realization of high-efficiency LEDs. In order to implement super-efficient blue-violet LEDs with an energy conversion efficiency of 40% and an internal quantum efficiency of 90%, the most important task at the present moment is to clarify the light emission mechanism of GaN-based light-emitting elements and, based on that, to map out paths towards practical implementation of high-efficiency elements.

Thus, in order to clarify the light emission mechanism of GaN-based compound semiconductors, the present study was carried out with a view 1) to clarify the mechanism of light emission in GaInN-based light-emitting layers, and 2) to clarify the relationship between defects, dislocations, and the mechanism of light emission.

The main results obtained in 1998-1999 are summarized below.

By investigating the effects of adding Si (donor) to GaInN/GaN quantum wells, it was found that piezoelectric effects exert considerable influence on the light emission characteristics, and these influences can be practically eliminated by the addition of donors to quantum wells in the amount of approximately  $10^{18}$  cm<sup>-3</sup>. The piezoelectric field reduces carrier recombination inside the quantum wells, and in devices operating at low carrier densities, such as LEDs, the elimination of the piezoelectric field is very important. On the other hand, it has been pointed out that since the addition of a high concentration of Si to quantum well layer brings about an increase in the threshold value of the induced stimulated emission, the crystal properties of GaInN deteriorate [5].

We have conducted a systematic investigation into emission characteristics of GaInN/GaN quantum well LEDs with different In concentrations over a wide temperature range (7~540K) and discovered (a) that the dependence of the emission lifetime on temperature was different in three different temperature regions, (b) that these three temperature regions were observed in samples with different In compositions, and, furthermore, (c) that the temperature at which carriers underwent a transition from a localized state to a delocalized state increased with the increase in the In composition. Based on that, it was found that the localization energy of the carriers increased with an increase in the In composition ratio.

## **3.2 Summary of Research and Development in 2000**

Just as in 1999, in 2000 we continued our investigations concerning the emission characteristics of GaInN/GaN quantum well structures in connection with crystal growth parameters or structure. It is believed that the physical phenomena involved in the mechanism of light emission vary depending on the device structure and crystal growth conditions, such as the In composition and the density of the Si dopant impurities in the active layer of the GaInN. For this reason, we prepared a systematic series of samples used for measurements, in which parameters were varied depending on the intended purpose, and subjected them to evaluation and investigation.

Below, we provide a summary of the objectives and results obtained in the four areas of research included in the present report.

### **3.2.1 Examination of light emission mechanism of GaInN/GaN multiple quantum well LEDs with different In compositions**

The effect of spatial localization of carriers in GaInN is believed to be of crucial importance to the understanding of the mechanism of light emission. The emission characteristics (in particular, carrier localization effects) of GaInN are believed to be strongly dependent on the In composition, and a systematic evaluation of samples with different In compositions is important for the clarification of the origin of carrier localization. However, reports published so far have provided evaluations for a narrow range of In compositions and described different device structures. For this reason, our investigation focused primarily on the localization state of carriers while varying the In composition of the GaInN active layer in the LED structures. As a result, based on the temperature dependence of the emission lifetime over a wide range of temperatures (7~540K) and on simulation using a simplified localization model, we discovered that, with the increase in the In composition, the localization energy increases, and, on the other hand, the density of non-radiative centers increases as well.

### **3.2.2 Examination of emission lifetime characteristics of LEDs of different luminescence efficiencies**

Based on the examination of the carrier localization state carried out in 1), we evaluated differences in the emission lifetime characteristics of LED samples with different luminescence efficiencies at the same emission wavelengths and investigated the relationship between the luminescence efficiency and the carrier localization state. Based on these results, we found that, in samples exhibiting a high-efficiency, carriers are localized deeper and the transition to non-radiative recombination centers is suppressed, thereby improving the efficiency of luminescence.

### **3.2.3 Examination of in-plane distribution of light emission**

We used a high spatial resolution near-field probe PL system, introduced in 2000, in order to evaluate the in-plane distribution of light emission spectra of GaInN/GaN quantum well LEDs and summarized its usefulness based on the obtained basic data.

### **3.2.4 Reverse bias PL characteristics of Si-doped quantum well LEDs**

The addition of Si to GaInN/GaN quantum wells is believed to be efficient in the elimination of piezoelectric effects. However, the addition of donors to the active layer also affects the LED band structure, and these influences must be taken into consideration. In the present study, we investigated the influence exerted on the device characteristics by the addition of donors to the active layer using reverse biased PL and time resolved PL characteristics of LED samples.

## **3.3 Methods and Means**

### **3.3.1 PL and Time Resolved PL Measurement System**

The PL measurements, for which we conducted measurements of the temperature dependence and PL excitation power density dependence at room temperature or low temperatures, as well as measurements of the carrier lifetime by time-resolved PL and measurements of its temperature dependence, etc., were carried out in cooperation with Yamaguchi University. As concerns the excitation light sources used for the measurement of the excitation power density, for weak excitation we used a He-Cd laser (325 nm, cw, 2 mW), and for high density excitation a Xe-Cl excimer laser (308 nm, pulse width: 2.5 ns, repetition rate: 70 Hz, peak power: 91 kW, average power: 16 mW) and a Nd YAG laser (355 nm, pulse width: 5 ns, repetition rate: 10 Hz). For the time-resolved PL measurements, we used the third harmonic of an Ar laser-excited mode-locked titanium sapphire laser (266 nm, pulse width: 200 fs, repetition rate: 250 kHz, peak power: 1.6 MW, average power: 80 mW) to produce the excitation light and a multichannel spectrometer and a streak camera for detection, with the measurements conducted using three-dimensional data made up of wavelength, time, and luminescence intensity. In order to measure the emission characteristics over a wide temperature range, for temperature dependence measurements, we used a temperature-variable cryostat for the range 7~300K and a heater for the range 300~540K.

### **3.3.2 Reverse Biased PL and Time-Resolved PL Measurements of LED Samples**

Measurements of light emission characteristics under an external electric field applied to quantum wells were carried out by measuring PL in a state, wherein a reverse bias was applied to the LEDs. We used the second harmonic (400 nm) of a mode-locked titanium sapphire laser to selectively excite quantum wells in LEDs emitting in the blue-green region. For ordinary PL measurements, we employed a spectrometer and a CCD detector, and for time-resolved PL measurements we used a spectrometer and a streak camera system. In order to quantitatively evaluate the intensity of the internal electric field in quantum wells in experiments in which a reverse bias is applied, it is important to estimate the externally applied electric field acting on the quantum wells. To estimate the externally applied electric field, we used an LCR meter to measure the pn junction capacitance of the LED samples, to which the reverse bias was applied, estimated the width of the depletion layer, and assumed that the externally applied voltage was applied to the entire depletion layer. In addition, we investigated the contribution of carriers generated by photo-excitation to the photocurrent and to radiative recombination by measuring the photocurrent in conjunction with luminescence spectra (emission peak energy, luminescence intensity).

### **3.3.3 High Spatial Resolution PL Mapping System Utilizing a Near-Field Optical Probe**

The evaluation of the in-plane distribution of light emission was carried out using a high spatial resolution PL mapping system utilizing a near-field optical probe, which was introduced in 2000. In the system, a semiconductor sample is excited by the near-field light of a laser originating from a microscopic opening (100-500 nm) at the tip of an optical fiber probe, and emission is detected via the same probe (illumination-collection mode). It was estimated that the spatial resolution was about 250 nm when using a probe with an

opening of 500 nm. Generally speaking, the measurement of the in-plane distribution of light emission is based on the use of CL (cathodo-luminescence) and micro PL systems. Because in the case of CL the lateral diffusion length of primary electrons is approximately 1  $\mu\text{m}$ , the spatial resolution power is limited by the lateral diffusion width. In addition, in samples of a multilayer structure, such as LEDs, the interpretation of the emission distribution data is made difficult by the fact that carriers are excited in all the layers from the surface to a depth of approximately 1  $\mu\text{m}$ . On the other hand, in a micro PL system, the light of the laser is focused with a microscope object lens, and although a high spatial resolution power is indeed obtained, the theoretical spatial resolution power does not exceed the diffraction limit ( $\sim\lambda/\text{NA}$ ). Because as compared with these conventional methods, near-field probe PL possesses a higher spatial resolution and can selectively excite quantum wells in the device structure, it is believed to facilitate the interpretation of mapping and other data.

FIG. 3.3.3-(1) shows a schematic diagram of the system. The laser used for excitation (325 nm or 441 nm) was coupled to a fiber, and the quantum wells of the LED structures were excited using near-field light from a microscopic opening at the tip of the optical fiber. Emission was collected using the same microscopic opening in the optical fiber and the measurement of the spectra was carried out using a monochromator and a CCD detector. Using feedback (shear force control), the distance between the tip of the fiber and the sample was controlled so as to maintain a constant distance, and, from the voltage applied to the piezoelectric elements along the Z axis, it was possible to simultaneously obtain information on surface irregularities, as information obtained by AFM. In addition, the newly introduced system equipped with a cryostat used for low temperature (5K) measurements.

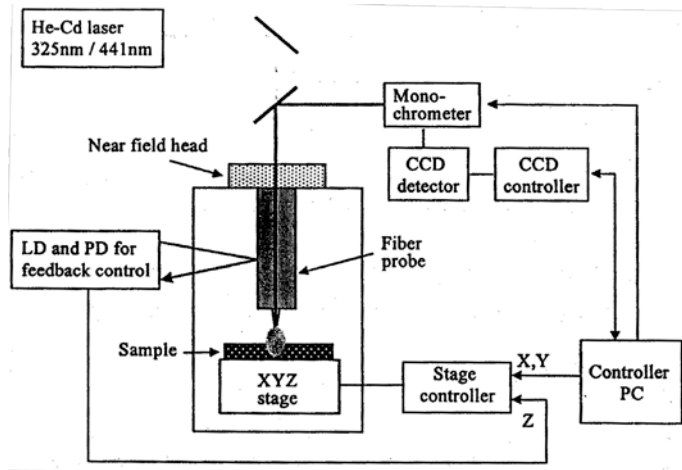
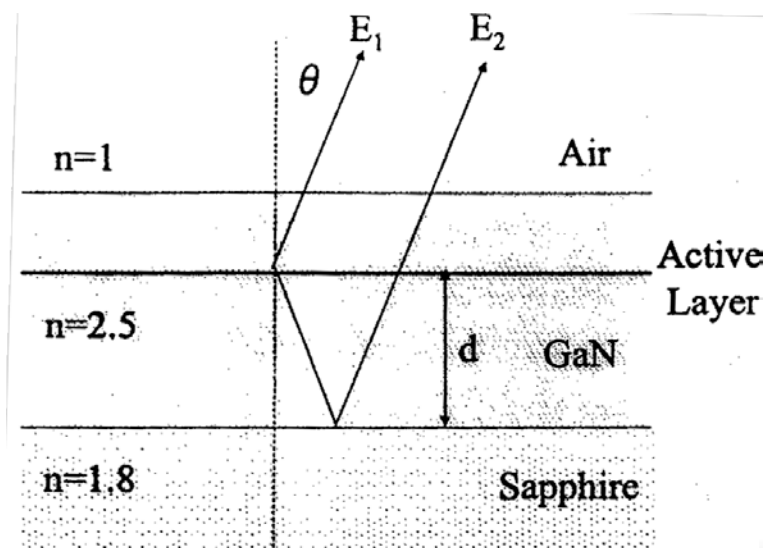


Figure 3.3.3-(1) Block diagram of near-probe PL system.

### 3.3.4 Method of Interference-Free Measurement of Emission Spectra

Due to the wide emission half-width of GaInN (which is about 120 meV in the blue region at 470 nm) and the difference in the indexes of refraction between the GaN epilayer and the sapphire typically used for the substrate, during the optical evaluation of GaInN-based light-emitting elements and materials, fringes caused by Fabry-Perot interference often appear in the emission spectra. The fringes resulting from interference quantitatively influence the half-width and peak position of the spectra, and complicate the interpretation of the emission process. Although principle it is possible to eliminate the influence of the interference by subjecting the measured spectra to numerical processing, it is in fact quite difficult to remove the interference fringes completely.

Figure 3.3.4-(1) Conceptual diagram of Fabry-Perot interference



such  
was  
field

effect

*in GaN-based light emitting elements on sapphire.*

Here, we will describe the method used in the present study for interference-free measurement of spectra. FIG. 3.3.4-(1) is a typical diagram showing the origin of interference in the PL and EL spectra of GaN-based light-emitting elements on sapphire substrates. Because of the difference in the indexes of refraction between the sapphire and the GaN, light emitted from the active layer undergoes repeated multiple reflection in the epilayer of the GaN, and the emission components guided to the detection system are represented by a direct component  $E_1$  originating from the active layer and component  $E_2$  reflected at the interface of GaN/sapphire. Here, with  $E$  representing the electric field of the light, the respective components are given by the following formulae:

$$E_1(\lambda) = A_0(\lambda)T \exp j(\omega t + kr_1) \quad (1)$$

$$E_2(\lambda) = A_0(\lambda)T \exp j(\omega t + kr_2) \quad (2)$$

(Where  $A_0(\lambda)$  represents the actual emission spectrum of the active layer,  $R$  represents the reflection coefficient at the GaN/sapphire interface, and  $T$  represents the transmission coefficient of the GaN/air interface.) In addition, the optical path difference between components  $E_1$  and  $E_2$  is given by:

$$r_1 - r_2 = \frac{2d}{\cos \theta} \quad (3)$$

In this case, light intensity in a direction orientated at an angle  $\theta$  to the center of the optical axis is given by:

$$I_\theta(\lambda) = |E_1 + E_2|^2 = A_0(\lambda)^2 T^2 \left\{ 1 + R^2 + 2R \cos \left( \frac{2k_0 nd}{\cos \theta} \right) \right\} \quad (4)$$

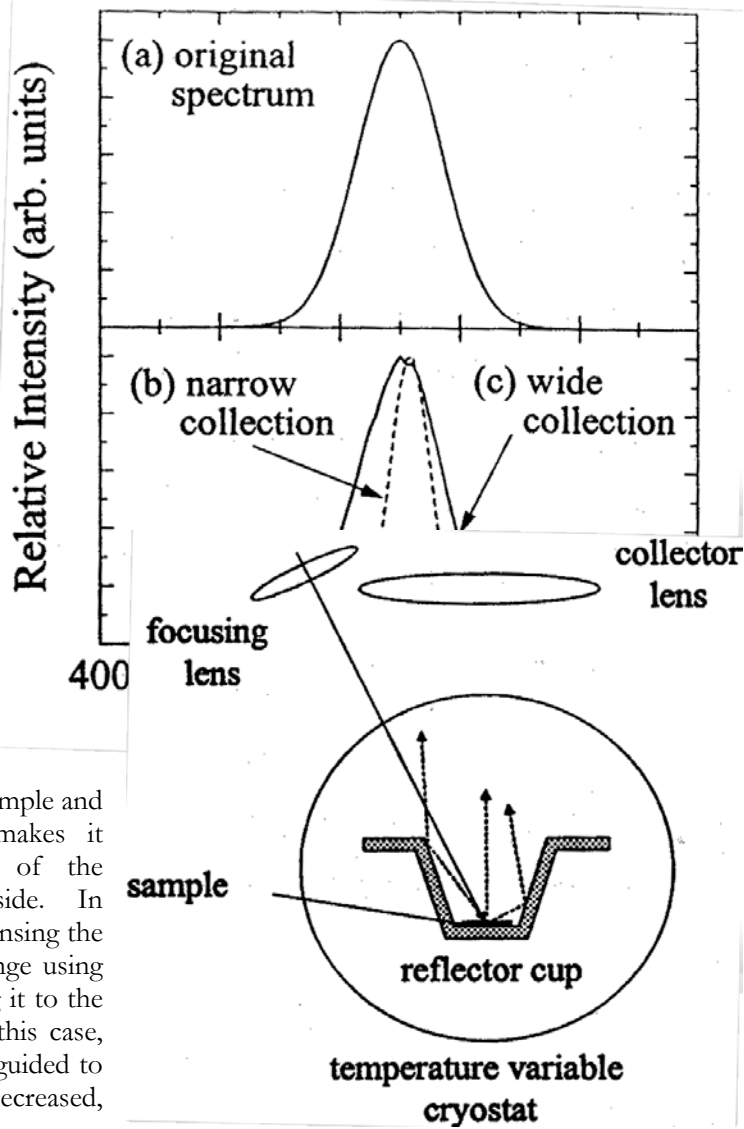
Because the light directed by the condenser lens into the detection system is given by an integral over a certain angle to the central axis, the actually measured spectrum is represented in the following manner as a dependence of the light intensity on the wavelength:

$$I(\lambda) = \int_0^{\theta_1} I_\theta(\lambda) d\theta = A_0(\lambda)^2 T^2 \left\{ \theta_1 + R^2 \theta_1 + 2R \int_0^{\theta_1} \cos \left( \frac{2k_0 nd}{\cos \theta} \right) d\theta \right\} \quad (5)$$

Now, based on the actual emission spectrum (a) of FIG. 3.3.4-(2), the computation of formula (5) in case (b), in which the detected emission component corresponds to a relatively narrow angle range of  $\theta_1 = 10^\circ$  (N.A. = 0.1), and in case (c), wherein the emission is collected over a wide angle of  $\theta_1 = 60^\circ$  (N.A. = 0.8), gives us the lower portion of FIG. 3.3.4-(2). The index of refraction used here for the GaN and the sapphire was, assuming that  $d = 2.8 \mu\text{m}$ , the value shown in FIG. 3.3.4-(1). Case (b), wherein the light was detected only over a narrow angle range from the central axis, reveals a spectrum influenced by interference, with the interference period being 14 nm, which is in agreement with the value calculated from  $\Delta\lambda = \lambda^2/2nd$ . On the other hand, when the light is collected over a wide angular range, and the N.A. of the detection system is relatively large, it is possible to reproduce the original emission spectrum so that it is free from the influence of interference.

Figure 3.3.4-(2) (a) Original spectrum used for calculations, and calculation results in case of (b)  $N.A. = 0.1$ , and (c)  $N.A. = 0.8$ .

As a method of increasing the of the detection system, it is possible to use a lens with a large (0.5 or more). However, during typical PL measurements, it is necessary to focus the laser used excitation with a lens and irradiate the sample with its light, addition, because the sample has placed in a cryostat etc. during temperature measurements, there be a certain distance between the sample and condenser lens, which usually makes it difficult to increase the N.A. of the condenser lens on the detector side. In addition, one might consider condensing the emitted light over a wide angle range using integrating sphere and then guiding it to the detection system with a lens. In this case, however, the intensity of the light guided to detection system is noticeably decreased, renders the method impractical.



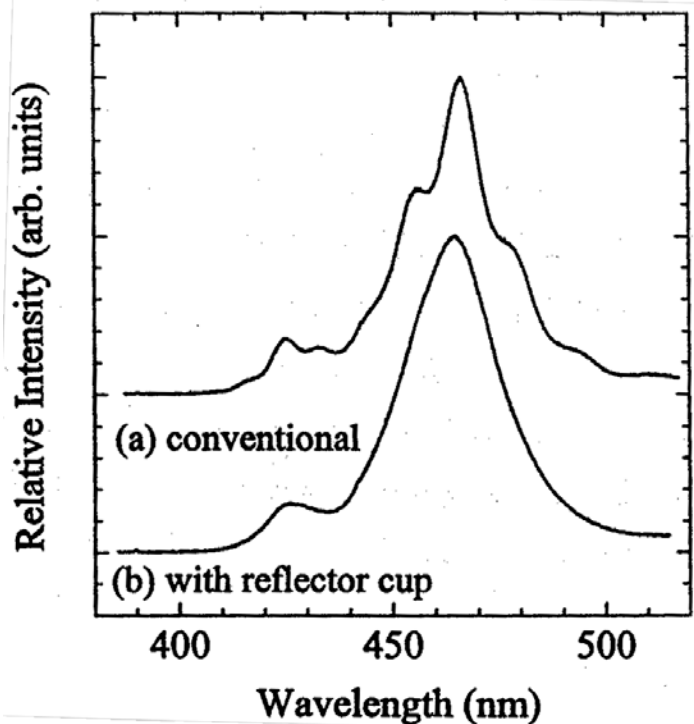
N.A.  
N.A.  
for  
and in  
to be  
low  
has to  
the  
an  
the  
which

Figure 3.3.4-(3) PL measurement system utilizing a reflector cup.

Thus, in order to eliminate the interference effect by increasing the N.A. of the detection system, we used a reflector cup such as the one shown in FIG. 3.3.4-(3). The reflector cup has a bottom face diameter of 8 mm and sidewalls inclined at an angle of approximately  $20^\circ$ , which allows it to guide a wide-angle component of the emission from the **aperture** of the condenser lens. In order to obtain a flat and high reflectance ratio in the desired wavelength region, the cup was electroplated with silver. In addition, the cup could be easily placed into the cryostat for temperature dependence measurements.

FIG. 3.3.4-(4) shows a typical example of PL measurements carried out on a blue LED sample. The figure shows emission spectra obtained in the case of (a) using an ordinary condenser lens with an N.A.= 0.1, and in the case of (b) conducting measurements using a reflector cup. In the case of ordinary measurements, the influence of interference on the spectrum is obvious and it is difficult to distinguish the original emission peak from interference. On the other hand, it is believed that in the case (b), in which a reflector cup was used, there is no influence from interference and the spectrum under measurement is the original spectrum. It can be seen that the spectrum of the emission is composed of a main peak with a central wavelength of 465 nm and a half-width of 150 meV and various peaks on the high-energy side (425 nm). With the exception of certain measurements, such as time resolved measurements, etc., emission spectrum measurements in the present study have been carried out by the method of 3.3.4-(3) in order to eliminate the influence of interference. A patent pending on the emission spectrum measurement method shown above (Emission spectrum measurement apparatus and measurement method, Japanese Patent Application JPA 2001-011214).

Figure 3.3.4-(4) (a) Measurement obtained using a conventional measurement system, (b) Measurement obtained using a reflector cup.



## 3.4 Results and Discussion

### 3.4.1 Investigation of Emission Characteristics of GaInN/GaN Quantum Well Structure LEDs with Different In Compositions

#### 3.4.1.1 Sample structure

Crystal growth was conducted by the MOVPE (Metalorganic Vapor Phase Epitaxy) method, and LED structures were fabricated on c-plane sapphire. The active layer was composed of Ga<sub>1-x</sub>In<sub>x</sub>N/GaN multiple quantum wells, with no doping in the quantum well layer and Si added to the barrier layer. The concentration of the Si dopant was approximately  $2\sim 3 \times 10^{18} \text{ cm}^{-3}$ . Based on the cross-sectional TEM observations, the thickness of the well layer was approximately 2 nm, and the thickness of the barrier layer was approximately 7.5 nm. In order to systematically investigate changes in the emission characteristics associated with the changes in the In composition of the GaInN active layer, we varied the In composition alone to prepare 3 samples with (a)  $x = 0.06$  ( $\lambda_p = 410 \text{ nm}$ ), (b)  $x = 0.18$  ( $\lambda_p = 445 \text{ nm}$ ), and (c)  $x = 0.22$  ( $\lambda_p = 475 \text{ nm}$ ). Beyond the In composition of the quantum wells, the three samples were identical in terms of the LED structure and crystal growth conditions. The emission wavelength shown here is the emission peak wavelength obtained when an electric current ( $20 \text{ mA/cm}^2$ ) was injected into the LEDs.

#### 3.4.1.2 Comparison of LED efficiencies

FIG. 3.4.1-(1) shows a comparison of efficiencies obtained when an electrical current (20 A/cm<sup>2</sup>) was injected into three LEDs. The values shown here are relative values of the external quantum efficiency normalized to the efficiency of the LED with  $x = 0.18$  (b). Because the highest efficiency among the three samples was obtained at  $x = 0.18$  (445 nm) it is believed that under the growth conditions used in the experiment, in the wavelength range from 410 nm to 175 nm, the efficiency is achieved by an LED with an emission wavelength of approximately 450 nm. The differences in the efficiencies obtained at this injection current correspond to the differences in the PL emission intensity, and are believed to be due to differences in the internal quantum efficiencies of GaInN quantum wells with different In compositions.

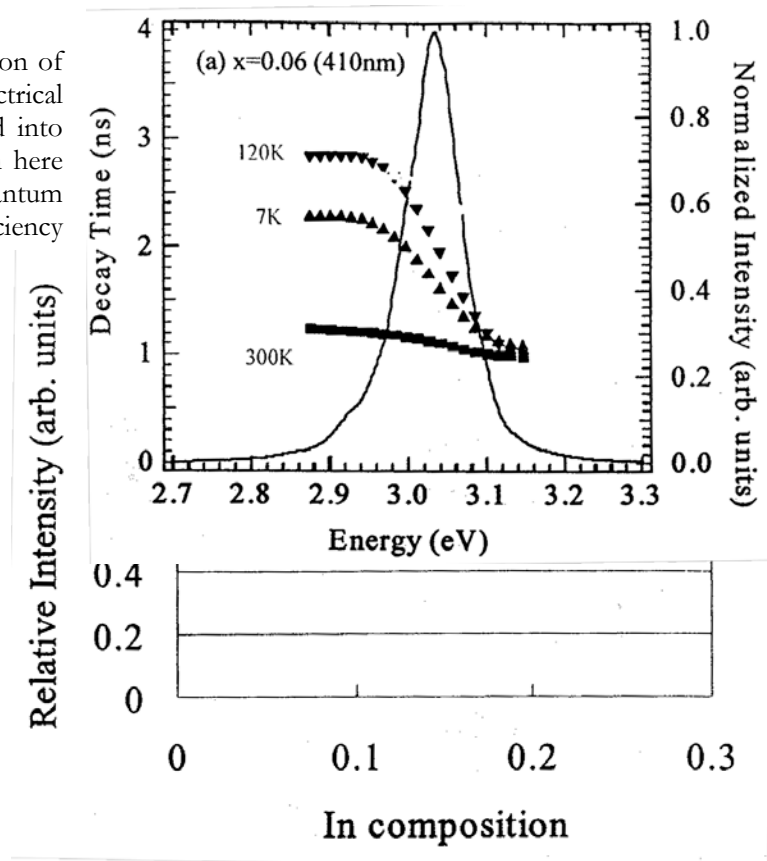


Figure 3.4.1-(1) Relative external quantum efficiencies of LED samples with different In compositions ((a)  $x = 0.06$ , 410 nm, (b)  $x = 0.18$ , 445 nm, (c)  $x = 0.22$ , 475 nm). Normalized to efficiency at 445 nm.

**3.4.1.3 Temperature dependence of emission lifetime**

Data on the PL excitation intensity dependence (emission peak energy shift, spectrum half-width) and time resolved PL measurements at room temperature were summarized in the 1999 Achievement Report.

Next, in order to investigate the localization state of carriers in each sample in detail we examined the temperature dependence of the emission lifetime. Measurements were carried out over a wide temperature range, from 7K to 540K. FIG. 3.4.1-(2) shows the dependence of the emission lifetime on the emission energy at various temperatures for sample (a) with  $x = 0.06$ . In this case, we defined the emission lifetime as the time required for the emission intensity to reach 1/e of the peak value, which appears to be somewhat different from the decay lifetime obtained by fitting. In particular, we believe that there will be different values in the decay waveform, which cannot be expressed using a single exponential function. However, here we are most interested in temperature-dependent emission lifetime changes and this won't present a problem for a discussion of the trend of the changes.

Figure 3.4.1-(2) Dependence of emission lifetime on the emission energy at various temperatures in the range of from 7K to 300K for LED (a) with  $x = 0.06$  (410 nm).

As can be seen from the figure, the dependence of the emission lifetime on the emission energy exhibits a characteristic behavior depending on the temperature. It is easier to understand if it is plotted in the same

manner as in FIG. 3.4.1-(3). FIG. 3.4.1-(3) shows the temperature dependence of the emission lifetime of the three LED samples at various emission energies of the emission spectrum ranging from low energies to high energies.

First of all, referring to figure (a) with  $x = 0.06$ , temperature-dependent changes in the emission lifetime can be divided into three regions: I, II, and III. In region I (7K~90K), the difference between the emission lifetime on the high-energy side and low energy side of the emission spectrum increases with increasing temperature. In region II (120K~240K), the large difference between the emission lifetime on the high-energy side and low energy side decreases with increasing temperature and the curve of emission lifetime versus emission energy becomes almost flat. In region III (240K~540K), the emission lifetime, whose curve is now almost flat, rapidly becomes very short as the temperature increases.

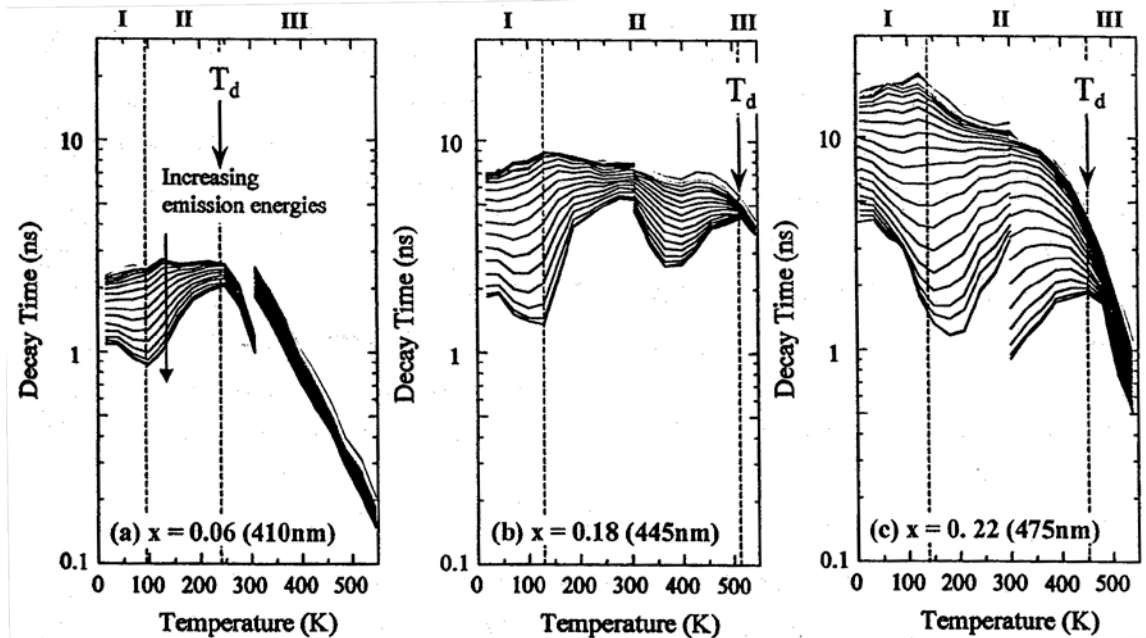
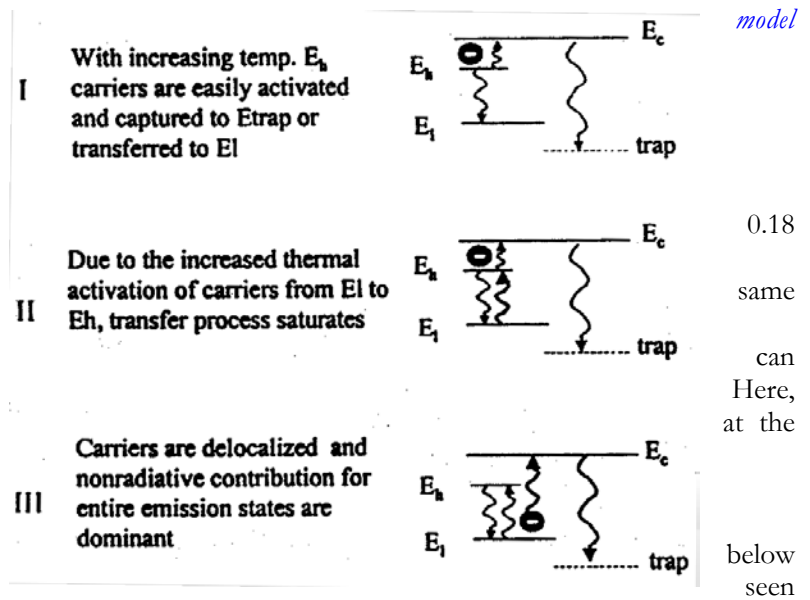


Figure 3.4.1-(3) Dependence of emission lifetime on temperature at various emission energies in the low energy portion and high energy portion of the emission spectrum for various LEDs. (a)  $x = 0.06$  (410 nm), (b)  $x = 0.18$  (445 nm), (c)  $x = 0.22$  (475 nm).

It is believed that the temperature-dependent changes in the emission decay time can be explained by changes in the localization state of carriers. Although Si was added to the barrier layers of these LED samples in the amount of approximately  $2\sim 3 \times 10^{18} \text{ cm}^{-3}$  and the influence of the piezoelectric effects in the quantum wells could be considered moderated to a certain degree, it is believed that the influence of the piezoelectric effects was still affecting the emission lifetime differences between the samples with different In compositions. However, because the temperature dependence of the piezoelectric effects is believed to be negligibly small, we think that the trend of the temperature dependence of the emission lifetime can be discussed by primarily taking into consideration the changes in the localization state of carriers.

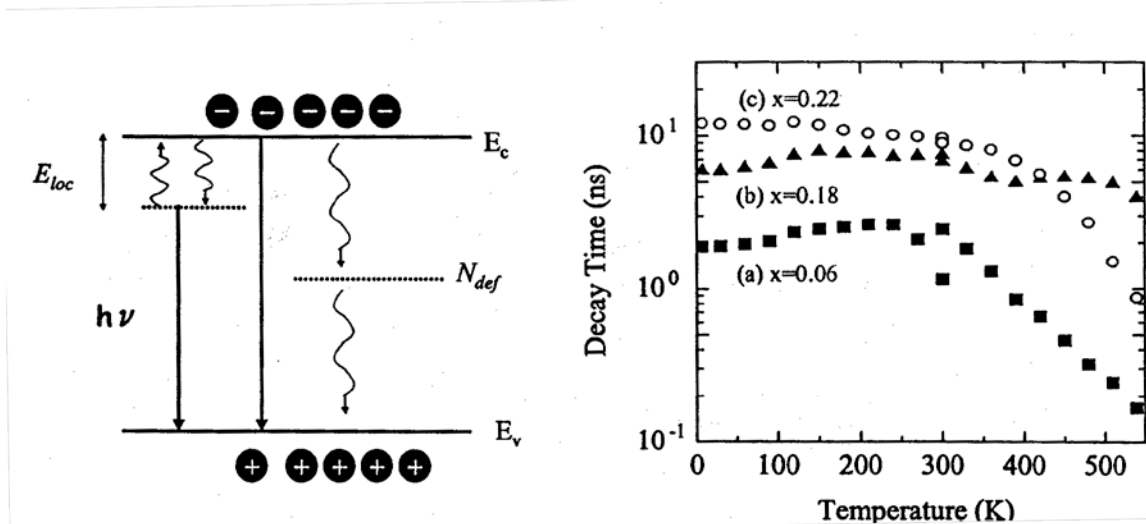
One possible model is illustrated in FIG. 3.4.1-(4), which is explained hereinbelow. First of all, in region I, as the temperature increases from low temperatures, in the localization level distribution inside the band, carriers possessing particularly high energy levels get delocalized first, and the percentage of carriers captured into non-radiative recombination centers increases. Thus, at first, high-energy lifetime becomes shorter as the temperature rises. Furthermore, in region II, which is characterized by an elevated temperature, carriers in a deep localized state are thermally excited and undergo a transition to a high-energy level. As a result, observation shows that, conversely, the lifetime on the high-energy side tends to increase. In region III, the lifetime becomes shorter for all emission energies, which is believed to indicate that almost all carriers that were in a localized state have been delocalized by thermal excitation and the proportion of carriers captured into non-radiative recombination centers such as dislocations and point defects rapidly increases.

Figure 3.4.1-(4) Conceptual diagram of used for explanation of emission lifetime changes in temperature regions I, II, III.



As concerns samples with different In compositions, in case of (b) with  $x = 0.18$  and (c) with  $x = 0.22$ , which are shown in FIG. 3.4.1-(3), basically the three temperature regions are observed and it is believed that they can be explained using the same model. Here, at the discontinuity of the data observed temperature of 300K is due to a difference in the excitation intensity associated with different experimental conditions in the temperature region 300K and above 300K. As can be seen from FIG. 3.4.1-(3), the temperatures corresponding to the boundaries between the regions increase as the In composition increases. In particular, the temperature that marks the transition from region II to region III is believed to be the temperature at which a transition from a localized state of carriers to a delocalized state takes place. If we designate this temperature as  $T_d$ , then in case of (a)  $T_d = 240K$ , and in case of (b) with  $x = 0.18$  and (c) with  $x = 0.22$  the value of  $T_d$  increases to approximately 450K~510K.

Next, in order to investigate the physical parameters governing the changes in the temperature dependence of the emission lifetime shown in FIG. 3.4.1-(3), we calculated the temperature dependence of the carrier lifetime from a rate equation based on a simple model assuming a density  $N_{def}$  of non-radiative recombination centers and an energy depth  $E_{loc}$  of localized level in the band, as shown in FIG. 3.4.1-(5). First of all, we used the values of FIG. 3.4.1-(3) to plot the temperature dependence of the emission lifetime of the three samples at the emission peak energy only in FIG. 3.4.1-(6). In case of (a) with  $x = 0.06$ , the emission lifetime rapidly decreased starting in the vicinity of 240K, whereas samples (b) and (c), which had different In compositions, exhibited a flat characteristic up to 400K. What we would like to point out here is that when (b) with  $x = 0.18$  and (c) with  $x = 0.22$  were compared, the degree of decrease in emission lifetime at temperatures above  $T_d$  was conspicuously larger for (c) with  $x = 0.22$ .



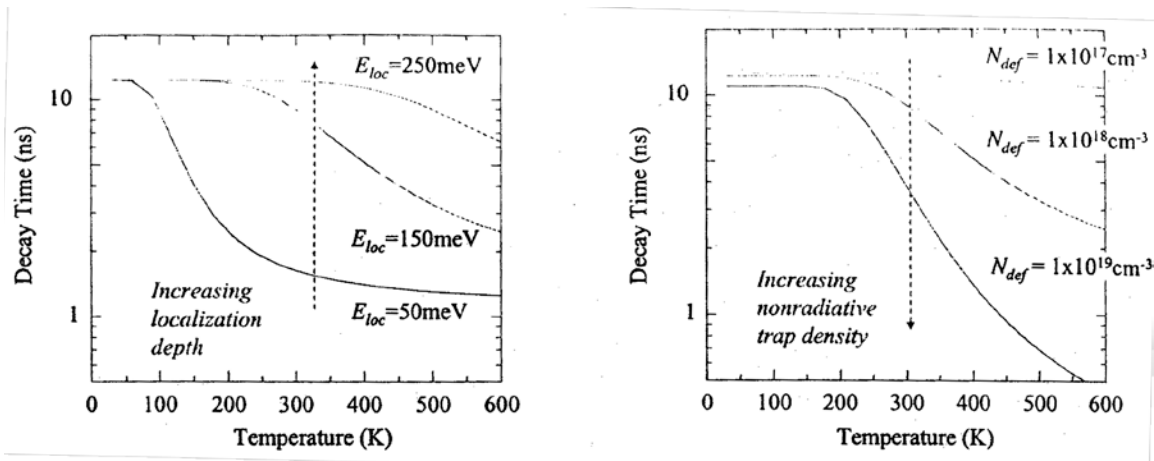
Left: Figure 3.4.1-5) Simulation model based on presence of non-radiative recombination centers and localization levels inside band.

Right: Figure 3.4.1-6) Temperature dependence of emission lifetime at emission peak energy for different LEDs.

An explanation of the simulation results is provided next. However, here we will focus our attention only on the energy depth  $E_{loc}$  of the localized level and the density  $N_{def}$  of the non-radiative recombination centers, while substituting values obtained from literature or values considered appropriate for other parameters used in the rate equation. Here, we investigated the contribution of the two parameters,  $E_{loc}$  and  $N_{def}$ , to temperature-dependent changes in the emission lifetime based on a comparison between the data obtained by measurement and the results of calculation of the temperature dependence of the carrier lifetime associated with changes in  $E_{loc}$  and  $N_{def}$ , and did not quantitatively estimate the parameters by fitting etc.

FIG. 3.4.1-7) represents results of calculation of the carrier lifetime at the localized level in the case where  $E_{loc}$  was varied and  $N_{def}$  remained constant at  $N_{def} = 1 \times 10^{18} \text{ cm}^{-3}$ . From the figure, it is evident that as the energy depth of the localized level increases, the temperature at which a rapid decrease in the emission lifetime starts increases. The temperature at which the decrease in the emission lifetime starts corresponds to the temperature  $T_d$  (the temperature marking the boundary between region II and region III) defined in FIG. 3.4.1-3), which leads us to believe that the energy depth of carrier localization increases with the increase in the In composition.

In addition, FIG. 3.4.1-8) shows the results of carrier lifetime calculations, in which  $N_{def}$  was varied at a constant  $E_{loc} = 150 \text{ meV}$ . From this figure, it is evident that as  $N_{def}$  increases, the tendency towards emission lifetime decay associated with a temperature increase in the region above  $T_d$  increases. Based on the fact that, as shown in FIG. 3.4.1-6), the tendency towards emission lifetime decay at temperatures higher than 400K is greater for sample (c) with  $x = 0.22$  than for sample (b) with  $x = 0.18$ , it is believed that the density of non-radiative centers in sample (c) with  $x = 0.22$  is increased. Because the crystal growth conditions of the three samples are practically the same with the exception of the In composition, the threading dislocation density of the crystals is a constant. Therefore, the increase in the non-radiative recombination center density is believed to be due to an increase in the point defect density associated with the increase in the In composition.



Left: Figure 3.4.1-(7) Temperature dependence of emission lifetime obtained by varying localization level energy depth ( $E_{loc}$ ) at constant non-radiative recombination center density ( $N_{def} = 1 \times 10^{18} \text{ cm}^{-3}$ ).

Right: Figure 3.4.1-(8) Temperature dependence of emission lifetime obtained by varying non-radiative recombination center density ( $N_{def}$ ) at constant localization level energy depth ( $E_{loc} = 150 \text{ meV}$ ).

The fact that sample (b) with  $x = 0.18$  exhibits the maximum value at the LED efficiency shown in FIG. 3.4.1-(1) and the result that its emission lifetime remains practically constant all the way to the high temperature region are in agreement from a qualitative standpoint. Generally speaking, it is believed that if the In composition increases and the energy of carrier localization increases, the percentage of carriers captured into defects decreases and the quantum efficiency increases, but because point defects exhibit a tendency to increase with increasing In composition, in case of sample (c) with  $x = 0.18$  the efficiency drops in comparison with sample (b) with  $x = 0.18$ . Based on the above, it is believed that the localization energy and the point defect density act as the controlling parameters of the quantum efficiency of the LEDs.

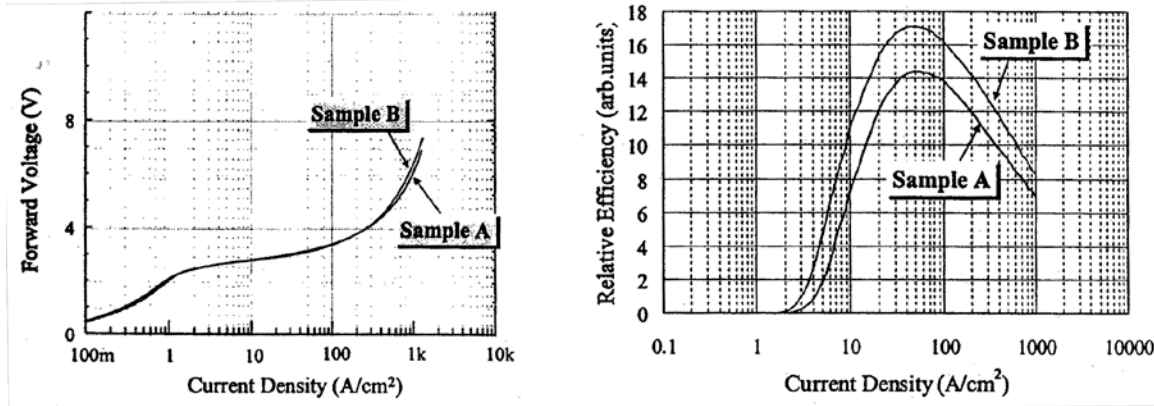
### 3.4.2 Investigation of Emission Lifetime Characteristics of LEDs with Different Emission Efficiencies

In 3.4.1 we discussed the emission lifetime characteristics and the carrier localization state. Here, based on these results and the results of measurements of the temperature dependence of the emission lifetime for LED samples with different emission efficiencies, we will discuss the influence of the carrier localization state on the emission efficiency.

Two LED samples (Sample A and Sample B) were prepared, which had an emission wavelength of 470 nm, an identical quantum well structure, and different emission efficiencies. Their basic structure was identical to the structure of the samples investigated in 3.4.1, the quantum well layer thickness being approximately 2 nm, the barrier layer thickness being approximately 7.5 nm, and the concentration of Si added to the barrier layers being approximately  $2 \sim 3 \times 10^{18} \text{ cm}^{-3}$ . The difference between Samples A and B consisted in the n-type layers that preceded the growth of the active layers.

The current-voltage characteristics (I-V characteristics) of the two LEDs are shown in FIG. 3.4.2-(1). Because there are no significant differences between the I-V characteristics of Samples A and B, the differences in the structure of the n-type layers obviously do not influence their electrical transmission characteristics. FIG. 3.4.2-(2) shows the relative external quantum efficiencies of Samples A and B as functions of the injection current density. The quantum efficiencies shown in the figure are used to compare the relative differences between the two samples, with the values indicated being different from the external quantum efficiencies obtained when measurements are carried out using ordinary resin moldings. In both cases the position of the peaks of efficiency is at approximately  $40 \sim 50 \text{ A/cm}^2$ , with the efficiency of sample B being approximately 20% higher in comparison with sample A at the position of the efficiency peaks. In

addition, the efficiency of sample B is approximately twice as high as that of sample A in the low current region starting at 5 A/cm<sup>2</sup>.



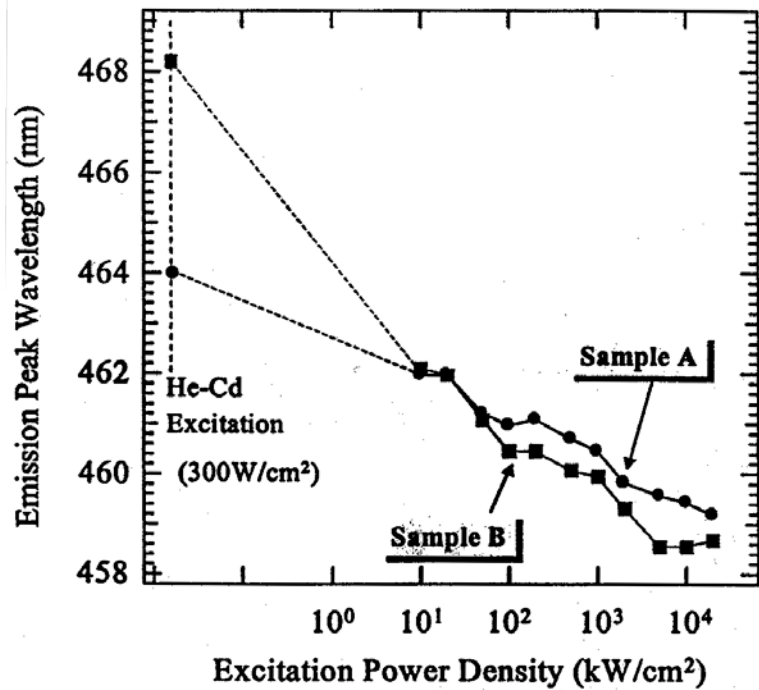
Left: Figure 3.4.2-(1) Voltage-current density characteristics of Samples A and B.

Right: Figure 3.4.2-(2) External quantum efficiency-current density characteristics of Samples A and B.

FIG. 3.4.2-(3) shows the dependence of the PL spectrum peak position on the excitation intensity under weak excitation (300 W/cm<sup>2</sup>) using a He-Cd laser and strong excitation (10k~2×10<sup>4</sup> kW/cm<sup>2</sup>) using a Xe-Cl laser. In this excitation intensity range, the emission peak of sample A undergoes a five-nm shift towards shorter wavelengths while a considerably larger peak shift of about 10 nm is observed in case of sample B.

Figure 3.4.2-(3) Dependence of PL emission peak wavelength on excitation intensity for sample A and sample B.

Next, we carried out measurements of the temperature dependence of the emission lifetime characteristics based on time-resolved PL measurements. FIG. 3.4.2-(4) shows the dependence of the emission lifetime of samples A and B at room temperature on the emission energy. In both cases the emission lifetime is shorter in the high-energy portion and in the low-energy portion, and expected that carriers undergo relaxation (localization) from high-energy side to the low-energy side. In particular, in the case of sample B, the energy dependence of the emission lifetime is more noticeable, the emission lifetime on the low-energy side being as long as 25 ns.



longer  
it is  
the  
case  
with  
low-  
ns.

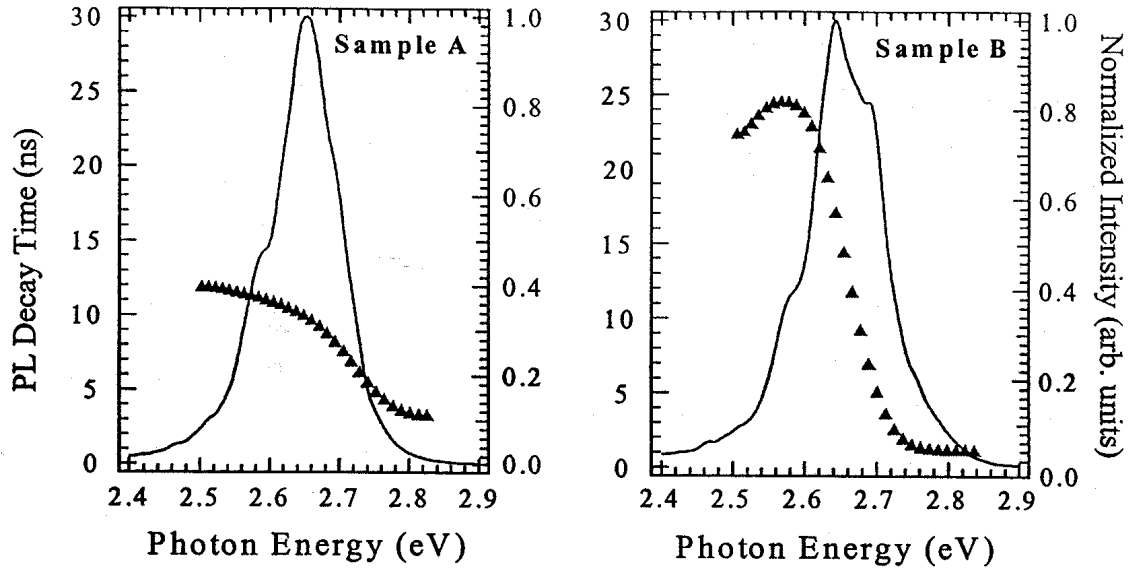


Figure 3.4.2-(4) Dependency of emission lifetime on emission energy at room temperature for sample A and sample B.

Next, FIG. 3.4.2-(5) shows the dependence of the emission lifetime on temperature (7K~300K) at various emission energies of the emission spectrum ranging from the low-energy side to the high-energy side. The energy interval between the curves in figure is 10 meV.

First of all, in the case of sample A, in the range between low temperatures and approximately 150K, the energy dependency of the emission lifetime increases, and when the temperature increases further, the energy dependence decreases. On the other hand, in case of sample B, with the exception of the data discontinuity at 120K, the energy dependency of the emission lifetime increases practically monotonically. Therefore, it is evident that, in this temperature range, both temperature regions I and II defined in FIG. 3.4.1-(3) are observed in case of sample A and only region I is observed in case of sample B. The model discussed in Section 3.4.1 points to a considerable energy depth of carrier localization in case of sample B.

This phenomenon qualitatively corresponds to the large peak shift observed in sample B. Although the mechanism whereby the difference in the n-type underlayer structures of sample A and B exerts influence on the localization energy is unclear, it is believed that in the highly efficient sample B, from the standpoint of energy, carriers are localized deeper, and their transition to non-radiative recombination centers is suppressed.

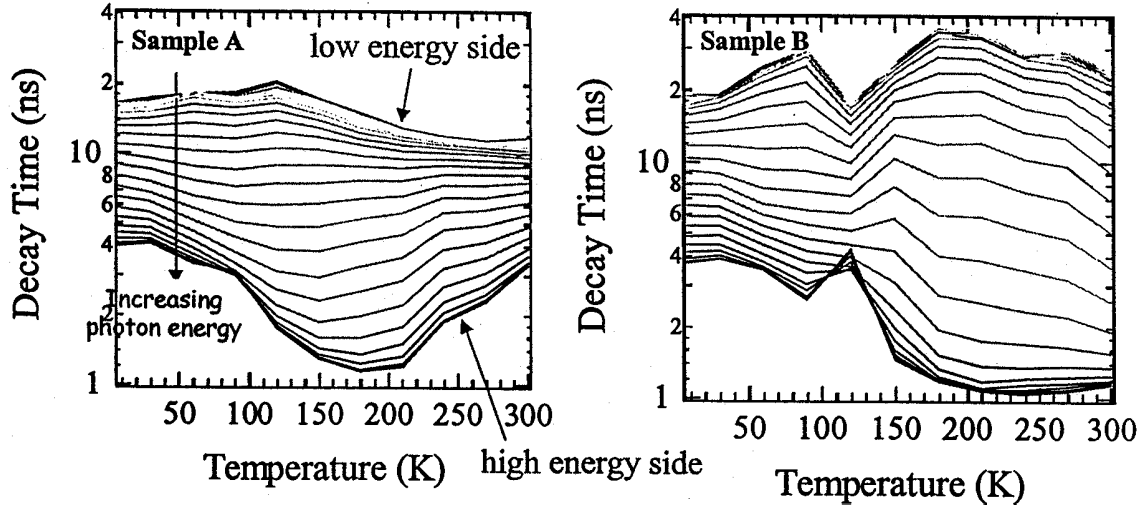


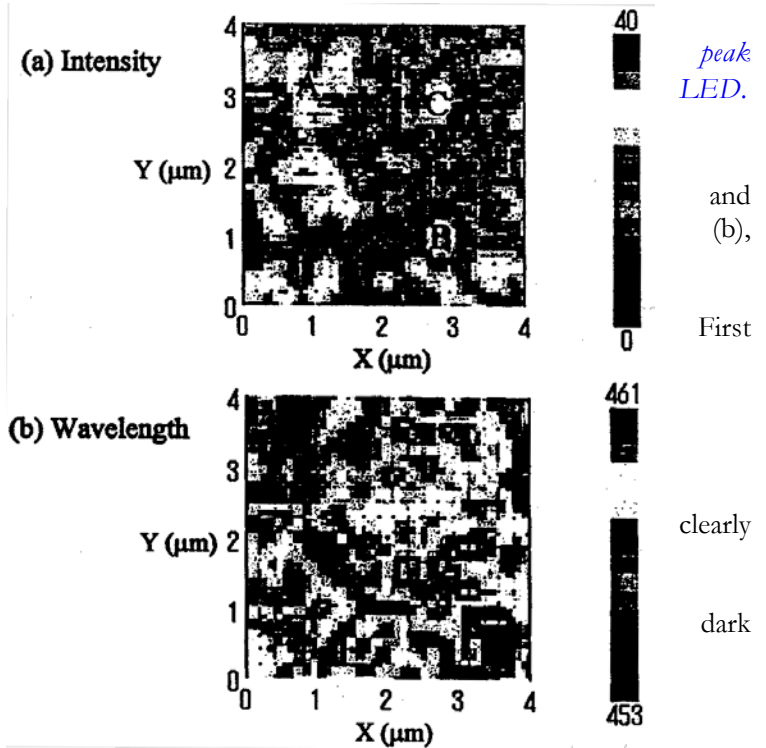
Figure 3.4.2-(5) Dependency of emission lifetime on temperature at various emission energies ranging from low-energy portion to high-energy portion of light emission for sample A and sample B.

### 3.4.3 Investigation of In-Plane Distribution of Light Emission

In 2000 we introduced a near-field probe PL system, shown in FIG. 3.3.3-(1), in order to measure the in-plane distribution of light emission with high spatial resolution. Here, in order to obtain basic data, we carried out measurements using typical multiple quantum well LEDs with an emission wavelength of 460 nm. For excitation, we used a He-Cd laser (441 nm), which allowed for selective excitation of the quantum well active layer in the LED samples. The PL mapping measurements were conducted at room temperature using 20×20 points in a 4 μm×4 μm region.

Figure 3.4.3-(1) (a) Distribution of PL emission intensity, and (b) distribution of PL wavelength in a 4 μm×4 μm region of a blue

The emission intensity distribution (a) and the emission peak wavelength distribution which were calculated from the PL spectra obtained in each measurement position, are shown in FIG. 3.4.3-(1). In all, we examined the in-plane distribution of the emission intensity shown in (a). It was confirmed that the instability of the system at the time of measurement was insignificant and it is believed that the distribution measured showed the in-plane distribution of the emission intensity. The intensity distribution was observed as light and dark regions with a size of approximately 0.3~0.5 μm. The respective spectra in positions A, B, and C inside the measurement region are shown in FIG.



(2). The figure shows that, in comparison with the position of maximum intensity, the PL intensity in low-level positions constituted approximately 25%.

Also, in case of the peak wavelength distribution (b), a distribution of approximately 8 nm could be seen in-plane, and it could be appreciated from a comparison with the emission intensity distribution (a) that in regions showing emission at long wavelengths the intensity of light emission tended to be higher. These results indicated that there was a clear in-plane distribution of light emission of a submicron size.

The data shown here are preliminary data, order to correctly interpret the measurement data, it is necessary to accumulate further data including confirmation of reproducibility. At present, we are conducting evaluation of samples with different efficiencies or wavelengths and carrying out detailed investigations into the relationship between in-plane distribution of light emission and efficiency of LEDs.

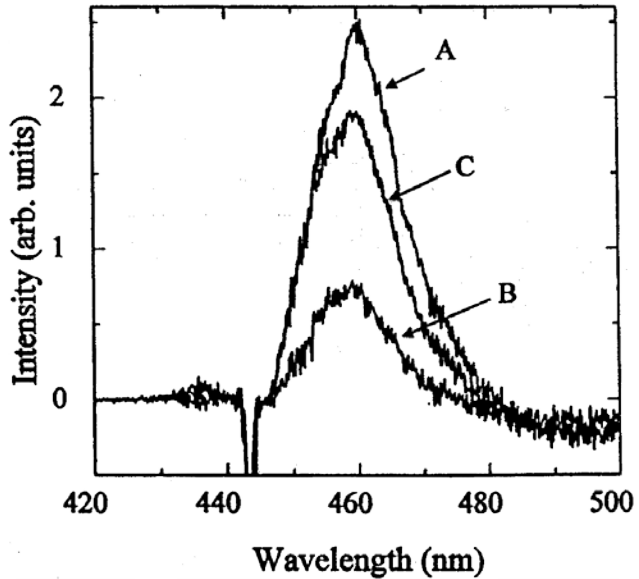


Figure 3.4.3-(2) Emission spectra in various positions. "A," "B," and "C" correspond to shown in FIG. 3.4.3-(1).

and in  
the  
the  
points

### 3.4.4 Reverse Bias PL Characteristics of Si-Doped Quantum Well LEDs

#### 3.4.4.1 Sample structure

As mentioned in the 1999 Report, it was found that the addition of Si to quantum wells was important in the elimination of the internal electric field applied to quantum wells [5]. However, because in the case of LED structures the addition of Si to quantum wells exerts influence on the band structure of the pn junction, it is necessary to investigate the influence of Si doping with account taken of the device characteristics. Thus, we conducted an investigation into the effects of the addition of silicon to quantum wells in LED structures.

The samples were multiple quantum well LEDs with an emission center wavelength of approximately 510 nm, a quantum well width of 2.5 nm, a barrier layer width of 15 nm, and a quantum well number of four. The In composition of the quantum well layer was estimated to be  $x=0.23$ . We prepared sample C, in which the concentration of silicon added to the barrier layer was  $4 \times 10^{17} \text{ cm}^{-3}$ , and sample D with a concentration of  $4 \times 10^{18} \text{ cm}^{-3}$ . The quantum well layer was not doped. In addition, the concentration of Si (donors) in the n-type layers of the LEDs was approximately  $5 \times 10^{18} \text{ cm}^{-3}$  and the concentration of Mg (acceptors) in the p-type layer was approximately  $5 \times 10^{19} \text{ cm}^{-3}$ .

#### 3.4.4.2 Measurement of depletion layer width

In order to estimate the external electric field applied to the quantum wells under reverse bias, we estimated the depletion layer width from measurements of the depletion layer capacitance. FIG. 3.4.4-(1) shows the results (a) of measurements of the depletion layer capacitance under reverse bias for samples C and D. In addition, (b) shows the depletion layer width estimated from the depletion layer capacitance based on the formula:

$$L = \epsilon_0 \epsilon \frac{S}{C} \quad (6)$$

Here, the area of the pn junction was  $S = 9 \times 10^{-4} \text{ cm}^2$ , and the value for GaN,  $\epsilon = 8.9$ , was used as the dielectric constant. The results show that the higher the donor concentration of the quantum wells, the narrower the depletion layer width, and, as a result, the higher the junction capacitance.

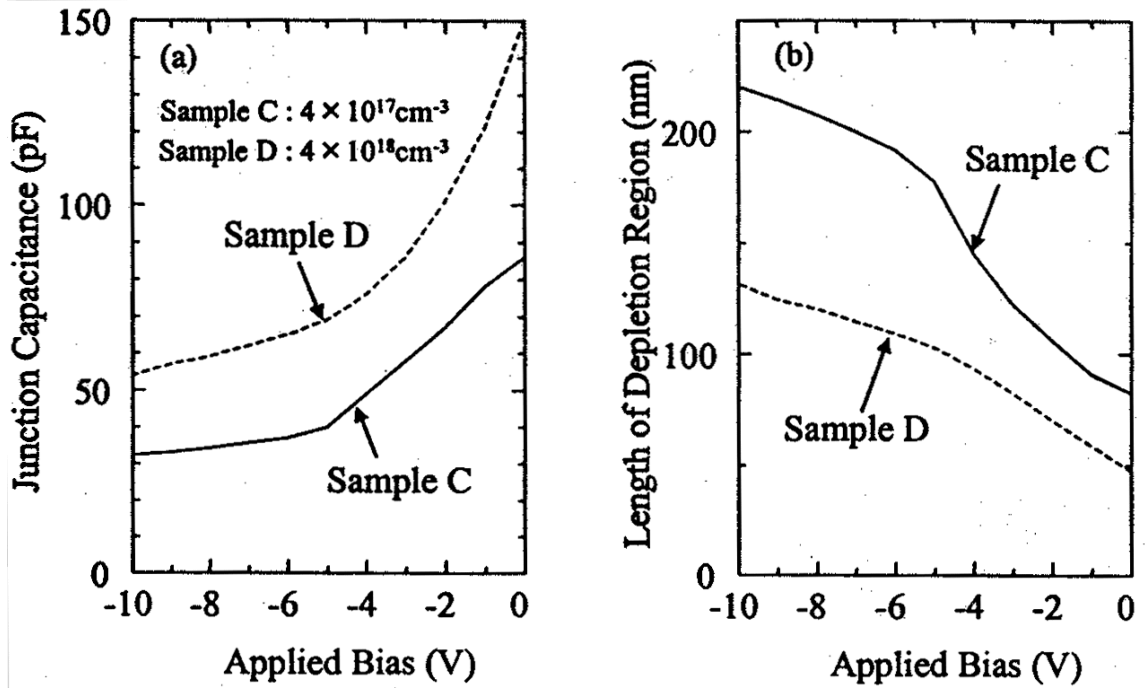


Figure 3.4.4-(1) (a) Changes in pn junction depletion layer capacitance, and (b) changes in depletion layer width under reverse bias in LED samples C and D.

The depletion layer width of samples C and D under zero bias was, respectively, approximately 82 nm and 47 nm. In the case of sample C the width was practically equal to the multiple quantum well active layer width of 85 nm, which shows that the quantum well region had been practically depleted. On the other hand, because in case of sample D the depletion layer constituted approximately 50% of the quantum well region, we expected half of the quantum wells to be depleted, and half of them to be n-type.

#### 3.4.4.3 PL measurements under reverse bias

Changes in the PL spectrum associated with the application of a reverse bias are shown in FIG. 3.4.4-(2). The wavelength of the laser used for excitation was 400 nm, which was the condition of selective excitation for the quantum wells of the sample. The measurements were carried out at 77 K. Spectrum measurements were carried out under conditions preventing the influence of the interference. A shift towards the high-energy side of the spectrum associated with the applied bias is clearly observed in the case of sample C. On the other hand, in the case of sample D, the measurements were carried out under the same conditions, but a large spectral width was observed at 0V and multiple peaks appeared as the applied bias increased. However, no noticeable peak shift was observed. Changes in the emission peak energy associated with the applied external electric field are shown in FIG. 3.4.4-(3). Here, the bias voltage is applied to the depletion layer width estimated in FIG. 3.4.4-(1) and the x-axis of the diagram represents the external electric field applied to the quantum well layer. In addition, as far as the bias of the external electric field is concerned, the forward direction of the pn junction (from the surface to the substrate) was considered as positive. In other words, the gradient of the applied external electric field was the same as the gradient of the internal electric field.

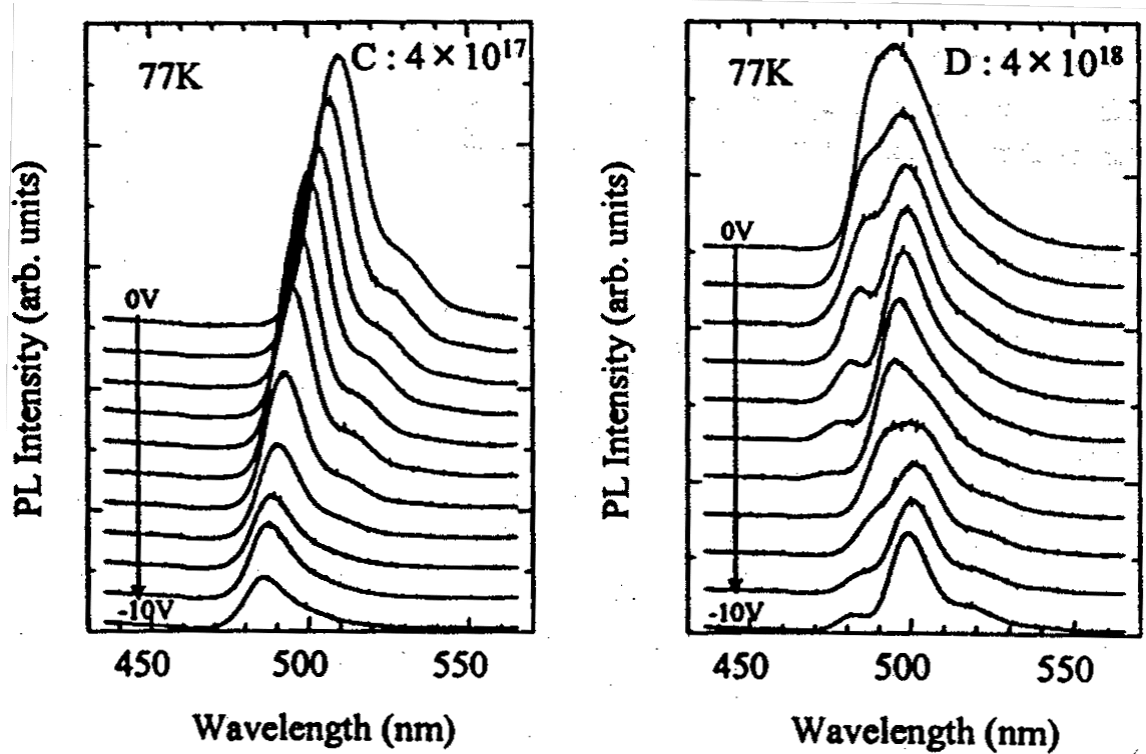
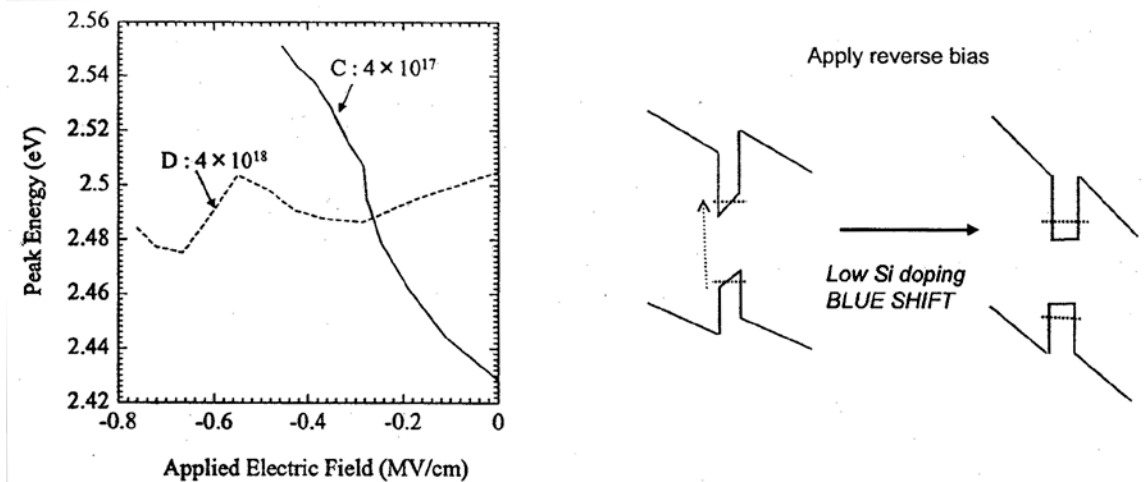


Figure 3.4.4-(2) Dependence of PL spectra on reverse bias at 77 K. (a) Sample C ( $4 \times 10^{17} \text{ cm}^{-3}$ ), (b) Sample D ( $4 \times 10^{18} \text{ cm}^{-3}$ ).

In the case of sample C, the emission peak exhibited a shift of approximately 110 meV towards the high-energy side when the external electric field ranged from zero to approximately  $-0.4 \text{ MV/cm}$ , whereas in case of sample D there was a shift of approximately 25 meV towards the low-energy side when the external electric field ranged from zero to approximately  $-0.7 \text{ MV/cm}$ . Figure 3.4.4-(4) shows a conceptual diagram of changes in the band structure associated with the application of an external electric field in sample C. Because in sample C the emission peak shifts towards the high-energy side following the application of an external electric field of the same direction as the internal electric field, it is believed that the band in the quantum wells biased by the internal electric field was close to a flat band. This phenomenon is in good agreement with the previous report [7], in which it was indicated that the piezoelectric field due to the strain within the quantum wells of GaInN was oriented in a direction opposite to the direction of the internal electric field (from the surface to the substrate).

Next, in order to estimate the piezoelectric field present in the quantum wells, we performed fitting to transition energy obtained by calculation. Results obtained for sample C are shown in FIG. 3.4.4-(6). However, as for calculations of the transition energy associated with the application of the bias, at present we are conducting further detailed investigations and the results presented here are merely preliminary results. For fitting, we used an In composition of  $x = 0.23$ , and the estimated piezoelectric constant was a value constituting 40% of the value reported by Bernardini *et al.* [8]. Based on this, the piezoelectric field in the quantum wells was determined to be approximately  $1.48 \text{ MV/cm}$ . Here, the estimated value is close to the values reported previously [7, 9, 10].



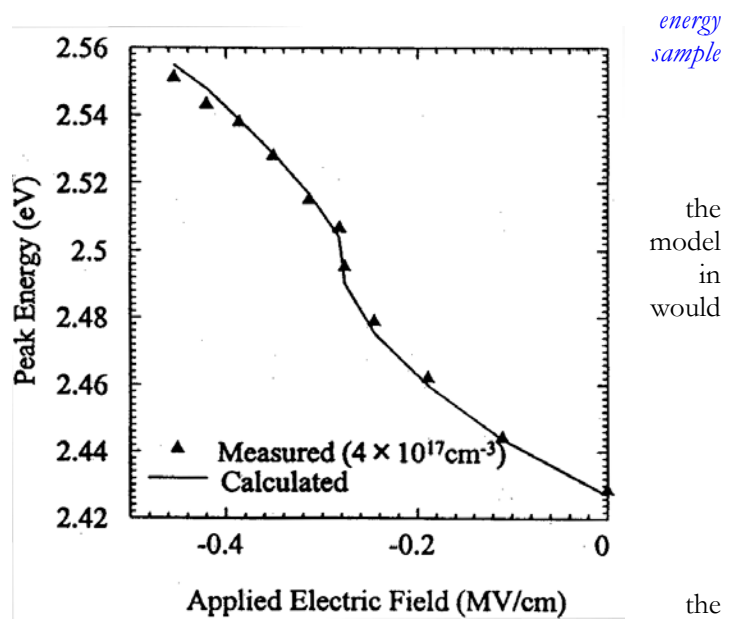
Left: Figure 3.4.4-(3) PL peak energy shift versus applied electric field for LED sample C and D.

Right: Figure 3.4.4-(4) Schematic diagram illustrating changes in band structure associated with application of external electric field in quantum wells of sample C with low Si doping.

On the other hand, in case of sample D with a high silicon doping concentration, as expected based on the measurements of the depletion layer width, the electric field in almost half of the quantum wells under zero bias is canceled by free electrons. However, it is believed that in the remaining half of the quantum wells depletion takes place and the band is biased by the internal electric field. It is believed that these quantum wells possess different emission transition energies, and as a result, under zero bias, as shown in FIG. 3.4.4-(2), a wide spectrum was observed. When the reverse bias is applied, in quantum wells that have been depleted under zero bias, the transition energy becomes higher due to the cancellation of the internal electric field and in those quantum wells that have not been depleted (in which the internal electric field has been screened by free electrons) depletion takes place with the increase in the reverse bias and the emission transmission energy becomes lower. Therefore, it is believed that there was practically no change in the overall emission peak energy.

Figure 3.4.4-(5) Results of fitting of transition versus external electric field for quantum wells of C with low Si doping.

FIG. 3.4.4-(6) shows the PL intensity (a), photocurrent (b), and dark current (c) observed when a reverse bias is applied to two samples. Based on the band structure shown in FIG. 3.4.4-(4), it was expected that case of sample C the internal electric field be canceled and the PL intensity would increase with the increase in the reverse bias. However, in the same manner as in the previously reported results [7], the PL intensity decreased with the increase in the applied reverse bias. It is believed that this decrease in the PL intensity can be understood based on an increase in the photocurrent, where carriers excited inside quantum wells are caused to drift by the electric field and the proportion of the carriers contributing to the



energy sample

the model in would

the

photocurrent increases. In addition, the increase in the dark current associated with the reverse bias in the entire photocurrent is negligibly small.

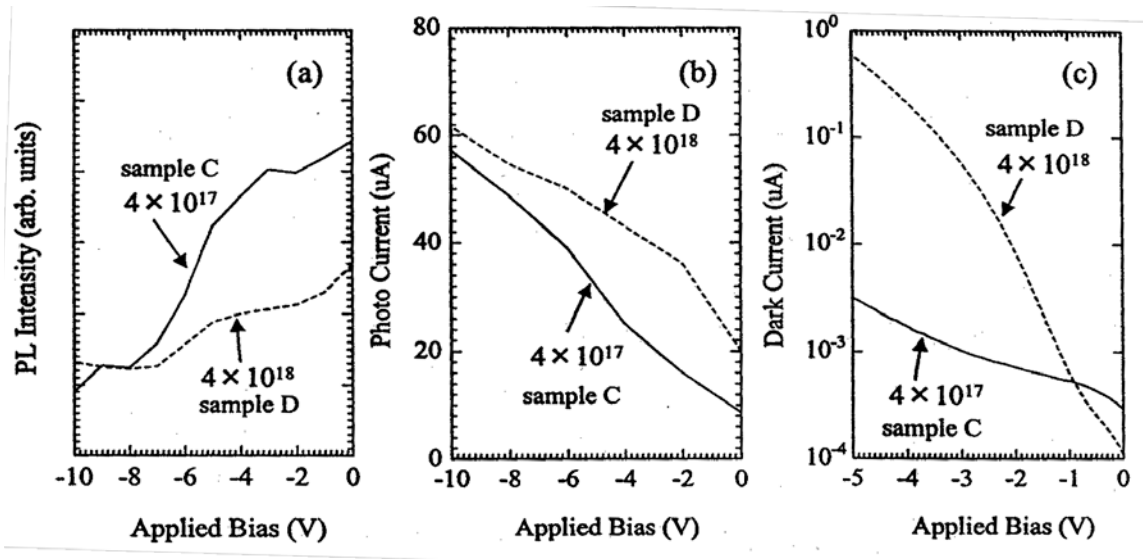


Figure 3.4.4-(6) Changes in (a) PL intensity, (b) photocurrent, (c) dark current versus applied reverse bias for LED samples C and D.

#### 3.4.4.4 Time resolved PL measurements under bias

Subsequently, we conducted measurements of the PL lifetime associated with the application of the reverse bias. The measurements were conducted at 77K using an excitation wavelength of 400 nm and an excitation intensity of  $3.5 \mu\text{J}/\text{cm}^2$ . FIG. 3.4.4-(7) shows changes in the time-resolved spectrum of the PL peak and FIG. 3.4.4-(8) shows the emission lifetime. The emission lifetime of sample C under zero bias was as long as 52 ns and became as short as approximately 10 ns when a bias of  $-10$  volts was applied. On the other hand, when a bias of  $-10$  volts was applied in case of sample D, the emission lifetime, which had been approximately 10 ns under zero bias, reached approximately 14 ns, that is, it became slightly longer.

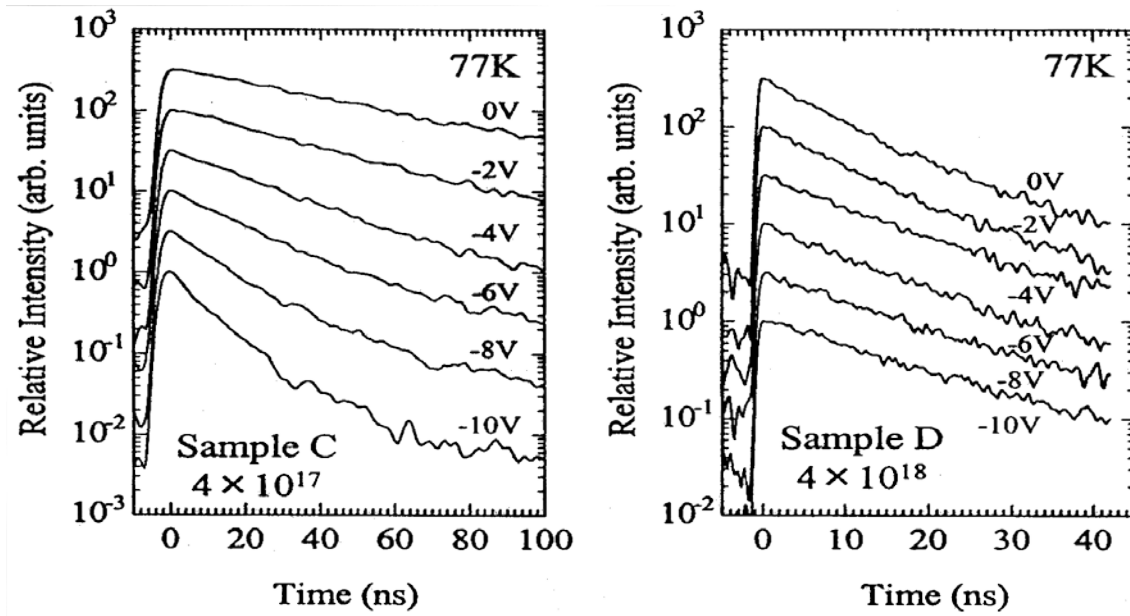


Figure 3.4.4-(7) Dependence of time resolved spectra on reverse bias for (a) sample C and (b) sample D.

It is believed that the factors that contribute to the changes in the carrier lifetime associated with the application of the reverse bias are primarily (1) changes in the emission lifetime associated with the changes in that internal electric field in quantum wells, (2) the increase in the photocurrent due to carrier leakage from inside the quantum wells, and (3) the dependence of the non-radiative recombination process on the bias. As shown in FIG. 3.4.4-(6), there are no extreme differences between the bias-dependent changes in the PL intensity and the photocurrent of the two samples, and, for this reason, it is believed that the conspicuous differences in the PL lifetime changes shown in FIG. 3.4.4-(8) are governed by the contribution of (1) the internal electric field (changes in the emission lifetime due to the biasing of the band).

The above described PL measurements under reverse bias permits the conclusion that the addition of silicon to the active layer is important in canceling the internal electric field but because it affects the widening of the depletion layer in the pn junction, the determination of its optimal value is extremely important.

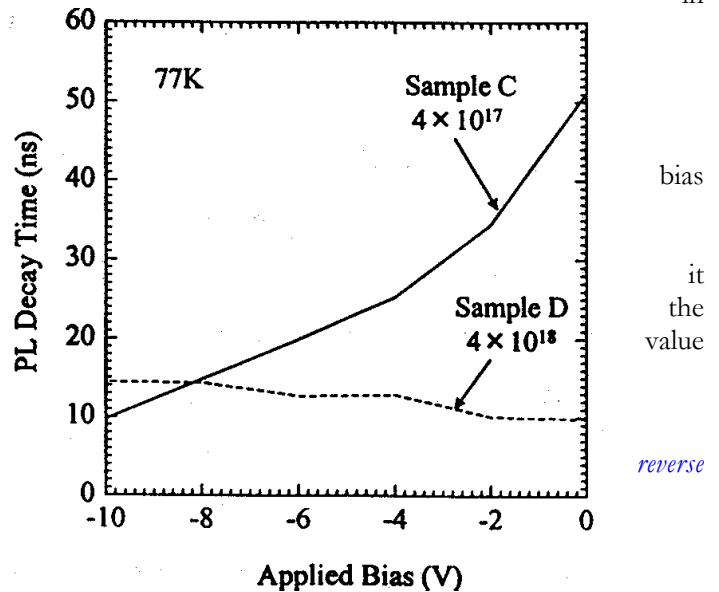


Figure 3.4.4-(8) Dependence of PL lifetime on reverse bias for (a) sample C and (b) sample D.

## 3.5 Summary

Just as in 1999, in 2000 we continued systematic investigations concerning the emission characteristics of GaInN/GaN quantum well structures in connection with the crystal growth parameters or structure. The results are summarized below.

1) Based on the investigations of the emission properties of GaInN conducted by numerous research organizations, it is believed that the key to the elucidation of the emission mechanism consists in the effect of spatial localization of carriers in GaInN. The emission characteristics (in particular, carrier localization effects) of GaInN are believed to be strongly dependent on the In composition, and for this purpose it is important to conduct a systematic evaluation of samples with different In compositions. For this reason, we conducted a systematic investigation into light emission characteristics of GaInN/GaN quantum well LEDs with different In compositions (emission wavelengths) over a wide temperature range (7K~540K). As a result, it was shown that the temperature dependence of the emission lifetime was split into three temperature regions and this temperature dependence could be explained by changes in the localization state of the carriers. In addition, based on simulation using a simplified localization level model, it was found that, with increasing In composition, the localization energy of the carriers increases, and, on the other hand, the point defect density increases as well. Based on a correlation between the In composition-induced differences in the temperature dependences of the emission lifetime and the quantum efficiencies of the LEDs, it is believed that the localization energy and the point defect density act as the controlling parameters of LED efficiency.

2) In order to examine the relationship between the carrier localization characteristics and the quantum efficiency, we conducted PL and time-resolved PL measurements on two LED samples with identical emission wavelengths and different quantum efficiencies. As a result, it was found that in the sample that had a high quantum efficiency there was a large shift of the PL peak towards the high-energy side associated with the excitation intensity, a considerable dependence of the emission lifetime on the energy, and a long emission lifetime at the emission peak. Based on these experimental results, it is believed that in the sample that had a high quantum efficiency, carriers were in a deeper localization state, and their transition to non-radiative recombination centers was suppressed. It is believed that the deep localization state of the carriers is the main reason why the sample exhibited the high quantum efficiency.

3) In order to measure the in-plane distribution of emission, this year we introduced a near-field probe-based PL system. First of all, we collected basic data using typical multiple quantum well LED samples with a wavelength of 460 nm. As a result, we found that an emission intensity distribution with a size of about  $0.3\sim 0.5\ \mu\text{m}$  could be observed in a  $4\ \mu\text{m} \times 4\ \mu\text{m}$  measurement region and the PL intensity in low-level positions was approximately 25% less than in the position of maximum intensity. The data provided here are preliminary data, and it is necessary to accumulate further data, including confirmation of reproducibility, in order to correctly interpret the data obtained by the measurements. Currently, we are conducting detailed investigations.

4) As concerns the effects of Si-doping in the quantum well active layer, based on reverse bias PL and time resolved PL measurements, we conducted evaluation from the standpoint of the quantum well band structure, including the piezoelectric effects. We measured the capacitance of the depletion layer under bias and, based on the calculated value of the depletion layer width, estimated the external electric field applied to the quantum wells and measured spectral changes depending on the applied external electric field. As a result, in the sample with low Si doping ( $4 \times 10^{17}\ \text{cm}^{-3}$ ), we observed a shift of the emission peak towards the high-energy side associated with the application of the external electric field, a long emission lifetime (52 ns) under zero bias, and a decrease in the emission lifetime associated with the application of the electric field. Based on the experimental results concerning the peak shift and the results of calculation of the transition energy, it was estimated that for an In composition of  $x = 0.23$  the piezoelectric field applied to the quantum wells was about 1.48 MV/cm. On the other hand, in the sample that had a higher concentration of Si dopant ( $4 \times 10^{18}\ \text{cm}^{-3}$ ), there was observed a slight shift of the emission peak towards the low-energy side. In

addition, because the emission lifetime was approximately 10~14 ns irrespective of the bias, the electric field generated by the piezoelectric effect was believed to be canceled by the carriers generated by the donor impurities. The addition of Si to the active layer is important for canceling the internal electric field, but because it affects the spread of the depletion layer in the pn junction, the determination of its optimal value is important for highly efficient current injection.

### 3.6 Future plans

In 2001, we will continue investigations conducted in the past year and use selective excitation PL to examine the Stokes shift and the depth of the localization level or the spatial distribution of quantum wells in a two-dimensional plane, as well as investigate the origin of carrier localization. Furthermore, we will examine the relationship between the LED sample structure, crystal growth conditions and carrier localization characteristics, and investigate ways to obtain higher efficiencies.

Also, in the last part of the project, based on the findings obtained up till now, we will examine the relationship between the crystal growth parameters and emission characteristics of light-emitting layers in the near ultra-violet region, which is the goal of the current project, and investigate methods for obtaining high efficiencies. To this end, we will conduct active exchange of information and samples between the Epitaxial Group and Yamaguchi University. In particular, by comparing the crystals obtained in the course of the current project with ultraviolet LEDs from other companies, we will try to clarify the parameters that contribute to high-efficiency emission in the ultraviolet region.

Specifically, we will conduct our research by focusing it on:

- differences due to heteroepitaxy and homoepitaxy in the influence of crystal dislocations and crystal strain on the emission characteristics (efficiency) and differences in the In doping effects
- effects of doping with impurities in the UV emission active layer
- optimization of the doping profile based on simulation

to obtain findings useful in the optimization of UV LED structures.

### 3.7 References

- [1] S.D. Lester, F. A. Ponce, M. G. Craford and D. A. Steigerward, *Appl. Phys. Lett.*, 66 (1995) 1249.
- [2] Y. Narukawa, Y. Kawakami, Sz. Fujita, and S. Nakamura, *Phys. Rev. B* 55, R1938 (1997); Y. Narukawa, Y. Kawakami, M. Funato, Sz. Fujita, Sg. Fujita and S. Nakamura, *Appl. Phys. Lett.* 70 981 (1997).
- [3] S. Chichibu, T. Azuhata, T. Sota, and S. Nakamura, *Appl. Phys. Lett.* 70, 2822 (1997); S. Chichibu, T. Azuhata, T. Sota and S. Nakamura, *Appl. Phys. Lett.* 69, 4188 (1996).
- [4] T. Taguchi, H. Kudo, H. Ishibashi, R. Zheng, and Y. Yamada, *Conference on Solid State Devices and Materials*, Tokyo, 1999, present patent. 194~195.
- [5] S. Watanabe, N. Yamada, Y. Yamada, T. Taguchi, T. Takeuchi, H. Amano, and I. Akasaki, *Phys. Stat. Sol.* (b) 216, 335 (1999).
- [6] S. Watanabe, M. S. Minsky, N. Yamada, T. Takeuchi, R. Schneider, C. Sasaki, M. Iwata, Y. Yamada and T. Taguchi: *Proc. IWN2000, IPAP Conf. Series* 1 532 (2000).
- [7] T. Takeuchi, C. Wetzel, S. Yamaguchi, H. Sakai, H. Amano, and I. Akasaki, *Appl. Phys. Lett.*, 73, 1691 (1998).
- [8] F. Bernardini, V. Fiorentini and D. Vanderbilt, *Phys. Rev. B* 56, 10024 (1997).

[9] C. Wetzel, S. Nitta, T. Takeuchi, S. Yamaguchi, H. Amano and I. Akasaki, MRS, MIJ-NSR Volume 3, Article 31 (1998).

[10] S. Chichibu, T. Azuhata, T. Sota, T. Nukai and S. Nakamura, Proc. IWN2000, IPAP Conf. Series 1 528 (2000).

# 4 Basic Research Concerning GaN Single Crystals Grown by the Solution Growth Method

## 4.1 Achievements in 1998 and 1999

High-pressure solution growth (HP-SG: High-Pressure Solution Growth) is a crystal growth method which permits growth of bulk GaN single crystals of the highest quality and allows for obtaining bulk GaN single crystals of crystal quality so high that the density of dislocations in the crystals is lower than  $10^4 \text{ cm}^{-2}$  [1-3]. In addition, it is known that homoepitaxial thin films grown on such crystals, as well as light-emitting diodes (LED: Light Emitting Diode) fabricated using such crystals possess extremely superior characteristics in comparison with heteroepitaxial thin films grown on sapphire substrates [4,5]. However, mass production based on the HP-SG method presents difficulties because under large temperature gradients of  $50\sim 150^\circ\text{C}/\text{cm}$ , growing a crystal requires six to ten days. Another problem is that the size of the crystal is  $104 \text{ mm}^2$  at the maximum, which is small for industrial use.

In the course of the present study we developed a new pressure-controlled solution growth method (PC-SG: Pressure-Controlled Solution Growth) with a view to develop a technology for inexpensively mass producing high-quality large bulk GaN single crystal substrates possessing a crystal quality equal to or higher than that obtained by the HP-SG method, and started research concerning the growth of bulk GaN single crystals based on this method. The evaluation of the characteristics of the resultant bulk GaN single crystals was carried out in cooperation with the Taguchi Laboratory at Yamaguchi University.

In 1998, we carried out investigations regarding the crystal growth process and crystal growth conditions using an ultrahigh HIP apparatus and successfully grew bulk GaN single crystals with a surface diameter of 7 mm, which showed that it was possible to grow bulk GaN single crystals by the PC-SG method. We found that the resultant GaN single crystals possessed excellent crystal characteristics. In addition, we investigated the specifications of the newly introduced ultrahigh pressure crystal growth apparatus.

In 1999, in order to substantiate the effectiveness of the PC-SG method, we obtained basic data regarding single crystal growth conditions and investigated factors exerting influence on the speed of growth. We examined the mechanism of growth of GaN crystals and showed that the process of diffusion of nitrogen atoms in the Ga melt is the rate-determining process. Based on these research results, we conducted bulk GaN single crystal growth and obtained GaN single crystals with a diameter of 12 mm, which exceeded the target for 2001 (10 mm on the side or larger). These bulk GaN single crystals exhibited structural characteristics superior to those of GaN single crystals grown heteroepitaxially by the metal organic chemical vapor deposition method (MOCVD: Metal Organic Chemical Vapor Deposition), etc., and optical characteristics exceeding those of GaN single crystals grown by the HP-SG method. These results demonstrated the effectiveness of the PC-SG method as a method that can be used for growing bulk GaN single crystals. In addition, we installed an ultrahigh pressure growth apparatus at the Japan Ultrahigh Temperature Materials Research Center (Inc.) and completed preparation for full-scale research starting from 2001.

## 4.2 Summary of Research and Development in 2000

In 2000, we conducted research aimed at the clarification of effects produced by the degree of supersaturation of nitrogen in the Ga melt on the growth of bulk GaN single crystals under the PC-SG method. We also investigated the effects produced by seed crystals, crystal growth time, equilibrium pressure, and pressure increase rate used when the pressure of nitrogen is increased in excess of the equilibrium pressure to the final crystal growth pressure, in order to gain an understanding of the conditions required for growing large bulk GaN single crystals of excellent crystal quality.

By using a lower pressure increase rate in the ultrahigh HIP apparatus, we obtained large bulk GaN single crystals of excellent surface condition. GaN single crystals with a size of 334 mm<sup>2</sup> (which corresponds to a diameter of 20.6 mm) were obtained in the ultrahigh pressure crystal growth apparatus at a pressure increase rate of 69 MPa/h. These data represent the top size of GaN single crystals grown under the solution growth method. Although GaN single crystals of excellent surface condition were obtained at a pressure increase rate of 9 MPa/h, the size of the crystals was approximately 18 nm, and the effect of GaN single crystal enlargement by means of reducing the pressure increase rate was not observed. Based on the examination on the results and the relationship between the nucleation density of the GaN crystals and temperature fluctuations, it was found that a reduction in the pressure increase rate was an efficient measure for obtaining bulk GaN single crystals of excellent surface condition and that, in order to obtain large bulk GaN single crystals, it was necessary to reduce temperature fluctuations and try to achieve a reduction in the nucleation density of the GaN crystals.

In addition, we also evaluated the characteristics of the resultant GaN bulk single crystals and examined the relationship between the surface condition of the bulk GaN single crystals and crystal quality. It was found that differences in the surface condition of GaN single crystals reflected differences in the state of crystal growth, so that single crystals exhibiting excellent surface condition possessed excellent crystal characteristics.

## 4.3 Methods and Means

### 4.3.1 Principles of the pressure-controlled solution growth method

The solution growth (SG: Solution Growth) method is a method of depositing crystals by bringing a solute dissolved in a solvent into a supersaturated state. In the case of GaN, where the atmosphere (nitrogen) itself is the solute, as shown in FIG. 4.3.1, a supersaturated state can be attained by applying nitrogen overpressure exceeding the equilibrium pressure. The PC-SG method was developed with account taken of this phenomenon. Whereas in the HP-SG method the driving force of crystal growth is the concentration differential associated with the temperature gradient, under the PC-SG method, the driving force of crystal growth is the concentration differential associated with a pressure differential.

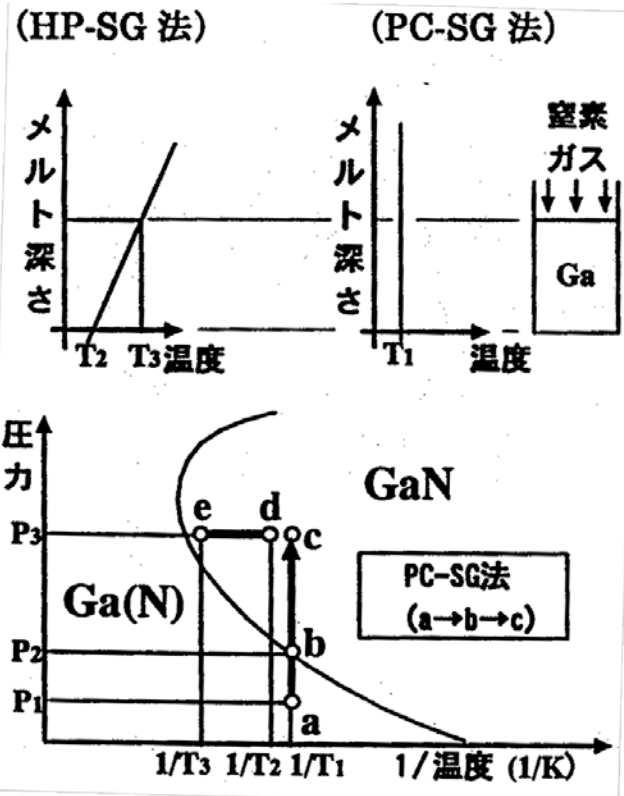
Figure 4.3.1 Comparison of high pressure solution growth (HP-SG) method and pressure-controlled solution growth (PC-SG) method.

[Keys for FIG. 4.3.1]

(HP-SG method) (PC-SG method)

(Y-axis) Melt depth; (Y-axis) Melt depth; (arrows) Nitrogen gas; (X-axis) Temperature; (X-axis) Temperature

(Bottom figure): (Y-axis) Pressure; (X-axis) Temperature; (Box) PC-SG method



(above X-

Under the PC-SG method, a supersaturated state is obtained by raising temperature of the entire system to a temperature  $T_1$  and holding it at this temperature, followed by raising the pressure of the system from  $P_1$  to  $P_3$  and changing the state of the system from  $a \rightarrow b \rightarrow c$ . Continuous crystal growth is possible because the nitrogen required for crystal growth can be continuously supplied doing crystal growth by maintaining the temperature at  $T_1$  and continuously increasing and maintaining the nitrogen pressure. In this method, it is important to maintain a constant concentration of nitrogen in the Ga melt and it is necessary to precisely control the temperature of the system and the nitrogen pressure.

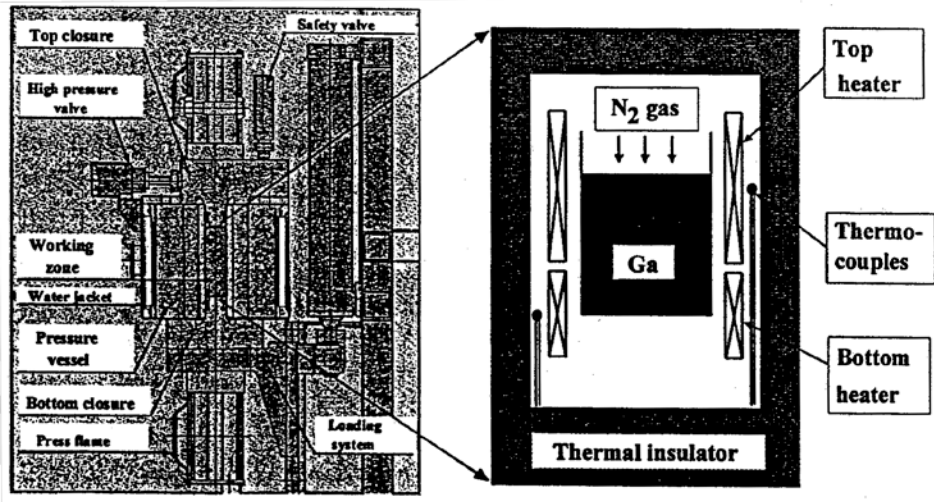
the

### 4.3.2 Laboratory equipment

#### 4.3.2.1 Ultrahigh pressure HIP apparatus

Before the ultrahigh crystal growth apparatus introduced in 1999 was put into operation, we used an ultrahigh pressure HIP apparatus for GaN single crystal growth experiments. A conceptual diagram of the apparatus and the heating equipment is shown in FIG. 4.3.2-(1). According to the principle of operation of the apparatus, after increasing the pressure to 175 MPa with the help of a compressor, the reactor pressure is raised by using cubic expansion caused by gas compression and heating produced by pushing in the lower lid. The reactor pressure is obtained by calculation from the hydraulic pressure used for pushing in the lower lid and the ratio between the hydraulic push-in area and the lower lid push-in area. The apparatus is capable of increasing the pressure up to 980 MPa, with the pressure controlled with a precision of  $\pm 0.1\%$  (1 MPa). The heating equipment, which is made up of top and bottom graphite heaters, two W-5%Re/W-26%Re thermocouples and a temperature regulator, is capable of increasing the temperature to a maximum temperature of 2000°C.

Figure 4.3.2-(1)  
Conceptual diagram of ultrahigh pressure HIP apparatus and heating equipment.



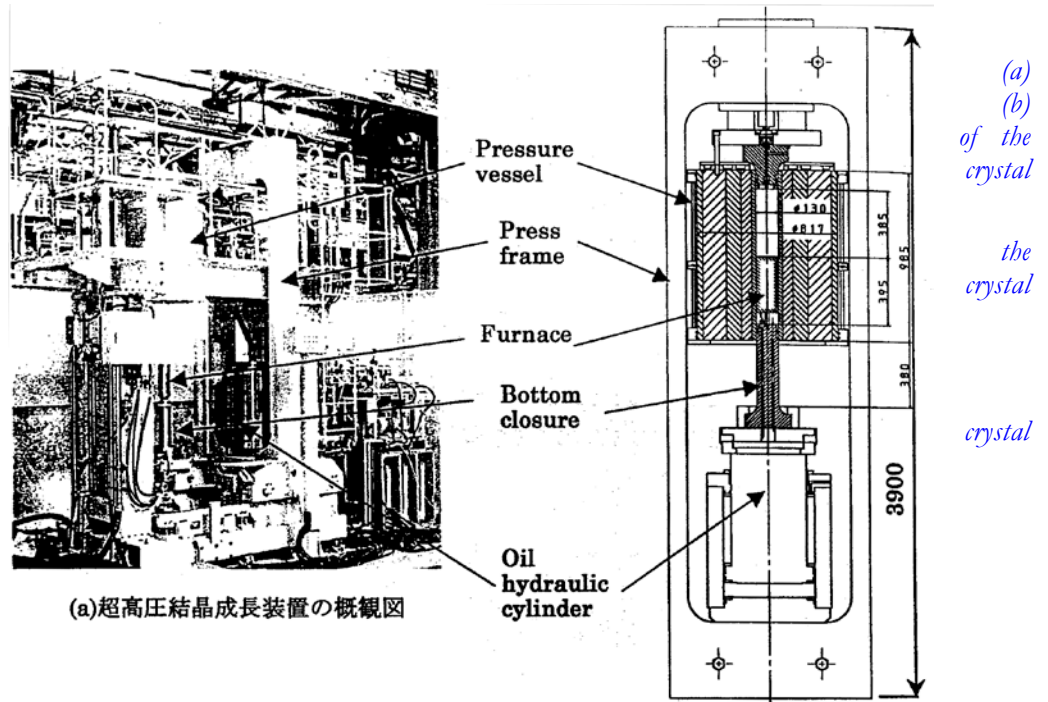
#### 4.3.2.2 Ultrahigh pressure crystal growth apparatus

The apparatus was designed and manufactured based on data obtained in the course of GaN solution growth experiments conducted using the ultrahigh pressure HIP apparatus in order to make growth of large GaN single crystals possible. A general view and a conceptual diagram of the apparatus are shown in FIG. 4.3.2-(2), with its main specifications listed in Table 4.3.2. The maximum pressure used in the apparatus is 1000 MPa, with the pressure controlled with a precision of  $\pm 0.1\%$  (1 MPa). The maximum temperature used in the apparatus was 1600°C.

Figure 4.3.2-(2)  
General view, and conceptual diagram ultrahigh pressure growth apparatus.

(a) General view of ultrahigh pressure growth apparatus.

(b) Conceptual diagram of the ultrahigh pressure growth apparatus.



(a)超高压結晶成長装置の概観図

Characteristics \ Apparatus	Ultra-High Pressure Crystal Growth Apparatus (newly designed)	Ultra-High Pressure HIP Apparatus (used in the past)
Max. pressure	1,000 Mpa {9,869 atm} {10,240 kgf/cm <sup>2</sup> }	980 Mpa {9,672 atm} {10,000 kgf/cm <sup>2</sup> }
Max. temperature	1600°C	2000°C
Inner dia. of pressure vessel	130 mm	100 mm
Continuous operation time	(Estimate) ≥ 14 days	Practically ≤ 2 days
Process chamber space	Dia. 70 mm Max. 150 mm	50 mm Max. 100 mm
Height		
Max. outside dia. of susceptor	60~64 mm	40 mm
Max. inner dia. of crucible	52~56 mm	38 mm

*Table 4.3.2 Main specifications of the ultrahigh pressure crystal growth apparatus. [Note] The maximum internal diameter of the crucible corresponds to the maximum external diameter of the substrate in the case of using a hetero seed substrate.*

**4.3.2.3 Multiple stage crucible system**

Under the PC-SG method, GaN crystal growth is made possible even when the temperature gradient in the Ga melt is practically zero [6]. In addition, because the diffusion of nitrogen in the Ga melt is a rate-determining factor, a shallower Ga melt is more advantageous for GaN crystal growth [6,7]. We have proposed a multi-stage crucible system (FIG. 4.3.2-(3)) as a method that allows us to make the most of these characteristics of the PC-SG method. The method offers possibility of high productivity because the crystal growth conditions inside each of the crucibles are individually adjusted without imparting a temperature gradient. In addition, in this system, on the bottom of the crucibles, are provided structures in which hetero seeds can be placed, which permits use of the system for crystal growth experiments utilizing seed crystals.

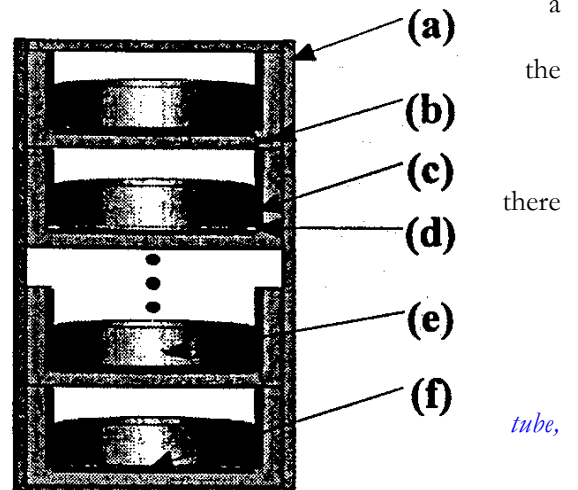


*Figure 4.3.2-(3) Conceptual diagram of the multi-stage crucible system. (a) Graphite susceptor, (b) graphite crucible, (c) pBN mask, (d) pBN mask, (e) the Ga melt, (f) hetero seed.*

### 4.3.3 GaN single crystal growth method

#### 4.3.3.1 Charging of source material

Source material charging conditions are shown in Table 4.3.3. 6N-Ga is charged to pBN crucibles and a predetermined number of crucibles are stacked on a graphite susceptor and placed inside the apparatus. Nitrogen gas is used for atmosphere substitution inside the furnace, whereupon the temperature is raised to 1475°C and the pressure is raised to 400 Mpa, and the state (state depicted in (a) of FIG. 4.3.1) is maintained for certain time.

Apparatus	Ultra-high Pressure HIP Apparatus	Ultra-high Pressure Crystal Growth Apparatus
Characteristics		
6N-Ga weight	50g	80g
pBN crucible dia.	38 mm	52 mm
pBN crucible number	5~6	10~9

*Table 4.3.3 Source material charging conditions. [Note] The number of the pBN crucibles is the number of crucibles that can be stacked in the multi-stage crucible system.*

#### 4.3.3.2 Equilibrium pressure measurement

In the GaN equilibrium pressure measurement experiments, the pressure was raised from 400 MPa to 590, 730, 830, and 980 MPa while maintaining a temperature of 1475°C, and, after maintaining the state (state (c) in FIG. 4.3.1) for 16 hours, the system was cooled down to room temperature over a period of 1.5~2 hours.

The amount of increase in the weight of the pBN crucibles charged with Ga was due to the increased amount of nitrogen resulting from the growth of the GaN crystal. Gallium adhered to the GaN crystals was removed by etching with aqua regia (HCl:HNO<sub>3</sub> = 1:1).

#### 4.3.3.3 GaN single crystal growth experiments using ultrahigh pressure HIP apparatus

Because the PC-SG method is a method, in which a supersaturated state is obtained by applying overpressure, it is believed that crystal growth is influenced not only by the nitrogen pressure during crystal growth, but also by the rate of increase of the pressure. For this reason, in the course of the GaN single crystal growth experiments, starting from a state characterized by a temperature of 1475°C and a pressure of 400 MPa, the pressure was increased to 980 MPa at a pressure increase rate of 8, 12, 49, and 293 MPa/h while maintaining the temperature constant. Seed crystals were not used, and crystal growth was based on natural nucleation. The temperature gradient in the direction of growth was not higher than 1°C/cm. After maintaining the state for a certain time, the system was cooled to room temperature over a period of 1.5~2 hours.

#### 4.3.3.4 GaN single crystal growth experiments using ultrahigh pressure crystal growth apparatus

After putting the ultrahigh pressure crystal growth apparatus into operation, we conducted GaN single crystal growth experiments by the PC-SG method using the multi-stage crucible system. Starting from a state characterized by a temperature of 1475°C and a pressure of 400 MPa, we increased the pressure to 1000 MPa using a pressure increase rate of 9.1, 34, and 69 MPa/h while maintaining the temperature constant. The pressure gradient in the direction of growth was not higher than 0.5°C/cm. After maintaining this state for certain time, the system was cooled down to room temperature over a period of 1.5~2 hours.

In order to investigate the relationship between the crystal growth time and the size of the GaN single crystal, we conducted crystal growth by varying the crystal growth time. The pressure increase rate was 34 MPa/h.

In order to investigate the effects of seed crystals on the enlargement of the GaN single crystals, in parallel to the above described experiments, we conducted GaN single crystal growth experiments by placing graphite plates and c-plane sapphire substrates with a diameter of two inches on the bottom of the crucibles.

#### **4.3.4 Crystal evaluation method**

The GaN single crystals obtained under the PC-SG method were evaluated using the method described below.

##### **4.3.4.1 X-ray diffraction**

Using a four-crystal x-ray diffractometer (X'Pert-MRD from PHILIPS), we measured the x-ray diffraction peak of the GaN crystals' (0002) plane in order to evaluate crystal quality based on its half-width. We used monochromatic x-rays of  $\text{CuK}_{\alpha 1}$  from a Ge (220) four-crystal monochromator. The measurements were carried out at an electron beam accelerating voltage of 45 kV and a beam current of 40 mA using a Cu target.

##### **4.3.4.2 Atomic force microscopy (AFM: Atomic Force Microscopy) observations**

In order to investigate the process of crystal growth in GaN single crystals, we carried out AFM observations of as-grown GaN single crystals using a Nano Scope III analyzer. The head used was a J.-type head and the probe was an NCH-10V (125 Wide). The observations were carried out in a **tapping mode** at an applied voltage of 1.3 volts.

##### **4.3.4.3 Transmission electron microscopy (TEM: Transmission Electron Microscopy) observations**

In order to investigate dislocations and crystal defects in the GaN single crystals, we conducted planar TEM observations. After subjecting the surface of the samples to ion milling to obtain a thickness allowing for a sufficient penetration of the electron beam, we conducted observations using a TEM microscope, the "H-9000" from Hitachi. The accelerating voltage of the electron beam was 300 kV and the observed magnification was 9,000~3,000,000 times (magnification accuracy:  $\pm 10\%$ ).

##### **4.3.4.4 Photoluminescence (PL: Photoluminescence) measurements**

In order to evaluate the optical characteristics of the GaN single crystals, we measured the PL spectra of the GaN single crystals at 4.2 K and 300 K. A He-Cd laser (CW, oscillation wavelength: 325 nm, output: 10 mW) was used as the excitation light source. After reflecting the excitation light with mirrors and adjusting its intensity with filters it was focused with a quartz lens on a sample in a He dewar. PL from the sample was focused on a spectrometer with a quartz lens, with its intensity measured using image pickup elements (CCD: Charge Coupled Device). For the measurement of the temperature dependence, which was carried out in the temperature range of from 5K to 300K, we used a temperature-variable cryostat.

##### **4.3.4.5 Electrical characteristics**

Based on Hall effect measurements, we obtained the carrier density of the GaN crystals. The samples used for measurements were obtained by cutting GaN crystals grown on sapphire substrates placed on the bottom of the crucibles into squares 10 mm on a side.

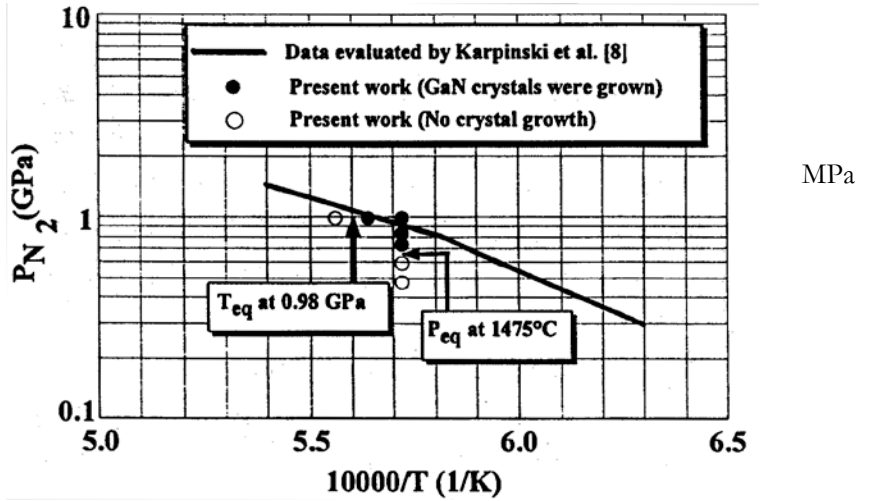
## **4.4 Experimental Results and Discussion**

### **4.4.1 Results of GaN single crystal growth experiments**

#### **4.4.1.1 Results of equilibrium pressure measurement experiments**

The results of GaN equilibrium pressure measurements are shown in FIG. 4.4.1-(1). The equilibrium pressure of GaN at a heater temperature of 1475°C was 590~730 MPa. Therefore, overpressure at a heater temperature of 1475°C and a crystal growth pressure of 980 MPa was approximately 300 MPa.

Figure 4.4.1-(1) Results of GaN equilibrium pressure measurements.

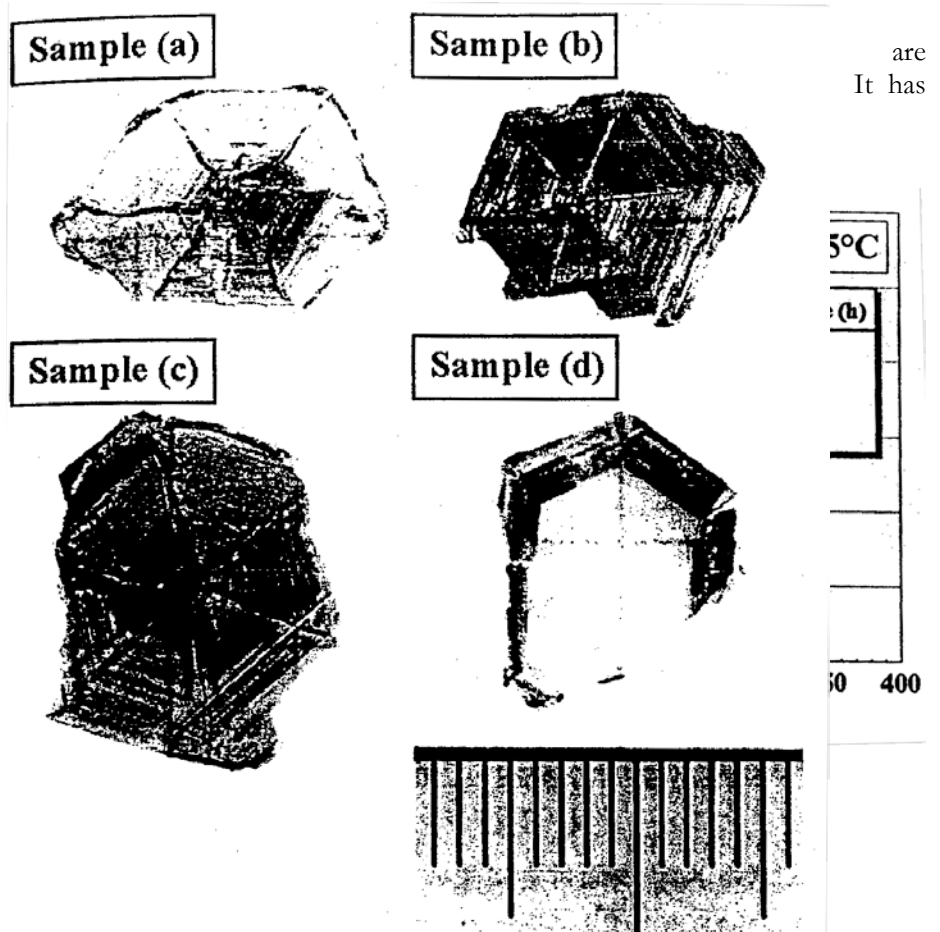


**4.4.1.2 Results of GaN single crystal growth experiments using ultrahigh pressure H.I.D. apparatus**

The relationship between the pressure increase rate ( $\Delta P/\Delta t$ ) and the surface area of a GaN single crystal produced in the vicinity of the surface of the Ga melt via natural nucleation, obtained using the ultrahigh pressure HIP apparatus, is shown in FIG. 4.4.1-(2). It was found that there was a strong correlation between  $\Delta P/\Delta t$  and the surface of the single crystal, and large GaN single crystals were obtained at 49 MPa/h. A GaN single crystal possessing a surface area of 120 mm<sup>2</sup>, which exceeded the single crystal surface of 104 mm<sup>2</sup> grown by UNIPRESS in Poland, was obtained at a pressure increase rate of 12 MPa/h [3]. The thickness of the single crystals (a)~(d) was 20~30 micrometers.

Figure 4.4.1-(2) Relationship between pressure increase rate ( $\Delta P/\Delta t$ ) and surface area of a GaN single crystal grown in the vicinity of Ga melt surface by natural nucleation.

Photographs of crystals (a)~(d) of FIG. 4.4.1-(2) shown in FIG. 4.4.1-(3). It has been found that the pressure increase rate  $\Delta P/\Delta t$  exerts influence not only on the size of the GaN single crystals, but also on their surface condition. In other words, the contrast of the hexagon-forming facets becomes weaker in single crystals (a), (b), and (c) with a decrease in  $\Delta P/\Delta t$ , and in case of single crystal D the contrast disappears altogether and a smooth surface is obtained. Furthermore, speaking of the lines extending from the center



are  
It has

of the GaN single crystal (which are formed by the joining of the facets): in the case of single crystal (a) they are considerably distorted (and the shape of the hexagon is significantly changed in the process of growth), in the case of single crystals (b) and (c) they are practically rectilinear (the growth takes place with the hexagon-like shape maintained), and in the case of single crystal (d), they appear only on the periphery of the crystal.

*Figure 4.4.1-(3) Relationship between pressure increase rate ( $\Delta P/\Delta t$ ) and the surface condition of GaN single crystals produced in the vicinity of Ga melt surface by natural nucleation: (a) 293 MPa/h, (b) 49 MPa/h, (c) 12 MPa/h, (d) 8 MPa/h.*

#### 4.4.1.3 Results of GaN single crystal growth experiments using ultrahigh pressure crystal growth apparatus

The relationship between the pressure increase rate ( $\Delta P/\Delta t$ ) and GaN single crystals produced in the vicinity of the Ga melt surface by natural nucleation, obtained using the ultrahigh pressure crystal growth apparatus, is shown in FIG. 4.4.1-(4). A GaN single crystal possessing a surface area of 334 mm<sup>2</sup> (which corresponded to a diameter of 20.6 mm) was obtained at a  $\Delta P/\Delta t$  of 69 MPa/h. As far as the size of the GaN single crystals is concerned, for the solution growth method these are top data. However, unlike the results obtained using the super high pressure HIP apparatus, no increase in the surface of the single crystal due to a decrease in  $\Delta P/\Delta t$  was observed. On the other hand, the surface condition of the crystal improved with decreasing pressure increase rate, and single crystals possessing an excellent crystal surface were obtained at 9.1 MPa/h. The thickness of single crystals (e)~(g) was 20~30 micrometers.

At a pressure increase rate of 34 MPa/h, we extended the time, during which the system was maintained at the crystal growth temperature of 1475°C and a pressure of 1000 MPa, from 16 hours 254 hours in order to investigate the effects of the extension on the size of the crystal, but observed no effect. This means that the size of the crystal is determined by the process of raising the pressure up to the final pressure. In addition, no increase was observed in crystal thickness due to the extension of the hold time. This has to be confirmed by further extending the hold time.

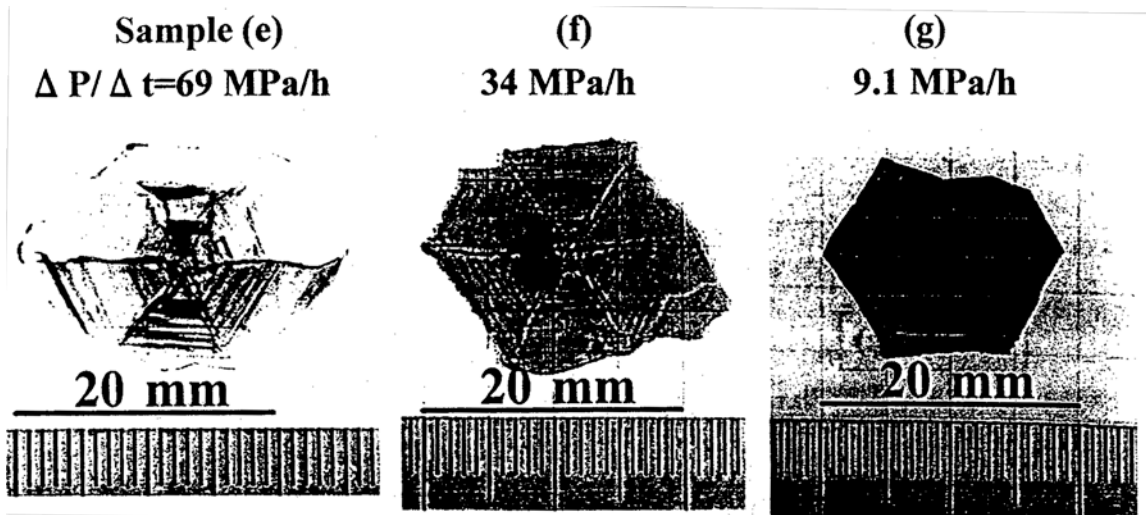


*Figure 4.4.1-(4) Relationship between pressure increase rate ( $\Delta P/\Delta t$ ) and surface area of a GaN single crystal produced in the vicinity of Ga melt surface by natural nucleation.*

The results of investigation regarding the effects of seed crystals on the enlargement of GaN single crystals are shown in FIG. 4.4.1-(5). In all cases, GaN single crystals produced in the vicinity of the surface of the Ga

melt by natural nucleation exhibited a greater tendency towards enlargement when c-plane sapphire substrates were placed on the bottom of the crucibles than when graphite plates were placed on the bottom. All of the GaN single crystals shown in FIG. 4.4.1-(4) are crystals grown by placing a sapphire substrate on the bottom of the crucibles.

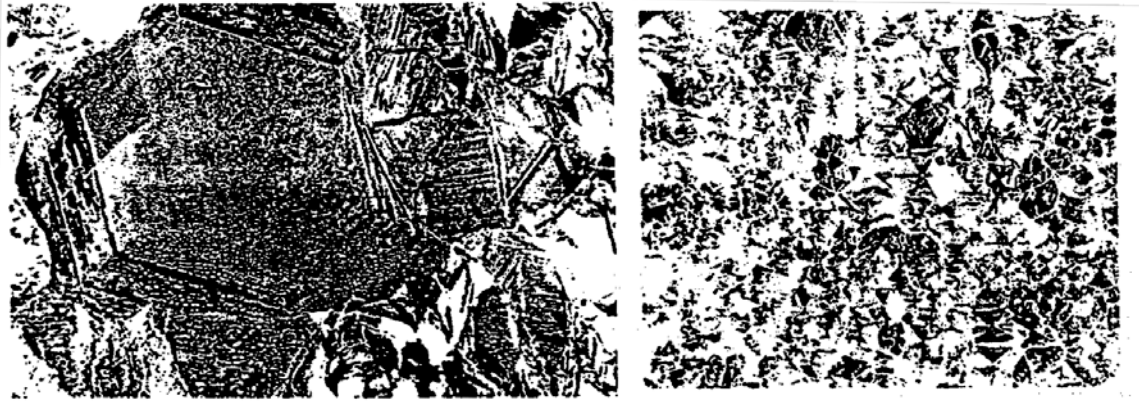


Figure 4.4.1-(5) GaN crystals produced in the vicinity of Ga melt surface by natural nucleation when seed crystals (a) and (b) were placed on the bottom of the crucibles.

- (a) C-plane just sapphire substrate
- (b) Graphite plate

On the other hand, apart from GaN single crystals produced in the vicinity of the Ga melt surface by natural nucleation, films of GaN crystals also grew on the sapphire substrates placed on the bottom of the crucibles (FIG. 4.4.1-(6)). XRD data showed that the growth face of these crystals was in the (0001) plane, oriented along the c-axis. As can be seen from the electron microscope photographs shown in figure, the GaN crystal was a columnar crystal, which was also confirmed by the fact that there were a large number of holes remaining after polishing. Because the growth mode of the GaN crystals is strongly dependent on the crystal growth conditions, such as temperature and pressure, it is believed that the growth mode can be switched from columnar (three-dimensional) growth to (two dimensional) growth adjusting the conditions. GaN crystals of specified quality could be grown by method, then reproducibility and mass production could be dramatically improved.

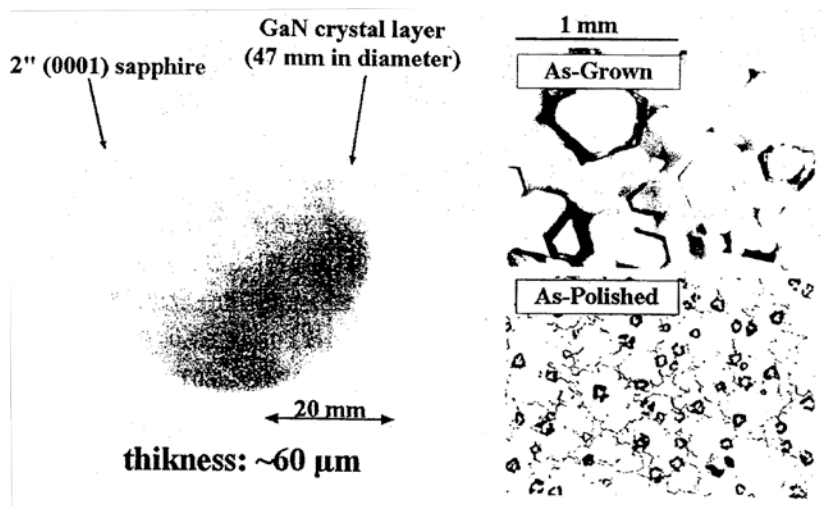


Figure 4.4.1-(6) Photographs of GaN crystals on sapphire substrates placed bottom of crucibles.

planar  
by  
If  
this  
  
grown  
at

**4.4.1.4 Discussion of crystal growth experiment results**

Regardless of whether the ultrahigh pressure HIP apparatus or the ultrahigh pressure crystal growth apparatus was used, the pressure increase rate exerted influence on the surface condition of the crystals, and crystals possessing excellent crystal surfaces were obtained at a  $\Delta P/\Delta t$  of 10 MPa/h or lower. On the other

hand, the size of the GaN single crystals exhibited a dependence on the equipment used. In the case of the ultrahigh pressure HIP apparatus, no increase in the single crystal surface area was observed as a result of a decrease in  $\Delta P/\Delta t$ , but in the case of the ultrahigh pressure crystal growth apparatus, there was no increase in the single crystal surface area and there was even a slight decrease in the surface area. A discussion of the above-mentioned phenomena is presented hereinbelow.

A strong contrast between the facets and the distorted lines formed by the joining of the facets are believed to be due to the fact that the rate of increase in nitrogen pressure, in other words, the rate of increase in the degree of supersaturation, is greater than the rate, at which nitrogen is supplied in the form of GaN crystal. In other words, because crystallization takes place at the point in time when the degree of nitrogen supersaturation exceeds a certain level, the shape of the GaN crystal reflects the distribution of supersaturation at that point, so that some of the facets become longer, some of the facets become shorter, and the lines formed along the joints between the facets become distorted. In addition, it is believed that in the newly grown crystal portions and already grown crystal portions, the thickness of the crystal becomes uneven and the contrast between the facets becomes more pronounced. On the other hand, when the increase rate of the nitrogen pressure is small, the degree of nitrogen supersaturation is maintained below a certain level, with nitrogen continuously supplied to the crystal as GaN, and, for this reason, crystals with excellent surface condition can grow without developing in a stepwise fashion. This explanation is supported by the results of the AFM observations of Section 4.4.2 (2).

Because the size of the crystal is determined by the nucleus density of the crystal, the fact that a large (small) single crystal is obtained means that the density of the generated nuclei has been low (high). Thus, it is believed that there is no direct relationship between the pressure increase rate, in other words, the rate of increase in the level of nitrogen supersaturation, and the nucleus density of the crystal. In general, the nucleus density strongly correlates with temperature fluctuations, with the nucleus density of the crystal increasing under conditions characterized by significant temperature fluctuations. This is also true for the present study, and it is believed that the fact that large (small) single crystals are grown is due to a low (high) nucleus density of the crystals. Evidence in support of this point is shown hereinbelow.

In accordance with the PC-SG method, the temperature was maintained constant and the applied pressure was increased, following the increase in the pressure, the heater power required for maintaining the temperature increased as well. Because under super high pressures of 700~1000 MPa nitrogen changes from a gas to a near-liquid state, the equalization of temperature due to gas mixing is made more difficult. Because the flow rate of nitrogen in a liquid state is slower and mixing is made more difficult, the temperature of the entire system can easily become inhomogeneous, and precise control of the temperature becomes an extremely difficult practical problem. In particular, in case of the super high pressure HIP apparatus, whose heating system is relatively small, the distribution of the discharged heat becomes inhomogeneous due to the small size of the heater, and temperature fluctuations are liable to increase. This tendency is even more noticeable when the applied nitrogen pressure is increased, and, in the super high pressure HIP apparatus, the larger the pressure increase rate, the larger the temperature fluctuations (full width), which may reach 4.0~5.0°C. When  $\Delta P/\Delta t$  is small, the power change rate of the heater is also small, and for this reason, the temperature fluctuations are also small, reaching approximately 2.0~4.0 °C. In the case of the super high pressure crystal growth apparatus, as shown in Table 4.3.2, the volume of the heating system is approximately three times larger (approximately two times larger based on the diameter ratio, and 1.5 times larger based on the height ratio), but the supplied electric power is increased only approximately 1.5 times. The temperature fluctuations are typically within 1.0~2.0°C, which represents a tremendous improvement in comparison with the super high pressure HIP apparatus. However, the size of the temperature fluctuations varies for each run of the experiment regardless of the pressure increase rate  $\Delta P/\Delta t$ . Temperature fluctuation obtained from temperature charts used during the growth of GaN single crystals (e)~(g), which are shown in FIG. 4.4.1-(4), was 0.3~0.9 °C in case (e), 0.5 ~1.5°C in case (f), and 1.0~2.8°C in case (g).

From the above-mentioned facts it is evident that the size of the GaN single crystal is strongly correlated with the temperature fluctuations, and a reduction in temperature fluctuations is efficient in growing large GaN single crystals. In order to achieve the goal set for 2002 (single crystals with a diameter of 1 inch or

larger) it is necessary to further reduce the temperature fluctuations in the super high pressure crystal growth apparatus and reduce them to at least 0.3~0.9°C or lower.

The reasons, due to which the GaN single crystals grown in the vicinity of the Ga melt surface became larger when sapphire substrates were placed on the bottom of the crucibles than when graphite plates were placed in the crucibles, are still unclear, but it is certain that the nucleus density of the GaN single crystals decreased when the sapphire substrates were placed on the bottom of the crucibles. It is believed that because in this case the nitrogen in the Ga melt was spent both on GaN growth in the vicinity of the melt surface and on GaN growth on the sapphire substrates, the pressure increase rate was effectively reduced. If we assume that this is true, then reducing the pressure increase rate is expected to exert no adverse influence on increasing the size of GaN single crystals.

## 4.4.2 Results of crystal evaluation

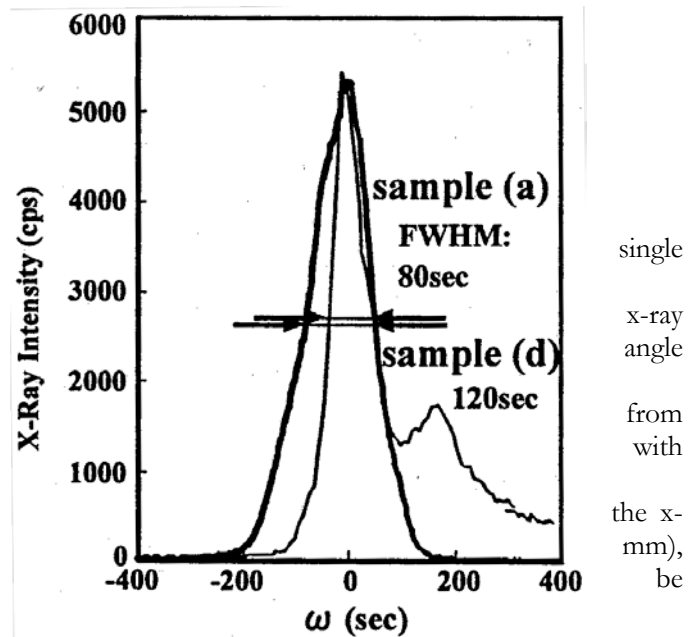
Differences in the surface condition of GaN single crystals reflect differences in the state of crystal growth, and single crystals possessing excellent surface condition are expected to exhibit excellent crystal properties. We evaluated GaN single crystals (a) and (d) shown in FIG. 4.4.1-(3) using x-ray diffraction, AFM observations, TEM observations, and PL in order to investigate the effects of the pressure increase rate on the crystal quality.

### 4.4.2.1 X-ray diffraction results

An x-ray rocking curve of reflection from the (0002) plane obtained by four crystal x-ray diffraction is shown in FIG. 4.4.2-(1). It was found that the half width of the (0002) plane reflection peak of single crystal (a), which contained low-angle (approximately 170 arcsec) grain boundaries, was 80 arcsec, with the crystal exhibiting excellent crystal properties. In case of single crystal (d), no distinct small-angle grain boundaries were observed, but its half-width increased to 120 arcsec.

Figure 4.4.2-(1) Rocking curve obtained by x-ray diffraction ( $\omega/2\theta$ ).

A discussion of the increase in the half-width is provided below. As shown by a detailed comparison of the peak shapes, the peak of crystal (d) appears to be composed of two superimposed peaks of approximately the same intensity. This indicates the presence of small grain boundaries in single crystal (d) and a decrease in this angle. The angle, as estimated from the locking curve, is approximately 60 arcsec, the peak half width being approximately 80 arcsec, on par with single crystal (a). Based on ray incident area (width: 0.5 mm, height: 0.5 mm), the size of the grain boundaries is expected to be approximately 0.1~0.5 mm or higher. The presence of small-angle grain boundaries in undoped GaN crystals grown by the HP-SG method has been also reported, with the angle being approximately 60 arcsec [3].



Thus, so as to get rid of the influence due to the small-angle grain boundaries, the locking curve of single crystal (d) was measured by setting the width of the x-ray slit to 0.05 mm and its height was set to 0.5 mm. The results are shown in FIG. 4.4.2-(2). The tilt angle determined from the locking curve profile for the (0002) plane was 43 arcsec, and the twist angle obtained from measurements in the (10-10) plane was 18

arcsec. Polowski *et al.* have reported a tilt angle of 18~25 arcsec and twist angle of ~20 arcsec as optimum values for undoped bulk GaN single crystals [3]. The fact that the tilt angle of the GaN single crystal (d) obtained in the present study was slightly larger is most likely due to a significant bowing of the substrate. On the other hand, the twist angles are practically the same and we can say that both crystals possess identical crystal properties.

In addition, Polowski *et al.* have reported that the crystal properties of GaN single crystals are considerably improved by the addition of Mg (0.5% of Ga by weight) [3], and we can expect to obtain the same effects under the present method as well.

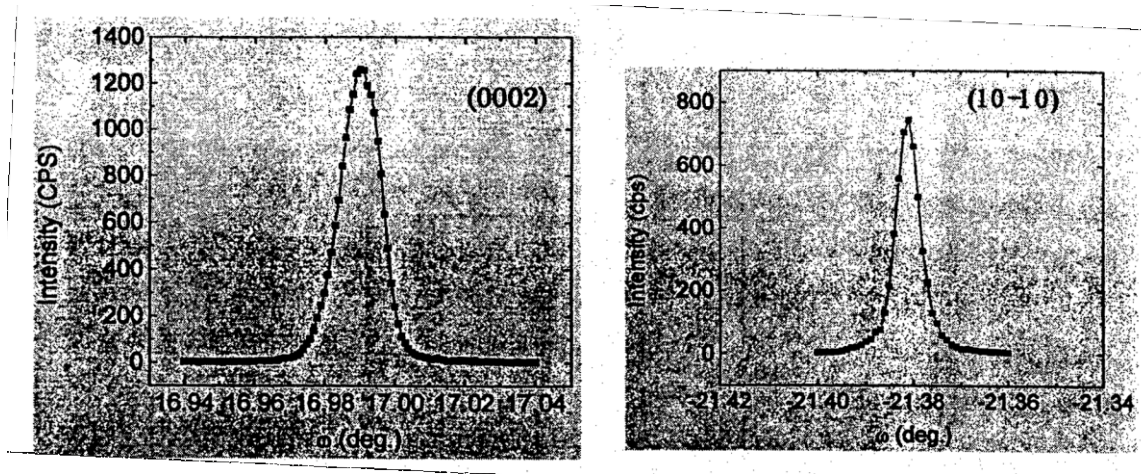


Figure 4.4.2-(2) Rocking curves obtained by x-ray diffraction.

#### 4.4.2.2 AFM observation results

The front and back faces of the GaN single crystals exhibit patterns so different that the difference can be seen during visual examination. In case of single crystal (a), a strong contrast, such as the one shown in FIG. 4.4.1-(3), can be observed on one of the faces, and the other face is smooth. In case of single crystal (d), some contrast, albeit extremely faint, is observed on one of the faces, and the other face is smooth.

AFM observation results for GaN single crystals (a) and (d) are shown in FIG. 4.4.2-(3) and FIG. 4.4.2-(4). To distinguish observation planes, the smooth face will be called the smooth face, and the other face (the face where contrast is visible) will be called the rough face. The results obtained during AFM observations were the same as during the visual observation. Namely, steps corresponding to a strong contrast were observed in case of single crystal (a) on the rough face. The height of the steps was about 100 nm or so from the line profile. The interval between the steps was not less than 20  $\mu\text{m}$ . Insular growth (size: 20  $\mu\text{m}$  in diameter, height: 30~70 nm) was observed in both single crystals (a) and (d) as a feature of the rough face.

On the other hand, step-flow growth was observed in both single crystals (a) and (d) on the smooth side. In case of single crystal (a), however, the step width is larger (1~2  $\mu\text{m}$ ) and the steps are higher (2~5 nm). In case of single crystal (d), the step width is narrower (~0.7  $\mu\text{m}$ ), and the steps are lower (0.3~0.5 nm). In

addition, there are considerable differences in the flatness of the steps (RMS: Root Mean Square), with that of single crystal (a) being 0.579 nm and that of single crystal (d) being 0.138 nm. Moreover, the RMS of single crystal (d) is a value that also includes step-related fluctuations. Thus, it was found that the smooth face of single crystal (d) possesses flatness at a monatomic-layer-high level. Its flatness is equivalent to the flatness of a GaN crystal grown by the MOCVD method or exceeds its level.

Figure 4.4.2-(3) AFM observation results for rough faces of GaN single crystals (top: single crystal (d), bottom: single crystal (a)).

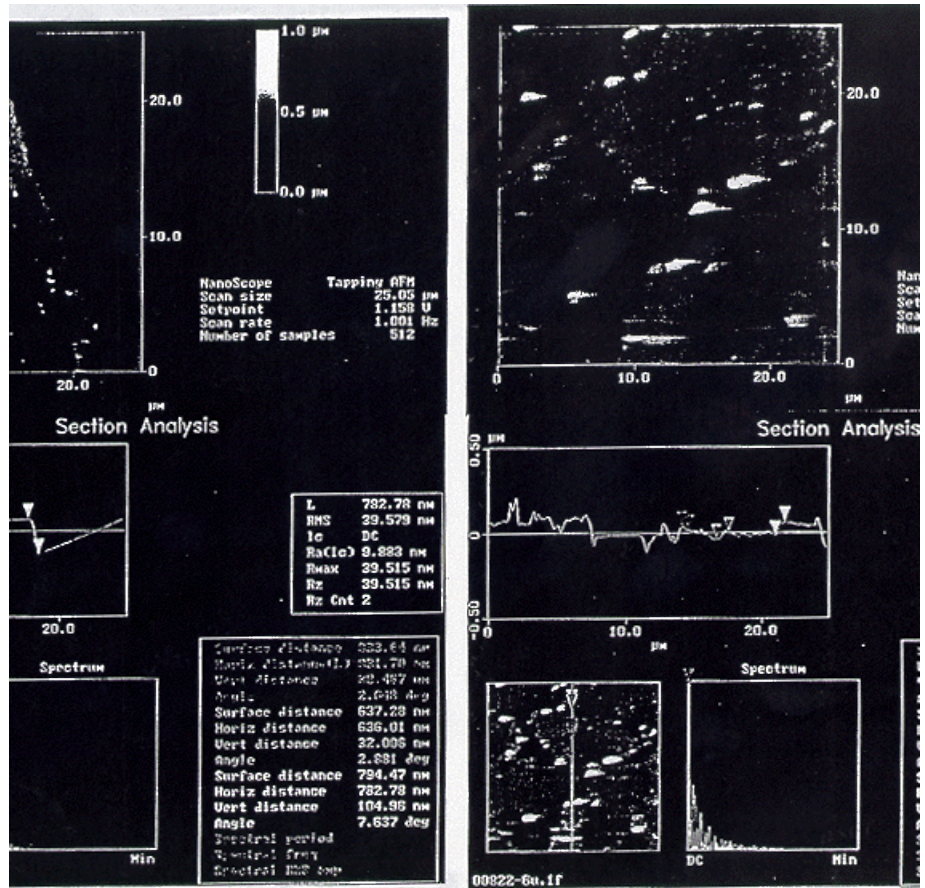
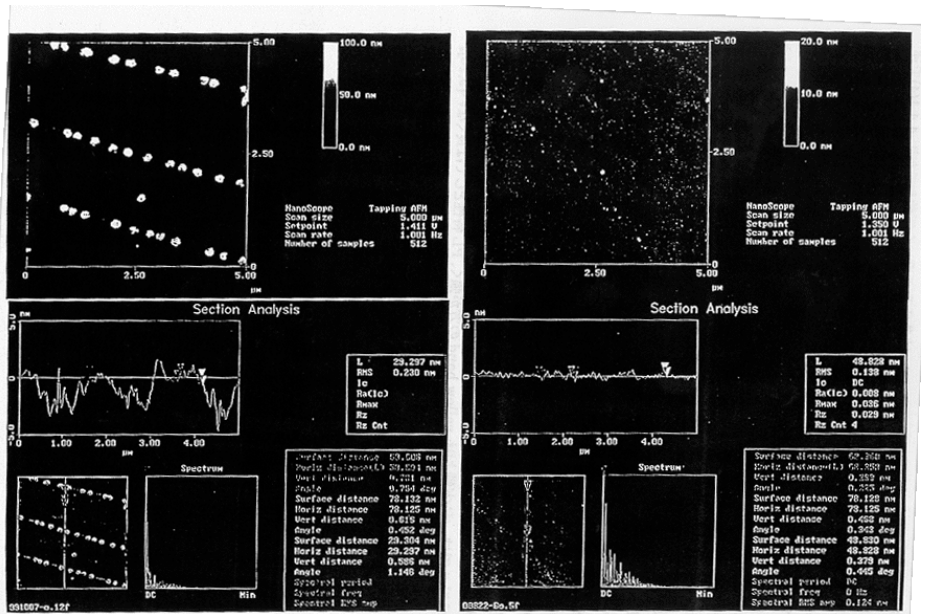


Figure 4.4.2-(4) AFM observation results for smooth faces of GaN single crystals (top: single crystal (d), bottom: single crystal (a)).

[Note] Bright dots in figures (in particular, in case of single crystal (a)) result from contamination (particles) adhered during washing and drying.



Differences in the characteristics of single crystals (a) and (b) reflect differences in crystal growth and support the discussion of the differences in growth provided in Section 4.4.1(4). Namely, the model says that in case of single crystal (a), the GaN crystal grows in a discontinuous (stepwise) manner, and in case of single crystal (d) crystal growth proceeds in a continuous manner.

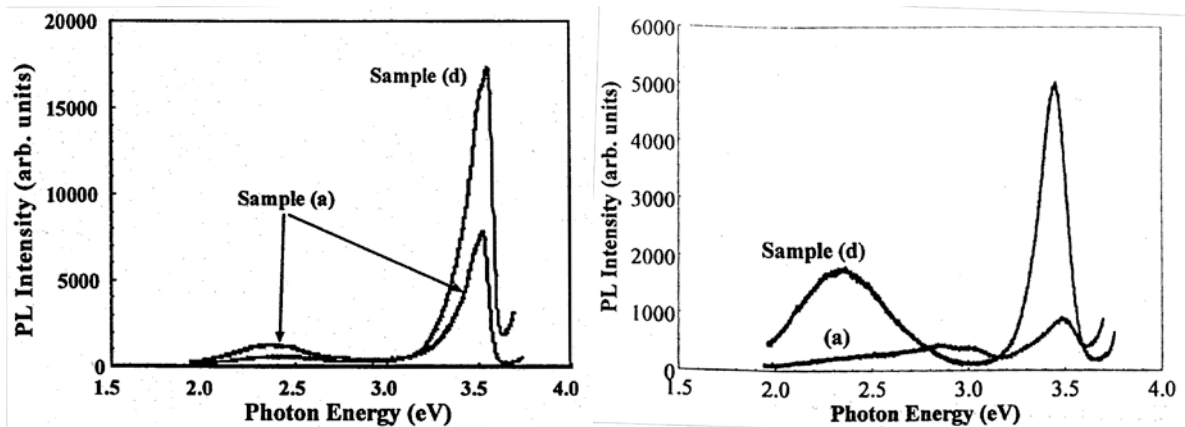
#### 4.4.2.3 TEM observation results

As reported in last year's Research Achievement Report regarding single crystal (a) shown in FIG. 4.4.1-(3), crystal defects were not found during low-magnification TEM observations either. Therefore, the defect density of undoped GaN crystals grown by the PC-SG method was low, with the defect density of GaN single crystals in the observation field estimated to be not more than  $10^5 \text{ cm}^{-2}$ . The defect density of single crystal (d) can be expected to be of the same magnitude as that of single crystal (a).

#### 4.4.2.4 Results of PL observation

PL spectra of GaN single crystals (a) and (d) at 4.2K are shown in FIG. 4.4.2-(5). In addition to band-edge emission at 3.5 eV, peaks were also observed from a deep level at 2.3 eV, which is called the yellow band. In both single crystals (a) and (d), the band edge exhibits excellent PL characteristics stronger than those of the yellow band. It is evident, however, that in terms of the PL intensity ratio of the band edge and the yellow band as well as relative PL intensity at band edge, single crystal (d) possesses considerably superior PL characteristics. These characteristics are more pronounced in PL spectra at room temperature (FIG. 4.4.2-(6)), and in GaN single crystals possessing crystal surfaces such as those of single crystal (a), sometimes it is impossible to measure the PL spectrum. In addition, the yellow band is stronger than the band edge in the room-temperature PL spectra of GaN crystals grown by the HP-SG method, which is not a good PL characteristic [9, 10].

*Left: Figure 4.4.2-(5) PL spectra of bulk GaN single crystals (a) and (d) at 4.2K.*

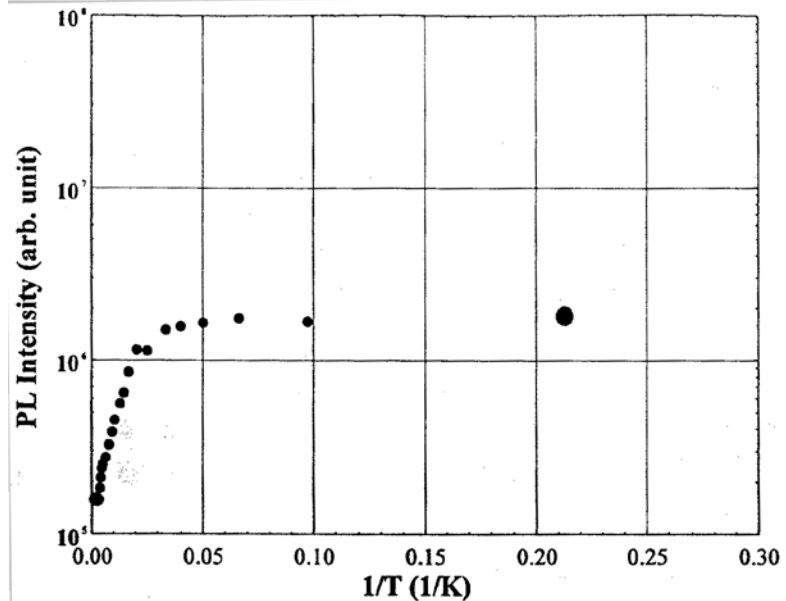


*Right: Figure 4.4.2-(6) Room-temperature PL spectra of bulk GaN single crystals (a) and (d).*

Discussions have been going on for a long time about the origin of the yellow band at 2.3 eV, with popular explanations including one attributing its origin to impurities, such as carbon, etc., and another one putting it down to crystal defects. As is evident from the relationship between the crystal quality and the PL spectrum, the yellow band is sensitive to crystal properties, and might possibly represent emission related to crystal defects.

The temperature dependence of the PL intensity of the band edge emission of single crystal (d), which exhibited excellent PL characteristics, is shown in FIG. 4.4.2-(7). Although the PL intensity of the band-edge emission is known to decrease by 3~4 orders of magnitude in GaN crystals grown by the MOCVD method, it decreased by only one order of magnitude in the crystals grown by the PC-SG method. This means that emission centers are effectively present at room temperature. The reason for this is believed to be a lower crystal density in GaN crystals grown by the PC-SG method compared with GaN crystals grown by the MOCVD method.

*Figure 4.4.2-(7) Temperature dependence of PL intensity of edge emission of bulk GaN crystals (d) having excellent surface.*



that is  
in

band  
single  
crystal

#### 4.4.2.5 Results of electrical characteristic evaluation

GaN grown on sapphire substrates was subjected to measurement of the hole effect at 300K. As a result, it was found that the crystals, which belonged to the n-type, had a carrier density of  $1.3\sim 1.9\times 10^{19}\text{ cm}^{-3}$ , and a mobility of  $36\sim 67\text{ cm}^2/\text{V}\cdot\text{s}$ . Although the data do not provide direct information about bulk GaN crystals, bulk crystals are expected to possess equivalent characteristics. In addition, the values obtained by measurement were in good agreement with values for crystals grown by the HP-CG method [11], as well as exhibited good agreement with mobility and carrier density obtained from the half value of the band-edge emission peak obtained in the course of the PL measurements [12].

## 4.5 Summary

The effects of seed crystals, crystal growth time, nitrogen pressure increase rate, and equilibrium pressure were subjected to investigation using the ultra-high HIP apparatus and the ultra-high crystal growth apparatus introduced in 1999 in order to clarify the effects produced by the degree of supersaturation of nitrogen in the Ga melt under the PC-GS method on bulk GaN single crystal growth and to determine conditions for growing large bulk GaN single crystals of excellent crystal quality. In addition, we evaluated the characteristics of the resultant GaN bulk single crystals to study the relationship between the surface condition and crystal quality of GaN bulk single crystals. The results are summarized below.

- (1) The equilibrium pressure of GaN at a heater temperature of 1475°C was 590~730 MPa, and overpressure at a crystal growth pressure of 980 MPa was approximately 300 MPa.

(2) GaN single crystals of excellent surface condition with a size of 120 mm<sup>2</sup> were obtained by reducing the increase rate of nitrogen pressure in the ultra-high HIP apparatus. This size exceeded the size of 104 mm<sup>2</sup> of GaN single crystals grown by the HP-SG method.

(3) GaN single crystals with a size of 334 mm<sup>2</sup> (which corresponds to a diameter of 20.6 mm) were obtained in the ultra-high crystal growth apparatus at a nitrogen pressure increase rate of 69 MPa/h. These data represent the top size of GaN single crystals grown under the solution growth method. Although GaN single crystals of excellent surface condition were obtained at a pressure increase rate of 9 MPa/h, the size of the crystals was approximately 18 mm in diameter, and there was no GaN single crystal enlargement effect due to reduction in the pressure increase rate. At a pressure increase rate of 9 MPa/h, GaN single crystals with excellent surface condition were obtained, but the size of the crystal was 18 mm, and there was no GaN single crystal enlargement effect due to the reduction in the pressure increase rate.

(4) Based on (2) and (3), it was found that a reduction in the increase rate of the nitrogen pressure was effective in terms of obtaining bulk GaN single crystals of excellent surface conditions.

(5) Based on (2), (3), and examination of the relationship between the nucleation density of GaN crystals and temperature fluctuations, it was found that in order to grow large bulk GaN single crystals, it was necessary to try to reduced the temperature fluctuations and to reduce the nucleation density of GaN crystals.

(6) The relationship between the size of the GaN single crystals produced in the vicinity of the Ga melt surface by natural nucleation and the seed crystals placed on the bottom of the crucibles showed that larger GaN single crystals were obtained in the case of c-plane just sapphire substrates than in the case of graphite plates.

(7) Extending the hold time at the final crystal growth pressure had no effects on enlargement of GaN single crystals and suggested that the size of the crystals was determined by the process of raising the pressure to the final pressure.

(8) Based on the results of evaluation of the characteristics of the resultant GaN bulk single crystals, it was found that differences in the surface condition of the GaN single crystals reflected differences in the state of crystal growth, with single crystals of excellent surface condition possessing excellent crystal properties.

(a) The tilt angle value of 43 arcsec and twist angle value of 18 arcsec obtained from a four-crystal X-ray locking curve profile show that the crystals were at an equivalent level as compared with undoped GaN single crystals grown by the HP-SG method and possessed superior crystal properties.

(b) AFM observations showed that they had monatomic layer-level flatness.

(c) PL spectrum measurements at 4.2K and room temperature showed that they had excellent PL characteristics, with the PL intensity at band edge being stronger than that of the yellow band.

## 4.6 Future Plans

Prospects and future plans aimed at achieving the goals of the final year of the present study (GaN single crystal size: not less than 25 mm in diameter, defect (dislocation) density: not more than 10<sup>5</sup> cm<sup>-2</sup>) are described hereinbelow.

The crystal defect density of bulk GaN single crystals grown by the PC-SG method, as determined by TEM observations, is below 10<sup>5</sup> cm<sup>-2</sup>, and we can expect to reach our goal. However, when the crystal defect density exceeds 10<sup>6</sup> cm<sup>-2</sup>, accurate evaluation of the defect density by TEM observations is practically impossible, and it is necessary to conduct the evaluation by means of etch pitting. In addition, as far as crystal properties other than crystal defect density is concerned, it was found that bulk GaN single crystals grown by the PC-SG method had excellent crystal properties, in particular, superior PL characteristics. However, it has not been confirmed whether crystals possessing such superior crystal properties are also superior as substrates for epitaxial growth. Therefore, issues that have to be confirmed or resolved in the

course of the present study in the future include (1) confirmation of performance as a homoepitaxial substrate, and (2) increasing the size of bulk GaN single crystals.

As far as (1) is concerned, the evaluation of homoepitaxial growth on bulk GaN single crystal substrates grown in the present study based on cooperation between the Taguchi Lab at Yamaguchi University and organizations participating in the present project started in at the end of 2000. Because the evaluation of bulk crystal characteristics requires a certain size and number of specimens, we will have to be able to fabricate single crystals with a size of at least 10~15 mm in diameter with good reproducibility. In addition, because handling presents difficulties at the current crystal thickness (20~30  $\mu\text{m}$ ), we are planning to investigate the crystal growth process and the limiting factors of crystal thickness. Investigations into polarity control are necessary as well, and we are planning to confirm the Mg doping-related effects. The crystals will be passed on to organizations in charge of epitaxial growth technology development and LED development and we expect that their use for epitaxial substrates will be made possible as a result of feedback from the results of their evaluation.

As far as (2) is concerned, a GaN single crystal with a surface area of 334 mm<sup>2</sup> (which corresponds to a diameter of 20.6 mm), i.e. the highest value in terms of size for GaN single crystals grown by the solution growth method, was obtained using the PC-SG method utilizing a multiple stage crucible system in an ultra-high pressure crystal growth apparatus. This result holds much significance, giving us the confidence that the attainment of the goal set for the final year (single crystal size: not less than 25 mm) is quite possible. However, making this goal a reality requires yet another breakthrough or improvement in the level of the technology. In this connection, as discussed in Section 4.4.1(4), it is believed that reducing temperature fluctuations will be most effective, and we are planning to implement modifications to the ultra-high pressure crystal growth apparatus and heating equipment in the coming year. Improvements in terms of temperature fluctuations are expected to not only enable enlargement of single crystals due to crystal nucleus density reduction, but also to contribute to an improvement in reproducibility resulting from the stabilization of the temperature environment.

Based on the above-described technological research combined with this year's research results, we expect to be able to reproducibly fabricate large bulk GaN single crystals with a diameter exceeding 25 mm and excellent crystal surfaces, i.e. excellent crystal properties.

## 4.7 References

- [1] S. Porowski, I. Grzegory, and J. Jun: High Pressure Chemical Synthesis, eds. J. Jurczak and B. Baranowski (Elsevier, Amsterdam, 1989) Chap. 3, p. 21.
- [2] S. Porowski and I. Grzegory: *J. Cryst. Growth* 178 (1997) 174.
- [3] S. Porowski: *MRS Internet J. Nitride Semicond. Res.* 4S1 (1999) G. 1.3
- [4] S. Porowski: Extended Abstracts of the 1999 Int. Conf. On Solid State Devices and Materials, p. 58, Tokyo, Japan, September 1999.
- [5] M. Kamp, V. Schwegler, C. Kirchner, H. Y. Chung, C. Wang, M. Seyboth, M. Scherer and K. J. Ebeling: 3<sup>rd</sup> Int. Symp. On Blue Laser and Light Emitting Diodes, Berlin, Germany, No. WeC2, March 2000.
- [6] T. Inoue, Y. Seki, O. Oda, S. Kurai, Y. Yamada, and T. Taguchi: *Jpn. J. Appl. Phys.* 39 (2000) 2394.
- [7] S. Krukowski: Proc. 15<sup>th</sup> Melt Growth Meeting, Sendai, 1999 (Tohoku Univ., Sendai, 1999) p. 279.
- [8] J. Karpinski, J. Jun, and S. Porowski: *J. Cryst. Growth* 66 (1984) 1.
- [9] P. Perlin, J. Camassel, W. Knapp, T. Talefcio, J. C. Chervin, T. Suski, I. Grzegory, and S. Porowski, *Appl. Phys. Lett.* 67 (1995) 2524.

- [10] A. Pelzmann, C. Kirchner, M. Mayer, V. Schwegler, M. Schauler, M. Kamp, K. J. Ebeling, I. Grzegory, M. Leszczynski, G. Nowak, and S. Porowski: *J. Cryst. Growth* 189/190 (1998) 167.
- [11] K. Pakula, A. Wysmolek, K. P. Korona, J. M. Baranowski, R. Stepniewski, I. Grzegory, M. Bockowski, J. Jun, S. Krukowski, M. Wroblewski, and S. Porowski, *Solid State Communications* 97 (1996) 919.
- [12] E. Iliopoulos, D. Doppalapudi, H. M. Ng, and T. D. Moustakas, *Appl. Phys. Lett.* 73 (1999) 375.

# 5 Research Concerning Substrate Surface Morphology

## 5.1 Achievements in 1998 ~1999

It was found that the surface morphology of sapphire substrates exerted considerable influence on the physical properties of GaN and on the characteristics of LEDs when GaN was heteroepitaxially grown on sapphire substrates for the purpose of fabricating light-emitting elements for LEDs.

Objectives of the present study included extreme abrasive modification of sapphire substrates to understand the influence exerted upon the physical properties of GaN heteroepitaxially grown thereon and introduction of basic technologies to be used for drastically improving the physical properties of GaN. Furthermore, yet another objective was to establish a technology for polishing GaN substrates by applying the polishing technology used for sapphire substrates.

In terms of practical results, we have been able to achieve a surface roughness of  $R_y \leq 1$  nm, a face inclination of  $\leq 0.05^\circ$  with respect to the designated axis, and a flatness of  $\leq 1$   $\mu\text{m}$ , which exceeded the surface precision goal for sapphire substrates (face roughness:  $R_y \leq 2$  nm, face inclination:  $0.1^\circ$  with respect to the designated axis, flatness:  $\leq 1$   $\mu\text{m}$ ). Here,  $R_y$  is the same parameter as the one previously designated by  $R_{\text{max}}$ . In particular, surface roughness measurements were taken within a  $1$   $\mu\text{m}$  by  $1$   $\mu\text{m}$  field of view, and the roughness was practically monoatomic ( $R_y \leq 0.3$  nm); if we take into consideration the fact that it was an off-orientation substrate, we can say that it was almost absolutely flat.

Although single-point measurement in the central portion of the substrate was used for  $c$ -axis orientation, it was confirmed it was possible to fabricate off-orientation substrates inclined at an angle of  $\pm 0.05^\circ$  with respect to any arbitrary axial direction. As for variation in the axis orientation on the surface of the substrate, five-point measurement results showed that a  $\pm 0.02^\circ$  precision could be maintained.

As for variation in the thickness of the substrate, five-point measurements showed that an excellent parallelism of not more than  $1$   $\mu\text{m}$  was achieved.

Although certain practical problems were indeed encountered, such as imperfections called "latent flaws" and contamination due to inadequate cleaning, it was confirmed that several methods allowing for improvement were available, such as, respectively, enhanced MCP (Mechanical Chemical Polish) and changing the cleaning equipment from an ultrasonic multi-tank cleaning machine to a single wafer cleaning machine.

The polishing of GaN substrates was carried out using the same technology as that used for the polishing of sapphire substrates. We determined the polishing method, selected the polishing equipment (a High-Press lapping machine), and installed it in August of 1999.

We carried out polishing tests on GaN substrates and confirmed that polishing was possible; in the future, we are going to work on practical improvements.

As far as a transition to the mass production of sapphire substrates is concerned, we have implemented improvements in important processes such as axis orientation alignment, polishing, latent flaw removal, and cleaning, and gathered data related to the transition to mass production.

## 5.2 Summary of Research and Development in 2000

As for substrate surface precision, in 1998 and 1999 we were able to achieve the target precision (surface roughness:  $R_y \leq 2\text{nm}$ , face inclination:  $\leq 0.1^\circ$  with respect to the designated axis, flatness:  $\leq 1\ \mu\text{m}$ ).

In 2000, we studied the influence exerted by sapphire substrates on the physical properties of GaN by epitaxially growing GaN on substrates whose precision we could ensure. The method we used consisted in fabricating  $c$ -plane substrates with various off-angles (five levels:  $0^\circ$ ,  $0.15^\circ$ ,  $0.3^\circ$ ,  $0.5^\circ$ , and  $1^\circ$ ) and off-directions (two levels:  $a$ -axis direction and  $m$ -axis direction) and investigating the results of epitaxial growth. As a result, it was found that excellent results in terms of epitaxial growth could be obtained on  $c$ -plane substrates inclined at an off-angle of  $0.15^\circ$  with respect to the  $m$ -axis direction.

In addition, along with using enhanced MCP to solve the practical problem of latent flaws, which reveal themselves during epitaxial growth, we eliminated the problem of the influence exerted by substrate contamination on epitaxially grown films by using an enhanced cleaning process (switching from multi-tank ultrasonic cleaning to single-wafer cleaning).

Regarding the polishing of GaN substrates, we conducted polishing experiments using the newly introduced polishing equipment. Currently we are still in the stage of conducting polishing experiments and results concerning GaN substrate evaluation have not been obtained yet, but, at the same time, we are also conducting experiments aimed at obtaining superior surface morphology by reforming GaN surface.

## 5.3 Introduction of High Precision Processing Technology for Sapphire Substrates

Objectives of the present stage in research and development include introduction of a processing technology intended for the finishing of the surface morphology of sapphire substrates used in LEDs to a consistent precision and a study of the influence exerted by the surface morphology of the substrates on the physical properties of the heteroepitaxially grown GaN.

The target surface precision of 2-inch sapphire substrates was as follows:

- Surface roughness  $R_y \leq 2\ \text{nm}$ , Face inclination, with respect to designated axis  $\leq 0.1$
- Flatness  $\leq 1\ \mu\text{m}$

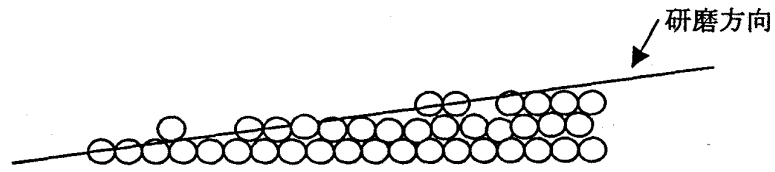
In addition, as concerns the evaluation of substrates obtained by finishing the surface morphology of sapphire substrates to a predetermined degree of precision, we have carried out such evaluation using heteroepitaxial growth on GaN by means of MBE in a joint study with Yamaguchi University.

### 5.3.1 Methods and Means

In 1998 and 1999, in order to increase the precision of processing in accordance with the new evaluation criteria used for high precision sapphire substrates, we developed a quick method for increasing processing precision, in which we followed prior-art processing steps while varying the processing speed and time, and making the most of already established know-how (maintenance and control of polishing plate, selection of abrasive materials, etc.). Furthermore, we tried to achieve improvements not only in terms of substrate surface precision, but also in terms of eliminating latent flaws in the substrates, enhancing the cleaning process, stabilizing the axial orientation of the substrates, and controlling bowing and thickness.

This year's objectives included establishing evaluation methods and achieving further progress in terms of the above mentioned topics. The specific objectives we tried to achieve included research on surface roughness, axis orientation, orientation flat orientation, bowing, parallelism, latent flaws, cleaning, surface reforming, and substrate evaluation methods [1,2,3].

In order to maintain a constant surface roughness, carried out measurements, inspection, and adjustment in to maintain the degree of flatness of the polishing within 1  $\mu\text{m}$ .



we  
order  
plates

Along with establishing a method permitting the measurement of the orientation flat orientation in a simple manner using x-rays, we conducted a series of whole number measurements to verify its precision.

Because the direction of bowing occurring at room temperature after growth is different from the direction during epitaxial growth, the standards preferably used for bowing are: 5  $\mu\text{m}$  or less, concave epi-surface (cupping down). However, the regulation of bowing is difficult, and it is preferable to regulate the bowing of sapphire substrates in accordance with the relative importance of bowing during epitaxial growth and bowing at room temperature after growth. Regulation of bowing is possible by adjusting the polishing roughness of the front and back sides of sapphire substrates, and experiments are underway to investigate this technique.

As far as parallelism is concerned, 1  $\mu\text{m}$  or less, as determined by five-point measurements, is a very good degree of parallelism, and, for this reason, parallelism has not been selected as a research topic for this year.

Latent flaws were eliminated by enhancing MCP. Furthermore, inspection based on the use of special microscopes was used for checking substrates for latent flaws [4].

As far as cleaning was concerned, along with confirming the limitations of the previously used ultrasonic multi-tank cleaning equipment, we tested a single-wafer cleaning machine and confirmed its effectiveness [5].

### 5.3.2 Results and Discussion

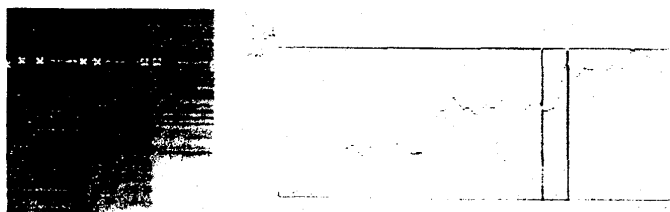
#### 5.3.2.1 Surface roughness

In terms of surface roughness, as described in connection with the results obtained in 1998 and 1999, surface irregularities were reduced to 0.3 nm or less. This is believed to be due to the fact that, with monoatomic irregularities, as depicted in FIG. 5.3.2-(1) (schematic representation), which shows an off-angle substrate surface, atoms are shaved off along the off-angle (along the direction of polishing in the figure). Incidentally, it was confirmed that when the steps were formed by heat treating an off-orientation substrate, the ratio of the step width to the step height was proportionate to the off-angle.

FIG. 5.3.2-(2) shows an AFM image of a stepped substrate with a 0.05° off-angle, in which the number of steps was confirmed to be practically the same as the number determined by calculation.

*Figure 5.3.2-(1) Off-angle substrate surface (schematic representation) [Keys for FIG. 5.3.2-(1)] (Arrow) Direction of polishing.*

Quite naturally, in order to maintain the precision of the surface, it is important to guarantee the precision of the polishing plate, and this is why we took all the necessary measurements in order to guarantee a flatness of not more than 1  $\mu\text{m}$  across the entire surface. In particular, we enhanced polishing plate adjustment in the MCP



the  
stage.

*FIG. 5.3.2-(2) AFM image of stepped substrate.*

### 5.3.2.2 Axis orientation

As for axis orientation control points, first of all, they are used for determining the plane orientation of the  $c$ -plane; at the present moment, substrates with an off-orientation of approximately  $0.2^\circ$  with respect to the  $m$ -axis direction have become mainstream. Experiments have been conducted using substrates with an off-orientation of up to  $1^\circ$  with respect to the  $m$ -axis direction (five levels:  $0^\circ$ ,  $0.15^\circ$ ,  $0.3^\circ$ ,  $0.5^\circ$ , and  $1^\circ$ ) and an off-orientation of up to  $1^\circ$  with respect to the  $a$ -axis direction, but results better than those afforded by substrates with an off-orientation of  $0.2^\circ$  with respect to the  $m$ -axis have not been obtained.

Another important issue is the angle of the orientation flat. At the present moment, the angle is controlled to  $\pm 0.3^\circ$  with respect to the  $a$ -axis direction, but for some applications it is necessary to control the angle to  $\pm 0.1^\circ$ . At the present moment, inspection and grading are necessary in order to control the angle to  $\pm 0.1^\circ$ , because variations caused by chamfering etc. during post-processing after initial adjustment cannot be controlled to within  $0.1^\circ$ .

### 5.3.2.3 Bowing

The currently used bowing standard for 2-inch substrates is:  $5\ \mu\text{m}$  or less, concave (down). This is a practical standard. Namely, it has been found that because the coefficient of thermal expansion of GaN is smaller than that of the sapphire substrate when GaN is epitaxially grown thereon, bowing occurs on the sapphire substrate side (an originally concave surface becomes convex), and the bowing of the sapphire substrate has come to be used as the benchmark for determining the bowing produced after GaN growth.

In the present study we accumulated know-how concerning bowing control methods. Namely, because the surface roughness of the front and back sides of a substrate is an important bowing factor, we created a polishing method, in which the roughness of the front and back sides of a substrate is varied in order to control bowing, and, in addition, experiments are currently underway, in which we are investigating methods that can be used for varying the thickness of substrates.

### 5.3.2.4 Latent flaws

Imperfections sometimes occur in epitaxially grown GaN layers. These imperfections are called latent flaws because they are difficult to detect by inspection under an ordinary optical microscope after polishing a substrate. Because the presence of such flaws can be now determined using special microscopes, such as the "Magic-Mirror microscope" etc., it has become possible to prevent latent flaws from escaping detection in the technological process, thereby permitting fabrication of substrates free from flaws.

### 5.3.2.5 Contamination

The operation of the multi-tank ultrasonic cleaning system employed in the past was followed by cleaning with a mixed solution of concentrated sulfuric acid and hydrogen peroxide (acid cleaning) intended for the removal of organic contamination. Although a considerable reduction in the degree of organic contamination was indeed obtained as a result of such cleaning, it was found that there was practically no decrease in the level of metallic elements (for example, Fe). Notwithstanding the fact that cleaning is now performed via the re-circulating filtration of the solution in the ultrasonic tanks, metallic elements are not removed and remain in the solution, and because multiple wafers are cleaned at the same time, metallic contamination accumulates.

In order to get rid of the metallic elements, it is necessary to constantly use a clean cleaning solution, but the above-mentioned multi-tank ultrasonic cleaning system has limitations as far as such a requirement is concerned, because the system needs a considerable amount of cleaning solution. In this connection, we tested a single-wafer cleaning system, and found that the amount of metallic elements could be reduced to below 1/10 without increasing the amount of the cleaning solution being used (it was possible, for example, to reduce the amount of Fe to  $10^{10}/\text{cm}^2$ , as determined by total reflection fluorescent x-ray spectroscopy),

and we are now designing equipment based on the experimental apparatus in order to further confirm its efficiency.

## 5.4 Introduction of GaN Substrate Precision Processing Technology

Based on literature data concerning the physical properties [6] of GaN and actual processing results [7], for the precision processing of GaN substrates, we used a rough grinding machine and a finishing machine, which were introduced in 1999, followed by MCP with KOH as an etchant. The process, which consists of a series of steps including rough grinding, finishing, and MCP, is expected to provide a surface roughness of not more than 1 nm.

### 5.4.1 Methods and Means

For the precision polishing of GaN substrates it is necessary to achieve a surface roughness of not more than 1  $\mu\text{m}$  by carrying out polishing as a series of steps including rough grinding, finishing, and MCP. Furthermore, it is essential to maintain the flatness of the surface of the polishing plate, and a device called a biaxial facing apparatus is used to constantly control the surface precision of the polishing plate to not more than 1  $\mu\text{m}$ .

The rough grinding machine required special specifications for a cooling system for the polishing plate in order to avoid thermal deformation of the polishing plate, and forced driving (using a device that forcibly moved the workpiece) was used as the processing mode.

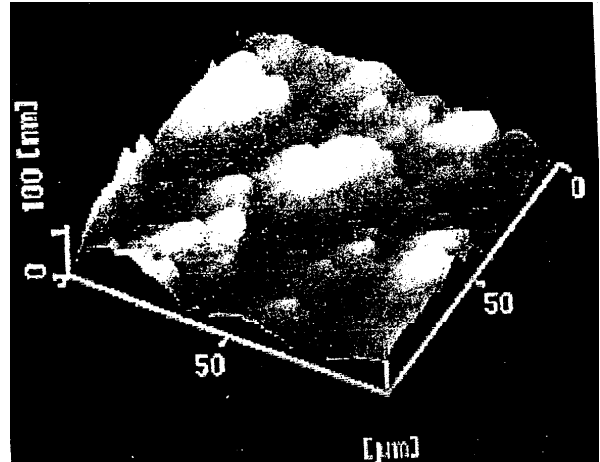
The finishing machine and the MCP apparatus were both desktop polishing machines, with the surface precision of their polishing plates maintained at not more than 1  $\mu\text{m}$  using the above described biaxial facing apparatus. Controlling their precision makes it possible to guarantee that the surface precision of the polished workpieces is on the order of nm.

A problem encountered in the process of polishing is the residual stress remaining between the GaN layer and the sapphire layer, which makes achieving a perfectly polished state rather difficult. The best method is probably not to continue directly polishing the GaN layer, but to provide a sapphire layer around its periphery in order to achieve a uniform and constant load with respect to the GaN layer. In practice, the target polished state can be achieved by carrying out the polishing operation several times.

### 5.4.2 Results and discussion

The experimental polishing of GaN substrates has previously been carried out by Japanese universities and companies, but unlike in the present project, they reported results regarding experimental polishing of GaN substrates manufactured by HVPE purchased in the United States.

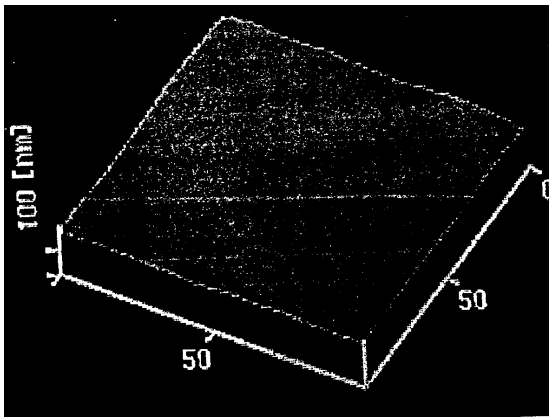
FIG. 5.4.2-(1) is an AFM image of an as-grown GaN substrate showing the surface of the GaN substrate. As-grown GaN crystals on the surface appeared to be of a columnar shape, and the flatness of the surface was rather low, at approximately 50  $\mu\text{m}$ , which precluded its use as a GaN substrate without additional processing.



In order to produce a flat surface by polishing, we removed approximately five  $\mu\text{m}$  of the GaN layer, which had a thickness of 15  $\mu\text{m}$ . As a result, the flatness of the surface was improved, as shown in FIG. 5.4.2-(2), which is an AFM image of the GaN substrate after polishing.

FIG. 5.4.2-(1) AFM image of as-grown GaN substrate.

When an enlarged photograph of the substrate was taken in order to determine whether the substrate met requirements for practical use, it was confirmed that, as shown in the enlarged AFM image of the GaN substrate after polishing, there were numerous large pits visible in the enlarged image, which made the surface condition worse than that found in ordinary MOCVD substrates.



Left: FIG. 5.4.2-(2) AFM image of GaN substrate after polishing.

Right: FIG. 5.4.2-(3) Enlarged AFM image of GaN substrate after polishing.

In addition, even when the thickness of the layer removed by polishing was increased from five  $\mu\text{m}$  to 10  $\mu\text{m}$ , the AFM images did not change. This fact indicates that it was impossible to reduce crystal imperfections by polishing. Our objectives for the next year include research aimed at determining the effects produced when

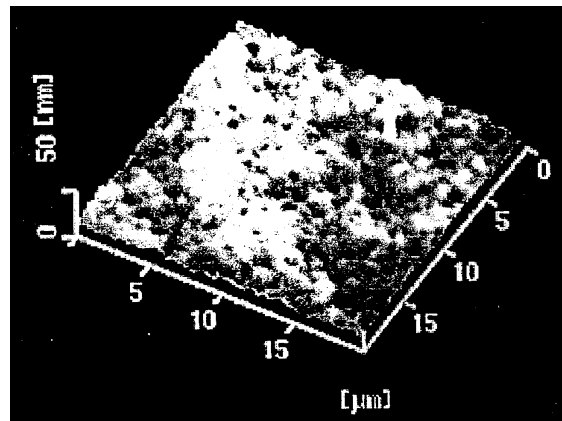
epitaxial growth is carried out on flat surfaces improved by polishing, as well as methods of polishing that make surface improvement possible.

## 5.5 Summary

As far as the technology for high precision polishing of sapphire substrate surfaces is concerned, using MCP as the last stage of the ordinary polishing process, we have been able to completely eliminate surface flaws, achieving a surface roughness of not more than 0.3 nm. In addition, we conducted measurements using AFM.

Additionally, special microscopes, such as Magic-Mirror microscopes etc., permit definitive determination of flaws and contamination, which allows for evaluation at the substrate stage. As for cleaning, by switching from the multi-tank ultrasonic cleaning system to a single-wafer cleaning system, we have been able to reduce metallic element contamination to under 1/10. Analysis was conducted using the total reflection fluorescent x-ray method.

Additionally, the precision of the  $c$ -plane orientation was controlled to within  $\pm 0.05^\circ$  or less with respect to the designated axis (an off-angle of  $0.15^\circ$  relative to the  $m$ -axis direction is considered standard), and users



have told us that there has been a decrease in the variation in epitaxial growth results due to variation in the off-angle of the substrates.

As far as the polishing of GaN substrates is concerned, experimental polishing was conducted using polishing equipment introduced in the course of the present study (High-Press lapping machine). Although polishing was possible, the crystal surface of the GaN used in this study was coarse, and the surface roughness target could not be met.

## 5.6 Plans for the Future

In a joint study conducted in cooperation with the Yamaguchi University, we will evaluate MBE-based heteroepitaxial growth on GaN to try to obtain better substrates. Specifically, we will try to reduce the number of imperfections in GaN epitaxial films by maintaining a high level of substrate surface precision and by varying surface characteristics, such as step-forming, etc.

In addition, by polishing the surface of GaN substrates, we will try to reduce the surface roughness to 1 nm or less, and will investigate methods for achieving a substantial reduction in the amount of imperfections on GaN surfaces.

## 5.7 References

- [1] 1998 Annual book of ASTM standards, Section 10, Electrical Insulation and Electronics.
- [2] 1997 SEMI Standards, Vol. 5, Material traceability FPD.
- [3] Techniques for fabrication and evaluation of ultra-precise surface interfaces, by M. Matsunaga, Y. Sakurai, J. Chikawa (or: Sengawa), Science Forum Co., Ltd.
- [4] Techniques for fabricating and evaluating perfect wafer surfaces, by H. Tsuya, Science Forum Co., Ltd.
- [5] Ultra-precise wafer surface control techniques, by K. Matsushita, S. Fukaya, H. Tsuya, S. Takasu, Science Forum Co., Ltd.
- [6] Hardness and fractured roughness of bulk single crystal gallium nitride, M. D. Drory, J. W. Ager, T. Suski, I. Grzegory, and S. Porowski, Appl. Phys. Lett., Vol. 69, No. 26, 4044, December 1996.
- [7] Chemical polishing of bulk and epitaxial GaN, J. L. Weyher, S. Muller, I. Grzegory, S. Porowski, Journal of Crystal Growth, 182 (1997) 17~22.

# 6 Research and Development of GaNAsP-based Multicolored Light Emitting Materials Using MOCVD

## 6.1 Achievements in 1998 – 1999

A large degree of band gap bowing is expected from III-V-N type mixed crystals. For example, the band gap of  $\text{GaN}_{1-x}\text{P}_x$ , which is created by adding P to GaN, does not decrease monotonically as one moves from GaN to GaP. Rather, it curves convexly downwards and the band gap takes on a negative value near  $x=0.5$ , as suggested by band structure calculations. By taking advantage of this characteristic and regulating the  $x$  of  $\text{GaN}_{1-x}\text{P}_x$  to about 10%, the primary colors red, green, and blue can be formed from a united family of materials with promise for photonic devices.

In 1998, an experiment was conducted using MOCVD (metal organic chemical vapor deposition) in which a high concentration of As was added to GaN to form GaNAs with a high As component. The photonic characteristics of this composition were then studied. Additionally, GaNP was grown using MOCVD with DMHy (Dimethylhydrazine) and  $\text{PH}_3$  (Phosphine) as raw materials. And, a new laser-assisted MOCVD method was also investigated to raise the P concentration.

SIMS (Secondary Ion Mass Spectrometer) analysis of films grown by MOCVD using DMHy with a constant V/III ratio but varying growth temperature confirmed that it is possible to mix in phosphorus on the order of several percent by setting the growth temperature low. Yet, we were unable to observe peak shifts in the band edge of the GaN caused by the addition of phosphorus (P).

In 1999, laser-assisted MOCVD was further studied and GaNP films were grown. Laser exposure was employed because it breaks down the source gases via light energy and results in more efficient crystal growth. To increase the effect of the laser exposure, an ArF laser was used, as well as TBP (tertiarybutyl phosphine) as the phosphorus source since it easily decomposes at the ArF excitation wavelength. At a growth temperature of 850° C, a crystal with a high P composition was attained. PL (photoluminescence) measurements showed that we were able to achieve  $\text{GaN}_{1-x}\text{P}_x$  with a 100 meV shift in the wavelength of the band edge as compared to GaN.

The  $x$  composition was estimated from an analysis using EDX (energy dispersive X-ray spectrometer), SIMS, and X-ray diffraction. Since the surface of the specimen had large irregularities, the  $x$  values varied greatly and could not be established. Nevertheless, the existence of P was clear and it is thought that a GaNP film was achieved. The SIMS analysis showed a P composition of about 0.02 but EDX showed a significantly higher composition. What's more, the degree of red shift was greater than that reported in previous announcements, and we believe that we have confirmed band bowing in GaNP, although not quantitatively. Thus, the red shift of the PL spectrum of GaNP using laser-assisted MOCVD has been shown to be two to three times that of conventional MOCVD, making laser-assisted MOCVD a promising crystal growth technology.

While not possible with InGaN, the large band gap bowing effect of  $\text{GaN}_{1-x}\text{P}_x$ -based materials makes it possible to emit red, green, and blue light by changing the ratio of mixed crystals. Determining the level of potential held by these materials is now the main objective of research.

Our aim is to grow a  $\text{GaN}_{1-x}\text{P}_x$  crystal with a high P composition and through photonic measurements like photoluminescence, establish a larger peak shift toward the long wavelength from that of GaN. Moreover, we aim to fabricate a GaNP LED and show light emission by current injection.

## 6.2 Summary of Research and Development of 2000

$\text{GaN}_{1-x}\text{P}_x$  with a high P composition was grown using two growth methods: laser-assisted MOCVD and MOCVD without photon excitation. The photonic characteristics were then evaluated. We also created a  $\text{GaN}_{1-x}\text{P}_x$  SQW (single quantum well), fabricated an LED and then investigated its light emission characteristics.

Together with Tokyo University's Onabe Research Lab, GaNP was grown using MOCVD at Tokyo University's leading Science Research Center. GaNP was also grown at low temperature using MOCVD with photon excitation. Uncovering the photonic characteristics was performed jointly by Yamaguchi University's Taguchi Research Lab and Tokyo University's Onabe Research Lab.

To be more concrete, growth of GaNP using laser-assisted MOCVD was performed through exposure with an ArF laser using TMG (Trimethylgallium),  $\text{NH}_3$  (Ammonia) and TBP as source gases. For MOCVD without photon excitation, DMHy,  $\text{PH}_3$ , and TMG were used. We studied the conditions needed to attain high quality GaNP by changing growth parameters. We further evaluated the crystals' optical properties using PL measurements, SEM (secondary electron microscopy) for crystal observation, X-ray diffraction for crystal evaluation, and SIMS for composition analysis. We also studied electrical properties of LEDs and light emission characteristics through EL (electroluminescence).

Due to the large band gap bowing of III-V-N-type crystals, it is possible to achieve a material uniting the three primary colors red, green, and blue by varying slightly the P or As crystal mix ratio. These materials hold promise as photonic device materials. To uncover the potential of these new materials, this project pressed forward development beginning in 1998, growing and evaluating GaNAs and GaNP crystals through MOCVD methods. For GaNAs, 0.2% As was added to GaN and the peak shift of band edge light was observed through photoluminescence measurement, but we were unable to mix a sufficient quantity of As. Therefore, we began development of GaNP in earnest in 1999.

In order to increase the incorporation of P, we began a new crystal growth method using laser-assisted MOCVD. This method involves exposing the substrate surface to an ArF laser during growth, thereby decomposing the source gases at low temperature and raising the incorporation of P. By using this method, we were able to attain a mixed crystal with a P composition of about 10%. We also fabricated a GaNP and GaN SQW (single quantum well) and were first to realize blue light emission with a GaNP LED.

## 6.3 Development of $\text{GaN}_{1-x}\text{P}_x$ Multicolored Light Emitting Materials through Laser-Assisted MOCVD

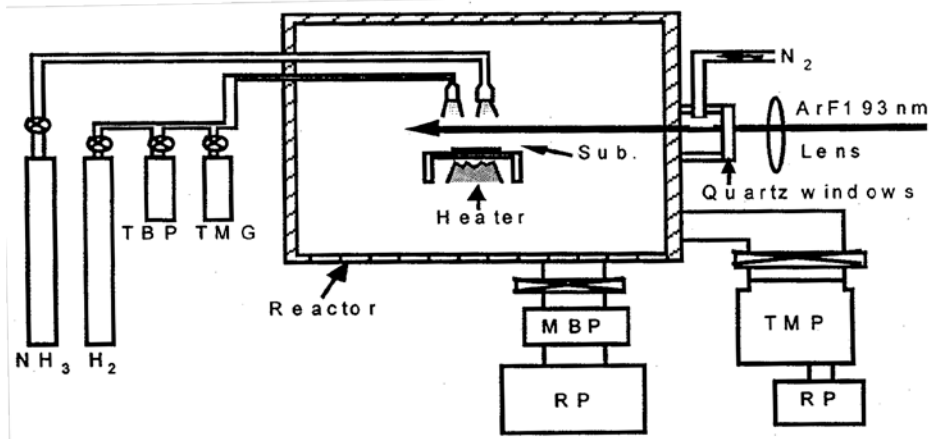
### 6.3.1 Methods and Means

Figure 6.3.1-(1) shows a diagram of the crystal growth platform used in this research. TMG was used as the Ga source,  $\text{NH}_3$  as the N source, and TBP as the additive P source. TMG and TBP are maintained in a thermostatic chamber at a constant temperature and then pulled as source gases at a constant volumetric flow via a MFC (mass flow controller).

Thereafter, acceleration is achieved by mixing in a large amount of oxygen gas and then introducing it into the reactor. Heat by a graphite heater is applied to the substrate used for growth and the gases are supplied to the susceptor. In contrast,  $\text{NH}_3$  is delivered from above via a separate system and is mixed in directly

above the substrate. The growth temperature is calibrated using both a thermocouple integrated into the heater and a radiant heat thermometer which monitors the substrate surface.

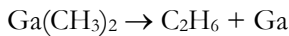
Figure 6.3.1-(1):  
Assisted  
MOCVD  
Platform.



The primary feature of this crystal growth platform is that MOCVD with photon excitation. An laser (LPX200 by Lambda Physik) is used for excitation, introducing from outside the growth chamber and scanned horizontally 2 mm above the substrate surface. The laser wavelength is 193 nm and the output is 100 mJ, modulated at a pulse repetition rate of 100 Hz.

The main benefit of photon-excitation lies in the elementary process of source gas decomposition, accelerating normal heat decomposition with decomposition caused by photon excitation. This elementary process is as follows.

Light absorption by TMG reaches its peak at around 195 nm and at 170°C has an absorption cross section of  $1.3 \times 10^{-16} \text{ cm}^2\text{mol}^{-1}$ . Decomposition begins around 250 nm and as it passes from a singlet state to a triplet state due to excitation through light absorption, the metal-carbon bond breaks [4]. At a wavelength of 280 nm the following reaction begins:



The following reaction begins at a wavelength of 240 nm [5, 6]:

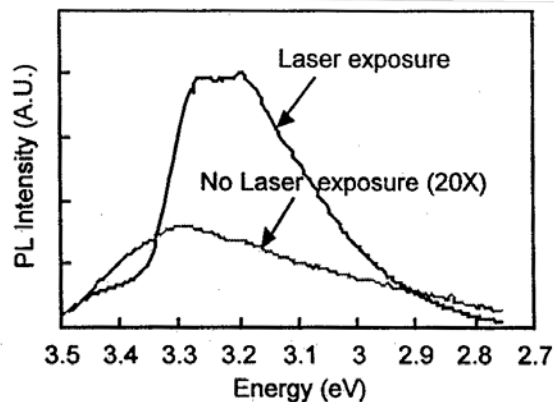
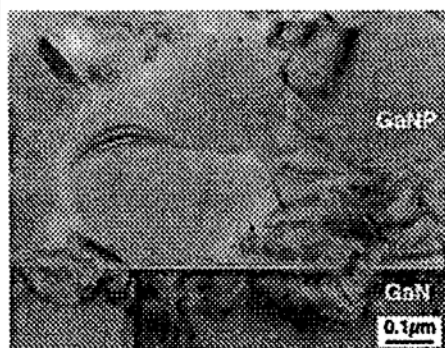


Absorption of light with  $\text{NH}_3$  begins at 210 nm and peaks at 190 nm. An absorption value of 500 to 600  $\text{cm}^{-1}$  has been reported [7]. The wavelength of the excitation laser used for growth is 193 nm so it covers the absorption band of TMG and  $\text{NH}_3$  and promises to facilitate source gas decomposition.

## 6.3.2 Results and Considerations for Growth of GaNP

### 6.3.2.1 The effect of photon excitation

A low temperature GaN buffer layer of 50 nm was grown on a sapphire substrate (0001), then another 1  $\mu\text{m}$  of GaN was grown on top of that. This was then used as the substrate for growing GaNP. When growing GaNP, the surface morphology worsens as the temperature is lowered to the level where islands easily form. GaNP was grown between 850°C and 950°C. Near 900°C we were able to attain a smooth surface. Figure 6.3.2-(1) shows the TEM (transmission electron microscopy) photo showing the cross section of the GaN/GaNP interface. GaNP is shown in a large domain. The crystal structure was found to be hexagonal through SAD (selected area diffraction) measurements.

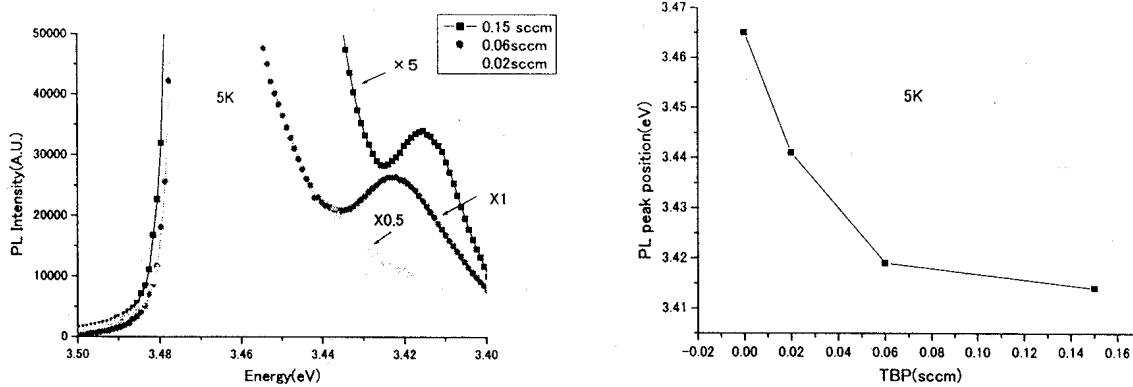


*Left: Figure 6.3.2-(1): Cross Section TEM Photo of GaN/GaNP Boundary.*

*Right: Figure 6.3.2-(2): Effect of Laser Exposure.*

Next, GaNP was grown on a substrate with a GaN buffer layer doped with Mg and a comparison was made between laser-assisted and non-laser-assisted methods. The GaNP was grown at a temperature of 900°C with a growth duration of 60 minutes, then annealed at 1050°C for 1 hour. The PL spectrum of the specimen is shown in Figure 6.3.2-(2).

The specimen which underwent laser exposure has a clear peak and an unmistakable difference in intensity that is several tens of times that of the specimen with no laser exposure. Yet, because the growth style differs when it is subjected to laser exposure and when it is not, we cannot state that the intensity difference is an effect of the laser exposure. Further study is necessary. When growing GaNP, the P composition is an important element. We verified the P composition dependency while growing GaNP crystals with TBP as the P source gas. They were grown at a temperature of 900°C for 60 minutes and annealed at 1050°C for 30 minutes. The TBP flow rate was at 4 levels: 0, 0.02, 0.06, and 0.15 sccm.



Left: Figure 6.3.2-(3): PL spectra at various flow rates.

Right: Figure 6.3.2-(4): PL peak position as a function of TBP flow rate.

Figure 6.3.2-(3) shows the PL intensity of each flow rate level at 5K. The GaNP peak can be seen as a small shoulder at the GaN edge emission peak.

Figure 6.3.2-(4) plots the GaNP PL position as a function of flow rate. A condition of saturation can be seen at a flow rate of 0.06 sccm. The amount of shift in the PL peak position becomes about 0.5% and, when one estimates the P composition of GaNP from results by Iwata and others [8], we find that saturation begins at a very low P composition.

### 6.3.2.2 Thoughts on Optical Evaluation of GaNP (Role of P<sub>N</sub> in GaNP)

Among the III-V and II-VI compound semiconductors, the behavior of substitutional charged impurities within a semiconductor has been researched most with GaP. It is well known that, among substitutional charged impurities of GaP, specific atoms, N or Bi for example, are bound exciton defects [9].

The electronegativity of an N atom is quite large at 3.0 compared to 1.64 for a P atom. For this reason, an N atom strongly traps nearby electrons and the potential of these trapped electrons attracts positive holes to form excitons. Additionally, the electronegativity of a Bi atom is small at 1.24 relative to a P atom, trapping positive holes and attracting electrons to form excitons. Such impurities appear electrically neutral except in their immediate vicinity, and therefore at short distances their potential operates to create deep levels.

Likewise with GaN, differences in the electronegativity between P or As atoms and the N atoms of the mother crystal result in trapped positive holes, causing electrons to be drawn by Coulomb potential in the same fashion as Bi atoms in GaP. The resulting neutral donor type exciton-binding defects are easy to observe.

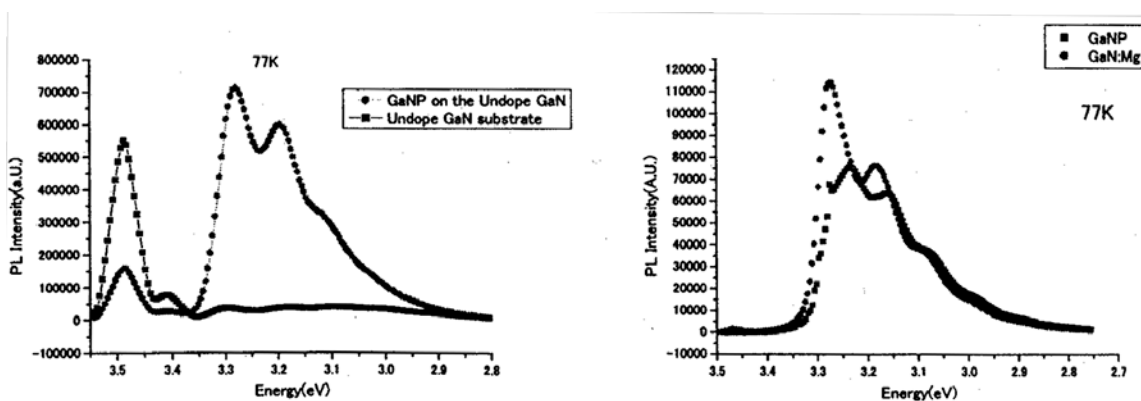
Among research on the introduction of substitutional charged impurities, such as P and As atoms, into GaN, there are a relatively large number of papers on As, but very few on P. Ion implantation is one method of introducing P that was reported by Pankove et al [10] many years ago. More recent research has been performed by Jadwisienczak et al [11], in which the light emission of a P isoelectronic trap peaks at 2.88 to 2.9 eV. On another front, Ogino et al [12] pursued a mixed crystal of P and GaN, producing a reaction between a Ga melt and NH<sub>3</sub> to create a powder which was then measured for photoluminescence. In this experiment too, the P atom serving as an isoelectronic trap showed a peak at 2.88 to 2.9 eV.

If P<sub>N</sub> in GaNP works as a neutral donor-type isoelectronic trap, it is thought that the conductivity of the host crystal should exert a large influence. Thus we grew GaNP with a P composition of 0.1% to 1% on p-type and n-type non-doped substrates. Then, through PL measurements, we confirmed the behavior of the P atom as a bound exciton defect.

### 6.3.2.3 Evaluation of GaNP Grown on GaN Epitaxial Sapphire Substrate

GaNP was grown on a GaN epitaxial sapphire substrate. Three GaN epitaxial substrates were used: one which was not intentionally doped, one doped with Mg, and another doped with Si. The quantity of each dopant was found through SIMS measurements to be  $1.8 \times 10^{19} \text{ cm}^{-3}$  for the p-type substrate and  $3.1 \times 10^{18} \text{ cm}^{-3}$  for the n-type substrate. The true carrier concentration is unknown since we did not perform Hall measurements, but it is thought that the activation rate of Mg is about 1% and of Si is about 10%, so we estimate that a carrier concentration of about  $1 \times 10^{17} \text{ cm}^{-3}$  exists on both p and n-type substrates. GaNP was grown by MOCVD with photon excitation at a temperature between 850°C and 950°C. The grown GaNP epitaxial layers were 0.5 to 1  $\mu\text{m}$  thick and the P compositions were estimated to be 0.5 to 1% based on SIMS and X-ray analysis, although establishing this quantitatively was difficult because the surface morphology of the GaNP was very poor. Moreover, SIMS measurement detected dopants of each substrate in the GaNP epitaxial layer, with Mg on the p-type substrate and Si on the n-type substrate. Even though no intentional doping was carried out, it is thought that p-like and n-like GaNP epitaxial layers formed by an auto-doping effect.

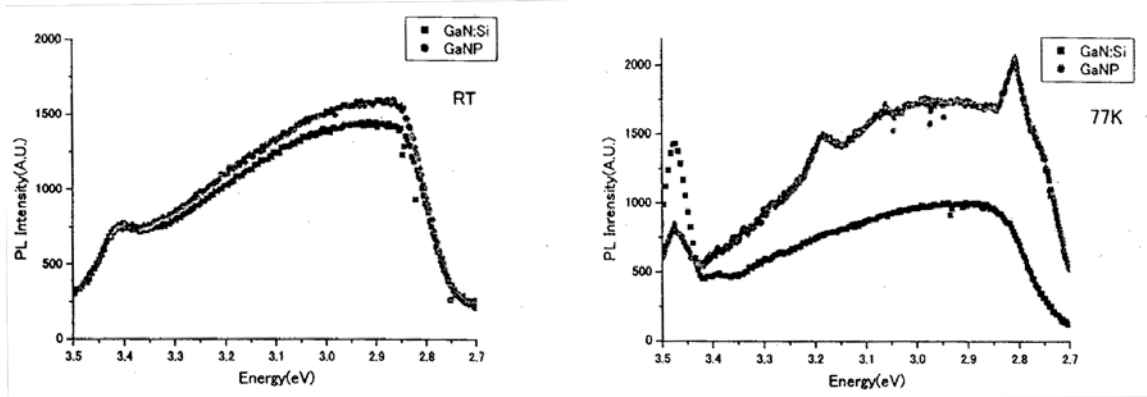
PL measurements were performed at 77K and at room temperature. As the source for photon excitation we used a He-Cd laser with a wavelength of 325 nm and an output of 50 mW. The light intensity density at the specimens was about  $1 \text{ Wcm}^{-2}$ . The PL measurement of the GaNP epitaxial film was, of course, effected by the underlying GaN substrate. To measure the photoluminescence of the underlying GaN substrate for comparison, we used three methods: (1) measure the substrate prior to GaNP growth, (2) measure after growth, and (3) turn over the experimental material and expose the GaN to photon excitation from the side of the sapphire substrate. We did this thinking that it is possible that the GaN of the substrate receives residual heat (heat history) from the growth of GaNP and is somehow transformed. However, the results show no significant difference between the PL measurement of the pre-growth substrate and that measured from the back side of the substrate after regrowth of GaNP.



Left: Figure 6.3.2-(5): Spectrum (77K) of GaNP on Undoped Substrate.

Right: Figure 6.3.2-(6): Spectrum (77K) of GaNP on p-type Substrate.

Figures 6.3.2-(5), (6) and (8) show the PL spectra at 77K of GaNP films grown on the undoped substrate, the p-type substrate, and the n-type substrate. Each figure shows the PL spectra of both the GaNP and the underlying GaN for the purpose of comparison. The GaNP spectra from both the undoped substrate and the p-type substrate are similar, but the GaNP of the n-type substrate is quite different in both shape and intensity. The GaNP of the p-type substrate shows strong exciton luminescence and phonon replica. The spectrum shape is similar to the substrate but shows a subtle difference in the peak near 3.27 to 3.25 eV.



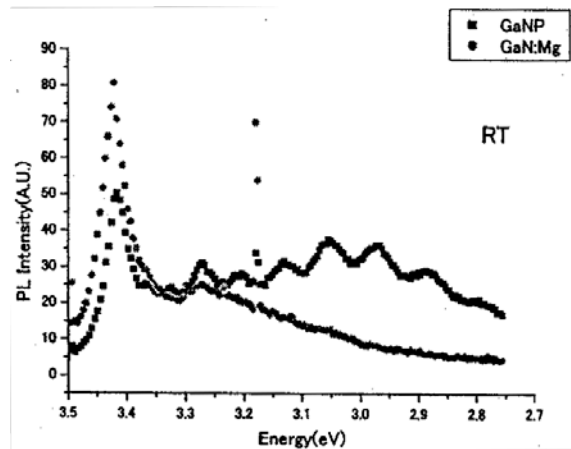
Left: Figure 6.3.2-(7): Spectrum (room temperature) of GaNP on n-type Substrate.

Right: Figure 6.3.2-(8): Spectrum (77K) of GaNP on n-type Substrate.

The shape of the GaNP on the undoped substrate clearly differs from the substrate, but closely resembles the GaNP on the p-type substrate. On the other hand, the GaNP on the n-type substrate shows only broad light emission with no exciton luminescence and is very similar to the substrate photoluminescence. Also, the intensity is two orders of magnitude weaker than that of the undoped or p-type substrates.

Figure 6.3.2-(8) shows the PL spectrum of GaNP on an n-type substrate at 77K. Figure 6.3.2-(9) shows the PL spectrum of GaNP on a p-type substrate at room temperature. The PL spectra of both the GaNP and the underlying GaN are plotted together for comparison. The PL spectra of GaNP on the n-substrate shows little difference between 77K room temperature. The PL intensity of GaNP on type substrate at room temperature is weaker by orders of magnitude compared to that at 77K. phonon replica in GaNP is remarkable compared that at 77K (shown in Figure 6.3.2-(6)).

Figure 6.3.2-(9): Spectrum (room temperature) of GaNP on p-type Substrate.



type  
and  
the p-  
four  
The  
to

These results, as viewed from the substrate’s conductivity, are as follows.

Exciton luminescence is predominant in GaNP on a p-type substrate in which holes are the majority carrier, and its intensity is strongly dependent on temperature. In GaNP on a n-type substrate in which holes are the minority carrier, exciton luminescence is not seen and the intensity shows little dependence on temperature. On the other hand, with GaNP on the undoped substrate – which is thought to be n-type – the PL spectrum is similar to that of the GaNP on the p-type substrate.

These results can be explained quantitatively as follows.

$P_N$  as a neutral donor works as a hole trap only with the existence of a reasonable concentration of positively charged holes. With GaNP on a p-type substrate, holes are the majority carrier so  $P_N$  can work effectively as a neutral donor. Because electrons are the majority carrier in GaNP on an n-type substrate, only generated holes exist nearby  $P_N$  during photon excitation and  $P_N$  does not work as an effective neutral donor due to competition with the non-radiating center of inactivated Si atoms and the numerous electrons surrounding

$P_N$ . Although GaNP on the undoped substrate is n-type, the quantity of electrons differs greatly compared to the n-type substrate and so the behavior resembles that of GaNP on a p-type substrate.

### 6.3.2.4 Evaluation of Photonic Properties of GaNP with Different Substrates (Strong Mutual Interaction with Lattice)

The phonon replica is peculiar to GaNP on a p-type substrate. In particular, as the measurement temperature rises the PL intensity falls, yet mutual phonon replica can be clearly observed. Figure 6.3.2-(10) shows the PL measurement results from 7K to room temperature. The peak energy and peak number have been separated for each replica and are shown in Figure 6.3.2-(11) as a Gaussian distribution. The spacing between each peak is 80 meV and the intensity distribution has been fit using LO phonon scattering.

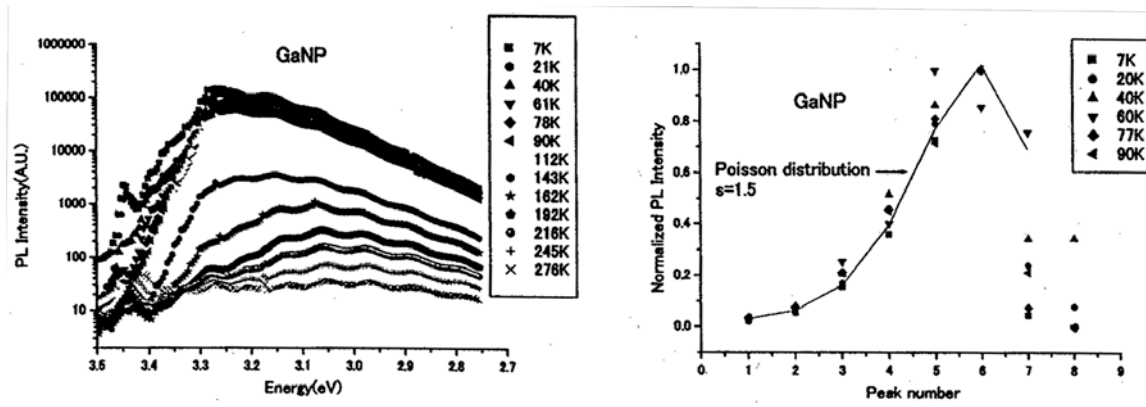
The peak PL intensity can be found by

$$I(E) = \sum \exp(-S) \frac{S^i}{i!} \times \frac{1}{1 + (E - E_0 + iE_{LO})^2 / \gamma^2}$$

$$S = I_1 / I_0$$

and the relationship to the phonon-exciton coupling can be derived. In Figure 6.3.2-(11) the zero phonon line is unclear so the intensity of each phonon replica was approximated using a Poisson distribution to derive [14] the phonon-exciton coupling coefficient of  $S = 1.5$ . This value is quite large compared to the value of  $S = 0.2$  calculated from the phonon replica observed by InGaN electroluminescence and we see that it has a strong localized center.

In this way, we observed that  $P_N$  in GaNP has the characteristics of an effective neutral donor when holes are the majority carrier and has a localized center that strongly interacts with the lattice.

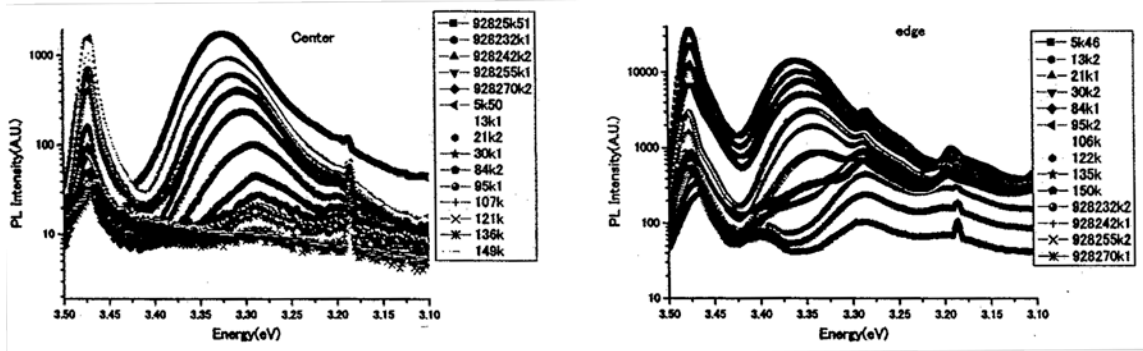


Left: Figure 6.3.2-(10): Spectrum of GaNP on p-Type Substrate.

Right: Figure 6.3.2-(11): Phonon Replica Peak Separation.

### 6.3.2.5 Temperature Dependence of GaNP Photonic Characteristics

To research the photonic characteristics of GaNP, GaNP with differing P compositions was grown and then PL measurements were performed. The specimen was grown on an undoped GaN substrate at a growth temperature of 900°C for 60 minutes with TBP flow rates of 0.1 sccm and 0.2 sccm, and then annealed for 60 minutes at 1050°C. Among the substrates there was some variation in the GaNP epitaxial film but the strongest PL intensity was used for comparison. The observed temperature dependence of the PL spectra is shown in Figures 6.3.2-(12) and (13).

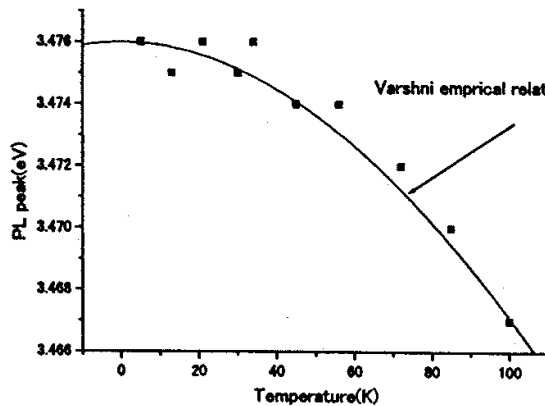


Left: Figure 6.3.2-(12): Temperature Dependency of PL Spectrum of GaNP (TBP: 0.2 sccm).

Right: Figure 6.3.2-(13): Temperature Dependency of PL Spectrum of GaNP (TBP: 0.1 sccm).

The peak around 3.476 eV is the band emission of GaN and shows no large variation with regard to temperature between 5K and 40K, but thereafter gradually shows red shifting. Figure 6.3.2-(14) shows the temperature dependence of this peak. Shown by the solid line in this figure, the measured values represented by the black squares were fit using the Varshni empirical relationship of the W. Shan model [15] ( $\alpha : 8.32 \times 10^{-4}$  eV/K,  $\beta : 835.6$  K), confirming the GaN band emission.

On the other hand, the fact that the peak position in the vicinity of 3.35 eV varies according to the GaNP composition leads us to believe that it is GaNP luminescence. This temperature dependence, unlike the band emission of GaN, is shown as a red shift relative to a rise in temperature from 5K.

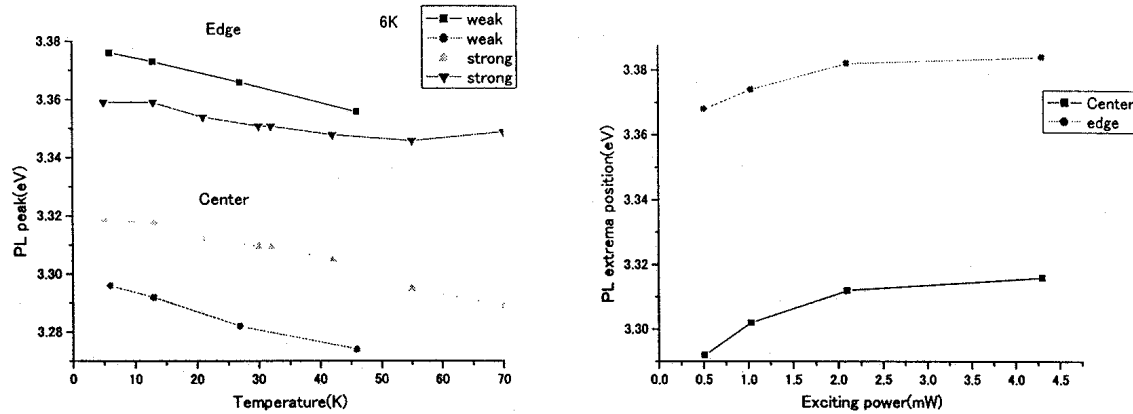


(Varshni empirical relationship)

$$E_g(T) = E_g(0) - \frac{\alpha T^2}{\beta + T}$$

Figure 6.3.2-(14): Temperature Dependency of GaN Band Emission.

Next, the dependence on excitation power using the same specimen was measured using PL measurement. The results are shown in Figure 6.3.2-(15). The temperature dependence of the GaNP peak was measured by setting the excitation light intensity to 0.5 mW for weak excitation, and to 4.5mW for strong excitation. The results are shown in Figure 6.3.2-(16).



Left: Figure 6.3.2-(15): Relationship between PL Peak and Excitation Light Intensity.

Right: Figure 6.3.2-(16): Relationship among PL Peak and Excitation Light Intensity and Temperature.

### 6.3.2.6 Discussion

The PL spectrum of GaNP – unlike the band emission of GaN – appears to experience a red shift proportional to the temperature. A dependence like this can also be seen in the PL emission band tailing of semiconductors doped with both high quantities of n and p impurities.

In semiconductors containing a high quantity of both n and p impurities, tailing occurs at the end of each band, both conduction and valence bands. The peak wavelength during recombination between the free electrons neighboring the Fermi level within the semiconductor and holes bound to the tailing valence band is expressed by the following equation [16, 17, 18].

$$\omega \approx E_g + \mu_n - \sqrt{2}\gamma - \varepsilon_p^o$$

Here,  $E_g$  represents the band gap energy when undoped,  $\mu_n$  represents the Fermi level,  $\gamma$  is the rms value of the potential fluctuation caused by impurities, and  $\varepsilon$  – found by the following equation – is the equivalent thermal depth of bound holes produced by potential fluctuation.

$$\varepsilon_p = T \ln \left[ N_v [p + n\theta(\varepsilon)]^{-1} \right]$$

In this equation, T is the absolute temperature,  $N_v$  is the effective state density of the valence band, and p and n represent the hole and electron densities, respectively.  $\theta$  is the ratio of the recombination coefficient between free electrons and localized holes and the binding coefficient caused by the localization center of the free holes. In this case, the temperature dependence of the PL spectrum peak wavelength is defined primarily by  $\varepsilon$  and results in a negative factor with regard to temperature (experiencing red shift).

On the other hand, the photoluminescence excitation intensity and the density of excited carriers ( $p + n$ ) within the semiconductor have a positive correlation, therefore if we tentatively assume that the correlation is linear, we should find from the equation that  $\exp(\varepsilon/T) \propto 1/(\text{excitation intensity})$ .

If we recalculate the variable in Figure 6.3.2-(15) we arrive at Figure 6.3.2-(17) with a sectionally linear slope. In reality the excitation intensity and carrier occurrence is not linear and since the Fermi level changes, the explanation is not this simple. Moreover, in Figure 6.3.2-(17) the peak position temperature dependency factor in relation to photoluminescence excitation intensity is larger when GaNP has a high P composition than when it has a low P composition. The difference in P composition in the GaNP can be explained qualitatively by noting that when the composition is increased by varying the carrier binding and recombination state, it results in a weaker photoluminescence intensity during recombination,  $\theta$  becomes smaller and the apparent  $\varepsilon$  grows larger.

Figure 6.3.2-(17):  $\exp(\varepsilon/T) \propto 1/(\text{Excitation Intensity})$ .

Further study is required in order to apply the analogy of band tail transition of high doped semiconductors to GaNP, as shown above. here, let's consider the concentration and distribution of P atoms in GaNP as seen from PL spectra.

The PL spectra of the GaNP can be categorized into two cases – when the P composition is extremely low, and when the density of P atoms is near 1%.

As reported above, in the GaNP specimens created with ion implantation of P atoms, there is a P density of about  $1 \times 10^{17}$  to  $1 \times 10^{18} \text{ cm}^{-3}$  and nearly all of the P atoms are isolated, showing light emission as an isoelectronic trap around 2.97 eV [10, 11].

In contrast, when the P atom density rises to  $1 \times 10^{19}$  to  $1 \times 10^{20}$ , the P atoms are no longer isolated and show characteristics of bulk GaNP, exhibiting a photoluminescence peak near the area of band emission of GaN. It has been reported that as the P atom density increases further, photoluminescence becomes difficult around 2% and at 8% separation into GaN-rich GaP and GaP-rich GaN occurs [8].

In what fashion are P atoms distributed within the GaNP crystal? If we assume a totally random distribution and zinblende lattice, the number of nearest neighbor and next nearest neighbor atoms to a particular P atom are 12 and 22, respectively. Therefore, taking  $x$  as the P atom density, the number of isolated P atoms (with only N nearest neighbors) and the number of nearest-neighbor P atom pairs (with only N next-nearest neighbors) can be calculated [19] to be  $N_s = x(1-x)^{12}$  and  $N_p = x^2(1-x)^{22}$ , respectively.

According to this, the probability of existence for an opposing P atom is about 1% of the isolated P atoms, even if density  $x$  becomes 10%, which means there is an overwhelmingly high number of isolated P atoms.

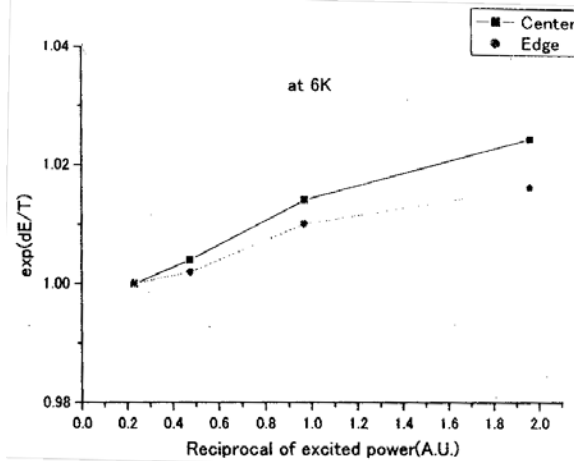
This contradicts the reality that even in GaNP with a density of about 0.1%, the photoluminescence of the bulk GaNP is stronger than the photoluminescence by the isoelectronic trap made up of isolated P atoms.

Now let's look at crystal structures with arsenic or simple phosphorus. Arsenic and phosphorus have a coordination number of 3 and is the most stable polymorphism. Among the bonds positioned at the vertex of the simple cubic lattice, three are deviant, thereby skewing the entire structure. With black phosphorus, it bonds in two locations at an angle of  $102^\circ$  and one location at  $96.5^\circ$ .

Figure 6.3.2-(18) shows the number and distance of neighboring atoms within arsenic and phosphorus crystalline structures. The first most-proximate atom is comprised of four atoms in a pyramidal formation. Figure 6.3.2-(19) shows the most stable structure of a monovalent 3s or 3p valence electron bound molecule, as predicted by first principle calculations. According to this, it is estimated that initially there are only isolated P atoms, but gradually a pyramid of four P atoms forms, the pyramids themselves form into clusters of six, and then the six pyramidal clusters form into clusters of twelve [20].

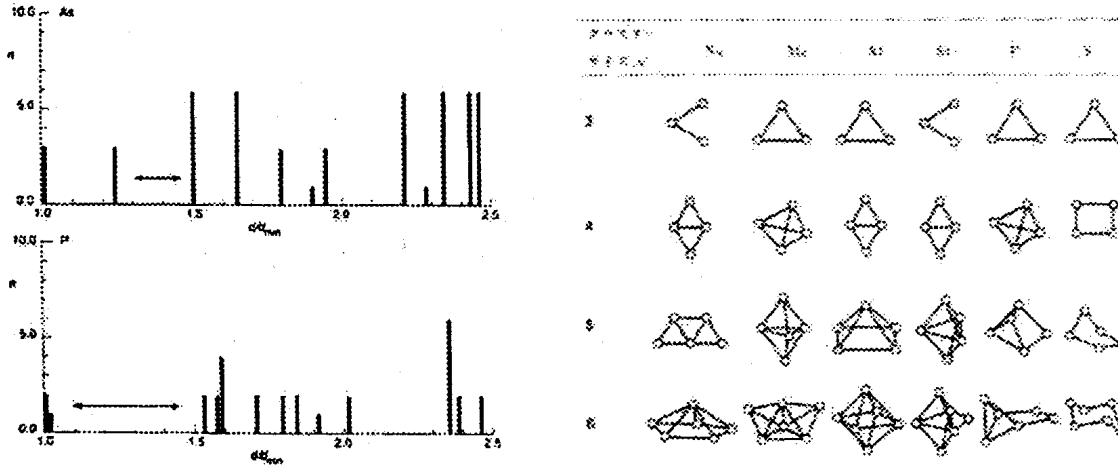
We can't imagine that the distribution of P atoms within the GaN host crystal is exactly as pictured above, but it can be easily imagined that if a large Ga-P bond is present among the short, strong bonds of GaN, the Ga-N bond will break once and the next P atom is easily accepted near the Ga-P bond, unlike near other Ga-N bonds. In other words, pairs of P atoms are formed and gradually cluster into near-pyramidal forms.

The photoluminescence spectra of GaNP clearly show that it exhibits the properties of the bulk GaNP even though the P density is comparatively low. It is surmised that this is because clusters form from the time that P atom density is low, rather than following a random distribution. It is believed that this clustering has a



From  
the

spatial composition distribution and behaves in a way similar to the band tailing produced by potential fluctuations in heavily doped semiconductors



Left: Figure 6.3.2-(18): Histogram of Neighboring Atoms of Black Phosphorus and Arsenic.

Right: Figure 6.3.2-(19): First Principle Calculations (H.S. Lim)[21].

## 6.4 GaNP Growth (DMHy/PH<sub>3</sub>/TMG) through Nonradiated MOCVD

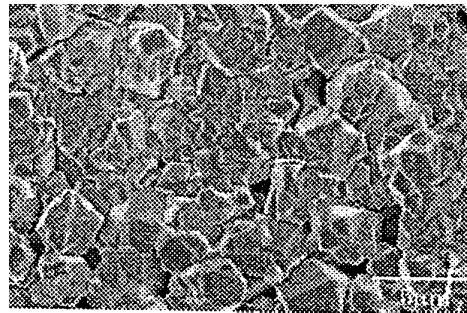
### 6.4.1 Methods and Means

Growth of GaNP on a sapphire substrate by MOVPE was examined. The growth procedure consisted of growing a high quality GaN layer at 1000°C with the introduction of an AlN buffer layer at a low temperature of 850°C. Then GaNP was grown epitaxially at 850°C. The source gases for Ga, Al, N, and P were TMG, TMA, DMHy and PH<sub>3</sub>, respectively. The growth pressure was 160 Torr. The temperature of the thermostatic chambers holding the organic source materials were set to 0°C for TMG, +15°C for DMHy, and +20°C for TMA. The saturated vapor pressures were 66.8 mmHg, about 95 mmHg, and 9.36 mmHg, respectively. The PH<sub>3</sub> was diluted 10% in hydrogen.

Oxide film was first removed from the sapphire surface through heat treatment at 1050°C. Thereafter the temperature was reduced to 850°C and an AlN buffer layer was grown (TMA: 9.1 sccm. DMHy: 220 sccm). AlN is used to relieve the large difference between the lattice constants of sapphire and GaN and becomes a crystalline nucleus, making growth thereafter of GaN a smooth process. GaN with a layer thickness of about 1.2 μm is then grown for 25 minutes and used as a substrate (TMG: 7.6 sccm. DMHy: 40 sccm). After lowering the temperature to 850°C, a layer of GaNP is grown for 20 minutes. The rate of flow for each source gas during growth of the GaNP layer was 29.8 μmol/min (7.6 sccm) for TMG, 220 μmol/min (40 sccm) for DMHy, and 135 to 450 μmol/min (30 to 100 sccm) for PH<sub>3</sub>.

### 6.4.2 Results and Observations

The surface of all specimens fabricated according to the growth conditions noted above turned yellowish and the growth layer of the film was extremely rough and difficult to see. Figure 6.4.2-(1) shows an SEM image of the surface. The GaN surface is formed by multiple grains, as can be seen in Figure 6.4.2-(1). It is thought that because the flow rate of PH<sub>3</sub> is quite high, the GaNP grown on the surface is not N-rich, rather it is P-rich or simply a GaNP layer. If GaP-rich, elimination is possible



layer

through etching via aqueous treatment, thus this treatment was performed for 15 minutes. Consequently, after etching, the layer that had existed on the specimen surface was eliminated, so the characteristics of the surface after etching was also examined.

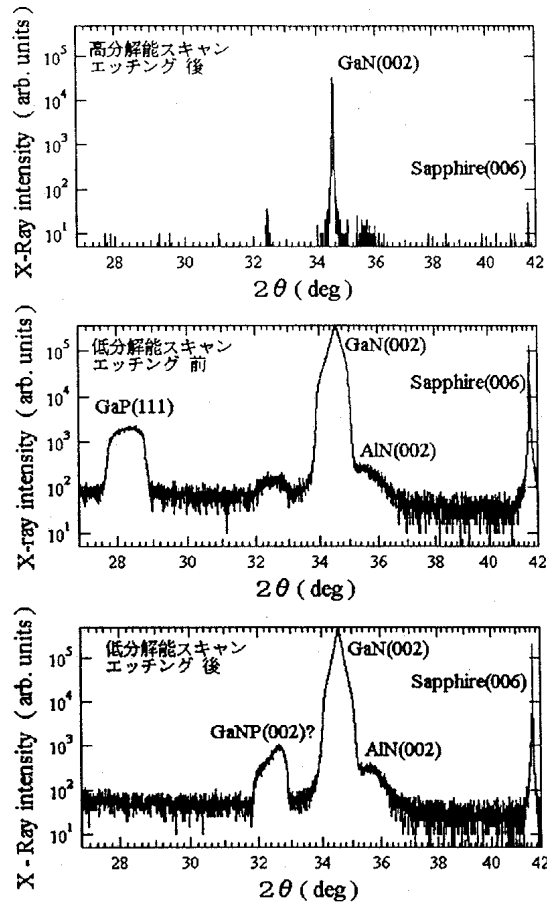
*Figure 6.4.2-(1): SEM Image of GaNP Mixed Crystal Surface.*

Figure 6.4.2-(2) shows the results of X-ray diffraction measurement (002) of the specimen before and after etching of the GaP-rich surface layer. The peak shown at about 41.7° is caused by the surface (006) of the sapphire substrate while the peak at about 34.7° is due primarily to the surface (002) of the underlying GaN layer. At high resolution, the remaining peaks are difficult to verify since their intensity is very weak, so a low resolution X-ray diffraction measurement was employed.

With low resolution measurement, the peak width height becomes extremely broad, allowing verification of the AlN buffer peak around 36°. an X-ray diffraction peak from the GaP surface was confirmed at about 28.3° (calculated to be 28.334°) with the pre-etched specimen only. This us that while the crystallization is extremely poor, crystal growth of GaP did occur.

Additionally, although the diffraction peak from (111) on the etched specimen disappeared, another peak appeared instead at around 32.4°. source of this peak is unknown, but since it was after etching and because it is not seen with the growth, it is believed to be a diffraction peak from initial GaNP growth layer.

*Figure 6.4.2-(2): (0002) X-Ray diffraction spectra to and after aqua regia etching of GaNP. (Top to bottom: high-resolution measurement after etching, and resolution measurements prior to and after etching.) (Top to bottom): High-resolution scan, after etching; resolution scan prior to etching; Low-resolution scan after etching.*



at half  
Also, (111)  
tells  
GaP  
The found GaN the  
prior  
low-Keys  
Low-after

Figure 6.4.2-(3) shows the photoluminescence spectra before and after etching. Because a GaP-rich layer is thickly applied, a GaNP peak near 3.5 eV and a GaN peak is not observed. Instead broad emissions near 1.9 eV and 2.25 eV are found. Since these emissions disappear after etching it is thought to be emissions from the GaP-rich layer. The peak at 1.9 eV appears at the same location as seen in the PL measurement when a four dimensional mixed crystal was evaluated so it is thought to be an emission from the GaPN mixed crystal. If this peak position is from GaPN, the N concentration equates to approximately 3%. Also, the peak at 2.25 eV is thought to be due to reflection from the GaP growth.

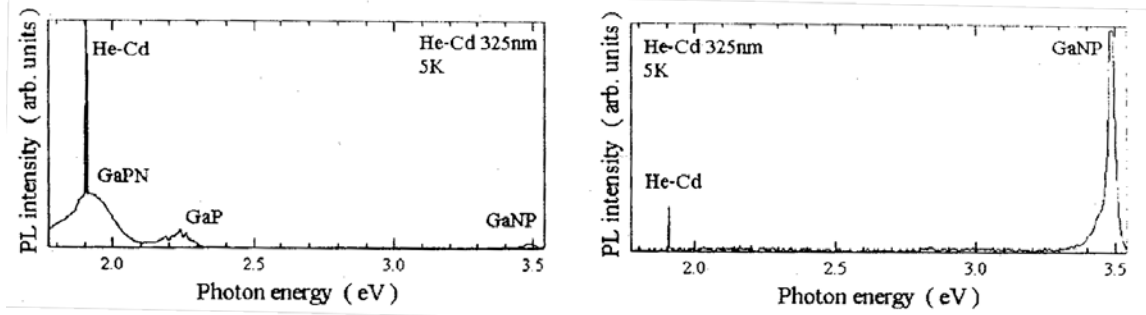


Figure 6.4.2-(3): PL Spectra Before and After Etching (left: before, right: after).

The peak near 3.5 eV on the etched specimen is an emission observed from a location different from the GaN PL peak position. This peak shifts systematically as the flow rate of  $\text{PH}_3$  is varied and no emission from the substrate's GaN can be seen. Since, even after etching, something is growing on the GaN, this is thought to be a result of inhibition of emission from the GaN buffer layer of the substrate.

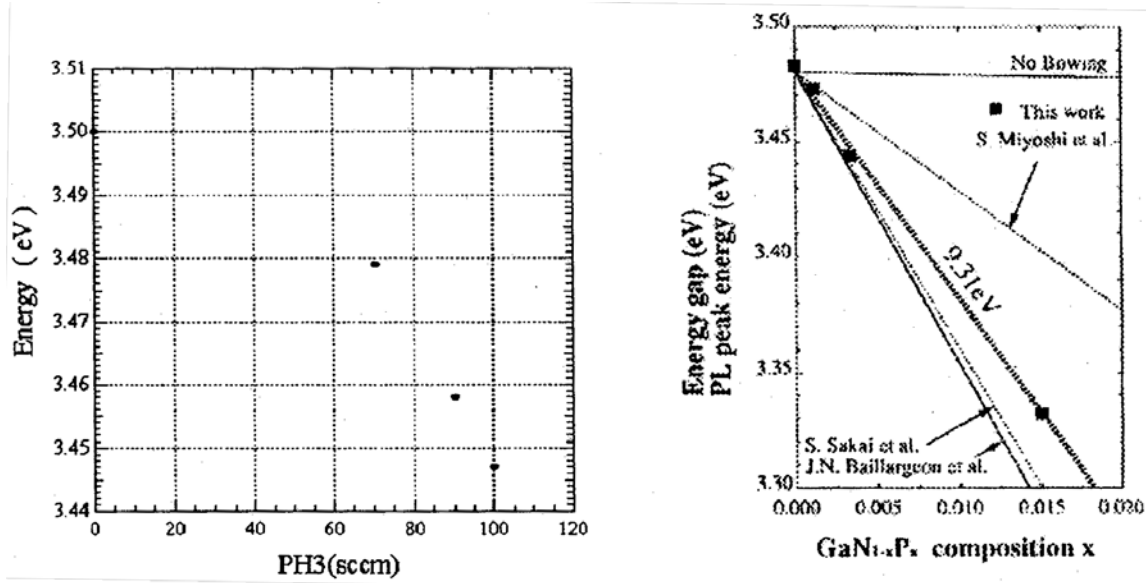
Next, GaP was grown on GaN with a  $\text{PH}_3$  flow rate of 100 sccm. Observation of the photoluminescence spectrum of the surface after etching showed no shifting of the PL peak with only emission from the GaN.

Next, the  $\text{PH}_3$  flow rate dependency of the PL peak energy was examined by varying the  $\text{PH}_3$  flow rate from 30 sccm to 100 sccm at 850°C. The findings are shown in Figure 6.4.2-(4), illustrating a PL peak shift dependent on the  $\text{PH}_3$  flow rate. At 875°C and 835°C, band edge emission occurs at 3.498 eV and 3.496 eV.

Figure 6.4.2-(5) shows test values for PL peak energy of a GaNP mixed crystal fabricated by MBE and the theoretical equation for band gap. The composition was determined from the band edge PL peak energy by referencing the band gap bowing of 9.3 eV that was derived experimentally from a GaNP mixed crystal up to 8.2%. As a result, we found a P density of 0.6% at 100 sccm.

From the results above, growth of GaNP mixed crystals on a sapphire (0001) substrate under conditions of 850°C with a  $\text{PH}_3$  flow rate from 30 to 100 sccm resulted in a GaP-rich layer having a very rough surface. Since the GaP-rich layer was eliminated by aqueous etching, neither X-ray diffraction or PL measurements could confirm that it was GaP-rich. Additionally, emissions from the GaNP were confirmed from the surface after etching.

By estimating the P density from the PL peak energy of GaNP, we found that we were capable of fabricating GaNP mixed crystals with a P density of approximately 0.25, 0.5, and 0.6%.



Left: Figure 6.4.2-(4): PH<sub>3</sub> Flow Rate Dependency of Band Edge PL Peak Energy.

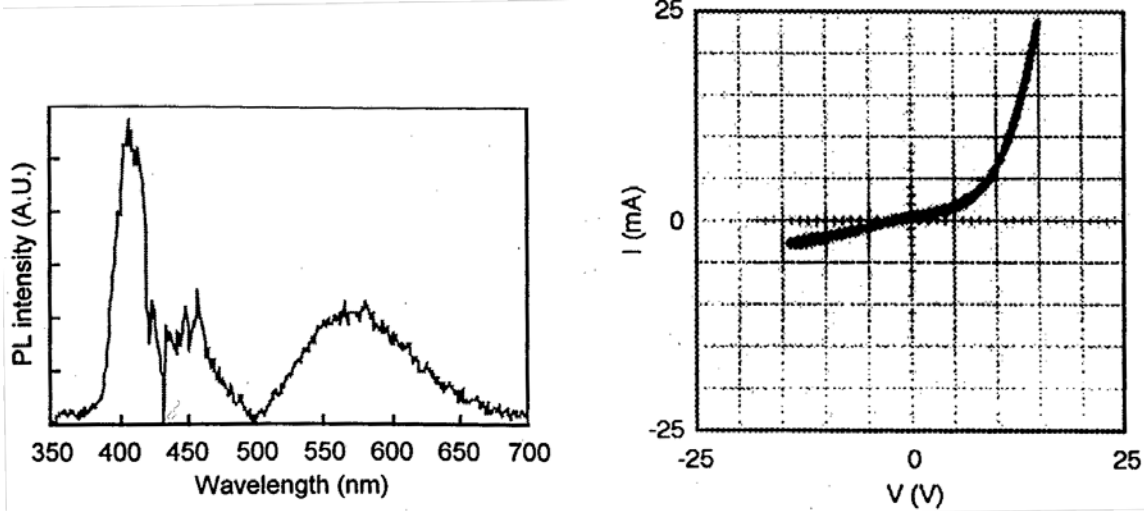
Right: Figure 6.4.2-(5): Band Gap Bowing of GaNP Mixed Crystal.

## 6.5 GaNP LEDs

### 6.5.1 Methods and Means

Using laser-assisted MOCVD, we were able to grow GaNP with a high P composition (up to 10%) on the N-rich side. We examined the photoluminescence characteristics of these mixed crystals and confirmed a maximum shift in the band edge emission peak by 0.2 eV from the GaN band edge toward the long wavelength. Based on these results, we fabricated a prototype SQW GaNP LED.

First, a Mg-doped GaN film was grown 2 μm thick on a sapphire substrate. Then, using laser-assisted MOCVD, undoped n-GaNP was grown to a thickness of 1 μm at 950°C using TMG, TBP, and NH<sub>3</sub> while exposed with an ArF laser at 30 nm. The photoluminescence characteristics of the resulting crystals were examined. Figure 6.5.1-(1) shows the PL spectrum. We observed a sharp peak near 410 nm, a sub peak at 450 nm, and a broad peak around 575 nm. This sample was used to fabricate the LED structure. After depositing SiO<sub>2</sub> on the GaN epitaxial surface, photo-resist was used to create the pattern and then portions of the n-GaN and GaNP layers were removed through dry etching to form p-type electrodes. ECR (electron cyclotron resonance) plasma etching with Ar (7 sccm) / H<sub>2</sub> (15 sccm) / CH<sub>4</sub> (5 sccm) combined gas was used for dry etching. Subsequent to etching, an LED was fabricated through vapor deposition of Al/Ti/Au for the n-type electrode and Pt/Au for the p-type electrode.



Left: Figure 6.5.1-(1): PL Spectrum.

Right: Figure 6.5.2-(1): I-V Characteristics of LEDs.

### 6.5.2 Results and Observations

Figure 6.5.2-(1) shows the I-V characteristics of the fabricated LED.

Onset characteristics of the forward current were poor and it is believed that this is because the n-GaN layer is undoped, resulting in a high resistance.

We plan on improving the equipment so it is possible to dope with Si as an n-type impurity. The LED's ability to withstand voltage in the reverse direction is greater than 20 V. We next performed EL measurements of the GaNP LED. Figure 6.5.2-(2) shows the EL spectrum. It shows a sharp peak around 425 nm and a broad peak around 590 nm. The emission color is a visible blue. An image of the LED emission is shown in Figure 6.5.2-(3). Deep level emission around 590 nm is thought to be caused by crystal defects in the GaNP. When a GaNP LED is fabricated with the GaNP layer thickness at 100 nm, the broad emission at 590 nm is stronger than the peak at 420 nm, as shown in Figure 6.5.2-(4), and the color of the emission becomes a bluish white. By thinning the emission layer and raising the crystallinity, deep level emission is suppressed and it is thought that this is because the band edge emission has become stronger.

The results above show that GaNP, apart from InGaN-based materials, holds promise as a new light emitting diode material.

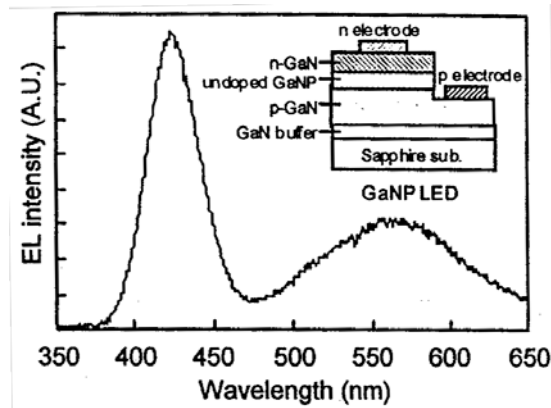
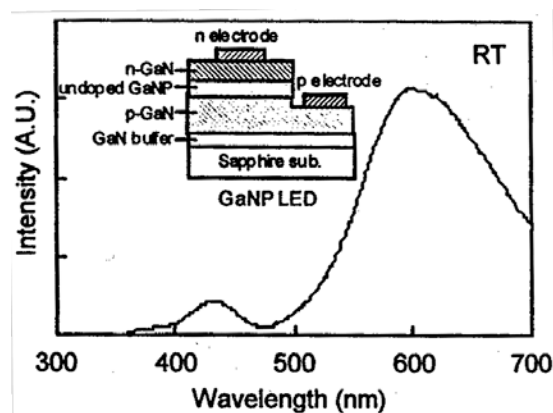


Figure 6.5.2-(2): EL Spectrum (with a thin GaNP

blue film).



Left: Figure 6.5.2-(3): Image of Blue Light Emission from LED.

Right: Figure 6.5.2-(4): EL Spectrum (with a thick GaNP film).

## 6.6 Summary

Growth of GaNP with a high P composition was examined using two methods: MOCVD using DMHy and PH<sub>3</sub> source gases, and laser-assisted MOCVD.

Through an experiment with MOCVD using DMHy and PH<sub>3</sub>, and keeping the V/III ratio of the source gases constant while varying the growth temperature, SIMS analysis found 0.5% P was combined when the temperature was set low. Among the optical characteristics we observed a peak shift in the band edge caused by the addition of P to GaN with respect to the PH<sub>3</sub> flow rate.

Additionally, GaNP was grown by a new laser-assisted MOCVD method. The results show the the source gases were photodecomposed at low temperature and SIMS analysis found a P addition of about 10%. Using TBP – which is easily decomposed – as the P source, we were able to attain a crystal with a high P composition at a growth temperature of 850°C. PL measurements showed a shift of 0.2 eV in the band edge peak in the long wavelength direction compared to GaN. Moreover, while inadequate from a quantitative perspective, we observed a large red shift compared to previous reports and believe we have confirmed band bowing in GaNP. The degree of red shift shown in the photoluminescence spectra from our GaNP specimens is two to three times that of conventional MOVPE. Laser-assisted MOCVD has thus been shown to have high potential.

It is necessary to move forward with more emphasis on quantitative research in 2001. With the creation of a prototype GaNP SQW LED, we were the first to prove blue and blue white light emission by current injection. This shows that, at a minimum, GaNP LEDs hold promise as a blue LED.

## 6.7 Future Course

In 2001, we intend to work with Professor Onabe of Tokyo University in growing GaNP (As) crystals and finding the optimum growth conditions under laser-assisted MOCVD by raising the intensity of the laser and improving the equipment itself.

Tokyo University will examine crystal growth of GaNAs or GaNP by gas source MBE which has a stronger non-equilibrium state, large band gap bowing, and a high expectation for wave length shifting. We will also work on optimizing the design of equipment used for laser-assisted MOCVD. In other words, we will optimize the growth conditions to achieve GaNP with a high P composition by making modifications to the substrate susceptor, heater construction, and gas inlets.

We will raise the photoluminescence intensity of the LED by further studying GaNP multiple quantum well structures and epitaxial structures. To understand the light emission mechanism of GaNP we will continue to research in detail photonic characteristics through photoluminescence measurements. We will use selective epitaxial growth to increase the brightness of the LED and to improve the crystal quality. Stated differently, selective epitaxial growth, where epitaxial growth is performed locally and at specified locations of the substrate surface instead of across the entire surface, is thought to be more effective in attaining high quality. Evaluation of photonic characteristics and the light emission mechanism will be researched together with Professor Taguchi of Yamaguchi University. Lastly, we will work on raising the P composition and discovering the optimum growth structures and conditions for high-brightness luminescence.

## 6.8 References

- [1] J. Kikawa, S. Yoshida, and Y. Itoh, Workshop on Nitride Semicond. IPAP Conf. Ser. 1 (2000) 429.
- [2] J. Kikawa, S. Yoshida, and Y. Itoh, J. Crystal Growth (2000) May in Press.
- [3] J. Kikawa, S. Yoshida, and Y. Itoh, Mat. Res. Soc. Symp. Proc. (2001) G2.2, in press.
- [4] Fundamentals of the Photon Excitation Process, K. Takahashi (1994) Kogyochosakai.
- [5] H. Okabe, J. Appl. Phys. 69, 1730 (1991).
- [6] Th. Beuermann, Chemicals, 3, 230 (1988).
- [7] K. Watanabe, J. Chem. Phys., 22, 1564 (1954).
- [8] Kakuya Iwata, Molecular Beam Crystal Growth of III-V Nitride Semiconductors, Osaka University Academic Dissertation (1998).
- [9] P. J. Dean, Prog. Crystal. Growth Charact. 1982, Vol. 5, pp. 89-174.
- [10] J. I. Pankove and J. A. Hutchby, J. Appl. Phys. 47 (1976) 5387.
- [11] W. M. Jadwisieniczak and H. J. Lozykowski, Mat. Res. Soc. Symp. Proc. Vol. 482 (1998) 1033.
- [12] T. Ogino and M. Aoki, Jpn. J. Appl. Phys. 18 (1979) 1049.
- [13] C. Onodera and T. Taguchi, J. Crystal Growth, 101 (1990) 502.
- [14] T. H. Kell, Phys. Rev. 140 (1965) A601.
- [15] Development of Compound Semiconductors for High-Efficiency Optoelectronic Conversion (Light for the 21<sup>st</sup> Century) Report of Results, p17, Japan Research and Development Center for Metals, (March, 2000).
- [16] A. P. Levanyuk and V. V. Osipov, Sov. Phys. Usp, 24, 187 (1981).
- [17] V.V. Osipov, T. I. Soboleva and M. G. Foigel, Sov. Phys. Semicond., 13, (1979) 319.
- [18] A. P. Levanyuk and V. V. Osipov, Sov. Phys. Semicond., 7, 751 (1973).
- [19] T. Fukushima and S. Shinoyama, Jpn. J. Appl. Phys. 12 (1973) 549.
- [20] Bonds and Structures of Molecules and Solids, D. Pettifor (translated by M. Aoki and S. Nishiya), GIHODO SHUPPAN Co., Ltd. (1997).

# 7 Development of MOCVD-grown Low-Defect GaN Thin Film Epi-Substrates

## 7.1 Achievements in 1998 and 1999

Development of GaN-on-Sapphire substrates used for the homoepitaxial growth of high-efficiency UV-emitting LEDs was continued. Although the currently used technique, which is based on MOCVD, is capable of easily and inexpensively producing large surface area substrates and numerous practical expectations are pinned on it, it has certain problems, such as the high density of dislocation defects and substrate bowing. In this project, our goal is to implement 2-inch substrates of practical value, in which the density of dislocations would be reduced from the current  $10^9$  cm<sup>-2</sup> to not more than  $10^4$  cm<sup>-2</sup>.

Prior to 1999, we conducted basic research concerning the reduction of dislocation density and systematically investigated the influence of the growth temperature, pressure, growth atmosphere, mask material, crystal directions, etc. in 10-mm substrates using ELOG (Epitaxial Lateral Overgrowth), which is a well-known powerful technique. In terms of dislocation density, we reached a level of  $10^6$  cm<sup>-2</sup>. Our main achievements are listed below.

(1) It was discovered that low-defect GaN was obtained by ELOG growth if we changed the ordinary SiO<sub>2</sub> mask to a W mask. It was confirmed by X-ray diffraction, TEM observations, and PL observations that it was a high-quality crystal that had an insignificant amount of *c*-axis wobble, in other words, no low-angle tilt grain boundaries, and, in addition, no dislocations caused thereby. Based on this, we assumed that although active hydrogen generated by the contact reaction between the W mask and ammonia etched away GaN in the vicinity of the W mask, creating gaps, it did not tilt the laterally growing GaN on the mask.

(2) A novel “facet-controlled ELOG technique” (“FACELO” technique), a type of ELOG, was developed. It was discovered that the morphology of the facets growing in the window areas was dependent on the growth temperature and pressure and could change to {11 $\bar{2}$ 0} rectangular facets as well as to {11 $\bar{2}$ 2} facets. Furthermore, it was determined that because the propagation behavior of dislocations was different depending on the morphology of the facets, by efficiently controlling the facet morphology, we could expect to achieve a reduction in the density of dislocations without the dislocations reaching the top face of the crystal.

(3) Simulations of substrate bowing were carried out to obtain a relationship between the amount of bowing and the thickness of the GaN film, etc. With the target amount of bowing in 2-inch substrates being 50  $\mu$ m or less, it was found that for the present the objective in terms of GaN film thickness should be 10  $\mu$ m.

(4) In order to conduct observations of dislocations in GaN crystals, we developed a FIB (Focused Ion Beam processing) - TEM observation technique, which has been demonstrated to be an effective technique for microscopic observation of dislocations. In addition, for the measurement of dislocation density, we investigated the GPD (Growth Pit Density) technique in comparison with the conventional EPD (Etch Pit Density) technique and determined characteristics under both observation techniques, as well as the fact that density according to both techniques was identical.

(5) In order to investigate the effects of dislocation reduction on the luminescence efficiency of LEDs, we fabricated blue LED structures consisting of AlGa<sub>N</sub>/InGa<sub>N</sub>/Ga<sub>N</sub> single quantum wells on substrates. When using samples with a dislocation density of  $10^8$  cm<sup>-2</sup>  $\sim$   $10^9$  cm<sup>-2</sup> on ordinary GaN-on-sapphire

substrates without ELOG, the PL intensity tended to increase with decreasing dislocation density. However, in case of EL emission in HVPE samples, whose dislocation density had been reduced to  $2 \times 10^8 \text{ cm}^{-2}$ , no conspicuous difference was confirmed.

## 7.2 Summary of Research and Development in 2000

Sapphire is commonly utilized in LED substrates used for GaN growth. However, because there is a considerable difference in lattice constants and thermal expansion coefficients between sapphire and GaN, even after developing and optimizing the technology of inserting low-temperature buffer layers of GaN and AlN, the threading dislocation density is still extremely high, at  $10^8 \sim 10^{10} \text{ cm}^{-2}$  [1,2], which is believed to be an important factor that significantly reduces the efficiency of luminescence in ultraviolet LEDs with an emission wavelength of not more than 400 nm.

As in 1999, we continued to focus our investigations on the ELOG technique in order to implement practical 2-inch low-dislocation-density GaN-on-sapphire substrates with a dislocation density of not more than  $10^4 \text{ cm}^{-2}$  for use in epitaxial growth of high-efficiency UV-emitting LEDs. We used the MOCVD equipment introduced in 1999, trying to achieve a dislocation density of  $10^5 \text{ cm}^{-2} \sim 10^4 \text{ cm}^{-2}$  by investigating the core technologies of dislocation reduction while further expanding the use of the newly developed FACELO (Facet Controlled ELO: facet-controlled ELOG) technique or effectively combining and integrating it with other core technologies. Furthermore, although at present we are conducting investigations using 10-mm substrates, we have started investigations aimed at reproducing dislocation reduction in 2-inch substrates. A thorough understanding of the mechanism of dislocation reduction is necessary for this purpose as well, and in this connection we are trying to make the most of the analysis of information concerning GaN crystal micro-regions. We decided to concentrate our efforts on limited-field TEM, micro photoluminescence, etc.

The following results were obtained in 2000.

- (1) We arrived at a level of dislocation density of  $10^6 \text{ cm}^{-2} \sim 10^4 \text{ cm}^{-2}$ . Dislocation density was successively reduced by means of carrying out FACELO growth on underlying GaN crystals with a dislocation density of  $10^7 \text{ cm}^{-2}$ , in which the initial nucleus density was controlled, by using a two step process consisting of  $\{11\bar{2}2\}$  FACELO and then  $\{11\bar{2}0\}$  FACELO, which allowed us to obtain low dislocation density Ga-on-sapphire substrates which, to the best of our knowledge, had the best quality in the world. We have started investigations into 2-inch substrates, but we are still dealing with substrates of inadequate surface condition due to incomplete burial.
- (2) TEM observations etc. confirmed that the crucial point in the reduction of dislocations by means of FACELO was the fact that dislocations were bent by the  $\{11\bar{2}2\}$  triangular facets in a direction normal to the  $c$ -axis and propagation could be terminated by the void formed in the central portion of the mask, and the fact that new dislocations originating from the top edge of the void could be prevented from propagating all the way to the surface by the  $\{11\bar{2}0\}$  rectangular facets.

## 7.3 Investigations into Dislocation Defect Reduction by ELOG Growth

The selective lateral growth (Epitaxial Lateral Overgrowth: ELOG) technique, in which a mask of insulating material, such as  $\text{SiO}_2$ , is patterned to the desired shape on a GaN substrate and GaN is then selectively grown in the window areas, has been attracting attention as a dislocation reduction technique. GaN ELOG started in 1997 with thick film growth by the HVPE method, which permitted reduction of the threading dislocation density to a level of  $10^7 \text{ cm}^{-2}$  [3]. In addition, as far as the mechanism of dislocation reduction is concerned, it was discovered that it was related to a phenomenon in which dislocations were bent by the  $\{11\bar{0}1\}$  facets formed by the selective growth [4]. Subsequently, ELO was used in the MOCVD method by

Nam *et al.* [5] and Nakamura *et al.* [6], and although dislocations propagated and remained in the window areas, considerable reductions over the mask were reported.

In the course of the present project, it has been reported prior to last year [7] that the morphology of MOCVD ELO facets could be controlled by controlling the growth temperature and pressure [7]. Subsequently, the “facet-controlled ELOG” (facet controlled ELO: FACELO) was proposed, which is a technique for controlling the propagation of dislocations by controlling the morphology of facets formed by selective growth [8]. FIG. 7.3 shows a model of two varieties of FACELO used for dislocation propagation control.

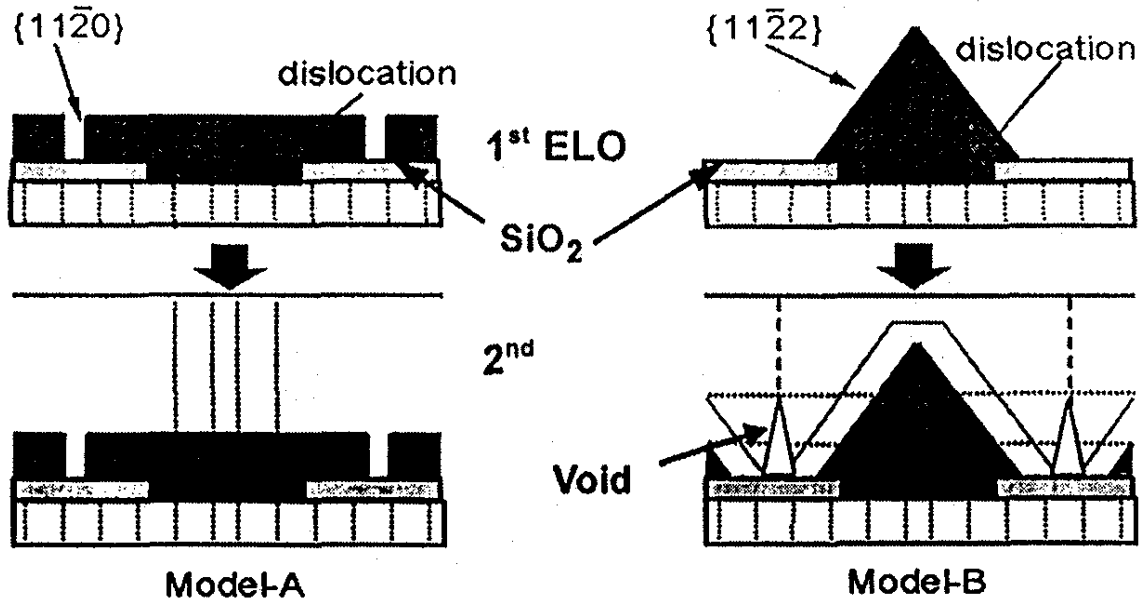


FIG. 7.3 Control of propagation of dislocations and facet morphology by FACELO.

This year, we continued our investigations into dislocation density reduction by FACELO in cooperation with Mie University in order to establish a technology for the fabrication of low-dislocation-density GaN. In addition, with a view to further reduce the density of dislocations by using the FACELO method, we achieved further evolution in research and realized a defect density of  $10^5 \text{ cm}^{-2}$  and are planning to achieve a defect density on the order of  $10^4 \text{ cm}^{-2}$  or less.

In {11 $\bar{2}$ 2} FACELO, we were able to reduce the dislocation density to a level of  $10^6 \text{ cm}^{-2}$ . Dislocations remaining after {11 $\bar{2}$ 2} FACELO are dislocations rectilinearly arranged in the center of the mask, namely, dislocations generated in the portion where the ELO-GaN coalesces above the void and propagating to the surface. For this reason, we carried out 2-step FACELO growth in an attempt to further reduce the dislocation density by blocking the dislocations remaining after the first step of {11 $\bar{2}$ 2} FACELO growth with a film grown in a second step of {11 $\bar{2}$ 0} FACELO growth.

In order to investigate the reduction of density dislocations in 2-inch substrates, we examined the suitability of the MOCVD equipment introduced in 1999 and decided to keep the growth conditions expected to influence the ELOG process under strict control. In addition, in a parallel investigation, we initiated research concerning facet morphology control using the HVPE apparatus installed at the Mie University in 2000 in order to understand the mechanism of dislocation reduction in comparison with the MOCVD method.

### 7.3.1 Methods and Means (Investigation into ELOG Growth for Reduced Dislocation Density)

#### 7.3.1.1 Investigations into facet-controlled ELOG growth

Samples obtained by growing approximately 4  $\mu\text{m}$  of GaN on sapphire (0001), with a low-temperature GaN buffer layer interposed in between, were used as the underlying substrates. A  $\text{SiO}_2$  film with a thickness of about 80 nm was deposited on the underlying substrates, and photolithography was used to form three striped patterns with a mask/window ratio of 7/3, 5/5, and 3/3  $\mu\text{m}$ . The stripes were formed in parallel to  $\langle 1100 \rangle$ , where the velocity of lateral growth by ELOG is high and which permits the use of the facet control technology. The TMG of the source material and the flow rate of  $\text{NH}_3$  were 46  $\mu\text{mol}/\text{min}$  and 1.0~1.5 slm, with  $\text{H}_2$  used as the carrier gas. In order to form the target ELO-GaN facets, the growth temperature and pressure were varied within the range of from 950~1050°C and 80~500 Torr. In addition, approximately 250 nm of InGaN was grown at a growth temperature of 800°C. Growth pits formed by InGaN thin film growth have been reported to be in a one-to-one correspondence with threading dislocations ( $a$  and  $a+c$ ) [9]. The FACELO growth process is shown in FIG. 7.3.1-(1).

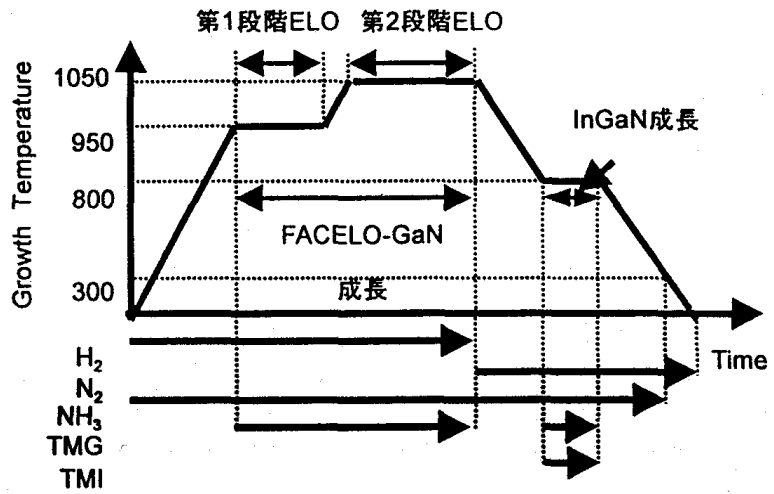
FIG. 7.3.1-(1) FACELO growth process

[Keys, FIG. 7.3.1-(1)]

(Across top): First-stage ELO  
Second-stage ELO

(Middle, right) InGaN growth

(Bottom) FACELO-GaN growth



In the case of two-step double FACELO, after conducting a {1122} FACELO as a first step of FACELO, we tested two methods for use as a second step [10, 11]. The corresponding models and mask pattern alignment are shown in FIG. 7.3.1-(2).

FIG. 7.3.1-(2) Models and mask pattern alignment of two-step double FACELO

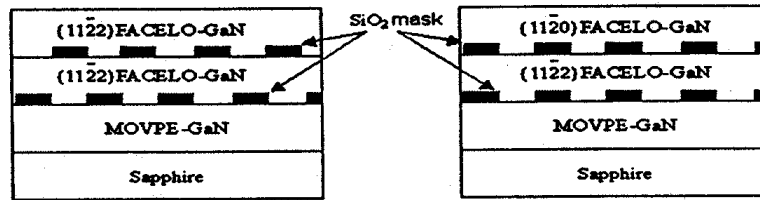
[Keys, FIG. 7.3.1-(2)]

(Underneath two drawings at top) Models (cross sections)

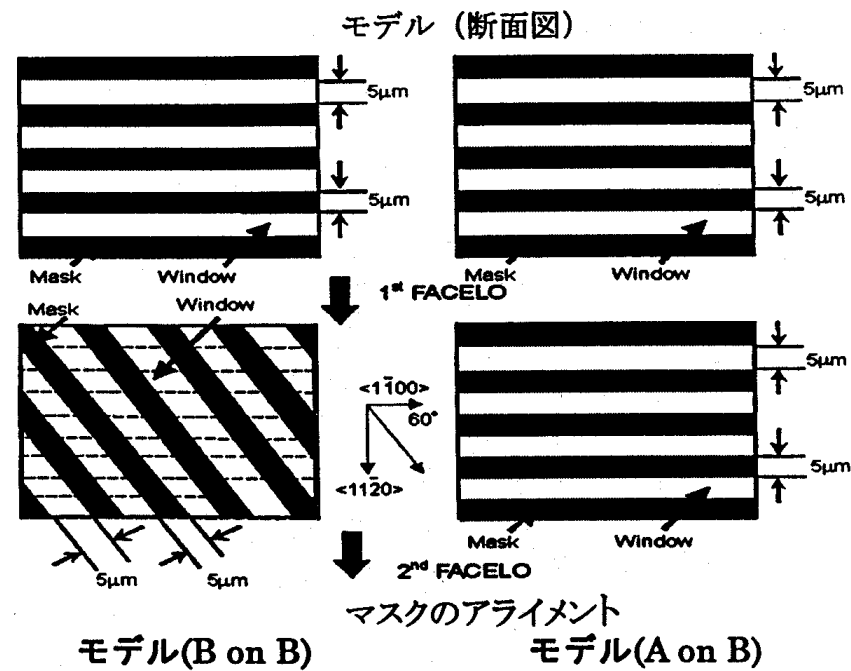
(Underneath two drawings at bottom) alignment

(Left) Model (B on B)

(Right) Model (A on B)



Mask



in FIG.

Models of dislocation propagation are shown FIG. 7.3.1-(3) and 7.3.1-(4). In case of

growth based on Model (B on B), {1122} FACELO according to model B, which is shown in FIG. 7.3.1-(2) (first-stage ELOG using a growth pressure of 500 Torr, a growth temperature of 950°C, a growth time of 45 min; second stage ELOG using a growth pressure of 500 Torr, a growth temperature of 1050°C, and a growth time of 105 min), was carried out by forming a mask along the <1100> direction, and, after that, a mask stripe was patterned along the <1010> direction. In other words, the second mask was formed by rotating it 60° with respect to the first mask, and then a second-stage FACELO was conducted under the same growth conditions as the first-stage FACELO. In this case, the second mask was simply geometrically rotated 60°, and mask formation presented no difficulties.

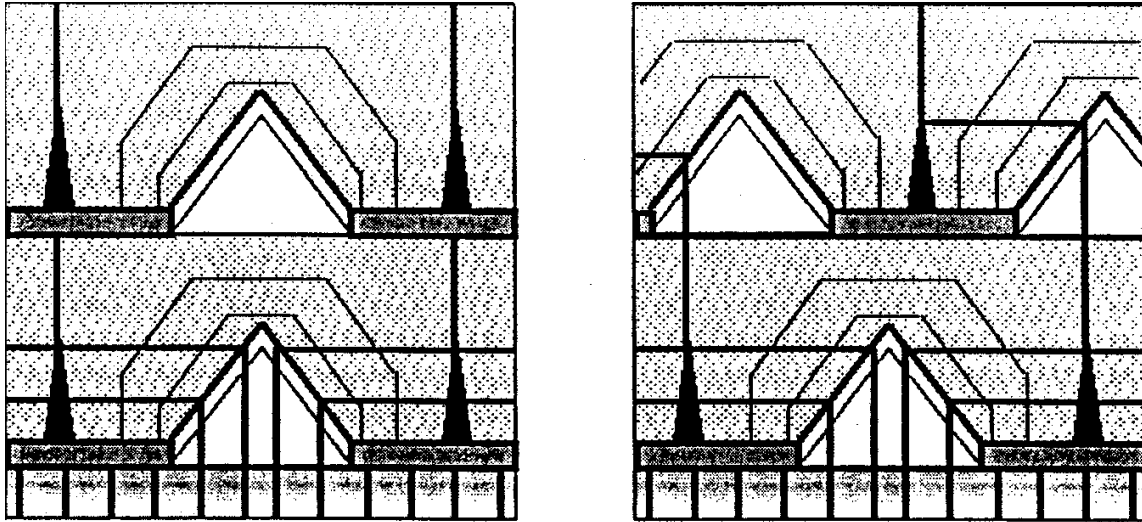


FIG. 7.3.1-(3) Model of dislocation propagation in 2-step double FACELO model (B on B)

[Keys, FIG. 7.3.1-(3)]

(Underneath figure on the left) When first and second masks are aligned

(Same on the right) When first and second masks are not aligned

In case of model (A on B), {1122} FACELO based on model B (first-stage ELOG using a growth pressure of 500 Torr, a growth temperature of 950°C, a growth time of 45 min; second stage ELOG using a growth pressure of 500 Torr, a growth temperature of 1050°C, and a growth time of 105 min) was carried out, whereupon a stripe mask was formed so that the second mask was positioned exactly above the first mask, that is, in parallel to <1100>. Then, second-stage FACELO was carried out using model A-based {1120} FACELO (using a growth pressure of Torr, a growth temperature of 1050°C, growth time of 60 min). In this case, our was to get rid of dislocations in the second-stage FACELO by using the second mask to terminate the rectilinearly arranged dislocations of the stage FACELO.

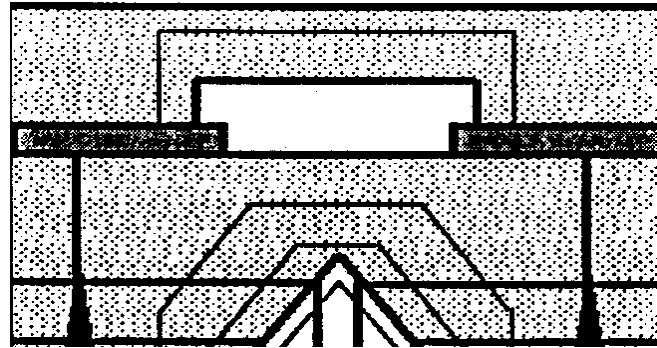
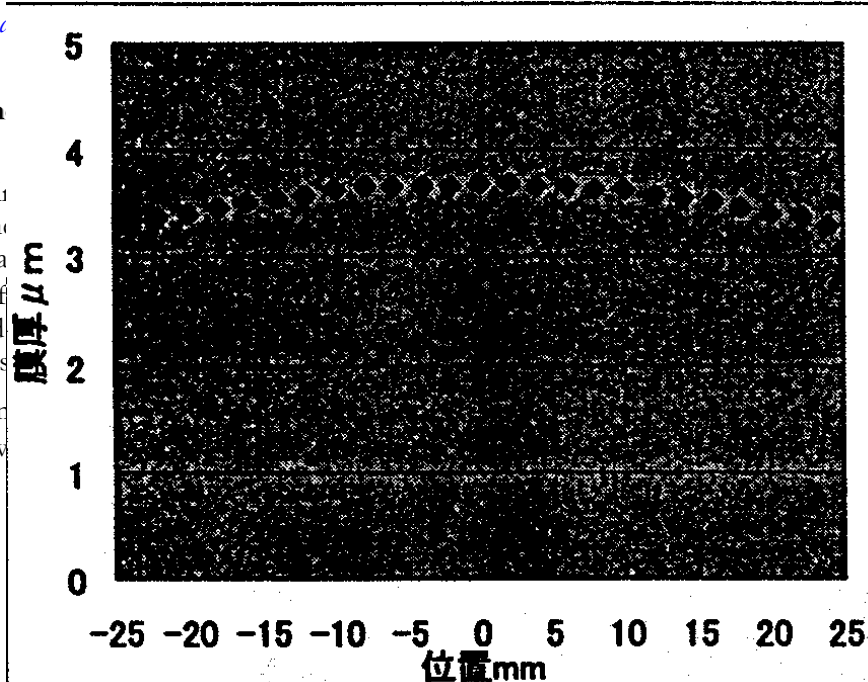


FIG. 7.3.1-(4) Model of dislocation propagation in 2-step (A on B)

7.3.1.2 Research on substrates

In the course of our growth temperature, the parameters on growth a approximately 3 μm of surface a stripe-shaped ammonia (NH<sub>3</sub>) were used. Prior to the ELOG it confirmed that, as show



300 and a goal first-model

e of the growth growing on its (Ga) and face and in ±2%

within a 30-mm radius from the center. The mask pattern used for the ELOG investigation is shown in Table 7.3.1.

*FIG. 7.3.1-(5) Uniformity across surface of 2-inch substrate*

*[Keys, FIG. 7.3.1-(5)]*

*(X-axis) Position, mm*

*(Y-axis) Film thickness,  $\mu\text{m}$ .*

	SiO <sub>2</sub> mask width (L)	Window width (S)
Pattern ①	2 $\mu\text{m}$	8 $\mu\text{m}$
Pattern ②	5 $\mu\text{m}$	5 $\mu\text{m}$
Pattern ③	2 $\mu\text{m}$	2 $\mu\text{m}$

*Table 7.3.1 Mask patterns*

### 7.3.1.3 Investigation of HVPE-based ELOG

The HVPE apparatus introduced in the present study was a horizontal reactor. The electric furnace was a resistance-heating furnace divided into 7 zones, with the upstream 4 zones used as a gallium chloride (GaCl) production region, and the downstream 3 zones used as a growth region. GaCl supplied to the growth region was produced by reacting metallic Ga with a purity of 6N with HCl at about 850°C. In addition, NH<sub>3</sub> was used as a Group V source material. N<sub>2</sub> and H<sub>2</sub>, in mixed gas form, were used as the carrier gas. The susceptor permits rotation for uniform film growth on the substrate.

On the substrates used for the ELOG of GaN, the SiO<sub>2</sub> masks formed stripe patterns with a mask/window ratio of 5/5  $\mu\text{m}$  in the <1100> direction and <1120> direction of the GaN. The carrier gas N<sub>2</sub> and the source gas NH<sub>3</sub> were supplied from the start of the temperature rise. NH<sub>3</sub> was introduced in order to suppress desorption of nitrogen from the GaN substrates at elevated temperatures. When deposition was conducted in a mixed atmosphere of N<sub>2</sub> and H<sub>2</sub> upon reaching the growth temperature, H<sub>2</sub> was introduced in the carrier gas and GaN growth was initiated by simultaneously introducing HCl. In addition, NH<sub>3</sub> was supplied until a temperature of 500°C was reached in order to control desorption during the lowering of the temperature. The rotation velocity of the susceptor was 10 rpm, the growth temperature was 1070°C, and the total gas flow rate was 2.5 slm (with an NH<sub>3</sub>-based total of 2.0 slm, and an HCl-based total of 0.5 slm).

## 7.3.2 Results and discussion (investigation of ELOG growth-based dislocation defect reduction)

### 7.3.2.1 Investigations of facet-controlled ELOG

To carry out {1120} FACELO, which forms dislocation-free regions above the mask, as shown Model (A) illustrated in FIG. 7.3, a rectangular morphology, in which {1120} constituted the side faces, was created during the first-stage ELOG. Then, during the second-stage ELOG, the lateral growth velocity was increased in order to bury the mask. During the experiment, the first-stage ELOG was carried out on substrates with mask/window ratio of 7/3  $\mu\text{m}$  using a growth pressure of 80 Torr, a growth temperature of 950°C, and a growth time of 30 minutes, and the second-stage ELOG was conducted using a growth pressure of 500 Torr, a growth temperature of 1050°C, and a growth time of 90 minutes. FIG. 7.3.2-(1) shows an SEM image of a sample. As shown in the surface SEM image, dislocations are distributed largely in the window areas, and their amount is greatly decreased in the mask areas. In addition, the center of the mask areas, the dislocations are arranged in a rectilinear fashion. The dislocations are believed to be due to a lattice plane shift during the coalescence of the ELO-GaN and to the influence of the strain generated thereby. The average dislocation density, including the window areas and the mask areas of the sample, was  $6.0 \times 10^7 \text{ cm}^{-2}$ , which constituted approximately 1/3 of the dislocation density of the underlying GaN.

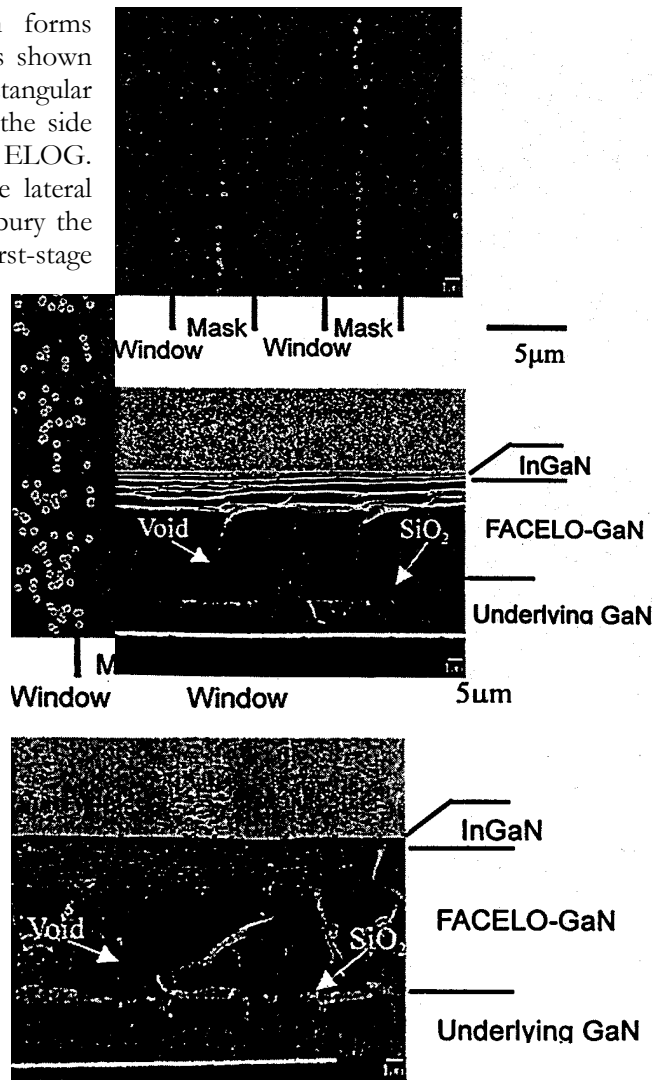


FIG. 7.3.2-(1) {1120} FACELO-GaN (Mask/Window = 7  $\mu\text{m}$ /3  $\mu\text{m}$ )

[Keys, FIG. 7.3.2-(1)]

(Top diagram, on the left) Surface image.

(Bottom diagram, same) Bird's eye view.

It is believed that in case of {1122} FACELO based on Model B, as a result of the formation of the {1122} plane during the first-stage ELOG, dislocations can be bent to switch from a direction normal, to a direction parallel, to the (0001) plane. Then the bent dislocations coalesce together and disappear or propagate to the surface when the ELOG layer coalesces in the center of the mask during the second-stage ELOG. For this reason, the dislocations concentrate in the central portion of the mask. In the experiments, the first-stage ELOG was conducted at a growth pressure of 500 Torr and a growth temperature of 950°C, and in the second-stage ELOG, the growth pressure of 500 Torr was left unchanged while the growth temperature was raised to 1050°C.

FIG. 7.3.2-(2) shows an SEM image of a sample obtained by conducting {1122} FACELO (first-stage ELOG: 45 min, second-stage ELOG: 105 min) on a substrate with a mask/window ratio of 5/5  $\mu\text{m}$ . As can

be confirmed by examining the cross-section SEM image, a void with a height of 5~7  $\mu\text{m}$  was formed in the coalescence portion of the ELOG layer. As is also evident from the surface SEM image, the dislocations were arranged in a rectilinear fashion in the center of the mask area only, with the remaining region (region with a width of 10  $\mu\text{m}$ ) being practically dislocation-free.

FIG. 7.3.2-(2)  $\{11\bar{2}2\}$  FACELO GaN

[Keys, FIG. 7.3.2-(2)]

(Top figure, on the left) Surface image.

(Bottom figure, same) Cross-section.

The bending of the dislocations by the  $\{11\bar{2}2\}$  plane is expected based on the fact that dislocations do not propagate to the surface above the window areas in the cross-section SEM image, and, as will be described later, this is also confirmed by TEM observations. Then, since the amount of dislocations arranged in the center of the mask area is considerably reduced, it is believed that the dislocations are terminated by the void. The dislocation density of the sample was  $6 \sim 10 \times 10^6 \text{ cm}^{-2}$ , which points to a reduction by more than an order of magnitude in comparison with the dislocation density of  $2 \sim 4 \times 10^8 \text{ cm}^{-2}$  of the underlying GaN.

Results of the double FACELO are shown below. First of all, SEM images of the two-step FACELO-GaN based on Model (B on B) are shown in FIG. 7.3.2-(3). Partially dislocation-free regions are confirmed based on the distribution of InGaN growth pits shown in the surface SEM images, but there remained dislocations believed to be produced in the coalescence portion of the second-step FACELO. The dislocation density of the sample was  $2 \sim 10 \times 10^6 \text{ cm}^{-2}$ , which means there was a reduction by about 1/2 in comparison with the dislocation density of  $6 \sim 10 \times 10^6 \text{ cm}^{-2}$  of the one-step FACELO; however, a reduction in the amount of dislocations located in the ELOG coalescence portion is critical for achieving further reductions in the dislocation density.

FIG. 7.3.2-(3) Surface and cross-sectional SEM images of second FACELO-GaN based on Model (B on B)

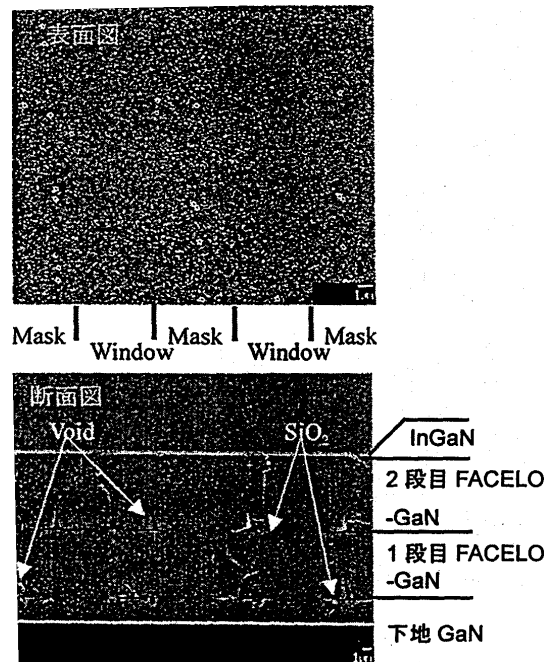
[Keys, FIG. 7.3.2-(3)]

(Top figure, inside) Surface image.

(Bottom figure, inside) Cross-sectional view.

(Bottom figure, right, top to bottom) InGaN; Second FACELO -GaN; First FACELO -GaN; Underlying GaN

Next, a cross-section image of the two-step FACELO-GaN based on Model (A on B) is shown in FIG. 7.3.2-(4). It can be seen that the second mask is placed directly above the first mask. As a result, as shown in the model, the dislocations remaining in the coalescence portion in the first FACELO are terminated by the second mask, and because the first window areas are dislocation-free, there are no dislocations propagating to the second window areas. As a result, there are no dislocations on the surface.



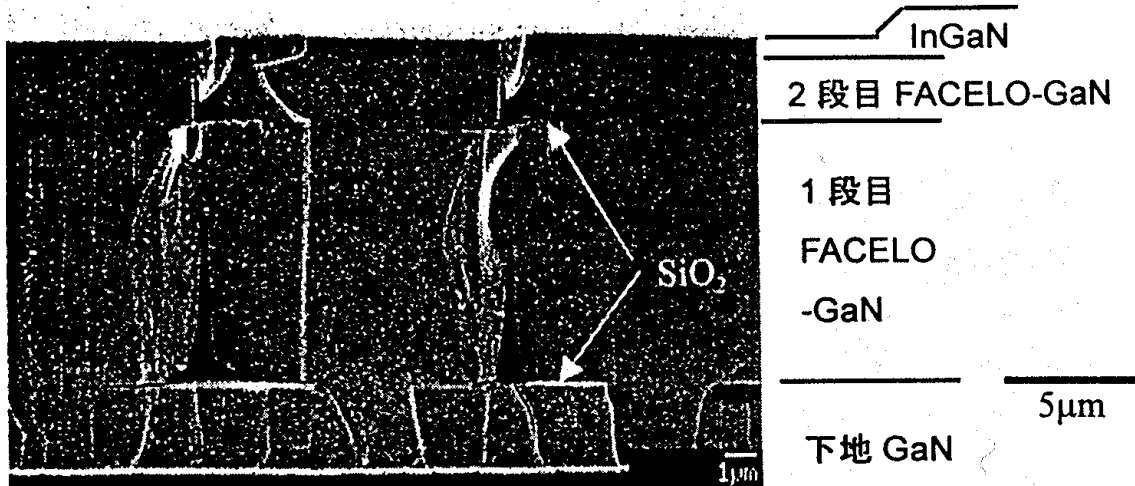


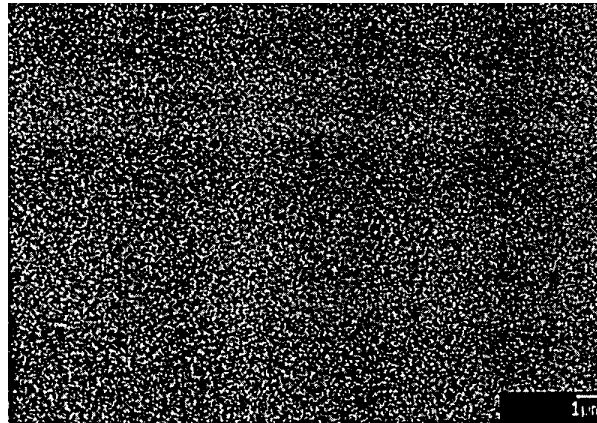
FIG. 7.3.2-(4) Bird's eye view SEM image of second FACELO-GaN based on Model (A on B)

[Keys, FIG. 7.3.2-(4)]

(Right, top to bottom) Surface; Second FACELO-GaN; First; FACELO; -GaN; Underlying GaN

A surface SEM image is shown in FIG. 7.3.2-(5). The surface area of the image is  $4.4 \times 10^6 \text{ cm}^2$ , with absolutely no dislocations found within this region. In other words, one can say that the dislocation density is not more than  $2 \times 10^5 \text{ cm}^{-2}$ . Dislocations arranged in a rectilinear fashion were observed in the portions the second mask did not coincide with first mask. In addition, in certain areas, confirmed the presence of dislocations generated in the coalescence portion of second FACELO, and it is believed that further optimization of growth conditions is necessary.

FIG. 7.3.2-(5) Surface SEM of second FACELO-GaN based on Model (A on B).



where  
the  
we  
the

As shown above, our purpose was to achieve a reduction in the amount of dislocations based on an ELOG technique (FACELO) intended for controlling the propagation of dislocations by means of controlling the facet morphology generated by selective growth. In case of the  $\{11\bar{2}0\}$  FACELO shown in Model A, the density of dislocations is determined by the ratio of the size of the mask and the window, and if the wobble of the  $c$ -axis of the crystal is taken into consideration, the ratio cannot be large. However, the advantage is that burial can be carried out using a thin ELO layer. On the other hand, a dislocation density reduction down to a level of  $10^4 \text{ cm}^{-2}$  proved possible in case of the  $\{11\bar{2}2\}$  FACELO based on Model B. Rectilinearly arranged dislocations remained only in the coalescence portion in the center of the mask, and there were no dislocations in the window areas. In order to achieve a dislocation density on the order of  $10^4 \text{ cm}^{-2}$  or less, which is the goal of the present project, we repeated FACELO in two steps. In the  $\{11\bar{2}2\}$  FACELO, dislocations rectilinearly arranged in the center of the mask were terminated by a second mask. The realized dislocation density was not more than  $2 \times 10^5 \text{ cm}^{-2}$ , which nearly met the target value. In the future, we are planning to achieve a further reduction in the density of defects by means of further optimizing mask material, morphology, and growth conditions along with conducting research into the application of this technology to 2-inch substrates of practical value.

**7.3.2.2 Investigations of 2-inch substrates**

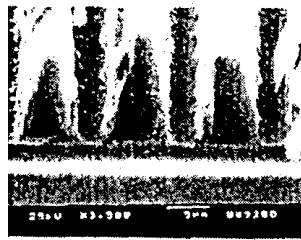
FIG. 7.3.2-(6) shows results concerning the differences in the SiO<sub>2</sub> mask width (L) and window width (S) depending on the growth temperature.

FIG. 7.3.2-(6) Differences in the growth pattern depending on changes in growth temperature

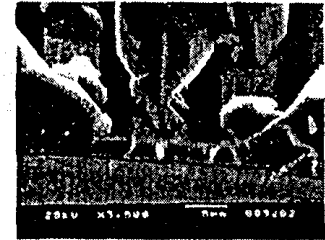
[Keys, FIG. 7.3.2-(6)]

- (a) Pattern ①, 1130°C (b) Pattern ②, 1130°C
- (c) Pattern ①, 1110°C (d) Pattern ②, 1110°C
- (e) Pattern ①, 1080°C (f) Pattern ②, 1080°C
- (g) Pattern ①, 1060°C (h) Pattern ②, 1060°C
- (i) Pattern ①, 1040°C (j) Pattern ②, 1040°C

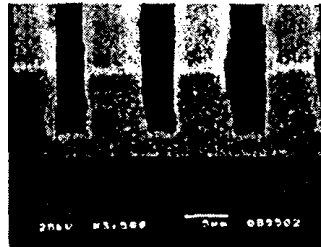
At elevated growth temperatures of 1130°C and 1110°C, the action of etching was clearly visible, and the presence of no-growth regions was confirmed in patterns with a small window width. When the growth temperature was decreased from 1130°C to 1110°C, the etching action was reduced. When the growth temperature was further decreased to 1080°C, in pattern ①, voids appeared above the mask, growth from the window areas proceeded in a reverse mesa shape, and a flat C-plane appeared on the top face. In pattern ②, growth occurred along the window areas. At 1060°C, in case of pattern ①, the voids above the mask became smaller, forming a near-square cross-section. The adjacent crystal above SiO<sub>2</sub> was in contact therewith, but no coalescence took place. In case of pattern ②, the entire cross section assumed the same shape, with a C-plane observed on the top face and planes, believed to be {1122} planes, observed on the inclined faces. At 1040°C, in pattern ①, no voids were generated above the SiO<sub>2</sub> mask. C-planes appeared on the top face, and inclined faces, believed to be {1122} planes, became wider than at 1060°C. In pattern ②, the inclined faces were clearly



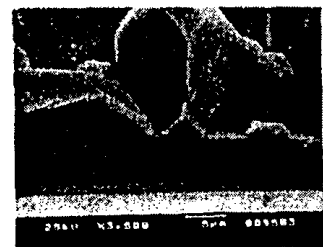
(a) パターン①、1130°C



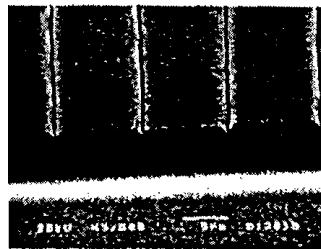
(b) パターン②、1130°C



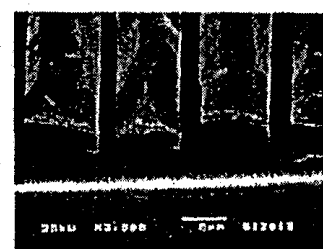
(c) パターン①、1110°C



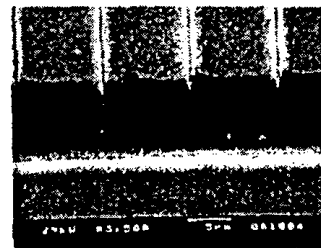
(d) パターン②、1110°C



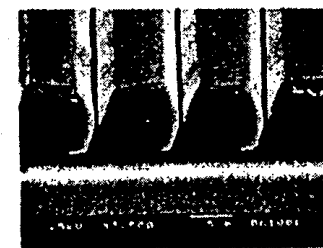
(e) パターン①、1080°C



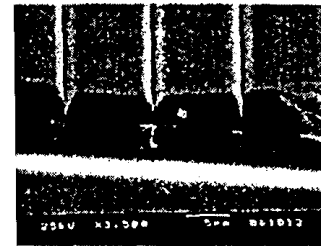
(f) パターン②、1080°C



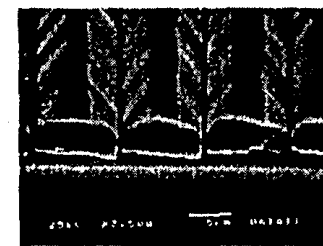
(g) パターン①、1060°C



(h) パターン②、1060°C



(i) パターン①、1040°C



(j) パターン②、1040°C

visible, and the flat region of the top face became narrower. These phenomena, as described above, coincide with the tendency of {1122} planes to emerge easily during low temperature growth.

FIG. 7.3.2-(7) shows results obtained by growth conducted by varying only the amount of the supplied ammonia in order to study the influence of the V/III ratio. In the case of pattern ①, when the amount of the supplied ammonia was 3 slm, the cross section was triangular in shape, but when it was set to 1 slm, a flat surface appeared on the top face and the proportion of the inclined faces decreased, resulting in a cross section close to a square in shape (a, b). In pattern ③, the coalescence of the triangular crystals started at 3 slm, leaving behind residual V-shaped trenches. At 1 slm, a flat surface appeared on the stripe-shaped top portion, with trenches between crystals becoming shallower. However, there was no coalescence of crystals (c, d).

FIG. 7.3.2-(7) Differences in growth pattern depending on amount of supplied ammonia

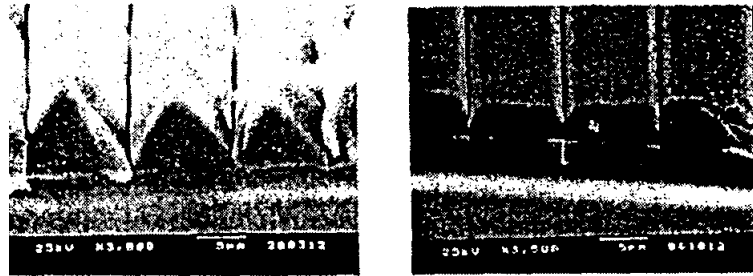
[Keys, FIG. 7.3.2-(7)]

(a) Pattern ①, NH<sub>3</sub>: 3slm (b) Pattern ①, NH<sub>3</sub>: 1slm

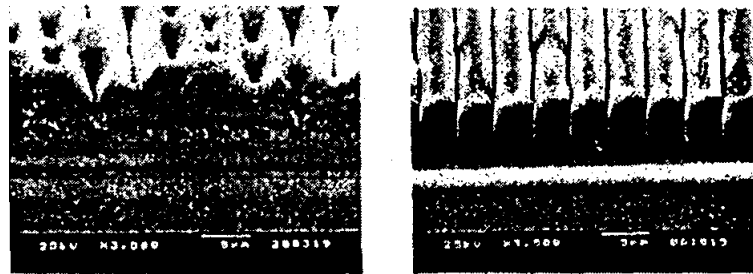
(c) Pattern ③, NH<sub>3</sub>: 3slm (d) Pattern ③, NH<sub>3</sub>: 1slm

(e) Pattern ①, NH<sub>3</sub>: 1slm

(f) Pattern ①, NH<sub>3</sub>: 0.75slm



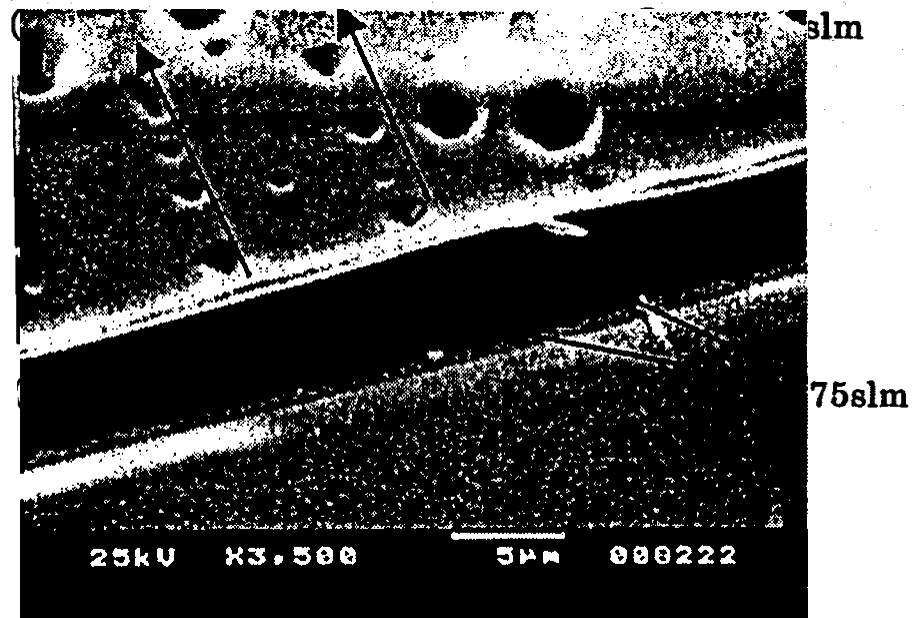
(a) パターン①、NH<sub>3</sub>:3slm (b) パターン①、NH<sub>3</sub>:1slm



As shown in (e) and (f) of FIG. 7.3.2-(7), when there were slightly inclined faces along with a flat surface on the top face (amount of supplied ammonia: 1 slm), after reducing the amount of supplied ammonia to 0.75 slm the inclined faces disappeared, producing voids between adjacent crystals.

The results above coincide with the tendency of inclined faces to grow and produce a near-triangular cross section when the V/III ratio is increased and to produce near-square cross section when the V/III ratio is reduced.

FIG. 7.3.2-(8) shows results obtained by conducting growth under the conditions, under which triangular-shaped crystals are obtained in (c) of FIG.



25kV X3,500 5μm 000222

7.3.2-(7) using pattern ③, and then conducting growth under conditions, under which a flat surface is formed on the top face and trenches become shallower, as shown in (d). Although it could be confirmed that the flat surface occupied most of the face, coalescence was insufficient, and the condition of the surface was poor. It was confirmed that pits were generated above the SiO<sub>2</sub> mask where the coalescence of the crystals takes place. The pits were arranged in the same  $\langle 1\bar{1}00 \rangle$  direction as the direction of the stripes.

*FIG. 7.3.2-(8) Results of second ELOG*

*[Keys, FIG. 7.3.2-(8)]*

*(Top)  $\langle 1\bar{1}00 \rangle$  direction*

*(Right) SiO<sub>2</sub> mask.*

Based on the above, we started investigations into 2-inch low-dislocation substrates. The current results indicate insufficient burial. We have conducted investigations into the influence exerted by growth temperature, V/III ratio, and other parameters during ELOG growth under normal pressure. When the growth temperature is high, a flat surface forms easily on the top portion, and when the growth temperature is low, inclined faces tend to form easily. The growth pattern changes greatly with slight changes in the growth temperature (about 20°C). When the V/III ratio is large, inclined faces are formed and triangular-shaped crystals grow, whereas when the V/III ratio is small, a flat surface is formed on the top face and square-shaped crystals are obtained. Thus, it is concluded that the amount of supplied ammonia also exerted a strong influence on the growth pattern.

In the present study, observations showed that adjacent crystals did come in contact with each other above the SiO<sub>2</sub> mask, but it is believed that there was no coalescence. In addition, even if the coalescence did occur, V-shaped trenches and pits were generated, and a flat surface over the entire face was not obtained. This is believed to be due to the fact that the lateral growth velocity on the SiO<sub>2</sub> mask is small and the crystal axis is slightly inclined, and we believe that the lateral growth velocity has to be increased. In the future, we are planning to conduct investigations including growth parameters such as growth pressure and atmosphere, which are believed to exert influence on lateral growth.

### **7.3.2.3 Investigation of HVPE-based ELOG**

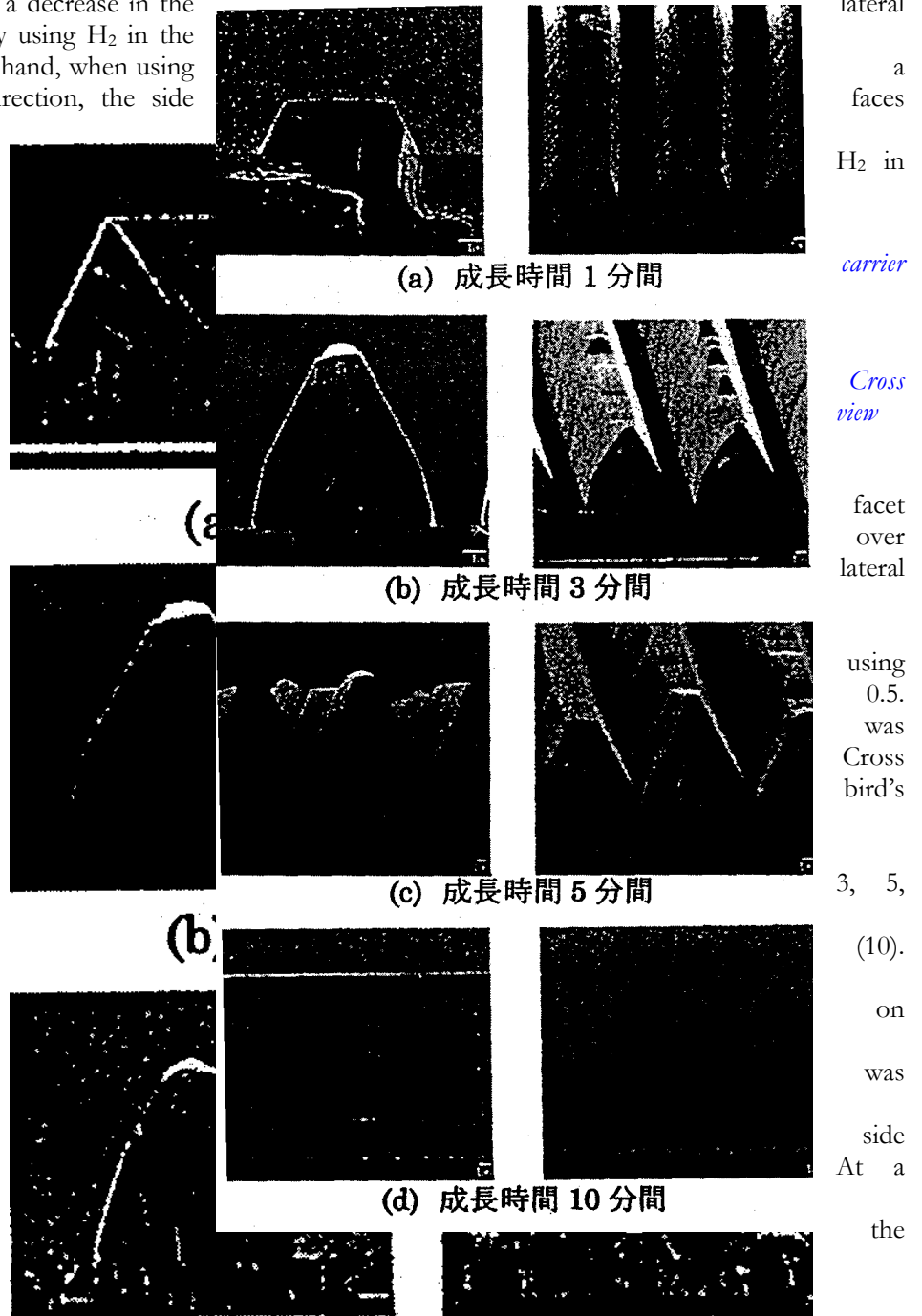
In order to investigate the effects of the carrier gas on the morphology of facets produced by selective lateral growth, we studied morphological changes produced by variations in the proportion of H<sub>2</sub> in the carrier gas. Cross sectional views and perspective view SEM images of crystals obtained by conducting growth for three minutes on substrates with a mask/window ratio of 5 μm/5 μm in the  $\langle 1\bar{1}00 \rangle$  direction of the GaN using a carrier gas with a H<sub>2</sub>/(N<sub>2</sub>+H<sub>2</sub>) ratio of 0, 0.5, and 0.9 are shown in FIG. 7.3.2-(9).

When H<sub>2</sub> was not used, in other words, when the ratio H<sub>2</sub>/(N<sub>2</sub>+H<sub>2</sub>) was 0, only {1122} and (0001) facets emerged. These planes were identical to the facet planes formed in the initial stage of selective growth by the MOCVD method. By contrast, when the H<sub>2</sub>/(N<sub>2</sub>+H<sub>2</sub>) ratio was 0.5, {1122} facets emerged on the side faces and, closer to the mask, there emerged 75~77° faces, and so far as we know, these 75~77° faces have not been previously reported. In terms of the index of these faces, the most likely candidate is {3362}. At a H<sub>2</sub>/(N<sub>2</sub>+H<sub>2</sub>) ratio of 0.9, the proportion of {3362} facets became even larger. These morphological changes are believed to be due to a decrease in the growth velocity caused by using H<sub>2</sub> in the carrier gas.

FIG. 7.3.2-(9) Surface morphology depending on gas ratios

[Keys, FIG. 7.3.2-(9)]  
(Across top, left to right) sectional view, perspective

In order to study how morphology changes time during selective growth, we observed changes in crystal morphology over time a H<sub>2</sub>/(N<sub>2</sub>+H<sub>2</sub>) ratio of 0.5. The <1100> direction used for the SiO<sub>2</sub> mask. sectional views and eye view SEM images of crystals obtained by conducting growth for 1, and 10 minutes are shown in FIG. 7.3.2- In the case of 1-minute growth, {1122} emerged the side faces. By contrast, when growth conducted for 3 minutes, {1122} emerged on the faces and {3362} below. growth time of 5 minutes, the {1122} and {3362} in the lower portion remained unchanged, and coalescence of the ELOG crystal was starting to show. At 10



(c) H<sub>2</sub>/(N<sub>2</sub>+H<sub>2</sub>)=0.9

minutes, the coalescence was complete, and the SiO<sub>2</sub> mask was buried. A smooth crystal with a thickness of 40~60  $\mu\text{m}$  was obtained by conducting growth for 60 minutes. In order to investigate the effects of the mixed carrier gas, X-ray rocking curve measurements were carried out for crystals obtained by 60-min ELOG. The  $c$ -axis of the crystal on the mask had been reported to wobble when using a SiO<sub>2</sub> mask with a stripe pattern. (0004) diffraction X-ray rocking curves were measured in two cases, i.e. when the incident X-rays were oriented in the horizontal direction ( $\phi=0^\circ$ ) and in the vertical direction ( $\phi=90^\circ$ ) with respect to the mask. The half-width in the case of  $\phi=90^\circ$  was larger than that in case of  $\phi=0^\circ$ , and it was believed that the  $c$ -axis of the crystal was tilted. However, the half-width at  $\phi=0^\circ$  was 216 arcsec, an indication of the high quality of the crystal.

*FIG. 7.3.2-(10) Surface morphology depending on growth time*

*[Keys, FIG. 7.3.2-(10)]*

*(Across top, left to right) Cross sectional view, perspective view*

*(a) Growth time: 1 minute*

*(b) Growth time: 3 minutes*

*(c) Growth time: 5 minutes*

*(d) Growth time: 10 minutes*

As mentioned above, we obtained and installed HVPE equipment and investigated growth conditions in a study for comparison with the MOCVD method. We investigated ELOG-GaN obtained by using a mixed carrier gas of H<sub>2</sub> and N<sub>2</sub> by focusing on the study of changes in facet morphology. When a mask with stripes arranged in the  $\langle 11\bar{1}00 \rangle$  direction was used, the addition of H<sub>2</sub> resulted in  $\{11\bar{2}2\}$  and (0001) at a growth time of 1 minute, and when growth was conducted for 3 minutes,  $\{33\bar{6}2\}$  emerged, with complete burial achieved at 10 minutes. The emergence of  $\{33\bar{6}2\}$  was due to the decrease in the lateral growth velocity due to the addition of H<sub>2</sub>. In the case of a  $\langle 11\bar{2}0 \rangle$ -direction mask, only  $\{1\bar{1}01\}$  facets emerged on the side faces.

In the future, we are going to study the relationship between the facet morphology and the propagation of dislocations and investigate optimum growth conditions.

## 7.4 Evaluation of ELOG-grown substrates

As mentioned in the previous section, which described investigations of ELOG growth, we developed a novel FACELO technique, which is a technology for controlling the direction of propagation of dislocation lines by means of controlling facets in order to reduce the density of dislocations. By using SEM observations of growth pits of FACELO-GaN, we compared the distribution of dislocations in different samples grown by FACELO under different conditions and proposed a model of the dislocation reduction mechanism. FIG. 7.4 shows typical growth models of FACELO-GaN. In model A,  $\{11\bar{2}0\}$  facets are produced during growth in the first stage and the lateral growth velocity is increased in the second stage. Under such conditions, dislocation lines do not bend during the FACELO process, with multiple dislocation lines reaching the surface and corresponding growth pits observed on the surface. In model B,  $\{11\bar{2}2\}$  facets are produced during growth in the first stage and the lateral growth velocity is increased in the second stage. In such a case, the dislocation lines bend towards the mask region(s) and are terminated by the void produced above the mask. Only dislocations produced in the junction portion at the top of the void reach the surface, with growth pits appearing to be arranged only parallel to the stripes of the mask. In order to ascertain the adequacy of this model, we carried out observations of dislocation lines using TEM. Furthermore, analysis of Burger's vectors was also conducted in order to study the nature of the dislocations.

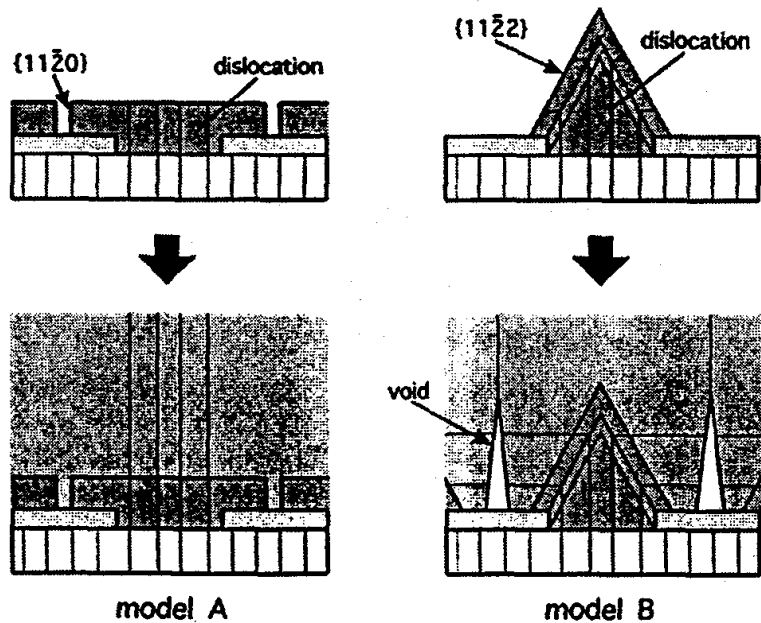
FIG. 7.4 FACELO-GaN growth models

It is known that in ELO-grown samples, depending on the mask material, there may be differences in the physical properties of the material above the mask pattern (wing portions) and above the opening portions [13-15]. When LED structures are grown on top of ELOG-GaN crystals, it is important to control this difference in characteristics. In order to study the positional relationship with respect to the mask pattern, in this study, to conduct this evaluation, we used the newly introduced micro-photoluminescence (micro-PL) technique because of its superior position analysis capabilities. Furthermore, the influence of the material of the SiO<sub>2</sub> mask and the W mask on the ELOG-GaN crystal was evaluated at the Yamaguchi University by means of time resolved photoluminescence.

### 7.4.1 Methods and Means

#### 7.4.1.1 TEM of substrates grown by facet-controlled ELOG

The samples used for evaluation were grown by ELOG in the following manner. A low-temperature buffer and an underlying GaN layer were grown on (0001) sapphire substrates by MOVPE. SiO<sub>2</sub> vapor deposited thereon by RF sputtering, and a stripe-shaped mask pattern was formed along the  $\langle 1100 \rangle$  direction of the GaN by photolithography. Two types of FACELO-GaN layers were grown. One of them was obtained by using samples corresponding to Model A (Sample A), on which a mask with width of 7  $\mu\text{m}$  was grown with a periodicity of 10  $\mu\text{m}$  by conducting first-stage growth at 80 Torr and 1000°C for 30 minutes and second-stage growth at 500 Torr and 1050°C for 90 minutes. Finally, in order to produce growth pits, InGaN was grown thereon. Another type of layer was obtained by using samples corresponding to Model B (Sample B) and growing a mask with a width of 5  $\mu\text{m}$  with a periodicity of 10  $\mu\text{m}$  at 500 Torr and 950°C for 45 minutes



in the first stage, at 500 Torr and 1025°C for 105 minutes in the second stage, and then conducting additional growth at 1070°C for 30 minutes. InGaN was grown as a final step. For TEM analysis, we prepared cross sectional samples with a thickness of approximately 100 nm by using the Focused Ion Beam technique and analyzed them using the JEM-4000FX from NEC at an accelerating voltage of 350 kV.

#### **7.4.1.2 Micro-photoluminescence of facet-controlled ELOG-GaN**

Samples (1)~(4), which were used for evaluation, were obtained by varying the conditions of ELOG growth on GaN, on which SiO<sub>2</sub> masks had been patterned to produce a striped shape in the <1100> direction.

- ① Sample illustrating process of burial starting from triangular facets
- ② Sample illustrating process of burial starting from square facets
- ③ Sample illustrating burial by one-step regrowth
- ④ Sample obtained by forming triangular facets and then completing burial using square facets

① and ② are samples grown at atmospheric pressure by Sumitomo Chemical Co., Ltd., whereas ③ and ④ are samples grown at reduced pressure (~0.4 atmospheres) by Mie University. The pitch of the mask pattern was 10 μm in either case, but the width of the mask pattern was 2 μm in case of ① and ② and 5 μm in case of ③ and ④. A micro-PL apparatus from Atago Bussan Co., Ltd. was used. A He-Ne laser was used as an excitation light source, with the position analysis resolution being approximately one μm.

#### **7.4.1.3 Time resolved photoluminescence of ELOG-GaN**

ELOG-GaN samples utilizing W- and SiO<sub>2</sub> masks were subjected to time resolved PL measurements using a femtosecond laser and PL measurements using a He-Cd laser in order to study the respective excitation density dependences and temperature dependences. The time resolved PL measurement system is shown in FIG. 7.4.1.

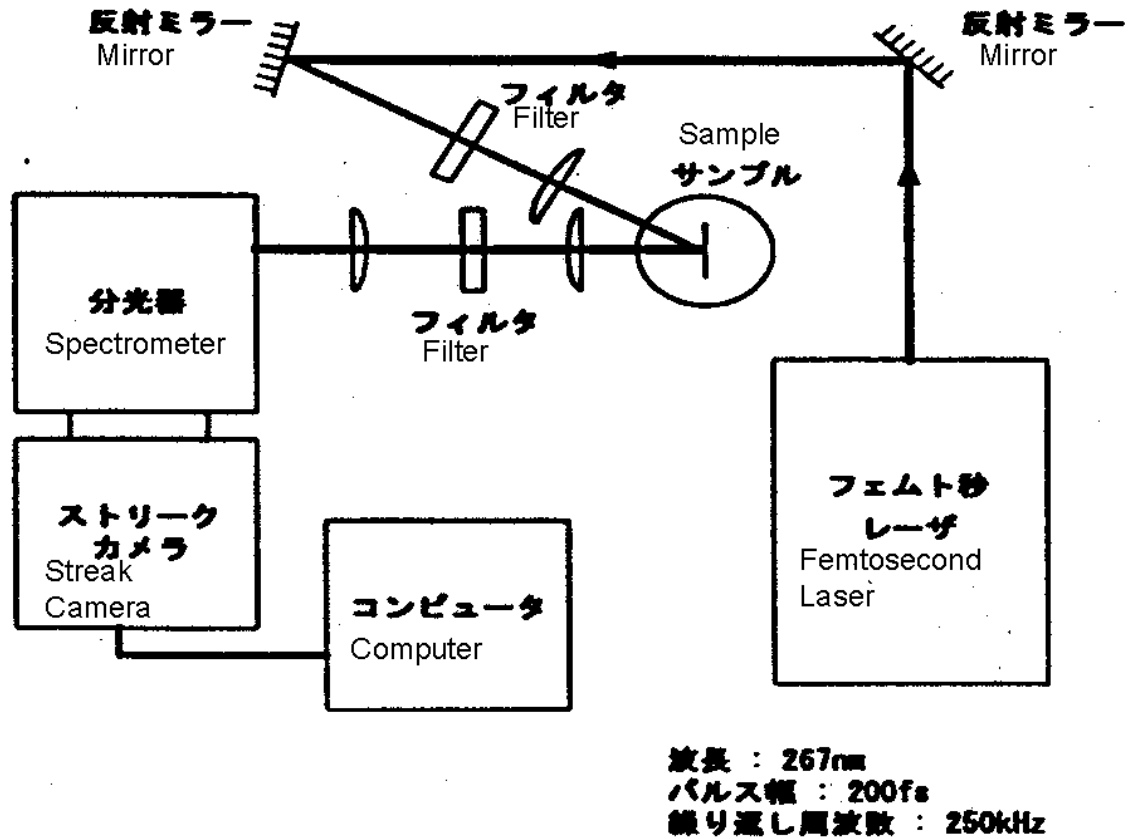


FIG. 7.4.1 Time resolved spectroscopy measurement system

[Keys, FIG. 7.4.1]

Wavelength: 267 nm

Pulse width: 200 fs

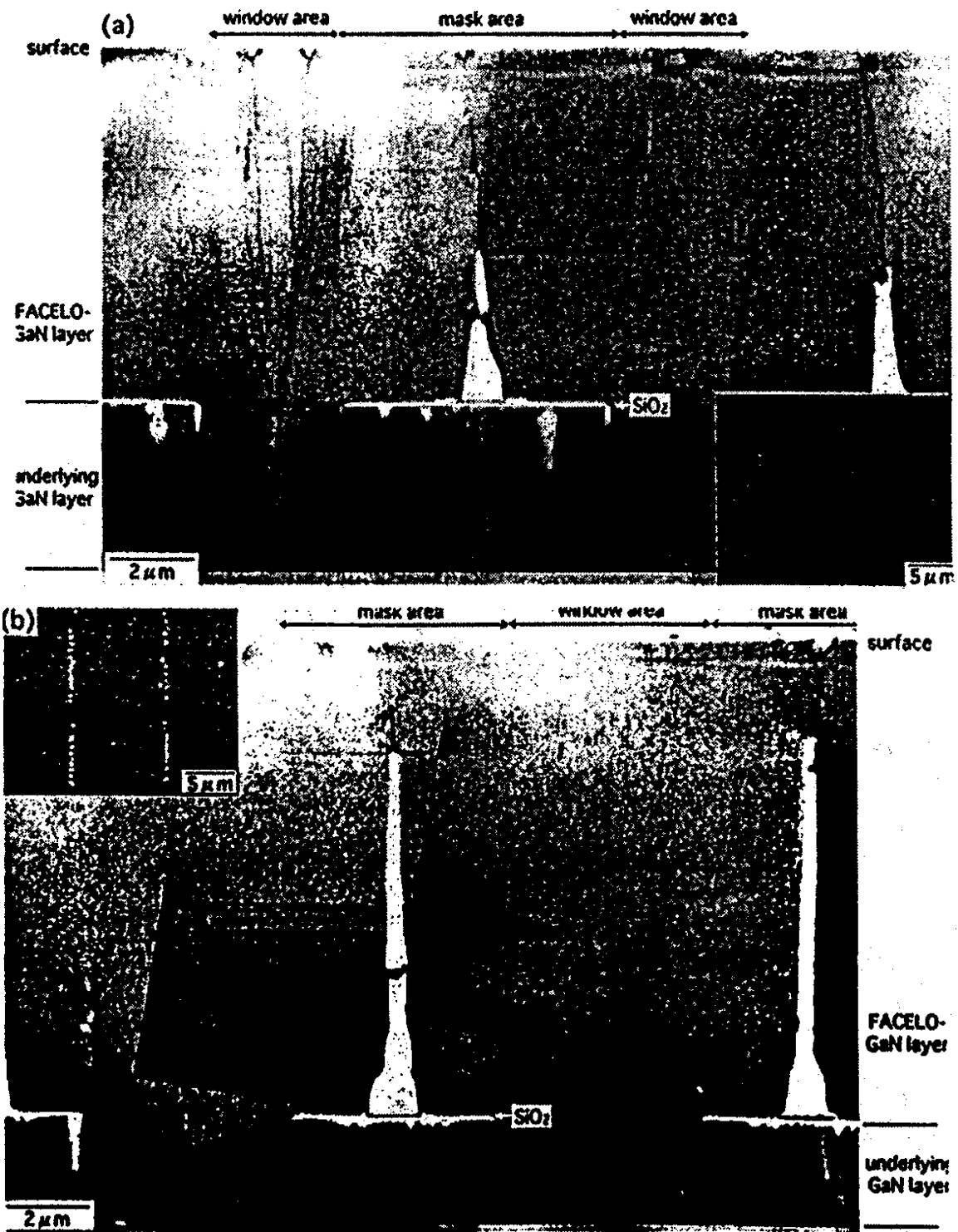
Repetition rate: 250 kHz

The third harmonic of a titanium-sapphire laser was used as the excitation light with an excitation wavelength of 267 nm, a pulse width of 200 fs, and a repetition rate of 250 kHz. The light emitted from the samples was detected using a streak camera attached to a spectrometer, and three-dimensional data were collected, including light intensity, light wavelength, and time. The time resolution capability was 10 ps or less.

## 7.4.2 Results and Discussion

### 7.4.2.1 TEM of facet-controlled ELOG substrates

TEM images of  $\{11\bar{2}0\}$  square-facet FACELO samples and  $\{11\bar{2}2\}$  triangular-facet FACELO samples are shown, respectively, in FIG. 7.4.2-(1a) and FIG. 7.4.2-(1b). The figures inserted in the corners are SEM images of growth pits. The dark circular structures were produced during the fabrication of the cross sections and do not correspond to structures of the samples themselves.



Top: FIG. 7.4.2-(1a) TEM of {1120} square-facet FACELO-GaN substrate.

Bottom: FIG. 7.4.2-(1b) TEM image of {1122} triangular-facet FACELO-GaN substrate.

In Sample A, the dislocation lines of the mask region are terminated by the mask, but the numerous dislocation lines of the window region reach the surface. On the other hand, in Sample B, the multiple dislocation lines of the window region are bent in the direction of the mask region and terminated by the void in the top portion of the mask. The remaining dislocation lines disappear at the  $\{11\bar{2}2\}$  facet comprising the edge portion of the mask. These are bent in a direction parallel to the stripes of the mask (direction normal to the surface of the paper in the figure) and are believed to extend outside the sample, which was thinned for TEM observations. Only the dislocation lines generated at the top edge of the void reached all the way to the surface.

Next, in order to study the relationship between the nature of the dislocations and the direction of bending, we carried out a Burger's vector analysis. FIG. 7.4.2-(2) is a TEM image of the vicinity of the edge of the mask in Sample B, where (a) is a bright field image, and (b) and (c) are dark field images obtained using  $(11\bar{2}0)$  and  $(0002)$  diffraction waves, respectively. Dislocation lines bent in the direction of the mask region are observed in both dark field images, whereas dislocation lines bent in the direction of the stripes of the mask are only observed in the image in which  $(11\bar{2}0)$  diffraction waves were used. Based on these results, it is evident that mixed dislocations are bent in the direction of the mask region and are terminated by the void, whereas edge dislocations are bent in a direction parallel to the stripes of the mask.



FIG. 7.4.2-(2) TEM image of the vicinity of the mask edge (Sample B). (a) Bright field image; (b), (c) Dark field images

FIG. 7.4.2-(3) shows dark field images of dislocation lines generated at the top edge of the void. Judging by the contrast of the images, it was determined that both mixed dislocations and edge dislocations were present among the dislocation lines generated at the top edge of the void and both types of dislocations generated growth pits.

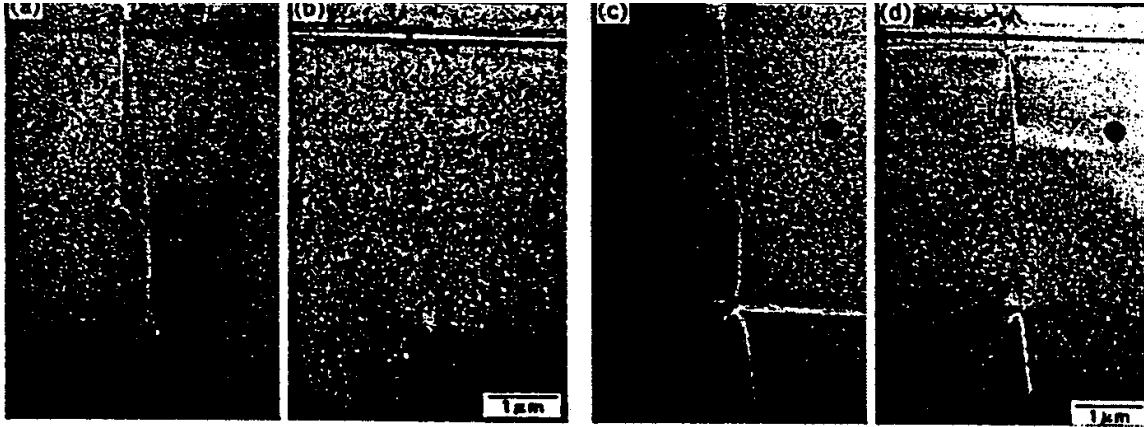


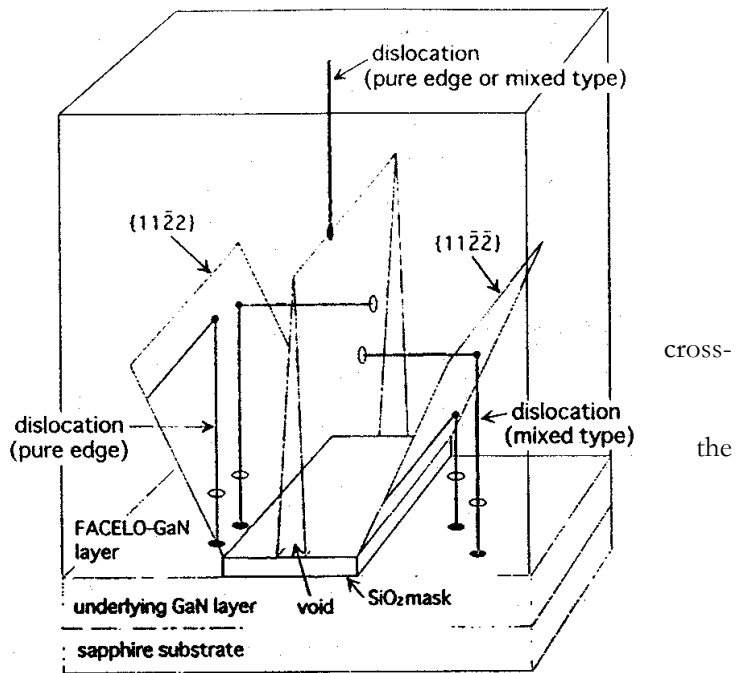
FIG. 7.4.2-(3) TEM images of the top edge of the void (dark field images)

FIG. 7.4.2-(4) shows a three-dimensional sketch of the dislocation reduction mechanism in FACELO-GaN, as confirmed in the present study. It is noteworthy that reduction of dislocations in FACELO-GaN requires growing only 10 μm.

FIG. 7.4.2-(4) Dislocation propagation mechanism in FACELO-GaN

**7.4.2.2 Micro-photoluminescence of facet-controlled ELOG-GaN**

FIG. 7.4.2-(5)~FIG. 7.4.2-(8) show two-dimensional maps of peak intensity in sections made in a direction normal to the stripes of the samples. In the figures, the bottom side represents the substrate, and top side represents the surface of the crystal. In all cases, measurements were conducted with a pitch of 1 μm and mapping was subjected to smoothing. Results obtained for each sample are described below.



① A sample illustrating the process of starting from triangular facets is shown in FIG. 7.4.2-(5). It exhibits a characteristic peak intensity distribution, where the peak intensity is stronger on the facet-forming slanted faces ( $\{11\bar{2}2\}$  faces) and weaker above the opening portions, with an intensity ratio of approximately one order of magnitude. The

same distribution has been reported for observations of cross sections in HVPE samples using cathodoluminescence (CL), and is believed to be due to the generation of defects on the faces, where facets are formed. Also, it has been confirmed by micro-PL that the peak wavelength is longer and the half-width becomes wider in positions of high peak intensity, and these results are believed to indicate an increase in the incorporation of defects or impurities in this portion.

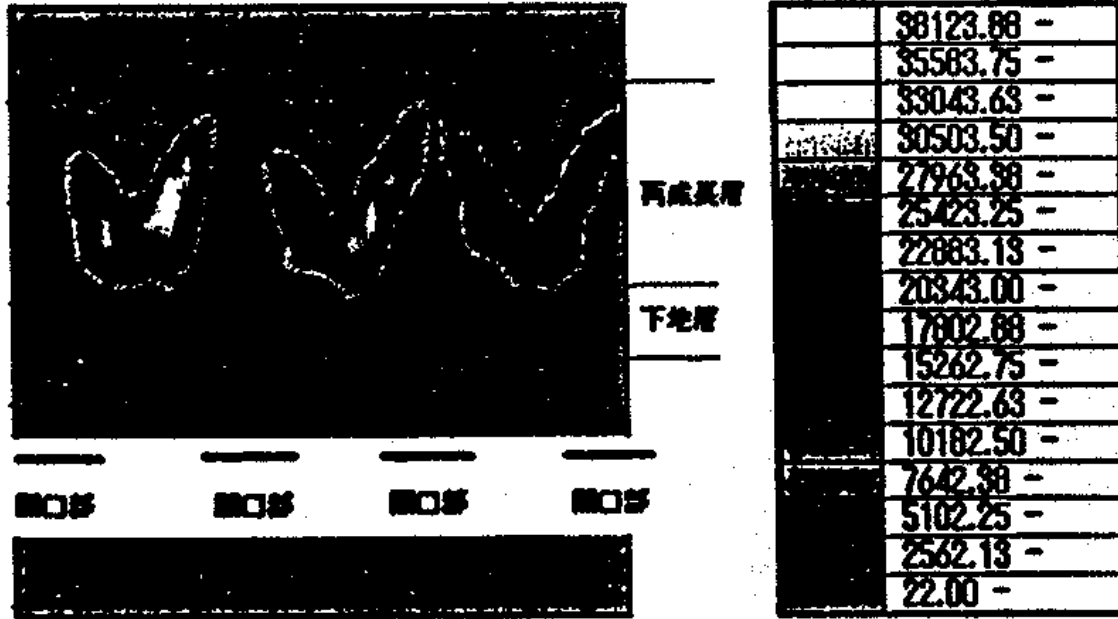


FIG. 7.4.2-(5) Cross sectional PL intensity mapping for a sample illustrating process of burial starting from triangular facets

[Keys, FIG. 7.4.2-(5)]

(Right, top to bottom) Regrowth layer; Buffer layer

(Across bottom) Opening Opening Opening Opening

② An example illustrating the process of burial starting from square facets is shown in FIG. 7.4.2-(6). In this sample, above the mask pattern, there are high-intensity portions rectilinear in the direction of growth. Based on the fact that this is a square-facet sample, it is evident that these portions of high peak intensity are interfaces ( $\{11\bar{2}0\}$  faces) of growth in the lateral direction. The fact that portions of large half-width and portions of large peak wavelength coincide with the portions of high peak intensity and there is considerable incorporation of defects or impurities at the facet growth interfaces is identical to the results of ①.

③ A sample illustrating burial by one-step regrowth is shown in FIG. 7.4.2-(7). There is high peak intensity at the growth interfaces of the square facets, and the peak wavelength and half-width exhibit basically the same distribution as in ②. At the very surface, the peak intensity declines, and, after facets from the two edges coalesce above the mask, in the same manner as in other areas, the incorporation of defects or impurities is reduced.

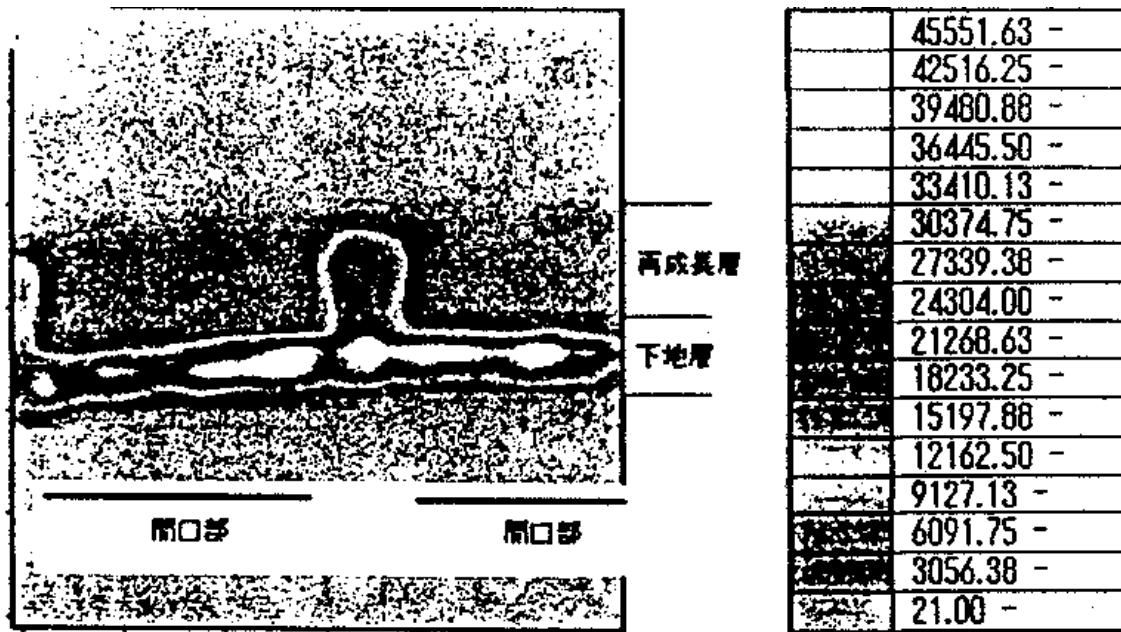


FIG. 7.4.2-(6) Cross sectional PL intensity mapping of sample illustrating process of burial starting from formation of square facets

[Keys, FIG. 7.4.2-(6)]

(Right, top to bottom) Overgrowth layer; Underlayer  
 (Across bottom) Opening Opening

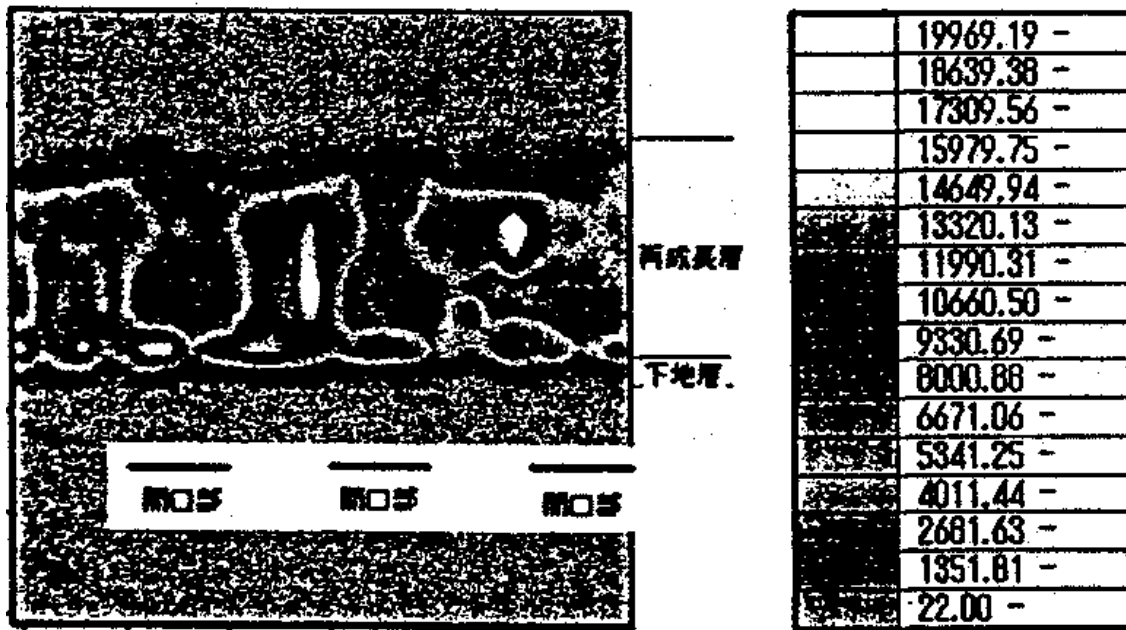


FIG. 7.4.2-(7) Cross sectional PL intensity mapping of sample illustrating process of burial starting from square facets in one step

[Keys, FIG. 7.4.2-(7)]

(Right, top to bottom) Overgrowth layer; Underlayer  
 (Across bottom) Opening Opening Opening

A sample obtained by completing burial using square facets upon formation of triangular facets is shown in FIG. 7.4.2-(8). This sample also exhibits practically the same distribution as in ③. Namely, the peak intensity is strong only in the coalescence region of the square facets. In the sample of ①, which illustrates the process of triangular facet burial, a distribution corresponding to the growth interfaces of the triangular facets was visible, but in this sample it was not clearly observed, and the incorporation of defects and impurities at the growth interfaces of the vertical facets is believed to be greater than at the interfaces of the triangular facets.

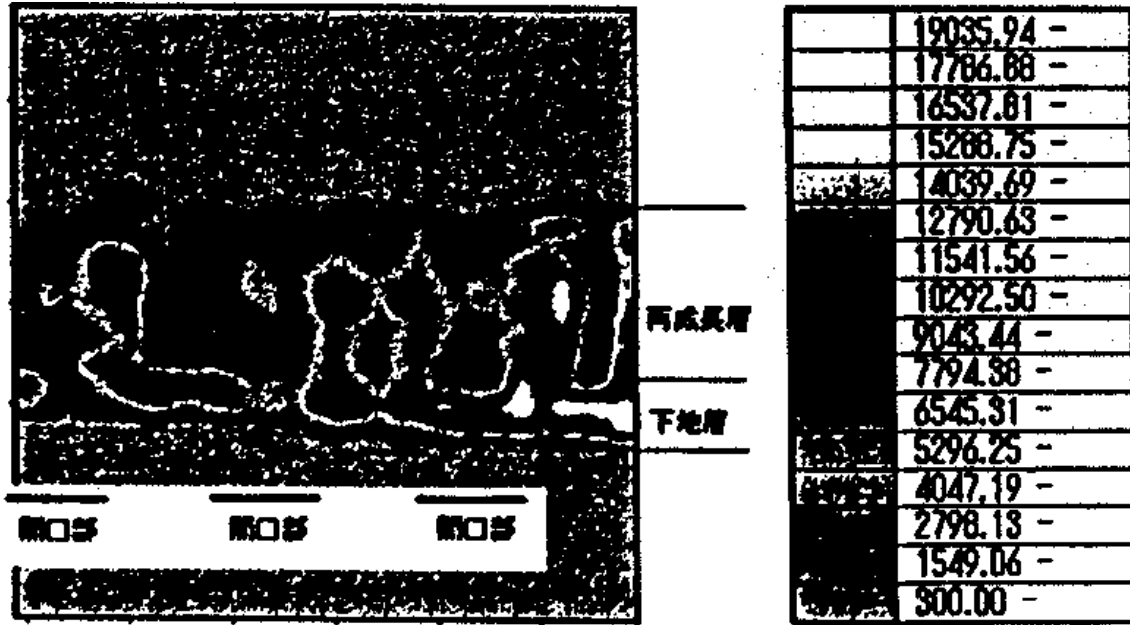


FIG. 7.4.2-(8) Cross sectional PL intensity mapping of sample illustrating two-step burial with triangular and square facets

[Keys, FIG. 7.4.2-(8)]  
 (Right, top to bottom) Overgrowth layer; Underlayer  
 (Across bottom) Opening Opening Opening

To sum up all of the above, it was found that the distribution of PL spectra related to the growth mechanism could be obtained by means of the micro-PL technique. It is believed that the overgrowth interfaces of the facets contain defects and impurities, and, as far as the tendency relative to the facet surfaces is concerned, for *c*-plane, incorporation of defects and impurities is the least of all, for {112̄2} it is larger, and for {112̄0} it is largest. In the future, in order to study the fine structure of the spectrum, we will conduct measurements at low temperatures.

**7.4.2.3 Time resolved photoluminescence of ELOG-GaN**

The 3.4786-eV neutral donor bound exciton emission line (I<sub>2</sub>) is dominant in the PL spectra of the ELOG-GaN samples, and emission lines corresponding to the free exciton resonance energy of the reflection spectra are observed at 3.4850 eV (Ex<sup>A</sup>) and 3.4924 eV (Ex<sup>B</sup>). In addition, the free exciton emission becomes dominant with temperature and is observed at room temperature.

FIG. 7.4.2-(9) and FIG. 7.4.2-(10) show the dependence of time-integrated emission spectra on the excitation energy density in ELOG-GaN with W masks and ELOG-GaN with SiO<sub>2</sub>-masks, respectively.

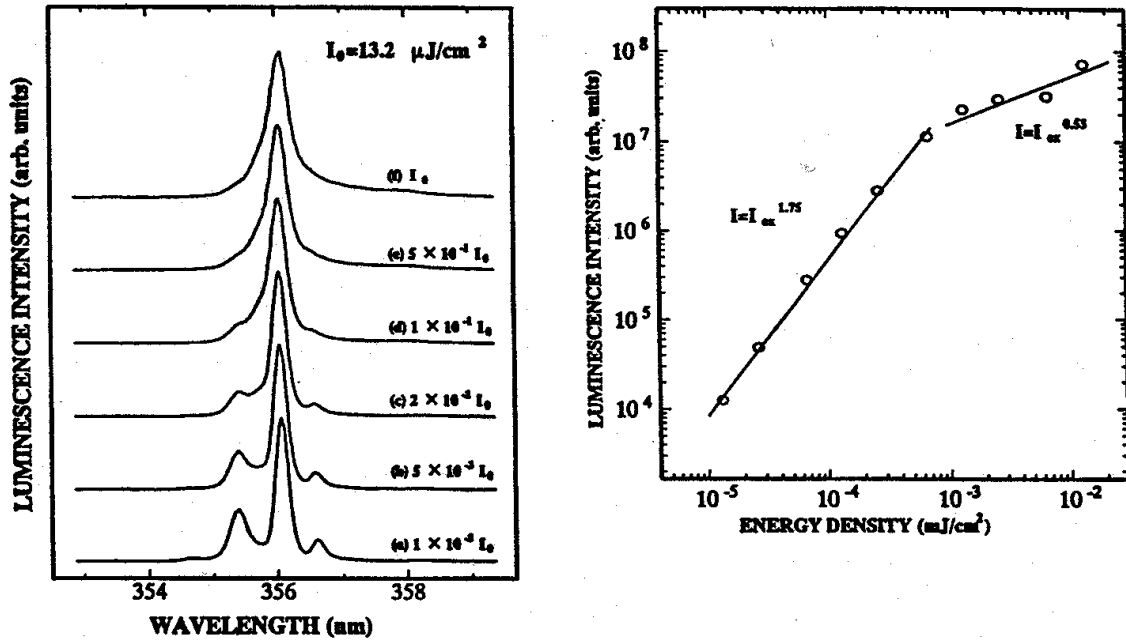


FIG. 7.4.2-(9) Time integrated emission spectra of ELOG-GaN using W masks

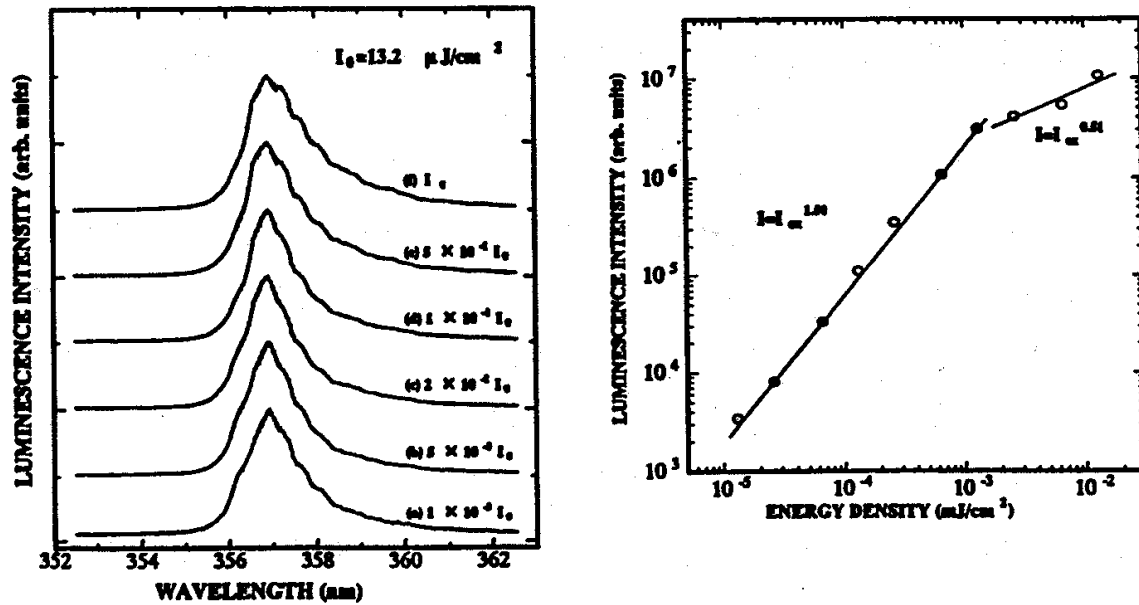


FIG. 7.4.2-(10) Time integrated emission spectra of ELOG-GaN using SiO<sub>2</sub>-masks

In ELOG-GaN with W masks, for Ex<sup>A</sup>, which is clearly observed at the excitation energy density of (a), the relative intensity ratio with respect to (D<sup>0</sup>,X) decreases with increasing excitation energy density, and practically no peak can be observed in (f). This is believed to be due to the fact that exciton emission in the vicinity of the (D<sup>0</sup>,X) energy position becomes more pronounced with increasing excitation energy density. The same can be said about ELOG-GaN using SiO<sub>2</sub> masks, but because of the large half-width at (D<sup>0</sup>,X), it was not observed as markedly as in the case of ELOG-GaN with W masks.

In addition, plots obtained by plotting the peak intensity against the excitation energy density are shown on the right-hand side of the respective figures. The characteristic dependence of exciton emission, in accordance with which there is a super-linear increase as a function of the excitation energy density in the vicinity of the ( $D^0, X$ ) energy position, can be observed in this figure as well. However, it was found that its slope was 1.50 for ELOG-GaN with  $\text{SiO}_2$  masks and 1.75 for ELOG-GaN with W masks, with the W mask ELOG-GaN exhibiting a stronger increase.

FIG. 7.4.2-(11) shows time-decay spectra of free exciton emission. Both for the W mask and  $\text{SiO}_2$ -mask samples, the emission lifetime became longer with increasing excitation energy density, with the emission lifetime saturating at the excitation energy density of (d)~(f) and becoming practically constant. In the W mask ELOG-GaN, the emission lifetime is 42 ps in (a) and reaches 143 ps in (f), and in the  $\text{SiO}_2$ -mask ELOG-GaN, the emission lifetime is 48 ps in (a) and 117 ps in (f).

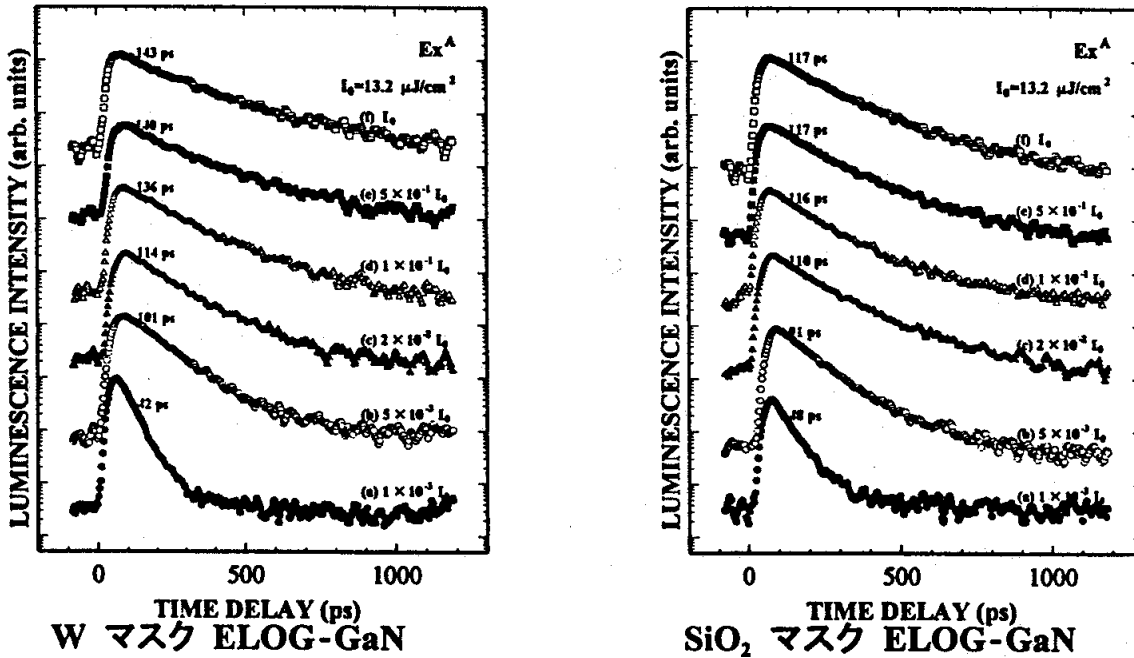


FIG. 7.4.2-(11) Dependence of free exciton emission decay time spectra on excitation energy density for W mask (left) and  $\text{SiO}_2$  mask (right) ELOG.

The tendency of the excitation lifetime to increase with excitation energy density is believed to be due to the fact that, as the excitation energy density increases, the impurity level becomes more saturated, and, as a result, carrier transport related to the impurity level is suppressed. It is believed that, in the low excitation energy density region of (a), carriers are trapped by the impurity level at an early stage, and, as a result, the emission lifetime becomes shorter, while in (f), in the region of excitation energy density where the impurity level is saturated, the transport of carriers to the impurity level is suppressed, and, as a result, the emission lifetime becomes longer. In addition, the fact that the emission lifetime in (f) is 143 ps for the W mask ELOG-GaN and much shorter, 117 ps, for  $\text{SiO}_2$ -mask ELOG-GaN, is believed to be due to the fact that  $\text{SiO}_2$ -mask ELOG-GaN is strongly influenced by non-radiative recombination centers, while in W mask ELOG-GaN samples the non-radiative recombination centers are evidently suppressed.

The same tendency was observed in the time decay spectra of the exciton emission. As for emission components, in regions (a)~(c), neutral donor bound exciton emission saturates, and exciton emission becomes dominant. The emission lifetime becomes longer with increasing excitation energy density, saturating and becoming practically constant in regions (d)~(f). In addition, the emission lifetime at excitation energy (f) is 134 ps for the  $\text{SiO}_2$ -mask ELOG-GaN and 192 ps for the W mask ELOG-GaN, with

the emission lifetime of excitons of the W mask ELOG-GaN being longer, which indicates that the non-radiative recombination centers of the W mask ELOG-GaN are suppressed.

Based on the above-described results, it became evident that W mask ELOG-GaN has better crystal properties than SiO<sub>2</sub>-mask ELOG-GaN, and that in such samples the non-radiative recombination centers are suppressed. Thus, it was confirmed that the material of the mask exerts an influence on the optical characteristics of ELOG-GaN.

## 7.5 Summary

By using the newly developed FACELO technique, we were able to reduce the dislocation density to a level of  $10^6 \text{ cm}^{-2} \sim 10^4 \text{ cm}^{-2}$ . The dislocation density was successively reduced by controlling the initial nucleus density and carrying out two-step FACELO growth on a underlying low-dislocation GaN crystal (10 mm on a side) in two steps including  $\{11\bar{2}2\}$  FACELO and then  $\{11\bar{2}0\}$  FACELO. So far as we know, the resulting GaN-on-sapphire substrates have the lowest dislocation density in the world. We have determined that a crucial point in dislocation reduction is that dislocations with  $\{11\bar{2}2\}$  triangular facets are bent in a horizontal direction with respect to the  $c$ -axis and propagation is terminated by the void formed in the central portion of the mask. In addition, new dislocations originating from the top edge of the void and reaching the surface, where they remain in a linear pattern, can be efficiently prevented from reaching the surface by  $\{11\bar{2}0\}$  rectangular facets. We have started investigations into 2-inch substrates, but because of insufficient burial we are still dealing with substrates of insufficient surface condition. A parallel effort has been going into accumulation of data on the basic technology of ELOG growth by means of HVPE.

Based on analysis of dislocation lines in FACELO-GaN by TEM, it has been determined that mixed dislocations are bent towards the mask regions and terminated by the void, whereas edge dislocations are bent in a direction parallel to the stripes of the mask. It has been determined that, based on this mechanism, dislocation lines generated at the interface of the substrate and GaN do not reach the surface, and the dislocation density is greatly reduced.

It has been determined that a PL spectrum distribution related to the growth mechanism is obtained using the micro-PL technique. A considerable amount of defects and impurities is believed to be contained at the facet regrowth interface. The tendency to incorporate impurities via facet surfaces is believed to be least pronounced in the case of the  $c$ -plane, more pronounced in the case of the  $\{11\bar{2}2\}$  planes, and strongest in the case of the  $\{11\bar{2}0\}$  planes.

Results of time-resolved spectroscopy measurements have confirmed that, in comparison with ELOG-GaN with a SiO<sub>2</sub> mask, ELOG-GaN with a W mask has a longer free exciton emission life and its non-radiative recombination process is suppressed.

## 7.6 Future plans

In our pursuit of core technologies of dislocation defect reduction in 10-mm substrates, we have been able to accumulate a large number of technologies by developing a novel FACELO method, using W masks, etc. The dislocation density is now  $10^6 \sim 10^4 \text{ cm}^{-2}$ , which is practically at the target level. However, in our investigations into 2-inch substrates, for which we changed the MOCVD growth equipment, we have been unable to reproduce the current FACELO results, with the current post-burial surface morphology remaining inadequate.

In the future, in order to realize 2-inch GaN-on-sapphire substrates of practical value with a dislocation density of not more than  $10^4 \text{ cm}^{-2}$ , which is the target of the current project, we will focus our efforts on the study of 2-inch substrates. To this end, along with conducting basic research aimed at further dislocation density reduction, we will try to reduce dislocations by efficiently combining the core technologies accumulated up until now. In order to achieve an efficient combination, it will be necessary to further

elucidate the mechanism of dislocation propagation or extinction using TEM observations. We believe that the characteristic mechanism of the MOCVD method will also become apparent from a comparative study of the HVPE method. In addition, in connection with the different crystal quality of GaN on the mask and above the window areas in ELOG-GaN, we are going to focus on the evaluation of crystal quality in micro-regions by means of micro-photoluminescence, time resolved photoluminescence, cathodoluminescence, etc.

We plan to develop high-quality GaN-on-sapphire substrates of practical value in a timely fashion by applying the findings obtained above in our investigations to 2-inch substrates. The fabricated substrates will be supplied to the UV LED Epi-Group as substrates for homoepitaxy or to the Substrate Group as high-grade seed crystals for confirmation of the effects of the low-dislocation substrates.

## 7.7 References

- [1] H. Amano, N. Sawaki, I. Akasaki, and Y. Toyoda: *Appl. Phys. Lett.* 48, 358 (1986)
- [2] S. Nakamura: *Jpn. J. Appl. Phys.* 30 (1991) L1705
- [3] A. Usui, H. Sunakawa, A. Sakai, and A. Yamaguchi: *Jpn. J. Appl. Phys.* 36 (1997) L899
- [4] A. Sakai, H. Sunakawa, and A. Usui: *Appl. Phys. Lett.* 71 (1997) 2259
- [5] O. H. Nam, M. D. Bremser, T. S. Zheleva, and R. F. Davis: *Appl. Phys. Lett.*, 71 (1997) 2638
- [6] S. Nakamura, M. Senoh, S. Nagahama, N. Iwase, T. Yamada, T. Matsushita, H. Kiyoku, Y. Sugitomo, T. Kozaki, H. Umemoto, M. Sano, and K. Chocho: *Jpn. J. Appl. Phys.* 36 (1997) L1568
- [7] H. Miyake, A. Motogaito, and K. Hiramatsu: *Jpn. J. Appl. Phys.* 38 (1999) L1000
- [8] K. Hiramatsu, K. Nishiyama, M. Onishi, H. Mizutani, M. Narukawa, A. Motogaito, H. Miyake, Y. Iyechika, and T. Maeda: *J. Crystal Growth*, 221 (2000) 316
- [9] K. Kagawa, K. Tsukamoto, N. Kuwano, K. Oki, and K. Hiramatsu: *Proc. of IWN 2000, IPAP Conf. Series 1* (2000) 471
- [10] H. Miyake, H. Mizutani, K. Nishiyama, A. Motogaito, K. Hiramatsu, Y. Iyechika, and T. Maeda: *Proc. of IWN 2000, IPAP Conf. Series 1* (2000) 324
- [11] H. Miyake, H. Mizutani, K. Hiramatsu, Y. Honda, Y. Iyechika, and T. Maeda: *Proc. of MRS 2000 Fall Meeting* (2001) G5.3
- [12] S. Nagahama, N. Iwasa, M. Senoh, T. Matsushita, Y. Sugimoto, H. Kiyoku, T. Kazaki, M. Sano, H. Matsumura, H. Umemoto, K. Chocho, and T. Mukai: *Jpn. J. Appl. Phys.* 39, (2000) L647
- [13] A. Kaschner, A. Hoffman, C. Thomsen, F. Bertram, T. Riemann, J. Christen, K. Hiramatsu, H. Sone, N. Sawaki, *Appl. Phys. Lett.*, 76 (2000) 3418
- [14] S. J. Rosner, E. C. Carr, M. J. Ludowise, G. Girolami, H. I. Erikson, *Appl. Phys. Lett.*, 70 (1997) 420.
- [15] J. S. Speck, H. Marchand, P. Kozodoy, P. T. Fini, X. H. Wu, J. P. Ibbetson, S. Keller, S. P. Denbaars, U. K. Mishra, S. J. Rosner, *Proc. 2<sup>nd</sup> International Symposium on Blue Laser and Light Emitting Diodes*, p. 37.

# 8 Development of GaN Epitaxial Substrates Based on Low Pressure Gas Phase Technique

## 8.1 Achievements in 1998 and 1999

In the future, in the process of transition to industrial production, the cost of manufacture per unit of luminance of white illumination LEDs will have to be made equivalent to that of already existing means of illumination. In addition to being plagued by poor efficiency of electricity-to-light conversion, the GaN LEDs currently available on the commercial market are expensive in spite of the use of sapphire substrates, which are very close to industrial production at the present moment. Thus, in the course of the present project, it is necessary to seek increased efficiency and improvements in the reliability of white illumination LEDs by practically implementing GaN substrates, and, on the other hand, to investigate possible low-cost fabrication methods with a view to start industrial production in the future.

As far as current techniques of gas phase growth of GaN are concerned, methods that have been reported to achieve successful synthesis include MOCVD, the sandwich technique, as well as HVPE and other open-tube growth methods; all of the above methods, however, make use of expensive source materials, most of which are discharged from the system without contributing to the reaction. In addition, because of the high volume of the discharged toxic exhaust gases and by-products, it is necessary to install expensive environmental protection equipment and prevent environmental damage by frequently renewing the chemicals. Because the existing GaN gas phase growth methods, which have already allowed us to achieve high levels of quality, are open-tube type methods, it is difficult in principle to realize additional cost reductions in terms of source material expenses, equipment costs, and running costs. Thus, it is believed that transition to industrial production in case of fabrication methods used for illumination LED substrates will present serious difficulties. Therefore, with account taken of the future cost reduction needs, in the course of the present project we have been trying to develop GaN substrates for epitaxial growth using a new low pressure gas phase technique.

In 1998, no bulk crystals were obtained by using the low pressure gas phase technique, and, in order to decide on the preferable system for GaN growth, we conducted investigations into the processes of crystal growth (sublimation, transport, and reactions of source materials) in the low pressure gas phase technique. As a result, as shown below, it was determined that the application of the open-tube system created serious obstacles, and we concluded that it was more practical to use GaN growth based on the low pressure gas phase technique under a pseudo-open tube system, which is characterized by supplying source materials from outside the system.

(i) In order to obtain basic data regarding the reaction of Ga and N<sub>2</sub>, measurements were carried out to determine the GaN dissociation pressure and the presence/absence of GaN synthesis in the vicinity of 1000°C in an equilibrium system, and, as a result, it was experimentally confirmed that the dissociation pressure at 940°C was  $3.6 \times 10^5$  Pa, which was almost the same as the value expected based on data from literature. In addition, it was also confirmed that the rate of dissociation of N from GaN was extremely high.

(ii) Based on thermodynamic investigations and theoretical equations of Stephan flow, we performed growth velocity calculations for direct synthesis from Ga and N<sub>2</sub>, and concluded that improvements in the growth velocity of up to two orders of magnitude, with a maximum of 6 mm/h, were possible if trace amounts of carrier gases such as HCl were used.

(iii) Preliminary experiments confirmed that if nitrogen was activated with microwaves etc., it reacted with the Ga vapor, thereby making synthesis of GaN possible.

In 1999, our investigations into applicable systems to be used with the low pressure gas phase technique were narrowed down to the pseudo-open tube system, which is characterized by supplying source gases from outside the system and studies were conducted regarding GaN reactions involving the N<sub>2</sub> plasma created by microwave excitation. As a result,

(iv) using sapphire as seed crystals, we carried out growth in regions where a high concentration of plasma was created by adjusting the microwave output, and, based on the optimization of pressure, temperature, etc., achieved a relatively high rate of synthesis of 100  $\mu\text{m}/\text{h}$  for GaN in microcrystal powder form, which was more than 20 times the prior-art level. In addition, depending on the conditions used, we were able to obtain hexagonal-shaped single crystals as small as 30  $\mu\text{m}$ .

(v) In addition to GaN, an EDX analysis of SEM images of the resultant powdery material did not reveal any impurity peaks, and X-ray diffraction confirmed its orientation along the *c*-axis on the sapphire substrate.

(vi) Based on the findings obtained in the course of the above-described basic experiments, we designed and built a “Gas Phase Bulk Growth Furnace” intended for the systematic development of bulk GaN crystals.

## 8.2 Summary of Research & Development in 2000

A high quality (low dislocation density) and low cost are essential conditions for the development of illumination LED substrates, which constitutes the ultimate goal of the present project. Thus, it is believed that the pseudo-open tube design, which has a high source material yield, is preferable for bulk growth from the gas phase. In 2000, we have been optimizing the growth conditions of the pseudo-open tube system with a view to grow GaN single crystals with a diameter of several mm to 10 mm and in order to investigate the possibility of using the grown GaN single crystals as LED substrates. Specific problems included: ① improvement in the rate of GaN synthesis of up to 100  $\mu\text{m}/\text{h}$  or more. ② Clarification of the conditions of monocrystallization. ③ Determination of the growth conditions that should be used in the bulk growth furnace. ④ Conducting evaluation of crystals as substrates for UV LEDs.

### 8.2.1 Research on GaN-related transport and reaction phenomena

The growth velocity of bulk single crystals is an important factor in the fabrication of such crystals. Generally speaking, the velocity of crystal growth from the gas phase is slower in comparison with that of growth from the liquid phase, and from the standpoint of its practical application in the future, it is necessary to achieve a good understanding of the various possibilities of further improvement. In 1999, we attained a GaN rate of synthesis of 100  $\mu\text{m}/\text{h}$  and demonstrated that such rates were possible. Thus, based on the obtained findings, we have been trying to further improve the rate of synthesis and achieve even higher crystal growth velocities.

In this system, reactions are believed to take place instantaneously, and transport is believed to act as the rate-determining factor. For this reason, we have been trying to optimize the temperature and pressure conditions and the structure of the reaction system to improve the rate of transport. In addition, we have been investigating high-frequency wave-based plasma as a method for generating activated nitrogen. Because the use of this method makes it easier to control the position of the plasma and allows for increasing the activation ratio by raising the pressure of nitrogen, it offers the possibility of raising the rate of the GaN synthesis reaction. Moreover, because it has the advantage of requiring equipment that is smaller in size and less expensive in comparison with the microwave system, it is believed that the study of growth based on this system will be necessary from the standpoint of our future cost-reduction efforts.

In 2000, our achievements have included the determination of the essential conditions necessary for further crystal property improvements at the maximum rate of synthesis of 100  $\mu\text{m}/\text{h}$  under the microwave system

and the experimental confirmation of the possibility of improvement of up to 1 mm/h under the high-frequency wave system.

## 8.2.2 Research on single crystal growth techniques

In 2000, we have been using existing furnace equipment in order to continue investigations into the conditions of monocrystallization, in particular, conditions such as the substrate temperature and the pressure of the supplied nitrogen. As a parallel effort, we have studied monocrystallization within a wider range of controllable conditions using the bulk growth furnace that was introduced in 1999. In addition, with a view to eventually grow large 10-mm GaN single crystals, we have been using GaN single crystals as seed crystals, which are indispensable for monocrystallization. In addition, in order to make sure the crystals can be used as LED substrates, we have been conducting evaluation of crystal properties and optical characteristics. In 2000, our achievements have included confirmation of growth of a dense film-like GaN crystal oriented along the *c*-axis within a 10 × 4 mm area on a sapphire substrate, and, furthermore, successful synthesis of crystals exhibiting no surface roughness and possessing a highly symmetric surface morphology along with an X-ray rocking curve half-width of 6 minutes.

## 8.3 Microwave-based GaN Synthesis Experiments

### 8.3.1 Methods and means

#### 8.3.1.1 Avenues of research

In order to stably synthesize bulk single crystals from a gas phase, it is necessary to build a system capable of realizing diffusion-controlled constant mass transport. Diffusion-controlled gas transport phenomena in closed-tube systems are described by the so-called Stephan flow, in which the difference in vapor pressure between the source materials and the synthesis section acts as the driving force, and were investigated during the first year of the study. In a pseudo-open tube system, in which nitrogen is introduced from outside, it is important to control the temperature of the seed crystal and the Ga source material, which determines the vapor pressure difference, as well as the stability of the N<sub>2</sub> flow rate. To this end, we have put into operation the gas phase bulk growth furnace (introduced last year), and we currently working to establish its controllability characteristics.

In addition, as regards the phenomenon of transport of reactive radicals activated by the plasma state, in addition to the above-mentioned diffusion-controlled mass transport, the reactive radicals, when charged, are acted upon by the electric field and drift-controlled. In this connection, we are working to better appreciate the respective influence exerted in the case of microwave excitation, where the electric field is presumed to be zero when integrated over time, and in the case of high-frequency wave pulse excitation, which has been adopted as a new method of activation.

As regards microwave excitation, the vapor pressure of Ga in the vicinity of 1000°C is low, approximately 1 Pa, and nitrogen is supplied such that a constant pressure is maintained within the range of efficient Ga transport rates, in other words, at a pressure of about several hundred Pa. For this reason, the difference between the vapor pressure in the outlet section and in the reaction zone is usually larger in comparison with the difference between the vapor pressure of Ga and the Ga source material section, and, as result, the nitrogen transport rate does not determine the rate of synthesis. Because in this system synthesis is carried out in the above-mentioned pressure range, the mean free path of the plasma is short, and, as a result, a diffuse plasma undergoes repeated generation and extinction. The density distribution of the plasma determines the quantity of the synthesized GaN and the region of synthesis. In this connection, we have been trying to determine the position of the substrate based on experimental findings regarding the density distribution, which we obtained the year before by plasma spectroscopy measurements.

Although it has been confirmed that, due to the extremely high activation energy of GaN in the vicinity of 1000°C, in a thermal equilibrium state dissociation does not proceed, in a non-equilibrium plasma state the

energy of the plasma may impart dissociation energy to the surface and cause decomposition, and, therefore, it is essential to have a clear understanding of this state in order to proceed. In other words, when other parameters are predetermined, maximal values are expected to be present in the relationship between the microwave output and the rate of synthesis and crystal properties, and we will proceed to further investigate these values.

Additionally, although sapphire is commonly used as the seed crystal substrate, it is necessary to carry out observations of the growth mode and surface morphology obtained with various substrates to have a clear picture of the range of applicability of the present method of synthesis. In addition, in the process of carrying out the above-mentioned experiments, it is important to regulate the relationship between the problems to be solved, parameters, and core technologies, as shown in FIG. 8.3.1-(1), to obtain a clear picture of their mutual influence while strengthening the understanding of the most important factors. In the present chapter, we describe the results obtained by the experimental study of Ga crucible temperature dependence, pressure dependence, microwave output dependence, substrate temperature dependence, and substrate seed crystal dependence.

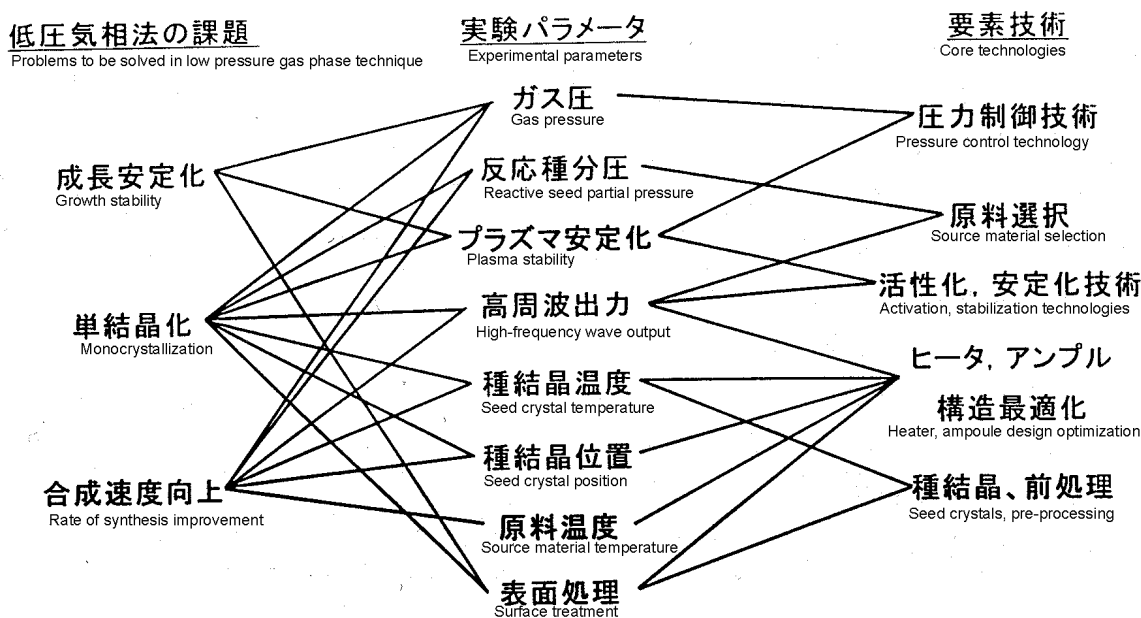


FIG. 8.3.1-(1) Problems to be solved and core technologies associated with low pressure gas phase technique

### 8.3.1.2 Experimental methods

Experiments were carried out using the gas phase bulk growth furnace designed and manufactured last year. As far as source material supply was concerned, we designed the experimental system so that Ga and N<sub>2</sub> gases were used as the supply sources and no by-products were generated, just as in the sublimated state in a closed-tube system. Ga was placed in a crucible and diffusion was carried out by using as the driving force the vapor pressure difference inside the reaction tube due to the temperature distribution created by the heater. In accordance with the principles of the gas phase method, nitrogen was supplied from outside in such a manner that a constant pressure was maintained and diffused onto the seed crystals in an activated plasma state. We set up an experimental system such as the one shown in FIG. 8.3.1-(2).

Because microwaves leaked outside via the thermocouple as an antenna when the plasma was ignited, we conducted temperature measurements by inserting the thermocouple in the center of the reaction tube after turning off the microwave output. For this reason, the temperature of the substrate during synthesis was expected to be several degrees higher than the measured values.

After taking the synthesized crystals out, they were cleaned with aqua regia and evaluated using Nomarski microscope observations, X-ray measurements, electron microscope observations, photoluminescence, etc.

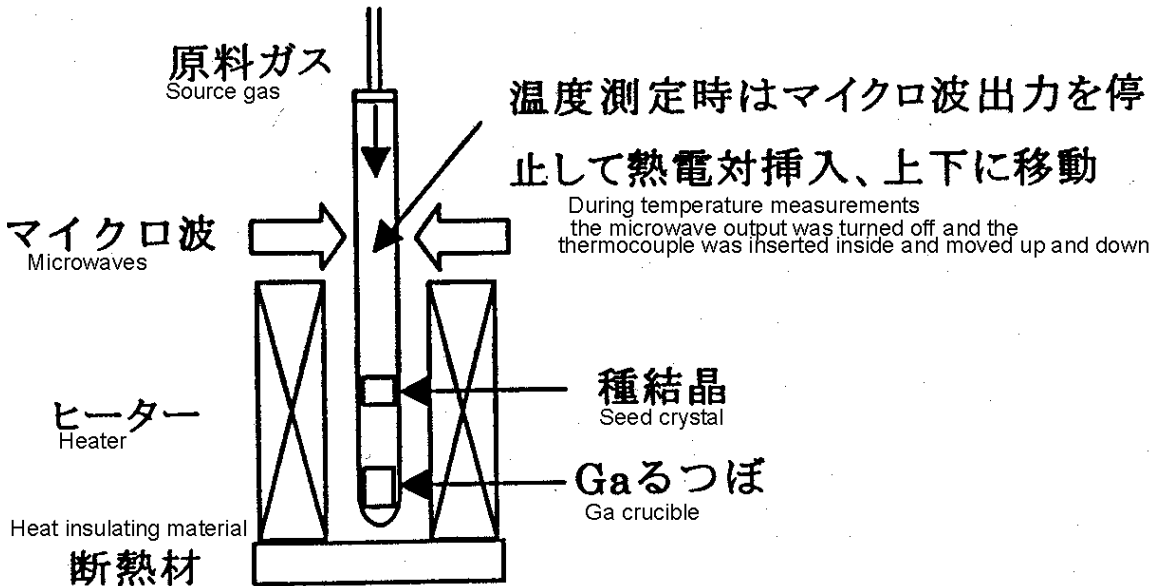


FIG. 8.3.1-(2) Experimental system for GaN synthesis using microwaves

(i) Ga crucible temperature

In order to form a GaN single crystal, first of all, it was necessary to set the temperature of the Ga crucible to the range in which a Ga transport amount necessary for GaN crystal formation could be obtained. Because in the present system Ga was diffused in an inert N<sub>2</sub> gas having a sufficiently short mean free path, the Stephan flow model, which takes into consideration advection and which is the principle of the closed-tube method, is applicable in this case. Assuming that all of the Ga reacts in the vicinity of the substrate, and designating the diffusion coefficient of Ga as  $D$ , the total pressure as  $P$ , the Ga vapor pressure on the surface of the crucible as  $P_{\text{Ga}}$ , and the distance between Ga and the substrate as  $L$ , the Ga transport amount,  $J_{\text{Ga}}$ , is expressed by relationship (8.3.1), which is derived from Stephan flow.

$$J_{\text{Ga}} = (2D \cdot P \cdot P_{\text{Ga}}) / \{RTL \cdot (2P - P_{\text{Ga}})\} \quad (8.3.1)$$

In addition, because the synthesis is carried out at a constant pressure, (8.3.2) holds true.

$$J_{\text{Ga}} \propto (\text{rate of synthesis}) \propto (\text{quantity of consumed N}_2) \quad (8.3.2)$$

Based on the formulas and on the Ga vapor pressure curve, the quantity of consumed N<sub>2</sub> is expected to display a sensitive positive correlation with the temperature of the Ga crucible.

The synthesis experiments were carried out under the following conditions with a view to establish a suitable Ga temperature range based on the quantity of consumed N<sub>2</sub> and the crystal surface morphology, as observed under a Nomarski microscope. As for N<sub>2</sub> consumption, the current study utilized sapphire substrates with a diameter of 16 mm, and it was estimated at 61  $\mu\text{m}$  if all of the 10-cc N<sub>2</sub> gas was consumed in the synthesis of GaN on the substrate. The total pressure was 200 Pa, the microwave output was 300 W, and the temperature was:

- ① Ga temperature of 1000°C – substrate temperature of 800°C
- ② Ga temperature of 1070°C – substrate temperature of 1000°C
- ③ Ga temperature of 1100°C – substrate temperature of 1000°C

(ii) Pressure dependence

The pressure inside the reaction tube was varied to investigate the crystalline properties and the rate of synthesis. Based on formula (8.3.1), the rate of synthesis can be expected to improve when the total pressure  $P$  is low. However, in a state wherein the pressure of Ga vapor from GaN is higher than the saturated vapor pressure of Ga alone, a non-equilibrium reaction is stimulated, and, for this reason, GaN including Ga droplets may be synthesized if the V/III ratio is small. In addition, when the total pressure  $P$  is high, a decline in the quantity of transported Ga occurs, and GaN micropowder can be produced. With account taken of the above, experiments were conducted by varying the pressure of the supplied nitrogen under the following conditions.

- ① Microwave output: 300 W, Ga temperature: 1080°C, substrate temperature: 800°C, total pressure: 100 Pa
- ② Same as above, total pressure: 200 Pa
- ③ Same as above, total pressure: 500 Pa
- ④ Microwave output: 300 W, Ga temperature: 1100°C, substrate temperature: 1000°C, total pressure: 100 Pa
- ⑤ Same as above, total pressure: 200 Pa

In this series of experiments, in addition to the quantity of consumed N<sub>2</sub> and Nomarski micrographs, we conducted X-ray (0002)  $\omega$ -mode measurements to compare crystal properties based on the half-width.

#### (iii) Microwave output dependence

In the above-mentioned pressure and microwave output ranges, the generated nitrogen plasma consists mainly of the so-called 2<sup>nd</sup> positive system of N<sub>2</sub>, i.e. active radicals in the form of nitrogen molecules that are positive ions or are in a neutral excited state displaying the most intensive emission at 337 nm. Radicals etc., which are in the most highly reactive dissociation state in the nitrogen plasma, have not been observed under any conditions because of the short mean free path. As regards the distribution of the emission intensity, when the microwave output is changed, the intensity ratio does not change, only the absolute values change. In other words, in the reaction taking place on the substrate, only the density of the arriving active radicals changes, and it is necessary to keep the ratio of V/III and the Ga within an appropriate range. Based on the above considerations, we varied the microwave output to investigate the correlation with the quantity of synthesized material and crystal properties.

The experiments were conducted under the following conditions: a pressure of 200 Pa, a substrate temperature of 1000°C, a Ga temperature of 1100°C, and a microwave output of, respectively, ① 200 W, ② 300 W, ③ 400 W, and ④ 600 W.

#### (iv) Substrate temperature studies

During ordinary gas phase growth, the temperature of the substrate is one of the parameters exerting the strongest influence on monocrystallization, and it is believed to have a strong correlation with initial nucleation in the present growth method as well. This year, in order to conduct the experiments with high precision, we made improvements to the furnace and at present we are trying to determine the conditions necessary for transition to higher substrate temperatures. While it is believed that higher temperatures are preferable in order to activate surface migration, on the other hand, if sufficient Ga supply amounts are not provided at higher temperatures, decomposition of GaN will take place, which is why it is believed that further fine-tuning of these parameters needs to be done.

#### (v) Seed crystal dependence

Monocrystallization on a sapphire substrate has not been realized yet, the reason being either insufficient control over initial nucleation or insufficiently clear understanding of the crucial factors of the synthesis method itself. Seed crystals were modified into GaN substrates, the influence of surface treatment on which was expected to be relatively weak, and synthesis experiments were carried out in order to determine at the earliest possible stage whether synthesis of GaN single crystals was possible by the present method.

## 8.3.2 Results and Discussion

### 8.3.2.1 Confirmation of performance of gas phase bulk growth furnace and crystalline GaN synthesis experiments

We completed the commissioning of the “Gas Phase Bulk Growth Furnace” a single-wafer crystal growth furnace designed and manufactured the year before. Its main specifications are shown in FIG. 8.3.2-(1). Whereas the basic experimental furnace was of the horizontal type, which permitted easy arrangement of jigs inside the furnace, the gas phase bulk growth furnace was of a vertical design in order to achieve uniformity of temperature distribution in the radial direction as well as a reduction in convection. In addition, the degree of freedom and controllability of each parameter was greatly improved in comparison with the existing furnace.

An essential condition for metallic Ga transport in the low-pressure gas phase technique consists in achieving a higher degree of ultimate vacuum. Because the equilibrium vapor pressure of Ga at 1000°C is low, about 1 Pa, and because it is prone to form Ga<sub>2</sub>O<sub>3</sub> by reacting with residual oxygen in the gas phase, usually, the level of the residual oxygen is reduced while increasing the mean free path by using MBE and other ultra-high vacuum devices. On the other hand, although there was concern regarding oxidation in the basic experimental furnace because under the total pressure of 10<sup>1</sup>~10<sup>3</sup> Pa the mean free path in the low pressure gas phase technique is on the order of μm, considerable improvements have been achieved with respect to this aspect.

In addition, by combining the microwave generator with an automatic matching device, output fluctuations were reduced from the previous 20% to ±3%, enabling effective production of active radicals at low pressure and low output. Additionally, by using a PID flow rate controller, the pressure fluctuation range was stabilized below the lower limit of measurement, enabling synthesis with low convection. Based on the confirmation of above-described basic performance characteristics we were able to conduct synthesis experiments with high controllability.

	Gas phase bulk growth furnace	Basic experimental furnace (old)
System	Vertical furnace	Horizontal furnace
Maximum temperature	1150°C	1100°C
Ultimate vacuum	10 <sup>-5</sup> Pa	1 Pa
Pressure control system	PID control using flow rate controller	On/off control using electromagnetic valve
Microwave output	2 kW	1 kW
Output stability	±3%	±20%
Microwave matching system	Automatic matching device (stability for long period of time)	Manual stub (multiple stops during synthesis)
Maximum reaction tube OD	100 mm	50 mm

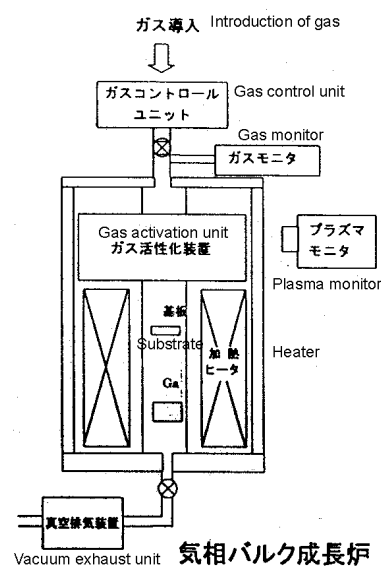


FIG. 8.3.2-(1) Main specifications and conceptual diagram of gas phase bulk growth furnace

Next, we used the device to conduct GaN crystallization by varying the microwave output, substrate position, Ga crucible position, temperature, and other conditions. As a result, at a substrate temperature of

approximately 1000°C, an adequate state was achieved in terms of the Ga transport amount and nitrogen plasma density and crystalline, albeit polycrystalline, GaN was successfully synthesized on a sapphire substrate.

On the other hand, we confirmed the phenomenon of GaN decomposition at a rate of several  $\mu\text{m}/\text{h}$  when synthesized GaN/sapphire was placed in a region characterized by a low Ga transport amount and a high density of plasma. Decomposition did not occur if the GaN was simply placed in a region of elevated temperature, and in that case no changes in surface morphology were noticed either. This makes the optimization of the ratio between the plasma density and Ga transport amount important, and, in case of a predetermined Ga supply amount, the amount synthesized and the flatness of the surface morphology are believed to assume extreme values through tweaking the plasma density. By taking the above results into consideration, we proceeded with experiments intended to study in detail the correlation between the parameters below and crystal properties.

### 8.3.2.2 Ga crucible temperature dependence

The results are shown in FIG. 8.3.2-(2) and FIG. 8.3.2-(3). There is a sensitive dependence between the temperature and the quantity of consumed  $\text{N}_2$ , which increases monotonically. The quantity of consumed  $\text{N}_2$  ① at a Ga temperature of 1000°C is just 2.4 cc/h, with powder-like GaN sparsely adhered to the surface of the sapphire, as shown in FIG. 8.3.2-(3). Although another issue to be considered in connection with crystalline properties is the temperature of the substrate, the sparsely synthesized GaN shows that the absolute quantity of transported Ga is insufficient, and it has been found that under the RF-MBE method, which is also based on a non-equilibrium reaction utilizing plasma, there is a suitable region on the higher temperature side as compared with temperatures of 900~1000°C. By contrast, a Ga temperature of ② 1070°C and ③ 1100°C resulted in a 10-cc/h  $\text{N}_2$  consumption, with GaN crystallizing in the form of a dense film over the entire surface of the substrate. Although there were fluctuations in the amount synthesized across the surface, on the average it was 30  $\mu\text{m}/\text{h}$ . This value was insufficient to proceed with investigations into monocrystallization, but further improvements in the rate of synthesis can be expected if the temperature is raised even higher. However, because based on formula (8.3.1) the quantity of transported Ga also depends on the total pressure and the distance to the substrate, improvements are achievable by varying these parameters. Based on the above, it was determined that the preferred Ga crucible temperature under this system was 1100°C, or, in case other conditions were predetermined, it had to be set to a higher temperature.

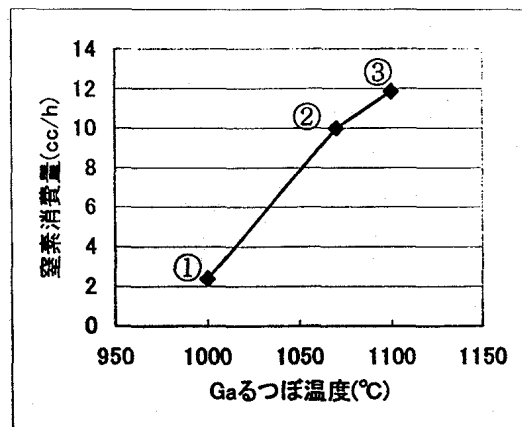


FIG.8.3.2-(2) Dependence of  $\text{N}_2$  consumption on Ga temperature

[Keys, FIG.8.3.2-(2)]

(X-axis) Ga crucible temperature (°C)

(Y-axis) Quantity of consumed nitrogen (cc/h)

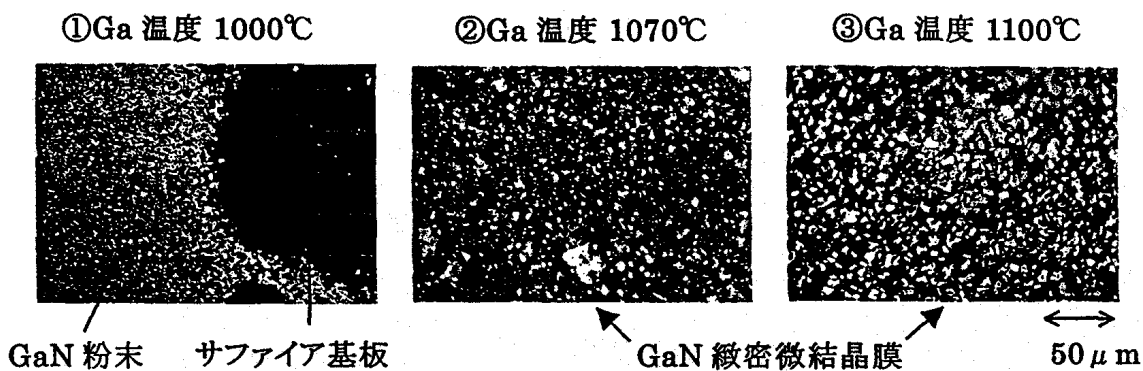


FIG.8.3.2-(3) Ga temperature and surface morphology

[Keys, FIG.8.3.2-(3)]

① Ga temperature 1000°C

② Ga temperature 1070°C

③ Ga temperature 1100°C

(Across bottom) GaN powder Sapphire substrate Dense microcrystalline GaN film

### 8.3.2.3 Pressure dependence

The results are shown in FIG. 8.3.2-(4) and FIG. 8.3.2-(5). As far as the rate of Ga transport was concerned, as shown on the left side of FIG. 8.3.2-(4), the quantity of consumed nitrogen decreased monotonically relative to the pressure at a constant temperature, and, notwithstanding the large difference in vapor pressure between the Ga crucible and the substrate at 500 Pa in ③, the transport amount remained small and GaN did not crystallize. In addition, when the substrate temperature was low at a constant pressure, the amount of consumed nitrogen rapidly increased. The above-mentioned phenomena were in good agreement with formula (8.3.1), showing that transport in the system was diffusion-controlled.

As far as crystal properties were concerned, according to Nomarski micrographs of FIG. 8.3.2-(5), the surface of the crystal in ①, which was obtained at 800°C and a pressure of 100 Pa, was covered with Ga droplets, and, for this reason, despite cleaning with aqua regia, dendritic microcrystals were obtained due a large amount of admixed Ga. The picture of the crystal in ②, which was obtained at 1000°C and 100 Pa, was taken prior to the aqua regia cleaning, and likewise, there were some Ga droplets observed; however, the transport of Ga was reduced in comparison with the 800°C case and GaN was synthesized in the form of a film, with the half-width, as determined by X-ray (0002)  $\omega$ -mode measurements, being 15 minutes. In this manner, at low pressure the amount of transported Ga was too large, producing Ga droplets, which affected crystal properties.

Next, in case of ② and ③, where the total pressure had been set to 200 Pa, a dense film of GaN crystal was synthesized. According to the X-ray measurement results shown on the right-hand side of FIG. 8.3.2-(4), in each case, the half-width was considerably improved, at 8 minutes, which was believed to be due to the V/III ratio approaching the right value. In addition, at 500 Pa in case of ③, due to the insufficient Ga transport amount, there was practically no synthesis on the substrate, and no (0002) peaks were obtained as a result of X-ray measurements. We concluded that the amount of transported Ga and crystal properties were extremely sensitive with respect to the total pressure, with changes being particularly large at low pressure. It was determined that the preferable range for excellent crystal properties and experiment controllability was approximately between 150~300 Pa.

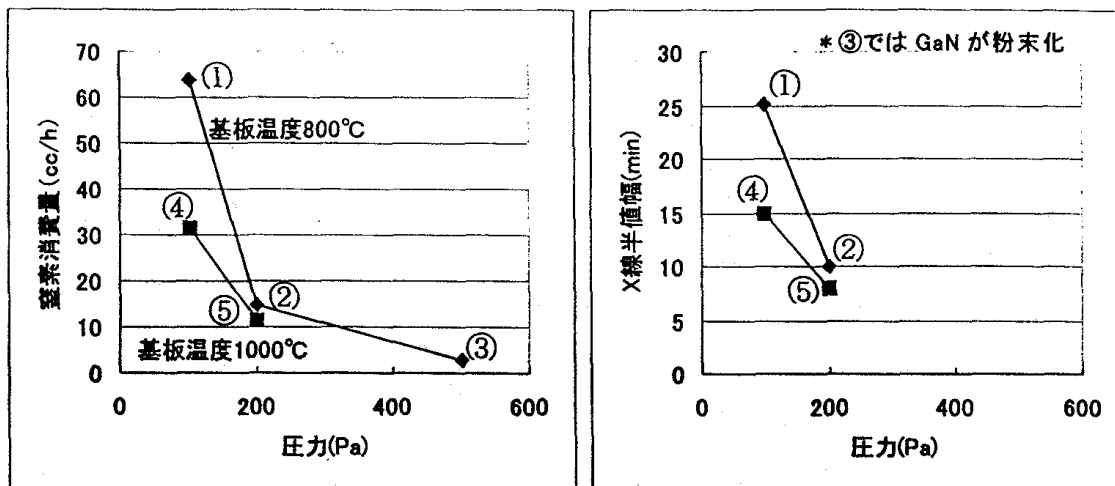


FIG. 8.3.2-(4) Dependence of nitrogen consumption and X-ray half-width on pressure

[Keys, FIG. 8.3.2-(4)]

(Figure on the left)

(X-axis)

Pressure (Pa)

(Y-axis)

Amount of consumed nitrogen (cc/h)

(Inside, top)

Substrate temperature: 800°C

(Inside, bottom)

Substrate temperature: 1000°C

(Figure on the right)

(X-axis)

Pressure (Pa)

(Y-axis)

X-ray half-width (min)

(Inside, top)

GaN was in powder form in case of ③\*.

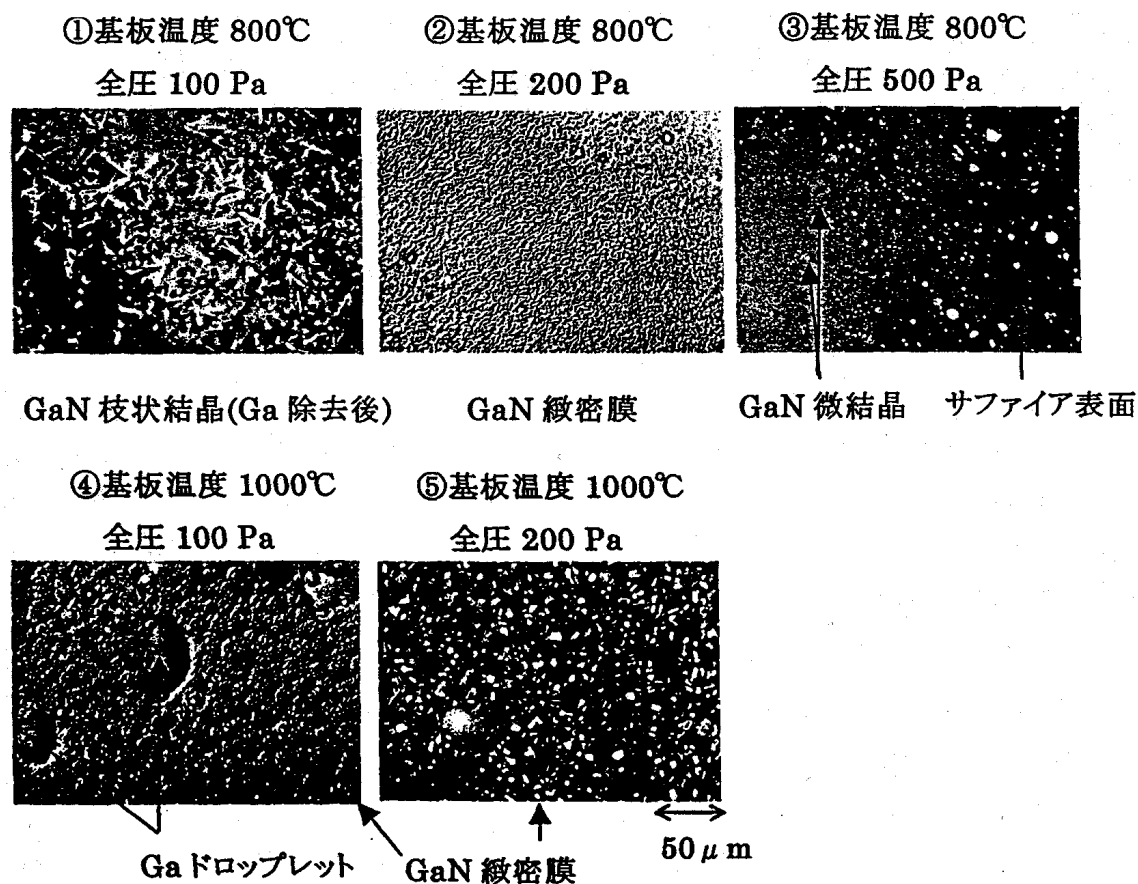


FIG. 8.3.2-(5) Synthesis pressure and surface morphology

[Keys, FIG. 8.3.2-(5)]

- ① Substrate temperature: 800℃  
Total pressure: 100 Pa  
(Underneath figure) Dendritic GaN crystals (after removal of Ga)
- ② Substrate temperature: 800℃  
Total pressure: 200 Pa  
(Underneath figure) Dense GaN film
- ③ Substrate temperature: 800℃  
Total pressure: 500 Pa  
(Underneath figure) GaN microcrystals      Sapphire substrate
- ④ Substrate temperature 1000℃  
Total pressure: 100 Pa  
(Underneath figure) Ga droplets
- ⑤ Substrate temperature: 1000℃  
Total pressure: 200 Pa  
(Underneath figure) Dense GaN film

#### 8.3.2.4 Microwave output dependence

The results are shown in FIG. 8.3.2-(6) and FIG. 8.3.2-(7). The amount of consumed nitrogen, in other words, the amount synthesized, showed a monotonic increase relative to the plasma output. Because in (2) and (3) the fluctuations of the area accessible to plasma were small, the GaN synthesis reaction proceeded

with the Ga supply acting as the rate-determining factor; however, because in the present experiment the range accessible to plasma varied depending on the changes in the microwave output, changes were accordingly observed in the amount of consumed N<sub>2</sub>.

As for the crystal properties of GaN, the X-ray half width reached its minimum at 400 W.

Then, in case of ① 200 W, a powder was formed, as shown in the Nomarski micrographs, and X-ray  $\omega$ -mode measurements were not taken. The reason for the formation of the powder was supposed to be the insignificant amount synthesized and the inability of GaN to bond with other nuclei on the surface. Also, in case of ② and ③, dense microcrystalline films with a narrow X-ray half-width were obtained. At ④ 600 W, the X-ray half-width was the widest, and although the surface was covered with a dense crystalline film, surface irregularities were still visible. This was believed to be due either to an increase in the V/III ratio and damage to GaN on the growth surface or to certain changes in the reaction mechanism, but the exact reason was not known. In this manner, we discovered that tweaking the microwave output resulted in extreme values with respect to crystal properties if other conditions were fixed.

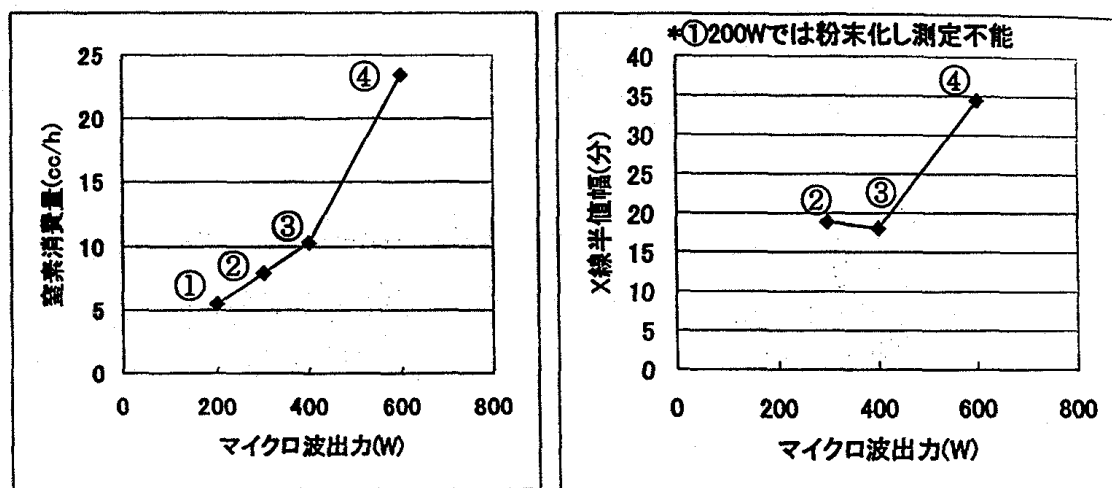


FIG. 8.3.2-(6) Dependence of N<sub>2</sub> consumption and X-ray half-width on microwave output

[Keys, FIG. 8.3.2-(6)]

(Figure on the left)

(X-axis) Microwave output (W)

(Y-axis) Amount of consumed nitrogen (cc/h)

(Figure on the right)

(X-axis) Microwave output (W)

(Y-axis) X-ray half-width (min)

(Across top) \*In case of ① 200 W, powder was formed, rendering measurement impossible

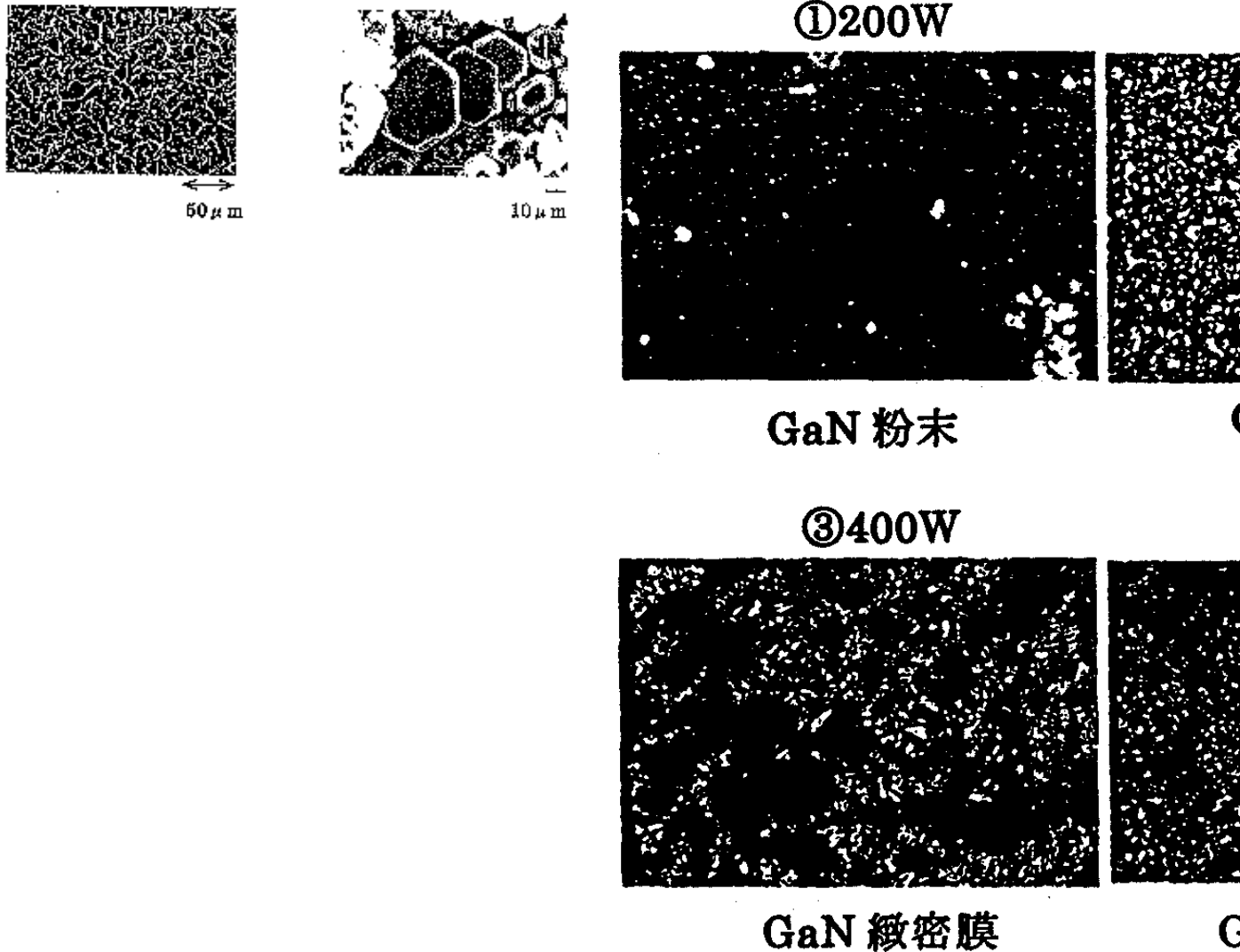


FIG. 8.3.2-(7) Microwave output and surface morphology

[Keys, FIG. 8.3.2-(7)]

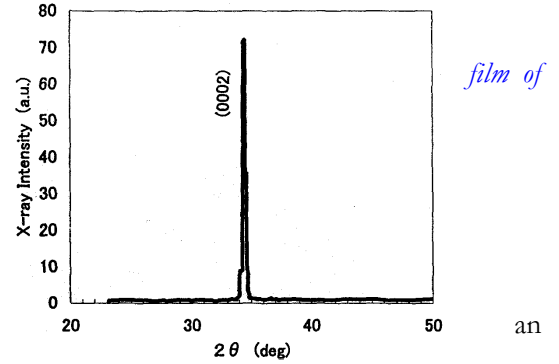
- ① 200 W, (underneath figure) GaN powder
- ② 300 W, dense GaN film
- ③ 400 W, dense GaN film
- ④ 600 W, dense GaN film

#### 8.3.2.5 Studies of substrate temperature

Although substrate temperature conditions could not be completely controlled and a clear picture of its precise temperature at all times could not be obtained, FIG. 8.3.2-(8) (on the left) shows an SEM photograph of the surface of a dense film obtained when the substrate temperature was maintained on the high-temperature side, and, for comparison, a photograph of a representative dense film (on the right). The film formed as a result of the increased temperature was produced by the binding of GaN crystals possessing a 6-fold rotational symmetry, and it was assumed that a change in growth mode had occurred. The X-ray spectrum of FIG. 8.3.2-(9) clearly shows that the resultant crystals possessed excellent orientation properties.

Left: FIG. 8.3.2-(8) SEM photographs of dense microcrystalline GaN (on sapphire substrate) prior to and after adjustment of temperature

Right: FIG. 8.3.2-(9) X-ray measurements of dense microcrystalline film of GaN synthesized on sapphire substrate



### 8.3.2.6 Seed crystal dependence

In the course of the above-described experiments we gained understanding of the necessary conditions of GaN crystal formation and thus were able to move beyond the powder-like forms available until last year and successfully synthesized dense films of excellent orientation properties. However, monocrystallization on sapphire substrates was not achieved, and we switched to using GaN substrates, the influence of surface treatment etc. on which was supposed to be relatively weak, as seed crystals, and conducted corresponding synthesis experiments. The results are shown in FIG. 8.3.2-(10) and FIG. 8.3.2-(11). The SEM photographs revealed clear rectilinear grain boundaries, with no surface irregularities visible anywhere on the entire 5-mm surface. In addition, excellent crystal properties were shown by X-ray diffraction measurements. The growth rate obtained was 40  $\mu\text{m}$ , which was 1 order of magnitude higher than in case of growth in other open-tube systems utilizing a nitrogen plasma, and bulk crystal growth was therefore within the range of practical applications. Thus, the concerns that we had regarding this method of growth, such as whether the use of plasma itself would block the monocrystallization of GaN, etc., were eliminated, demonstrating that the growth of large single crystals by means of controlling initial nucleation was indeed possible.

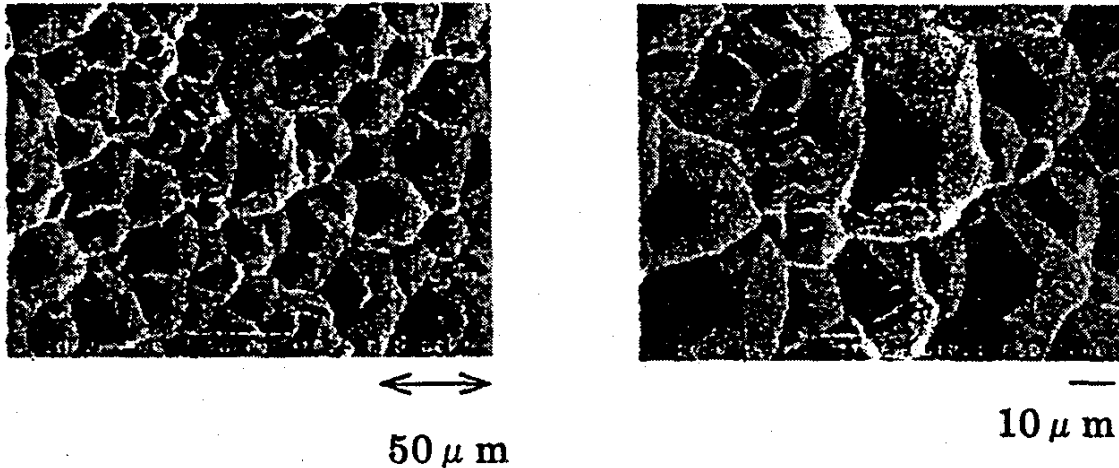


FIG. 8.3.2-(10) SEM photographs of crystals where GaN was used in seed crystals

In this manner, by synthesizing GaN with microwaves, we managed to carry out the crystallization of GaN, which had been previously obtained in microcrystalline powder form, and were able to synthesize dense films of excellent orientation properties, and, furthermore, were able to synthesize crystals without surface irregularities on GaN substrates. In the future, we are planning to continue investigations into the substrate temperature, growth velocity, and processes etc. of growth with a view to synthesize large GaN single crystals by controlling the initial nucleation.

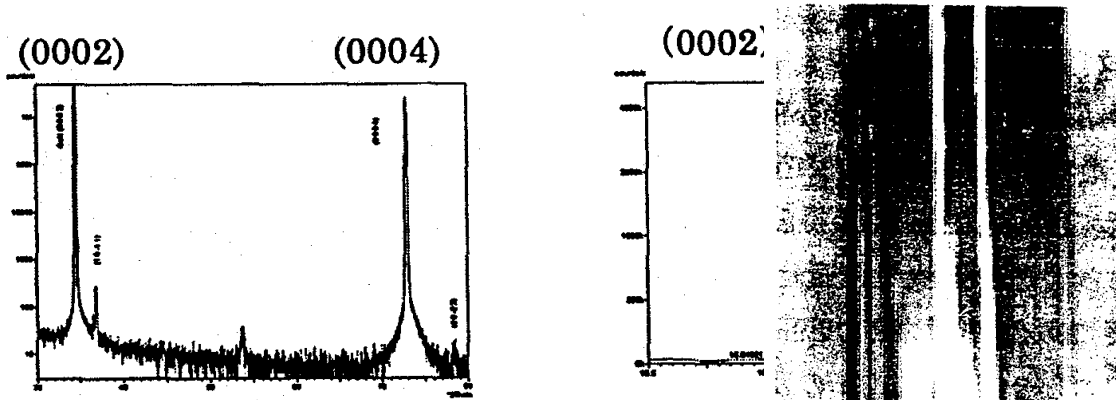


FIG. 8.3.2-(11) X-ray measurement results for crystals where GaN used in seed crystals

was

## 8.4 GaN Crystal Growth Method Utilizing Novel Plasma Generation Technique

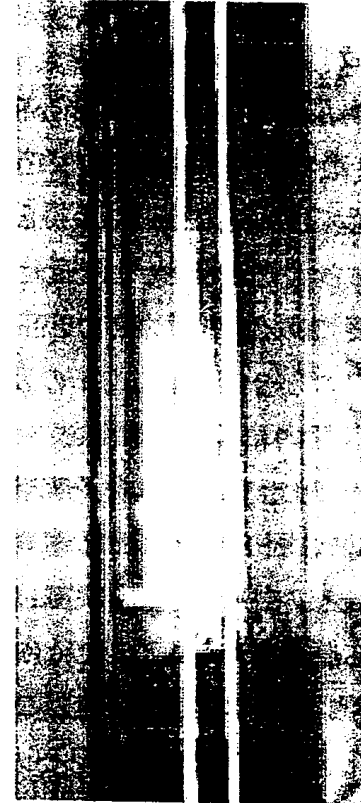
### 8.4.1 Methods and means

Among the methods of N<sub>2</sub> activation, in addition to the use of microwaves, there are methods that involve the generation of non-equilibrium plasma via application of a high-frequency electric field, DC electric field, etc. In the present chapter, we describe our attempts to synthesize GaN single crystals using N<sub>2</sub> plasma based on the use of an pulsed type high-frequency power supply other than microwaves. Impulse-type high-frequency wave-based techniques generate plasma via application of positive and negative pulse voltage and are characterized by ① a high plasma density, ② discharge at atmospheric pressure, ③ simple plasma control, ④ a higher degree of freedom in terms of electrode design, and ⑤ small size, light weight, etc. For this reason, they permit generation of plasma in various shapes and in various locations, and, due to the fact that they allow for setting the pressure of the reaction system to a higher pressure than in the case of microwaves, they are expected to permit an increase in the velocity of growth. On the downside, however, there is some possibility of discharge occurring in unexpected places because of the high pressure. For this reason, in a narrow reaction system, it is necessary to design the insulation very thoroughly to form a stable plasma.

FIG. 8.4.1 shows a high-frequency pulsed discharge. The GaN growth experiments were carried out at an applied voltage of not more than 4 kV. The pressure was 200 Pa and the temperature 1000°C. In addition, a whitish film was generated on the surface when a sapphire substrate was placed inside. X-ray diffraction measurements revealed a polycrystalline GaN peak and SEM observation results confirmed that 2 μm hexagonal plate-shaped microcrystals had been grown. In this manner, it was confirmed that GaN readily reacted in a plasma produced by using a high-frequency pulsed power supply. However, neither the growth velocity, nor the crystal size could come close to results obtained by using conventional microwave plasma.

Figure 8.4.1

Next, in order to explore the possibility of accelerating the rate of GaN synthesis reaction in the high-frequency plasma, we conducted experiments in a system, in which Ga and N<sub>2</sub> were violently reacted. In the system, Ga was supplied not by diffusion transport, but rather by means of a direct, albeit violent, contact between the N<sub>2</sub> gas and the Ga. The experiment was conducted by applying the principle of the so-called DC sputter making use of the polarity that the plasma power supply possessed. The experiments were carried out at a pressure of 200 Pa and a temperature of 1000°C in a vertical furnace. As a result, matter, which covered the Ga crucible, filled the inside of the reaction tube, as shown in FIG. 8.4.2. It was found that because reaction was conducted at an N<sub>2</sub> flow rate of 7 sccm, if GaN deposition on the crucible continued, its rate could reach approximately 1.2 mm/h. The material produced was in fact a mixture of GaN microcrystals and Ga, and if the crucible continued to be filled in that manner, as a result of the subsequent decrease in the reaction rate, GaN single crystals hardly grow in that state. However, one significant achievement that showed that in a GaN synthesis reaction conducted using Ga plasma-activated nitrogen, it was possible to achieve growth rates exceeding 1 mm/h, which had been impossible to reach using reactions based on thermal equilibrium.



the  
by  
Pa  
solid  
the  
could  
was  
and

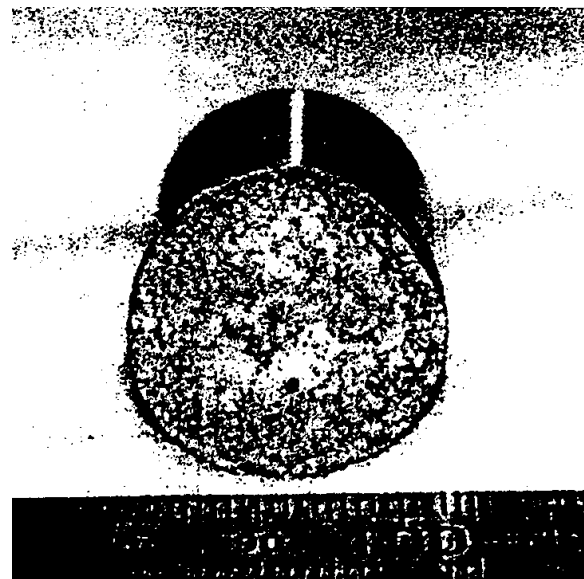
From the above-described results, it was evident that in order to growth of GaN single crystals, in the next step, it would be necessary to create a zone of high-density plasma by adjusting the high-frequency output, and continue the optimization of the temperature, pressure, and other parameters in the zone, as well as to conduct experiments and investigations into the reaction of GaN synthesis using the source material temperature, substrate temperature, relative position of the substrate and Ga crucible, N<sub>2</sub> pressure, etc. as parameters.

Figure 8.4.2

## 8.4.2 Results and discussion

### 8.4.2.1 Temperature dependence

As was described above, although the GaN reaction was confirmed, we could only obtain microcrystals, which called for the optimization growth conditions. First of all, we conducted growth experiments with the temperature used parameter by placing only Ga inside the reaction and maintaining the pressure and high-frequency output constant.



of the  
GaN  
as a  
tube

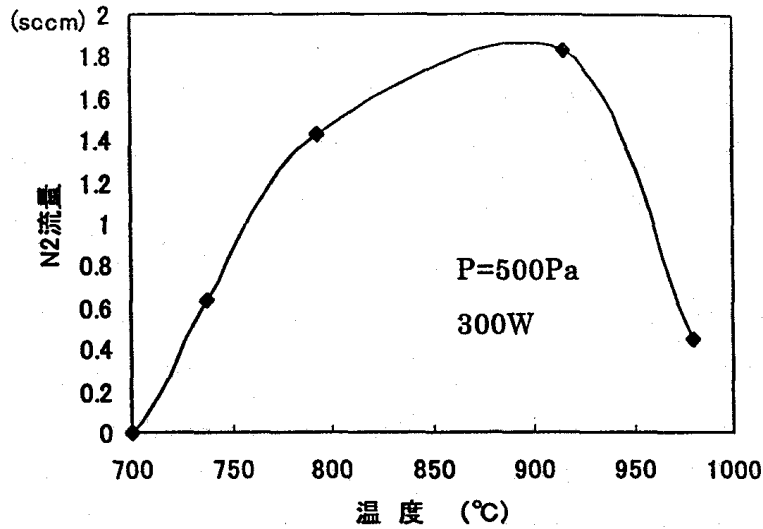
FIG. 8.4.3 Relationship between temperature and N<sub>2</sub> flow rate

[Keys, FIG. 8.4.3]

(X-axis) Temperature (°C).

(Y-axis) N<sub>2</sub> flow rate.

FIG. 8.4.3 shows, as an indicator of the reaction rate, relationship between the growth and the N<sub>2</sub> flow rate, which was plotted along the vertical axis. However, the term "temperature" here refers to the temperature of the sidewalls of reaction tube, and not to the internal reaction temperature.



From the figure, it is evident that the synthesis of GaN took place at the highest rate when growth was conducted in the range of from 800 to 900 degrees. The low rate exhibited at lower temperatures was believed to be due to the low growth temperature and the low amount of evaporated Ga. On the one hand, it is believed that the slowing down of the reaction at more elevated temperatures is attributable to the fact that in the region, where plasma existed, dissociation became stronger than the reaction, which made growth impossible, and, in low temperature portion, no activated nitrogen existed because of the remoteness from plasma, and therefore, no reaction occurred. SEM images of a crystal surface generated on the inner walls of the reaction tube (quartz tube) after the experiment are shown in FIG. 8.4.4. It was found that it was GaN in form of a dense film.

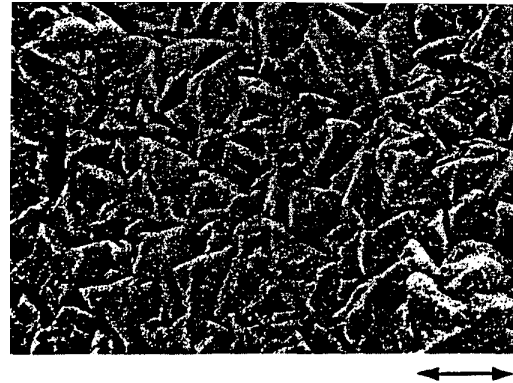


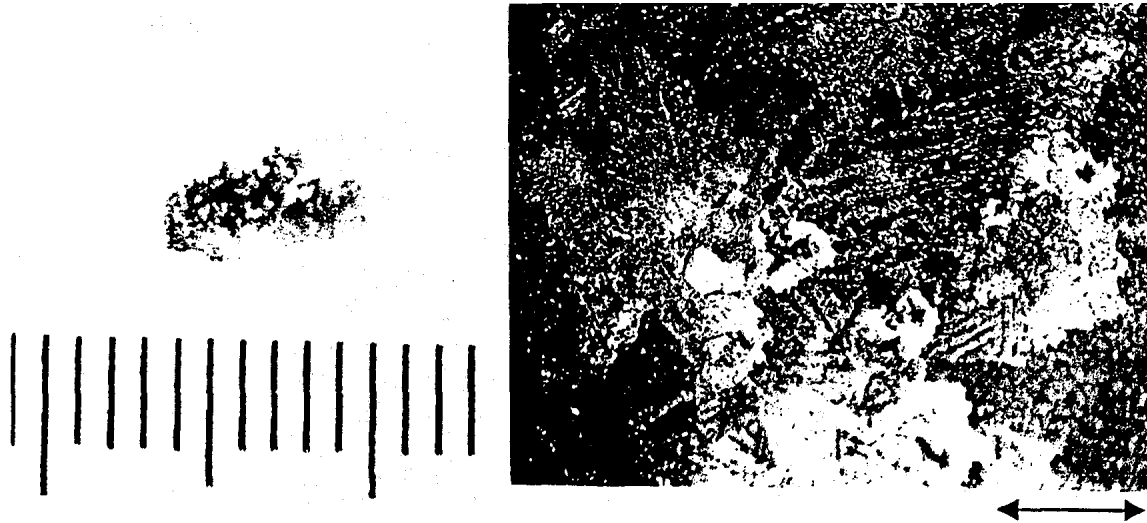
FIG. 8.4.4 SEM image

**8.4.2.2 Optimization of substrate position**

Considering that growth of films has been successfully realized even on amorphous substrates, such as quartz, it could be expected that it was possible to realize monocrystallization if the orientation substrate was arranged properly. Therefore, we carried out GaN single crystal growth experiments using sapphire substrates. Judging by the results of the growth experiments, in which microwave plasma was utilized, for the crystallization to take place, Ga and N<sub>2</sub> had to be supplied in a well-balanced proportion. Moreover, it was necessary to guarantee good Ga transport by making the temperature of the Ga higher than that of the substrate and to make sure the substrate was set to a temperature suitable for growth. In addition, in a situation where the Ga and the substrate were in a wide range of plasma, the Ga, simultaneously with evaporation, could come in contact with activated nitrogen, resulting in the production of GaN in the form of powder, and, for this reason, it was necessary to make sure that growth on the substrate was enhanced by setting the distance between the Ga and the substrate to a length not shorter than the average free path.

In this manner, with account taken of the conditions necessary for guiding reactive radicals to the substrate, we conducted various experiments by varying the pressure, temperature, and other conditions in a substrate position we considered the best, and, as a result, at 300 Pa, 900°C, a distance of 20 mm between Ga and the

substrate, and 300 W, in part of a 16-mm sapphire substrate, we grew a lump-shaped solid, which separated from the substrate when etched with aqua regia, producing a 3×6 mm crystal such as the one shown in FIG. 8.4.5. The resultant crystal was a thin plate with an apparent transparency of approximately 0.1~0.2 mm and a rough surface. FIG. 8.4.6 is an enlarged photograph of the crystal surface. It shows that the surface was made up of crystal grains with a size of several 10 to 200  $\mu\text{m}$ , with hexahedral crystals visible here and there. The surface was considerably rough, with ridges and valleys all over it.



*Left: FIG. 8.4.5 Lump-shaped crystal.*

*Right: FIG. 8.4.6 Micrograph of the surface.*

The results of X-ray diffraction measurements are shown in FIG. 8.4.7.  $\omega$ - $2\theta$  scanning yielded a (0002) orientation peak only, which showed that the crystal was oriented along the  $c$ -axis. Incidentally, when the rocking curve of the (0002) peak was measured, it was split into several peaks, as shown in FIG. 8.4.8, clearly indicating its polycrystalline nature. From the shift of the peaks, it was evident that in each crystal the  $c$ -axis was inclined approximately 20 minutes. FIG. 8.4.9 is a pole figure obtained by measurement in the (10-12) plane. (0002) diffraction appears in the vicinity of  $45^\circ$ , with the tilt component widened in the radial direction and the mosaic component in the direction of rotation. Diffraction in the (0002) plane appeared as spots in some places on a weak ring, with each of the  $\phi$  angles ( $\Psi$ ) shifted, matching the inclination of the rocking curve. In addition, it was found that the 6-fold rotational symmetry was destroyed, and, with the in-plane orientation in considerable disorder, growth proceeded with crystal grain boundaries remaining independent.

Left: FIG. 8.4.7  $\omega$ -2 $\theta$  spectrum.

Right: FIG. 8.4.8 Rocking curve.

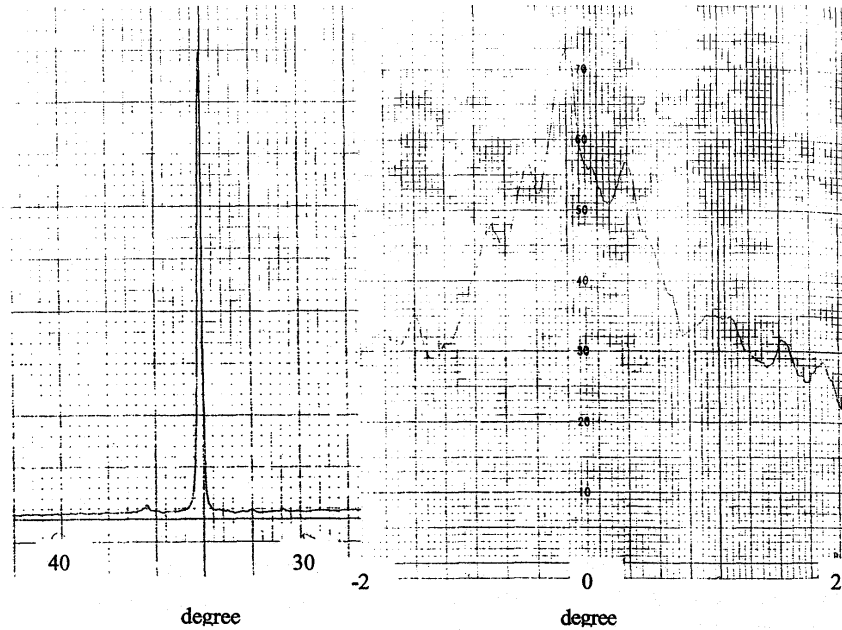


FIG. 8.4.9 Pole figure GaN crystal.

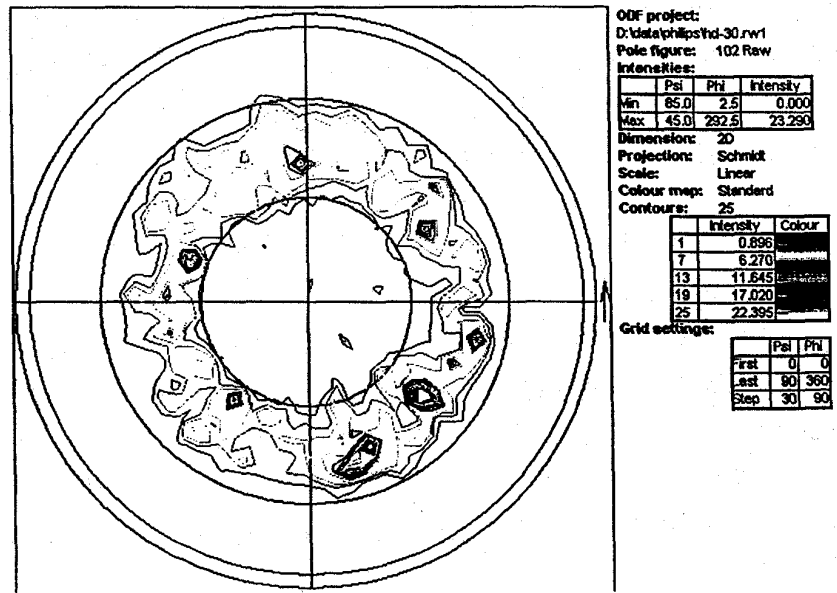


FIG. 8.4.10 shows room-temperature PL mapping results for the crystal. The excitation light source was a Hd-Cd laser with a generation wavelength of 325 nm and an intensity of 8 mW. Si was used as a detector. The mapping was carried out by means of a 1-mm pitch scan across a measurement range of from 340 nm to 700 nm. The vicinity of the center, where the PL intensity was high, was the location, from which the GaN polycrystals emitted light. There was a strong emission from the absorption edge in the GaN crystal, but its wavelength was somewhat low, at 371 nm, which was believed to be due to large residual strain. The fact that the ratio of the intensity of the absorption edge emission and the intensity of broad emission on the lower energy side varied depending on the location was believed to be due not only to the different growth orientation of the polycrystals, but also to the fact that the crystal structure, as well as the defect and impurity distribution, of the crystal grains were not uniform. In addition, the peak observed at 410 nm was caused by the underlying glass used to secure the sample. The reason why polycrystals were grown was believed to be

due to the lack of satisfactory growth along the surface due to the high reaction rate of GaN and the insufficient diffusion of atoms on the substrate. Thus, to achieve monocrystallization, it is necessary to raise the temperature of the substrate to stimulate crystallization. In addition, the reason for peeling was believed to be bowing generated by mismatch with the sapphire substrate and a difference in coefficients of thermal expansion. Thus, to avoid it, the use of improved substrate crystals, in other words, SiC substrates and GaN substrates, is believed necessary.

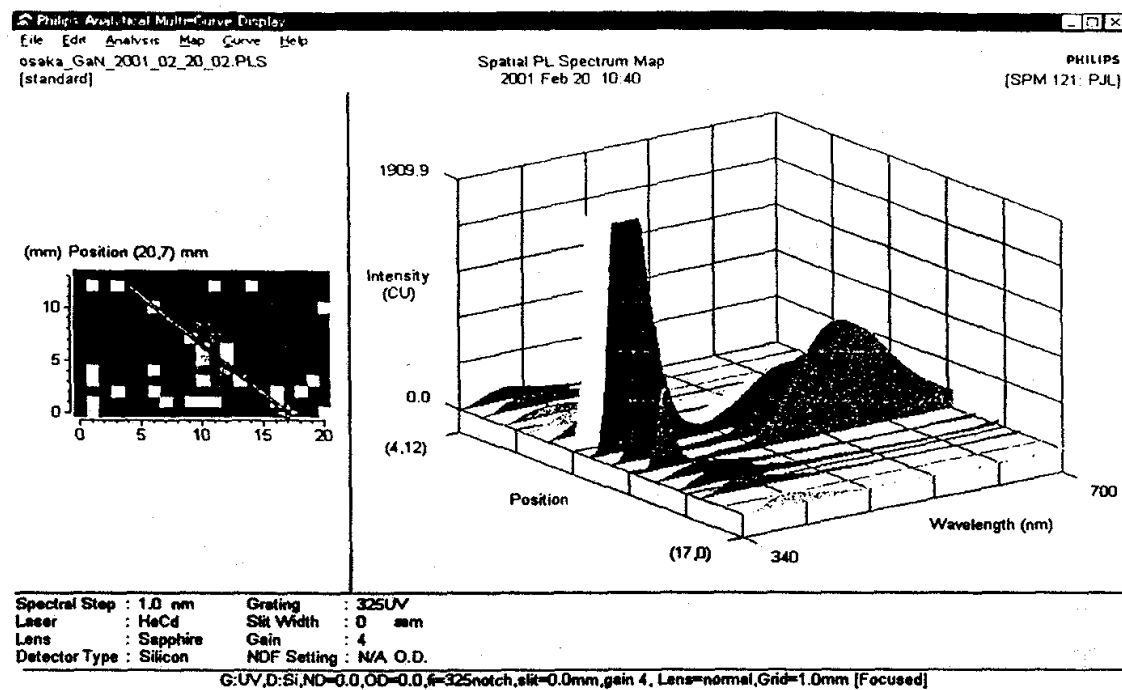


Figure 8.4.10.

As described above, as a result of growing GaN crystals using high-frequency plasma, it was confirmed that a GaN synthesis reaction based on nitrogen activation took place in the same manner as under the microwave system, and experiments, in which a forced reaction with Ga was carried out, demonstrated that growth rates as high as 1 mm/h were possible. Furthermore, as a result of conducting growth experiments by placing sapphire substrates in the vicinity of the Ga source material, we were able to grow mm-sized, albeit polycrystalline, crystals. In the future, in order to conduct growth characterized by both monocrystallization and higher reaction rates, we are planning to carry out growth experiments at an increased rate of activation, which cannot be easily carried out under the microwave system, by generating plasma at a high density in a narrow region in the vicinity of the substrate by raising the pressure and narrowing down the plasma discharge area. Furthermore, another important task is to apply the obtained results to the microwave system to further optimize the growth conditions.

## 8.5 Summary

As a result of conducting further optimization of the pressure, temperature, etc. in the region of high-density plasma and carrying out investigations into the process of GaN synthesis by using the source material temperature, substrate temperature, relative position of the substrate and the Ga crucible, and the N<sub>2</sub> pressure as parameters, we were able to effect transition from micropowder to a dense film-shaped GaN crystal oriented along the *c*-axis over a 10×4 mm<sup>2</sup> area on a sapphire substrate, as confirmed by the SEM photographs shown in FIG. 8.3.2-(8), with the above crystal displaying a strong (0002) single peak without a

sapphire peak, as shown by the X-ray diffraction spectrum of FIG. 8.3.2-(9). Furthermore, we were able to synthesize a crystal oriented along the  $c$ -axis that displayed a surface morphology of excellent symmetry without surface irregularities, as shown in the SEM photographs of FIG. 8.3.2-(10).

In addition, we experimentally established the correlation of the maximum rate of synthesis of 100  $\mu\text{m}/\text{h}$  with various parameters, which gave us the necessary degree of freedom in terms of improving the crystal properties. Furthermore, with regard to the rate of synthesis, varying the growth conditions, such as the partial pressure of reactive radicals and the method of activation, allowed us to confirm that improvement of up to a maximum level of 1 mm/h was feasible under the gas phase growth method for compound semiconductors, albeit in micro-crystal form.

## 8.6 Future Plans

Recent research concerning GaN substrates has seen considerable progress in terms of the development of GaN single crystals in thick film form based on the hydride gas phase technique (HVPE) and bulk single crystals based on the high-pressure solution technique, as well as the expanded use of SiC substrates aimed at increasing substrate quality and diameter. However, at present we are facing numerous problems due to a large number of threading dislocations and the mosaic-shaped low tilt angle grain boundaries characteristic of hexagonal crystals. In addition, there are numerous problems arising in connection with supplying crystals for illumination LEDs at a low cost. Based on theoretical investigations, the possible rate of synthesis of GaN by the low-pressure gas phase technique is expected to be 1~6 mm/h, and if we are able to achieve a growth rate of 1 mm/h for direct GaN synthesis using the pseudo-open tube system and establish a production technology permitting fabrication of large size substrates and high growth rates, the cost of substrates for epitaxial growth will be dramatically reduced, allowing for low cost equivalent to that of the currently used GaAs substrates.

In the future, we are planning to grow large GaN bulk single crystals with a diameter of not less than 10 mm by moving ahead with our investigations into a wide range of conditions based on the already obtained findings and exploring the possibility of using the grown GaN single crystals as LED substrates. One important specific problem is how best to control the stoichiometry of Ga and N<sub>2</sub>. For this, it will be necessary to carry out further optimization by conducting theoretical studies and systematic experiments concerning single crystal growth conditions such as temperature and pressure. In addition, we will work on another promising technique for improving the rate of growth, i.e. the addition of reactive gases, such as H<sub>2</sub> and HCl. Furthermore, yet another goal will be to grow low dislocation density crystals with reduced defect generation by using SiC and GaN crystals etc. as substrates or by carrying out substrate surface processing and low supersaturated growth during the initial stage of growth.

# 9 Development of LED Epi Process Technology

## 9.1 Achievements in 1998 and 1999

The study of emitting layers, crystal dislocation density reduction, and ways to increase the concentration of p-type layers are considered important issues in the development of high-efficiency UV light-emitting diodes (LEDs) possessing an external quantum efficiency of not less than 40%. In this study, we carried out crystal growth using the molecular beam epitaxy (MBE) technique and the metalorganic chemical vapor deposition (MOCVD) technique. In 1998, we conducted investigations into the fabrication of blue LEDs by the MBE technique, and in 1999, we conducted investigations into MOCVD-grown high-brightness blue LEDs and into ways of shortening the emission wavelength of UV LEDs.

### 9.1.1 Achievements in 1998

#### 9.1.1.1 Epi-growth based on MBE technique

We carried out epitaxial growth using the MBE technique, which permits high p-doping upon growth without heat treatment, fabrication of quantum well structures of excellent interface sharpness, and fabrication of ultra-thin films necessary for improvement in element characteristics. Examination of p-type GaN confirmed that it had a p-type carrier concentration of  $1 \times 10^{18} \text{ cm}^{-3}$ . Emission spectra with an emission wavelength of 420 nm and a half-width of 20 nm were observed in LED structures obtained by superimposing an n-type GaN layer, GaInN multiple quantum well (MQW) emitting layers, and a p-type GaN layer. However, the emission intensity was lower than in LEDs fabricated by the MOCVD technique by 1 or 2 orders of magnitude.

#### 9.1.1.2 Introduction of small-size MOCVD apparatus

We evaluated the performance characteristics of the apparatus using growth of GaInN and undoped GaN. The in-plane distribution of the film thickness of the undoped GaN was confirmed to be within 4%. The  $\omega$ -scan X-ray diffraction half-width was about 370 arcsec in the case of (0002) diffraction and 540 arcsec in the case of asymmetric plane (10 $\bar{1}2$ ) diffraction, and, according to Hall measurements, the electron concentration was  $1.7 \times 10^{17} \text{ cm}^{-3}$  and the mobility was 560  $\text{cm}^2/\text{Vs}$ . In addition, the non-uniformity of GaInN film composition was around 4%, which resulted in a film of excellent in-plane uniformity.

### 9.1.2 Achievements in 1999

#### 9.1.2.1 Commissioning of small-size MOCVD apparatus

To confirm the proper functioning of the MOCVD apparatus introduced in 1998, we conducted studies of blue LED structures. It was confirmed that blue LEDs with an emission wavelength of 475 nm and a luminous intensity equivalent to 2 candelas were obtained from LED structures, in which MQWs consisting of GaN barrier layers/GaInN well layers were used as emitting layers.

#### 9.1.2.2 Studies of UV LED structures

We conducted investigations into the shortening of the emission wavelength using GaN/GaInN MQW structures suitable for use in blue LED structures. Although the shortening of the wavelength was achieved by raising the growth temperature, the intensity of photoluminescence (PL) from the UV MQW (emission wavelength: 388 nm) decreased by 1/2. It was believed that factors involved in the decreased emission intensity included the weaker confinement of the carriers to the well layers as a result of the shortening of the

wavelength, which prevented their functioning as a quantum structure, and the weakening of the effects of In that contribute to the PL emission [1]. Fabrication of LED structures demonstrated that their peak wavelength was 398 nm and their emission output was 0.5 mW, which was lower in comparison with blue LEDs.

### 9.1.2.3 Dislocation density reduction by ELO technique

We investigated the ELO technique for the purpose of reducing the amount of dislocations in the GaN layer. It was found that the tilt of the (0001) axis, which created problems in case of ordinary SiO<sub>2</sub> films, could be prevented by using plasma CVD-grown SiN<sub>x</sub> as the mask material. We introduced a dislocation density evaluation method based on observations of etch pits caused by sulfuric and phosphoric acid. The dislocation density of ELO-GaN, as evaluated by the same method, was  $1 \times 10^8$  cm<sup>-2</sup> in the windows and  $2 \times 10^7$  cm<sup>-2</sup> on the mask. The study confirmed that since the density of dislocations of GaN before ELO was  $5 \times 10^8$  cm<sup>-2</sup>, the dislocation density reduction was 1/5 in the windows and 1/25 on the mask.

### 9.1.2.4 High-concentration p-type

We carried out investigations into the growth of p-type GaN possessing a high carrier concentration with a view to improve the piezoelectric efficiency of LED elements. By optimizing the growth temperature, the amount of supplied Mg source material, and the conditions of activation annealing, we were able to obtain p-type GaN with a concentration of positive holes as high as  $1 \times 10^{18}$  cm<sup>-3</sup>.

### 9.1.2.5 Introduction of new facilities

An MOCVD apparatus for simultaneous processing of six 2-inch substrates was introduced in March 2000. The proper functioning of the apparatus was evaluated using GaN and GaInN single quantum well structure (SQW) growth. It was confirmed that the in-plane distribution of film thickness in the GaN layer was within 4% at 15 points on the 2-inch wafer surface and was within 4% across the six wafers. The carrier concentration was  $1 \times 10^{17}$  cm<sup>-3</sup> and the degree of mobility was 640 cm<sup>2</sup>/Vsec. As a result of a PL evaluation using GaInN SQW structures, it was confirmed that the peak wavelength distribution was within 5% at 25 points on the wafers and within 5% across the six wafers, which was indicative of excellent uniformity.

## 9.2 Summary of Research and Development in 2000

During the present project, we developed UV LEDs with an emission wavelength of not longer than 400 nm and white LEDs utilizing fluorescent materials in order to build illumination light sources with an energy efficiency exceeding that of fluorescent lamps. When GaN/GaInN MQW structures typically used in blue LEDs were used for UV LEDs, the emission output turned out to be lower in comparison with blue LEDs. It is believed that, as a result of decreasing the molar fraction of InN of GaInN in the well layers for the purpose of shortening the wavelength, the well bandgaps approached the bandgap of the GaN barrier layers, which made it impossible to efficiently confine electrons in the well layers, and the MQW stopped functioning as a quantum structure, causing a decrease in the emission intensity. For this reason, AlGaIn cladding layers and AlGaIn barrier layers with a large bandgap are essential in terms of efficiently confining electrons to the well layers in UV LEDs.

This year, our most important task has been to boost the efficiency of UV LEDs. In order to achieve increased efficiency, it is necessary to optimize the MQW growth conditions and the structure of the emitting layers for UV emission. The present study demonstrates that MQW structures of excellent interface sharpness, as well as excellent UV emission characteristics, can be obtained by improving the growth process and optimizing the structure of UV MQWs. Here, explanations will be provided regarding the characteristics of the elements of UV LEDs and investigations into AlGaIn cladding layers with high AlN molar fractions, which are essential for efficient LEDs.

## 9.3 Fabrication of AlGa<sub>N</sub>/GaIn<sub>N</sub> UV MQW Structures

In the case of GaN/GaIn<sub>N</sub> MQW structures, in which GaN is used in the barrier layers and GaIn<sub>N</sub> is used in the well layers, a decrease in the PL intensity occurs in the UV region [1]. This is believed to be due to the fact that in the UV region the In<sub>N</sub> molar fraction of the well layers decreases, the difference between the bandgaps of the well layers and the barrier layers becomes smaller, and, for this reason, the effect of carrier confinement weakens and the emission intensity declines. Thus, in order to efficiently confine carriers to the well layers, it is necessary to use AlGa<sub>N</sub> with a large bandgap to secure the energy difference relative to GaIn<sub>N</sub> well layers with low In<sub>N</sub> molar fractions. In connection with this, we are investigating ① ways to improve the emission efficiency in the UV region using AlGa<sub>N</sub> barrier layers, and ② ways to optimize the growth conditions in order to fabricate high-quality MQWs.

### 9.3.1 Methods and means

All of the samples were fabricated by MOCVD. (0001) sapphire was used for the substrates. After depositing a low-temperature buffer GaN layer on a sapphire substrate, undoped GaN was grown at an elevated temperature. The pressure used for the high-temperature growth of GaN was 20 kPa. The AlGa<sub>N</sub>/GaIn<sub>N</sub> MQW structure utilizing the AlGa<sub>N</sub> barrier layers investigated in the present experiment is shown in FIG. 9.3.1-(1). The thicknesses of the AlGa<sub>N</sub> barrier and the GaIn<sub>N</sub> well layers were, respectively, 8 nm and 2 nm, with the AlGa<sub>N</sub> barrier layers doped with Si and the GaIn<sub>N</sub> well layers left undoped. The growth sequence of the MQW is shown in FIG. 9.3.1-(2). The growth temperature was 860°C in the case of the GaIn<sub>N</sub> layers, and, in the case of the AlGa<sub>N</sub> layers, we studied two cases, namely, ① growth at 860°C and ② growth at 1100°C. The mixed crystal composition of the AlGa<sub>N</sub> barrier layers and GaIn<sub>N</sub> well layers, as determined by X-ray diffraction, showed that the molar fraction of Al<sub>N</sub> was 12% and the molar fraction of In<sub>N</sub> was 5%.

The surface condition of the MQW layers was examined under an atomic force microscope (AFM), and transmission electron microscope (TEM) observations were carried out for the purpose of structure evaluation. PL measurements were done using a He-Cd laser with a wavelength of 325 nm as the excitation light source in order to evaluate the optical characteristics. Furthermore, the dependence of the PL intensity on temperature was investigated by varying the sample temperature from 10 to 300 K.

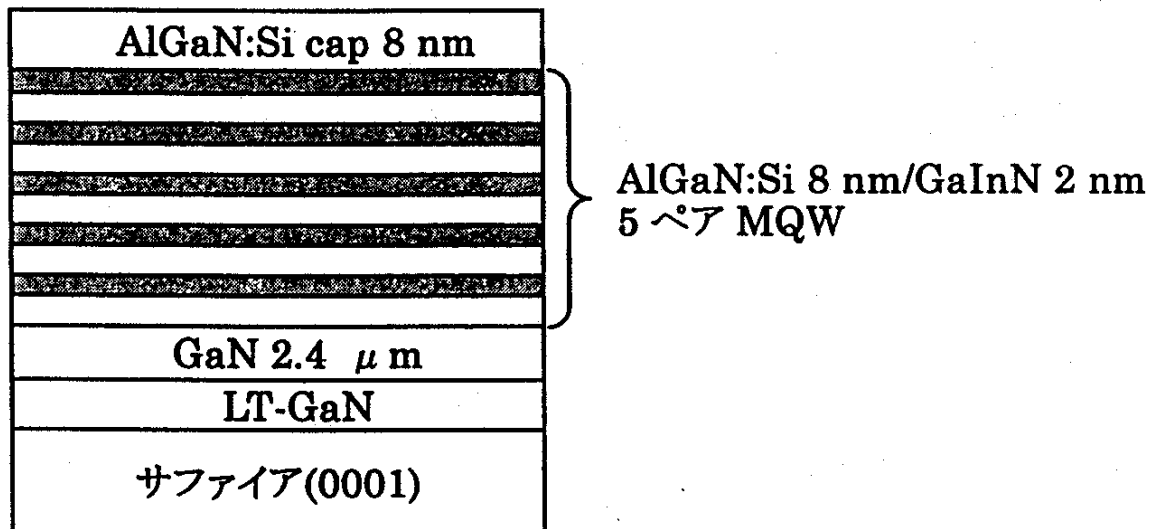


FIG. 9.3.1-(1) Schematic diagram of AlGa<sub>N</sub>/GaIn<sub>N</sub> MQW structure

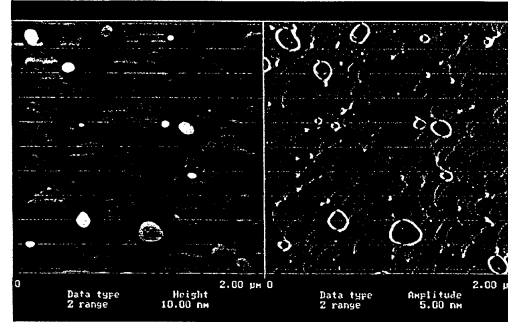
[Keys, FIG. 9.3.1-(1)]

(On the right) AlGa<sub>N</sub>: Si 8 nm / GaIn<sub>N</sub> 2 nm; 5-pair MQW

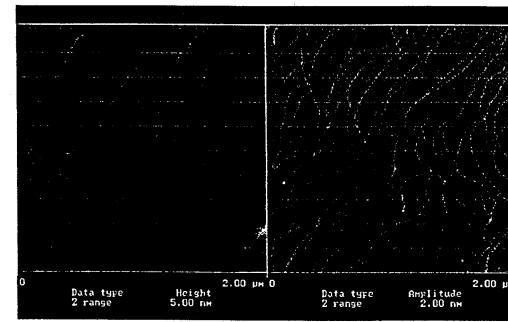
(Bottom layer) Sapphire (0001)

In process ①, both the AlGa<sub>N</sub> barrier and the GaIn<sub>N</sub> well layers were grown at 860°C, and in process ② the AlGa<sub>N</sub> barrier layers were grown at 1100°C while GaIn<sub>N</sub> layers were grown at 860°C.

During the growth of the MQW, trimethylaluminum (TMAI), triethylgallium (TEGa), and trimethylindium (TMI<sub>N</sub>) used as Group III source materials, with ammonia (NH<sub>3</sub>) used as the Group V source material and monosilane (SiH<sub>4</sub>) as the dopant material.



(a) AlGa<sub>N</sub> 層および GaIn<sub>N</sub> 層をともに 860°C で成長させた AlGa<sub>N</sub>/GaIn<sub>N</sub> MQW



(b) AlGa<sub>N</sub> 層を 1100°C で、GaIn<sub>N</sub> 層を 860°C で成長させた AlGa<sub>N</sub>/GaIn<sub>N</sub> MQW

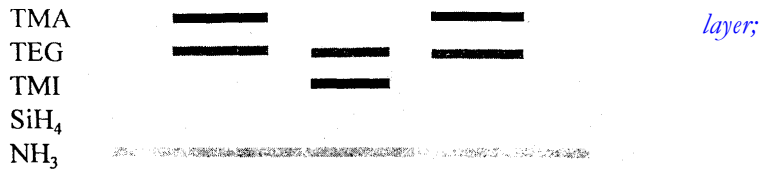
FIG. 9.3.1-(2) MQW growth sequence

[Keys, FIG. 9.3.1-(2)]

(X-axis) Time.

(Y-axis) Temperature [°C].

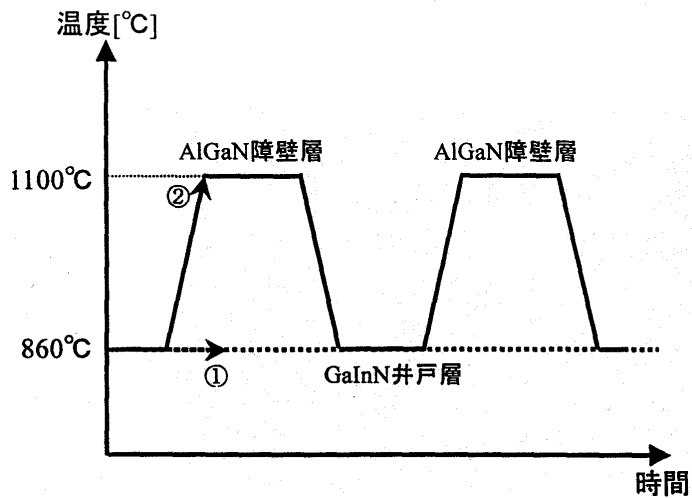
(Inside, left to right) AlGa<sub>N</sub> barrier  
GaIn<sub>N</sub> well layer; AlGa<sub>N</sub> barrier layer.



### 9.3.2 Results and discussion

#### 9.3.2.1 AFM observations of surface condition

The surface condition of MQW layers obtained during the fabrication of the MQW in accordance with the growth sequence of FIG. 9.3.1-(2) in case ①, wherein both the AlGa<sub>N</sub> barrier layers the GaIn<sub>N</sub> well layers were grown at 860°C, and in case ②, wherein the AlGa<sub>N</sub> barrier layers were grown at 1100°C and the GaIn<sub>N</sub> layers were grown at 860°C, is shown in FIG.



layers

the

were

used

layer;

and

9.3.2-

(1). In case ①, a lot of pits were generated, whereas in case ② there were almost no pits, and the surface condition was excellent.

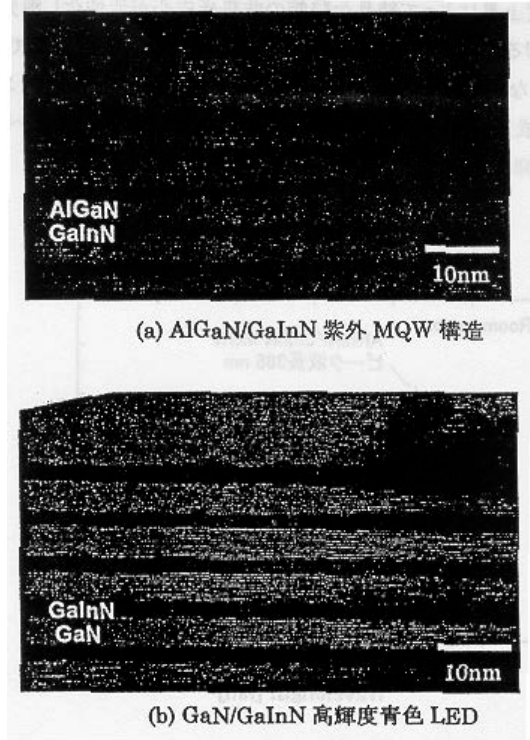
FIG. 9.3.2-(1) AFM images of MQW layers ( $2\ \mu\text{m} \times 2\ \mu\text{m}$ )

Left: actual image, right: derivative image.

[Keys, FIG. 9.3.2-(1)]

(a) (case ①) AlGaIn/GaInN MQW with both AlGaIn layers and GaInN layers grown at  $860^\circ\text{C}$

(b) (case ②) AlGaIn/GaInN MQW with AlGaIn layers grown at  $1100^\circ\text{C}$  and GaInN layers grown at  $860^\circ\text{C}$



### 9.3.2.2 TEM observations

The quality of the interfaces in the MQW were evaluated using cross-sectional TEM. FIG. 9.3.2-(2) (a) is a cross-sectional TEM image of an AlGaIn/GaInN MQW structure with an excellent surface condition, which was obtained when the AlGaIn layers were grown at an elevated temperature. From the results of (1), it is evident that in order to obtain MQW layers of excellent surface condition it is necessary to grow the AlGaIn layers at an elevated temperature. On the other hand, in order to incorporate In during the growth of GaInN, it is necessary to maintain a low growth temperature. Although it was believed that as a result of the temperature rise during the growth of AlGaIn, the GaInN layers were subject to thermal damage, it was found that in FIG. 9.3.2-(2) (a) there was no visible damage to the MQW layers and excellent hetero-interfaces were formed. For comparison, a cross-sectional TEM image of a high-brightness blue LED with a GaN (7 nm)/GaInN (3 nm) MQW structure is shown in (b) of the same figure. There was no marked difference in terms of the interface sharpness between the two figures. From this, we concluded that UV MQW's utilizing AlGaIn barrier layers had structures that compared very well with those of high-brightness blue MQW's utilizing GaN barrier layers.

FIG. 9.3.2-(2) Cross-sectional TEM images captured in the vicinity of MQW's

[Keys, FIG. 9.3.2-(2)]

(a) AlGaIn/GaInN UV MQW structure

(b) GaN/GaInN high-brightness blue LED

**9.3.2.3 Evaluation of optical characteristics using PL**

To evaluate the optical characteristics of the MQW structures, we carried out PL measurements. FIG. 9.3.2-(3) shows a PL spectrum obtained from an AlGaInN/GaInN MQW structure with AlGaInN barrier layers grown at an elevated temperature. For comparison, a PL spectrum of a high-brightness blue MQW is shown with a dotted line in the same figure. UV emission with a peak wavelength of 385 nm was observed. The emission intensity was approximately the same as that obtained in the case of the blue MQW structure. In the case of MQW structures utilizing GaN barrier layers, the PL intensity decreases as the emission wavelength is shortened (FIG. 9.3.2-(4)) [1]. This is believed to be due to the fact that, as described above, as a result of a reduction in the InN molar fraction of the well layers for the purpose of shortening the wavelength, the bandgaps of the MQW layers approach the bandgap of the GaN barrier layers and stop functioning as quantum structures, resulting in a decrease in intensity. On the other hand, it is believed that when the AlGaInN barrier layers are used, it is possible to efficiently confine electrons to the well layers because the energy difference with respect to the well layers can be reduced, thereby suppressing the decrease in the PL intensity.

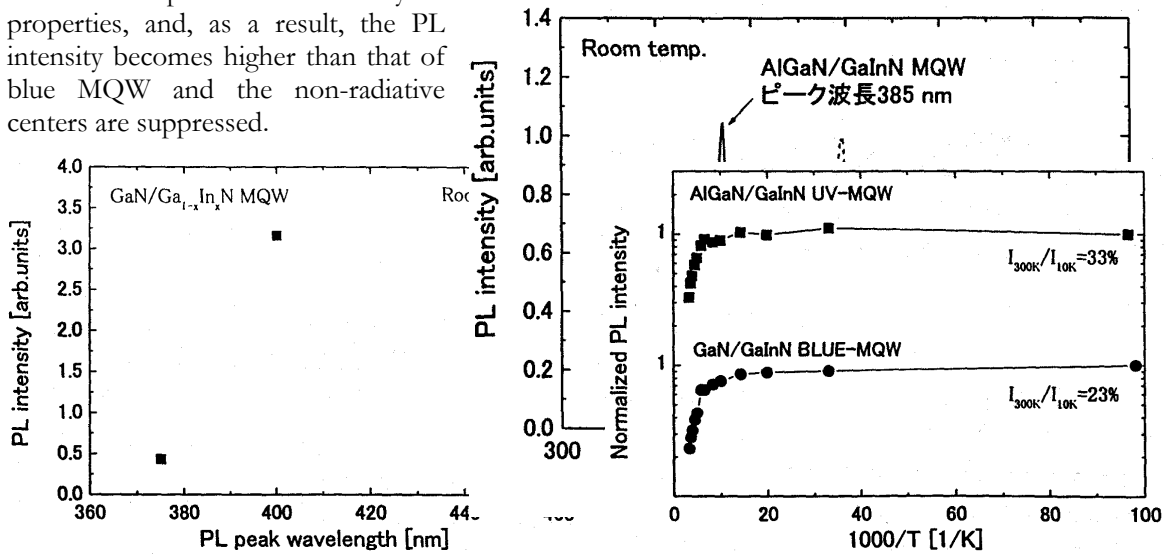
FIG. 9.3.2-(3) PL spectra obtained from UV MQW and blue MQW structures

[Keys, FIG. 9.3.2-(3)]

(Peak on left) AlGaInN/GaInN MQW; peak wavelength: 385 nm

(Peak on right) GaN/GaInN MQW; peak wavelength: 448 nm

FIG. 9.3.2-(5) shows the dependence of the PL intensity on the temperature, which was obtained by varying the sample temperature from 10 K to 300 K. Results obtained for an AlGaInN/GaInN MQW with AlGaInN grown at an elevated temperature and, for comparison, a GaN/GaInN blue MQW, are shown in the same figure. It was found that as the temperature increased, the PL intensity decreased (temperature-induced extinction). This is believed to be due to the fact that as the temperature rises, non-radiative centers, such as crystal defects, etc., become activated, which leads to extinction. The ratio of the PL intensities at 300 K and at 10 K ( $I_{300\text{K}}/I_{10\text{K}}$ ) was 33% for the UV MQW and 23% for the blue MQW. In addition, when AlGaInN was grown at 860°C, the ratio was 22%. In this connection, it is believed that growing the AlGaInN barrier layers at 1100°C improves the crystal properties, and, as a result, the PL intensity becomes higher than that of blue MQW and the non-radiative centers are suppressed.



the

Left: FIG. 9.3.2-(4) Relationship between PL peak wavelength and PL intensity

Right: FIG. 9.3.2-(5) Dependence of PL intensity of UV MQW on temperature

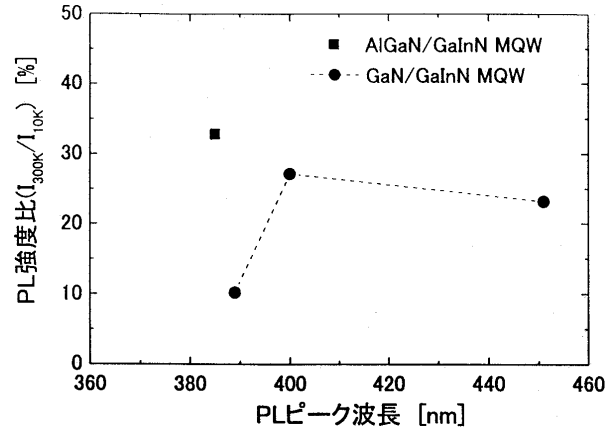
FIG. 9.3.2-(6) shows the peak wavelength and the PL intensity ratio  $I_{300\text{ K}}/I_{10\text{ K}}$ . When GaN barrier layers were used, a decrease in the PL intensity ratio was observed in the UV region below 400 nm, with the  $I_{300\text{ K}}/I_{10\text{ K}}$  ratio at a peak wavelength of 389 nm being approximately 10%; the ratio, however, was almost tripled, to 33%, when AlGaIn barrier layers were used. This can demonstrate that AlGaIn/GaInN MQWs effectively increase efficiency in the UV region.

FIG. 9.3.2-(6) Relationship between PL peak wavelength and PL intensity ratio

[Keys, FIG. 9.3.2-(6)]

(X-axis) PL peak wavelength [nm].

(Y-axis) PL intensity ratio ( $I_{300\text{ K}}/I_{10\text{ K}}$ ) [%]



## 9.4 Study of AlGaIn cladding layers with high AlN molar fraction

As a result of the decreased InN molar fractions of the GaInN used in the emitting layer, in order to efficiently confine carriers to the well layers, it is essential to use not only the AlGaIn barrier layers described in 9.3, but also a AlGaIn cladding layer with a high AlN molar fraction. The AlN molar fraction of the AlGaIn cladding layer currently used in UV LEDs is about 20% [2]. However, as the AlN molar fraction increases, the growth of p-type AlGaIn is rendered more difficult, and problems arise in terms of p-type conductivity control. In addition, the risk of parasitic reactions between  $\text{NH}_3$  and TMAI, which is used as the Al source material, presents a problem in the commonly used normal-pressure MOCVD technique, which makes growth at high AlN molar fractions difficult. To grow AlGaIn, it is important to suppress the parasitic reactions. The MOCVD apparatus used in the present study allows for growth at a reduced pressure, which is believed to be advantageous in terms of suppressing the parasitic reactions and growing AlGaIn with a high AlN molar fraction. In this connection, we have been investigating the growth of single thin films of AlGaIn with a high AlN molar fraction (an AlN molar fraction of about 20%) for use in UV LEDs.

### 9.4.1 Methods and means

Single thin films of AlGaIn were grown on undoped GaN layers. The thicknesses of the AlGaIn layers was  $0.3\ \mu\text{m}$ . The conditions, under which the AlGaIn layers were grown are shown in Table 9.4.1. The growth pressure used for growing the GaN was 20 kPa and the total gas flow rate was 10 slm. In the case of AlGaIn growth, at a growth pressure of 20 kPa, the AlN molar fraction was high, about 15%, regardless of the TMAI gas composition, which made high-concentration growth difficult. For this reason, in this study we investigated AlGaIn growth at 10 kPa, i.e. a pressure lower than the growth pressure used for GaN. The AlN molar fraction of the AlGaIn layer was obtained using X-ray diffraction in a  $2\theta/\omega$  scan.

---

Growth temperature

1180°C

---

---

Growth pressure	10 kPa
TMGa molar flow rate	$7.8 \times 10^{-5}$ mol/min
TMAI molar flow rate	$2.6 \sim 7.8 \times 10^{-5}$ mol/min
NH <sub>3</sub> molar flow rate	$1 \times 10^{-1}$ mol/min
Total gas flow rate	10~18 slm

---

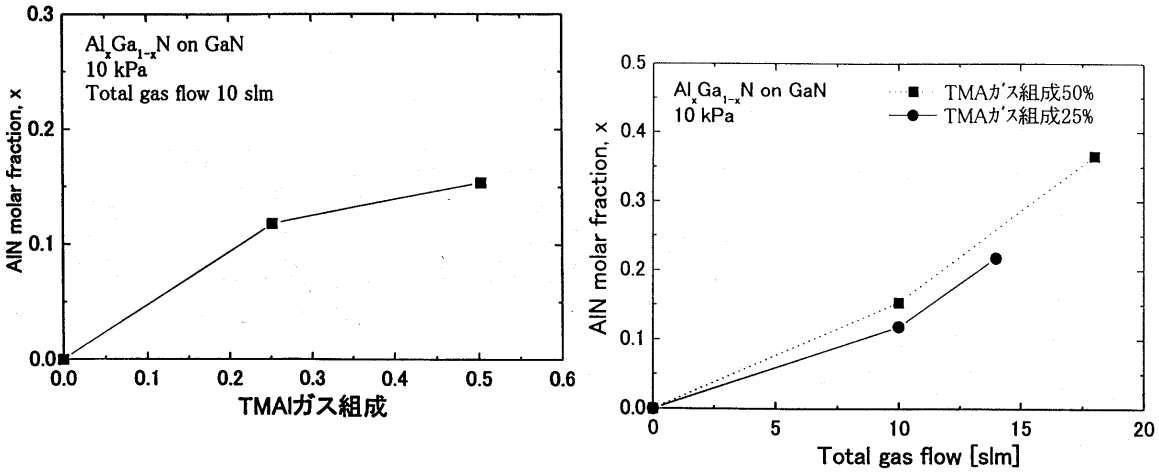
*Table 9.4.1 AlGaN Growth Conditions*

## 9.4.2 Results and discussion

FIG. 9.4.2-(1) shows the relationship between the TMAI gas composition and the AlN molar fraction under a total gas flow rate of 10 slm. At a TMAI gas composition of 25%, the AlN molar fraction was 12%, and at 50%, the AlN molar fraction was 15%. These results show that an increased concentration is difficult to achieve by simply increasing the TMAI gas composition. This is believed to be due to the fact that, at a total gas flow rate of 10 slm, the high flow velocity results in a decrease in the incorporation of Al into the solid phase.

FIG. 9.4.2-(2) shows the relationship between the total gas flow rate and the AlN molar fraction. In the case of a total gas flow rate of 14 slm, the AlN molar fraction at the TMAI gas composition of 25% was 22%, and in case of a total gas flow rate of 18 slm, the AlN molar fraction at a TMAI gas composition of 50% was 37%, obtaining an AlGaN layer with an AlN molar fraction of approximately 20%, which is necessary for UV LEDs.

The relationship between the flow velocity during the growth of AlGaN and the AlN molar fraction is shown in FIG. 9.4.2-(3). To suppress parasitic reactions and obtain AlGaN layers with an AlN molar fraction exceeding 20%, it is necessary to increase the flow velocity to 100 cm/sec or higher.



Left: FIG. 9.4.2-(1) Relationship between TMAI composition and AlN molar fraction (total gas flow rate: 10 L)

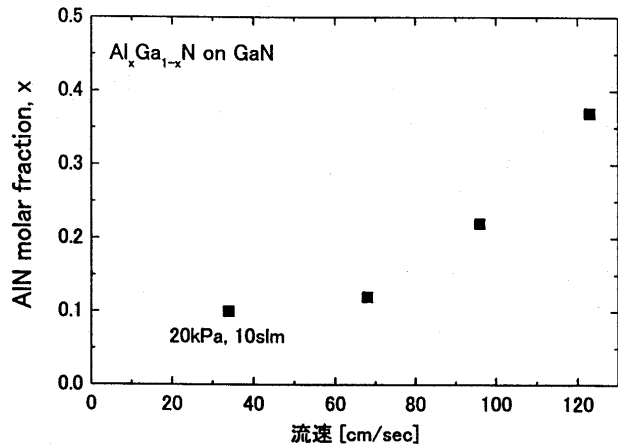
Right: FIG. 9.4.2-(2) Relationship between total gas flow rate and AlN molar fraction

[Keys, FIG. 9.4.2-(2)]: TMA gas composition 50%; TMA gas composition 25%

The results above show that an increase in the flow velocity achieved by increasing the total gas flow rate 1.5~2 times and a reduction in the growth temperature during AlGa<sub>x</sub>N growth by 1/2 comparison with the growth conditions in case of GaN (20→10 kPa) provides for efficient growth with a high AlN molar fraction.

FIG. 9.4.2-(3) Relationship between flow velocity during AlGa<sub>x</sub>N growth and AlN molar fraction

[Keys, FIG. 9.4.2-(3)]: (X-axis) Flow velocity [cm/sec].



## 9.5 Fabrication of UV LED Structures

This section describes the fabrication, emission characteristics, and electrical characteristics of UV LED structures obtained based on results of the investigations described in 9.3 and 9.4.

### 9.5.1 Methods and means

A UV LED structure is shown in FIG. 9.5.1. An undoped GaN layer, an n-type GaN:Si layer, an AlGa<sub>x</sub>N/GaInN 5-pair MQW, a p-type Al<sub>0.2</sub>Ga<sub>0.8</sub>N:Mg cladding layer, and a p-type GaN:Mg layer were deposited on a sapphire substrate. The carrier concentration of the p-type AlGa<sub>x</sub>N:Mg was  $1 \times 10^{17} \text{ cm}^{-3}$ . Al was used as the n-type electrode, and Ni/Au was used as the p-type electrode. The alloying of the p-side electrode was conducted for 10 min at a pressure of 1 atmosphere and a temperature of 540°C in a 5000 sccm stream of mixed gas consisting of oxygen and argon. The emission spectrum of the electroluminescence (EL) of the LED element was measured using a wavelength measurement apparatus

with an auto-prober. The wavelength range was 300~800 nm. The current/voltage characteristic of the LED element was measured using a current/voltage source monitor. DC

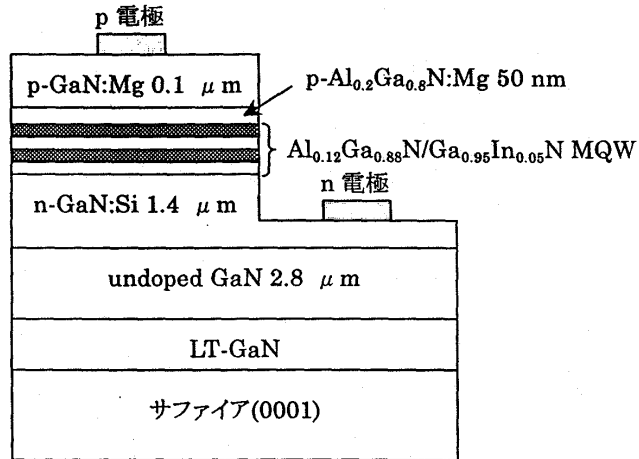
FIG. 9.5.1 UV LED Structure

[Keys, FIG. 9.5.1]

(Top) P-electrode.

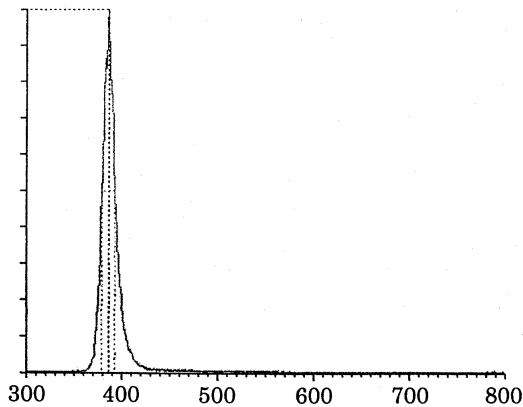
(Middle, right) N-electrode.

(Lowest layer) Sapphire (0001).



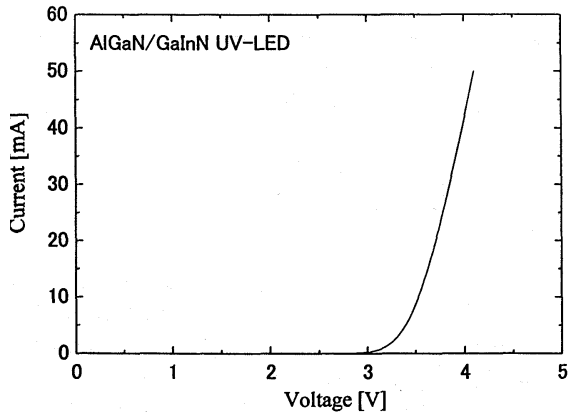
### 9.5.2 Results and discussion

FIG. 9.5.2-(1) shows the EL spectrum. It was confirmed that UV emission at a wavelength of 390 nm occurred after current injection. The operating voltage at 20 mA was 3.7V (FIG. 9.5.2-(2)). The emission power, converted to lamp-equivalent output, corresponded to 1 mW (measured using an auto-probe), with the output of the UV LED being lower in comparison with that of the blue LED. In case of PL induced by light excitation, no PL intensity decrease due to the shortening of the wavelength was observed; however, with current injection, the EL intensity decreased, which was believed to be due to the formation of non-radiative centers. It is necessary to improve the crystal quality and reduce the non-radiative recombination rate by carrying out further optimization of the growth conditions.



Left: FIG. 9.5.2-(1) Current injection emission spectrum of UV LED.

[Keys, FIG. 9.5.2-(1)]: (X-axis) Wavelength [nm]; (Y-axis) Intensity [a.u.].



Right: FIG. 9.5.2-(2) I-V characteristic of UV LED.

## 9.6 Summary

### 9.6.1 Fabrication of AlGaInN UV MQW structures

We investigated AlGaInN MQW emitting layers designed for use in the emitting layers of UV LEDs. MQW structures of excellent surface condition and interface sharpness were obtained by growing AlGaIn barrier layers at an elevated temperature of 1100°C. PL measurements showed that excellent UV emission

characteristics were obtained, with a peak wavelength of 385 nm and an emission intensity equivalent to that of the PL from a blue MQW. As a result of investigating the ratio of PL intensities ( $I_{300\text{ K}}/I_{10\text{ K}}$ ), it was established that the ratio reached 33% in UV MQWs utilizing AlGa<sub>x</sub>N barrier layers, which was higher than the 23% in the case of blue QWs utilizing GaN barrier layers. By using AlGa<sub>x</sub>N barrier layers, we were able to suppress the decrease in the PL intensity ratio in the UV region of GaN barrier layer MQWs.

### **9.6.2 Study of AlGa<sub>x</sub>N cladding layer with high AlN molar fraction**

We investigated the growth of a AlGa<sub>x</sub>N cladding layer with a high AlN molar fraction for use in UV LEDs. It was found that parameters such as growth pressure and total gas flow rate could effectively influence the growth of the AlGa<sub>x</sub>N with a high AlN molar fraction. As a result, a AlGa<sub>x</sub>N layer with AlN molar fractions exceeding 20% was obtained.

### **9.6.3 Fabrication of UV LED element structures**

We fabricated LED structures utilizing AlGa<sub>x</sub>N/GaInN MQW as emitting layers. The presence of 390-nm UV current injection emission was confirmed. The operating voltage at 20 mA was 3.7V. As converted to lamp output, the emission output corresponded to 1 mW, which was lower in comparison with that of blue LEDs, and, therefore, called for further investigations into the optimization of the growth conditions in order to increase the efficiency.

## **9.7 Future Plans**

In the future, we are planning to carry out further optimization of the growth conditions and establish an epitaxial technology for high-efficiency UV LEDs. The topics for future research are shown below.

### **9.7.1 Non-radiative recombination rate reduction**

Further optimization of the growth conditions, and, especially, an increase in the quality of the MQWs, are necessary in order to reduce the non-radiative recombination rate, which causes the decreased output of UV LEDs. In addition, we would like to study the influence of the introduction of a superlattice cladding layer in terms of improving the crystal properties of MQW layers and in terms of the LED emission brightness.

In addition, from the I-V characteristic we concluded that the cause of the non-radiative recombination rate was in the interface (pn junction) between the MQW layer and the p-layer, and we believe that it is important to investigate p-AlGa<sub>x</sub>N cladding layers as well. It is necessary not only to improve the interface sharpness of the pn junction, but also to continue investigating the growth of high-carrier-concentration p-AlGa<sub>x</sub>N in order to improve electrical characteristics.

### **9.7.2 AlGaInN emitting layer (high InN molar fraction)**

In the UV region, the InN molar fraction of the GaInN emitting layer decreases. For this reason, the effects of In weaken, and the PL intensity decreases. It is believed that enhanced In effects can be expected in case of an AlGaInN emitting layer, because a high InN molar fraction can be achieved. 360-nm UV current injection emission from LED structures utilizing MQW structures made of quaternary mixed crystals such as AlGaInN has been observed [3]. In previous investigations into AlGaInN emitting layers their intensity has been lower by one order of magnitude as compared with blue MQWs. The introduction of Al in the emitting layer results in a deterioration of the surface flatness, bringing about a decrease in the PL intensity. By optimizing the growth conditions, we are planning to increase the quality of the AlGaInN layer and achieve high-efficiency UV emission.

### 9.7.3 ELO technique

Regarding the ELO technique, we will work on the optimization of the regrowth conditions and further reduction of dislocations. We will fabricate UV LED structures on ELO-GaN substrates to confirm the dislocation reduction effect.

### 9.7.4 Large-size MOCVD apparatus

We would like to make use of multiple wafer growth in order to clarify the effects of the substrate on the LED emission efficiency. The density of dislocations, the amount of strain applied to the emitting layers, and control of the substrate surface condition are believed to exert considerable influence on the emission efficiency. A large MOCVD apparatus permits comparison, under the same growth conditions, of substrates exhibiting different dislocation densities, differences in the degree of lattice matching, and differences in the methods of surface processing. We would like to investigate the effects produced on the efficiency of LED emission by different dislocation densities of ELO-GaN substrates and GaN substrates, different degrees of lattice matching of SiC substrates, by sapphire substrates, as well as by differences in the corresponding pre-processing conditions. Furthermore, an in-situ observation system based on the surface reflectivity of visible light could be a powerful tool in controlling the condition of the substrate surface immediately prior to growth.

### 9.7.5 Application of SiC substrates

The use of SiC substrates offers certain advantages in terms of LED fabrication, such as a smaller degree of lattice mismatch in comparison with sapphire substrates, electrical conductivity of the substrate, etc. We would like to confirm the influence exerted by the use of SiC substrates on LED characteristics.

## 9.8 References

- [1] High-efficiency photoelectric conversion compound semiconductor research activity report (1999), Research and Development Center for Metals, p. 157.
- [2] T. Mukai, M. Yamada, and S. Nakamura: Jpn. J. Appl. Phys. 37 (1998) L1358.
- [3] A. Kinoshita, H. Hirayama, M. Ainoya, Y. Yamahi, A. Hirata, Y. Aoyagi: Materials of Scientific Symposium No. 61 of Applied Physics Society, 7a-L-7, p. 332.

# 10 Development of High-Output UV Light-Emitting Components

## 10.1 Achievements in 1998 and 1999

In 1998 and 1999, as a result of carrying out fundamental investigations of UV light-emitting components using existing MOVPE (Metalorganic Vapor Phase Epitaxy) crystal growth equipment, as well as fundamental investigations of the ELO (Epitaxially Lateral Overgrowth) technique, which offers a promising technology for dislocation reduction, we obtained the information necessary to determine our approach to component design.

### 10.1.1 Achievements in 1998

Based on the blue LED (Light Emitting Diode) fabrication technology, which our company had been developing and maintaining in-house as a proprietary technology, we conducted investigations into the fundamental film-forming conditions necessary for  $\text{In}_x\text{Ga}_{1-x}\text{N}$  ( $0 \leq x \leq 0.12$ , wavelength: 362~400 nm), which is used in the emitting layer of UV LEDs, and carried out evaluation of its characteristics with special emphasis on PL (Photo-Luminescence) measurements. ① The PL intensity of  $\text{In}_x\text{Ga}_{1-x}\text{N}$  single films ( $0 \leq x \leq 0.12$ , 50 nm,  $n = 2 \times 10^{18} \text{ cm}^{-3}$ ) peaked in the vicinity of In composition  $x = 0.05$  (emission wavelength: 378 nm). ② We investigated the dependence of the PL intensity of  $\text{In}_x\text{Ga}_{1-x}\text{N}$  ( $0 \leq x \leq 0.12$ ,  $w = 2 \text{ nm} \sim 10 \text{ nm}$ ,  $n = 2 \times 10^{18} \text{ cm}^{-3}$ )/AlGaIn-SQW (Single Quantum Well) structures on  $x$  and well width ( $w$ ) and strengthened our grasp on the PL characteristics that are strongly dependent on  $x$  and  $w$ . It was found that a well width of 3 nm was the optimal value for all tested  $x$ . The PL intensity decreased with decreasing In composition, and the elucidation of the causes and development of countermeasures against this phenomenon were put on our agenda for the next year. ③ We verified the dislocation reduction effects afforded by the ELO technique and found that although the dislocation reduction effects did exist, there were various problems, which included substrate bowing, crystal axis ( $c$ -axis) wobble, etc.

### 10.1.2 Achievements in 1999

Using the InGaIn-SQW-UV LED as a basic structure, we ① investigated the dependence of the optical characteristics (temperature characteristics of PL) of InGaIn-SQW structures on the In composition, ② built prototypes of UV LEDs, ③ examined the dependence of the emission intensity on the dislocation density, ④ investigated the ELO technique, and ⑤ designed and introduced a novel MOVPE apparatus (property of NEDO) [*NEDO: New Energy and Industrial Technology Development Organization – trans.*].

① By evaluating the PL temperature characteristics of InGaIn-SQW structures, it was confirmed that as the In composition decreased, the intensity of room-temperature PL decreased and the temperature extinction of the PL intensity increased. ② Results of UV LED prototyping showed a decrease in the emission output associated with the shortening of the emission wavelength. ③ Examination of the relationship between the density of dislocation-related pits on the surface of InGaIn-MQW (Multi-Quantum Well) structures and the PL intensity confirmed that there was a negative correlation between the density of dislocations and the PL intensity. Thus, we concluded that ①, ②, and ③ in the 1998 achievements section were due to the powerful influence of dislocations and other defects in the UV emission wavelength region, and determined that dislocation defect reduction was essential to the practical implementation of high-output UV LEDs and that it was important to optimize crystal growth conditions (especially the conditions of the initial stage of crystal growth) in order to determine the conditions necessary for reducing the number of dislocation defects.

④ With a view to reduce the warping of the substrate and the wobble of the crystal axis, which present serious problems in ELO-GaN layers, we conducted investigations into the use of fine-striped masks in the ELO technique. As a result, by setting the ratio of masked/open width to  $0.5 \mu\text{m}/0.5 \mu\text{m}$ , we were able to fabricate thin ELO-GaN and successfully reduced the  $c$ -axis wobble. Although we did achieve a dislocation density reduction as a result of introducing ELO-GaN, it did not amount to a substantial improvement in the optical characteristics of the UV InGaN-SQW structures formed thereon, which attested to the need to develop novel ELO techniques. In addition, we ⑤ completed the design and commissioning of a novel MOVPE apparatus and started research aimed at determining the appropriate crystal growth conditions.

Based on the above-described achievements, our top-priority development tasks for 2000 include ① optimization of the initial stage of crystal growth and crystal growth conditions of the emitting layer, ② development of dislocation defect reduction techniques, such as ELO, etc., ③ development of component structures suitable for short-wavelength LEDs.

## 10.2 Summary of Research and Development in 2000

Based on the previously set tasks, we conducted the following investigations.

- Optimization of the amount of Si used for the doping of InGaN-MQW structures
- Investigation into new dislocation density reduction techniques based on problems that had been uncovered in ELO
- Building of UV LED prototypes by applying the results of the above-described investigations
- Building of blue LED prototypes for the purpose of comparison with the UV LEDs
- Building of white LED prototypes by applying the results obtained by building the UV and blue LED prototypes

As a result of the above-mentioned investigations, it was found that the emission output of UV LEDs could be improved by adding trace amounts of Si to the barrier layers.

In addition, we proposed a technique called LEPS (Lateral Epitaxy on the Patterned Substrate) as a novel technique for dislocation reduction. As a result, it has been confirmed that this method is extremely effective in improving the output of UV LEDs and in terms of dislocation reduction.

## 10.3 Building of prototypes of UV-emitting components

When we conducted preliminary studies of MQW layers last year, we obtained results indicating that their emission characteristics could be improved by Si doping. In this report we present the results of our investigations into the influence exerted on the optical characteristics and device characteristics by the Si doping of the barrier layers of UV LEDs.

### 10.3.1 Experimental method

The structure of the samples used in the experiments is shown in FIG. 10.3.1. The samples were fabricated using a vertical-type atmospheric pressure MOVPE apparatus.  $C$ -plane sapphire was used for the substrate, and, after subjecting it to thermal cleaning treatment in a hydrogen atmosphere at approximately  $1150^\circ\text{C}$ , a GaN buffer layer (thickness  $t = 27 \text{ nm}$ ) was grown thereon at a temperature of  $450^\circ\text{C}$ . A Si-doped n-GaN layer ( $4 \mu\text{m}$ ), a Si-doped n- $\text{Al}_y\text{Ga}_{1-y}\text{N}$  layer ( $y = 0.1$ ,  $50 \text{ nm}$ ), an MQW structure (number of wells = 4), which was made up of  $\text{In}_x\text{Ga}_{1-x}\text{N}$  ( $x = 0.08$ ,  $3 \text{ nm}$ ) well layers and Si-doped n-GaN ( $6 \text{ nm}$ ) barrier layers, a Mg-

doped p-Al<sub>y</sub>Ga<sub>1-y</sub>N layer (y = 0.1, 50 nm), and a Mg-doped p-GaN contact layer (100 nm) were successively grown thereon.

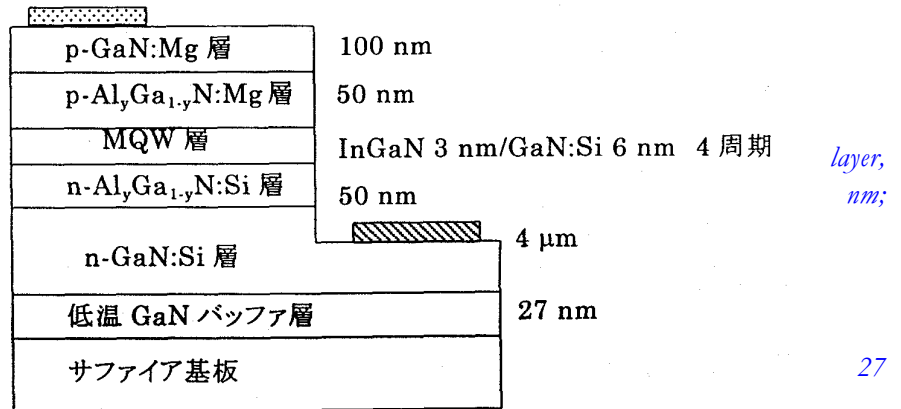
The amount of Si used to dope the barrier layers was varied ( $2.4 \times 10^{18} \text{ cm}^{-3}$ ,  $8 \times 10^{17} \text{ cm}^{-3}$ ,  $2 \times 10^{17} \text{ cm}^{-3}$ , and no doping). Upon completion of growth, some of the p-type layer of the wafer was removed by dry etching to expose the n-GaN layer and an n-electrode was formed thereon. In addition, after forming a p-electrode in the p-GaN contact layer, device isolation was carried out, resulting in an LED chip.

Using a PL apparatus installed at Yamaguchi University, the fabricated samples were subjected to optical measurements in order to examine their PL spectra under excitation (using a He-Cd laser with an excitation density of 25 mW/cm<sup>2</sup>) and the temperature dependence of the PL intensity across a temperature range from 4K to room temperature.

FIG. 10.3.1 Structure of LED prototype

[Keys, FIG. 10.3.1]

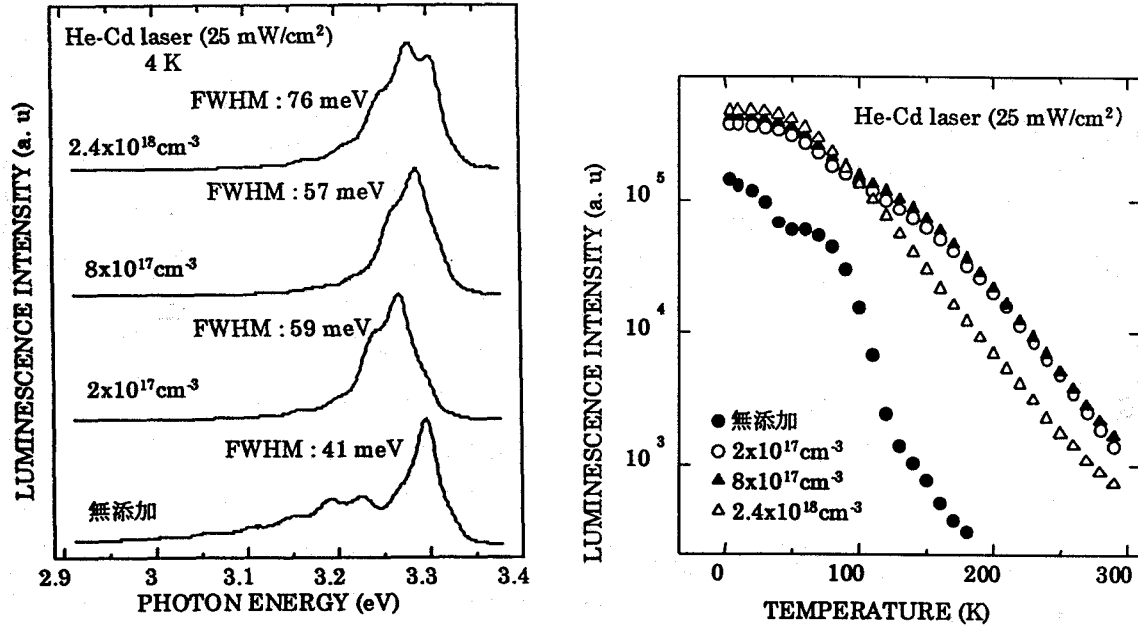
(Top to bottom) p-GaN:Mg 100 nm; p-Al<sub>y</sub>Ga<sub>1-y</sub>N layer, 50 nm MQW layers, InGaN 3 nm/GaN:Si 6 nm, 4 cycles; n-Al<sub>y</sub>Ga<sub>1-y</sub>N:Si layer, 50 nm; n-GaN:Si, 4 μm; Low-temperature GaN buffer layer, 27 nm.



### 10.3.2 Results and discussion

#### 10.3.2.1 Results and discussion of optical evaluation by PL

The PL spectra of the UV LED prototypes obtained at 4 K are shown in FIG. 10.3.2-(1), and changes in the PL emission intensity of the active layer across the range of from 4 K to room temperature are shown in FIG. 10.3.2-(2).



Left: FIG. 10.3.2-(1) Comparison of PL spectra (active layer) obtained at 4 K

[Keys, FIG. 10.3.1-(1)]: (Inside, bottom left) No doping.

Right: FIG. 10.3.2-(2) Temperature dependence (active layer) of PL emission intensity.

[Keys, FIG. 10.3.1-(2)]: No doping

Mg-related emission was observed in the vicinity of 3.2 eV in undoped samples, where the barrier layers were not subjected to Si doping. On the other hand, this emission was not observed in Si-doped samples. In this connection, it is believed that the Si doping of the barrier layers produces suppressing effects on the diffusion of Mg from the p-type layer into the emitting layer.

Examination of the temperature dependence of the PL emission intensity showed that, in comparison with the Si-doped samples, samples that had not been doped with Si exhibited a weaker intensity in all temperature zones. This is believed to be due to the formation of non-radiative recombination centers as a result of Mg diffusion in the emitting layer. In addition, as a result of subjecting the barrier layers to high-level doping, the PL emission intensity at low temperatures was high, but, as a result of a considerable temperature extinction, the PL emission intensity at room temperature decreased. Examination of the full width half maximum (FWHM) of the PL spectra of FIG. 10.3.2-(1) showed that the FWHM widened when the amount of Si used for doping was increased. Based on this, we believe that excessive Si doping brings about a deterioration in crystal properties.

### 10.3.2.2 LED prototyping results and discussion

The relationship between the LED chip output and the amount of Si used for the doping of the barrier layers is shown in FIG. 10.3.2-(3).

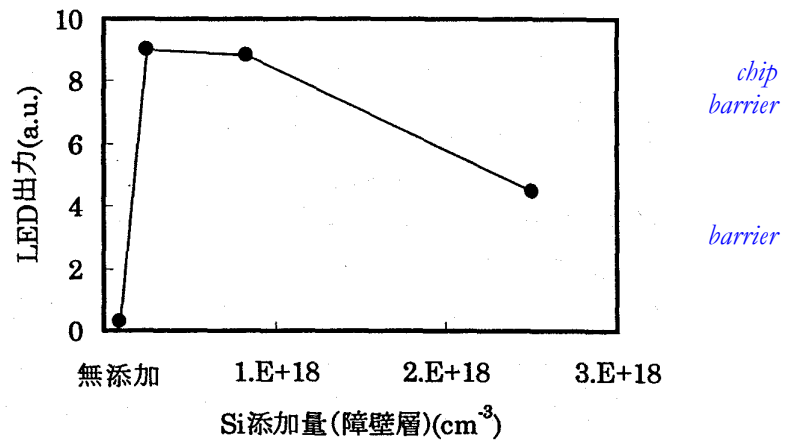
FIG. 10.3.2-(3) Dependence of LED output on amount of Si used for doping (of layers)

[Keys, FIG. 10.3.2-(3)]

(X-axis) Amount of Si used for doping (of layers) ( $\text{cm}^{-3}$ )

(X-axis, point of origin) No doping.

(Y-axis) LED output (a. u.).



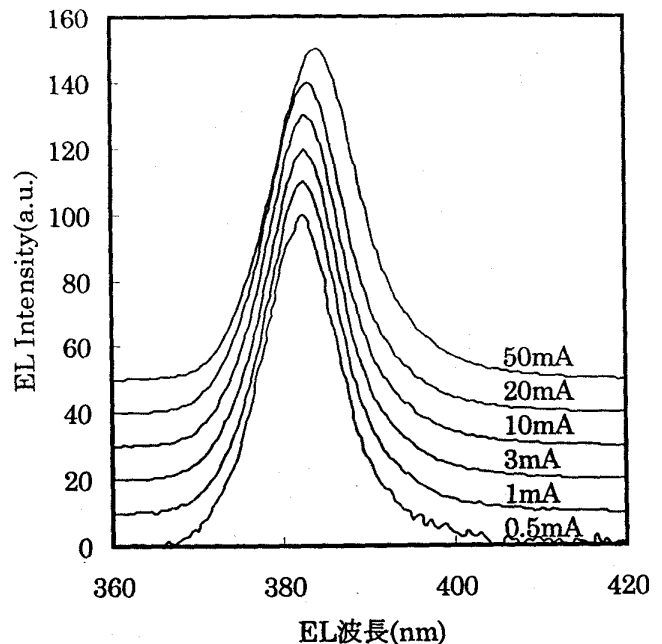
The output peaked at a Si doping amount of  $2 \times 10^{17} \text{ cm}^{-3}$ . The sample was mounted on a TO-18 STEM [scanning transmission electron microscope – trans.] stage and an integrating sphere was used to measure the output, which was 1.2 mW (at 20 mA). Although the emission output did increase as the amount of Si used for doping was decreased, but with no doping at all, there was a considerable drop in the output. This was in good agreement with the results of the PL-based optical characteristic evaluation and was believed to be due to the fact that absence of doping caused a decrease in the emission output due to the Mg diffusion from the p-layer into the emitting layer, with the emission output dropping because of deterioration in crystal quality when the carrier concentration was increased.

A current value dependence of the EL spectrum of an LED chip doped with Si at a level of  $2 \times 10^{17} \text{ cm}^{-3}$  is shown in FIG. 10.3.2-(4). The blue shift, which is observed in blue LEDs, was not observed as the current value was increased. On the other hand, when the current value was increased to 20 mA and higher, we observed a red shift, which was believed to be due to the shrinking of the bandgap caused by heat. These results are believed to be due to the fact that because in UV LEDs the In composition of the InGaN well layers is low, In composition fluctuations have practically no effect, and no blue shift is generated as a result of the increase in the current value.

FIG. 10.3.2-(4) Dependence of EL spectrum on current value.

[Keys, FIG. 10.3.2-(4)]

(X-axis) EL wavelength (nm).



### 10.3.3 Building of white LED prototypes

UV epi-wafers manufactured by our company were processed by Stanley Electric Co., Ltd., who used

them to fabricate LED chips subsequently die-bonded in a flip chip fashion on a TO-18 STEM stage [1] and subjected to measurements. In addition, a prototype of a white LED lamp was build [2] from the UV LED chips based on the technique of RGB (red/green/blue) fluorescent material excitation.

Results obtained for LED chips die bonded using face-up mounting by our company and die bonded using flip-chip mounting by Stanley Electric Co., Ltd. are shown in Table 10.3.1.

Die Bonding Technique	LED Output (mW)
Face up	1.2
Flip chip	2.9

*Table 10.3.1 Differences in LED output due to die bonding techniques (TO-18: bare chip: at 20 mA)*

Thus, by using flip-chip mounting, the LED output was increased approximately 2.4 times, obtaining an output of 2.9 mW and an external quantum efficiency of 4.3%. This improvement in LED output was believed to be due to improvement in light extraction efficiency and corroborated the double increase effects that have been reported [1]. In addition, although in the present study we did not do any resin sealing, we believe that in the future the output will be improved even more by means of resin sealing [1].

The luminous efficacy of the white LED lamp obtained by exciting the RGB fluorescent materials was 1.7 lm/W.

## 10.4 Investigations into new dislocation reduction techniques

In addition to the ELO technique and the Pendeo-Epitaxy technique [3, 4], recent efforts aimed at dislocation density reduction by means of selective growth have included investigations into the air-bridge technique [5] and facet-controlled ELO [6]. In case of ordinary ELO growth, it is necessary to grow a GaN layer as an underlying layer and carry out the operations of mask-forming and ELO growth, and, therefore, growth has to be carried out twice. In addition, there is the problem of the auto-doping Si contamination of the growth layer by the mask layer material (SiO<sub>2</sub>) and the problem that selective growth of AlGaN cannot not be carried out by reacting TMA (trimethylaluminum) and SiO<sub>2</sub>. In this study, we attempted to further reduce the dislocation density of GaN by mask-less one-step growth by the LEPS technique, in which the substrate is processed to impart it with a groove-and-ridge topography and create preferential conditions for lateral growth from the ridges.

### 10.4.1 LEPS technique

Schematic diagrams illustrating the commonly used ELO technique and the LEPS technique are shown in FIG. 10.4.1.

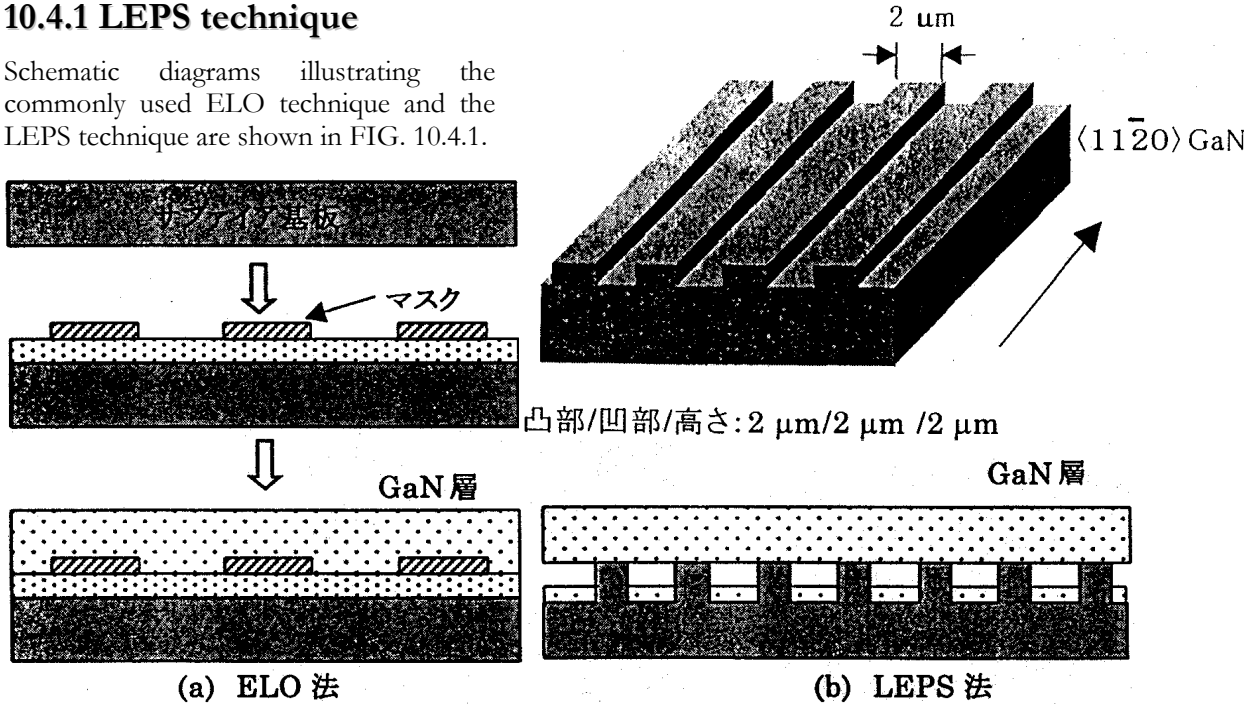


FIG. 10.4.1 Schematic representation of ELO and LEPS techniques

[Keys, FIG. 10.4.1]

(Left column) Sapphire substrate; Mask; GaN layer; GaN layer; (a) ELO technique

(Right column) Sapphire substrate processed to impart groove-and-ridge topography; GaN layer; (b) LEPS technique

While the ELO technique requires crystal growth to be carried out twice or more times, the same effects are believed to be attainable by the LEPS technique, where growth has to be conducted only once.

### 10.4.2 Experimental (LEPS-GaN growth)

The structure of a processed substrate used for growth is shown in FIG. 10.4.2. A ridge-and-groove stripe with 2- $\mu\text{m}$  ridges and 2- $\mu\text{m}$  grooves with a depth of 2  $\mu\text{m}$ , whose length direction coincided with  $\langle 11\bar{2}0 \rangle$  of the GaN, was formed on a  $c$ -plane sapphire substrate. The ridge-and-groove pattern was formed by dry etching using an ICP (Inductive Coupled Plasma)-type RIE (Reactive Ion Etching) apparatus introduced the year before.

GaN was grown in an atmospheric pressure MOVPE apparatus, with GaN buffer layers grown at low temperatures, and GaN layers grown at elevated temperatures. The shape of the fabricated samples was examined using scanning electron microscopy (SEM). In addition, dislocation behavior was observed using transmission electron microscopy (TEM) and dislocation density distribution was studied by observing pits formed as a result of dry etching.

FIG. 10.4.2 Structure of processed substrate.

[Keys, FIG. 10.4.2]

(Underneath image) Ridge/groove/height: 2 μm/2 μm/2 μm

### 10.4.3 Results and discussion

Results obtained by varying the growth time and observing the process of growth by means of cross-sectional SEM are shown in FIG. 10.4.3-(1).

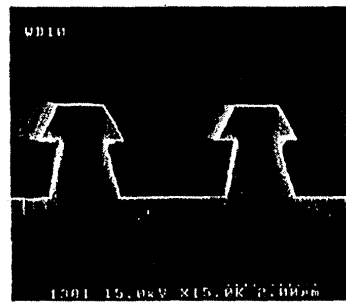
FIG. 10.4.3-(1) Cross-sectional SEM photos of LEPS-GaN

[Keys, FIG. 10.4.3-(1)]

(Top row) After growing for 15 min After growing for 30 min

(Bottom photo) After growing for 60 min

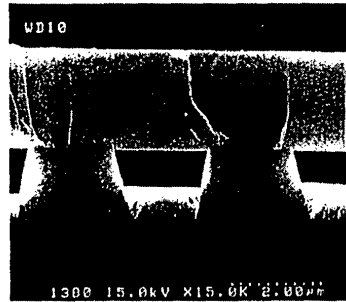
Although the growth of takes place both in the and groove portions, it confirmed that film originating from the portions grew in the direction. The shape formed in the process growth is enclosed by a {0001} face and a {1122} face, which is a face. As the growth continues, the laterally grown film coalesces, forming a flat film made {0001} only. As a of the above-described growth, the supply of source materials to the groove portions is shut off, so that growth can no longer continue and hollow portions are formed therein.



15 min 成長



30 min 成長



60 min 成長

GaN ridge was ridge lateral

of

stable

図 10.4.3(1) LEPS-GaN の断面 SEM 写真

up of result lateral

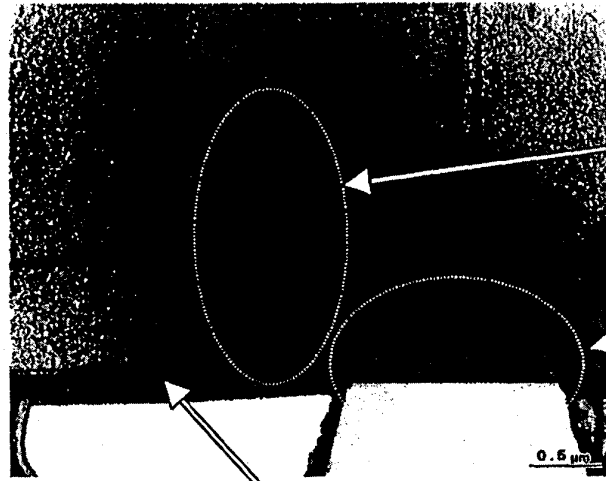
TEM observations were carried out in order to examine dislocation behavior. A cross-sectional TEM image is shown in FIG. 10.4.3-(2). Whereas in the portions above the ridges dislocations generated at the substrate/GaN interface extended upwards, no dislocations were observed in the portions above the grooves, where growth in the lateral direction took place. On the other hand, generation of new dislocations was observed in locations where the laterally grown film coalesced. This means that while in the portions above the ridges dislocations propagate upwards, in the portions above the grooves, where growth in the lateral direction takes place, a reduction in the density of dislocations can be achieved. Because the {1122}

face was revealed in the process of growth, it is believed that the propagation and reduction of these dislocations occur in accordance with the same mechanism as the one reported in case of FIELO [7].

FIG. 10.4.3-(2) Cross-sectional TEM image of LEPS-GaN.

[Keys, FIG. 10.4.3-(2)]

(Left, top to bottom) dislocations observed lateral growth portions; High-of dislocations observed above sapphire; (Directly image) Dislocations observed in central sections of concave portions



横方向成長部  
で転位観測されず

サファイア上部で  
高密度転位観測

凹部中央部で転位観測

No  
in

density

under

check

pits

Next, in order to the dislocation density of the resultant film, we carried out observations of

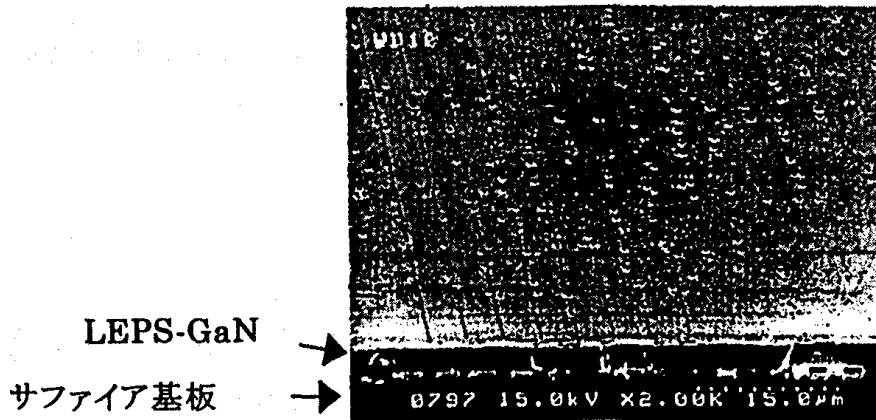
(which corresponded to certain dislocations) detected during dry etching. An SEM image of the film is shown in FIG. 10.4.3-(3).

It was confirmed that while pits corresponding to dislocations were visible above the ridges, the number of pits in the locations of lateral growth above the grooves was considerably reduced.

FIG. 10.4.3-(3) Pits produced by dry etching on an LEPS-GaN film

[Keys, FIG. 10.4.3-(3)]

(Bottom, left): Sapphire substrate.



LEPS-GaN

サファイア基板

## 10.5 Application of LEPS technique to LEDs

The LEPS technique had been confirmed as an effective method of dislocation density reduction. For this reason, we decided to see if it could be applied to UV LEDs, whose emission output was believed to be amenable to improvement by dislocation density reduction.

### 10.5.1 Experimental methods

The structure of the fabricated UV LEDs is shown in FIG. 10.5.1.

FIG. 10.5.1 Structure of LED prototypes

[Keys, FIG. 10.5.1]

(Top to bottom) p-GaN contact layer

p-AlGaN cladding layer

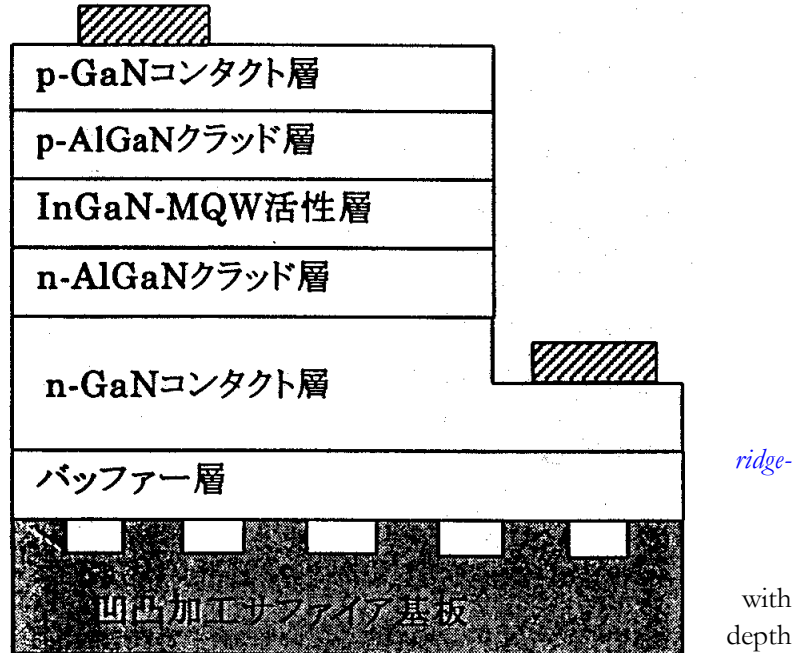
InGaN-MQW active layer

n-AlGaN cladding layer

n-GaN contact layer

Buffer layer

Sapphire substrate processed to impart and-groove topography



First of all, ridge-and-groove stripes 2- $\mu\text{m}$  ridges and 2- $\mu\text{m}$  grooves with a of 2  $\mu\text{m}$ , whose length direction coincided with  $\langle 11\text{-}20 \rangle$  of the GaN, were formed on a  $c$ -plane sapphire substrate. The growth of LED structures on processed substrates was carried out based on the structure shown in FIG. 10.3.1. Also, the amount of Si used for the doping of the barrier layers was  $2 \times 10^{17} \text{ cm}^{-3}$ . LED wafers were obtained by etching away part of the p-type layer and emitting layer, and then forming n- and p-type electrodes. After component isolation, the LED wafers were mounted by ordinary die bonding on a TO-18 STEM stage and subjected to measurements. The evaluation of dislocation density was carried out by means of cathodoluminescence (CL). LED chips were characterized by measuring the current value dependence of the output. Samples, in which ordinary substrates without ridge-and-groove processing were used, were fabricated and compared.

### 10.5.2 Results and discussion

CL observation results obtained for a sample that had undergone the ridge-and-groove processing are shown in FIG. 10.5.2-(1).

Because the emission spectrum intensity of the emitting layer during the CL measurements in the present study was extremely weak and thus made CL observations very difficult, to conduct measurements, the wavelength was set to a wavelength of 366 nm, at which the emission of the n-GaN contact layer takes place.

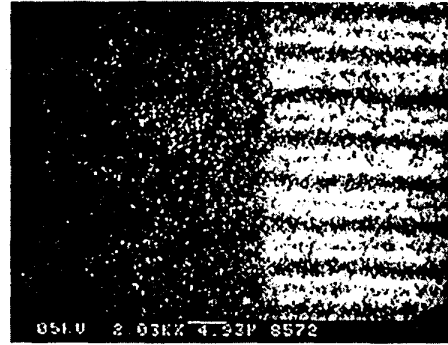
FIG. 10.5.2-(1) CL (366 nm) image of UV LED: comparison of processed and unprocessed portions.

[Keys, FIG. 10.5.2-(1)]

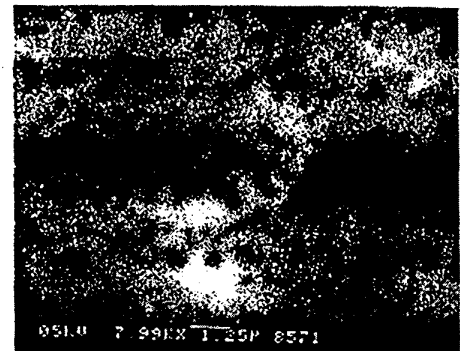
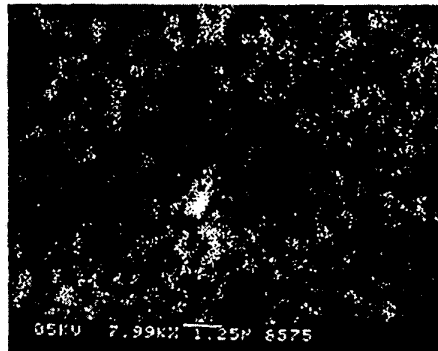
(Top) Unprocessed and processed portions (2000x)

(Bottom, left) Unprocessed portion (8000x)

(Bottom, right) Processed portion (8000x)



非加工部と加工部(2000倍)



Dark spots corresponding to dislocations in the amount of approximately  $1 \times 10^9$  spots/cm<sup>2</sup> were observed in the unprocessed portion. Above the ridges, the number of spots was approximately the same. Above the center of the grooves it was  $3 \times 10^8$  spots/cm<sup>2</sup> and on the order of  $10^7$  spots/cm<sup>2</sup> in other portions of the groove.

The spots observed in the central portion of the grooves were believed to originate from newly generated dislocations produced by coalescence. The distribution shown in the CL image was in good agreement with the behavior of dislocations shown in the cross-sectional TEM of FIG. 10.4.4 and was identical to the distribution obtained under ELO [8].

The LED chips were mounted on the TO-18 STEM stage and emission output measurements were carried out using an integrating sphere. The LED output and dislocation density (CL dark spots) results were summarized in Table 10.5.2 for LEDs fabricated on ordinary substrates and for LEDs fabricated by the LEPS technique.

	Ordinary growth	LEPS growth
Dislocation density (cm <sup>-2</sup> )	$1 \times 10^9$	$6 \times 10^8$
Output (mW)	0.9	2.5

Table 10.5.2 Comparison of UV LED Characteristics (wavelength: 380 nm) (\*Dislocation density of samples fabricated by LEPS is an average value.)

The emission output was almost tripled by applying the LEPS technique. Such a considerable improvement in the emission output in comparison with that reported for ELO-grown UV LEDs [9] strengthens the case for the superiority of the LEPS technique.

FIG. 10.5.2-(2) shows the current value dependences of the external quantum efficiency and output of LEDs grown on ordinary substrates and LEDs grown on LEPS substrates.

FIG. 10.5.2-(2) Current value dependence of efficiency and output.

[Keys, FIG. 10.5.2-(2)]

(X-axis) Current (mA).

(Y-axis, left) External quantum efficiency

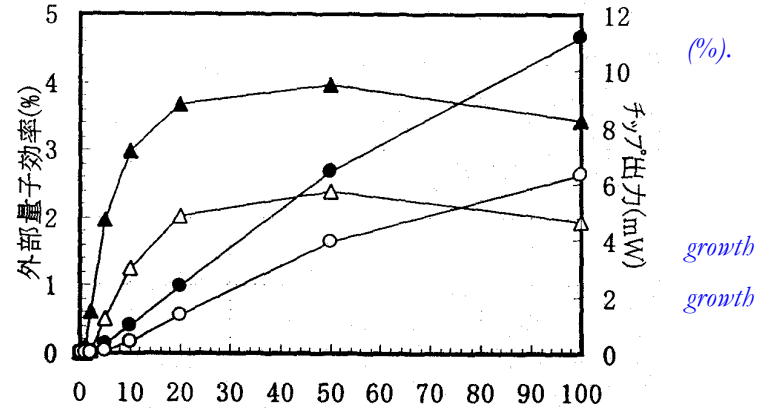
(Y-axis, right) Chip output (mW).

○ Chip output: regular growth

● Chip output: LEPS growth

△ External quantum efficiency: ordinary

▲ External quantum efficiency: LEPS



It was found that in both LEDs the

current at which the external quantum efficiency peaked was 50 mA, a value considerably higher in comparison with values reported for blue and green LEDs [10]. This is believed to be due to the trapping of injected carriers in non-radiative centers in the micro-current region, and it is believed that in UV diodes, as compared with blue diodes, the influence of the non-radiative centers, such as dislocations, etc., is stronger. It is believed that this attests to the need to reduce the density of dislocations in UV LEDs.

Considering the differences between the substrates, we can see that LEPS-grown LEDs exhibit an improved buildup in the low current region. This is believed to be due to a decrease in the number of non-radiative recombination centers as a result of the dislocation density reduction.

The external quantum efficiency of LEPS-grown UV LEDs at 20 mA was 3.7%. It can be expected to increase to up to 8.9% if we add the approximately 2.4-fold improvement in light extraction efficiency afforded by the use of flip chip mounting, as described in 10.3.4. Furthermore, it is reasonable to expect lamps with efficiencies exceeding 10% to be fabricated if we also consider the light extraction efficiency improvement effects produced by resin sealing [1].

In the present study, the dislocation density was still just  $6 \times 10^8/\text{cm}^2$ . It is believed that in the future we can expect the output to be improved and external quantum efficiencies to exceed 20% as a result of achieving further reductions in the dislocation density by optimizing the growth conditions and improving the LEPS technique.

## 10.6 Building of white LED prototypes utilizing blue LEDs

In addition to using a combination of RGB fluorescent materials and UV LEDs, which has been suggested in the course of the project, white LEDs can be fabricated using blue LEDs + yellow fluorescent materials. In this study, for the purpose of comparison with white LEDs fabricated using UV LEDs, we fabricated blue LED prototypes and white LEDs utilizing the blue LEDs.

### 10.6.1 Experimental method

With the exception of increasing the In composition of the emitting layer in order to increase the wavelength, LED wafers were fabricated by the same method as in Section 10.3. The epi-wafers were used by Stanley Electric Co., Ltd. to make chips, made into lamps, and combined with yellow fluorescent materials to fabricate white LEDs.

### 10.6.2 Results and discussion

The current value dependence of the external quantum efficiency of resin-sealed blue LED lamps is shown in FIG. 10.6.1, and the characteristics of the lamps are shown in Table 10.6.1.

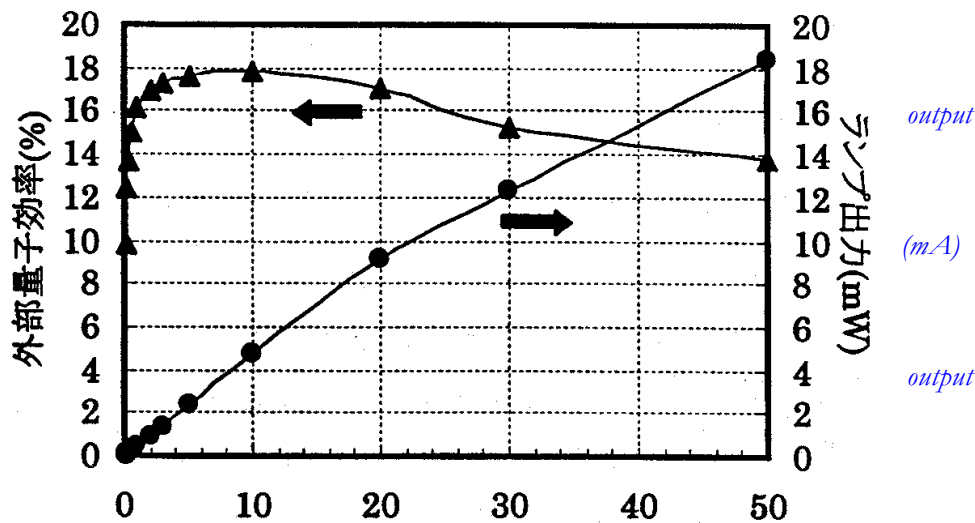
FIG. 10.6.1 Current dependence of external quantum efficiency and of blue LED lamps

[Keys, FIG. 10.6.1]

(X-axis) Current value

(Y-axis, left) External quantum efficiency.

(Y-axis, right) Chip (mW).



Emission wavelength	FWHM	Lamp Output	External Quantum Efficiency
468.6 nm	22.9 nm	9.11 mW	17.1%

Table 10.6.1 Characteristics of blue LED lamps (at 20 mA)

The value of the electric current at which the external quantum efficiency reached a maximum was 10 mA, which was a lower current value in comparison with the value (50 mA) for UV LEDs. This is believed to be due to the fact that, in comparison with UV LEDs, the influence of dislocations and other non-radiative centers in blue LEDs is unlikely to be stronger. As concerns the LED characteristics obtained at 20 mA, a lamp output of 9.1 mW and a high luminous efficacy with an external quantum efficiency of 17.1% were obtained. The efficacy of the white LED lamps fabricated using the chips was 12 lm/W.

## 10.7 Summary

As a result of studies conducted to determine the correct amount of Si to be used for the doping of the barrier layers in UV LEDs, we obtained an output of 1.2 mW (at 20 mA) at a Si doping level of approximately  $2 \times 10^{17} \text{ cm}^{-3}$ . It is believed that there is a coexistence of an effect in which Mg diffusion is suppressed by Si doping on the emitting layer, and an effect whereby Si doping decreases the crystal quality. Using the chips to fabricate flip chip-type LEDs resulted in an approximately 2.4-fold improvement in the output. Furthermore, as a result of building a prototype of a white LED lamp utilizing RGB fluorescent materials, we obtained a luminous efficacy of 1.7 lm/W.

To achieve a reduction in the dislocation density of GaN by mask-less one-step growth, we used a technique (LEPS technique), in which the substrate was processed to impart it with a groove-and-ridge topography and create preferential conditions for lateral growth from the ridges. As a result, we were able to significantly reduce the dislocation density in the lateral growth portions. In addition, as a result of applying the LEPS technique to UV LEDs, we obtained an output of 2.5 mW, which was approximately 3 times higher in comparison with growth on ordinary substrates. This demonstrated that the LEPS technique was an efficient method of dislocation density reduction and emission output improvement.

For the purpose of comparison with UV LEDs, we fabricated a blue LED lamp prototype and a white LED lamp, with the blue LED lamp displaying an output of 9.1 mW and an external quantum efficiency of 17.1%. In addition, the efficacy of the white LED was 12 lm/W.

## 10.8 Future Plans

In this study, we were able to substantiate the ability of the LEPS technique to provide dislocation density reduction and improvements in terms of the UV emission output. However, even in the low dislocation region the dislocation density, as observed by CL, is still on the order of  $10^7/\text{cm}^2$ , or  $6 \times 10^8/\text{cm}^2$  on the average. In the future, we are planning to go ahead with investigations into the LEPS technique so as to achieve further reductions in the density of dislocations. The use of the LEPS technique has allowed us to improve the external quantum efficiency of UV LEDs at 20 mA to 3.7%. We believe that in the future it will be possible to realize UV LED lamps with an external quantum efficiency exceeding 20% by further optimizing the growth conditions and component design and by improving the light extraction efficiency by means of flip chip mounting and resin sealing. In the future, we are planning to develop our cooperation with the Optical Source Device Group and continue further development of high-output UV LED lamps and white-light lamps using RGB fluorescent materials.

Furthermore, we are planning to conduct investigations into the application to UV LEDs of new substrates, such as the low-dislocation GaN substrates fabricated by the enterprises of the Substrate Group, which will be replacing the currently used sapphire substrates. We are planning to achieve lower dislocation densities than those achievable in current LEPS-GaN and realize UV LEDs of higher outputs. In addition, we are planning to examine the relationship between the output improvements due to dislocation density reduction and the wavelength and realize light-emitting components with the highest possible output in the UV region.

## 10.9 References

- [1] 1999 Achievement Report for Light for the 21<sup>st</sup> Century Project, 12.4, p. 217.
- [2] 1999 Achievement Report for Light for the 21<sup>st</sup> Century Project, 12.4, p. 222.
- [3] A. Usui, H. Sunakawa, A. Sakai, and A. Yamaguchi: Jpn. J. Appl. Phys. 36 (1997) L899
- [4] K. Linthicum, T. Gehrke, D. Thomson, E. Carlson, P. Rajagopal, T. Smith, D. Batchelor, and R. Davis: Appl. Phys. Lett. 75 (1999) 196.
- [5] I. Kidoguchi, A. Ishibashi, G. Sugahara, A. Tsujimura, and Y. Ban: Jpn. J. Appl. Phys. 39 (2000) L453.
- [6] Mizutani et al.: Preprints of Applied Physics Society, Spring of 2000, 28p-YQ-5.
- [7] For example, A. Sakai, H. Sunakawa, and A. Usui: Appl. Phys. Lett. 71 (1997) p. 2259.
- [8] For example, S. Nagahama, N. Iwasa, M. Senoh, T. Matsushita, Y. Sugimoto, H. Kiyoku, T. Kozaki, M. Sano, H. Matsumura, H. Umemoto, K. Chodo, and T. Mukai: Jpn. J. Appl. Phys. 39 (2000) L647.
- [9] T. Mukai, and S. Nakamura: Jpn. J. Appl. Phys. 38 (1999) p. 5735.
- [10] T. Mukai, M. Yamada, and S. Nakamura: Jpn. J. Appl. Phys. 38 (1999) p. 3976.

# 11 Development of High-efficiency Phosphors

## 11.1 Achievements in 1998 and 1999

The “Light for the 21<sup>st</sup> Century” Project, whose objective is the use of light from white LEDs for illumination purposes, requires phosphors permitting efficient conversion of UV light emitted by GaN-based LEDs into visible light. Because various other characteristics are required of the phosphors in addition to the conversion efficiency, we have been studying methods of examination and evaluation of such characteristics while at the same time striving to select suitable phosphors from among the existing phosphors and develop new materials with a view to achieve a quantum efficiency of  $\geq 90\%$ . The results obtained in 1998 and 1999 are described below.

### 11.1.1 Review of phosphors and selection of model phosphors

Based on data accumulated from literature, patent searches, and measurement of available samples, to obtain high color rendering 3-wavelength-type fluorescent lamps, we decided to proceed based on the principle of producing white light by means of mixing phosphors emitting in the blue, green, and red regions of the long wavelength UV. We selected 5 different kinds of model phosphors in order to further investigate their luminance and lifetime characteristics under various packaging conditions.

### 11.1.2 Improvements in characteristics of red phosphors

Among the blue, green, and red model phosphors, the luminance of the red materials is the lowest, which decreases the overall luminance obtained when colors are mixed to produce white light. Hence, we started our research by narrowing down the development objective to red phosphors. The model red phosphor we used was europium-activated yttrium oxysulfide ( $Y_2O_2S:Eu$ ), which is utilized as a red phosphor in TVs. To improve its practical characteristics, numerous studies ranging from manufacturing methods to the emission theory had been conducted on the material, but it had never been the subject of research related to UV excitation. Based on information on electron-beam excitation, we carried out synthesis experiments by adding various chemical elements and substituting them for portions of the host composition. As a result, a tendency towards increased intensity in the 360~380 nm region of the excitation spectrum was observed with several elements, such as Ga, Lu, Sc, Mn, Mg, etc., but these effects were insufficient.

### 11.1.3 Introduction of equipment for phosphor firing

The basic characteristics of phosphors are dependent primarily on a combination of raw material selection, firing temperature, firing time, and firing atmosphere. To be able to investigate the widest possible range of synthesis conditions for the red phosphors and other phosphors, we conducted in-depth investigations into the necessary raw materials, furnace construction, and specifications and then designed and installed an experimental furnace.

### 11.1.4 Precise measurements and evaluation of phosphor emission characteristics

To obtain improved quantum efficiency, we examined available literature, and, at the same time, gained practical experience in system design by trial and error, which finally allowed us to introduce precise

measurement and evaluation equipment in 1999. Using NBS standard phosphors as test samples, we conducted material makeup verification, and the results were confirmed to be relatively satisfactory.

## 11.2 Summary of Research and Development in 2000

The light sources produced in the course of the “Light for the 21<sup>st</sup> Century” Project are evaluated by the total efficiency of the LEDs, which serve as the excitation light sources, the phosphors, and the lighting fixtures, whereas the efficiency of the phosphors themselves is evaluated by the quantum efficiency. In the project, a target value was set for the quantum efficiency of the phosphors. The quantum efficiency of phosphors, unlike that of LEDs, is seldom subjected to measurements. The measurements are limited to optical techniques and precise measurements require considerable time and labor, and, in addition to that, the methods of measurements cannot be considered fully established and there is considerable disagreement between previously reported values. However, the value of the quantum efficiency is very significant in that it makes it possible to confirm the current level and see possibilities via comparison with target values (theoretical values) of phosphor efficiency. In addition, because phosphors are usually white and have a considerably reduced capacity for absorption of excitation light in the long wavelength UV ~ blue region, it is believed that an important task will be to calculate the efficiency of emission by precisely separating and measuring absorption and emission. With account taken of the above, in 1999 we introduced a system for the precise measurement and evaluation of phosphor emission characteristics and completed preliminary evaluation of its functional properties.

This year, our research objectives have included a search for high-efficiency phosphors by re-evaluating conventional phosphors from a quantum efficiency standpoint and applying the measurement data to the development of new high-efficiency phosphors. In the present report, we focus first of all on the method of quantum efficiency measurement, on simple and straightforward verification of measurement values, as well as on discovering problems and application to actual measurements, and then discuss the relationship of the current phosphor measurement results with respect to the target being sought, endorse a novel candidate for a second model green phosphor, and discuss the results of experiments aimed at improving the efficiency of red phosphors.

## 11.3 Quantum Efficiency Measurements

### 11.3.1 Methods and means

#### 11.3.1.1 Definition of quantum efficiency

Quantum efficiency is the proportion, in which the excitation light is converted into emission of light, and is represented by the following formula:

[Internal] Quantum efficiency = number of photons converted into emission / number of photons absorbed by the phosphor

The formula does not take into consideration the energy loss due to the Stokes shift. If we exclude from consideration certain rare cases of special emission processes, such as double photon emission, avalanche emission, etc., the ideal quantum efficiency will be 1. There have been reports [1, 2, 3] describing phosphor measurement results where the actual efficiency values were close to 1.

The proportion of photons of the excitation light absorbed by the phosphor is an important characteristic in quantum efficiency measurements. Albeit related to the intrinsic physical properties of the phosphor, the value varies greatly depending on the way the phosphor is used, such as positioning with respect to the excitation light source, film thickness in case of using it in the form of a coating film, etc. The coefficient of absorption is defined by the following formula:

Coefficient of absorption = (number of photons used for irradiation – number of reflected photons) / number of photons used for irradiation

Another definition of quantum efficiency is used for external quantum efficiency, which is expressed by the following formula:

External quantum efficiency = number of photons converted into emission / number of photons used to irradiate the phosphor

In case of absolute evaluation of the external quantum efficiency as a phosphor characteristic, a problem arises in connection with the coefficient of absorption. In the present report, it is assumed that the term “quantum efficiency” stands for “internal quantum efficiency,” and, in order to avoid confusion, the term “emission efficiency” is used in the sense of “external quantum efficiency.” Because improvements in quantum efficiency depend on the phosphors used and improvements in the efficiency of emission have to be studied by fine-tuning the characteristics of the phosphors and packaging conditions, in the future we will proceed by paying particular attention to three characteristics.

### 11.3.1.2 Summary of instrumentation equipment

Light of a specified wavelength was extracted from a xenon lamp using a spectrometer and guided to a 4-inch integrating sphere via a condenser lens and a mirror. Phosphor powder was charged in a cell and placed on the bottom of the integrating sphere. All of the luminous energy of the phosphor emitted under the action of the excitation light was guided to an instantaneous spectrophotometer MCPD-2000 via an optical fiber. The number of photons absorbed by the phosphor was calculated by placing a white plate of known reflectance in the same position as the phosphor sample, performing identical measurements, and then using the data regarding the difference between the two spectra in the excitation light wavelength region; in addition, the number of emitted photons was calculated from the emission spectrum in the visible region (400~780 nm). A formula we used for the calculations, a description of the instrumentation equipment, and a flow-chart are provided below.

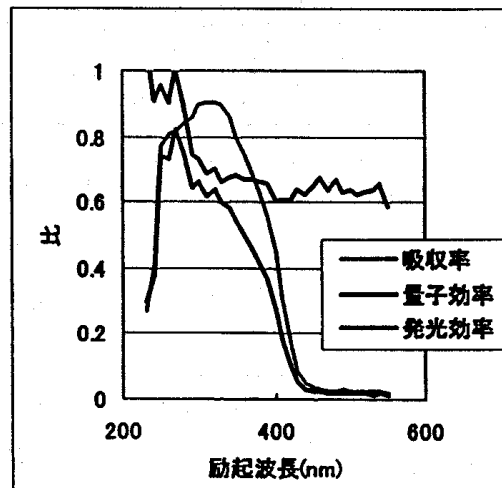
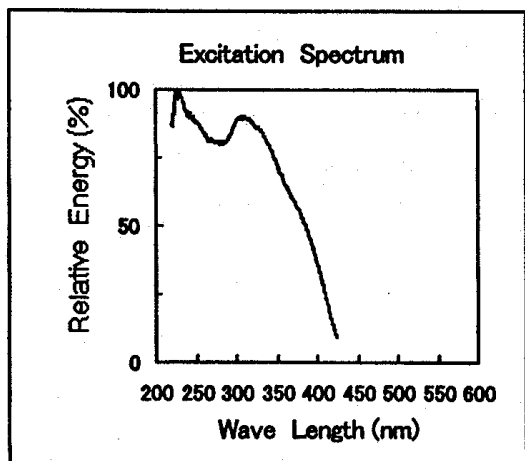
$$\text{Quantum efficiency}_\eta = \frac{\int \lambda \cdot P(\lambda) d\lambda}{\int \lambda \cdot [E(\lambda) - R(\lambda)] d\lambda}, \text{ where}$$

E( $\lambda$ ): Excitation spectrum used to irradiate phosphor

R( $\lambda$ ): Reflection spectrum of excitation light

P( $\lambda$ ): Emission spectrum





Left: FIG. 11.3.2-(1) BAM excitation spectrum

Right: FIG. 11.3.2-(2) BAM emission characteristics

[Keys, FIG. 11.3.2-(2)]

(X-axis) Excitation wavelength (nm)

(Box, top to bottom) Coefficient of absorption

Quantum efficiency

Emission efficiency

Data concerning the quantum efficiency of BaMgAl<sub>10</sub>O<sub>17</sub>:Eu under short wavelength UV excitation reported up till now are shown in Table 11.3.2-(1).

	Measured by	Excitation wavelength (nm)	Quantum efficiency	References
1	A	254	0.84	(1)
2	B	254	1.03	(2)
3	A	147	0.67	(1)
4	Present study	254	0.98	
5	Present study	370	0.68	

Table 11.3.2-(1) Reported values of quantum efficiency

The differences between the measurement values in the table above are believed to be due to differences in the samples.

The samples in the present study were randomly selected. At 254 nm the value came close to 1, and dropped below 0.7 at 370 nm. This reduction was much greater than initially expected, and in the future it will be necessary to analyze its mechanism and consider ways to improve the efficiency.

**11.3.2.2 Measurement results for blue and green phosphors**

Reported here are characteristic results selected from the results we obtained for red, green, and blue emission of model phosphors. Below, the phosphors discussed in the present report are represented by abbreviations listed in the following table.

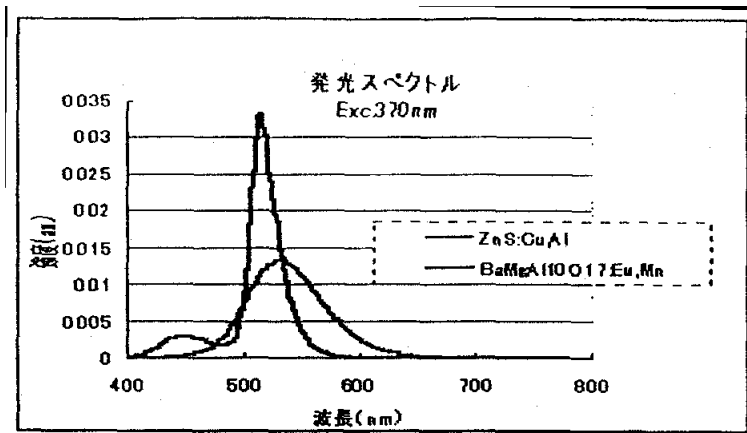
Emission color	Composition	Name (abbreviation)	Notes
Blue	BaMgAl <sub>10</sub> O <sub>17</sub> :Eu	BAM	Primary model
	(Sr,Ca,Ba,Mg) <sub>10</sub> (PO <sub>4</sub> ) <sub>6</sub> Cl <sub>2</sub> :Eu	SCA	Primary model
	Ca <sub>2</sub> B <sub>5</sub> O <sub>9</sub> Cl:Eu	CCB	
Green	ZnS:Cu,Al	P22-GN	Primary model
	BaMgAl <sub>10</sub> O <sub>17</sub> :Eu,Mn	LP-G3	
Orange	(Y,Gd) <sub>3</sub> Al <sub>5</sub> O <sub>12</sub> :Ce	P46Y	Primary model
Red	Y <sub>2</sub> O <sub>2</sub> S:Eu	P22-RE3	Primary model

Table 11.3.2-(2) Composition and names of phosphors

CCB phosphor was developed for use in lamps, in the same manner as the other two kinds of blue model phosphors. The results obtained by measuring their respective quantum, absorption, and emission characteristics are as shown in FIGs. 11.3.2-(4), (6), (8). While there was absolutely no difference in terms of quantum efficiency, the absorption coefficient of CCB was approximately 10% higher, and its emission efficiency was also better.

As far green phosphors were concerned, P22-GN, which had been subjected to the same measurements, did not exhibit any degradation problems when used in a LED; however, generally speaking, atmosphere exposure test results had shown that it could in no way be considered stable. LP-G3 was another candidate used as insurance in case P22-GN exhibited degradation problems. LP-G3 has a BAM composition and exhibits a narrower emission spectrum than P22-GN with two peaks, as shown in FIG. 11.3.2-(3). Since the start of the project, its luminance at 254 nm has been improved.

FIG. 11.3.2-(3) Green phosphor  
[Keys, FIG. 11.3.2-(3)]  
(X-axis) Wavelength (nm).  
(Y-axis) Illegible  
(Across top) Emission spectra



spectra

The results of the measurements shown in FIGs. 11.3.2-(5), -(7), (9).

When excitation was carried out nm, the quantum efficiency of G3 was higher than that of P22- and exhibited almost the same characteristics as in case of blue However, because the coefficient of absorption of P22-GN was higher, approximately the same characteristics were obtained in terms of the efficiency of emission. LP-G3 was recommended as a second model green phosphor.

are and - at 370 LP-GN BAM.

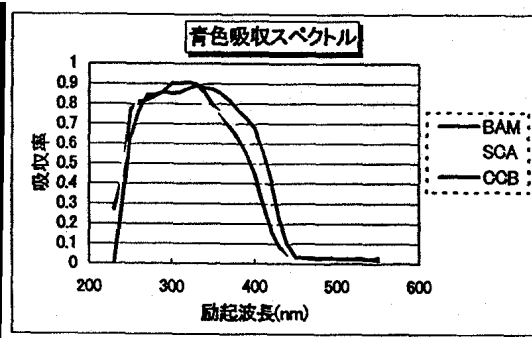


図11.3.2-(4) 青色蛍光体吸収スペクトル

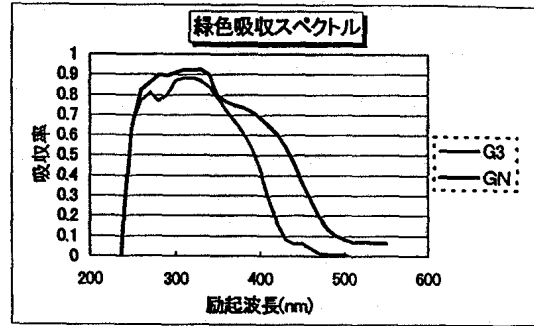


図11.3.2-(5) 緑色蛍光体吸収スペクトル

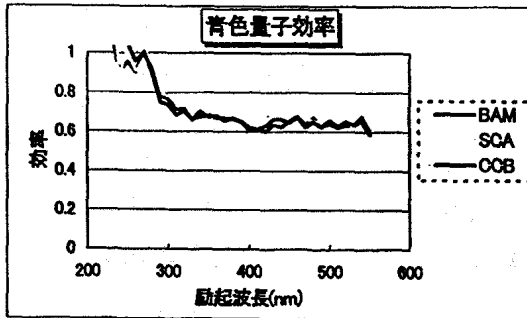


図11.3.2-(6) 青色蛍光体量子効率

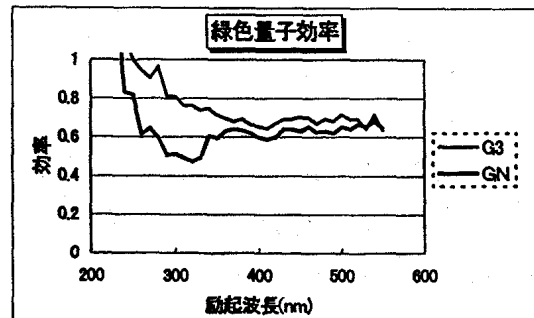


図11.3.2-(7) 緑色蛍光体量子効率

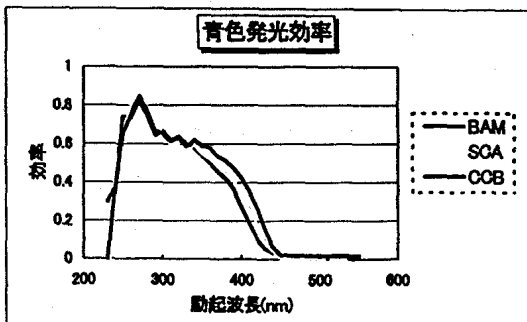


図11.3.2-(8) 青色蛍光体発光効率

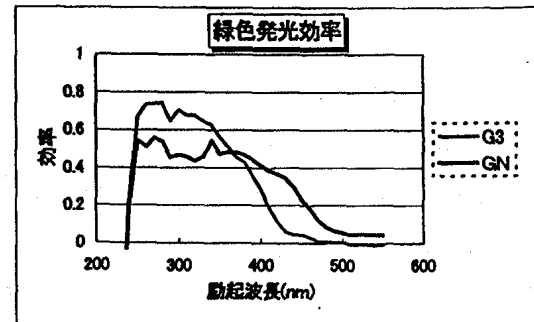


図11.3.2-(9) 緑色蛍光体発光効率

FIG. 11.3.2-(4) Blue phosphor absorption spectrum

FIG. 11.3.2-(5) Green phosphor absorption spectrum

FIG. 11.3.2-(6) Blue phosphor quantum efficiency

FIG. 11.3.2-(7) Green phosphor quantum efficiency

FIG. 11.3.2-(8) Blue phosphor emission efficiency

FIG. 11.3.2-(9) Green phosphor emission efficiency

[Keys, FIGs. 11.3.2-(4), (5)]: (X-axis) Excitation wavelength (nm); (Y-axis) Absorption coefficient

[Keys, FIGs. 11.3.2-(6), (7), (8), (9)]: (X-axis) Excitation wavelength (nm); (Y-axis) Efficiency.

### 11.3.2.3 Simulation of white-color-producing color mixing

We estimated the brightness obtained in synthesizing white light by combining the red, green, and blue phosphors used in the present study. The color temperature of white light was 6700K, CIE(x,y)=(0.3089,0.3252). We used computation software we developed ourselves.

Phosphors			Mixing Ratios			
Green	Red	Blue	Green	Red	Blue	Relative luminance
P22-GN	P22-RE3	BAM	22.8%	55.8%	21.3%	100.0%
LP-G3	P22-RE3	BAM	18.5%	65.0%	16.5%	88.7%
P22-GN	P22-RE3	CCB	32.7%	53.7%	13.6%	107.8%
P22-GN	P22-RE3	SCA	25.7%	54.4%	19.9%	105.2%
LP-G3	P22-RE3	CCB	24.1%	66.4%	9.6%	90.7%
LP-G3	P22-RE3	SCA	20.2%	64.8%	15.0%	91.4%

*Table 11.3.2-(3) Mixing ratios and luminance estimates of white phosphors*

As can be seen from the simulation results, in comparison with BAM, admixture of CCB and SCA produces a higher luminance. The CCB mixing ratio becomes smaller. In case of the green color, the mixing ratio of P22-GN is higher than that of LP-G3, and the white color luminance is higher. When a combination of GN-CCB was used, the brightness results obtained were approximately 8% better than in case of using the model phosphor. In the future we will examine the corresponding color rendering properties.

### 11.3.2.4 Study of red phosphors

We are currently evaluating and analyzing the relationship between the absorption efficiency and quantum efficiency under various phosphor composition conditions. Because we have obtained samples that are close to 150~200% in terms of emission efficiency, we will continue our investigations.

## 11.4 Evaluation of Temperature Characteristics

### 11.4.1 Methods and means

Considering the possible forms in which phosphors will be incorporated in LEDs and used for illumination in the future, it becomes apparent that it will be very important to be able to maintain excellent emission within a wide range of temperature conditions, taking into consideration generation of heat in case of densely packed LED assemblies, outdoor illumination in cold regions, etc. We are building a phosphor temperature characteristic evaluation system for investigating changes in the phosphor emission characteristics by controlling the ambient temperature and will use it in selecting phosphors and improving temperature characteristics.

### 11.4.2 Results and discussion

#### 11.4.2.1 Equipment specifications

The specifications of the installed system include the following.

- Temperature control range (−20~250°C)
- Excitation light sources (black lights, sterilizing lamps, xenon spectroscopic lights)

- Light source monitoring function
- Computation software
- Measurement parameters (luminance, emission spectrum, temperature)

#### 11.4.2.2 Measurements

Operation confirmation and final acceptance will be completed.

In 2001, we will measure the temperature characteristics of the phosphors and create a database.

## 11.5 Summary

We have decided on the method of phosphor quantum efficiency measurements. The measurements involve a process of separate evaluation of three characteristics: the coefficient of absorption, the quantum efficiency, and the emission efficiency, and, as a result of establishing feedback between the obtained information and experiments aimed at improving the composition of the red phosphors, we have managed to improve their emission efficiency by 150~200%. In addition, some green and blue phosphors exhibiting a higher quantum efficiency than that of the primary models have also been discovered. However, it has been found that even in the best samples, the quantum efficiency of the current phosphors, including not only red phosphors, but also blue and green ones, as shown in the table below, is at the level of about 60%, which is still far from the target 90%.

Emission color	Composition	Quantum Efficiency
Blue	BaMgAl <sub>10</sub> O <sub>17</sub> :Eu (Sr,Ca,Ba,Mg) <sub>10</sub> (PO <sub>4</sub> ) <sub>6</sub> Cl <sub>2</sub> :Eu	62%
Green	BaMgAl <sub>10</sub> O <sub>17</sub> :Eu,Mn	64%
Red	Y <sub>2</sub> O <sub>2</sub> S:Eu	60%
Mixed white		>60%

*Table 11.5 Current quantum efficiency*

## 11.6 Future Plans

### 11.6.1 Quantum efficiency improvement

We will continue our investigations by repeating the cycle depicted in the following figure. Specifically, we will focus on search for sensitizers capable of energy transfer to the Eu<sup>3+</sup> emission centers of the red phosphor Ln<sub>2</sub>O<sub>2</sub>S:Eu to improve its quantum and emission efficiency. The results will be carried over to other green and blue phosphors.

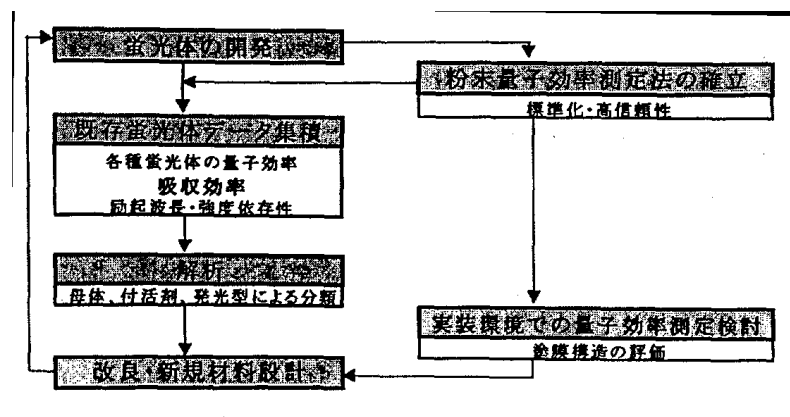
FIG. 11.6.- (1) Methods of quantum efficiency improvement

[Keys, FIG. 11.6.- (1)]

(Left column, top to bottom)

Phosphor development →  
 Collecting data on existing phosphors, including: quantum efficiency of various phosphors, coefficients of absorption, excitation wavelength & intensity dependence →  
 Analysis, including: classification by matrix, activating agent, type of emission

Improvement of existing and design of new materials



→

(Right column, top to bottom) Establishing methods of quantum efficiency measurement for powders, including: standardization, increasing reliability → Study of quantum efficiency measurement under actual packaging conditions, including: evaluation of coating film structure.

## 11.6.2 Methods of synthesis

We will focus on the study of firing in various kinds of atmosphere and expanding our research by selecting conditions different from those used before. Because we are still a long way from the target quantum efficiency value, we need new approaches and will explore possibilities offered by the use of thin films and ultra-fine microparticles, which have been said to improve the quantum efficiency.

## 11.6.3 Other

In anticipation of problems associated with practical applications, we will consider the following issues.

- Setting up a system for analysis of temperature characteristic measurements; instrumentation, evaluation.
- Design and introduction of degradation characteristic acceleration test equipment
- Mixed white color simulation
- Elucidation of the emission mechanism, joint research in cooperation with Yamaguchi University

## 11.7 References

- [1] Okubo, et al.: Journal of the Illuminating Engineering Institute of Japan, 83-2, pp. 87~93 (1999).
- [2] Narita, Kazuo: Journal of the Illuminating Engineering Institute of Japan, 69-2, pp. 15~19 (1985).
- [3] Brill, A.: Luminescence of Organic and Inorganic Materials. Pp. 479~493 (1962).

# 12 Electrode Attachment, Packaging, and White LED Development

## 12.1 Achievements in 1998~1999

### 12.1.1 Achievements in 1998

#### 12.1.1.1 Development of electrode forming techniques

In order to decrease resistance losses due to consumption by the electrodes, it is necessary to decrease the contact losses between the electrodes and GaN. First of all, we investigated methods of forming transparent electrodes and obtained a contact resistance of  $3 \times 10^{-3} \Omega\text{cm}^2$  and a 50% electrode transmittance by subjecting Ni 1 nm/Au 10 nm to heat treatment in an oxygen atmosphere. In addition, in the Mg/Au system, we obtained a contact resistance of  $1 \times 10^{-3} \Omega\text{cm}^2$  and a 70% electrode transmittance, but this involved problems with electrode handling.

#### 12.1.1.2 Improvements in light extraction efficiency

Light emitted from ordinary LEDs constitutes 30% of the light emitted from the light-emitting layer. The remaining 70% is confined inside the chip and ultimately turns into heat. Therefore, it is important to increase the light extraction efficiency. In order to suppress the internal reflection inside the chip, we formed an anti-reflective film (AR film) on a GaN epitaxial wafer having a thin-film Au/Ni electrode formed thereon; however, when the transmittance was estimated, it was found that the gain was only 6% or so. In addition, we conducted a study of high-reflectance electrodes in flip-chip type LEDs, which offer considerable advantages in terms of light extraction efficiency improvements.

#### 12.1.1.3 Development of UV-resistant sealing technology

We studied the characteristics of currently used epoxy resins.

### 12.1.2 Achievements in 1999

#### 12.1.2.1 Development of electrode forming techniques

We determined Ni/Ag electrode forming conditions for high-reflectance p-type electrodes used in flip-chip diodes and were able to obtain a contact resistance of  $3 \times 10^{-3} \Omega\text{cm}^2$  by means of subjecting a Ni 1 nm/Ag 200 nm structure to a 60-sec alloying treatment at 500°C in an electron beam vapor deposition apparatus.

As far as Ni/Rh is concerned, film forming by sputtering could not produce the necessary ohmic properties of the contact between the electrode and the p-GaN.

We studied pre-treatment procedures for forming electrode using p-GaN epitaxial wafers and discovered that contact resistances constituting 1/2 of the prior-art resistances could be obtained in the Ni/Au structure using ammonia boiling treatment instead of the conventional treatment with an aqueous solution of HCl or an aqueous solution of HF.

#### 12.1.2.2 Improvements in light extraction efficiency

We fabricated flip-chip type LEDs using UV GaN epitaxial wafers and confirmed that the light output was doubled in comparison with conventional transparent electrodes.

### 12.1.2.3 Development of white LEDs

In order to achieve the target light-generation efficiency, we used the spectra of model phosphors to estimate the light intensity of UV LEDs.

## 12.2 Summary of Research and Development in 2000

In the field of electrode forming technology, we studied materials possessing a higher reflectance and a lower contact resistance than the conventional materials used for p-type electrodes and n-type electrodes. In the case of n-type electrodes, we were able to achieve a reflectance of 70% and a contact resistance of  $2 \times 10^{-5} \Omega \text{cm}^2$  by optimizing the Ti/Al structure. In addition, we tried new materials, using ZnO/Ni/Ag for n-type electrodes, and obtained results equivalent to those of Ti/Al. As for p-type electrodes, we studied Rh, Pt-based electrode materials and obtained electrode materials possessing contact resistances lower than that of Ni/Ag.

In an attempt to improve the light extraction efficiency, we conducted studies of chip shape. Light emitted from the light-emitting section becomes bottled up in the GaN semiconductor layer, with part of it emitted below the chip, part from the edge faces of the chip, and part of it undergoing multiple reflection and absorbed in the semiconductor layer. It has been suggested that the semiconductor layer etching edge should be tilted in order to reflect internally absorbed light (light propagating inside the GaN layer). This year, we developed a technology for creating an inclined semiconductor layer surface using the dry etching technique.

In developing white LED devices, we studied phosphor coating techniques and conducted an evaluation of the basic characteristics of RGB model phosphors, and, based on the obtained results, conducted simulation of mixing of RGB phosphors to produce white light. In addition, we conducted a study of the methods used for forming the phosphor layer and control of the UV light transmitted via the phosphor layer. Furthermore, we conducted an evaluation of the color rendering properties and emission characteristics of a white-color LED lamp prototype. As a result, by means of forming an optical thin-film filter on top of the phosphor layer mounted on a UV LED chip such that the UV light was reflected from the filter while visible light passed through it, and, furthermore, by coating the edges of the LED chip with a phosphor, we were able to decrease the amount of transmitted UV light from 31% to 13% and confirmed a 30% improvement in the total flux of the white LED lamp.

In the development of UV-resistant sealing technology, our goal was to develop epoxy resins resistant to UV degradation by means of compounding epoxy resins. This year we investigated degradation behavior by means of UV irradiation tests, high-temperature tests, etc. As a result, a possibility of developing a resin with a low level of UV degradation was discovered by using an acid anhydride-curable epoxy resin composition, in which we used a phosphorus-based cure promoter and an epoxy monomer obtained by introducing alicyclic groups into hydrogenated bisphenol A glycidyl ether.

## 12.3 Development of electrode forming techniques

### 12.3.1 Methods and Means

#### 12.3.1.1 N-type electrodes

##### (a) Ti/Al electrodes

In order to study n-type electrode materials, we used an undoped GaN epitaxial wafer (carrier density:  $\sim 1 \times 10^{17} \text{ cm}^{-3}$ ), on which a round TLM (Transmission Line Model [1]) pattern was formed by means of photolithography. Using electron beam vapor deposition, we formed a Ti (0, 1, 2, 2.5 nm)/Al 300 nm film. An RTA (Rapid Thermal Annealing) apparatus was used to conduct alloying at  $400^\circ\text{C} \sim 700^\circ\text{C}$  for 10 to 120

sec, followed by measuring the contact resistance. Simultaneously, we formed a thin film on top of a quartz substrate (thickness: 1 mm) to [illegible – trans.] of the electrode.

#### (b) ZnO/Ni/Ag electrodes

[illegible – trans.] Sample fabrication techniques are described below. A round TLM pattern was formed on n-type GaN (carrier density:  $\sim 5 \times 10^{18} \text{ cm}^{-3}$ ) using photolithography, with a 64-nm ZnO thin film formed at room temperature using the DC arc-discharge ion plating technique. The carrier density of the ZnO thin film was  $\sim 2 \times 10^{21} \text{ cm}^{-3}$  and the mobility was  $\sim 12.8 \text{ cm}^2 \text{ V}^{-1} \text{ s}^{-1}$ . After that, a thin film of Ni 1 nm/Ag 300 nm was formed thereon, a pattern was formed by lift-off, and measurement of the contact resistance was carried out. Subsequently, in order to compare the Ti/Al electrode and the ZnO electrode, we fabricated LEDs, in which n-type electrode Ti/Al and ZnO were used to make n-type electrodes, and evaluation of the characteristics of the n-type electrodes was carried out by measuring their forward voltage.

#### 12.3.1.2 P-type electrodes

To study p-type electrode materials, we formed electrodes on a p-type GaN wafer with a hole carrier density of  $5 \times 10^{18} \text{ cm}^{-3}$  and carried out the same evaluation as in the case of n-type electrode materials.

### 12.3.2 Results and Discussion

#### 12.3.2.1 N-type electrodes

##### a) Ti/Al-based electrodes

Results of contact resistance measurement for Ti/Al-based electrodes on an undoped GaN epitaxial wafer are shown in Table 12.3.2-(1).

Electrodes	Alloying Conditions	Contact Resistance [ $\Omega \text{cm}^2$ ]
Al alone	-----	-----
Ti 1 nm/Al 300 nm	400~700°C, 10~120 sec	Schottky
Ti 2 nm/Al 300 nm	450°C, 1 min	$2.43 \times 10^{-5}$
Ti 25 nm/Al 300 nm	500°C, 20 sec	$4.18 \times 10^{-5}$

Table 12.3.2-(1) Contact resistant values for various electrodes

The Al electrode exhibited poor adhesion properties with respect to the GaN surface, and a working electrode could not be formed. In addition, according to the results of other studies, electrodes made up of Al alone could be formed but their contact resistance was very high, at  $10^{-3} \sim 10^{-4} \Omega \text{cm}^2$  [2], and it is believed that Al-only electrodes are unsuitable for application in electronic devices. Also, the alloying of the electrode made up of Ti 1 nm/Al 300 nm was carried out at 400~700°C for 10~120 sec, but no ohmic contact was obtained.

Sandwiching Ti between Al and GaN makes it possible to decrease the contact resistance of the electrode. This is believed to be due to the fact that Ti forms grains by absorbing oxygen from the naturally oxidized film, which is generated on the GaN surface as a result of the alloying treatment after electrode film forming, and oxygen-free GaN becomes exposed and Al comes in contact with it [3]. By contrast, it is believed that in case of Al alone, the effect of removal of the naturally oxidized film from the surface is absent, which leads to poor adhesion and an increase in the contact resistance. It is believed that in case of Ti 1 nm an ohmic contact is impossible to obtain without completely removing the oxygen from the surface. On the other

hand, an ohmic contact with n-type GaN was formed and a contact resistance of  $2.43 \times 10^{-5} \Omega\text{cm}^2$  was obtained in the Ti/Al electrode with a Ti layer of 2 nm or more.

Next, FIG. 12.3.2-(1) shows the reflectance of the Ti/Al electrodes. It was noted that the reflectance of the Ti 2 nm/Al 300 nm electrode exhibited a tendency to decrease with increasing alloying temperature. An ohmic contact with GaN cannot be obtained if alloying is not carried out at a temperature of 450°C or higher after film forming. In the past, the alloying treatment was carried out 500°C for 20 seconds. Under the above-mentioned conditions, the decrease in the reflectance was approximately 10%, but conducting the alloying treatment at 450°C for 1 minute allowed us to lower the decrease in the electrode reflectance to 6%. The decrease in the reflectance after alloying is believed to be caused by irregular reflection of light by grains formed as a result of Ti absorbing Al and surface oxygen during heating.

The results confirmed that the Ti 2 nm/Al 300 nm electrode for n-type GaN simultaneously meets the requirements for a high reflectance (70%) and a low contact resistance ( $2.43 \times 10^{-5} \Omega\text{cm}^2$ ) when the alloying treatment is conducted for 1 minute at 450°C.

FIG. 12.3.2-(1) Ti/Al film reflectance measured from the quartz side

[Keys, FIG. 12.3.2-(1)]

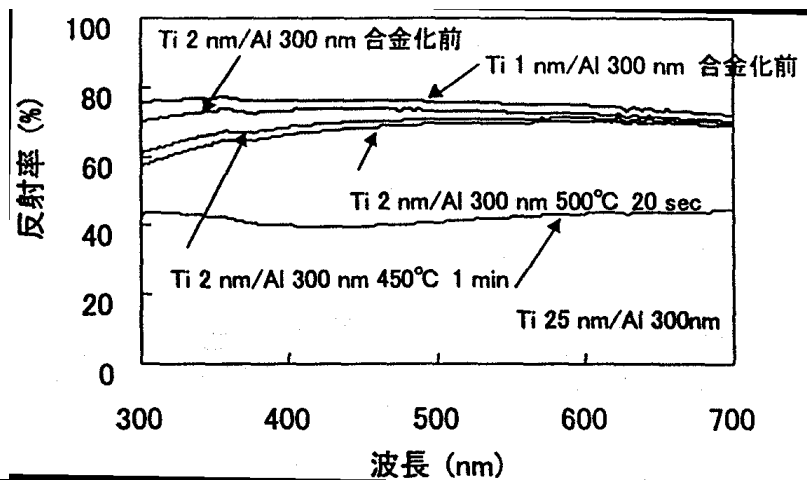
(X-axis) Wavelength (nm)

(Y-axis) Reflectance (%)

(Inside, top left) Ti 2 nm/Al 300 nm prior to alloying

(Inside, top right) Ti 1 nm/Al 300 nm prior to alloying

b) ZnO-based electrodes



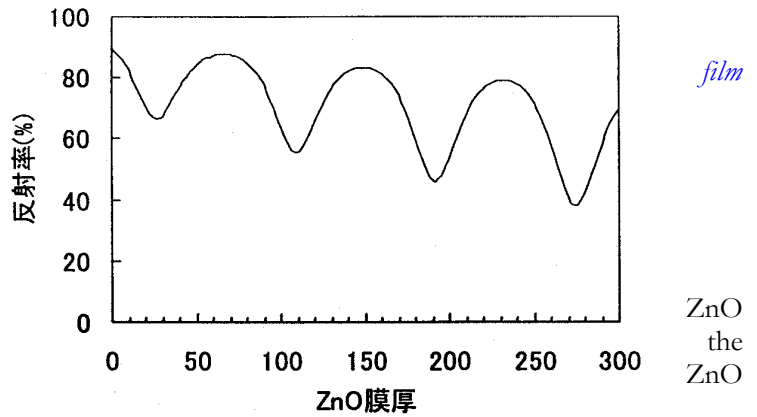
Ag
Ni

ZnO
n-type GaN

FIG. 12.3.2-(2) N-type ZnO-based electrode structure

The Ti/Al electrodes need alloying treatment at a temperature of not less than 450°C in order to obtain ohmic contact with respect to GaN. Therefore, the problem is that the alloying heat treatment of the Ti/Al electrodes brings about a deterioration in the characteristics of p-type electrodes. The ZnO-based electrodes investigated in the present study were transparent electrically conductive films with a transmittance of 80% at a wavelength of 370 nm. We invented a structure, depicted in FIG. 12.3.2-(3), in which the ZnO film serves as an ohmic contact layer for GaN and the light that propagates from the GaN side and passes through the ZnO film is reflected by the Ni/Ag electrode, and conducted appropriate contact resistance and reflectance studies. With account taken of light absorption, the thickness of Ni, which was used to suppress the peeling of Ag, was set to 0.3 nm. Optical thin film simulation results used to estimate the optimum thickness of the ZnO film for reflectance measurements are shown in FIG. 12.3.2-(3). Air/Glass 1 mm/ZnO/Ni 0.3 nm/Ag was used as the simulation model.

FIG.12.3.2-(3) ZnO film thickness dependence according to results of optical thin simulation (Air/Glass/ZnO/Ni/Ag model) Wavelength: 370 nm



As can be seen from FIG. 12.3.2-(3), the reflectance varies depending on the film thickness as a result of interference in the layer. Using the simulation, we obtained optimum ZnO film thickness, and used 64 nm/Ni 0.3 nm/Ag 300 nm as the structure of the samples, in which a thin film was formed on glass for the evaluation of reflectance and samples, in which a thin film was formed on GaN for the evaluation of contact resistance. Using the simulation, we obtained the optimum ZnO film thickness, and decided to used ZnO 64 nm/Ni 0.3 nm/Ag 300 nm as the structure of samples used for the evaluation reflectance, in which the thin film was formed on glass, and that of samples used for the evaluation of contact resistance, in which the thin film was formed on GaN.

Table 12.3.2-(2) shows the relationship between the alloying temperature/time and contact resistance in case of using the ZnO/Ni/Ag electrodes.

		Alloying time [sec]							
		5	20	40	60	80	100	120	180
Temperature [°C]	800		9.80E-03						
	700		2.62E-03						

	600		2.98E-04		4.77E-04			Schottky	
	500	2.78E-05	4.25E-05	3.36E-05	5.37E-05	5.58E-05	5.00E-05	Schottky	
	400		1.01E-05		9.78E-06			1.17E-05	
	300		0.13E-06						1.59E-05
No alloying treatment: 3.50E-06									

Table 12.3.2-(2) Contact resistance and alloying temperature [unit: Ωcm<sup>2</sup>]

The contact resistance was the lowest ( $3.5 \times 10^{-6} \Omega\text{cm}^2$ ) in samples that had not undergone alloying, and, as the alloying temperature rose, the contact resistance exhibited a tendency to increase.

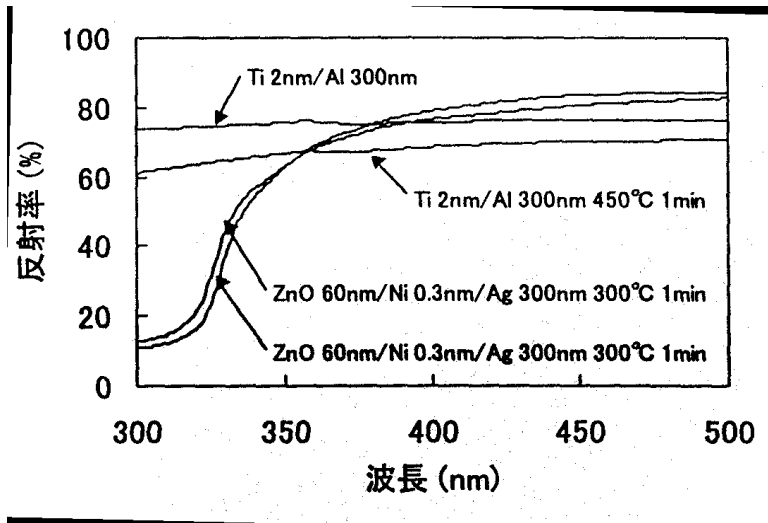
The reflectance of the ZnO/Ni/Ag electrode is shown in FIG. 12.3.2-(4). At a wavelength of 370 nm, the reflectance of the Ti/Al film was 67%, while that of the ZnO/Ni/Ag film was 70%. Although the reflectance of the ZnO-based electrodes was lower than the calculated value, it was due to the fact that the quartz substrate, on which the ZnO film was formed, was taken into consideration in the simulation, resulting in higher calculated values.

FIG. 12.3.2-(4) Reflectance of Ti/Al film and ZnO/Ni/Ag film

[Keys, FIG. 12.3.3-(4)]

(X-axis) Wavelength (nm)

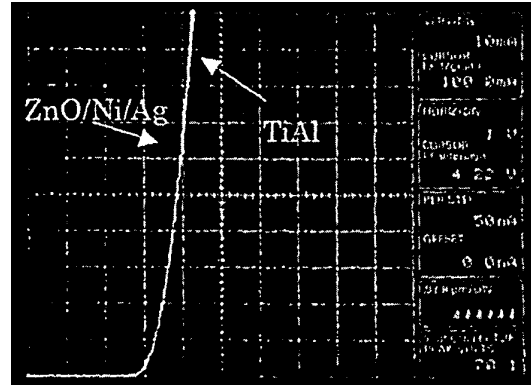
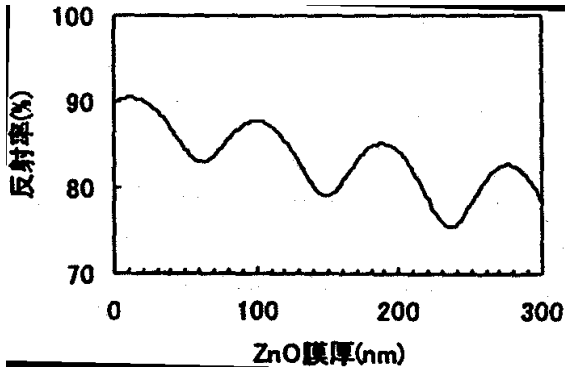
(Y-axis) Reflectance (%)



In addition, we also studied V characteristic of GaN-based using Ti/Al electrodes and ZnO/Ni/Ag electrodes. on the optical thin film simulation (FIG. 12.3.2-(5)), the thickness of the ZnO film formed on n-type GaN to 10 We fabricated LEDs with the type electrode structure and plotted their I-V characteristic FIG. 12.3.2-(6). To obtain the electric current density in the used at such time as in an

the I-LEDs Based we set nm. n- in same device

ordinary chip, we used a  $5 \times 100$  mA electric current. The leading edge voltage of the Ti/Al-based electrode  $V_f = 4.27$  V, while that of the ZnO-based electrode was  $V_f = 4.22$  V, which indicates that the ZnO-based electrode holds promise for n-type GaN.



Left: FIG. 12.3.2-5) GaN /ZnO /Ni/ Ag model

reflectance simulation

[Keys, FIG. 12.3.2-5): (X-axis) ZnO film thickness (nm); (Y-axis) Reflectance (%)

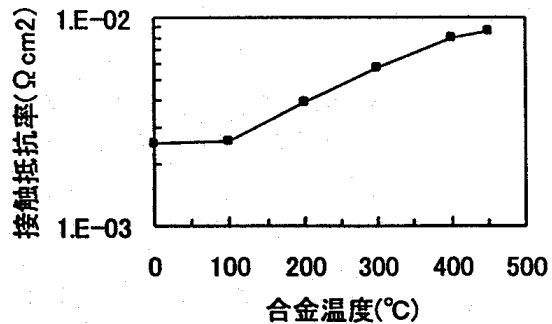
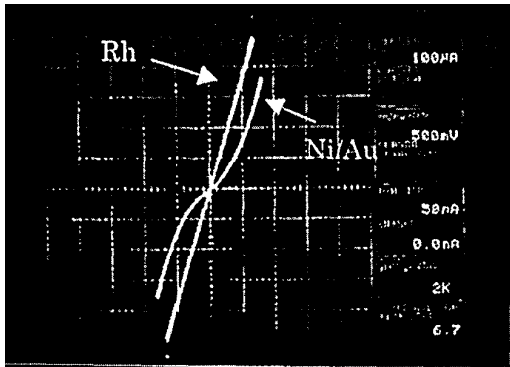
Right: FIG. 12.3.2-6) Leading edge voltage in case of using Ti/Al based and ZnO based electrodes

As far as electrical and optical characteristics and process flexibility (no alloying treatment) are concerned, the ZnO based electrode is by no means inferior to the Ti/Al based electrode, but there is the concern that its characteristics might deteriorate over time because of using Ag in the reflecting layer. This is a future research topic.

### 12.3.2.2 P-type electrodes

#### a) Rh electrodes

The I-V characteristic for the Rh-GaN electrode is shown in FIG. 12.3.2-7). An ohmic contact was confirmed without conducting heat treatment. The contact resistance at such time was  $2.48 \times 10^{-3} \Omega\text{cm}^2$ , which was two orders of magnitude better in comparison with the contact resistance of the thick-film Ni/Au.



Left: FIG. 12.3.2-7) I-V characteristics for Rh and Ni/Au electrodes on p-type GaN

Right: FIG. 12.3.2-8) Alloying temperature dependence of contact

resistance for Rh electrode on p-type GaN

[Keys, FIG. 12.3.2-8): (X-axis) Alloying temperature (°C); (Y-axis) Contact resistance ( $\Omega\text{cm}^2$ )

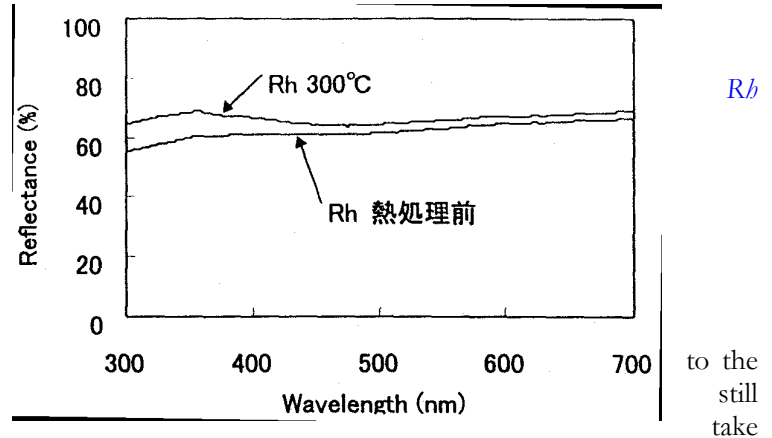
Next, the heat treatment temperature dependence of the contact resistance for the Rh electrode is shown in FIG. 12.3.2-8). Alloying was conducted in a nitrogen atmosphere for 20 second, followed by rapid cooling.

It was confirmed that a contact resistance of  $2.5 \times 10^{-3} \Omega \text{cm}^2$  could be obtained at alloying temperatures of  $100^\circ\text{C}$  or less, but at alloying temperatures of more than  $100^\circ\text{C}$  the contact resistance increased with rising temperature. This is believed to be due to a reaction at the GaN-Rh interface. In addition, a Schottky contact was obtained by treatment at temperatures higher than  $600^\circ\text{C}$ . For treatment at  $300^\circ\text{C}$ , which is the temperature used during chip bonding, the contact resistance increased to  $5.7 \times 10^{-3} \Omega \text{cm}^2$ , but even in this case this electrode appears more promising than Ni/Au. The reflectance of the Rh electrode is shown in FIG. 12.3.2-(9).

FIG. 12.3.2-(9) Reflectance of Rh electrode

[Keys, FIG. 12.3.2-(9)]: (Inside) Prior to heat treatment

At a wavelength of 370 nm, the reflectance of the electrode prior to heat treatment was 60.3%, while after a heat treatment at  $300^\circ\text{C}$  it rose to 67%. Although this result is somewhat inferior result obtained for Ni/Ag, the material is believed to be extremely promising if we the contact resistance into consideration as well.



#### (b) Rh/Ag electrodes

In order to obtain higher reflectances, we conducted studies of an Rh/Ag electrode, in which the Rh film thickness was reduced and the film was used as a contact layer for GaN, with Ag used to produce a high reflectance electrode.

The thickness of the Rh/Ag electrode was Rh 1 nm/Ag 200 nm. As far as the contact resistance was concerned, the results were almost the same as those obtained for the Rh electrode. However, in the same manner as with the Rh electrode, a rise in the contact resistance with increasing temperature was also observed. In this connection, using AES (Auger electron spectroscopy analysis), we confirmed that there were changes taking place inside the GaN/Rh/Ag sample. We conducted a comparison of two samples: one at a temperature (a temperature of  $600^\circ\text{C}$ , at which a Schottky contact is obtained) at which Rh is believed to have diffused into the GaN film; and one immediately after deposition.

FIG. 12.3.2-(10) shows that, after heat treatment in case of the as-dep. sample, the Rh profile is rather sharp, whereas after heat treatment at  $600^\circ\text{C}$ , the Rh profile can be confirmed to have diffused into the GaN film. This phenomenon is believed to bring about an increase in the contact resistance. Thus, with Rh-based electrodes, it is necessary to conduct device processing by applying as little heat as possible.

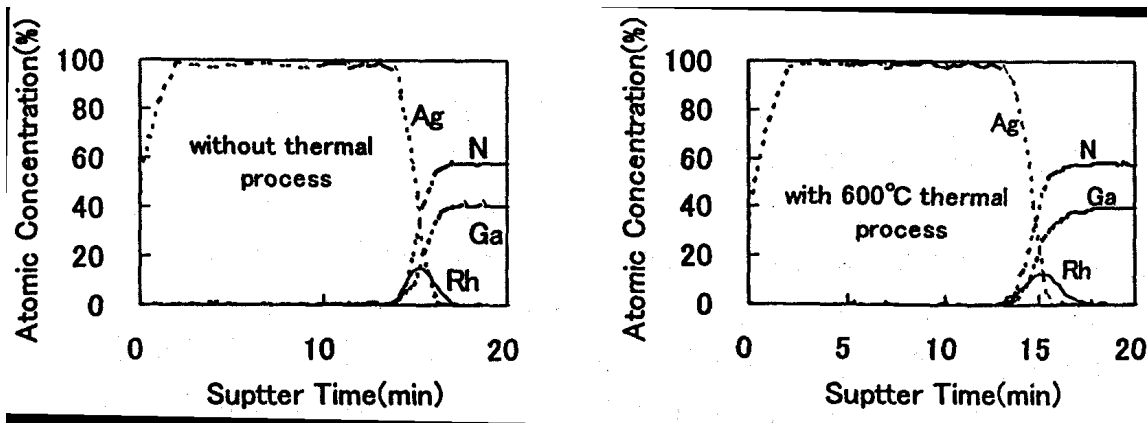


FIG. 12.3.2-(10) AES analysis of Rh/Ag electrode

(c) Pt-based electrodes

In case of the Pt-based electrode, in the same manner as with the Rh-based electrode, we evaluated the contact resistance using the alloying temperature as a parameter.

As shown in FIG. 12.3.2-(11), when using an electrode with a Pt film thickness of 200 nm, in the as-deposited state, the obtained contact resistance was as low as  $4.15 \times 10^{-4} \Omega\text{cm}^2$ . However, in the same manner as with the Rh-based electrode, an increase in the contact resistance was observed when heat treatment was conducted.

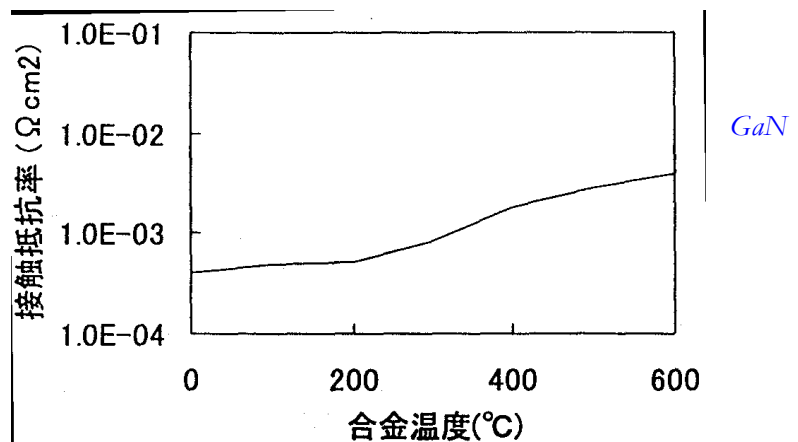
Although the contact resistance obtained after processing at the temperature necessary for chip bonding (300 °C, 1 min) increased to  $8.4 \times 10^{-4} \Omega\text{cm}^2$ , this is still the lowest contact resistance for p-type electrodes. However, with Pt electrodes, the reflectance at a wavelength of 370 nm was just 49.5%, and we could not expect high reflectances. Thus, in the same manner as with the Rh-based electrode, we attempted fabrication of a Pt/Ag electrode. In this case, the contact resistance was inferior to that obtained with Pt alone after 1-min treatment at 300°C, but the obtained resistance was  $2 \times 10^{-3} \Omega\text{cm}^2$  and, in terms of reflectance, the results exceeded 70%. The film structure used at such time was Pt 1 nm/Ag 200 nm. In case of p-type electrodes, this electrode is believed to be the most promising for obtaining electrodes with a low contact resistance and a high reflectance.

FIG. 12.3.2-(11) Annealing temperature dependence of contact resistance for Pt-based electrode on p-type

[Keys, FIG. 12.3.2-(11)]

(X-axis) Alloying temperature (°C)

(Y-axis) Contact resistance ( $\Omega\text{cm}^2$ ).



## 12.4 Investigations into increasing light extraction efficiency (edge tilting technology)

### 12.4.1 Methods and means

Currently, in the course of the “Light for the 21<sup>st</sup> Century Project,” we are conducting a study of white LEDs utilizing UV LED elements as excitation light sources, and we have to take into consideration the fact that when sealing resin is irradiated with excitation light, the optical and mechanical characteristics of the sealing resin will deteriorate. The light emanating from an excitation element is emitted not only from the light-emitting surface, but also from the edges of the element, with the emission from the edges being a major factor in the deterioration of the sealing resin. For this reason, the structure of the UV light-emitting element serving as the excitation light source has to be such that the entire element is covered with metal electrodes etc. so that excitation light does emanate from the edges of the chip. Thus, light extraction using a reflection horn, which is employed in ordinary LED lamps for increasing the light extraction efficiency, is impossible, which makes it difficult to increase the luminescence efficiency of white LEDs. For this reason, we chose to increase the luminescence efficiency of white LEDs by means of tilting the edges of the excitation element 45° to allow the element itself to act as a reflection horn.

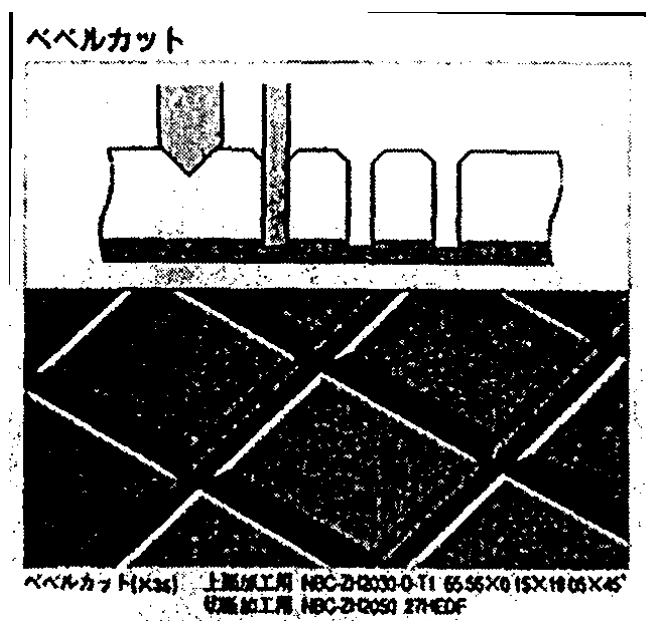
To implement GaN edge tilting, we considered methods based on the bevel cut technique (FIG. 12.4.1-(1)), which is one of the dicing techniques, and methods based on the reactive ion etching technique (Reactive Ion Etching: RIE). As for element edge tilting using the bevel cut technique, there have been reports [4], according to which the light extraction efficiency of elements was improved using the bevel cut technique to process the edges of InGaP devices, and we believe this procedure to be a promising technique for GaN edge tilting. However, experimental results showed that, because of the sapphire which is commonly used as a substrate for GaN-based light-emitting elements, the blades used for dicing were subject to severe wear (about 1.2 [ $\mu\text{m}/\text{line}$ ]) and the technique was not suitable for forming slanted edges in elements with high controllability. Thus, in the present study we focused our attention and investigated edge tilting methods based on the RIE technique.

*FIG. 12.4.1-(1) Bevel cut technique (From Disco DIAMOND WHEELS NBC-Z SERIES Catalog (1999)*

*[Keys, FIG. 12.4.1-(1) ]: (Top) Bevel cut.*

Although various materials are employed for the RIE mask, one of the most convenient methods is to use a photoresist mask. Incidentally, micromachining techniques used to form complicated shapes on the surface of Si substrates and glass using photoresist masks have attracted attention in recent years, and the use of a photoresist mask as a RIE mask for tilting the edge surfaces of GaN looks very promising.

Thus, in order to conduct an in-depth investigation into the use of photoresist masks as RIE masks for tilting the edges of GaN, we studied various photoresist mask fabrication conditions.



For the experiments, we prepared two kinds of positive photoresist of different viscosity. Table 12.4.1-(1) shows the conditions used in the photoresist experiments.

Photoresist	Type-A	Type-B
Viscosity	20 mPa	44 mPa
Rotational frequency used for coating	2000~5000 rpm	2000~5000 rpm
Post-bake temperature	110~140°C, without post-bake	110~140°C, without post-bake
Post-bake time	1~15 min	1~15 min

Table 12.4.1-(1) Photoresist used and conditions of experiment

Undoped GaN epitaxial wafers (film thickness: 4  $\mu\text{m}$ ) were used as samples. The photoresists shown in Table 12.4.2-(1) were used for patterning on the surface of a wafer. Using a parallel plate RIE apparatus, we conducted a 2-min RIE treatment (etching amount: about 1  $\mu\text{m}$ ) using an etching pressure of 7 Pa, an etching gas ( $\text{Cl}_2$ ) flow rate of 100 sccm, an etching substrate temperature of 30°C, and an RF power of 200 W. Subsequently, we used a scanning electron microscope (Scanning Electron Microscope: SEM) to examine the shape of the GaN edge of the sample that was tilted 20° from a vertical position to obtain the angle between the etched surface and the edge of the sample (see FIG. 12.4.1-(2)) and conducted a comparative study of the tendencies exhibited under various photoresist conditions. In addition, we also investigated the GaN orientation dependence of the GaN edge tilt angle. Furthermore, in order to evaluate reproducibility tendencies, we prepared multiple samples for several photoresist conditions and calculated the respective standard deviations.

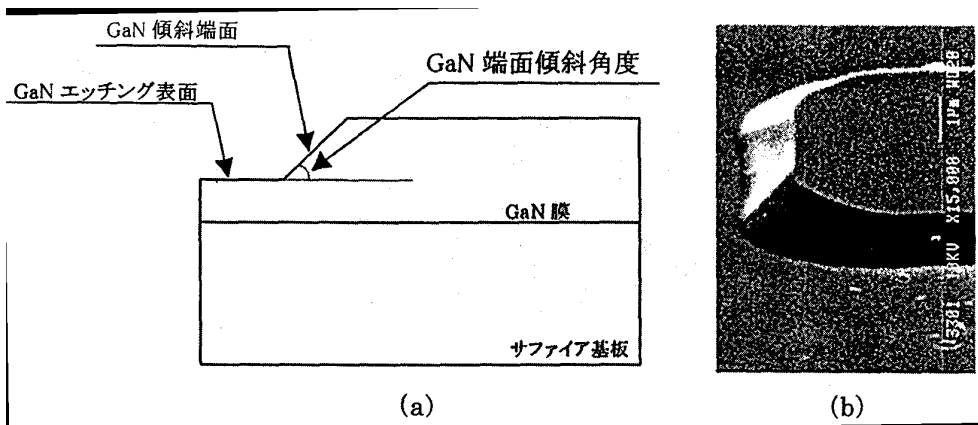


FIG. 12.4.1-(2) Explanatory diagram showing GaN tilted edge angle (FIG. (a)) and example of SEM microphotograph of GaN tilted edge surface (FIG. (b)).

[Keys, FIG. 12.4.1-(2)]

(a) (Left, top) GaN tilted edge surface.; (Left, below) GaN etched surface.; (Right, top) GaN tilted edge surface angle.; (Right, underneath) GaN film.; (Right, underneath) Sapphire substrate

## 12.4.2 Results and discussion

### 12.4.2.1 Photoresist film thickness dependence

The dependence of the photoresist film thickness for each photoresist on the rotational frequency of the spinner is shown in FIG. 12.4.2-(1). The rotational frequency of the spinner was varied between 2000 and 5000 rpm, with the thickness of the film obtained by the post-baking treatment of the resultant photoresist mask measured using a contact-type film thickness meter.

FIG. 12.4.2-(1) confirms that the thickness of the photoresist film obtained using the photoresist of Type-B, which had a higher viscosity, was greater than that obtained using the photoresist of Type-A. On the other hand, in case of Type-A photoresist films obtained by varying the post-bake temperature, there was no difference in the thickness of the resultant films.

FIG. 12.4.2-(1) Photoresist film thickness and rotational frequency of spinner

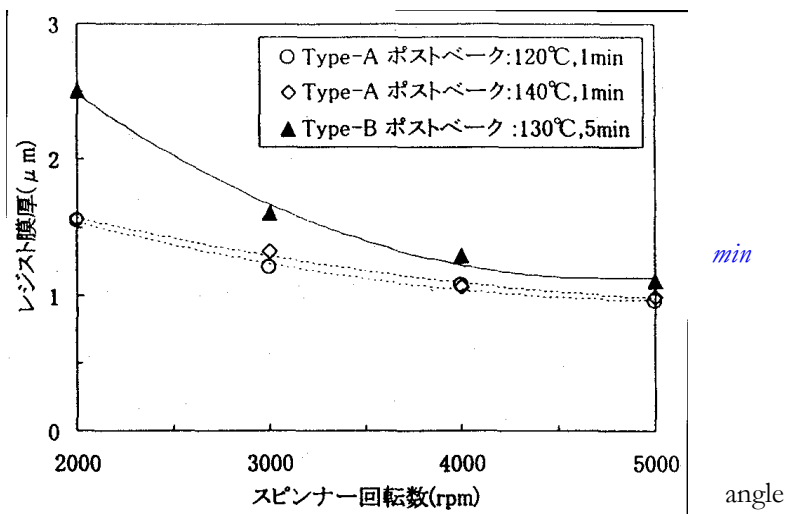
[Keys, FIG. 12.4.2-(1)]

(X-axis) Rotational frequency of spinner.

(Y-axis) Resist film thickness ( $\mu\text{m}$ )

(Box)  $\circ$  Type-A post-bake: 120°C, 1 min  
 $\diamond$  Type-A post-bake: 140°C, 1 min

$\blacktriangle$  Type-B post-bake: 130°C, 5 min



Next, the photoresist film thickness dependence of the GaN edge face angle is shown in FIG. 12.4.2-(2). In addition, the symbols used in the figure are the same as the ones used in FIG. 12.4.2-(1).

FIG. 12.4.2-(2) Photoresist film thickness dependence of GaN edge face angle

[Keys, FIG. 12.4.2-(2)]

(X-axis) Photoresist film thickness ( $\mu\text{m}$ )

(Y-axis) GaN edge face angle ( $^\circ$ )

(Box)  $\circ$  Type-A post-bake: 120°C, 1 min  
 $\diamond$  Type-A post-bake: 140°C, 1 min

$\blacktriangle$  Type-B post-bake: 130°C, 5 min

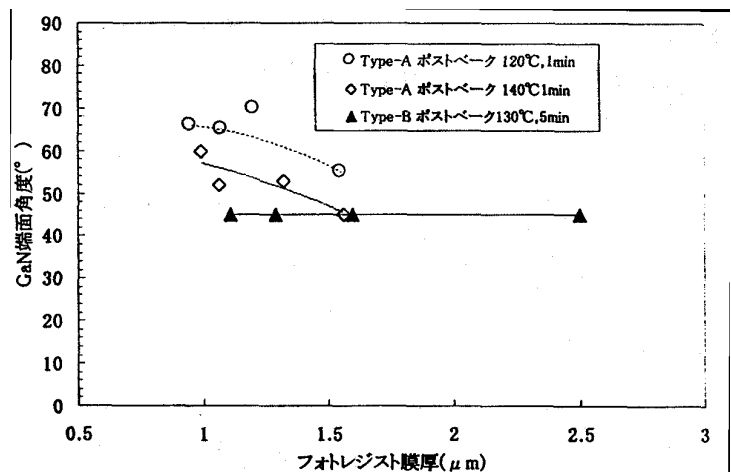


FIG. 12.4.2-(2) shows that in case of the Type-A photoresist, the GaN edge face angle tends to become smaller as the thickness of the photoresist film increases. In addition, although there

were no differences in the photoresist film thickness, as is evident from FIG. 12.4.2-(1), differences were observed in the edge face angle of the GaN film depending on the post-bake temperature, with the GaN edge face angle exhibiting a tendency to decrease with increasing post-bake temperature.

On the other hand, in case of the Type-B photoresist, at any photoresist film thickness, the GaN edge face angle was about 45°, which was smaller than the values of the GaN edge face angle obtained for the Type-A photoresist film. The fact that the resultant GaN edge face angle was smaller than that of the Type-A photoresist is believed to be due to the fact that, as compared with the Type-A photoresist,

- 1) the Type-B photoresist uses a relatively high post-bake temperature of 130°C,
- 2) the post-bake time was 5 min, considerably longer than that of Type-A, etc.

#### 12.4.2.2 Post-bake temperature dependence

FIG. 12.4.2-(3) shows the post-bake temperature dependence of the GaN edge face angle. The post-bake temperature was studied in the range of from 110°C to 140°C. In addition, we also studied samples that were not subjected to the post-bake treatment. In FIG. 12.4.2-(3), the round dots show results from a sample coated with the Type-A photoresist at 2000 rpm and subjected to a post-bake treatment for 1 minute. The square dots show results from a sample coated with the Type-A photoresist at 3000 rpm and subjected to a post-bake treatment for 1 minute. In addition, the triangular dots in the figure represent results from a sample coated with the Type-B photoresist at 3000 rpm and subjected to a post-bake treatment for 5 minutes.

As can be seen from FIG. 12.4.2-(3), at any rotational frequency of the spinner, up to a post-bake temperature of 130°C the Type-A photoresist produced practically constant GaN edge face angles, which was approximately 60° in case of samples coated at a rotational frequency of 2000 rpm and approximately 50° in case of samples coated at a rotational frequency of 3000 rpm. This result is in agreement with the tendency of the GaN edge face angle to decrease when the rotational frequency of the spinner decreases, as shown FIG. 12.4.2-(2). In addition, at any rotational frequency of the spinner, when the post-bake treatment was carried out at 140°C, the GaN edge face angle was approximately 46°.

On the other hand, in case of the Type-B photoresist, the GaN edge face angle was largest in samples that were not subjected to the post-bake treatment, and as the post-bake treatment temperature increased, the GaN edge face angle tended to become smaller. Furthermore, a GaN edge face angle of 45° could be obtained by conducting the post-bake treatment at 130°C or more.

FIG. 12.4.2-(3) Post-bake temperature dependence of GaN edge face angle

[Keys, FIG. 12.4.2-(3)]

(X-axis) Post-bake temperature (°C)

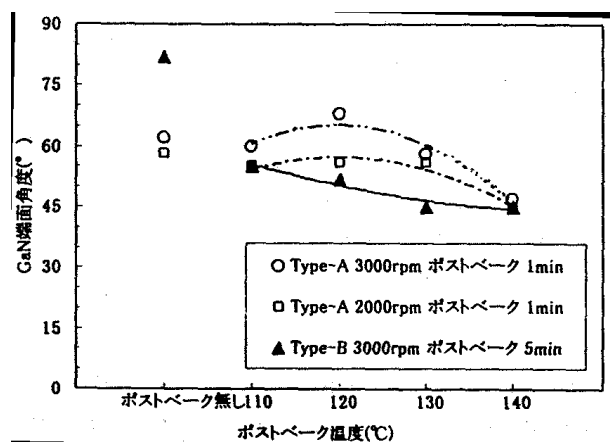
(X-axis, between 0 and 110) No post-bake treatment

(Y-axis) GaN edge face angle (°)

(Box) ○ Type-A 3000 rpm post-bake 1 min; □ Type-A 2000 rpm post-bake 1 min; ▲ Type-B 3000 rpm post-bake 5 min

#### 12.4.2.3 Post-bake time dependence

FIG. 12.4.2-(4) shows the post-bake time dependence of the GaN edge face angle. The post-bake time dependence was studied within a 1~15 min time interval. In FIG. 12.4.2-(4), the round dots show results obtained for samples fabricated by coating wafers with the Type-A photoresist at 3000 rpm and



conducting a post-bake treatment at a constant temperature of 120°C and the square dots show results obtained for samples fabricated by coating wafers with the Type-A photoresist at 2000 rpm and conducting a post-bake treatment at 120°C. In addition, in FIG. 12.4.2-(4), the rhombus-shaped dots show results obtained for samples fabricated by coating wafers with the Type-A photoresist at 2000 rpm and conducting a post-bake treatment at a constant temperature of 140°C, and the triangular dots show results obtained for samples fabricated by coating wafers with the Type-B photoresist at 3000 rpm and conducting a post-bake treatment at a temperature of 130°C.

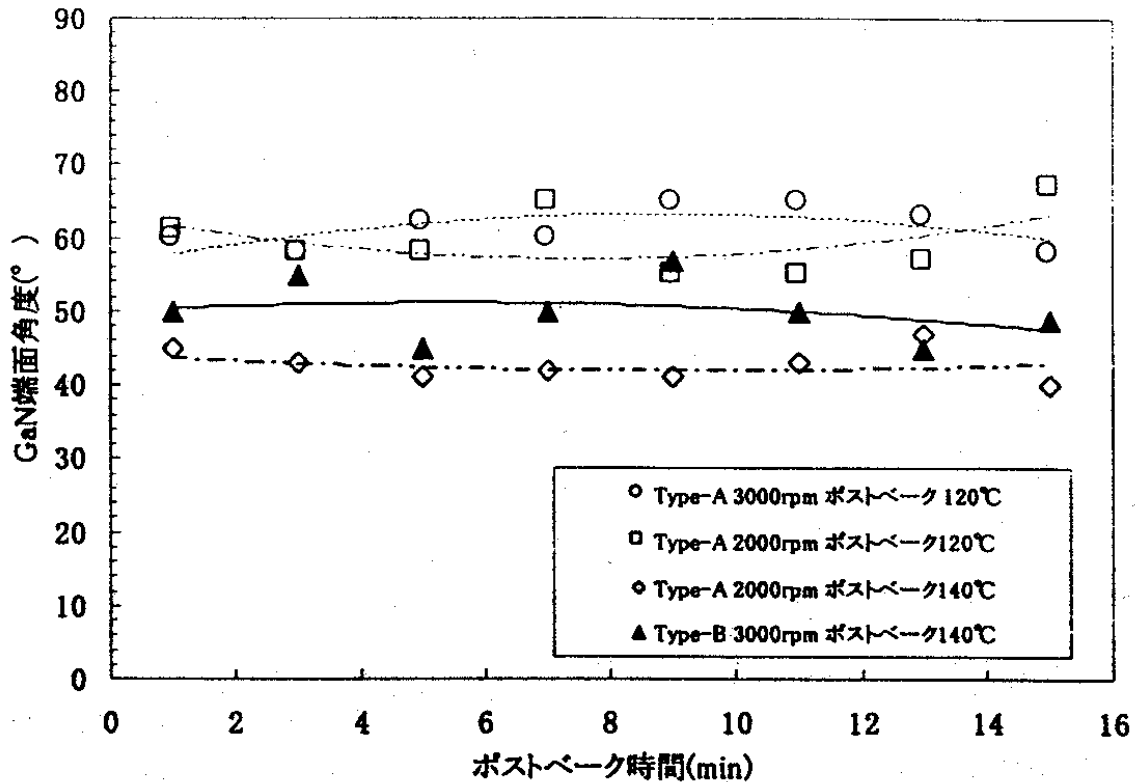


FIG. 12.4.2-(4) Post-bake time dependence of GaN edge face angle

(X-axis) Post-bake time (min)

(Y-axis) GaN edge face angle (°)

(Box) ○ Type-A 3000 rpm post-bake 120°C; □ Type-A 2000 rpm post-bake 120°C; Type-A 2000 rpm post-bake 140°C; ▲ Type-B 3000 rpm post-bake 140°C

As can be seen from FIG. 12.4.2-(4), in case of the Type-A photoresist, samples prepared using a spinner rotational frequency of 3000 rpm and a post-bake temperature of 120°C exhibited a maximum value of the GaN edge face angle, which was approximately 65°, when the post-bake treatment was conducted for 8~9 min. On the other hand, samples prepared using a spinner rotational frequency of 2000 rpm, including samples treated at a post-bake temperature of 120°C and those treated at 140°C, exhibited maximum values of the GaN edge face angle, which was respectively 57° for samples subjected to post-bake treatment at 120°C and 43° for samples subjected to post-bake treatment at 140°C, when the post-bake treatment was conducted for about 7 minutes.

Also, it was discovered that in the case of the Type-B photoresist, the maximum value of the GaN edge face angle, which was approximately 52~53°, was obtained by conducting the post-bake treatment at 130°C for 7 minutes. In addition, on the whole, the post-bake time dependence exhibited fluctuations.

#### 12.4.2.4 Plane orientation dependence in samples with inclined GaN edge faces

We used the Type-A photoresist for the photoresist mask. The patterning of the Type-A photoresist was carried out at a spinner rotational frequency of 2000 rpm, and the post-bake treatment was conducted for 1 minute at 120°C. The RIE treatment was carried out for 2 minutes under STD. conditions. After that, we used SEM to evaluate the GaN edge face tilt angle in a direction perpendicular (1-100) and parallel (11-20) to the orientation flat ((1-100); designated as O.F. below) along the sapphire c-plane. The results of the evaluation are shown in Table 12.4.2-(1).

	Parallel to O.F. ((1-100))	Perpendicular to O.F. ((11-20))
Sample A	57°	55°
Sample B	55°	56°

*Table 12.4.2-(1) Plane orientation dependence of GaN edge face angle*

As shown in FIG. 12.4.2-(1), there was no significant variation in the GaN edge face tilt angle neither in the perpendicular, nor in the parallel direction with respect to the O.F., with the angle being approximately 55°. This experiment shows that the tilt angle of the GaN edge faces was unrelated to the crystal plane orientation.

#### 12.4.2.5 GaN edge face reproducibility

We conducted a study of the reproducibility of the GaN edge face angle. According to the method we used for evaluation, we prepared several GaN substrates patterned using the Type-A photoresist under three types of conditions shown in Table 12.4.3-(3) and subjected each sample to RIE treatment under STD conditions. After that, the photoresist mask was completely removed using an aqueous solution of sulfuric acid/peroxide, and the GaN edge face tilt angle was evaluated using SEM. Using the obtained GaN edge face tilt angles, we obtained standard deviations for the GaN edge face tilt angles under each type of conditions and conducted a comparative study. The results of the study are shown in Table 12.4.2-(3).

Sample name	A	B	C
Spinner rotational frequency	3000	2000	2000
Post-bake temperature (°C)	120	120	140
Post-bake time (min)	1	1	1
Number of points	5 points	6 points	7 points
Average value of GaN edge face angle (°)	65.2	56.7	44.4
Standard deviation (°)	8.70	2.25	0.79

*Table 12.4.2-(3) GaN edge face tilt angle reproducibility*

If we compare the value of standard deviation of the GaN edge face tilt angle obtained under conditions A and the value of the standard deviation of the GaN edge face tilt angle obtained under conditions B, as listed in Table 12.4.2-(3), we will see that the value of standard deviation obtained under conditions B is smaller. This indicates that when the spinner rotational frequency is decreased, in other words, when the thickness of the photoresist film is increased, the variation in the GaN edge face tilt angle tends to decrease.

Furthermore, if we compared conditions B and conditions C, we can see that the value of the standard deviation of the GaN edge face angle obtained under conditions C is smaller. This is believed to be due to the fact that the variation in the GaN edge face tilt angle tends to become even smaller when the post-bake temperature is increased.

Summing up the above-described results, we can say that the value of standard deviation under conditions B, where the thickness of the photoresist film is greater, is smaller than under conditions A, and, furthermore, the value of standard deviation under conditions C, where the post-bake temperature is higher, is smaller than under conditions B. Based on the above, it is believed that a greater thickness of the photoresist mask film and a higher post-bake temperature are appropriate for the fabrication of tilted GaN edge faces with high reproducibility.

## 12.5 White LED development

### 12.5.1 Study of mixed white light production and emission characteristics of RGB model phosphors

#### 12.5.1.1 Methods and means

The physical properties of the RGB model phosphors used in the present development project are shown in Table 12.5.1. A fluorescence spectrophotometer (Hitachi F-4500) was used to conduct the measurement of the excitation spectra and emission spectra of the phosphors. Because in case of emission spectra the central wavelength of the UV LED emission is not fixed, we conducted measurements within a relatively wide range in the near-UV region. Based on the resultant emission spectra of the phosphors, we obtained CIE-based color specification values  $(Y_i, x_i, y_i)$  ( $i=R,G,B$ ) under the XYZ color specification system as specified in JIS [Japanese Industrial Standards – trans.] [5]. In addition, the measurement of the emission spectra at the same excitation wavelength for each of the phosphors was carried out under the same spectrometer settings. We used additive mixing [6] to obtain an estimate of the central wavelength of the UV LED emission and a theoretical Y-stimulus ratio  $(Y_R':Y_G':Y_B')$  in the target white color coordinates from the resultant chromaticity coordinates  $(x_i, y_i)$  ( $i=R,G,B$ ) of the samples. Based on the ratio  $((Y_R'/Y_R):(Y_G'/Y_G):(Y_B'/Y_B))$  of the theoretical Y-stimulus ratio  $(Y_R':Y_G':Y_B')$  and actual Y-stimulus ratios  $(Y_R:Y_G:Y_B)$  of the phosphors and the specific weights, we obtained white color mixing ratios for the phosphors.

Phosphors	Name	Specific weight	Average particle size ( $\mu\text{m}$ )	Composition
R	P22-RE3	5.0	5.73	$\text{Y}_2\text{O}_2\text{S:Eu}$
G	P22-GN4	4.1	6.67	$\text{ZnS:Cu,Al}$
B	LP-B1	4.3	4.98	$(\text{Sr,Ca,BaMg})_{10}(\text{PO}_4)_6\text{Cl}_2\text{:Eu}$

Table 12.5.1 Physical properties of RGB model phosphors

#### 12.5.1.2 Results and discussion

FIG. 12.5.1-(1) shows the excitation and emission spectra of the phosphors.

FIG. 12.5.1-(1)  
Excitation and emission  
of model phosphors

[Keys, FIG. 12.5.1-(1)]

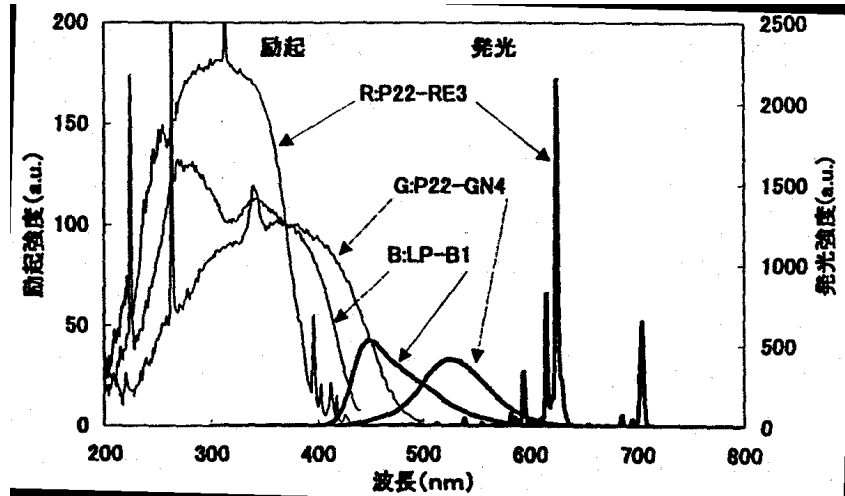
(X-axis) Wavelength (nm)

(Y-axis, left) Excitation  
intensity (a.u.)

(Y-axis, right) Emission  
intensity (a.u.)

(Inside, top, left)  
Excitation.

(Inside, top, right)  
Emission.



spectra

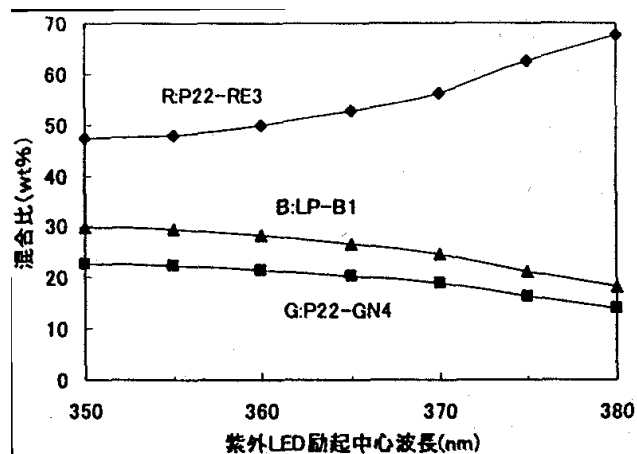
The excitation spectrum intensity was obtained by normalizing the intensity obtained at an excitation wavelength of 370 nm to 100. FIG. 12.5.1-(2) shows phosphor mixing ratios (wt%) vs the central wavelength of UV LED emission used to obtain the target chromaticity coordinate (x,y)=(0.31,0.31). Using the results shown in FIG. 12.5.1-(2) as a guide, we fabricated samples of mixed RGB phosphors. When we obtained their chromaticity coordinates from the emission spectra, it was confirmed that the resultant values were practically the same as the target chromaticity coordinates. As FIG. 12.5.1-(2) shows, in the RGB model phosphors used in the present experiment, the mixing ratio of the R phosphor was higher than the proportion of the G and B phosphors. This is believed to be due to the fact that the absolute luminance of the R phosphor is lower in comparison with the G and B phosphors, and, therefore, when the excitation wavelength is a short wavelength, even though the luminance of the R phosphor is increased, its absolute value is small, and thus the influence exerted on the mixing ratio is insignificant. In addition, there is a correlation between the Y-stimulus value at a given excitation wavelength and the excitation spectrum. Thus, it was confirmed that the phosphor mixing calculations could be simplified by converting a measured Y-stimulus value at a given excitation wavelength.

FIG. 12.5.1-(2) Phosphor mixing ratio in target chromaticity coordinates (0.31, 0.31)

[Keys, FIG. 12.5.1-(2)]

(X-axis) Central UV LED excitation wavelength (nm)

(Y-axis) Mixing ratio (wt%)



## 12.5.2 Study of phosphor layer forming techniques and transmitted UV light control

### 12.5.2.1 Methods and means

#### a. Study of phosphor layer forming techniques

Our method of forming a phosphor layer on a UV LED consisted in using the flat face of a sapphire substrate of a UV LED chip that had been assembled using the flip chip technique [7]. Here, we studied a technique, in which we used a phosphor-bearing surface to mount a phosphor chip obtained by micropatterning a glass substrate, on which a phosphor layer was formed in advance. An extremely thin glass plate with a thickness of 0.1 mm, which allowed for micropatterning, was used as the glass substrate. Spin coating was used for forming a phosphor layer on the glass substrate. A mixed white phosphor produced by combining RGB phosphors was used, with the mixing ratio determined in accordance with the wavelength of the evaluation UV LED, which is described below. In addition, we used SiO<sub>2</sub> inorganic binders to disperse the phosphors and obtained the optimum compounding ratio from the relationship between the compounding ratio of the phosphor with respect to the binder and the resultant coating film adhesive strength in order to maximize the packing density of the phosphor layer. Phosphor layer film thickness control was carried out by regulating the spinner rotational frequency, the phosphor compounding ratio with respect to the binder, and the slurry density. In the process of phosphor chip micropatterning, we applied the common LED wafer chip fabrication techniques. The size of the phosphor chip was 500  $\mu\text{m}$  on a side, with that of the UV LED chip being 350  $\mu\text{m}$ . The UV LED chip used for evaluation, which was mounted on a TO-18 STEM using the flip chip assembly technique, had a central wavelength of 372 nm and an output of 4 mW ( $I_f=20\text{mA}$ ). The architecture of a basic white LED lamp combining a UV LED and a phosphor chip is shown in FIG. 12.5.2-(1). Phosphor edge coating (designated as “EC treatment” below) was introduced in order to convert the UV light emitted from the edge faces of the UV LED chip into visible light. The measurement of the emission characteristics of the basic white LED lamp was carried out using a spectrometer (the CAS140B from INSTRUMENT SYSTEMS) with an attached integrating sphere.

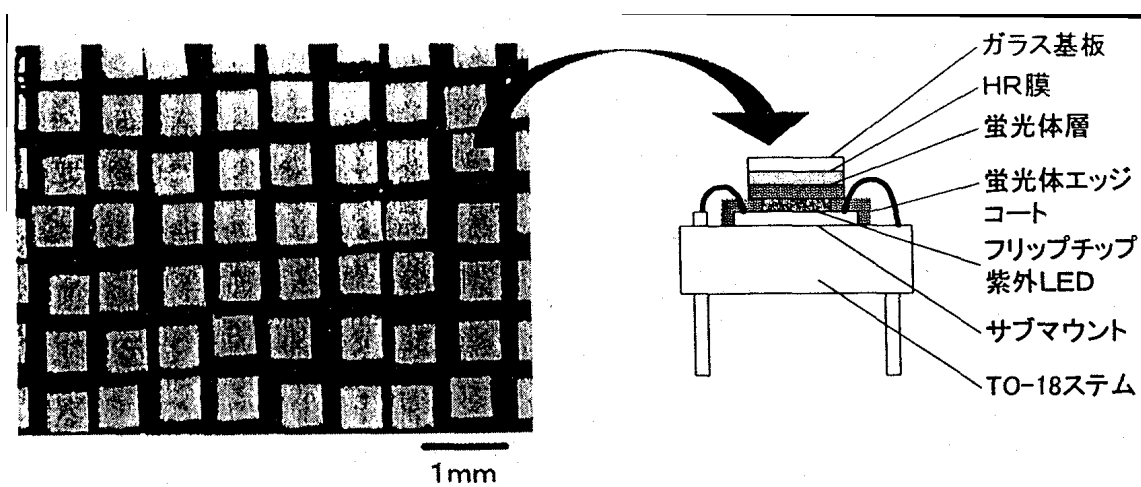


Figure 12.5.2-(1) Architecture of basic white LED lamp

[Keys, 12.5.2-(1)] (Right, top to bottom) Glass substrate; HR film; Phosphor layer; Phosphor edge coating; Flip-chip UV LED; Submount; TO-18 STEM

#### b. Study of transmitted UV light control

We studied a technique, in which an optical thin film filter (called the HR film below) possessing the ability to reflect transmitted UV light and transmit only visible light whose wavelength had undergone conversion in the phosphor layer is formed between the glass substrate and the phosphor layer as shown in FIG. 12.5.2-(1) in order to control the component of the UV light emitted from the UV LED that is not absorbed by the phosphor layer (transmitted UV light). The basic architecture of the HR layer consists of alternating layers of two kinds of thin film (for example, SiO<sub>2</sub>/TiO<sub>2</sub>) of different refractive indices. We conducted simulation analysis in order to obtain the number of layers and the film thickness providing a high reflectance in the UV

LED emission wavelength region and a high transmittance in the visible light region. Using the obtained conditions as a guide, we formed an HR film on a glass substrate using the vacuum deposition technique. In addition, assuming that the UV light transmitted through the phosphor layer would be randomly scattered in the phosphor layer, we evaluated the UV light incident angle dependence of the UV region reflectance by varying the cut-off wavelength (defined as the wavelength, at which reflectance constitutes 50%) representing the boundary between the reflected wavelength region and the transmitted wavelength region.

**12.5.2.2 Results and discussion**

a. Study of phosphor layer forming techniques

FIG. 12.5.2-(2) shows results obtained by mounting phosphor chips with varying phosphor layer film thickness on an evaluation UV LED chip and measuring the emission characteristics of the basic white LED lamp. As can be seen from the results, the visible light intensity of the white LED peaks in the vicinity of a phosphor layer film thickness of 30~40 μm, and decreases after the peak with increasing film thickness. In addition, the transmitted UV light decreases with increasing film thickness. This is in agreement with common tendencies encountered during transmission, and implies that the film thickness and phosphor packing density in this layer forming method are controlled with high accuracy. It was confirmed that if the phosphor layer on the UV LED chip edge faces is EC-treated as shown in FIG. 12.5.2-(2), then at the peak of the visible light intensity, the visible light intensity is increased 15% as compared with that obtained without the EC treatment, and the amount of transmitted UV light is decreased 9%. Measurements conducted on EC-treated samples only confirm that with this flip-chip LED architecture, approximately 13% of the UV light is emitted from the UV LED chip edge faces. The component emitted from the edge faces of the LED chips is believed to be converted to visible light and contribute to an increase in the visible light intensity.

FIG. 12.5.2-(2) Emission characteristics of basic white LED lamp with a phosphor chip

[Keys, FIG. 12.5.2-(2)]

(X-axis) Phosphor layer film thickness (μm)

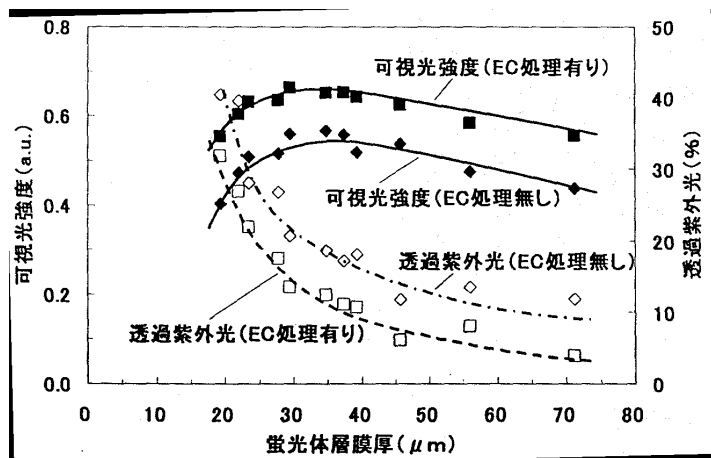
(Y-axis, left) Visible light intensity (a.u.)

(Y-axis, right) Transmitted UV light (%)

(Inside, top to bottom) Visible light intensity (EC-treated); Visible light intensity (no EC treatment); Transmitted UV light (no EC treatment); Transmitted UV light (EC-treated)

b. Study of transmitted UV light control

FIG. 12.5.2-(3) shows the reflectance characteristics of glass substrates with an HR film obtained by varying the cut-off wavelength defining the UV light reflection from 380 nm to 440 nm. Results obtained by irradiating the surface of HR films with UV light and measuring the incidence angle dependence of the amount of transmitted UV light transmitted the glass surface are shown in FIG. 12.5.2-(4). As can be seen from 12.5.2-(4), the incidence angle dependence of the amount of the transmitted UV light becomes less pronounced when the cut-off wavelength of the HR film is shifted towards longer wavelengths. Emission spectra, on the UV LED



by region the from FIG.

excitation axis, of samples obtained by superimposing HR film substrates and substrates spin-coated with a phosphor layer are shown in FIG. 12.5.2-(5). This figure shows that when the cut-off wavelength becomes greater than 430 nm, some of the blue phosphor emission spectrum component is reflected. FIG. 12.5.2-(6) shows relationships of the amount of the reflected UV light (value obtained by integration from the incident angle dependence) and the amount of light converted to visible light by the phosphor versus the cut-off wavelength. The results show that the optimum cut-off wavelength region taking into account the UV light reflectance and the amount of visible light converted by the phosphor lies somewhere between 400 nm and 420 nm.

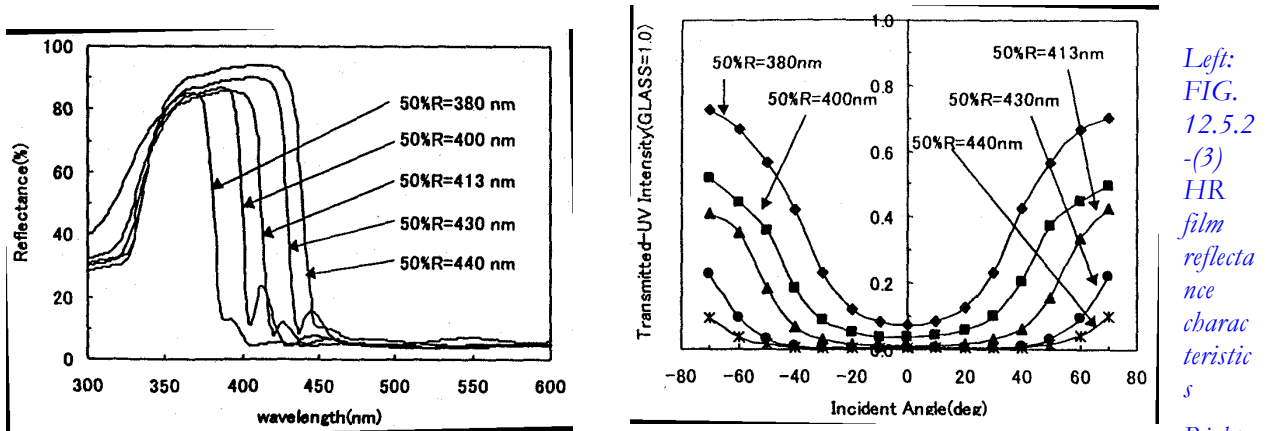
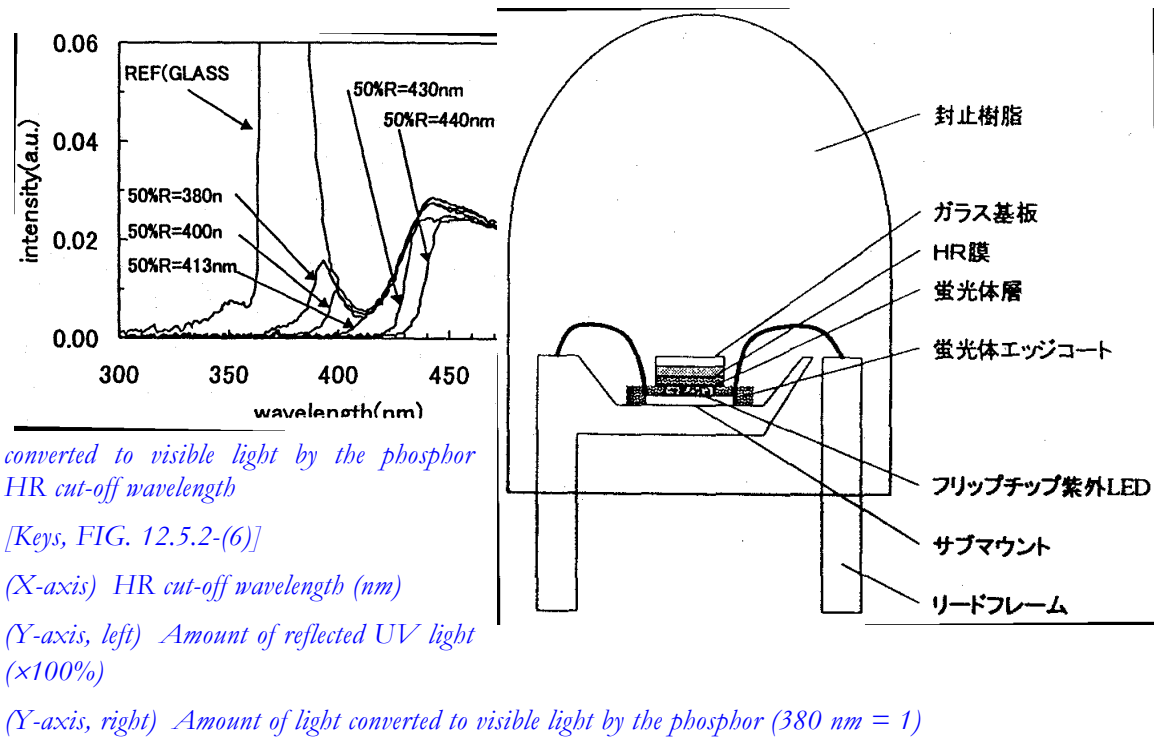


FIG. 12.5.2-(4) Incidence angle dependence of amount of transmitted UV light

Left: FIG. 12.5.2-(5) Emission spectra, on UV LED excitation axis, of samples obtained by superimposing HR film substrates and phosphor-coated substrates



## 12.5.3 Evaluation of emission characteristics and color rendering of a white LED lamp

### 12.5.3.1 Methods and means

The UV LED chips were made by forming high reflectance electrodes on UV LED wafers fabricated in the current project (central wavelength of emission: 382 nm), making chips with a size of 350  $\mu\text{m}$  on a side, assembling them on electrode wiring submounts using the flip-chip technique, and then mounting the resultant part on a lead frame and bonding the electrodes. In the fabrication of the phosphor chips mounted on the UV LED chips we used RGB model phosphors, with the fabrication of the chips carried out by forming a 40- $\mu\text{m}$  thick film of mixed phosphor (standard white phosphor (A)), which corresponded to the central emission wavelength of the UV LED, on a glass substrate with or without an HR film (cut-off wavelength: 413 nm) and making chips with a size of 500  $\mu\text{m}$  on a side. An inorganic adhesive was used for mounting the phosphor chips on the UV LEDs. In addition to samples with/without an HR film, samples were also prepared, in which the edge faces of the UV LED chip were either subjected an EC treatment or left untreated, and bullet type prototype white LED lamps were fabricated by sealing the frame with resin (FIG. 15.3-(1)). A spectrometer with an attached integrating sphere was used for conducting emission characteristic measurements.

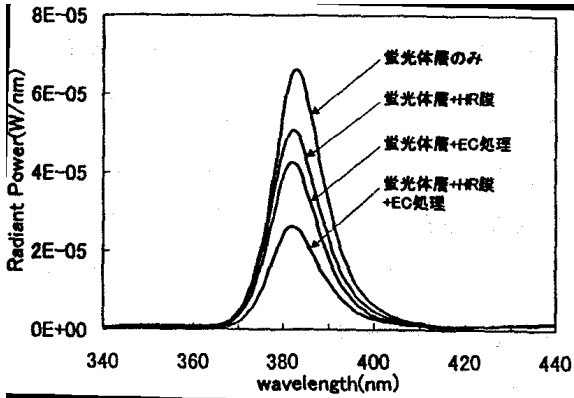


FIG. 12.5.3-(1) White LED lamp architecture

[Keys, FIG. 12.5.3-(1)]

(Top to bottom) Sealing resin; Glass substrate; HR film; Phosphor layer; Phosphor edge coating; Flip-chip UV LED; Submount; Lead frame

In order to investigate the influence exerted on color rendition by chromaticity coordinates and the emission spectrum shape, in addition to the above-mentioned standard white phosphor (A), we used a chromaticity-adjusted white phosphor (B), which was obtained by shifting the white color coordinates towards the blue side by changing the mixing ratio of the phosphors, and a comparative white phosphor (C) made of other phosphor materials with a different spectrum shape to form phosphor films on glass substrates and conducted evaluation of their color rendering properties based on the results of measurement of the emission spectra obtained by UV LED excitation.

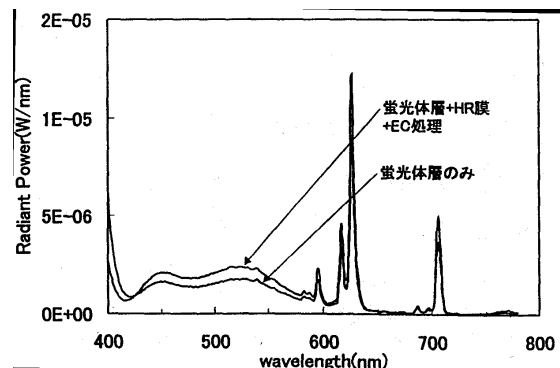
**12.5.3.2 Results and discussion**

FIG. 12.5.3-(2) shows UV-region spectra of white LED lamps with various peripheral architectures of the UV LED chip. FIG. 12.5.3-(3) shows visible-region spectra of white LED lamps having a phosphor layer only, as well as white LED lamps with a phosphor layer + an HR film + EC treatment. Table 12.5.3-(1) shows characteristics of white LED lamps with various architectures. As can be seen from FIG. 12.5.3-(2), FIG. 12.5.3-(3), and Table 12.5.3-(1), in comparison with the architecture having a phosphor layer only, the introduction of the HR film allows for decreasing the UV light transmitted by the phosphor layer, and, in addition, subjecting the edge faces of the UV LED chip to an EC treatment permits conversion of the UV light emitted from the edge faces of the UV LED to visible light, resulting in an increase in the total flux of the lamp and in the phosphor conversion efficiency (visible light flux from the phosphor/LED's UV flux). Based on these results, the amount of UV light reflected by the HR film is about 35%. Although an HR film-only architecture is supposed to produce a reflectance of not less than 80%, in the LED architecture evaluated in the present experiment, UV light is believed to be emitted not only by the phosphor layer on the UV LED chip, which caused a reduction in the reflection effect provided by the HR film in terms of the total amount of transmitted UV light. In addition, it is believed that because the central wavelength of the UV LED was not less than 380 nm, a relatively higher value than the value assumed (370 nm), this increased the UV light incidence angle dependence of the UV-region reflectance of the HR film. Thus, we found that in order to make the best of the reflection effects of the HR film, we had to investigate architectures capable of directing most of the light emitted from a UV LED to the phosphor layer under the HR film.

Left: FIG. 12.5.3-(2) UV-region spectra of white lamps with various peripheral architectures of UV chip

[Keys, FIG. 12.5.3-(2)]

(Inside, top to bottom) Phosphor layer only; Phosphor + HR film; Phosphor layer + EC treatment; Phosphor layer + HR film + EC treatment



LED LED layer

*Right: FIG. 12.5.3-(3) Visible-region spectra of white LED lamps with various peripheral architectures of UV LED chip*

*[Keys, FIG. 12.5.3-(3)]*

*(Inside, top to bottom) Phosphor layer + HR film + EC treatment; Phosphor layer only*

Peripheral architecture of UV LED chip	Transmitted light (%)	UV	Phosphor conversion efficiency (%)	Total flux (lm)
Phosphor layer only	31.4		10.7	0.099
Phosphor layer + EC treatment	19.5		12.6	0.120
Phosphor layer + HR film	24.2		10.8	0.100
Phosphor layer + HR film + EC treatment	12.8		13.8	0.129

*Table 12.5.3-(1) Characteristics of white LED lamps with various peripheral architectures of UV LED chip ( $I_f=20$  mA)*

FIG. 12.5.3-(4) shows results of measurement of UV LED-excited emission spectra in samples fabricated by forming a film of, respectively, standard white phosphor (A), chromaticity-adjusted white phosphor (B), and comparative white phosphor (C) on a glass substrate. Table 12.5.3-(2) lists the chromaticity coordinates and color rendering evaluation scores for each of the phosphors. As can be seen from FIG. 12.5.3-(4) and Table 12.5.3-(2), the color rendering properties of the chromaticity-adjusted white phosphor (B) obtained by increasing the blue component in the standard white phosphor (A) were greatly improved. In addition, it was found that the average color rendering evaluation score Ra obtained from the spectrum of the comparative white phosphor (C) was 43, a relatively low value as compared with other samples. As can be seen from the shape of the spectrum of comparative white phosphor (C) shown in FIG. 12.5.3-(4), its components in the vicinity of 480 nm and 580 nm were practically absent and its JIS test color reproducibility was lower than that of the model phosphors, which resulted in a decrease in color rendering properties.

These results show that white color from three-wavelength phosphors containing many components with a broad spectral distribution, as in the RGB model phosphors evaluated in the present project, is highly efficient in terms of improving the color rendering properties of light sources used for illumination.

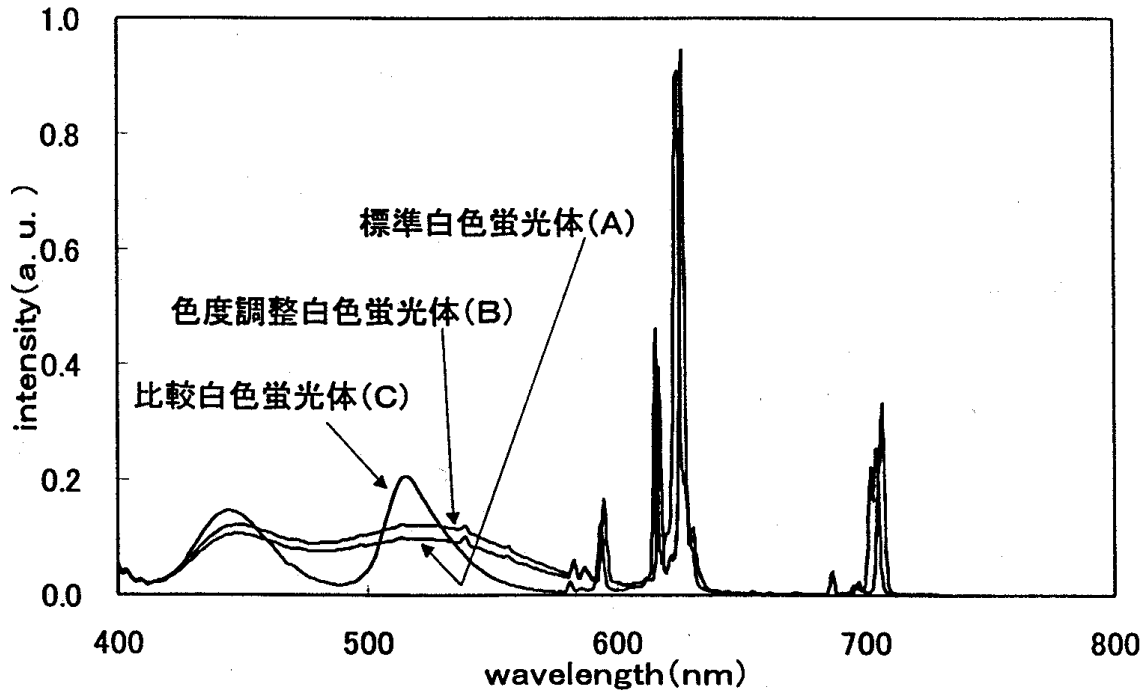


FIG. 12.5.3-(4) Emission spectra of model phosphor samples and comparative samples

[Keys, FIG. 12.5.3-(4)]

(Inside, top to bottom) Standard white phosphor (A)

Chromaticity-adjusted white phosphor (B)

Comparative white phosphor (C)

Samples	Standard white phosphor (A)	Chromaticity adjusted white phosphor (B)	Comparative white phosphor (C)
Color coordinate x	0.311	0.288	0.298
y	0.321	0.331	0.297
Reference light	D 6710	D 7860	D 8010
Average color rendering evaluation score Ra	76	90	43
Special color rendering evaluation score R <sub>1</sub>	69	91	26
R <sub>2</sub>	88	93	81
R <sub>3</sub>	85	90	61
R <sub>4</sub>	70	92	9
R <sub>5</sub>	76	94	40
R <sub>6</sub>	85	92	68
R <sub>7</sub>	82	89	57
R <sub>8</sub>	50	79	-2
R <sub>9</sub>	-29	44	-150
R <sub>10</sub>	78	88	56
R <sub>11</sub>	65	86	-13
R <sub>12</sub>	89	83	80
R <sub>13</sub>	74	89	40
R <sub>14</sub>	89	94	73
R <sub>15</sub>	61	90	18
Type of standard used	JIS Z 8726-1990		

*Table 12.5.3-(2) Color coordinates and color rendering evaluation scores of model phosphor samples and comparative samples*

## 12.6 Development of Sealing Resins for UV LEDs

### 12.6.1 Methods and means

#### 12.6.1.1 Samples and reagents

We used bisphenol A glycidyl ether (Epicoat 828, from Japan Epoxy Resin K.K) along with hydrogenated bisphenol A glycidyl ether (YL6663, from Japan Epoxy Resin K.K.), and 3,4-epoxycyclohexylmethylcarboxylate (Celoxide 2021 from Daicel Chemical Industries, Ltd.) as epoxy monomers and methylhexahydrophthalic anhydride (MH-700 from New Japan Chemical Co., Ltd.) as an acid anhydride.

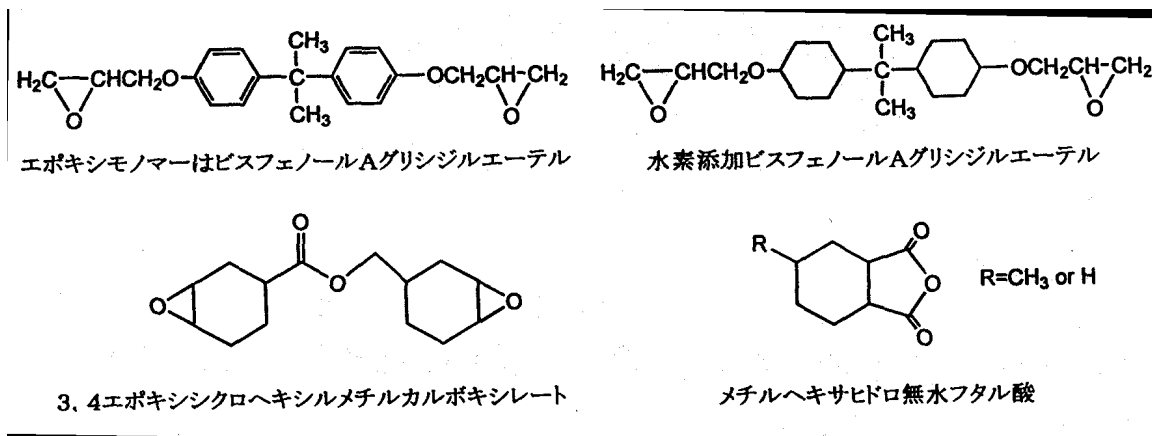


FIG. 12.6.1-(1) Epoxy monomers

[Keys, FIG. 12.6.1-(1)]

(Top row) Bisphenol A glycidyl ether, hydrogenated bisphenol A glycidyl ether

(Bottom row) 3,4-epoxycyclohexylmethylcarboxylate, methylhexahydrophthalic anhydride

As cure accelerators, we used 2-ethyl-4-methylimidazole (from Shikoku Corp.), benzyldimethylamine (reagent), tetraphenylphosphonium bromide (reagent), diazobicycloundeceneoctanoic acid salt (from SAN-APRO Limited), and tetrabutylphosphonium diethylphosphorodithioate (PX-4ET from Nippon Chemical Industry Co., Ltd.).

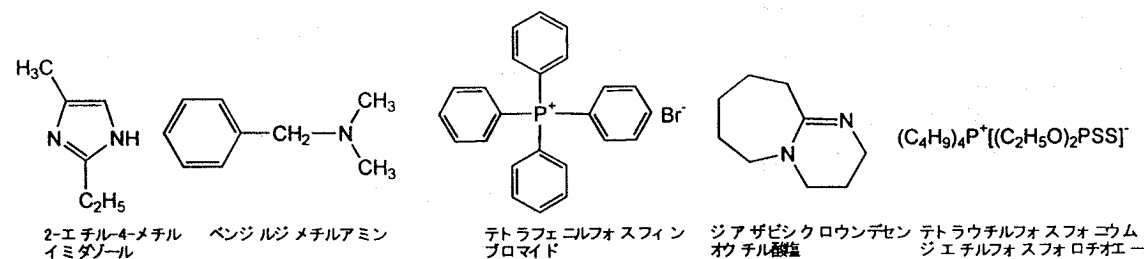


FIG. 12.6.1-(2) Cure accelerators

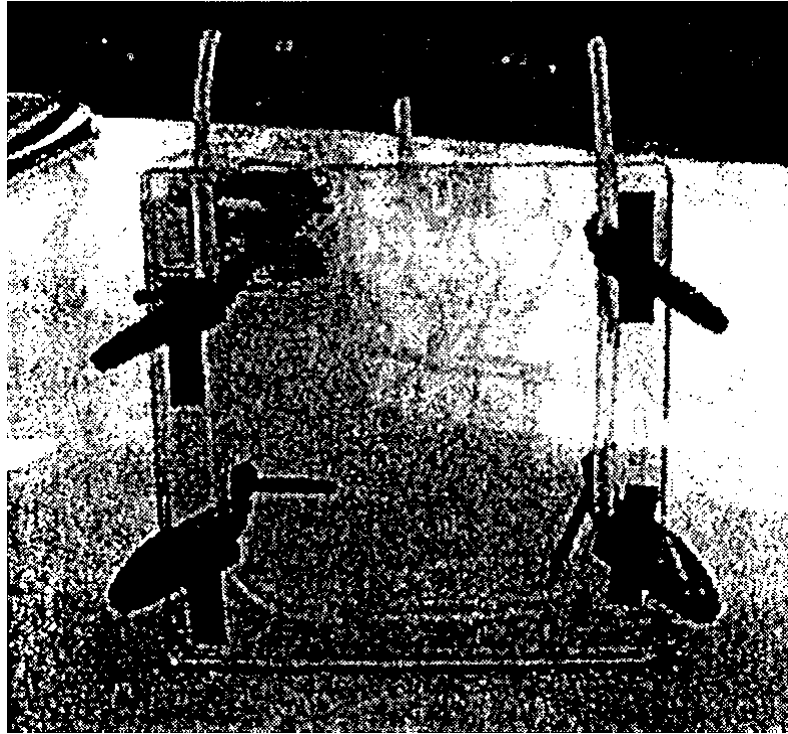
[Keys, FIG. 12.6.1-(2)]

(Left to right) 2-ethyl-4-methylimidazole, benzyldimethylamine, tetraphenylphosphonium bromide, diazobicycloundeceneoctanoic acid salt, and tetrabutylphosphonium diethylphosphorodithioate.

### 12.6.1.2 Fabrication of resin plate

The epoxy monomers, acid anhydride, and cure accelerators were combined in a predetermined mixing proportion, charged to jig for plate fabrication, which was made of reinforced glass plates, and by heating for a predetermined time at a predetermined temperature (primary cure). Subsequently, the jig was taken apart to remove the resin plate, which was then again heated for a predetermined time at a predetermined temperature (secondary cure). The resin plate was cut into 50 mm × 50 mm × 5 mm (thickness) pieces used as evaluation plates.

*FIG. 12.6.1-(3) Jig for epoxy plate fabrication*



in a  
resin  
made  
cured  
the jig  
the  
time  
The  
50  
pieces  
resin

### 12.6.1.3 UV irradiation testing

Irradiation with UV light was conducted for 100 hours using a Q-UV accelerated weathering tester from Q-Panel, in which a UV fluorescent lamp ( $\lambda_p=340$  nm) as the light source. The transmittance and yellow index before and after irradiation were measured using the UV-3100 spectrophotometer from Shimadzu Corporation.

### 12.6.1.4 Heat resistance testing

The epoxy plates were placed inside a thermostat maintained at 150°C, and the transmittance and yellow index were measured in the manner as above.

## 12.6.2 Results and discussion

In general, not less than about 95% of the components of epoxy resins used for LED sealing are made up of bisphenol A glycidyl ether or other epoxy monomers along with the methylhexahydrophthalic anhydride, added to which are several percent of amine- or phosphorus-based curing accelerators.

However, these components absorb UV light and oxidize, as shown in FIG. 12.6.2-(1). At such time, the resin assumes a yellowish hue as a result of production of carbonyl groups and absorption of visible light [9].

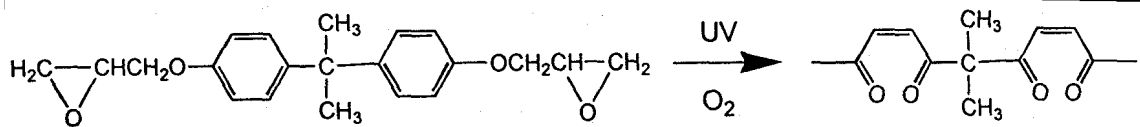


FIG. 12.6.2-(1) UV degradation of bisphenol A glycidyl ether

Therefore, in order to prevent the UV degradation, it is necessary to develop methods, in which bisphenol A glycidyl ether is not used.

Means for preventing the degradation include allowing all of the UV light to pass and using UV absorbers to convert UV light into heat energy and release it.

As far as the former technique is concerned, we know that cure accelerators that are capable of producing transparent epoxy resins and do not absorb UV light do not exist. However, because of their low concentration of less than 1 wt%, total UV absorption by the resin can be greatly reduced if UV absorption by the primary components is decreased.

On the other hand, in the second technique, conversion to heat energy and release based on the use of UV absorbers involves not only the need to provide high-performance absorbers, but also requires using a heat-radiating architecture for the LED, which imposes serious limitations on the design of LED architecture and which is impractical.

For this reason, in the present study, we focused mainly on techniques permitting UV light to pass through and investigated resin compounds based on hydrogenated bisphenol A glycidyl ether of FIG. 12.6.1-(1) that absorb little UV light.

#### 12.6.2.1 Influence of cure accelerators

First of all, we selected cure accelerators for the acid anhydride cure system. We conducted acid anhydride curing of hydrogenated bisphenol A glycidyl ether using methylhexahydrophthalic anhydride and investigated the relationship between the type of cure accelerator and UV degradation. In addition, it has been found that cure accelerators used in combination with bisphenol A glycidyl ether allow for obtaining transparent cured products [10].

As shown in Table 12.6.2-(1), compounds providing good initial characteristics included 2-ethyl-4-methylimidazole, tetraphenylphosphonium bromide, and tetrabutylphosphonium diethylphosphorodithioate. However, only tetrabutylphosphonium diethylphosphorodithioate was the compound exhibiting the least amount of UV degradation and maintaining a high transmittance after irradiation. The reason why considerable UV degradation developed when using tetraphenylphosphonium bromide was probably due to the four aromatic rings of tetraphenylphosphonium bromide that can easily absorb UV light.

Cure accelerators	Transmittance (% , 400 nm)		Yellow index,
	Initial	After irradiation	Initial
2-ethyl-4-methylimidazole (5)	86.4	84.8	2.02
Benzyl dimethylamine (6)	76.5	71.3	6.12
Tetraphenylphosphonium bromide (7)	87.1	37.9	1.14
Diazobicycloundeceneoctanoic acid salt (8)	73.0	71.9	2.31
Phosphorus-based cure accelerator PX-4ET (9)	89.8	87.8	1.02

Table 12.6.2-(1) Influence of different types of cure accelerators on UV degradation of epoxy resins [YL6663]:[MH700]:[Cure accelerator]=100:90:1

Thus, we decided on tetrabutylphosphonium diethylphosphorodithioate as the optimal, low UV degradation cure accelerator and carried out the subsequent experiments.

### 12.6.2.2 Improvement in heat resistance

One of the reasons for the wide use of bisphenol A glycidyl ether consists in the high stability of its aromatic rings. The heat resistance of the sealing resin is indispensable for securing reliability of semiconductors during soldering and operation. When cured with acid anhydride, as it is commonly done, its glass transition point is around 130°C.

On the other hand, in hydrogenated bisphenol A glycidyl ether, the stability of the cyclohexane rings is lower than that of the aromatic rings, and the glass transition point is also lower, in the vicinity of 100°C. This leads not only to problems in terms of reliability described above, but also facilitates oxidation of the resin under the action of heat, and may increase the tendency towards discoloration.

Therefore, with a view to improve the heat resistance, we added CEL2021, an alicyclic epoxy with a high glass transition point, to the composition and examined the discoloration properties of the cured product in a high-temperature weathering test. We found that adding 10 wt% of CEL2021 increased the glass transition point of the cured product to 130°C.

FIG. 12.6.2-(2) Relationship between concentration of alicyclic epoxy CEL2021 and thermal discoloration [YL6663+CEL2021]:[MH700]:[PX-4ET]=100:90:1

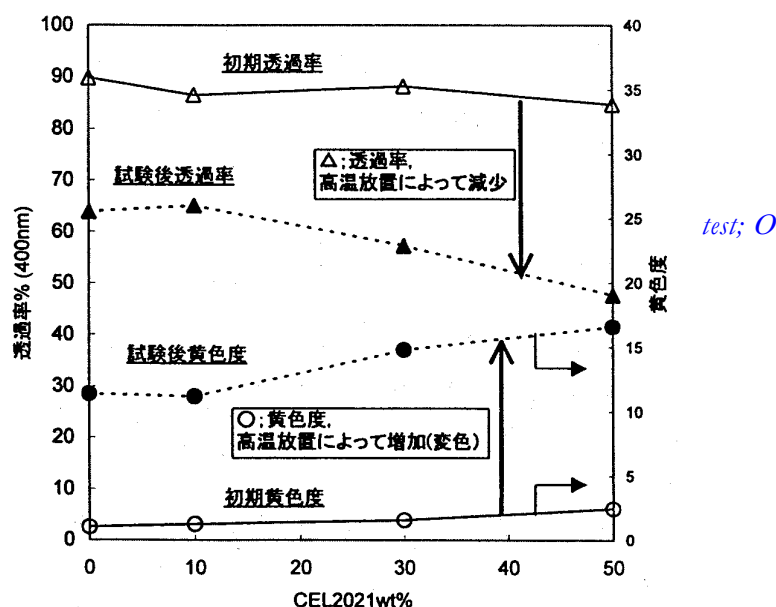
[Keys, FIG. 12.6.2-(2)]

(Y-axis, left) Transmittance, % (400 nm)

(Y-axis, right) Yellow index

(Inside) Initial transmittance;  
Transmittance after test  $\Delta$  Transmittance,  
decrease after weathering; Yellow index after  
Yellow index, increase after weathering  
(discoloration); Initial yellow index

As shown in FIG. 12.6.2, as the concentration of CEL2021 relative to YL6663 grew, the initial discoloration increased, and the transmittance slightly decreased. After high-temperature



weathering, if the concentration of CEL2021 exceeded 10 wt%, there was a conspicuous increase in the yellow index and a drop in transmittance.

Therefore, although it is possible to increase the glass transition point by adding CEL2021, the addition simultaneously leads to an increase in the initial discoloration and thermal discoloration. At present, we are studying the relationship between the concentration of CEL2021 and UV degradation, and believe that the appropriate concentration of CEL2021 should be within 10 wt%.

## 12.7 Summary

### 12.7.1 Electrode forming techniques

In the development of high-reflectance n-type electrodes, in addition to obtaining high reflectances by improving the conventional Ti/Al electrode, our research indicates that the use of electrodes based on a novel material, ZnO, is also promising.

P-type electrodes studied so far are shown in FIG. 12.7-(1).

FIG. 12.7-(1) Contact resistance and reflectance of p-type electrodes

[Keys, FIG. 12.7-(1)]

(Y-axis, left) Reflectance (%)

(Y-axis, right) Contact resistance ( $\Omega\text{cm}^2$ )

(Box, inside) ◆ Reflectance

✱ Contact resistance

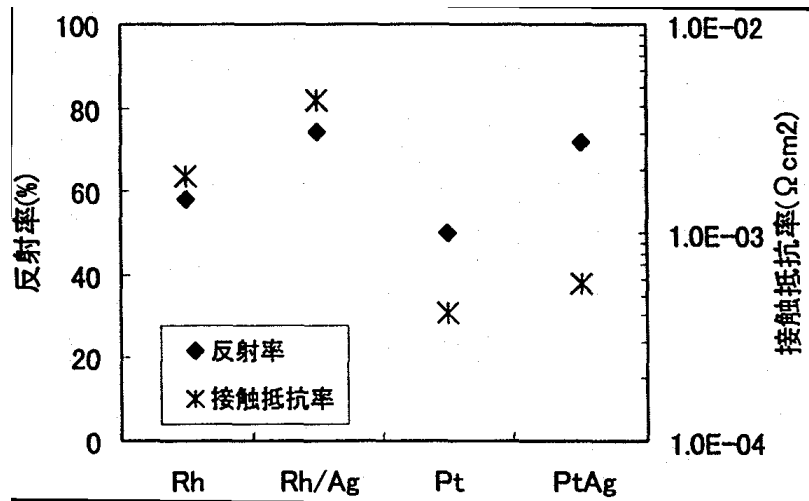


FIG. 12.7-(1) shows that the electrode was the Pt/Ag electrode. It was found that Pt/Ag electrode yielded excellent values of contact resistance, at  $10^{-4} \Omega\text{cm}^2$ , and reflectance, at 71.5%.

best  
the

### 12.7.2 Improvements in light extraction efficiency

We have been conducting investigations into the use of the edge face tilting method based on dry etching of GaN, which is believed to be an effective means not only for improving the light extraction efficiency, but also in terms of phosphor emission efficiency and UV-resistant sealing. To study specific techniques, we prepared masks of various two different kinds of photoresist with different viscosities and investigated various photoresist condition dependences of the GaN edge face angle.

A tendency towards smaller GaN edge face angles was observed when the thickness of the photoresist film was increased. In addition, when the post-bake temperature was increased, a tendency towards smaller GaN edge face angles was observed, although the thickness of the resultant photoresist film practically didn't change. Also, as a result of investigating the post-bake temperature dependence, it was found that in case of Type-A photoresist GaN edge face angles tended to remain practically unchanged at post-bake temperatures of up to 130°C, and carrying out the post-bake treatment at 140°C allowed to obtain a tilt of 45°, the target

value of the GaN edge face angle. Additionally, in case of Type-B photoresist, as the post-bake temperature increased, the GaN edge face angle exhibited a tendency to decrease, and GaN edge faces tilted 45° were obtained by means of post-bake treatment at 140°C.

As a result of studying the GaN face orientation dependence of the GaN edge face angle, no face orientation dependence of the GaN edge face angle was observed neither in a direction perpendicular to nor in a direction parallel to the c-plane sapphire substrate [1-100] direction. In addition, evaluation of the reproducibility of the GaN edge face angle under various photoresist mask conditions indicated that the edge faces of GaN could be tilted with good reproducibility if the photoresist mask was formed using a thick photoresist film and a high post-bake temperature.

### **12.7.3 Development of white LEDs**

White LED lamps were fabricated using UV LED chips and subjected to evaluation. As a result it was confirmed that when an optical thin film filter transmitting visible light and reflecting UV light was formed on the phosphor layer mounted on the UV LED chip, and, furthermore, when the UV LED chip edges were coated with phosphor, the amount of transmitted UV light in comparison with untreated samples was reduced from 31% to 13% and the total flux of the white LED lamp was improved 30%. In addition, it was found that in order to make the best of the optical thin film filter, it was necessary to investigate structures capable of directing most of the light emitted by a UV LED to the phosphor layer.

Evaluation of white color rendering using various phosphors conducted from the standpoint of emission spectrum shape confirmed that color rendering properties could be improved by regulating phosphors containing many components with a broad spectral distribution. White LED lamps combining phosphors with a broad spectral distribution, as in the RGB model phosphors evaluated in the present report, are of considerable practical importance as source of light for illumination.

### **12.7.4 Development of sealing resins for UV LEDs**

As a result of investigating cure accelerators added to mixtures of epoxy monomers and hydrogenated bisphenol A glycidyl ether, it was determined that optimal cure accelerators were phosphorus-based cure accelerators without double bonds. The problem with hydrogenated bisphenol A glycidyl ether is its low heat resistance, and it was found that thermal discoloration could be suppressed by adding an alicyclic epoxy with a high heat resistance.

## **12.8 Plans for the future**

In the area of electrode forming technique development, we will examine the influence of differences in electrode structure and electrode materials on the voltage efficiency and emission efficiency of UV LEDs in order to determine the best type of electrode in terms of device characteristics. In addition, we will evaluate electrode reliability based on LED characteristics and continue narrowing down our selection of electrode materials and electrode architectures.

In the area of light extraction efficiency, we will apply the RIE-based edge face tilting technology developed this year to the fabrication of LEDs to confirm the emission efficiency improvement effects. In addition, we will start development of chip micropatterning techniques and strive to realize at least 50% of the initial target for light extraction efficiency.

In the area of UV-resistant sealing technique development, we will not only continue the irradiation testing currently in progress, but we will also examine the use of anti-oxidants and UV absorbers in order to further suppress discoloration. In addition, we plan to investigate various characteristics of LED sealing resins (viscosity, heat resistance, water resistance, insulating properties, etc.) and examine them from the standpoint of reliability.

In terms of white LED development, we plan to confirm the behavior of visible light conversion efficiency using chips obtained by applying the edge face tilting technique. In addition, we will conduct investigations into the structure of the UV light reflecting film corresponding to the wavelength of the UV LED and further enhance the efficient use of the excitation light.

## 12.9 References

- [1] G. S. Marlow et al., Solid State Elec., 25, 91 (1982).
- [2] J. S. Foresi, T. D. Moustakas, Appl. Phys. Lett., 62(22), 2859 (1993).
- [3] Materials of Scientific Symposium No. 61 of Applied Physics Society (2000) 3a-ZN-2
- [4] M. R. Krames et al., Appl. Phys. Lett., 16, (1999), 2365.
- [5] JIS Handbook 33 "Color," JIS Z 8724-1983, p.275-286 (1992).
- [6] The Color Science Association of Japan, "Color Science Handbook," p. 151-152 (1982).
- [7] Development of high-efficiency photoelectric conversion compound semiconductors, 1999 Achievement Report, p. 217~222 (2000).
- [8] JIS Handbook 33 "Color," JIS Z 8726-1990, p. 222-231 (1992).
- [9] The Chemical Society of Japan, The Society of Polymer Science, "New Trends in Polymer Additives," Nikkan Kogyo Shinbunsha (1998)
- [10] Hirai (H. Kakiuchi), "New Trends in Curing Agents for Epoxy Resins," p. 183 CMC (1984)

# 13 Development of LED-based Light-Source Devices for Illumination

## 13.1 Achievements in 1998-1999

Because the per-element optical output of LEDs is lower than that of conventional light sources when LEDs are used as light sources for general illumination, it is necessary to try to increase their optical output by assembling the elements in the form of arrays or in the form of matrices. In the present study, we conducted an investigation into increasing the output of LED array light sources and confirmed that increased LED element temperature exerted considerable influence on the decrease in the optical output. Thus, as a result of examining various cooling methods (substrates, heat sinks, coolants) used for LED array light sources, we found out that the decrease in the optical output could be suppressed by creating conditions for highly efficient heat emission from LED elements, which made it possible to achieve increased light outputs.

On the other hand, in order to study the architecture of UV LED-based light source devices, we carried out optical measurements of UV-excitable phosphors capable of conversion to visible light [*“down-converting phosphors” – trans.*] and established optical simulation techniques for phosphor-converted light produced with the help of UV LEDs. As a result of comparing the characteristics of reflection and transmission of phosphor-converted light based on the simulation, it was conjectured that a reflective architecture making the most of reflected phosphor light would be efficient in increasing optical outputs. In this connection, we fabricated prototype models of light source devices of a transmitting-type architecture and of a reflective architecture, in which we combined blue LEDs and YAG phosphors, and subjected their optical output to measurement and comparison, as a result of which it was confirmed that higher optical outputs were obtained when using the reflective architecture.

In addition, in environment compatibility evaluation research, which included physiological and psychological influence exerted on humans by application of LED array light sources to living spaces, we focused on the problem of one-dimensional light-emitting surface luminance distribution in regular arrangements of point LED light sources and theoretically derived a formula for the estimation of visual discomfort using psychophysical parameters. In addition, using the estimation formula, we obtained a correlation for visual discomfort that took into consideration factors such as the spatial frequency, duty ratio, contrast ratio, and average luminous intensity and studied its tolerance values.

## 13.2 Summary of Research and Development in 2000

Results obtained prior to last year allowed us to confirm that a reflective architecture, when used for LED light source devices of the phosphor conversion type, could be efficient in increasing optical outputs and proposed a model reflective architecture. In this connection, this year, we conducted optical simulations of LED light source devices of the model reflective architecture using a phosphor conversion-based emission system combining blue LEDs and YAG phosphors and conducted a comparative study using real-life prototype models. It was confirmed that the results obtained from the simulation were close to the optical measurement values of the real-life models, which corroborated the effectiveness of the application of the present simulation technique to optical control and design optimization.

Subsequently, by combining white LEDs with LEDs emitting light of different colors, we were able to recreate multicolored light, and, based on the fact that the color tone could be easily changed by regulating optical outputs, we studied a correlated color temperature alteration technique based on combining red and green LEDs with white LEDs. Furthermore, because color rendering properties are a factor of considerable

importance for illumination light sources, we examined average color rendering property evaluation scores (Ra). As a result of investigating the spectral distributions of three kinds of LEDs based on the method of additive mixture of color stimuli, we obtained correlated color temperature conditions for incandescent light bulb color, warm white color, white color, daylight white color, and daylight color. In addition, it was confirmed that high color rendering properties with a Ra=95 could be obtained under daylight conditions.

In the area of environment compatibility evaluation, we conducted psychophysical experiments to determine the psychological influence exerted on test subjects by matrix-like two-dimensionally arranged LED array light sources. The verification did not allow us to determine the relationship of the visual stress to the spatial factors related to the arrangement of the LED point light sources, but it was confirmed that there was a strong correlation between “glare” and “discomfort.”

### **13.3 Study of phosphor conversion-based LED light source devices by optical simulation**

In recent years, development of high-brightness GaN-based LEDs has made considerable progress, with white LEDs based on the use of YAG phosphors attracting attention as a fourth type of illumination light sources in addition to incandescent lamps, fluorescent lamps, and HIDs. Against this background, LED-based solid semiconductor light sources, which are characterized by small size, long useful life, and by being mercury-free, have aroused even more interest from the standpoint of possible improvements in energy conversion efficiency, in other words, better energy savings. At present, the emission efficiency of white LEDs is 15~25 lm/W, i.e. its level already exceeds that of incandescent lamps, and since their commercial introduction in 1996, white light emitting diodes have made great strides in terms of efficiency improvements [1-5].

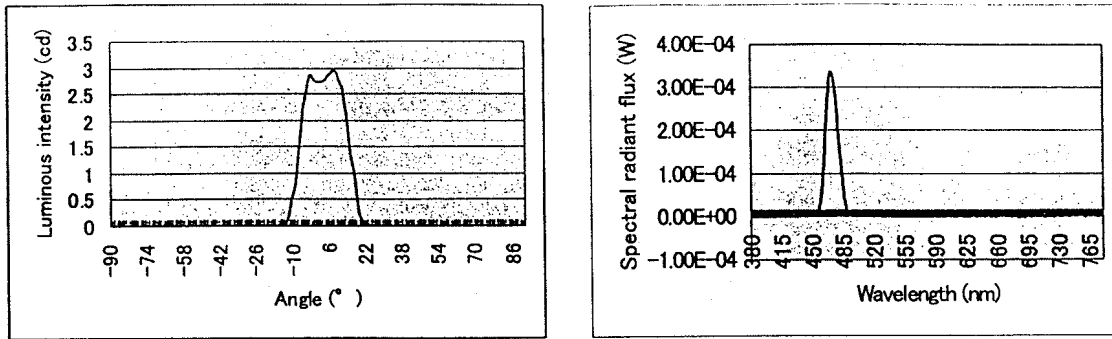
One of the objectives of the present project is to develop high-efficiency 80~100 lm/W LEDs before the end of 2003 to realize the goal of next-generation LED-based illumination that is coming to replace fluorescent lamps. In order to achieve the objective, during the present project, we have been developing LED light source devices for illumination using an emission system, in which high-efficiency LEDs based on GaN with emission wavelengths in the blue to near-UV region around 400 nm are combined with phosphors capable of efficient conversion to visible white light.

In the course of this development, we have realized the need to carry out design optimization and optical control of LED-based light source devices based on optical simulation. For this reason, last year, we conducted measurements of optical characteristics of UV-excitable phosphors capable of conversion to visible light, and, by introducing the obtained results in our optical simulation, conducted a basic investigation into simplified device models employing UV LEDs in order to determine whether a reflective architecture making efficient use of reflected phosphor light was desirable in terms of obtaining high optical outputs. On the other hand, in the course of our studies of phosphor conversion-based LED light source device architectures combining currently available GaN-type blue LEDs with YAG phosphors, we fabricated and examined real-life models, which corroborated the fact that high optical outputs were associated with the use of the reflective architecture. Therefore, this year, we studied the optical characteristics of LED light source devices of the reflective architecture that combined blue LEDs with YAG phosphors by carrying out actual measurements of optical characteristics of the YAG phosphors and introducing the resultant values into the optical simulation.

#### **13.3.1 Methods and means (simulation-based study of light source devices)**

First of all, in order to fully understand the characteristics of current GaN-based blue LEDs, we examined the light distribution characteristics and spectral distribution of currently available top-level bullet blue LEDs and, as a result, confirmed that such diodes emitted blue light with a peak wavelength of 467 nm and an optical output of 6.3 mW when a forward electric current with a rating of 20 mA was passed through the diodes. For this reason, in the experiments, in order to obtain the optical characteristic values of YAG

phosphors, we decided to make use of a spot light source (LA-250Xe from Hayashi Watch-Works Co., Ltd.), in which a Xenon lamp with an attached optical filter selectively transmitting light from the long wavelength region in the vicinity of 470 nm was used as a light source, on the assumption that the blue light (optical output: 6 mW) obtained from such a spot light source would be a good approximation of GaN blue LED emission. FIG. 13.3.1-(1) and FIG. 13.3.1-(2) show, respectively, the light distribution characteristic and spectral radiant flux of the spot light source.



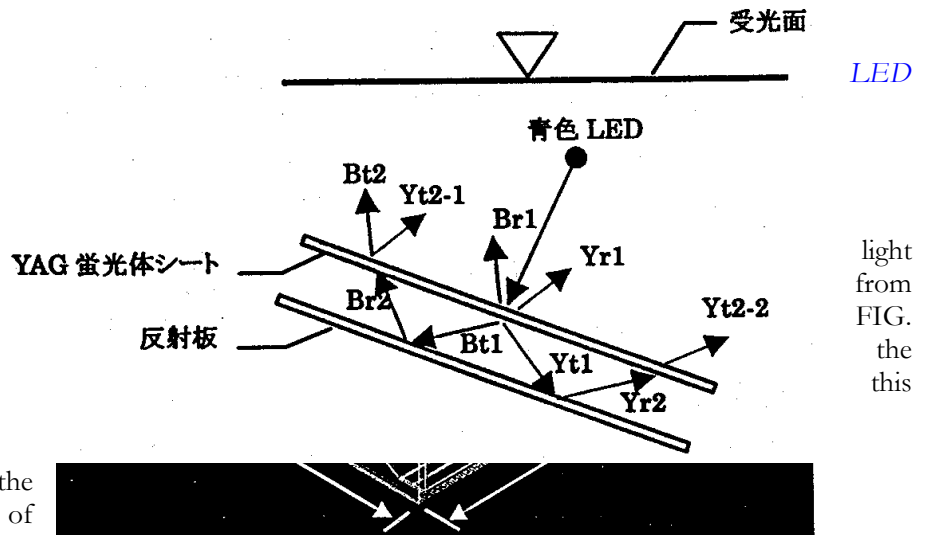
Left: FIG. 13.3.1-(1) Light distribution characteristic of spot light source

Right: FIG. 13.3.1-(2) Spectral radiant flux of spot light source

The YAG phosphors used in the experiments were commercially available products (P46-Y3 from Kasei Optonics, Inc.) whose structure was represented by the chemical formula  $Y_3Al_5O_{12}:Gd, Ce$ . To prepare YAG phosphor test samples (called YAG phosphor sheets below), YAG phosphor powders were introduced into silicone rubber sheets with a thickness of 0.3 mm so as to obtain a predetermined concentration of 10~60 wt%. The light distribution characteristics and spectral distributions of the transmitted light and reflected light resulting from irradiation of each sheet with light from the spot light source at an incidence angle varying between 0° to 70° were measured to investigate the optical characteristic values of the YAG phosphors, which we planned to introduce into the optical simulation.

The optical simulation was carried out using a ray tracing-type illumination design software program (Light Tools from Optical Research Associates), which was based on the Monte Carlo method. FIG. 13.3.1-(3) shows a reflective LED light source device model used to conduct the optical simulation. A 120° V-shaped reflecting plate and, above it, a YAG phosphor sheet, were installed inside a 122×122×36.5 mm box-shaped fixture, and array substrates having blue LEDs mounted thereon (10 LED per side) were arranged on both sides of the box at angles of 45° towards the inside. In this construction, light emitted by the blue LEDs was directed outside by traveling via the YAG phosphor sheet and reflecting plate and passing through a 100×100 mm diffuser plate provided in front of the box. In addition, as concerns the optical characteristic values (transmittance, reflectance) of the various constituent materials of the reflecting plates etc. used in this construction, we subjected the constituent materials of the real-life prototype models fabricated using commercially available surface-mounted GaN blue LEDs (rated optical output: 3.6 mW) to measurements using a C-light source [UV-C? – trans.] as a reference and employed the obtained values in the optical simulation. In addition, as far as the blue LED light source settings used in the simulations are concerned, 1,000 light rays were used as the number of rays (per 1 LED) and the optical output and light distribution characteristics of the spot light source were inputted as is because the blue light emitted from the spot light source when obtaining the optical characteristic values of the YAG phosphors was assumed to be equivalent to the emission of a GaN-based blue LED.

FIG. 13.3.1-(3) Reflective light source device model



The trajectory of a single ray in the light emitted a blue LED is shown in 13.3.1-(4). The target of calculations performed in simulation was the secondary light, which is usually crucial to the determination of the amount of illumination. When light

emitted from a blue LED reached the YAG phosphor sheet, it generated four kinds of light: ① wavelength-converted transmitted light (Yt1), ② unconverted transmitted light (Bt1), ③ wavelength-converted reflected light (Yr1), and ④ unconverted reflected light (Br1). The two kinds of reflected light (Yr1, Br1) were captured as primary light on the light-receiving surface. On the other hand, the light that passed through the YAG phosphor sheet (Yt1, Bt1) was reflected by the reflecting plate and again traveled to the YAG phosphor sheet (Yr2, Br2), generating wavelength-converted transmitted light (Yt2-1) and unconverted transmitted light (Yt2-1, Bt2), respectively. Therefore, the transmitted light (Yt2-1, Yt2-2, Bt2), generated when light reached the YAG phosphor sheet again, was captured as secondary light on the light-receiving surface. In addition, most of the calculations in the simulation were related to the radiant flux (W), with the long wavelength region of 380~500 nm used as the blue light component, the wavelength region of 501~780 nm used as the yellow light component, and the blue light component and yellow light component calculated separately.

LED  
light  
from  
FIG.  
the  
this

FIG. 13.3.1-(4) Single ray trajectory

[Keys, FIG. 13.3.1-(4)]

(Top to bottom) Light receiving surface; Blue LED; YAG phosphor sheet; Reflecting plate

### 13.3.2 Results and discussion (simulation-based study of light source devices)

FIG. 12.3.2-(1) shows the radiant fluxes of the components of the transmitted and reflected light versus the YAG phosphor content, which were obtained by irradiating a YAG phosphor sheet with a spot light source at an incidence angle of 0°. First of all, as far as the blue transmitted light and yellow transmitted light are concerned, it was confirmed that, as the content of YAG phosphor increased, the radiant flux of the blue transmitted light decreased, and, at the same time, as a result of conversion by the YAG phosphor, there was obtained yellow transmitted light; however, it was found that the radiant flux of the yellow transmitted light did not increase with the increase in the content of the YAG phosphor and remained in a saturated state. In addition, as the content of the YAG phosphor increased, the color of the transmitted light readily changed from blue to white to yellow, which can be seen from the ratio of the radiant flux of the blue transmitted light to that of the yellow transmitted light. On the other hand, as far as the blue reflected light and yellow reflected light are concerned, it was confirmed that as the content of YAG phosphor increased, the radiant flux of the blue reflected light did not undergo significant changes and remained almost constant, whereas the radiant flux of the yellow reflected light continuously increased and reached a saturated state when the content of the YAG phosphor was approximately 50~60 wt%. In addition, it was found that, as the content of the YAG phosphor increased, the color of the reflected light changed from a bluish white to white, with white light obtained under all conditions.

FIG. 13.3.2-(1) Relationship between YAG phosphor content and radiant flux

[Keys, FIG. 13.3.2-(1)]

(Box inside, top to bottom) Blue transmitted light

Yellow transmitted light

Blue reflected light

Yellow reflected light

FIG. 13.3.2-(2) shows the luminous flux versus the YAG phosphor content, obtained as a result of irradiating a YAG phosphor sheet with the spot light source at an incidence angle of 0°. It was found that as the content of the YAG phosphor increased, the luminous flux of the transmitted light tended to gradually decrease, while the luminous flux of the reflected light tended to undergo a considerable increase. In addition, it was confirmed that the total luminous flux reached a saturated state at a YAG phosphor content of 50 wt%. Thus, in order to study reflective LED light source devices, we made the decision to introduce the optical characteristic values obtained at the YAG phosphor content of 50 wt% into the optical simulation.

FIG. 13.3.2-(2) Relationship between YAG phosphor content and luminous flux

[Keys, FIG. 13.3.2-(2)]

(Box inside, top to bottom): Transmitted light; Reflected light; Total luminous flux

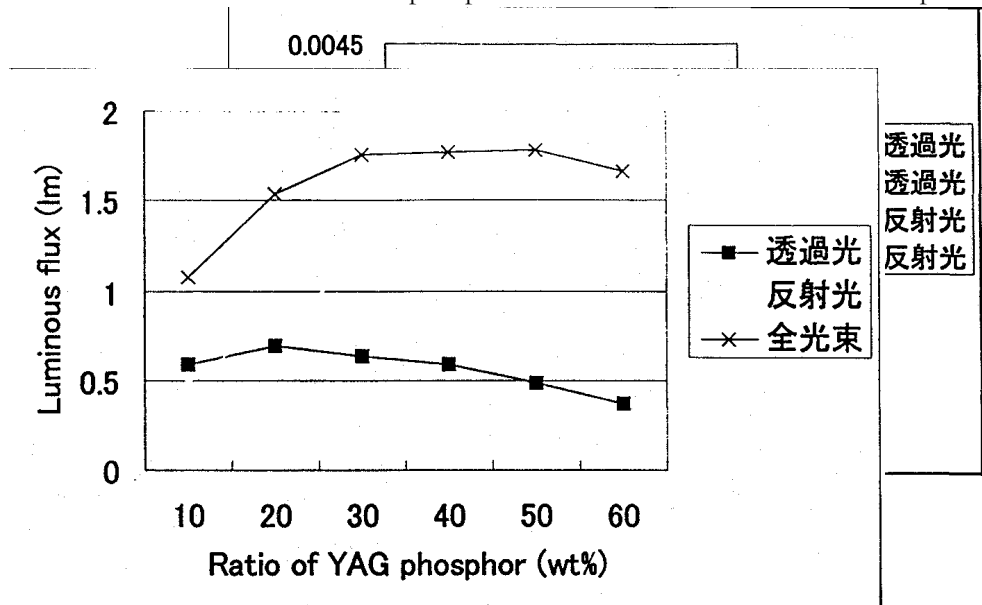
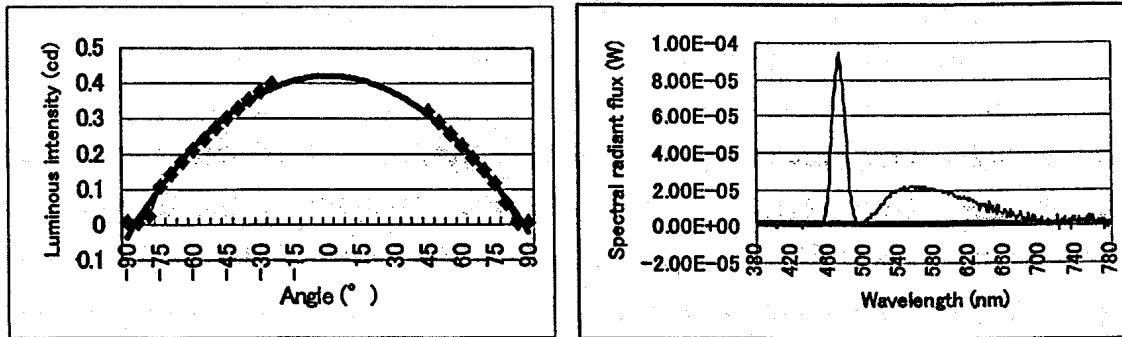


FIG. 13.3.2-(3) and FIG. 13.3.2-(4) show the light distribution characteristic and spectral radiant flux of reflected light obtained by irradiating a YAG phosphor sheet with a YAG phosphor content of 50 wt% at an incidence angle of 0°. In addition, because in case of measuring the light distribution characteristic of the reflected light the spot light source was itself an obstacle, there were some areas, where measurements could not be done; however, because in case of both transmitted light and reflected light generated from the YAG phosphor sheet it was assumed to be a type of diffused light, we obtained the desired values by using an approximation curve. In addition, for this reason, the light emitted from the YAG phosphor sheet in the optical simulation was treated as diffused light as well. From the spectral radiant flux results shown in FIG. 13.3.2-(4), it was determined that the radiant flux of the reflected light was 1.68 mW for the blue light component and 2.81 mW for the yellow light component, with the color of the emitted light being white, with chromaticity coordinates of  $x=0.31, y=0.33$ . Optical characteristics results obtained in the same manner for a YAG phosphor sheet with a YAG phosphor content of 50 wt% are shown in Table 13.3.2-(1).



Left: FIG. 13.3.2-(3) Light distribution characteristic of reflected light from YAG phosphor sheet (50 wt%, 0°)

Right: FIG. 13.3.2-(3) Spectral radiant flux of reflected light from YAG phosphor sheet (50 wt%, 0°)

Incidence angle	Transmitted light			Reflected light		
	Blue component (transmittance)	Yellow component (transmittance)	Chromaticity coordinates (x, y)	Blue component (reflectance)	Yellow component (reflectance)	Chromaticity coordinates (x, y)

0°	0.02 mW (0.004)	1.15 mW (0.191)	(0.45, 0.52)	1.68 mW (0.280)	2.81 mW (0.469)	(0.31, 0.33)
10°	0.02 mW (0.004)	1.13 mW (0.189)	(0.45, 0.52)	1.79 mW (0.298)	2.52 mW (0.420)	(0.30, 0.32)
20°	0.02 mW (0.004)	1.11 mW (0.185)	(0.45, 0.52)	1.66 mW (0.277)	2.56 mW (0.427)	(0.31, 0.33)
30°	0.02 mW (0.003)	1.09 mW (0.181)	(0.45, 0.52)	1.80 mW (0.300)	2.83 mW (0.472)	(0.31, 0.33)
40°	0.02 mW (0.003)	1.06 mW (0.177)	(0.45, 0.52)	1.85 mW (0.308)	2.94 mW (0.490)	(0.31, 0.33)
50°	0.02 mW (0.003)	1.02 mW (0.170)	(0.46, 0.52)	1.63 mW (0.272)	2.61 mW (0.435)	(0.31, 0.33)
60°	0.02 mW (0.003)	0.93 mW (0.155)	(0.46, 0.52)	1.57 mW (0.262)	2.53 mW (0.422)	(0.31, 0.33)
70°	0.01 mW (0.002)	0.79 mW (0.132)	(0.46, 0.52)	1.33 mW (0.222)	2.15 mW (0.358)	(0.31, 0.33)

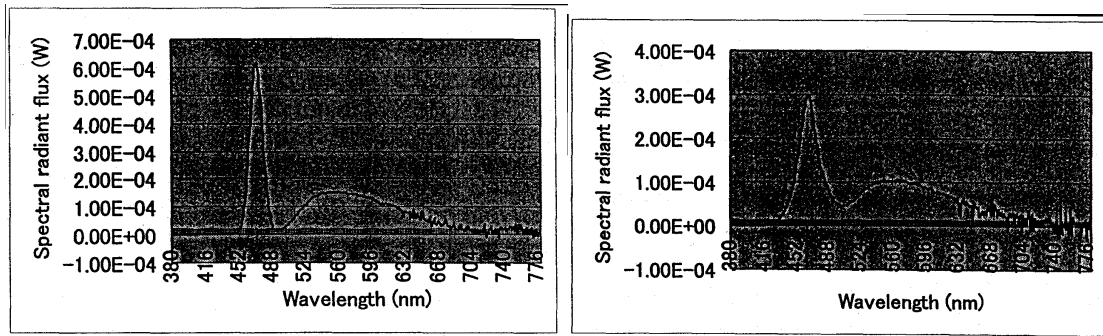
*Table 13.3.2-(1) Optical characteristic values of YAG phosphor sheet (YAG phosphor content: 50 wt%)*

Table 13.3.2-(2) shows the radiant flux of a reflective LED light source device obtained via simulation. In addition, FIG. 13.3.2-(5) shows the spectral radiant flux obtained based on the optical simulation results. From the simulation results it was conjectured that the radiant flux of the blue light component was 11 mW, and that of the yellow light component was 20 mW, and, upon conversion to luminous flux, the resultant optical output was approximately 9.1 lm, with the color of the emission at such time being white, with chromaticity coordinates of  $x=0.32$  and  $y=0.34$ . On the other hand, it was confirmed that the proportion of the primary light in the resultant total radiant flux accounted for the most of it, with the proportion of the secondary light being as small as to be safely ignored. This fact can be interpreted as a sign of the high reflectance and low transmittance of the YAG phosphor sheet used in the simulation, indicating that a reflective type architecture is efficient in terms of obtaining high optical outputs. However, because it was found that the total radiant flux obtained for blue light with an optical output of 120 mW ( $6 \text{ mW} \times 20$ ) was approximately 31 mW and there were considerable optical energy losses of more than 70% in the reflective type LED light source device, achieving further efficiency improvements based on simulation is an important task for the future.

FIG. 13.3.2-(6) shows the spectral radiant flux of a real-life prototype model. It was confirmed that in the real-life model, too, its total radiant flux was low, at 23 mW, and considering that in this case we used blue LEDs with an optical output of 3.6 mW/diode, the optical energy losses were also large, at about 70%. In addition, the total luminous flux of the real-life model was 6.4 lm and the color of the emission was white, with chromaticity coordinates of  $x=0.30$  and  $y=0.31$ , and if we consider the difference in optical outputs from this standpoint, this confirms that the results of the simulation were a good approximation of the results of the real-life model. This provides evidence in support of the possibility of applying the present simulation technique to the optical control and design optimization of LED light source devices.

Components	Radiant flux
Blue, reflected, primary (Br1)	11 mW
Yellow, reflected, primary (Yr1)	20 mW
Blue, transmitted, secondary (Bt2)	0.011 mW
Yellow, transmitted, secondary (Yt2-1)	0.026 mW
Yellow, transmitted, secondary (Yt2-2)	0.043 mW
Blue light radiant flux (Br1+Bt2)	11.011 mW
Yellow light radiant flux (Yr1+Yt2-1+Yt2-2)	20.069 mW
Total radiant flux (Br1+Bt2+Yr1+Yt2-1+Yt2-2)	31.080 mW

*Table 13.3.2-(2) Optical simulation results of reflective LED light source device*



Left: FIG. 13.3.2-(5) Spectral radiant flux obtained based on optical simulation results

Right: FIG. 13.3.2-(6) Spectral radiant flux of real-life prototype model

## 13.4 Correlated color temperature alteration techniques and color rendering property evaluation of mixed light from white, red, and green LEDs

Sunlight at the height of the day can be separated into red, orange, yellow, green, blue, indigo, and violet color light with a prism; however, because the human eye does not possess the capability for analyzing the components of light, it cannot tell whether the white light it sees is a mixture of yellow light and blue light or a mixture of red light, green light, and blue light. However, the human eye is quite sensitive to colors and perceives even the slightest difference in color tone, and the difference in color tone exerts considerable psychological influence on humans. For this reason, the color of light sources used for illumination is an important factor that not only affects the atmosphere of the interior and the impression of the space, but also exerts considerable influence on human perception and emotions. For example, one of the methods used to represent the color of a light source is to use the color temperature; in general, however, when the color temperature is less than 3000 K, the color feels warm, whereas when it is 5000 K or more, the color produces a cool sensation [6].

For light sources such as fluorescent lamps used for general illumination, the chromaticity range is stipulated by JIS Z 9112, where it is divided into 5 types of color, such as (starting from the lowest correlated color temperature ( $T_{cp}$ )): incandescent light-bulb (L:  $T_{cp}$ =2600~3150 K), warm white (WW:  $T_{cp}$ =3200~3700 K), white (W:  $T_{cp}$ =3900~4500 K), daylight white (N:  $T_{cp}$ =4600~5400 K), and daylight (D:  $T_{cp}$ =5700~7100 K) [7]. Therefore, although appropriately illuminated spaces can be created depending on the intended use and individual tastes by using different fluorescent lamps of the above various light source colors, in such a case, only one light source color can be selected for one type of fluorescent lamp and the needs of the user who might want to change the color temperature depending on seasonal or time-of-the-day variations in a simple and straightforward manner are not satisfied.

By contrast, LEDs exhibit various emission colors, including the three primary colors (red, green, blue), which permits full color lighting based on combining different LEDs and regulating their respective optical outputs. In addition, there are white LEDs manufactured by combining phosphors with blue LEDs, and using them together with colored LEDs allows for creating multi-colored lighting, the color tone of which can be easily tuned by regulating the respective optical outputs. In this connection, we studied a correlated color temperature alteration technique based on using white LEDs made by combining blue LEDs and phosphors as basic units and combining them with red and green LEDs, the other two primary colors besides blue. In addition, because color rendering properties are an important factor in creating high-quality illumination, we also studied their average color rendering property evaluation scores ( $R_a$ ).

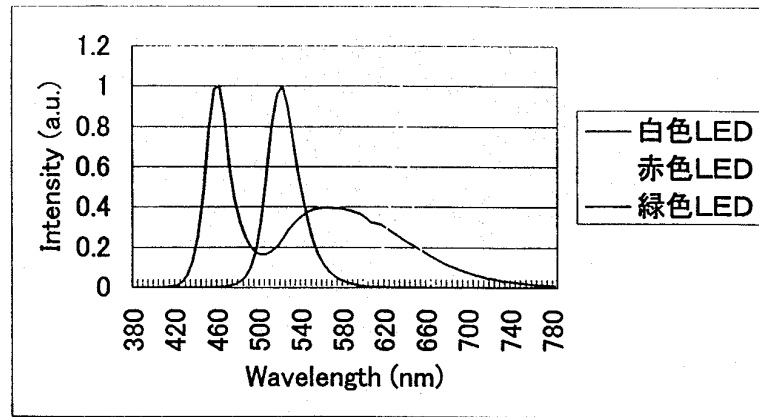
### 13.4.1 Methods and means (correlated color temperature alteration technique & color rendering property evaluation)

The spectral distributions of the white, red, and green LEDs used in the experiments are shown in FIG. 13.4.1. The white LEDs were based on a combination of an InGaN-based blue LED with a peak wavelength of 460 nm with a YAG phosphor emitting yellow light with a central wavelength of 565 nm, the red LEDs were based on AlGaInP with a peak wavelength of 635 nm, and the green LEDs were based on InGaN with a peak wavelength of 520 nm. In addition, the chromaticity coordinates of the white LEDs used in the experiments were  $x=0.31$  and  $y=0.29$ , with a correlated color temperature of  $T_{cp}=7200$  K and an average color rendering score of  $R_a=85$ .

FIG. 13.4.1 Spectral distributions of LEDs

[Keys, FIG. 13.4.1]

(Box inside, top to bottom): LED; Red LED; Green LED



White

color  
on

the

We studied the correlated temperature conditions based the method of additive mixture of color stimuli using spectral distributions of the LEDs.

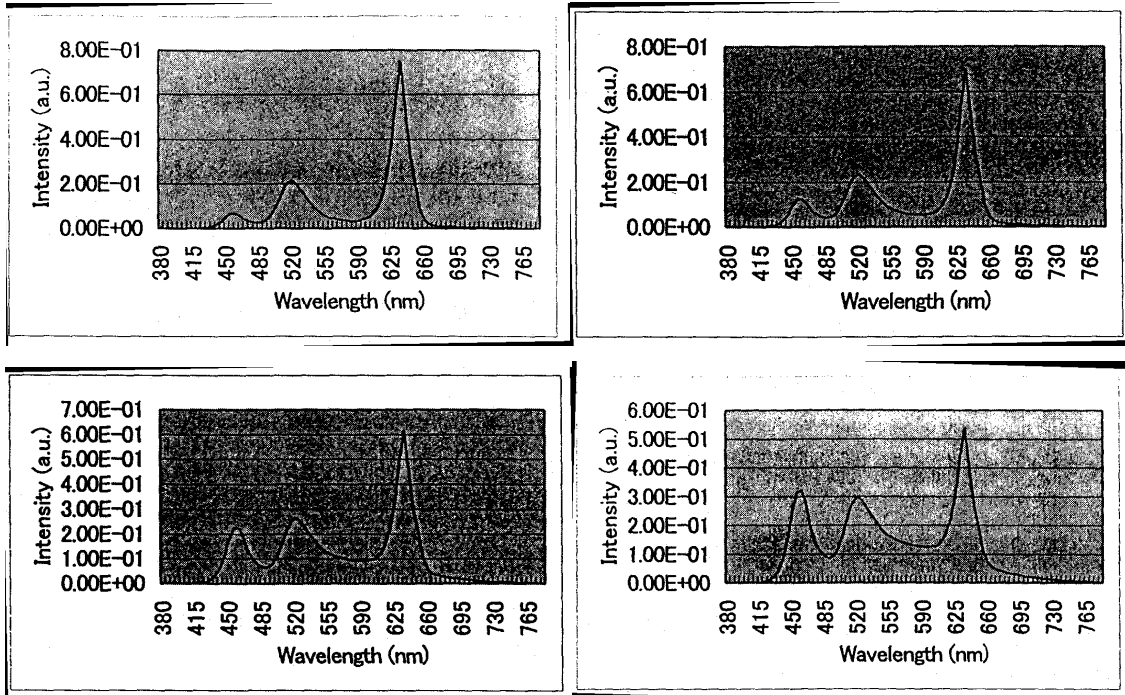
The values of the spectral distributions of mixed colors were inputted into an independently developed color rendering property evaluation score computation program, obtaining the chromaticity coordinates, correlated color temperature, and average color rendering property evaluation scores [8, 9].

### 13.4.2 Results and discussion (correlated color temperature alteration technique & color rendering property evaluation)

The average color rendering property evaluation scores, correlated color temperatures, chromaticity coordinates, and emission intensity ratios under various correlated color temperature conditions, which were obtained based on the method of additive mixture of color stimuli using the spectral distributions of the white, red, and green LEDs, are shown in Table 13.4.2. In addition, FIG. 13.4.2-(1) ~ FIG. 13.4.2-(5) show respective spectral distributions under various correlated color temperature conditions. The correlated color temperature conditions were obtained by setting the emission intensity ratio of the green LEDs to approximately 20% and varying the emission intensity ratio of the white LEDs and red LEDs. In other words, it was confirmed that arbitrary correlated color temperatures could be realized by lowering the emission intensity of the white LED ( $T_{cp}=7200$  K), which had a high correlated color temperature, and instead raising the emission intensity of the red LEDs.

Light source color	Emission intensity ratio (%)			Chromaticity coordinates (x, y)	Correlated color temperature T <sub>cp</sub> (K)	Average color rendering property evaluation score Ra
	White LED	Red LED	Green LED			
Incandescent light-bulb (L)	6.7	73.6	19.7	(0.45, 0.41)	2800	26
Warm white (WW)	12.4	67.1	20.5	(0.41, 0.39)	3370	42
White (W)	22.6	56.4	21.0	(0.37, 0.37)	4246	63
Daylight white (N)	31.8	46.2	22.0	(0.35, 0.36)	5026	78
Daylight (D)	53.5	26.7	19.8	(0.32, 0.34)	6186	95

Table 13.4.2 Correlated color temperature conditions



*Top Left: FIG. 13.4.2-(1) Spectral distribution of incandescent light bulb (L)*

*Top Right: FIG. 13.4.2-(2) Spectral distribution of warm white (WW)*

*Middle Left: FIG. 13.4.2-(3) Spectral distribution of white (W)*

*Middle Right: FIG. 13.4.2-(4) Spectral distribution of daylight white (N)*

*Lower Right: FIG. 13.4.2-(5) Spectral distribution of daylight (D)*

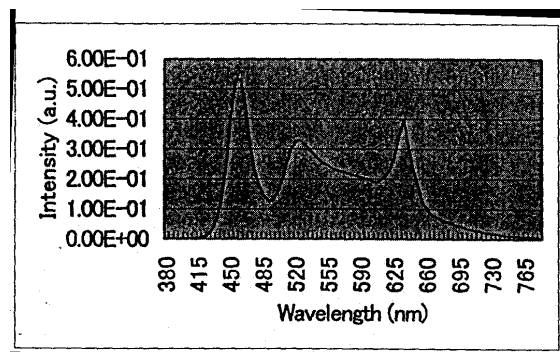
On the other hand, the average color rendering property evaluation score tended to increase with increasing correlated color temperature, with a particularly high value of  $R_a=95$  obtained for daylight, which exceeded the  $R_a=85$  of the white LED used in the experiments. In addition, generally speaking, color rendering properties are high in case of spectra that are uniform and continuous in the visible light region and low in case of spectra lacking in uniformity, which is also confirmed by the spectral distributions under various correlated color temperatures. However, because 3-wave length type fluorescent lamps, which are currently in widespread use, possess a spectral characteristic made up of broad red, green, and blue spectra, and, at the same time, provide high color rendering properties of  $R_a=80$  or greater, it is expected that color rendering properties can be improved by rigorously controlling the emission intensity ratios of the white (blue), red, and green LEDs under correlated color temperature conditions other than daylight, which was investigated in the present study.

## 13.5 Study of environmental compatibility evaluation of LED light source devices

In recent years, high-brightness white LEDs have grabbed the spotlight and have shown considerable promise to become a fourth type of light source after incandescent, fluorescent, and HID sources. However, their luminous flux per single LED is about 1 lm, and in order to be able to use LEDs for general illumination, it is necessary to obtain higher optical outputs by integrating them in matrix or array form. For this reason, when LED light source devices in which high brightness spot light sources such as LEDs are integrated together for illumination purposes are used in living spaces, their safety is a condition of paramount importance, and it is essential to carry out their environmental compatibility evaluation from the standpoint of visual stress and other factors of psychological influence.

To this end, last year we focused our research on measuring the sensation of visual discomfort caused by the one-dimensional light-emitting surface luminance distribution in regularly arranged integrated LED light sources using the spatial frequency, brightness amplitude modulation, and contrast as psychophysical parameters and theoretically derived a formula for its estimation. Subsequently, using the estimation formula, we examined tolerance values of visual discomfort by taking into consideration factors such as the duty ratio, contrast ratio, and average luminance. However, last year's research did not include an environmental compatibility evaluation based on psychophysical testing using real-life integrated LED-based light sources as stimuli, and estimation using actual test subjects remained an important task for future studies. Thus, in this year's research, we employed psychophysical techniques to conduct visual stress estimation experiments using integrated LED light sources dimensionally arranged in matrix form and found confirmation of the actual psychological influence exerted by visual stress.

A. J. Wilkins was the first to clearly define the concept of "visual stress" as a scientific term Wilkins developed a theory of visual discomfort caused by visual stimuli based on the fact that among visual stimuli there were stimuli causing



two-

[11].

discomfort when looked at by observers (including generally healthy individuals) and such visual stimuli caused attacks in light-sensitive epileptics and migraine headache sufferers. In other words, Wilkins proposed that visual stress was related to the functioning of the brain and when visual stimuli were subjected to information processing in the brain, they induced attacks in light-sensitive epileptics and migraine sufferers and caused a sensation of discomfort in generally healthy individuals.

Up until now, there have been very few examples of research approaching the problem of visual stress generated by visual stimuli in healthy individuals from the above-described standpoint. In addition, in current research related to light-sensitive epileptics and migraine sufferers, estimation is based mostly on physiological techniques while the number of examples of research based on psychological approaches is relatively small. Against this background, researchers from the Hibino Lab at the Chiyo University approached the problem of visual stress using psychophysical techniques. As a result, it was found that the method of magnitude estimation [12-15] was effective in the measurement of visual stress [16-20]. Thus, in this study, using the magnitude estimation method, we attempted an estimation of visual stress caused by integrated LED sources two-dimensionally arranged in matrix form.

### **13.5.1 Methods and means (environmental compatibility evaluation study)**

During the experiments, at first we conducted a basic study using integrated light source samples utilizing bullet-type LEDs of high directionality characteristics in order to obtain a clear picture of the fundamental tendencies imparted to human visual perception by spot light sources such as LEDs, and their characteristics. We prepared two types of bullet LED sample stimuli, which were made by mounting a matrix of commercially available bullet-type white LEDs (diameter: 5 mm, angle of visibility: 20°) arranged at 10 mm intervals (11×11 LEDs) and 15 mm intervals (16×16 LEDs) in a 150×150 mm central portion of a 200×200 mm glass-epoxy base plate that was painted white. The sample stimuli were lit using a DC source, and there were 3 kinds of illumination levels at a distance of 200 mm from the sample stimuli in a direction perpendicular to the stimulus: 4500 lx, 2700 lx, and 900 lx. In addition, sample stimuli were also mounted in a 150×150 mm central area of a white 450×450 mm holder. On the other hand, a flat surface light source with two 8-W inverter-type cold-cathode fluorescent lamps (from Fujicolor: Color Illuminator Pro B4) was used as a reference stimulus (luminance: 1500 cd/m<sup>2</sup>, correlated color temperature: about 5000 K), which was also mounted in a 150×150 mm central area of a white 450×450 mm holder.

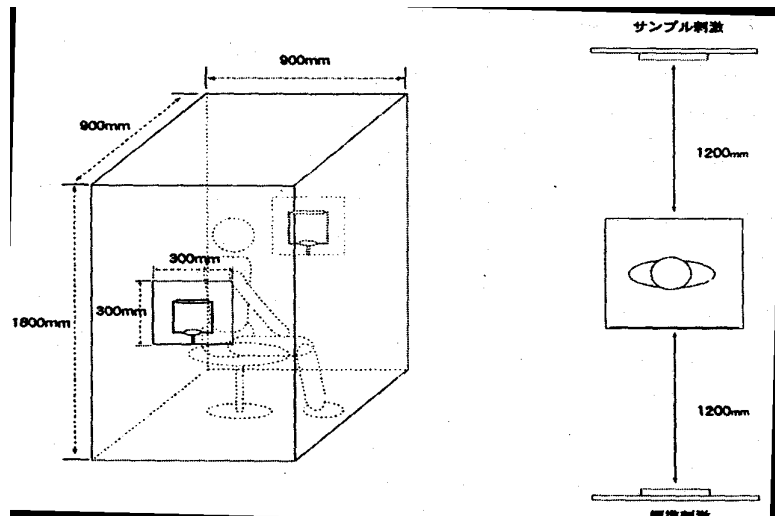
FIG. 13.5.1 shows a schematic view of the test environment used by test subjects to evaluate visual stress. All of the test subjects, i.e. nine students of the Chiyo University, had normal vision (including corrected vision). The lab where testing was conducted was shaded, and the test subjects were placed inside a 900×900×1800 mm darkroom inside, with the stimuli presented only at estimation time. In addition, the viewing distance was 1200 mm both for the sample stimuli and for the reference stimulus. Closable 300×300 mm windows were provided in the darkroom, both in the direction of the sample stimuli and that of the reference stimulus, with the stimuli shown through the windows to the test subjects, whose faces were securely positioned.

The magnitude estimation method was used for scaling the magnitude of the psychological effects produced by the sample stimuli. The test subjects were instructed to use the magnitude of the effect produced by the reference stimulus as 100 points and employ it as a reference in estimating the magnitude of the effects produced by the sample stimuli. The sample stimuli were presented for 2 seconds in random order, with three parameters measured at such time: “glare,” “discomfort,” and “pleasantness.” When possible, we tried to present one set (two kinds of stimulus samples × three kinds of illumination levels × three parameters of measurement = 18 estimations) per day, repeating the test a total of 5 times per person.

FIG. 13.5.1 Schematic view of test environment

[Keys, FIG. 13.5.1]

(Drawing on right, top to bottom) Sample stimulus; Reference stimulus



Next, we attempted to determine the degree of “glare” sensation depending on the directionality characteristics and, in order to confirm psychological influence due to spatial arrangement factors, we conducted a study using samples of integrated light sources utilizing surface-mounted type LEDs with relatively low directionality characteristics. We prepared three kinds of surface-mounted sample stimuli, in which commercially available surface-mounted white LEDs (2×3 mm, angle of visibility: 110°) were arranged in a 300×300 mm central portion of a 350×350 mm glass-epoxy base plate painted white in matrix form at intervals of 5 mm (60×60 diodes), 10 mm (30×30 diodes), and 20 mm (15×15 diodes). The sample stimuli were lit using a DC source to provide the illumination levels (200 mm away, in a direction normal to the stimulus) shown in Table13.5.1 and testing of the visual stress exerted on the subjects was carried out in the same manner as in the above-described method. In addition, the magnitude of the reference stimulus at such time was made closer to that of the sample stimuli by using a 260×260 mm central area and securing it to a white 450×450 mm holder.

Sample stimuli	Illumination levels of sample stimuli (per 1 LED)		
5 mm interval	20160 lx (5.6 lx)	5040 lx (1.4 lx)	1260 lx (0.35 lx)
10 mm interval	5040 lx (5.6 lx)	1260 lx (1.4 lx)	315 lx (0.35 lx)
20 mm interval	1260 lx (5.6 lx)	315 lx (1.4 lx)	78.8 lx (0.35 lx)

Table 13.5.1 Illumination levels of surface mounted-type sample stimuli

### 13.5.2 Results and discussion (environmental compatibility evaluation research)

FIG. 13.5.2-(1) shows estimations of the parameters depending on changes in the illumination of bullet-type sample stimuli. It was found that the estimations of “glare” and “discomfort” increased with increasing illumination, whereas the estimations of “pleasantness” tended to decrease as the illumination level increased. Furthermore, it was found that the estimations of “glare” were generally higher when the interval between LEDs was 10 mm than when it was 15 mm. This is believed to be due to the fact that when the interval was 10 mm, the density of LED arrangement was higher and the surface area of the light-emitting portion was larger at the same illumination level, which influenced the sensation of “glare” felt by the eye. On the other hand, no influence due to differences between the LED intervals was observed for “discomfort” and “pleasantness,” with both exhibiting the same tendencies in all cases. This was believed to be strongly related

to the directionality characteristics of the bullet LEDs, with light close to “beam light” with a visibility angle of 20° being an extremely strong stimulus for the test subjects, who could not differentiate the influence of the differences in the LED interval. In this connection, by switching from integrated light source samples utilizing bullet LEDs characterized by high directionality characteristics to integrated light source samples based on surface-mounted LEDs of relatively low directionality characteristics, we conducted visual stress estimation experiments in the same manner as above.

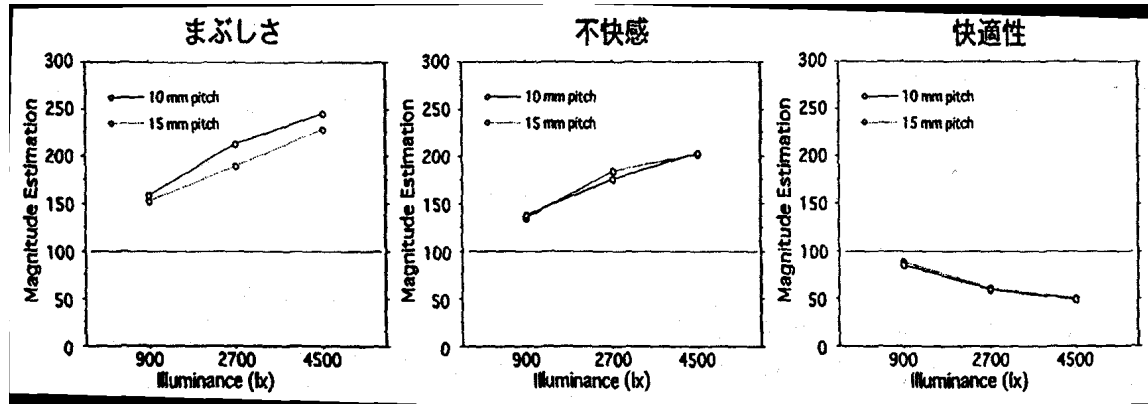


FIG. 13.5.2-(1) Estimations vs. illumination levels of bullet-type sample stimuli

[Keys, FIG. 13.5.2-(1)]

(Across top, left to right) Glare Discomfort Pleasantness

FIG. 13.5.2-(2) shows estimations of the parameters depending on illumination levels per LED in case of surface mounted type sample stimuli. In addition, FIG. 13.5.2-(3) shows the dependence of the estimations of “glare” and “discomfort” on the level of illumination of sample stimuli. Although the above data confirmed differences in estimation values for various parameters depending on illumination levels per 1 LED between sample stimuli with different LED intervals, in terms of the dependence of the estimation value on the illumination level of the sample stimuli taken as a whole, no differences in the estimation values depending on the LED interval were observed, and “glare and “discomfort” were conjectured to exhibit a tendency to change logarithmically with respect to the illumination level. Thus, we attempted to corroborate the logarithmic change tendency by means of regression analysis. In addition, as a result of conducting variance analysis of the measured estimation values, it was found that the main effects of integration density originating from the LED intervals and the illumination level per LED were statistically significant for all the parameters. On the other hand, for any of the parameters, no statistically significant differences were revealed in estimation values depending on the illumination level of the sample stimuli taken as a whole.

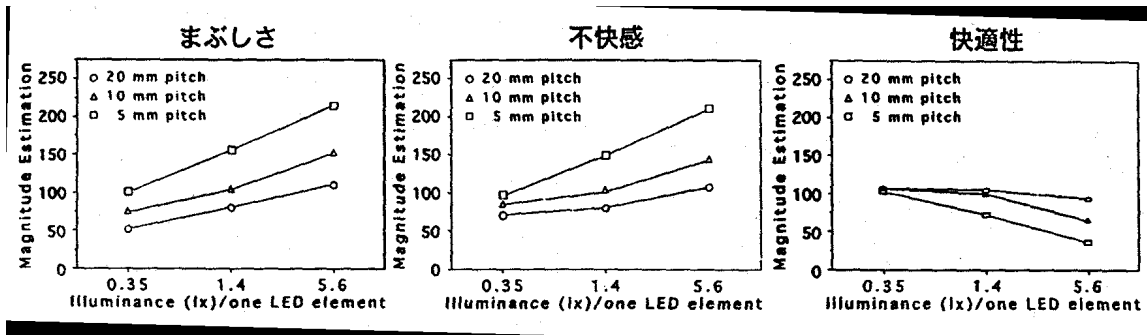


FIG. 13.5.2-(2) Estimation values of surface mounted type sample stimuli (depending on illumination level per 1 LED)

[Keys, FIG. 13.5.2-(2)]

(Across top, left to right) Glare Discomfort Pleasantness

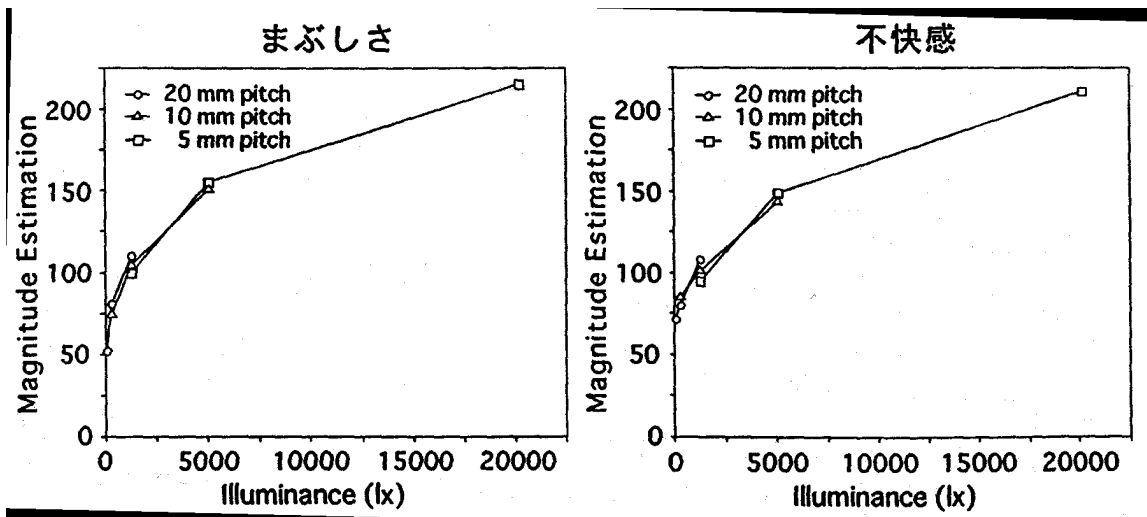


FIG. 13.5.2-(3) Dependence of estimation value on illumination level for surface mounted type sample stimuli

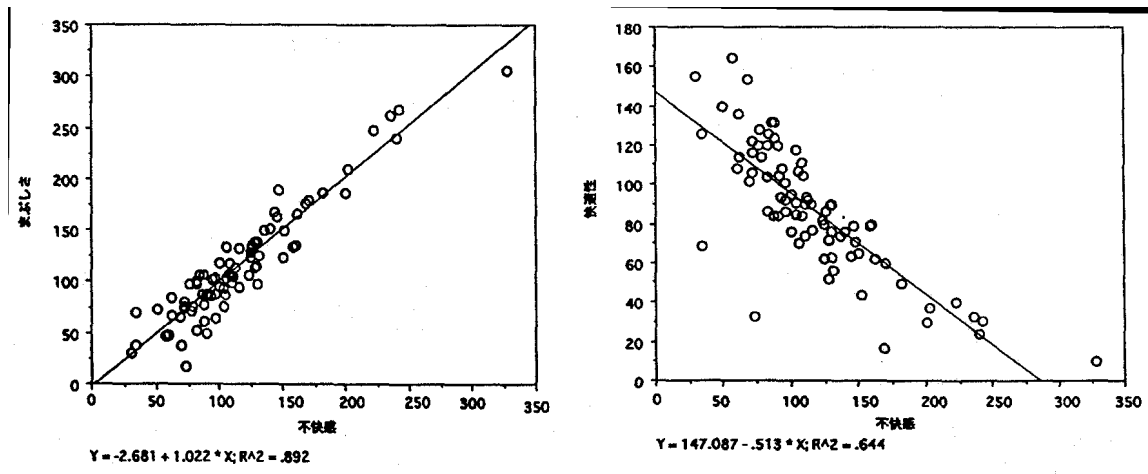
[Keys, FIG. 13.5.2-(3)]

(Across top, left to right) Glare Discomfort

FIG. 13.5.2-(4) shows the correlation between “glare” and “discomfort.” Regression analysis results showed that for “glare” the correlation coefficient was 0.972 and the explanatory ratio was 94.5%, whereas for “discomfort” the correlation ratio was 0.934 and the explanatory ratio was 87.2%, and there was a very strong linear relationship in both. In other words, it was confirmed that the estimation values of “glare” and “discomfort” were not related to the integration density of LEDs and were characterized by exhibiting a tendency towards logarithmic change with respect to the illumination level of the entire sample stimuli. Furthermore, as a result of subjecting the relationship between the two to correlation analysis, it was confirmed that there was a very strong positive correlation between the two, with a correlation coefficient of 0.944 and an explanatory ratio of 89.2%. In other words, it was confirmed that the estimation of the psychological effects of “glare” and that of “discomfort” strongly influenced each other, and, as a result, the estimation results for “glare” and “discomfort” were similar.

On the other hand, regarding the parameter of “pleasantness,” we used correlation analysis to probe the relationship between “pleasantness” and “glare” and between “pleasantness” and “discomfort.” As a result,

it was found that in the former case the correlation coefficient was  $-0.727$  and the explanatory ratio was 52.8% and in the latter the correlation coefficient was  $-0.802$  and the explanatory ratio was 64.4%, with “pleasantness” having a negative correlation with respect to both “glare” and “discomfort.” FIG. 15.5.2-(5) shows the correlation between “pleasantness” and “discomfort,” but the correlation observed here was not as strong as in the case of “glare” and “discomfort.” For this reason, it is believed that “pleasantness” and “discomfort” are not in a directly opposed relationship. This indicates that the relationships of “pleasantness” to “glare” and that of “discomfort” to “glare” do not yield completely opposed results. Therefore, it is necessary to proceed with further clarification of the parameter of “pleasantness.”



Left: FIG. 13.5.2-(4) Correlation between “glare” and “discomfort”

[Keys, FIG. 13.5.2-(4)]

(X-axis) Discomfort

(Y-axis) Glare

Right: FIG. 13.5.2-(5) Correlation between “pleasantness” and “discomfort”

[Keys, FIG. 13.5.2-(5)]

(X-axis) Discomfort

(Y-axis) Pleasantness

As described above, as a result of estimation of visual stress experienced by test subjects using various integrated light sources such as bullet type LEDs and surface-mounted type LEDs, it was found that with the increase in the illumination level of the sample stimuli, “glare” and “discomfort” increased and there was a strong correlation between the two. However, influence due to the LED intervals could not be confirmed, and it was not possible to establish its relationship to the visual stress generated by two-dimensional matrix-like arrangements of LED point light sources. Results of previous research into visual stress, in which healthy individuals were used as test subjects, indicate that, as far as geometric patterns are concerned, the discomfort increases when the spatial frequency is in the range of about 1~5 cpd. By contrast, as far as the LED arrangement patterns of the surface mounted type sample stimuli used in the present study are concerned, in terms of the spatial frequencies obtained when scanned in the horizontal direction, in case of the 5-mm interval, 10-mm interval, and 20-mm interval, we had frequencies of 4 cpd, 2 cpd, and 1 cpd, respectively, among which no differences in the estimations of discomfort were observed. Considering that the duty ratios of the sample stimuli were also changing, the fact that no differences between the estimations were observed is extremely interesting. In connection with this result, we should consider factors such as differences in the properties of the stimuli themselves (the ratio of illuminance at the edge of the pattern) and in the future it is necessary to conduct further investigations based on this point of view. In addition, although last year we conducted investigations using a theoretically derived estimation formula, but this study

has shown that corroboration by means of psychophysical testing using actual test subjects is extremely important in applied studies such as the environmental compatibility evaluation of illumination.

## 13.6 Summary

In this year's research, we determined the optical characteristics of YAG phosphors based on actual measurements and conducted an investigation into reflective LED light source devices combining blue LEDs with YAG phosphors using optical simulation. It was confirmed that the results of the simulation were close to the optical characteristic values of real-life prototype models fabricated using commercially available LEDs, which proved that the use of the present simulation technique was efficient in the optical control and design optimization of light source devices. In addition, based on the results of the simulation, it was found that light source devices of the reflective architecture investigated in the current study were characterized by optical energy losses of 70% or more, which makes improvements aimed at increasing the efficiency of the devices by suppressing the optical energy losses an important task for the future.

On the other hand, by combining currently available white LEDs with red and green LEDs, we conducted an investigation into a correlated color temperature alteration technique and also examined color rendering properties obtained in the process. As a result of studying the spectral distributions of three kinds of LEDs based on the method of additive mixture of color stimuli, we obtained correlated color temperature conditions for incandescent light-bulb (L:  $T_{cp}=2800$  K), warm white (WW:  $T_{cp}=3370$  K), white (W:  $T_{cp}=4246$  K), daylight white (N:  $T_{cp}=5026$  K), and daylight (D:  $T_{cp}=6186$  K) by setting the emission intensity ratio of the green LEDs to approximately 20% and controlling the emission intensity ratios of the white LEDs and red LEDs. In addition, it was confirmed that using daylight conditions resulted in high color rendering properties of  $R_a=95$ , which exceeded the  $R_a=85$  of currently available white LEDs.

In our research into environmental compatibility evaluation, we conducted psychophysical testing using test subjects to determine the psychological influence exerted by matrix-like two-dimensionally arranged integrated LED light sources. As a result, we were unable to determine how visual stress depended on the spatial factors of the LED point light sources. However, in the experiments, it was found that there was a strong correlation between the "glare" and "discomfort," and their estimations were proportionate to a logarithm of the illumination of the sample stimuli.

## 13.7 Future plans

This year's results have shown that optical energy losses of 70% or more occur in LED light source devices utilizing a reflective architecture; thus, in the future, we plan to increase the efficiency of LED light source devices by making the most of the optical simulation technique that has been developed. In addition, we will try and elucidate the heat-emitting structure of LED light source devices in search of possibilities of further efficiency improvements.

On the other hand, in the area of environmental compatibility evaluation research, we will conduct more detailed psychophysical testing to evaluate the "glare," "discomfort," and "pleasantness" of LED-illuminated environment while trying to clarify the characteristics of the influence exerted by discomfort glare and the influence of visual stress originating from factors related to the spatial arrangement of point light sources.

## 13.8 References

- [1] M. Miyazaki, Journal of Illuminating Engineering Institute of Japan, 81, 558 (1997).
- [2] T. Mukai, Journal of Illuminating Engineering Institute of Japan, 83, 447 (1999).
- [3] T. Taguchi, Display (monthly), No. 3, 1 (2000).

- [4] Y. Hirota, Materials of 2000 All-Japan Conference of Illuminating Engineering Institute of Japan (2000), pp. 277-278.
- [5] K. Bando, S. Koda, M. Kohashi, T. Nishioka, A. Sakano, K. Nagamine, K. Sakai, K. Arai, Y. Kiyomizu, Preprints of Joint Symposium on Fluorescent Materials No. 286 (2001), pp. 17~24.
- [6] N. Simazaki "Lighting Design Encyclopedia, Planning and Design Techniques for Lighting," Sangyo Chosakai (1986), p.70.
- [7] Illuminating Engineering Institute of Japan, "Lighting Handbook," Ohmsha (1987) pp. 64-65.
- [8] N. Ohta, "Color Engineering," Tokyo Denki University Press (1993).
- [9] K. Naya, "Industrial Color Science," Asakura Shoten (1980).
- [10] S. Kaneya, "Optics," 13, 331 (1984).
- [11] A. J. Wilkins, "Visual Stress," Oxford University Press (1995)
- [12] S. S. Stevens, American Psychology, 17, 29 (1962)
- [13] S. S. Stevens, "Psychophysics: Introduction to Its Perceptual, Neural, and Social Prospects," John Wiley (1975).
- [14] M. Ohyama, "Experimental Psychology," Tokyo University Press (1984).
- [15] N. Ichikawa, "Introduction to Measurement Methods in Psychology," Science (1991).
- [16] H. Hibino, Materials of Symposium of P&P Research Branch of Japanese Cognitive Science Society, 26, 19 (1998).
- [17] H. Hibino and Y. Sano, Perception, 28, Supplement (1999) p. 94.
- [18] H. Hibino, A. Itoh, Published Articles of 63<sup>rd</sup> Conference of Japanese Psychological Association (1999) p. 372.
- [19] H. Hibino, Y. Sano, "Animation Research," 2, 5 (2000)
- [20] H. Hibino, K. Tsubota, Published Articles of 64<sup>th</sup> Conference of Japanese Psychological Association (2000) p. 372.

# 14 Research and development of light-emitting-region conversion illumination systems

## 14.1 Achievements in 1998~1999

Illumination systems utilizing LEDs are facing two mutually exclusive requirements: ① integrated arrangement of LEDs for low cost and improvement maintenance, and ② providing two-dimensional light-emitting regions for improved visibility and pleasantness.

In the course of the present study, we conducted research and development in the area of optimization of light-emitting-region conversion optical systems as a first step towards making light-emitting-region-conversion illumination systems a reality.

In 1998~1999, as a first step towards making light-emitting region conversion-type illumination systems a reality, we compared three representative systems and identified problems associated with each one of them. The results are summarized in Table 14.1.1.

Based on the comparative results shown in Table 14.1.1 as well as the cost reduction and improved maintenance due to the fact that the light sources can be concentrated in one point, it is believed that the light guide panel system is more advantageous.

The uniformity of luminance of an illumination system is not commonly used as a criterion for the evaluation of illumination systems. However, in order to better illustrate the advantages of LED illumination as a new type of illumination system, or to try to develop a unique niche in the illumination market for LED illumination that would be different from general illumination, it is important to continue development of illumination systems capable of utilizing this unique effect of LED illumination.

Furthermore, in the present study, we developed an original vector radiation coupling theory [1, 2], built a prototype of a 4-inch light guide panel, and confirmed its effects. Based on these results, we decided to proceed with research and development aimed at practical realization of light guide panel systems.

	Light guide panel system	Direct downlight system	Indirect system
	Light guide panel LED module	LED Reflector plate	Reflector plate
<b>Light use efficiency</b>	92%	95%	96%
<b>Uniformity</b>	100% (in theory)*1 70% (sample)	100% (in theory)*2	—
<b>Thickness</b>	10 mm	50 mm	100 mm
<b>Advantages</b>	Higher degree of freedom in design of integrated structures made up of light sources	Slightly better light use efficiency	—
<b>Problems</b>	*1 Pattern visibility	*2 Non-uniformity due to variation of LED light output	—
<b>Notes</b>	—	—	Can be used for auxiliary illumination, difficult to use for primary illumination

Table 14.1.1. light-emitting region conversion-type illumination systems.

## 14.2 Summary of research and development in 2000

This year, to conduct our design work with account taken of possible mass production of light guide panels in the future, we conducted verification of improvements in terms of light use efficiency from the standpoint of tolerances used in the fabrication process. Specifically, using a computer simulation model, we calculated the correlation between parameters, for which unpredictable fluctuations are expected in the process of fabrication (sagging during formation of pattern shapes, LED installation position, etc.), and the light use efficiency, etc., in order to obtain the tolerances of the respective parameters. Furthermore, we proposed robust systems that can tolerate variation during fabrication, such as imparting a trapezoidal shape to the pattern, positioning of LEDs in the corner, etc., and confirmed their effects using computer simulation models.

In addition, in order to investigate high directivity applications such as footlights and spotlights, we studied the effects of directivity conversion systems utilizing prism sheets. This year, we used the prototype of the 4-inch light guide panel to confirm that the directivity of the emanating light is improved by the installation of a prism sheet in the light guide panel. Furthermore, it was confirmed that the uniformity of the luminance of the light guide panel did not decrease after the installation of the prism sheet.

### 14.3 Verification of improved efficiency of coupling elements

The basic configuration of a light guide panel system, based on the results of investigations conducted prior to last year, is shown in Fig. 14.3.1 (a), (b).

This system is made up of a reflector plate/diffuser plate, a light guide panel, and an LED module, which consists of an LED chip and a white frame. In addition, light guide panel coupling elements, which direct light from the LED module into the light guide panel, and radiation coupling elements (pattern), which cause the light guided through the light guide panel to be released in the direction of light emanation, are provided, respectively, in the portion, where the light emitting module and the light guide panel are coupled together, and on the surface of the reflector plate side of the light guide panel.

FIG. 14.3.1 Basic configuration

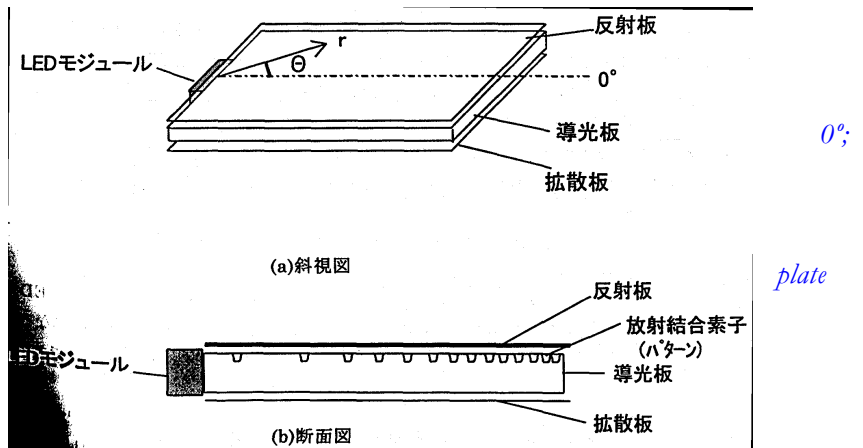
(a) Oblique view

(b) Cross sectional view.

[Keys, FIG. 14.3.1]

(a) LED module; Reflector plate; Light guide panel; Diffuser plate

(b) LED module Reflector plate Radiation coupling elements (pattern); Light guide plate; Diffuser



The light guide panel coupling elements and radiation coupling elements are suggested as the most important factors determining the light use efficiency of the light guide panel system. If we designate the luminance distribution of the light coming out of the light guide panel as  $P(r, \Theta)$ , the light emanating from the light guide panel coupling elements into the light guide panel as  $\Phi(\Theta)$ , and the distribution of the radiation coupling elements as  $H(r, \Theta)$ , then the respective correlation can be expressed in the following manner:

$$P(r, \Theta) = F[H(r, \Theta), \Phi(\Theta)] \quad (1)$$

In case of an ordinary light guide panel system, light propagates while undergoing diffusion, and the function  $F$ , which determines the coupling of  $H$  and  $\Phi$ , cannot be given analytically. However, in case of the vector radiation coupling system proposed in this study, light from the coupling section propagates through the light guide panel in a linear fashion. For this reason, light propagating in direction  $\Theta$  is influenced only by the radiation coupling pattern in direction  $\Theta$ , and  $F$  [sic; - trans.] is expressed by equation (2).

$$P(r, \Theta) = H(r, \Theta) \cdot \Phi(\Theta) \quad (2)$$

Equation (2) means that the influence exerted by the light guide panel coupling elements and influence exerted by the radiation coupling elements can be considered independently. For this reason, in this study we conducted investigations into light guide panel coupling elements and radiation coupling elements separately.

### 14.3.1 Methods and means

#### 14.3.1.1 Simulation model for radiation coupling elements

The simulation of the radiation coupling elements essentially consisted in using simulation tools to reproduce the portion emanating from the light guide panel coupling elements in the basic configuration shown in Fig. 14.3.1 and investigating its characteristics using a ray tracing simulation program. However, in case of ray tracing models that express even shapes that take into account fabrication tolerances, reproduction of the shapes requires building complicated shapes on a computer, and this, in turn, requires a huge amount of calculation time because of the huge number of points in the model.

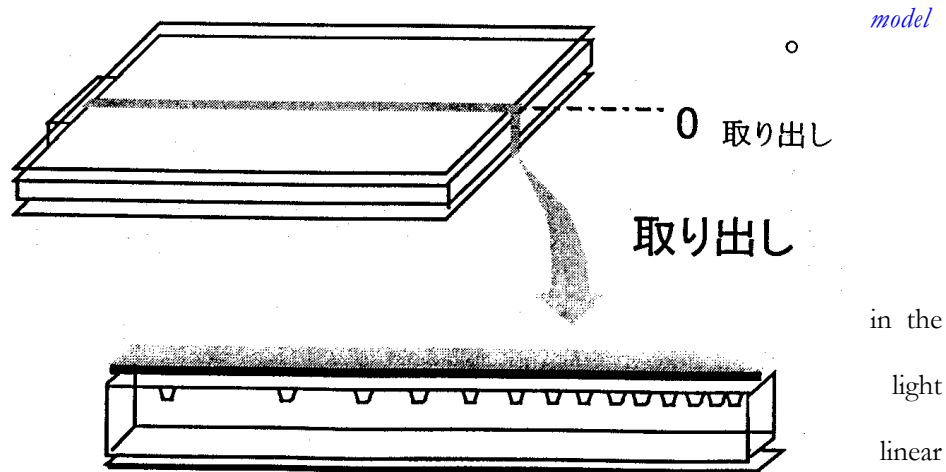
Thus, this year, in order to carry out the simulation within realistic calculation time limits, we used only part of a model obtained by selecting only a direction in the vicinity of  $\Theta=0^\circ$  in the basic configuration shown in Fig. 14.3.1. By doing so the computation load was reduced approximately 100 times. The simulation model used for radiation coupling elements is shown in Fig. 14.3.2

Fig. 14.3.2 Simulation

[Keys, Fig. 14.3.2]

0 extraction

Extraction



As was described above, vector radiation coupling system, light from the guide panel coupling portion propagates in a fashion to other edge

surfaces, with the respective angular directions being independent and the behavior of light being practically identical. Thus, because the correlation between fine shape changes of the radiation coupling pattern and the extraction efficiency, which is the purpose of the present simulation, is believed to be independent of the direction, in which light emanates from the light guide panel coupling elements, we decided to use the results obtained for direction  $\Theta=0^\circ$  as representative values.

The input parameter used in the present simulation was the pattern shape of the radiation coupling elements and the output was the amount of light emanating upwards. Other parameters were as follows.

Incident light	measured light intensity distribution of incident light
Pattern density	density, such that the luminance is constant in any location of the light guide panel (low density in the vicinity of the light source, high density at edge on the opposite side)
Light guide panel thickness	10 mm

**14.3.1.2 Simulation model for light guide panel coupling elements**

In models of light guide panels used prior to last year, the light-emitting module was located in the center at one of the edges of the light guide panel. However, we are aware of the fact that the efficiency of the light guide panel changes if the position of the light-emitting module is changed. Typically, the following positions are considered as positions at which the light-emitting module is installed:

- ① At the edge (Fig. 14.3.3 (a))
- ② In the corner (Fig. 14.3.3 (b))

*Fig. 14.3.3 Position of light-emitting module*

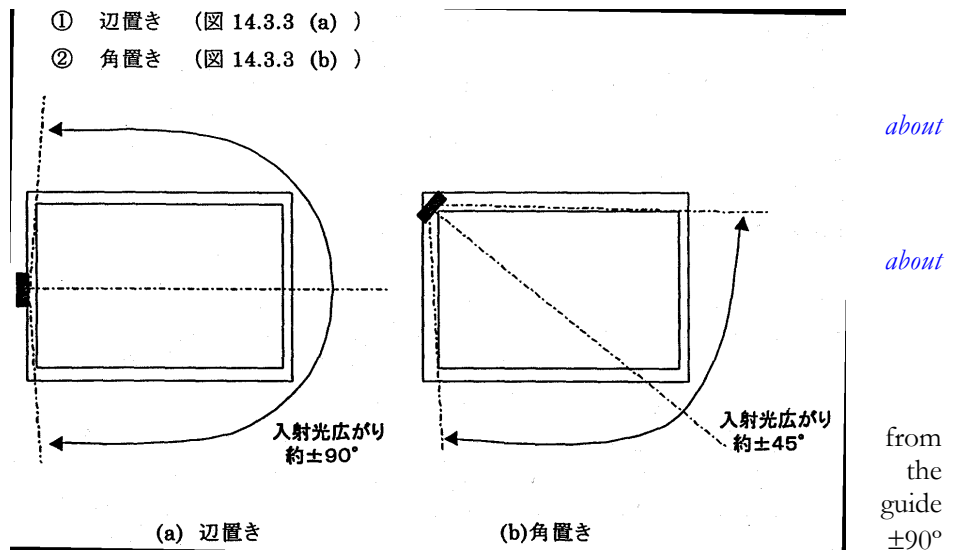
[Keys, Fig. 14.3.3]

(a) At the edge

*Spread of incident light:  $\pm 90^\circ$*

(b) In the corner

*Spread of incident light:  $\pm 45^\circ$*



In case of ①, in order to convert the incident light from the light source to cover entire surface of the light panel, a spread of about

is necessary in the light guide panel coupling elements. On the other hand, in case of ②, a spread of about  $\pm 45^\circ$  in the light guide panel coupling elements is enough. In these two models ① and ②, we used ray tracing simulation to determine the efficiency of light use obtained when the incident light is spread over the entire surface of the light guide panel and determined the optimum installation position for the light-emitting module.

**14.3.2 Results and discussion**

**14.3.2.1 Radiation coupling elements**

a. Effects of pattern shape fabrication tolerance

Fig. 14.3.4 shows a pattern in the shape of a cylindrical lens, which was proposed in the past. The parameters used in this simulation were as shown in Fig. 14.3.4. Defects due to fabrication irregularities in the pattern of Fig. 14.3.4 included edge R, which was caused by deformation of the edge section during injection molding, deformation of the width and height of the pattern due to the shrinkage and expansion of the resin, and variations in the refraction coefficient caused by variations in the characteristics of the resin and by differences in the process of curing.

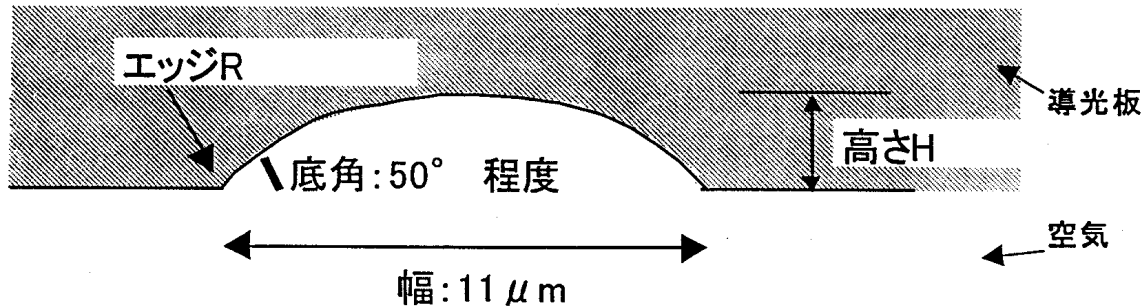


Fig. 14.3.4 Cylindrical lens-shaped pattern

[Keys, Fig. 14.3.4]

Edge R

Light guide panel

Height

Bottom angle: about 50°

Air

Width: 11  $\mu\text{m}$

First of all, we verified the correlation between changes in the edge R and the extraction efficiency.

The correlation between the edge R and extraction efficiency for the cylindrical lens-shaped pattern shown in Fig. 14.3.4 is shown in Fig. 14.3.5. The cylindrical lens height H was selected as the parameter.

According to the results of a simplified injection molding test, it was found that in case of a fine pattern of the specified size, the edge R could reach approximately 2  $\mu\text{m}$ . In Fig. 14.3.5, the value of  $R=2 \mu\text{m}$  gives us a decrease, as compared with the ideal state, of about 22% in case of  $H=2.8 \mu\text{m}$  and about 38% in case of  $H=3.5 \mu\text{m}$ . This edge irregularity does not occur uniformly and is subject to considerable variation depending on the fabrication conditions, etc. Thus, based on these results, it was found that in case of a cylindrical lens-shaped pattern, it was not resistant to edge R variation and could bring about a decrease in the extraction efficiency and considerable luminance non-uniformity.

Fig. 14.3.5 Effects of cylindrical lens edge R extraction efficiency

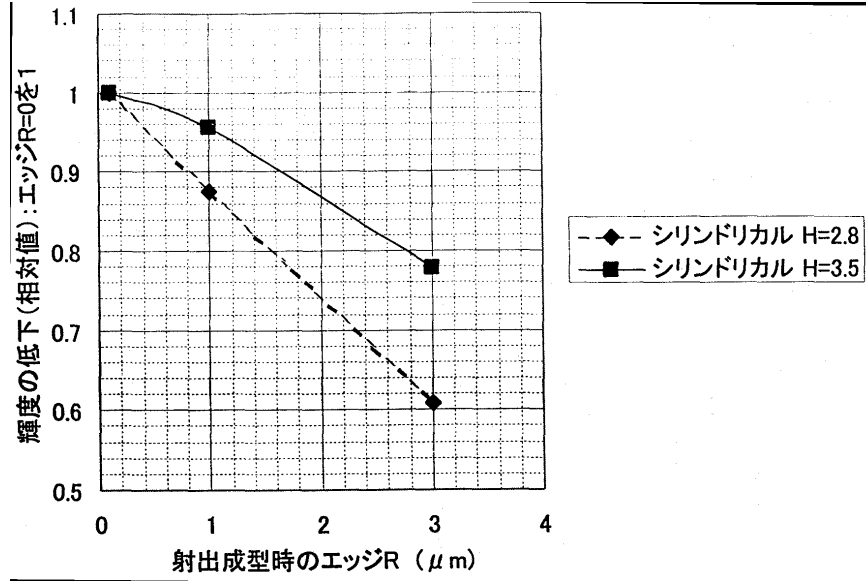
[Keys, Fig. 14.3.5]

(X-axis) Edge R due to injection molding ( $\mu\text{m}$ )

(Y-axis) Decrease in luminance (relative Edge R=0 as 1)

(Box) ◆ Cylindrical H=2.8

■ Cylindrical H=3.5



on

value):

For this reason, we proposed a trapezoidal pattern shown in Fig. 14.3.6 as a pattern resistant to edge R variation. Details related to the selection of the trapezoidal pattern are described below. In the same manner as with the cylindrical lens pattern, occurrence of fabrication irregularities is possible in case of the trapezoidal pattern.

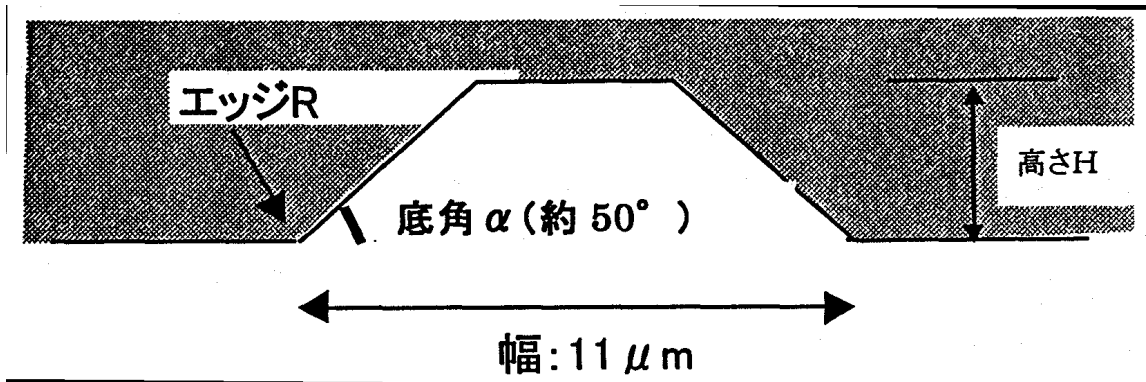


Fig. 14.3.6 Trapezoidal lens-shaped pattern

[Keys, Fig. 14.3.6]

Edge R

Height H

Bottom angle  $\alpha$  (about  $50^\circ$ )

Width:  $11 \mu\text{m}$

Fig. 14.3.7 Effects of trapezoidal lens edge R on efficiency

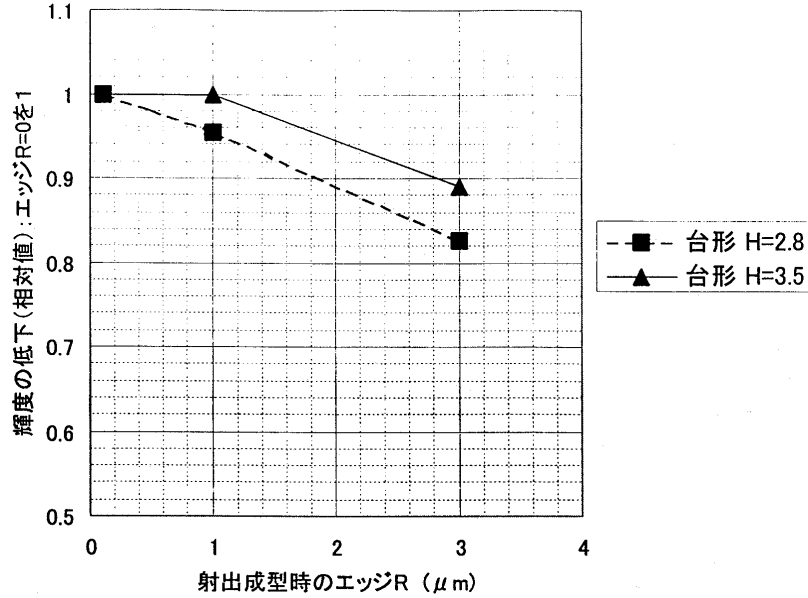
[Keys, Fig. 14.3.7]

(X-axis) Edge R due to injection molding ( $\mu\text{m}$ )

(Y-axis) Decrease in luminance (relative value): R=0 as 1

(Box) ◆ Trapezoidal H=2.8

■ Trapezoidal H=3.5



Edge

The results of the simulation allowed us to determine the correlation between the edge R of the trapezoidal pattern and extraction efficiency, which is shown in Fig. 14.3.7. As a result, we can see that while there was a decrease of not less than 15% in case of the cylindrical lens-shaped pattern, in case of the trapezoidal pattern, the corresponding decrease was approximately 10%. In addition, it was found that in case of a trapezoidal pattern with an H=3.5  $\mu\text{m}$ , the decrease in the extraction efficiency was maintained within 16%. These results indicate that the trapezoidal pattern exhibits a smaller decrease in the luminance at the same variation of the edge R and is a more robust pattern.

Thus, in connection with the conducted verification, we focused our further efforts on the study of the trapezoidal pattern.

b. Theoretical verification

Next, we will consider the theoretical basis of improvements due to the above-described trapezoidal pattern.

First of all, we will discuss the mechanism of light extraction depending on the pattern by using the simplified model shown in Fig. 14.3.8. In order for light propagating throughout the light guide panel to be extracted from the light guide panel by the pattern, during reflection from the pattern it has to be subject to changes in the propagation direction of 45° or more (up to an angle exceeding total reflection angle on the top face of the light guide panel). As a result of refraction, in some cases light is extracted towards the reflector plate side as well, but here, in order to facilitate possible changes, we will only consider extraction based on reflection.

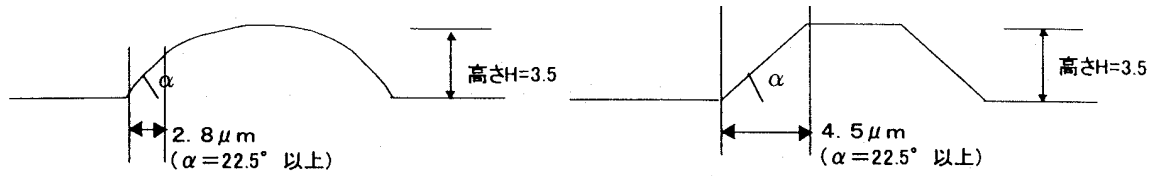


Fig. 14.3.8 Differences between efficient regions depending on pattern shape

[Keys, Fig. 14.3.8]

(Left) Height  $H=3.5$

$2.8 \mu m$

( $\alpha=22.5^\circ$  or larger)

(Right) Height  $H=3.5$

$4.5 \mu m$

( $\alpha=22.5^\circ$  or larger)

In order to bring about these changes of  $45^\circ$  or more, the bottom angle  $\alpha$  on the light source side of the pattern has to be  $22.5^\circ$  or more. Here, calculation of the length of the inclined surface with an angle exceeding  $\alpha=22.5^\circ$  among the inclined surfaces on the light source side of the cylindrical lens-shaped pattern and trapezoidal pattern gives  $2.8 \mu m$  for the cylindrical lens-shaped pattern and  $4.5 \mu m$  for the trapezoidal pattern (on the assumption that  $H=3.5 \mu m$  in both cases).

Changes in the edge R take place to the same extent for the respective patterns. Thus, if we consider a case, in which due to the sagging of the edge R the above mentioned inclined surface effective in terms of extraction is decreased  $1 \mu m$ , in case of the cylindrical shape pattern the decrease in the extraction efficiency is  $1/2.8=35\%$ , and in the case of a trapezoidal pattern the decrease is  $1/4.5=22\%$ , showing that the trapezoidal pattern, which has more effective inclined surface, is more robust with respect to edge R variation.

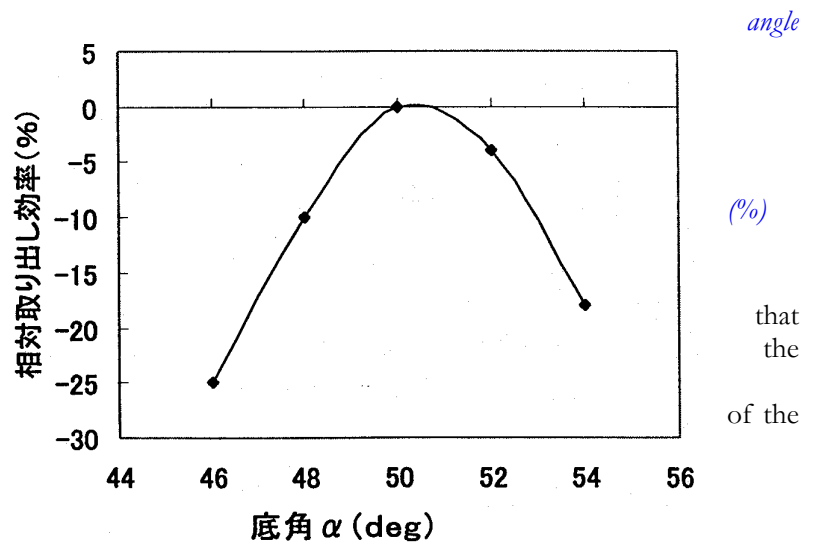
Also, Fig. 14.3.9 shows results obtained by studying the correlation between the bottom angle  $\alpha$  of the trapezoidal pattern and the extraction efficiency. From the results, it is evident that changes in the inclined surface of the trapezoidal pattern exert considerable influence on the extraction efficiency.

Fig. 14.3.9 Relationship between bottom  $\alpha$  and efficiency

[Keys, Fig. 14.3.9]

(X-axis) Bottom angle  $\alpha$  (deg)

(Y-axis) Relative extraction efficiency



Summing up the above, it is evident factors that exert strong influence on extraction efficiency include the bottom angle on the light source side pattern and the length of the effective inclined surface. Thus, when designing a pattern of high robustness, a pattern should be chosen, in which the bottom angle is not likely to deviate from the design value and the effective inclined surface is long. However, it is also necessary to pay attention to other constraints concerning the size of the pattern, such as pattern visibility, etc.

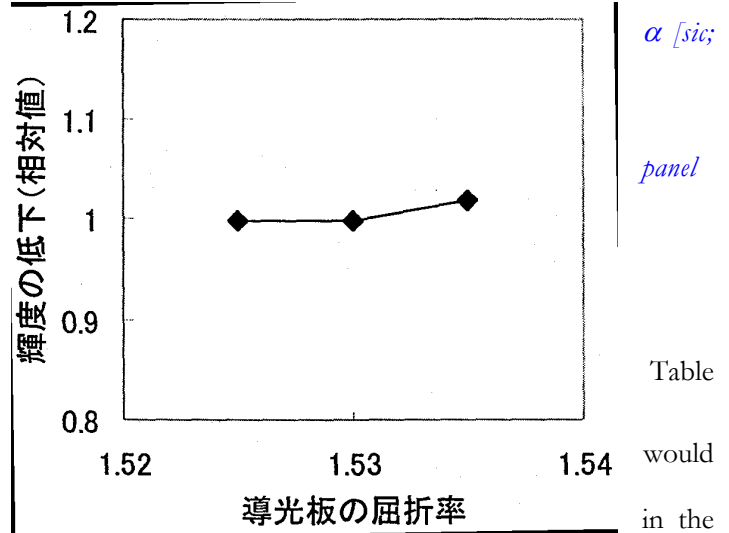
Next, a correlation between variation of the refractive coefficient believed to be caused by resin irregularities or curing condition irregularities and the extraction efficiency is shown in Fig. 14.3.10. As can be seen from the figure, the actual variation of the coefficient of refraction is about 0.005 at the most, and, for this reason, it has almost no effect on characteristics.

Fig. 14.3.10 Relationship between bottom angle - trans.] and efficiency

[Keys, Fig. 14.3.10]

(X-axis) Coefficient of refraction of light guide

(Y-axis) Decrease in luminance (relative value)



Results for other parameters are shown in 14.3.1.

Because there are no other parameters that exert adverse influence, no particular attention should be paid to these parameters design stage. For this reason, here their discussion is omitted.

Parameter	Verification region	Calculation results: Amount of deviation from design value (%)
Rear bottom angle (deg)	50+7	-0.6
	50-7	0
Pattern width (μm)	10+0.5	-2
	10-0.5	7

Table 14.3.1 Relationship between other parameters and efficiency

(c) Light guide panel coupling elements

Results of ray tracing for different positions of the LED module are shown in Fig. 14.3.11. In this figure, we used the symbol “O” to designate the LED, which is positioned at one of the edges or in a corner of the light guide panel. Light emitted by the LED is converted by the light guide panel coupling elements into the desired angular distribution. The distance from the light guide panel coupling elements corresponds to the luminous energy for each angle.

In Fig. 14.3.11, the luminous energy E2, which is shown with a thick black line, is the ideal luminous energy necessary for each angle. If we want to make constant the luminous energy emitted from the light-emitting face in any given position of the illumination system, the larger the distance from the LED to the edge on the opposite side, the more light will be necessary. In the figure, the distance from the light guide panel coupling

elements to the corner on the opposite side is the longest, and the ideal luminous energy for the corresponding angle is greater.

However, it is difficult to bring the luminous energy emitted from the light guide panel coupling elements in perfect correspondence with the ideal luminous energy. More realistically, it is easier to ensure proper control if we create an elliptical distribution of the emanating light. It is plotted in the figure as E1.

In the luminous energy E1 emanating at a certain angle from the light guide panel coupling elements, the E1–E2 portion of the luminous energy becomes unnecessary. On the other hand, the amount of emanating light can be increased by increasing the density of the pattern if we want to emphasize the efficiency of light use, but in this case the uniformity of luminance will deteriorate.

Results regarding light use efficiency E2/E1 in case of uniform luminance obtained by computer simulation are shown in Table 13.3.2.

	① Lateral position	② Corner position
Efficiency E2/E1	83%	95%

*Table 13.3.2 LED module position and light use efficiency*

As can be seen from the above results, the efficiency of light use is higher when the LED module is positioned in the corner (if we want to emphasize the efficiency of light use, positioning the module in the corner will decrease the non-uniformity of luminance). Thus, in the future, when designing prototypes of illumination systems, positioning the LED in the corner will be our first choice.

Fig. 14.3.11 Simulation for different positions of light emitting module

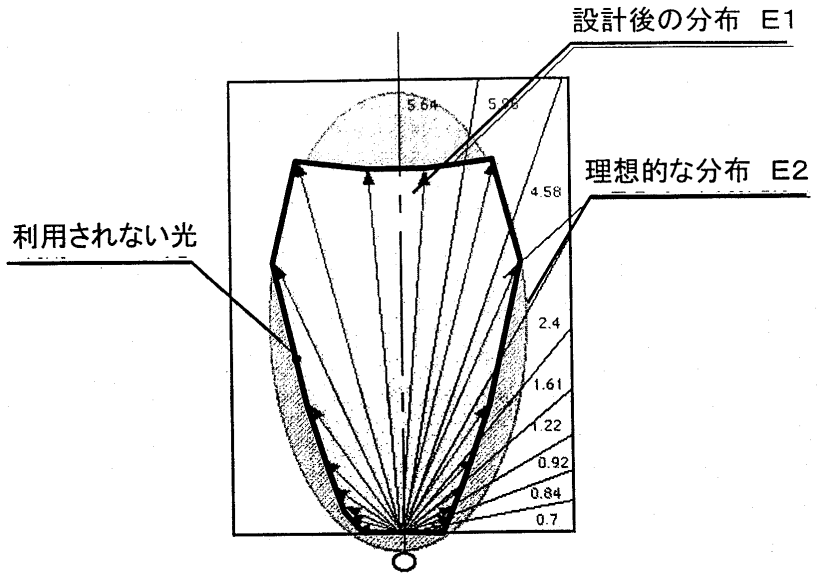
(a) ① Lateral position

(b) ② Corner position

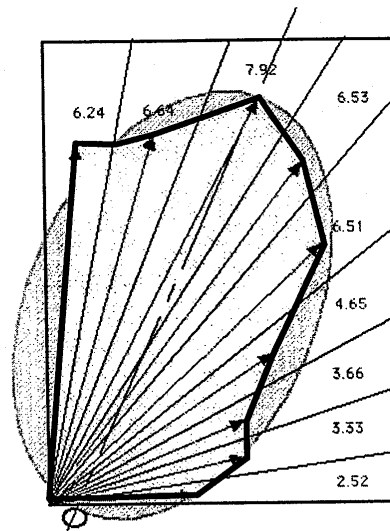
[Keys, Fig. 14.3.11 (a)]

(Left) Light that is not  
(Right, top to bottom) distribution E1

Ideal distribution E2



(a) ① 辺置き



(b) ② 角置き

results

used.  
Design

## 14.4 Conceptual design of directionality conversion system

### 14.4.1 Methods and means (conceptual design of directionality conversion system)

When illumination systems are considered from the standpoint of energy savings, it becomes important to consider conversion efficiency, which means how efficiently light from the light source is used to illuminate the desired illumination area at a uniform lighting level. In other words, the light that is emitted outside the desired illumination area is unnecessary, in other words, it is a waste of energy.

For example, in case of a footlight, from the standpoint of the purpose of the illumination system, the area that has to be illuminated is limited to the floor surface below the footlight. Specifically, if light is emitted with a directivity of approximately  $\pm 15^\circ$ , this will be enough for footlight functionality. However, when you look at actual illumination, you will find that light sometimes illuminates areas greater than  $\pm 15^\circ$ . Suppose, if inefficient lighting is used to illuminate, for example, a  $\pm 60^\circ$  area, then in terms of the magnitude of the solid angle, such an area will be about 15 times larger than  $\pm 15^\circ$ . In other words, although the ratio of the luminance of light emitted in the inefficient area to that of light emitted in the efficient area is 1/10, in terms of energy, more than half is emitted in the inefficient area, which cannot be simply ignored.

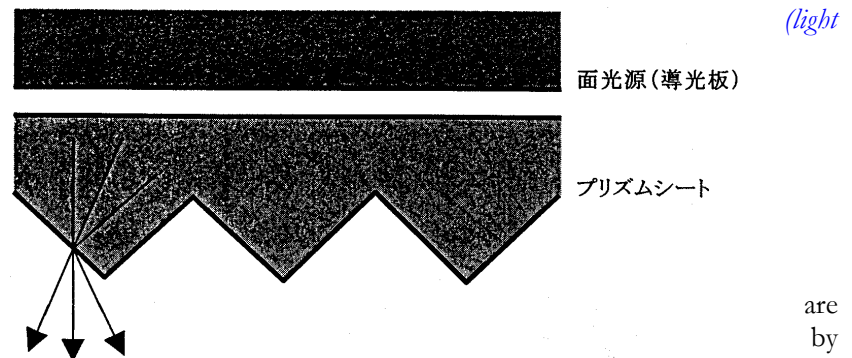
Reduction of this value requires a certain technology for converting the directivity of the light incident from the light source to the desired directivity. In case of typical conventional illumination, one of the most obvious approaches would be to improve directivity by installing reflectors. Furthermore, especially in case of illumination systems requiring high directivity, the shape of the reflectors is often curvilinear (for example, parabolic). However, these systems, especially curvilinear reflectors and such, are elements supposed to be used with point light sources and cannot be applied to a light guide panel, which is a surface light source, and, in addition, their use presents difficulties because it cancels out one of the advantages of the light guide panel system, i.e. the fact that it can be made very thin.

Fig. 14.4.1 Prism sheet

[Keys, Fig. 14.4.1]

(Top to bottom) Surface light source  
guide panel

Prism sheet



The above-described reflectors  
elements that convert directivity  
making use of light reflection.

There are, however, a type of element that converts directivity by making use of light refraction. Namely, as shown in Fig. 14.4.1, a prism sheet is a sheet, on which tiny prisms are molded in array form. Prism-like triangular shapes are formed on one side of the sheet, and the coefficient of refraction of the prism sheet is made higher than the coefficient of refraction of air. When light from a surface light source incident on the top face of the sheet passes through the sheet and emanates from the bottom face, the light is subjected to

refraction as shown in the figure by the prisms formed on the bottom face, which improves its directivity. Optimizing the sawtooth shape of the prisms makes it possible to convert the directivity of light to the desired directivity. In addition, the design can be made thinner by reducing the size (height, pitch) of the prisms, which is why one can expect prism sheets to find application as a directivity conversion element in illumination systems of the light guide panel type.

In this study, we conducted simplified tests for the purpose of confirming the applicability of the light guide panel/prism sheet combination. As shown in Fig. 14.4.2, two prism sheets (two sheets were necessary in order to improve directivity in the X direction and Y direction) were installed on the light-emitting side of a 4-inch light guide panel prototype, which we had previously fabricated, and a luminance meter was installed below the light guide panel to measure luminance in the center of the light guide panel. In addition, the light guide panel could be rotated about the X axis. Using this setup, we measured the distribution of the emanating light in the center of the light guide panel.

Fig. 14.4.2 Directivity measurement system

[Keys, Fig. 14.4.2]

(Left) \*Measurements of luminance were conducted by rotating the light guide panel the X-axis

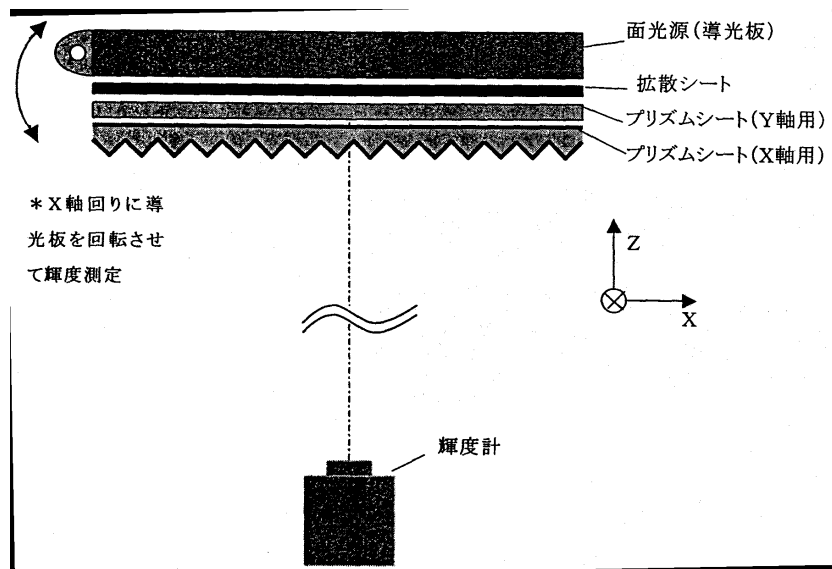
(Right, top to bottom)

Surface light source (light panel)

Diffuser sheet

Prism sheet (for Y-axis)

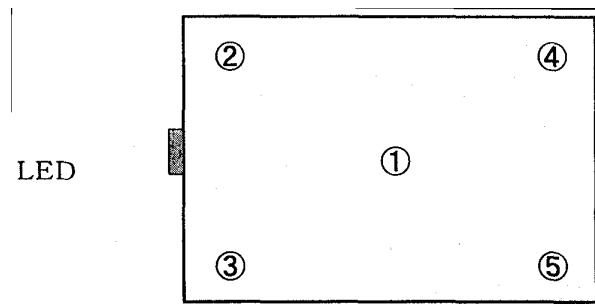
Prism sheet (for X-axis)



about  
guide  
axis)

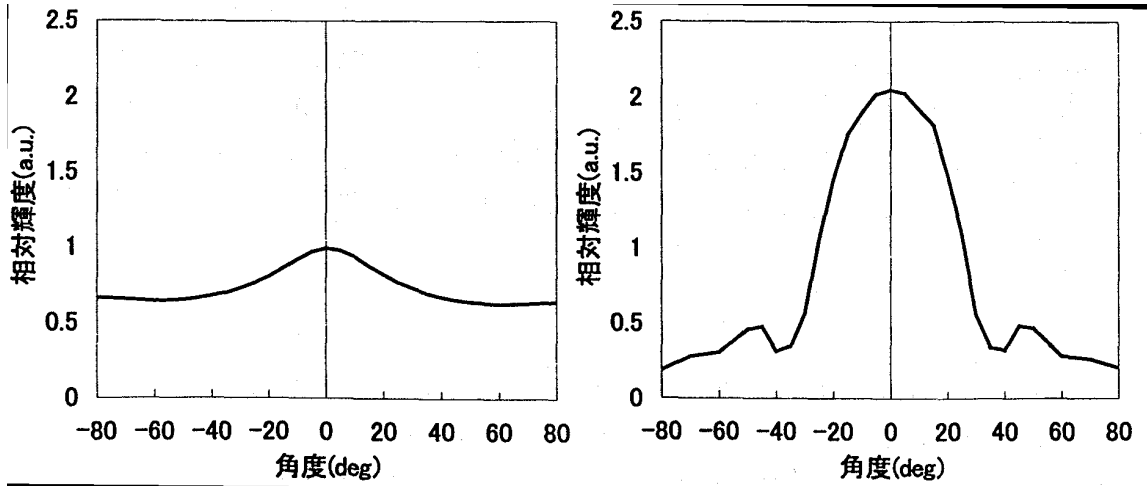
Furthermore, in order to confirm whether the installation of the prism sheets caused a deterioration in the uniformity of the luminance across the light guide panel's light-emitting surface, we also measured frontal luminance in five points: in the center and in the four corners of the light guide panel. The points, in which the luminance was measured, are shown in Fig. 14.4.3.

Fig. 14.4.3 Uniformity measurement points



### 14.4.2 Results and discussion (conceptual design of directionality conversion system)

Fig. 14.4.4 shows an emanating light distribution obtained when no prism sheets are installed, and Fig. 14.4.5 shows an emanating light distribution obtained with the prism sheets installed. As can be understood from the figures, when the prism sheets were installed, the directivity of the emanating light was improved up to  $\pm 17^\circ$ . In addition, Table 14.4.1 shows data obtained by subtracting frontal luminance from Fig. 14.4.4 and Fig. 14.4.5. From the table, it can be seen that the use of the prism sheets results in an improvement in the directivity and, at the same time, a doubling of the luminance, so that energy can be efficiently emitted across the desired area.



Left: Fig. 14.4.4 Directivity characteristic (without prism sheets)

[Keys, Fig. 14.4.4]

(X-axis) Degree (deg)

(Y-axis) Relative luminance (a.u.)

Right: Fig. 14.4.5 Directivity characteristic (with prism sheets installed)

[Keys, Fig. 14.4.5]

(X-axis) Degree (deg)

(Y-axis) Relative luminance (a.u.)

	Prism sheets	
	None	Installed
Relative luminance	1.00	2.05

Table 14.4.1 Luminance comparison

Furthermore, results of uniformity evaluation are shown in Table 14.4.2. As the table shows, even though the uniformity slightly decreased from 13% to 12% when the prism sheets were installed, it was within the tolerance of measurement. Thus, it was found that the prism sheets caused practically no decrease in the uniformity of the luminance of the light-emitting surface.

	Relative luminance	
	Prism sheets installed	Prism sheets not installed
①	1.00	2.05
②	1.05	2.08
③	0.96	1.95
④	1.08	2.05
⑤	1.01	1.99
Uniformity (%)	12	13

*Table 14.4.2 Results of uniformity evaluation*

It was found that, as shown above, if prism sheets were used in a light guide panel system, it was possible to improve the directivity while maintaining useful characteristics such as thin dimensions.

However, when the present directivity conversion system is applied to actual illumination systems, it is necessary to decide whether the present system needs to be used with account taken of the intended use of the illumination system. The present system is useful in illumination systems requiring high directivity, such as, for example, footlights, table lamps, road illumination, etc. However, because in the case of illumination systems such as signaling devices, signs, etc. the purpose of the system is to convey information to people in the surrounding vicinity, increasing directivity would actually be counterproductive, and the use of the present system would not be appropriate in many cases. Furthermore, it is believed that in case of indoor illumination, the distribution of light emitted by an illumination system is determined with account taken of the ergonomic properties, pleasantness, and intended use (direct illumination, indirect illumination, etc.) of the illumination, and corresponding decisions have to be made regarding the appropriateness of the use of the present system.

## 14.5 Summary

This year, in order to create a prototype of a light guide panel system intended for actual illumination, we built and practically used optical simulation tools using the ray tracing technique for design with account taken of fabrication errors etc. believed to occur during mass production. As a result, by elucidating the correlation between the variability of the shape of the light guide panel coupling elements and arrangement of radiation coupling elements in case of fabrication errors etc. and the efficiency of energy conversion, we reached the following conclusions.

1. With respect to the pattern formed in the light guide panel, it was found that a trapezoidal lens-shaped lens pattern exhibited a smaller decrease in the extraction efficiency due to molding errors than the cylindrical lens-shaped pattern, which had been proposed in the past.
2. With respect to the position of the module, it was found that positioning the module in a corner of the light guide panel provided for a higher light use efficiency than positioning it at one of the edges of the light guide panel.
3. With respect to other parameters, it was found that they exhibited high resistance to fabrication errors and required no special countermeasures.

In addition, we determined and decided that using prism sheets as a directivity conversion system for achieving further energy saving effects in illumination systems requiring high directivity was the best strategy

in case of a light guide panel system and, after installing such sheets in a prototype of a 4-inch light guide panel and measuring the corresponding optical characteristics, reached the following conclusions:

4. Installing prism sheets improves the directivity of light emanating from a light guide panel up to a directivity of  $\pm 17^\circ$  in terms of the half-value angle.
5. Inserting a prism sheet does not reduce the uniformity, which is an advantage of the light guide panel system.

## 14.6 Plans for the future

Using the shape precision/energy conversion efficiency correlation determined as a result of this year's investigations, next year, we will focus on determining the problems expected to arise in the production process and on their precision analysis with a view to develop actual illumination systems. In the verification process, we will concentrate mostly on the light guide panel coupling elements, which exert considerable influence on the optical characteristics.

In addition, we will combine it with studies related to the basic specification of the light guide panel system illumination device we plan to fabricate during the final year.

### (1) Robust design

Previously, with a view to determine the general principles of the light guide panel system, we have fabricated a prototype of a light guide panel using the 2P technique (Photo-Polymerization), which is superior in terms of simplicity and shape transfer properties. However, this molding technique, albeit superior in transferability of fine shapes, has numerous problems in terms of productivity indicators, such as tact, material costs, etc., as well as in terms of application to large surface areas. Therefore, injection molding, which will be superior in productivity as a production system for light guide panels, is believed to be a more advantageous technique. However, the problem with injection molding is its inferior shape transfer properties as compared with the 2P technique. Thus, next year we will try and elucidate the transferability of fine patterns under the injection molding method and will use the obtained characteristics as a basis for robust design of fine pattern shape and arrangement. Specifically, using transferred shape evaluation samples fabricated under the injection molding method, we will obtain new results related to the precision of shape transfer and its variation characteristics. As criteria for transfer characteristics evaluation, we are planning to use the linearity of the transferred shapes and the edge R. Using the obtained shape transfer characteristics, we will carry out optimal design using optical characteristics as evaluation criteria, and will verify its validity using computer simulation techniques.

In addition, in the vector radiation coupling system, it is essential to substantially localize the LED, and it is expected that the extent to which we will be able to improve the degree of LED integration will determine whether it will be possible to realize the system or not. It is believed that at 100 lm/W, i.e. the target of efficiency of the present project, the amount of released heat will be smaller than in a fluorescent lamp and even with integration, the optimization of the heat-removal structure of the module will permit suppression of temperature rise. However, the low reliability of heat-related simulations is a fact, and we will have to keep in mind the possibility that as a result of prototyping studies, we will not be able to raise the degree of integration. In addition, considering that we have reached the middle of the project with a lower LED efficiency than the one we planned to achieve, we will have to consider scenarios, in which the amount of released heat will be greater than expected and the degree of integration will be impossible to increase. Should such concerns prove realistic, we will study the possibility of integrate LEDs not in one location of the light guide panel, but rather in several locations of it. In addition, it is believed that in this case, for the purpose of maintaining uniformity, it will be better to divide the light guide panel into several portions, and this idea will be investigated at the same time.

### (2) Preparation of basic specification

We will define several different shapes of the light guide panel system LED illumination proto-sample, which will be fabricated in 2002, the final year of the project. We will further zero in on the intended use, shape and robust design criteria to prepare a general outline of the specification.

## 14.7 References

- [1] Masayuki Shinohara, Masataka Tei, Shigeru Aoyama, and Masashi Takeuchi, "Vector Radiation Coupling Method for High Efficiency and High Uniformity," *Diffractive Optics and Micro Optics*, 1998 OSA Technical Digest Series, Vol. 10, 189-191 (1998).
- [2] Masayuki Shinohara, Shigeru Aoyama, and Masashi Takeuchi, "Vector Radiation Coupling Type LED Backlight," *Optical Alliance*, Japan Industrial Publishing Co., Ltd., Vol. 9, No. 5, 13-16 (1998).

# 15 Lighting Fixture Development Based on Novel LED Concepts

## 15.1 Achievements in 1998~1999

We attempted to verify whether it was possible to use LEDs available on the market as light sources for illumination, and, assuming that it was possible, to determine what kind of fixtures could be employed. Furthermore, along with analyzing the characteristics and performance of LEDs and trying to determine ways in which they could be used as light sources, we created research prototypes of lighting fixtures based on novel concepts applicable to LEDs.

### 15.1.1 Achievements in 1998

- Commercially available LEDs were used to fabricate a test piece. As a result, we determined that the test piece input efficiency was 7.18 lm/W and the lamp efficiency was 9.65 lm/W.
- By measuring the light distribution characteristics of the above-mentioned test piece, we found that it could be utilized as a spot light for local lighting. In addition, we found that in such a case the light level was 131 lx at a distance of 100 cm, 524 lx at a distance of 50 cm, and 1450 lx at a distance of 30 cm, which met the requirements for reading (300~750 lx), handicrafts and sewing (750~2000 lx), specified as light level standards in JIS Z9110, and fell within a range permitting use in practical applications.
- Based on the above-described results, we created prototypes of various lighting fixtures that took advantage of LED characteristics.

### 15.1.2 Achievements in 1999

- Rectangular or round-shaped LED integrated light sources were fabricated to investigate the relationship between the size of the light sources and the temperature rise. As a result, we determined that in case of configurations consisting of closely packaged LEDs, their temperature increased to levels at which they could not operate.
- With regard to configurations of LED light sources used for lighting fixtures, we found that a “centerless” array obtained by removing the central portion of an array ensured the necessary luminous outputs and could suppress the temperature rise.
- We also found that the use of heat sinks was effective as a means for suppressing the temperature rise in LEDs. As a result, we implemented prototypes of lighting fixtures capable of achieving the current target of an illuminance of 1000 lx or more and a temperature rise of 30°C or less.

### 15.1.3 Discussion of Achievements in 1998~1999

Based on the above results, we summarized the relationship between the characteristics and market applications of LEDs as shown in Table 15.1.

	LED Characteristics	Lighting Fixture Concepts	Market Applications
1	Directionality of light	Reflectors are unnecessary, high fixture efficiency	Fixtures for local lighting
2	The freedom to combine circuits and lamps	The freedom to combine lamps, colors, and beam angles	Fixtures providing different light distribution depending on the intended use Appropriate illuminance at minimum power
3	Low heat generation	Thin lighting fixtures	Producing thinner downlights
4	Long service life	Maintenance-free	Makes maintenance easier and simpler due to reducing the amount of maintenance
5	Lightweight	Mounting on nonstationary equipment	Mounting on automobiles, Shinkansen (Japanese bullet) trains, and other means of transportation and equipment
6	Low temperature resistant	Fixtures used at low temperatures	Possible use in cold regions, cold storage facilities, etc. is being investigated
7	Impact resistant	High reliability under impact and vibration conditions	Mounting on mobile equipment

*Table 15.1 Characteristics and Market Applications of LEDs.*

With their current characteristics, modern LEDs produce insufficient luminous output for lighting applications and the field of their possible uses is limited to local lighting. In the future, the range of their uses in lighting applications is expected to expand as a result of a considerable increase in luminous output per LED.

## 15.2 Summary of Research and Development in 2000

On the basis of research results obtained up till this year, we investigated the characteristics of LEDs and their potential as light sources for illumination; this year, we focused our research on clarifying the benefits of LED light sources as revealed through comparisons with conventional light sources. We created prototypes of lighting fixtures using LEDs having the highest level of luminous efficiency (15 lm/W) among commercially available white LEDs. In particular, this year, in search of possibilities in the field of LED light sources and LED lighting fixtures, we investigated applications of chip-type LEDs and conducted research concerning fixture miniaturization and lighting characteristics.

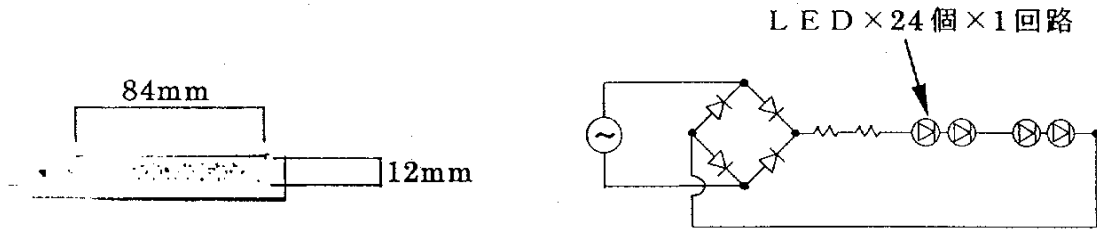
Guided by the new LED concepts, we conducted an investigation into various topics, such as how to miniaturize the dimensions of commercially available lighting fixtures, and, in this connection, what had to be done about the temperature of their various components, how to handle lighting characteristics, how to mount fixtures, etc.

In addition to providing evidence that miniaturization could be realized, and that design freedom in design could be increased while achieving a reduction in power consumption difficult to attain with conventional lighting fixtures, fabrication and evaluation of prototypes of LED table lamps and LED ceiling downlights also confirmed their advantages in terms of ease of installation.

## 15.3 Prototyping and Evaluation of LED Table Lamp

### 15.3.1 Methods and Means

As shown in FIG. 15.3.1-(1), an LED light source substrate was fabricated by mounting 24 chip-type LEDs on an aluminum substrate. A schematic diagram of its circuit is displayed in FIG. 15.3.1-(2). In the circuit, an AC power supply is full-wave rectified, and, through the medium of resistors, 24 LEDs are connected in series. The voltage-current, temperature and lighting characteristics of an LED table lamp prototype fabricated by combining the LED light source substrate and the circuit were evaluated, and its characteristics were further verified by comparing its dimensions and shape with table lamps utilizing conventional light sources.



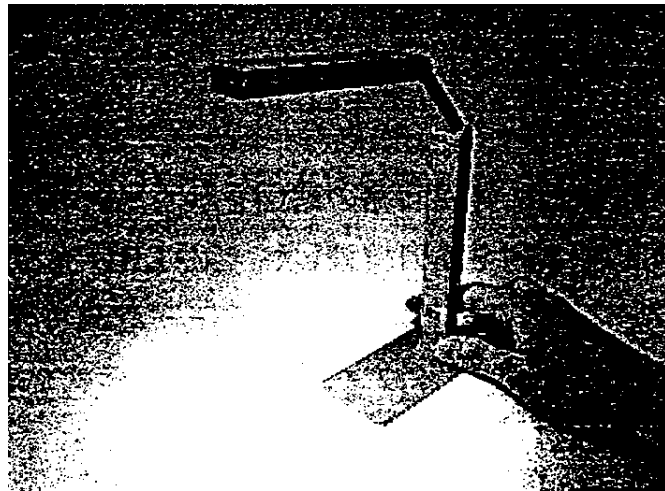
*Left:*

*FIG. 15.3.1-(1) LED light source substrate.*

*Right: FIG. 15.3.1-(2) Schematic circuit diagram. Labels: (Across top) LED x 24 x 1 circuit.*

### 15.3.2 Results and Discussion

A photograph of the LED table lamp prototype is shown in FIG. 15.3.2-(1). Evaluation results for the characteristics of the LED table lamp prototype are shown in FIG. 15.3.2-(2). We found that after applying AC 100V, the temperature rise in the LED junction portion (called the “LED portion” below) of the table lamp was 26.2°C, which satisfied the target value of 30.0°C or less. In addition, the temperature rise in the outer shell of the fixture reached 11.9°C; assuming that the ambient temperature 30.0°C, the temperature of the outer portion was 41.9°C, which was sufficient to meet the requirement of JIS C8109 (General Requirements for Luminaires) 55°C as the temperature limit for parts come in contact with human skin during operation.



was  
shell  
to  
of  
that

*FIG. 15.3.2-(1) LED Table Lamp Prototype*

Also, we found that after applying AC 100V, the illuminance was 490 lx, which was within the range 300~750 lx, i.e. the JIS standard for reading; therefore, the required illuminance conditions were satisfied as well. In addition, the input power at such time was extremely low, approximately 2.2W, which confirmed that the use of LEDs offered possibilities for power consumption reduction on a scale that was difficult to achieve with conventional lighting fixtures.

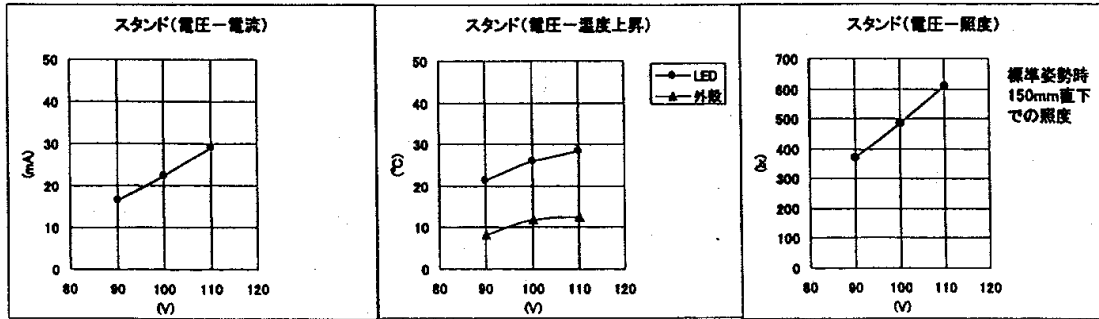


FIG. 15-3-2-(2) LED Table Lamp Prototype Evaluation Results

//Keys, FIG. 15.3.2-(2), left to right//

(Left, across top)

Table Lamp (Voltage-Current)

(Middle, across top)

Table Lamp (Voltage-Temperature Rise)

(Middle, box)

LED Outer Shell

(Right, across top)

Table Lamp (Voltage-Illuminance)

(Right, right-hand side)

Illuminance 150 mm directly below, standard posture

A comparison between the dimensions and shapes of the LED table lamp prototype and table lamps utilizing conventional light sources is shown in FIG. 15.3.2-(3). The volume ratio of the lamp bodies was about 1:27 in case of LED : incandescent lamp and about 1:80 in case of LED : fluorescent lamp, which was indicative of unprecedented miniaturization potential. Accordingly, the lamp could be considered a highly adaptable next-generation table lamp that, in addition to a higher degree of freedom in terms of design versatility, offered the advantage of being easily transportable.

	LED Table Lamp	Incandescent Table Lamp	Fluorescent Table Lamp
Shape	Lamp body portion	Lamp Body Portion	Lamp Body Portion
Method of attachment	Placed directly on tabletop	Placed directly on tabletop	Attached using special fittings
Lamp Body Portion Size	104×20×12 mm	Diameter 92×100 mm	163×248×50 mm

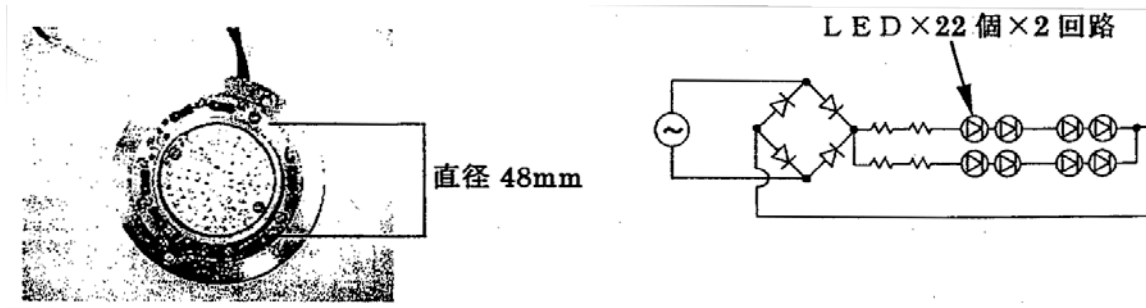
FIG. 15.3.2-(3) Comparison of table lamp dimensions and shapes

## 15.4 Prototyping and Evaluation of LED Ceiling Downlight

### 15.4.1 Methods and Means

As shown in FIG. 15.4.1-(1), an LED light source substrate was fabricated by mounting 44 chip-type LEDs on a glass-epoxy substrate. A schematic diagram of its circuit is shown in FIG. 15.4.1-(2). In the circuit, an

AC power supply is full-wave rectified and two series circuits made up of 22 LEDs with resistors interposed between are connected in parallel. The voltage-current, temperature and lighting characteristics of an LED ceiling downlight prototype fabricated by combining the LED light source substrate and the circuit were evaluated, and its characteristics were verified by comparing its dimension and shape with those of downlights utilizing conventional light sources.



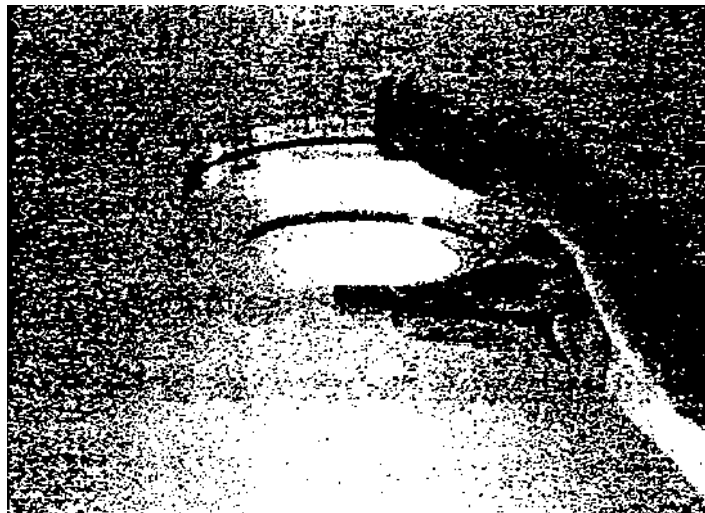
Left: FIG. 15.4.1-(1) LED light source substrate. //Keys, FIG. 15.4.1-(1)// (Right-hand side) Diameter 48 mm.

Right: FIG. 15.4.1-(2) Schematic circuit diagram. //Keys, FIG. 15.4.1-(2)// (Across top) LED  $\times$  22  $\times$  2 circuits.

## 15.4.2 Results and Discussion

A photograph of the LED ceiling downlight prototype is shown in FIG. 15.4.2-(1). An evaluation of characteristics for the LED ceiling downlight prototype is shown in FIG. 15.4.2-(2). We found that after applying AC 100V, the value of the temperature rise in the LED portion of the ceiling downlight was 40.9°C, which did not satisfy the target value 30.0°C or less. We assumed that was attributable to the use of an epoxy substrate for the LED light source substrate and that the temperature conditions could be corrected by using a heat-conductive aluminum substrate in the same manner as in the case of the above-described LED table lamp.

FIG. 15.4.2-(1) LED ceiling downlight prototype.



of  
this  
glass-

In addition, we found that temperature conditions that were close to the target value could be obtained and the temperature rise could be reduced by lowering the input voltage to AC 90V. In particular, the value of the temperature rise in the outer shell portion of the fixture was 13.1°C, and, assuming that the ambient temperature was 30.0°C, the temperature of the outer shell portion was 43.1°C, which was indicative of operational safety in the same manner as in the case of the above-described LED table lamp. Also, the outer shell portion temperature value of 43.1°C was acceptable even when working with vinyl materials (temperature limit: 60°C), which are said to be the least temperature resistant of all inner packaging materials. On the other hand, examination of illuminance after applying AC 90V showed that the light level at a distance of 300 mm directly below the fixture was 180 lx; and, when the ceiling downlight was mounted in a location that had a ceiling height of 2.4 m, an illuminance of 2.8 lx was obtained at the floor level, i.e. the fixture met requirements for night-time

safety lighting. It is believed that this illuminance level provides a basis for possible development of under-shelf lighting, etc. In addition, the input power at such time was approximately 2.6W, which showed a possibility for a large-scale reduction in power consumption in the same manner as in the case of the above-described LED table lamp.

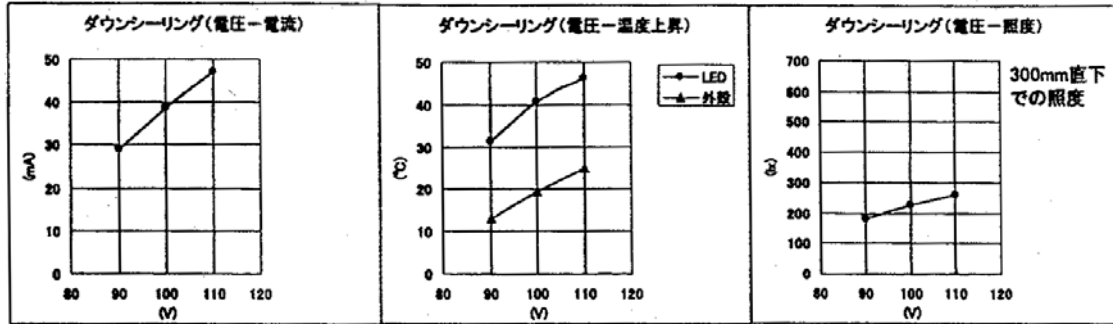


Figure 15.4.2-(2) LED ceiling downlight prototype evaluation results.

//Keys, FIG. 15.4.2-(3)//

(Left, across top)

Ceiling Downlight (Voltage-Current)

(Middle, across top)

Ceiling Downlight (Voltage-Temperature Rise)

(Middle, box)

LED Outer shell

(Right, across top)

Ceiling Downlight (Voltage-Illuminance)

(Right, right-hand side)

Illuminance 300 mm directly below, standard posture

A comparison between the dimensions and shape of the LED ceiling downlight prototype and downlights utilizing conventional light sources is shown in FIG. 15.2.2-(3). The volume ratio of the fixtures was about 1:21 both in case of LED : incandescent lamp and in case of LED : fluorescent lamp, which indicated that the use of LEDs permitted a high degree of miniaturization and could contribute to a reduction in labor because of eliminating the need for drilling holes in the ceiling.

	天井付けLED器具	天井付け白熱灯器具	天井付け蛍光灯器具
形状			
取付方法	天井面に直に取付	天井面に開口作業が必要	天井面に開口作業が必要
天井裏寸法		181mm	185mm
天井面からの下がり	19mm	5mm	5mm
外径寸法	直径 95mm	直径 142mm	直径 142mm

	Ceiling-mounted LED fixture	Ceiling-mounted incandescent light fixture	Ceiling-mounted fluorescent fixture
--	-----------------------------	--	-------------------------------------

Shape	Ceiling surface	Ceiling surface	Ceiling surface
Method of attachment	Attached directly to ceiling	Drilling of holes in ceiling was necessary	Drilling of holes in ceiling was necessary
Dimensions of recess in ceiling		181 mm	185 mm
Protrusion from ceiling surface	19 mm	5 mm	5 mm
Outside diameter	Dia. 95 mm	Dia. 142 mm	Dia. 142 mm

*FIG. 15.4.2-(3) Comparison of downlight dimensions and shapes.*

## 15.5 Conclusions

As a result of fabricating and evaluating the characteristics of lighting fixture prototypes comprising as their light sources chip-type LEDs possessing the highest level of commercially available luminous efficiency (15 lm/W), we arrived at the following conclusions:

- It is possible to realize ultra-miniature fixtures completely different from lighting fixtures used in the past..
- It is possible to realize fixtures generating energy savings on a scale difficult to achieve with conventional light sources.
- At present, practical application of such fixtures is possible for local lighting purposes.
- The degree of freedom in the selection of installation locations has increased because thermal constraints related to the mounting of fixtures have been reduced.

## 15.6 Agenda for the Future

So far, prototypes of light source substrates utilizing bullet LEDs and chip-type LEDs as light sources for illumination, as well as prototypes of lighting fixtures that take advantage of their characteristics, have been created and have confirmed the possibility, as well as the benefits, of putting them to practical use. A clear-cut development orientation addressing the needs of the market will be indispensable from now on. Table 15.6 illustrates how the LED lighting fixture concept, which was formulated when the research was in its initial phase, has evolved towards the Next Generation.

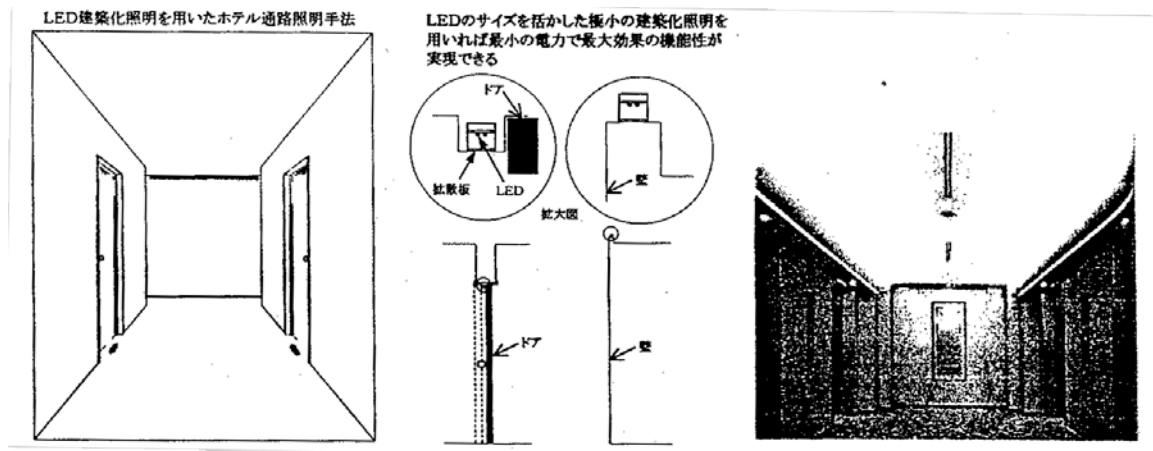
	LED Characteristics	Initial Concept	Next Generation Concept
1	Directionality of light	Reflectors are unnecessary, high fixture efficiency	Development of lighting fixtures that save resources
2	The freedom to combine circuits and lamps	The freedom to combine lamps, colors, and beam angles	Light distribution characteristics optimized for specific applications
3	Low heat generation	Thin lighting fixtures	Free choice of installation locations
4	Long service life	Maintenance-free	Applicability to an ageing society
5	Lightweight	Mounting on nonstationary	Fixture holders unnecessary, labor

		equipment	savings during installation
6	Low temperature resistant	Fixtures used at low temperatures	Fixtures used at low temperatures (continuing effort)
7	Impact resistant	High reliability under impact and vibration conditions	High reliability under impact and vibration conditions (continuing effort)

*Table 15.6 LED Characteristics and Next Generation Concept.*

FIG. 15.6-(1) and FIG. 15.6-(2) show an image of architectural lighting and specific lighting techniques used for comfortable space management that takes advantage of their functional superiority. In comparison with ordinary lighting fixtures, lighting fixtures used for architectural lighting have numerous mounting constraints (size, heat, etc.), and thus they are worth exploring as a research topic and in the future we will try to keep an eye on possibilities of expansion into the area of architectural lighting.

In addition, as far as problems related to light source levels are concerned, it should be noted that because modern LEDs were developed on the basis of a semiconductor component-oriented philosophy, they are not necessarily suitable for light sources used for illumination. Therefore, the downside of their benefits, such as the freedom of arrangement and combination of sources, etc., is the need to integrate multiple LEDs because their luminous output is low in comparison with conventional light sources. As a result, variations in light color, color rendition, etc. at the level of the integrated light source caused by variations in individual LEDs may present a problem. In addition, another problem to consider is the heat problem, which becomes aggravated as the number of LEDs grows. Therefore, now it is time to investigate LEDs as light sources for illumination at the structural level and to implement specific solutions based on efforts by all the groups involved in the project. In the future, we want to use LEDs of novel structures to create prototypes of lighting fixtures based on new concepts and to continue our support for the present project.



Left: Figure 15.6-(1) Lighting Techniques

// Keys, FIG. 15.6-(1) //

(Left, across top) Hotel corridor lighting technique using LED-based architectural lighting

(Right, above 2 circles) Functionality providing maximum effects can be realized at minimum power if very small architectural lighting fixtures taking advantage of LED size are employed

(Left circle, inside, top) Door

(Left circle, inside, left) Diffuser

(Right circle, inside) Wall

(Below & between 2 circles) Enlarged view

(Below left circle) Door

(Below right circle) Wall

Right: Figure 15.6-(2) Architectural lighting image.

As a specific course of action, we will be creating the following prototypes for the purpose of investigating and evaluating LED structures that can be used as new light sources for illumination.

- 1) Using commercially available LEDs, we will be creating prototypes of lighting fixtures designed for a luminous efficiency of 80 lm/W.
- 2) We will be creating prototypes of lighting fixtures utilizing LEDs of novel structures fabricated in the course of this project.
- 3) We will be creating prototypes of lighting fixtures incorporating new concepts (such as architectural lighting, etc.).

We will also strive to raise the efficiency of the lamp circuits we have implemented in this year's prototypes while continuing to investigate the following topics in order to ensure better reliability:

- 1) Selection and verification of reliability testing parameters for LED-based lighting devices.
- 2) Guidelines for ensuring safety in connection with the influence that may be exerted on the human body by increased LED output.

# 16 Conclusions and Future Course

## 16.1 Planning and Investigations

We have participated in symposia and academic meetings both domestically and overseas, researched technology trends, and conducted patent searches on GaN-based LEDs. In the future we shall continue our research to keep this project active.

## 16.2 Basic Research on Light Emission Mechanisms

(1) With regard to the two components of light emission from  $\text{In}_{0.08}\text{Ga}_{0.92}\text{N}$  thin films, PL measurements were performed at excitation energies both higher and lower than the GaN band gap. No large variations in the emission peak position of the two components were found. Nonetheless, when GaN is not excited the PL intensity is reduced, indicating a significant role for GaN as a carrier supply source, a role which grows in importance with increasing temperature.

(2) Excitation spectra of  $\text{In}_{0.08}\text{Ga}_{0.92}\text{N}$  thin films were measured and a clear absorption peak was observed in the temperature range from 4K to room temperature. It also became clear that at 4K the free A, B, and C excitons within GaN contribute to the photoluminescence of  $\text{In}_{0.08}\text{Ga}_{0.92}\text{N}$ . This suggests the possibility that the GaN belongs primarily to the buffer layer. The absorption positions of the two emission components are the same and it is surmised that the excited carriers first relax from the excitation energy position to the higher energy level and then transition to a lower energy level. Upon measuring the temperature dependence of the excitation spectrum there was no large variation in the peak position relative to temperature, so it is thought that the band gap of  $\text{In}_{0.08}\text{Ga}_{0.92}\text{N}$  shows no startling temperature dependence.

(3) Among the two light emission components, the emission peak position of the high energy component and the peak position of the excitation spectrum shifted in a parallel manner with temperature, indicating no temperature dependence of the Stokes shift of the high energy component and a value of about 50 meV. In the strain contributing to localized excitons, it is known that as the temperature rises, excitons delocalize and the energy difference (Stokes shift) between the absorption PL spectra becomes smaller. Considering this, the large Stokes shift observed in  $\text{In}_{0.08}\text{Ga}_{0.92}\text{N}$  is not likely due to localized excitons. With regard to the photoluminescence source of the high energy component, the Stokes shift is large and yet it is possible to maintain it to room temperature.

When thinking about the emission mechanism model into which a polaron concept has been introduced, as we proposed last year, the Stokes shift expected from the electron-polaron interaction is  $\alpha_e \eta \omega_l = 44.2$  meV ( $\alpha_e$ : Frohlich interaction constant.  $\eta \omega_l$ : LO phonon energy) and closely matches the results from this experiment, so we found that this could be explained without contradiction.

(4) From the fact that the peak positions in the absorption spectrum and excitation spectrum are at nearly the same energy position, we conclude that light absorbed by the  $\text{In}_{0.08}\text{Ga}_{0.92}\text{N}$  specimen excites carriers within the crystals and that these carriers contribute to the radiative recombination of  $\text{In}_{0.08}\text{Ga}_{0.92}\text{N}$  in the same manner as in typical semiconductors.

(5) Excitation spectroscopy was performed on InGaN with In compositions ranging from 4 to 14%. The lower the In composition the clearer the absorption peak was observed in the excitation spectra. Also, higher compositions of In showed a larger Stokes shift.

(6) Homoepitaxial growth by RF-MBE was conducted on a GaN bulk single crystal substrate fabricated by pressure controlled solution growth. As a result, epitaxial thin films that represented a continuation of the polarity of the GaN bulk single crystals used for the substrates were obtained. Also, it was confirmed that

when a GaN epitaxial thin film is grown on the N-face of the GaN bulk single crystal, it grows three dimensionally but when grown on the Ga-face, it grows two dimensionally. PL spectroscopy on these homoepitaxial thin films showed predominant emission lines produced by extremely sharp, strong neutral-donor-bound excitons with hardly any deep level emission observed. In comparison to heteroepitaxial growth on a sapphire substrate, huge improvements are seen, such as the emission peak width at half height narrows to less than 1/2, the PL intensity strengthens by 2 orders of magnitude, and the band-edge emission / deep level PL intensity ratio increases by 1 to 2 orders of magnitude.

(7) The effects of nitriding sapphire substrates with NH<sub>3</sub> gas and of AlN buffer layers on crystal polarity have been clarified with regard to control of initial stages of growth by NH<sub>3</sub> GS-MBE. N-face growth of GaN epitaxial thin film was found to be predominant regardless of the presence or absence of nitriding of the sapphire surface. In contrast to this, by introducing an AlN buffer layer prior to growth of the epitaxial thin film, it was found that Ga-face growth could be attained irrespective of the presence or absence of nitriding. The ability to control single polarity faces is valuable to high quality growth of crystals by NH<sub>3</sub> GS-MBE. Moreover, the results of RBS analysis of crystallinity of GaN epitaxial thin films grown by NH<sub>3</sub> GS-MBE using an AlN buffer layer show that the crystallinity of the attained epitaxial thin films was extremely high.

Future challenges and policies are noted below.

(1) There are insufficient experimental results to make clear conclusions regarding the low energy component of the two emission components. Still, based on numerous test results it is expected that the low-energy component contributes an important effect on the photoluminescence characteristics of In<sub>x</sub>Ga<sub>1-x</sub>N. At this time, it is unknown whether the low energy component observed at low temperature exists at high temperature. Also, from the fact that the strength of LO phonon replicas changes with different In compositions, it is expected that the low energy component is highly dependent on the In composition. In the future, the origin of the low energy component will be uncovered through more detailed measurements of specimens having different In compositions.

(2) The line width of the low energy component is wider than that of the high energy component and does not show dependences on external forces such as excitation strength or temperature. Additionally, the localization effect within the In<sub>x</sub>Ga<sub>1-x</sub>N among the specimens with wide emission line widths may shroud the emission characteristics of the In<sub>x</sub>Ga<sub>1-x</sub>N itself. Therefore, high quality crystals fabricated by joint R&D organizations will be used.

(3) When the photoluminescence of In<sub>x</sub>Ga<sub>1-x</sub>N was researched, there was no mistake that GaN contributes to the PL intensity. In particular, carriers from the GaN become crucial the higher the temperature, but more detailed examination of this mechanism will be conducted. This is extremely interesting from the perspective of device fabrication.

(4) Improvements will be made in the crystallinity of GaN thin films by homoepitaxial growth, especially with regard to surface flatness, which was inadequate this time. For the Ga-polar surface, which has stepped irregularities in the substrate surface, it is necessary to find techniques to fill in the substrate irregularities, such as lengthening the growth time or lengthening the source gas dispersion. With regard to N-polar surface, we will examine the introduction of shutter control techniques to reduce step-like three dimensional structures that form during homoepitaxial growth. We will also look at homoepitaxial growth by NH<sub>3</sub> GS-MBE, which easily attains films with good photoluminescence characteristics. High quality InGa<sub>1-x</sub>N mixed crystals will be grown on good homoepitaxial GaN buffer layers.

(5) Structural and optical characteristics of homoepitaxial thin films will be researched. To uncover the relationship between crystallinity and photoluminescence characteristics, RBS and X-ray diffraction measurement will be conducted on GaN epitaxial thin films and GaN bulk single crystals. With RBS measurement in particular, more detailed measurements of the channeling axes other than the <0001> axis evaluated this time will be performed.

## 16.3 Properties of GaN-based Semiconductors and Discovery of Light Emission Mechanisms

(1) Many research organizations have examined photoluminescence properties of GaInN and it is believed that the key to the light emitting mechanisms lies in the spatial localization effect of carriers in GaInN. It is thought that the photoluminescence characteristics (especially carrier localization) of GaInN are largely dependent on the In composition and evaluation while systematically varying the In composition is important. Therefore we systematically examined the photoluminescence characteristics over a broad range of temperatures (7K to 540K) using GaInN/GaN quantum well LEDs of varying In compositions (emission wavelengths). The results indicate an emission life temperature dependence split among three temperature regions and can be explained by changes in the carrier localization state. Additionally, simulation using a simple localization level model shows that an increase in the In composition ratio produces an increase in localization energy of the carriers and an increase in point defect density. The correlation between an LED's quantum efficiency and the differences in emission life temperature dependence according to In composition leads us to believe that localization energy and point defect density are predominant parameters affecting LED efficiency.

(2) To research the relationship between carrier localization characteristics and quantum efficiency, PL spectroscopy and time-resolved PL spectroscopy was conducted on two LED specimens having different quantum efficiencies but equivalent emission wavelengths. Results from the high quantum efficiency specimen show a large shift to higher energy in the PL peak accompanying excitation intensity, a large energy dependency with regard to the emission life, and a long emission life at the emission peak. From the results of these experiments, it is thought that the deep localization states of the carriers inhibit transition toward non-radiative recombination centers in the high quantum efficiency specimen. We believe the deep localization states of the carriers are a primary cause indicating high quantum efficiency.

(3) This year we introduced a near-probe PL system to measure at a high spatial resolution the in-plane distribution of light emission. First, basic data was collected from a typical multiple quantum well LED sample having an emission wavelength of 460 nm. A distribution of PL intensities ranging between 0.3 and 0.5  $\mu\text{m}$  was observed within the 4  $\mu\text{m}$  x 4  $\mu\text{m}$  area measured and the PL intensity at the low position was found to be 25% of the maximum intensity. The data is preliminary and requires accumulation of further data, including confirming reproducibility, to correctly interpret the data.

(4) The effects of Si doping of the quantum well activation layer were evaluated by reverse bias PL and time-resolved PL spectroscopy from the perspective of the quantum well band structure including piezoelectric effects. Changes in the spectrum of an applied electrical field were measured by measuring the depletion layer capacitance when a reverse bias was applied and estimating from the calculated value of the depletion layer width the external electrical field actually applied to the quantum well. The results from the low Si-doped specimens ( $4 \times 10^{17}\text{cm}^{-3}$ ) showed a shift of the PL peak to higher energy when an external electrical field is applied, a long life (52 ns) at zero bias, and a reduction in the life when an external electrical field is applied. It is estimated from the peak shift results and calculation of the transition energy that the piezoelectric field acting upon the quantum well is 1.48 MV/cm with In composition of  $x = 0.23$ . In contrast, a very slight shift of the PL peak to lower energy was observed with the high Si-doped specimen ( $4 \times 10^{18}\text{cm}^{-3}$ ). Also, since the life remained at 10 to 14 ns regardless of bias, it is believed that the electric field induced by the piezoelectric effect is neutralized by carriers from donor impurities. While Si doping of the activation layer is important to neutralize internal electrical fields since it influences spreading of the depletion layer in the pn connection, optimum design is important for efficient current injection.

Future plans are described here. First, as an extension of research conducted up to last year, we will explore the origin of carrier localization. We will study the two dimensional spatial distribution within a quantum well and investigate Stokes shift through selective excitation PL and the depth of localization levels. Additionally, LED specimen structures and the relationship between crystal growth conditions and carrier localization characteristics will be studied for the purpose of raising efficiencies still further.

The latter half of this project will focus on studying the knowledge obtained thus far and investigating the relationship between crystal growth parameters and photoluminescence characteristics of near ultraviolet light that is the goal of this project. To this end, information and samples will be closely shared between the epitaxial group and Yamaguchi University. Between the crystals grown within this project and the UV LEDs of other companies the conditions contributing to highly efficient emission of ultraviolet light will be uncovered. To be more concrete, the following main topics will be researched:

- effects from differences between heteroepitaxy and homoepitaxy, effects of crystal dislocation and skewing on photoluminescence characteristics, and differences in In doping effects
- effects of doping the UV emission activation layer with impurities
- optimization of doping profiles through simulation

This research will yield invaluable knowledge on optimal UV LED structures.

## 16.4 Basic Research on Bulk GaN Single Crystals by Solution Growth Method

The effects on the growth of bulk GaN single crystals of supersaturating a Ga melt with nitrogen using the PC-SG method were uncovered. With the intent of understanding the conditions needed to grow large, high quality bulk GaN single crystals, an ultra high pressure HIP device and an ultra high pressure crystal growth device introduced in 1999 were used to explore the effects of seed crystals, equilibrium pressure, acceleration speed of nitrogen pressure, and crystal growth time. Also, the characteristics of the GaN bulk single crystals attained were evaluated and the relationship between crystal quality and the surface condition of GaN bulk single crystals was examined. The details of the results are noted below.

(1) The equilibrium pressure of GaN at a heater temperature of 1475°C was 590 to 730 MPa. At a crystal growth pressure of 980 MPa, overpressure was about 300 MPa.

(2) By reducing the acceleration speed of nitrogen pressure in the ultra high pressure HIP device, a 120 mm<sup>2</sup> GaN single crystal with a good surface condition was attained. This is larger than the 104 mm<sup>2</sup> size GaN single crystal attained by HP-SG.

(3) A 334 mm<sup>2</sup> GaN single crystal (equivalent to diameter 20.6 mm) was attained using a ultra high pressure crystal growth device with the nitrogen pressure acceleration speed at 69 MPa/h. This is the best data regarding size of a GaN single crystal grown via a solution growth method. A GaN single crystal with a good surface condition was attained at a pressure acceleration speed of 9 MPa/h, but the crystal size was about 18 mm and did not enlarge the GaN single crystal by reducing the pressure acceleration speed.

(4) We found in (2) and (3) above that reducing the acceleration speed of nitrogen pressure is an effective means of attaining GaN single crystals with good surface condition.

(5) From observing the relationship between temperature fluctuations and cell nuclei occurrence density in (2) and (3) above, we've learned that reducing temperature fluctuations and lessening the nuclei occurrence density in GaN crystals is necessary to achieve large bulk GaN single crystals.

(6) Large GaN single crystals are more easily attained on a C-face just sapphire substrate than on a graphite plate, due to the relationship between seed crystals arranged in the crucible and the size of GaN single crystals that form near the surface of the Ga melt due to natural nuclei occurrence.

(7) Results suggest that prolonging the hold time of final crystal growth pressure has no effect on enlargement of the crystal size and that the size of the crystal is determined by the pressure rising process to final pressure.

(8) Results from the evaluation of GaN bulk single crystal characteristics show that differences in the GaN single crystal surface condition reflect differences in the crystal growth state. Single crystals having good surface condition are the same as those exhibiting good crystal characteristics.

- Tilt angle of 43 arcsec and twist angle of 18 arcsec attained with a four crystal x-ray rocking curve profile are values of a level equivalent to those of undoped GaN single crystals raised by HP-SG and show superior crystallinity.
- AFM observation showed flatness at a single atom layer level.
- PL spectroscopy at 4.2 K and room temperature showed good PL characteristics with band edge PL intensity greater than the yellow band. Additionally, with regard to PL intensity temperature dependency of band edge emissions, temperature variations in the PL intensity were small in the bulk GaN single crystals raised by PC-SG.

Predictions on the achievement of the goal (GaN single crystal size of 25 mm diameter or greater; defect density below  $10^5 \text{ cm}^{-2}$ ) and future plans are noted below.

In bulk GaN single crystals formed by PC-SG crystal defect density estimated by TEM observation is  $10^5 \text{ cm}^{-2}$  and it is predicted that the goal can be reached. Still, it is nearly impossible to correctly evaluate defect densities via TEM observation when the crystal defect density drops below  $10^6 \text{ cm}^{-2}$ , so it will be necessary to conduct evaluation by etch pitting. It was also found that bulk GaN single crystals formed by PC-SG show good crystal characteristics, especially superior PL characteristics. However, we were unable to confirm whether these crystals were superior as epitaxial substrates. Consequently, topics which should be confirmed or resolved include (1) suitability as a substrate for homoepitaxy, and (2) attainment of larger bulk GaN single crystals.

With regard to (1), evaluation of homoepitaxial growth on the bulk GaN single crystals formed by this research began at the end of 2000 with the cooperation of Yamaguchi University's Taguchi Research Lab and other organizations participating in this project. In order to evaluate characteristics of the bulk crystals it is necessary to have a fixed size and quantity so it is important to be able to consistently fabricate single crystals of at least 10 to 15 mm diameters. Moreover, the handling of crystals having a thickness of 20 to 30  $\mu\text{m}$  is difficult so we plan to examine the crystal growth process and crystal thickness inhibiting factors. Study of polarity control is also needed and we plan to verify effects of Mg doping. These crystals will be supplied to organizations performing research on LEDs and epitaxial growth techniques. By feeding back the results to growth technologies it is hoped that it will be possible to use them as epitaxial substrates.

With regard to (2), GaN single crystals with an area of 334  $\text{mm}^2$  (equivalent to a diameter of 20.6 mm) were attained by PC-SG using a multi-level crucible in an ultra high pressure crystal growth device. This gives us confidence that meeting the final year goal of 25 mm diameter crystals is not impossible. Nevertheless, technological improvements or breakthroughs are required to make this a reality. On this point, it is thought that reduction of temperature fluctuations is most effective, thus modifications to the heating device and the ultra high pressure crystal growth device are planned for this year. Improving temperature fluctuations will contribute not only to larger single crystals through reduction in crystal nuclei density, but will also improve reproducibility through a more stable temperature environment.

It is expected that the achievements of this year's research, through the technology studies noted above, will result in consistent fabrication of bulk GaN single crystals that exhibit good crystal surfaces, good crystal characteristics, and exceed 25 mm diameter in size.

## 16.5 Research into Crystalline Substrate Surfaces

With regard to techniques for precision lapping of the surface of a sapphire substrate, we were able to completely remove surface scratches by employing MCP in the latter part of normal lapping and achieved a surface roughness of 0.3 nm. Measurement was accomplished using AFM.

By using custom microscopes, scratches and contaminants can be detected, making evaluation at the substrate stage possible. Cleaning was changed from a multiple chamber ultrasound cleaning system to a single wafer cleaning system, reducing metallic element contaminants to less than 1/10<sup>th</sup> previous amounts. Analysis was conducted via total reflection fluorescent X-ray.

Additionally, precision of the C-face azimuth was controlled to less than  $\pm 0.05$  degrees relative to the specified axis (with m-axis at 0.15 degrees off as standard). Variation in the epitaxial effect due to off angle variation of the user's substrate has been reduced.

Lapping and polishing of the GaN substrate was performed experimentally with a high press lapping machine introduced to this research. Lapping is possible, but with the coarse surface of the GaN crystals this time, the target roughness could not be attained.

Future research plans with Yamaguchi University call for evaluation of GaN heteroepitaxial growth using MBE in pursuit of better substrates. In concrete terms, we intend to reduce GaN epitaxial film defects by varying the surface properties through stepping and the like while maintaining a high standard for surface roughness. We shall also research methods to greatly reduce GaN surface defects, aiming for a surface roughness of 1 nm or less.

## 16.6 Research and Development of GaNAsP-based Multicolored Light Emitting Materials by MOCVD

Two GaNP growth methods to achieve GaNP with a high P composition were studied: laser-assisted MOCVD and MOCVD using DMHy and PH<sub>3</sub> source gases.

The experiment with MOCVD using DMHy and PH<sub>3</sub> source gases was conducted keeping the ratio of V/III source gases constant and varying the growth temperature. With growth temperature set low, a P composition of 0.5% was confirmed using SIMS analysis. Among photoluminescence characteristics, a peak shift in the band edge caused by adding P to GaN via PH<sub>3</sub> was observed. Newly studied was growth of GaNP thin film using a laser-assisted MOCVD method. Results showed the source gas readily decomposed at low temperature due to the light energy and a P mix of about 10% was confirmed using SIMS analysis. TBP, which easily decomposes, was used as the P source. As a result, crystals with a high P composition were attained at a growth temperature of 850°C. PL measurements showed the band edge peak shift 0.2 eV toward the long wavelength compared to GaN. What's more, the degree of red shift was greater than that reported in previous announcements, and we believe that we've confirmed band bowing in the GaNP although not quantitatively. Thus the red shift of the PL spectrum of GaNP using laser-assisted MOCVD has been shown to be two to three times that of conventional MOVPE, making laser-assisted MOCVD a promising crystal growth technology.

It is necessary to move forward with more emphasis on quantitative research in 2001. With the creation of a prototype GaNP SQW LED, we were the first to confirm blue white light emission by current injection. This shows that, at a minimum, GaNP LEDs hold promise as a blue LED.

Future plans are noted below. In 2001, we intend to work with Professor Onabe of Tokyo University in growing GaNP (As) crystals and finding the optimum growth conditions under laser-assisted MOCVD by raising the intensity of the laser and improving the equipment itself. Tokyo University will examine crystal growth of GaNAs or GaNP by gas source MBE which has a stronger non-equilibrium state, large band gap

bowing, and a high expectation for wave length shifting. We will also work on optimizing the design of equipment used for laser-assisted MOCVD. In other words, we will optimize the growth conditions to achieve GaNP with a high P composition by making modifications to the substrate susceptor, heater construction, and gas inlets. We will raise the photoluminescence intensity of the LED by further studying GaNP multiple quantum well structures and epitaxial structures. To understand the light emission mechanism of GaNP we will continue to research in detail photonic characteristics through photoluminescence measurements. We will use selective epitaxial growth to increase high brightness of the LED and strive to raise the crystal quality. Stated differently, selective epitaxial growth, where epitaxial growth is performed locally and at specified locations of the substrate surface instead of across the entire surface, is thought to be more effective in attaining high quality. Evaluation of photonic characteristics and the light emission mechanism will be researched together with Professor Taguchi of Yamaguchi University. Lastly, we will work on raising the P composition and discovering the optimum growth structures and conditions for high brightness luminescence.

## 16.7 Development of Low Defect Density GaN Thin Film Epitaxial Substrates through MOCVD

Using a new FACELO (Facet Controlled Epitaxial Layer Overgrowth) method, dislocation density was reduced to an order between  $10^6 \text{ cm}^{-2}$  and  $10^4 \text{ cm}^{-2}$ . Controlling initial nuclei density, FACELO growth on a GaN substrate crystal (10 mm square) exhibiting low dislocation density was conducted by double FACELO – {11-22} FACELO, then {11-20} FACELO – to gradually reduce dislocation density.

To the best of our knowledge, we attained the world's lowest dislocation density in GaN on a sapphire substrate. We hypothesize that the dislocation reduction lies in dislocation bending horizontally along the c-axis through {11-22} triangular facet, resulting in propagation being terminated by voids formed at mask center.

Dislocation induced from the upper edge of the voids and arriving to persist as lines at the surface was found to be effectively blocked by {11-20} rectangular facet. We began study of 2 inch diameter specimens but it ended in incomplete embedding and inadequate surface morphology.

Results from TEM analysis of dislocation lines in FACELO-GaN make it clear that combined dislocations bend toward the mask region and are terminated by voids, and knife-shaped dislocations bend parallel to the mask stripe. Through this mechanism, dislocation lines occurring in the boundary between the GaN and sapphire substrate do not reach the surface, greatly reducing dislocation density.

It was found that a PL spectrum distribution in relation to the growth mechanism could be obtained through a micro PL method. It is believed that a large number of defects and impurities are contained in the regrowth boundary of the facet. It is thought that the trend to collect impurities by the facet is lowest in the c-face, followed by the {11-22} face, and then the {11-20} face.

Results from time-resolved spectroscopy confirm that the life of free excitons is longer in ELOG-GaN using a W mask than ELOG-GaN using an SiO<sub>2</sub> mask and that non-radiative recombination processes are inhibited.

Future plans are described here. We have accumulated many fundamental technologies, such as new FACELO methods and the use of W masks, that reduce dislocation defects on 10 mm square substrates. Dislocation density is on the order of  $10^6 - 10^4 \text{ cm}^{-2}$ , nearly reaching targeted levels. However, study of 2-inch diameters with a modified MOCVD growth device was unsuccessful in reproducing these FACELO results, ending in an inadequate surface morphology after embedding.

Further efforts at studying 2-inch diameters is needed to realize a practical 2-inch diameter GaN on sapphire substrate with dislocation density of less than  $10^4 \text{ cm}^{-2}$  targeted by this project. To this effect, we shall conduct additional basic research on reducing dislocation density and will combine elemental technologies

discovered thus far. To efficiently combine technologies, it is necessary to fully understand through TEM observation the propagation and elimination mechanisms of dislocation. The peculiar mechanisms of MOCVD will be better understood through examination and comparison with HPVE. Additionally, now that we understand differences in GaN crystal quality at the mask and at the window with ELOG-GaN, fine region crystal evaluation will be conducted through microphotoluminescence, time-resolved photoluminescence, and cathode luminescence.

By applying the above knowledge to 2-inch diameter GaN, timely development of practical, high quality GaN on sapphire substrate will occur. The fabricated substrate will be made available to the LED epitaxial group for use as a homoepitaxial substrate or to the substrate group for high-grade crystals to confirm the effects of low dislocation substrates.

## **16.8 Development of GaN Epitaxial Substrates through Low Pressure Vapor Phase Method**

We examined the synthesis condition of GaN by adjusting the microwave output to optimize temperature and pressure in the region where plasma exists in high density, taking source gas temperature, substrate temperature, relative position of the Ga crucible to the substrate, and N<sub>2</sub> pressure as parameters. Results show that what was heretofore a powder now shows growth of GaN crystals having a compact film arranged on the c-axis on sapphire substrates in the range of 10 x 4 mm<sup>2</sup>. X-ray diffraction spectroscopy also confirms a strong single peak in the sapphire (0002). Moreover, surface dilapidation was absent on 5 mm square GaN substrates, and synthesis of c-axis oriented crystals having surface morphology with good symmetry was achieved.

Additionally, with regard to synthesis speed of max. 100 μm/h, we experimentally uncovered correlations among various parameters, attaining the degree of freedom needed to improve crystallization. By changing growth parameters, such as the partial pressure of the reactive radicals and the activation method, we were also able to confirm that it is possible to raise synthesis speed to the highest level of 1 mm/h with vapor phase growth of compound semiconductors.

Future plans are described here. Among recent research surrounding GaN substrates, one sees progress in development of thick film GaN single crystals using HVPE and bulk single crystals by high pressure solution method, or increasing use of SiC substrates to attain higher quality or larger size. However, all of these methods involve hexagonal crystals with small inclination grain boundaries or thread dislocation and at present problems are piling up. There are also many challenges in establishing low cost supply as LEDs for general lighting. The synthesis speed of GaN via low pressure vapor phase has been estimated to logically be 1 to 6 mm/h. If manufacturing techniques can be established for direct synthesis of GaN at 1 mm/h or higher, the cost of epitaxial substrates will decrease dramatically to a level equivalent to present practical GaAs substrates.

In the future, we will further study a broad range of conditions together with the knowledge gained thus far and examine the potential as a GaN single crystal LED substrate, with the aim of fabricating large GaN bulk single crystals of 10 mm diameter or greater. How well the stoichiometry of Ga and N<sub>2</sub> can be controlled is crucial. To this end, single crystal growth conditions such as temperature and pressure must be optimized through logical observations and systematic experiments. Also, addition of reactive gases like H<sub>2</sub> or HCl will be tried as a promising means to raise growth speed. Moreover, we aim for growth of low dislocation density crystals by using SiC or GaN crystals as the substrate, or through substrate surface treatments, or by conducting low super saturation growth during initial growth processes.

## 16.9 Development of LED Epitaxial Process Technologies

### (1) Fabrication of AlGaIn/GaInN UV MQW Structures

The AlGaIn/GaInN MQW luminescent layer was examined as a luminescent layer for UV LEDs. By growing an AlGaIn barrier layer at a high temperature of 1100°C, a MQW structure exhibiting good surface morphology and interface sharpness was attained. PL measurement showed a peak wavelength of 385 nm and PL intensity on par with the photoluminescence of a blue MQW. Investigation of the PL intensity ratio ( $I_{300K}/I_{10K}$ ) showed 33% with the UV MQW using an AlGaIn barrier layer and was high compared with 23% exhibited by a blue MQW using a GaN barrier layer.

Reduction of the PL intensity ratio in the UV region of a GaN barrier layer MQW was suppressed by using a AlGaIn barrier layer.

### (2) Study of High AlN Mole Fraction AlGaIn Clad Layers

Growth of high AlN mole fraction AlGaIn clad layers for UV LEDs was examined. Growth pressure and the total gas flow was found to be effective parameters for high AlN mole fraction AlGaIn growth. An AlGaIn layer was attained with a AlN mole fraction exceeding 20%.

### (3) Fabrication of UV LED Element Structures

An LED structure using AlGaIn/GaInN MQW as the luminescence layer was fabricated. Current injection UV emission at an emission wavelength of 390 nm was confirmed. Operating voltage is 3.7 V when energized at 20 mA. Luminescence output was weaker as compared to blue LEDs with a lamp-translated equivalent of 1 mW. Optimization of growth conditions must be studied to make progress toward high efficiency.

Future plans include further optimization of growth conditions and establishment of highly efficient UV LED epitaxial technologies. Specific challenges are noted below.

#### (1) Reduction of Non-Radiative Paths

Further optimization of growth conditions is required to reduce non-radiative paths that decrease the output of UV LEDs and it is also necessary to raise the quality of MQW in particular. We wish to investigate the effects on LED brightness and improvements in the crystallinity of the MQW layer by introducing a super lattice clad layer.

Additionally, it is estimated from I-V characteristics that the cause lies in the boundary between the MQW layer and the p layer (pn connection) and examination of a p-AlGaIn clad layer is thought to be important. It is also important to study high carrier concentration p-AlGaIn growth as a means for good interface sharpness of the pn-connection and improvements in electrical characteristics.

#### (2) AlGaInN Light Emitting Layers (High InN Mole Fraction)

InN mole fraction in the GaInN luminescence layer becomes lower in the ultraviolet region. Consequently the effect of In weakens, reducing the PL intensity. With an AlGaInN luminescence layer, a high InN mole fraction is achieved so we have high expectations for In effect. UV emission at 360 nm was observed from an LED structure using a four-dimensional mixed crystal AlGaInN MQW structure by current injection. We previously studied AlGaInN luminescence layers but the strength decreased by about a factor of 1 compared with blue MQW. The introduction of Al into the luminescence layer worsens surface flatness and is a cause of reduced PL intensity. We shall aim for highly efficient UV luminescence by raising the quality of the AlGaInN layer through optimization of the growth conditions.

#### (3) ELO Method

With regard to ELO, further reduction of dislocation and optimization of regrowth conditions will be carried out. A UV LED structure on an ELO-GaN substrate shall be fabricated and the effect on low dislocation will be confirmed.

#### (4) Large MOCVD Equipment

We wish to uncover the effects of substrates on LED luminescence efficiency, making use of multiple charge characteristics. Dislocation density, luminescence layer skew, and control of the substrate surface condition are thought to effect luminescence efficiency. Using large MOCVD equipment, comparison is possible under fixed growth conditions with substrates with varying dislocation densities, differences in lattice inconsistencies with the luminescence layer, and different surface treatments. We wish to investigate how the different dislocation densities of GaN substrates and ELO-GaN substrates, the different lattice inconsistencies of SiC substrates and sapphire substrates, and the pre-processing conditions effect LED luminescence efficiency. Moreover, it is expected that observation systems using visible light surface reflectivity will be an effective tool for control of substrate surface conditions before growth.

#### (5) Applications with SiC Substrates

Compared to sapphire substrates, SiC substrates have characteristics advantageous to device fabrication such as substrate conductivity and a smaller lattice inconsistency with the GaN.

## 16.10 Development of High Output Ultraviolet Emitting Elements

(1) The amount of Si doping of the barrier layer in a UV LED were examined and an output of 1.2 mW (at 20 mA) was attained with Si doping of about  $2 \times 10^{17} \text{ cm}^{-3}$ . It is believed that Si doping has the effect of suppressing diffusion of Mg to the luminescence layer and at the same time works to degrade crystal quality. Upon making this chip into a flipchip LED, the output was improved by a factor of 2.4. Moreover, by fabricating a prototype blue LED lamp using RGB phosphors, we were able to attain a luminescence efficiency of 1.7 lm/W.

(2) By treating substrate irregularities and, by using a method which promotes lateral growth from protrusions (LEPS method) we attempted to reduce dislocation density of GaN with a single, maskless growth. The result was a dramatic reduction in the dislocation density of the laterally grown portion. Also, by applying LEPS method to UV LEDs, an output of 2.5 mW was attained, which is 3 times that on a conventional substrate. In this way, we found that LEPS was an effective method for reducing dislocation density and improving luminescence output.

(3) For the purpose of comparison to UV LEDs, we fabricated a blue LED lamp and a white LED lamp. The blue LED lamp exhibited an output of 9.1 mW with an external quantum efficiency of 17.1%. The white LED's luminescence efficiency was 12 lm/W.

Future plans are described here. This research has proven that LEPS can be used to reduce dislocation density and improve ultraviolet luminescence output. However, dislocation density observed in CL was still on the order of  $10^7 \text{ parts/cm}^2$ , even if within the low dislocation region, and on average was  $6 \times 10^8 \text{ parts/cm}^2$ . In the future further advances in the study of LEPS method will result in greater reductions in dislocation density. By using the LEPS method we improved the external quantum efficiency of a UV LED to 3.7% while energized at 20 mA. By improving light extraction efficiency through flipchip mounting technology and resin sealants, and with further optimization of device structures and growth conditions, it is thought that achievement of a UV LED with an external quantum efficiency exceeding 20% is possible. From here, we plan on working together with the light source device group to advance research on white lamps using RGB phosphors and high output UV LED lamps.

Additionally, we plan to study UV LED applications for new substrates, such as low dislocation GaN substrates fabricated by firms from the substrate group that will replace conventional sapphire substrates. We

also plan to further reduce dislocations and attain higher output UV LEDs. We shall also investigate the relationship between higher output through low dislocation density and wavelength and shall achieve an LED with the highest output in the ultraviolet region.

## 16.11 Development of Highly Efficient Phosphor Substances

A method of measuring the quantum efficiency of phosphors was determined. The measurement involves a process of separating three characteristics – absorption ratio, quantum efficiency, and luminescence efficiency – and the results are fed back to an experiment to improve composition of red phosphors. The results showed improvement in luminescence efficiency of 150 to 200%. Even with blue and green, a quantum efficiencies higher than 1-dimensional model were seen. However, even among phosphors showing the best quantum efficiency, red, green, and blue were all in the 60% range. This leaves a large gap between today and the goal of 90%.

Future plans are described below.

### 16.11.1 Improving Quantum Efficiency

Study shall proceed according to the cycle shown below. In concrete terms, improvements in quantum and luminescence efficiency will be targeted by searching for a sensitizer capable of communicating energy to the luminescence center  $\text{Eu}^{3+}$  of red phosphor  $\text{Ln}_2\text{O}_2\text{S}:\text{Eu}$ . Achievements here will then be expanded to green and blue colors.

*Figure 11.6-(1): Means to Improve Quantum Efficiency*

*Left Column, top to bottom: Phosphor development; Collect data on existing phosphors [quantum efficiency of each phosphor, absorption efficiency, excitation wavelength, intensity dependence]; Analysis [categorized according to host matrix, activating agents, luminescence type]; Improvement of existing materials and design of new materials.*

*Right Column, top to bottom: Establish method to measure powder quantum efficiency [standardization, reliability]; Study of quantum efficiency measurement in package environment [includes evaluation of coating film structure].*

### 16.11.2 Synthesis Method

We shall expand ambient atmospheric baking by choosing parameters different than in the past. Since the gap between current and target quantum efficiency is large, new concepts are needed. Ultra fine grains and thin film are said to improve quantum efficiency and the potential of these will be considered.

### 16.11.3 Other

Problems in making technologies practical and solutions thereof will be pursued, including:

- Ramp up, measurement, and evaluation of temperature characteristics.
- Design of equipment to experimentally accelerate degradation.
- Simulation of white color mixtures
- Full understanding of light emission mechanisms (joint research with Yamaguchi University)

## 16.12 Development of Lead Bonding Methods, Packaging Technologies, and White LEDs

### 16.12.1 Electrode Formation Technology

In addition to achieving high reflectivity in conventional Ti/Al electrodes, high reflectivity n-type electrode research suggests that electrodes based on new ZnO materials hold promise.

The optimum electrode is a Pt/Ag electrode. Pt/Ag electrodes have been found to achieve contact resistance of  $10^{-4} \Omega\text{cm}^2$  and reflectivity of 71.5%.

### 16.12.2 Improvement in Light Extraction Efficiency

Etching facet inclination techniques were examined. GaN dry etching is thought to be effective in not only raising efficiency of light extraction, but also for luminescence efficiency of phosphors and UV-resistant sealants. The method involved preparation of two photoresist masks, each with a different viscosity, and then study of dependencies among various photoresist conditions on the GaN facet angle.

The GaN facet angle showed a tendency to become smaller with an increase in the thickness of the photoresist film. It was also observed that the GaN facet angle tends to become smaller when the post bake temperature is raised, even though the resulting photoresist film thickness remains nearly the same. Examination of the post bake temperature dependence showed no perceptible change in the GaN facet angle at post bake temperatures up to 130°C on Type A photoresist. By post baking at 140°C, the GaN facet inclination reached the target 45° slant. With Type B photoresist a tendency toward reduction of the GaN facet angle with a rise in post bake temperature was observed. At a post bake temperature of 140°C a GaN inclined facet of 45° was attained.

A dependence on the orientation of the GaN facet angle was examined and none was observed either vertically or horizontally to the c-face sapphire substrate[1-100] direction. Evaluation of reproducibility of the GaN facet angle under differing photoresist conditions suggests that the GaN facet angle can be reproduced consistently when the photoresist mask is thick and the post bake temperature is high.

### 16.12.3 Development of White LEDs

A UV LED chip was used to fabricate a white LED and this was evaluated.

Ultraviolet light was shown on the phosphor layer mounted on a UV LED chip to form a photonic thin film filter transmitting visible light, then by coating the UV LED chip edge with phosphors we were able to verify an improvement of 30% in the white LED lamp's total luminous flux and transmitted ultraviolet light was suppressed from 31% to 13% compared to an unprocessed one. It was also realized that study of structures to draw the radiative light from the UV LED to the phosphor layer is needed to get the most out of photonic thin film filter characteristics.

White light color rendering of various phosphors was evaluated from the perspective of the luminescence spectrum shape. It was confirmed that color rendering can be improved by adjusting the phosphors containing high quantities of components having a broad spectrum distribution. White LED lamps combining phosphors with broad spectrum distribution, such as those G and B model phosphors evaluated here, hold promise as a practical light source for general illumination.

### 16.12.4 Development of Resin Sealants for UV LED

In studying hardening accelerators when using hydrogenised bisphenol A glycidyl ether as an epoxy monomer, we found that the optimum hardening accelerators were phosphorus-based ones which do not

have double bonds. Since hydrogenised bisphenol A glycidyl ether has a low resistance to heat, it was found that by doping with a heat tolerant alicyclic epoxy, heat discoloration could be suppressed.

Future plans are described here. Among development of electrode formation technologies, we plan to investigate electrode materials and the effects of different electrode structures on the potential efficiency and luminescence efficiency of UV LEDs and then identify electrodes with optimal device characteristics. We shall also evaluate electrode reliability from the LED characteristics and narrow down final electrode materials and structures.

We will apply facet inclination techniques established this year via RIE to LED fabrication and verify the effects of light extraction efficiency on improvements in luminescence efficiency. Additionally, we shall begin development of fine processing techniques for chips with the initial aim of achieving a light extraction efficiency of 50% or greater.

Within development of UV resistant resin technologies, we will not only continue the light experiments currently underway, but will also investigate oxidant inhibitors and ultraviolet absorbents to suppress discoloration. Also, we plan to study reliability and various characteristics (such as viscosity, heat resistance, water resistance, and insulation) needed for LED sealant resins.

On the white LED development front, we shall verify the behavior of visible light conversion efficiency using a chip to which facet inclination techniques have been applied. Also, we shall examine the structure of ultraviolet light reflective film that matches the wavelength of a UV LED and consider the benefit of using excitation photoluminescence.

## **16.13 Development of Light Emitting Diode Light Source Devices for Illumination**

In this year's research, photonic characteristics of a YAG phosphor were constructed using actual measurements and a reflective structured LED light source device combining a blue LED and a YAG phosphor were studied through optical simulation. The results of this simulation approximate the photonic characteristics of a real device model built from a blue LED sold in the marketplace. It was proven that this simulation method is effective in the design optimization and optical control of light source devices. Additionally, it was found that light source device using the reflection model structure examined this time resulted in an optical energy loss of greater than 70% and so improvement in efficiencies while suppressing optical energy loss is an important future research topic.

In contrast, correlated color temperature conversion techniques were studied by combining red and green LEDs with current blue LEDs and color rendering was explored. Examination of the relative spectral energy distribution of three types of LEDs via additive color mixture by setting the photoluminescence intensity ratio of the green LED to about 20% and then controlling the photoluminescence intensity ratio of the white LED and the red LED shows achievement of each correlated color temperature condition with bulb color (N:  $T_{cp} = 5026$  K), white white color (WW:  $T_{cp} = 3370$  K), white color (W:  $T_{cp} = 4246$  K), neutral white (N:  $T_{cp} = 5026$  K), dayglow color (D:  $T_{cp} = 6186$  K). What's more, high color rendering of  $R_a = 95$  was attained under dayglow conditions, thereby exceeding the  $R_a = 85$  of current white LEDs.

With regard to research into environmental suitability, a psychophysics experiment was conducted to verify the psychological effects on subjects that an integrated light source in which LEDs are arranged in a two-dimensional matrix may have. We were unable to understand the relationship of vision stress induced by the spatial factors of the LED points. Nevertheless, in this experiment we were able to establish that a strong correlation exists between glare and discomfort and that it is logarithmically proportional to the illumination intensity of the sample stimulus.

Future plans are described here. This year's research showed an optical energy loss of greater than 70% in light source devices using a reflection model structure. Using the established optical simulation methods we

will raise efficiency of LED light source devices. By introducing heat flow analysis and simulation we will come to understand heat-dissipating structures for LED light source devices and pursue even greater efficiencies.

With regard to environmental suitability, further detailed psychophysics experiments will be conducted to evaluate glare, discomfort, and comfort under an LED illumination environment. The effects of uncomfortable glare will be made clear and the effects of vision stress induced by the spatial factors of LED point light sources will be studied.

## 16.14 Research and Development of Zone Conversion Illumination Systems

This year an optical simulation tool using ray tracking was constructed and used to design practical illumination prototypes while considering fabrication errors expected to occur during mass production. As a result, the following came to be understood:

- A trapezoidal shape lens pattern, rather than the cylindrical-shaped lens pattern proposed before, results in less degradation in light extraction efficiency caused by fabrication errors.
- It was found that locating the LED module at the corner of the photo plate rather than along its side resulted in a higher light utilization factor.
- Other parameters are strongly resistant to fabrication errors and do not require any special methods.

Since illumination systems demand a high degree of directivity we found that using a prism sheet as a directional conversion means to achieve even greater energy saving effect was optimal for photonic plates. By creating a prototype with a prism mounted to a 4 inch photonic plate, optical characteristics were measured and the following was discovered.

- By attaching a prism sheet, the directivity of the light radiating from the photonic plate was half perpendicular, with directivity improvement to  $\pm 17^\circ$ .
- The uniformity of the photonic plate is not reduced with the introduction of the prism sheet.

Future plans are described here. Using the correlations between shape precision and energy conversion efficiency discovered in this year's research as guidelines, next year we shall conceptualize illumination systems, enumerate challenges thought to exist in the fabrication process, and analyze fabrication process precision. Our efforts will focus on photonic plate coupled elements that are greatly impacted by optical characteristics.

Additionally, we will begin assembling specifications for the illumination system planned in the final year.

### 16.14.1 Robust Design

To this point the objective has been to confirm the principles of photonic plates and to create prototypes using a simple 2P (photo-polymerization) method which has superior shape transfer. However, although this molding method is superior in transferring fine shapes, it has many problems with regard to manufacturing speed, materials cost, and large areas. Therefore, it is thought that injection molding is a better method for manufacturing, but it is not as good at transferring shapes as the 2P method. This year we shall investigate the ability of injection molding to transfer fine patterns and then use the results to create a robust design of fine pattern shapes and arrangements. To be specific, using transfer shape evaluation samples created by injection molding, knowledge will be acquired regarding precision and variability of shape transfer. Taking the transfer characteristics as an index, it will then be used for shape transfer of edge R and line formations.

Using the resulting transfer characteristics, the photonic characteristics will be taken as an evaluation index to optimize design, verifying suitability through simulation.

With a vector radiative coupling method, it is critical that the LED be fundamentally localized and the degree to which LED integration can be pushed is thought to be the determining factor in whether it will be realized or not. With regard to heat problems, heat dissipation of 100 lm/W targeted by this project is low compared to fluorescent lamps and it is believed that, even in integrated modules temperature rises can be suppressed through optimization of non-thermal structures. Still, reliability of heat simulation is low at present and it is conceivable that the prototype is unable to raise the level of integration.

It can also be thought that the LED efficiency at the halfway point of the project is lower than targeted and that the heat radiated will be greater than expected, preventing a rise in the level of integration. If this turns into a reality, breaking the LEDs among multiple photonic plates will be studied. Some think that this is better for the purposes of maintaining uniformity and this will be studied at the same time.

### 16.14.2 Fundamental Specifications

In 2002 – the final year of this project – several types of photonic plate LED illumination prototype samples will be extracted. From these, we will narrow it down from the perspective of application, shape, and design robustness to decide the summary specifications.

## 16.15 Development of Illumination Devices Based on New LED Concepts

We fabricated lighting fixtures using chip-type LEDs having the highest level luminescence efficiency (15 ml/W) in commercially available devices. Evaluation of their characteristics made the following clear.

- (1) It is possible to achieve extremely compact fixtures that are completely different from conventional lighting fixtures.
- (2) It is possible to achieve power-saving fixtures through a range difficult for conventional light sources.
- (3) It is possible to presently make practical LED illuminated devices for local light.
- (4) Heat restrictions for fixture attachment can be relaxed, creating greater freedom in where a fixture is affixed.

Future plans are described here. To this point we've created prototype light source substrates using shell-type LEDs and chip-type LEDs as the illumination source and made the most of these features in the formation of prototype light fixtures. We confirmed the practicality and merit of such approaches. From here, it is important to direct development toward meeting the needs of the marketplace. Thus, LED lighting fixture concepts held during the initial stages of this research are expanded to next generation concepts in the table below.

	LED Characteristic	Initial Concept	Next Generation Concept
1	Light having directivity	Reflective plate unnecessary. High fixture efficiency.	Resource saving lighting fixtures
2	Free arrangement of circuits and lamps	Free to arrange color, number of lamps, and beam angle	Arrange optimally according to application
3	Heat radiation low	Thin lighting fixtures	Freedom in fixture attachment
4	Long life	Maintenance-free	Perfect for aging society

5	Lightweight	Portable fixtures	Fixture holding materials unneeded. Less effort to install.
6	Withstand low temperatures	Low temperature use fixtures	Low temperature use fixtures (carried over)
7	Withstand shock	High reliability under shock and vibration	High reliability under shock and vibration (carried over)

*Table 16.15-(1): LED Characteristics and Next Generation Concepts*

Compared to general lighting fixtures, architectural lighting fixtures are subject to greater restrictions (such as size and heat). This research will expand its view to include these architectural lighting fixtures since there is adequate value in studying this as well.

With regard to light source level problems, present LEDs are thought up as semiconductor devices and are not necessarily suitable as an illumination light source. Consequently, while there are merits in freedom of arrangement and combination, the flip side to this is full of problems with variances in color rendering and the color of light emitted at the integration level due to differences among each LED. Moreover, when the LED integration density is increased it is conceivable that temperature-related troubles will occur with the increase in LED counts. This makes it important to examine at a structural level the form that LEDs as an illumination light source should take and this requires cooperation horizontally among the many groups involved in this project. In the future, we wish to support this project by creating prototype lighting fixtures based on new concepts using new LED structures.

The following prototypes will be created for the purpose of investigating and evaluating LED structures as a new illumination light source.

- 1) Using a commercially available LED, a prototype lighting fixture with a target luminescence efficiency of 80 lm/W will be created.
- 2) A prototype lighting fixture using a new LED structure devised by this project will be created.
- 3) A prototype lighting fixture introducing new concepts (architectural lighting, for example) will be created.

Additionally, we shall also advance high efficiency with a prototype circuit created this year and undertake the following studies with the aim of assuring reliability.

- 1) Examination of LED lighting fixture reliability
- 2) Establish safety after understanding the effects of LED high output on people.

# 17 List of Research Publications and Articles

Publication Subject	Authors	Where published/presented	When published/presented	Serial No.
Radiative Recombination Dynamics of Carriers in In <sub>x</sub> Ga <sub>1-x</sub> N Epitaxial Layers Revealed by Temperature Dependence of Time-resolved Photoluminescence Spectra	H. Kudo, T. Tanabe, H. Ishibashi, R. Zheng, Y. Yamada, and T. Taguchi	Physica Status Solidi (a) 180, pp. 27-21.	2000	
Optical properties of bound excitons and biexcitons in GaN	Y. Yamada, C. Sasaki, Y. Yoshida, S. Kurai, T. Taguchi, T. Sugahara, K. Nishino, and S. Sakai	IEICE Transactions on Electronics E83-C(4), pp. 605-611.	2000	
Effects of electric field on photoluminescence spectra in InGaN ultraviolet light-emitting diodes	H. Kudo, Y. Yamada, and T. Taguchi	Physica E7, pp. 949-952.	2000	
Homoepitaxial growth of GaN thin layer by molecular beam epitaxy with an RF nitrogen plasma	S. Kubo, S. Kurai, T. Okazaki, Y. Nanba, S. Manabe, and T. Taguchi	Vacuum, 59, pp. 277-283.	2000	
Fundamental characteristics of light sources utilizing InGaN semiconductor-based white LEDs (in Japanese)	T. Tamura, T. Setomoto, and T. Taguchi	Transactions of The Institute of Electrical Engineers of Japan, A 120.	2000	
Radiative recombination mechanisms in InGaN/AlGaIn single-quantum-well LED revealed by time-resolved photoluminescence spectra under	H. Kudo, T. Tanabe, H. Ishibashi, R. Zheng,	Proceedings of SPIE, "Optoelectronic Materials and Devices II," 4078, pp. 8-15.	July, 2000	

external electric fields	Y. Yamada, and T. Taguchi			
Effect of pre-treatment of GaN substrate for homoepitaxial growth by rf MBE	S. Kubo, T. Okazaki, S. Manabe, S. Kurai, and T. Taguchi	Proceedings of SPIE, "Optoelectronic Materials and Devices II," 4078, pp. 58-65.	July, 2000	
Characteristics of high-efficiency InGaN-based white LED Lighting	Y. Uchida, T. Setomoto, and T. Taguchi	Proc. of SPIE, "Display Technologies IV," 4079, pp. 120-126.	July, 2000	
White illumination characteristics of ZnS-based phosphor materials excited by InGaN-based ultraviolet Light-emitting diode	K. Murakami, T. Taguchi, and M. Yoshino	Proc. of SPIE, "Display Technologies III," 4079, pp. 112-118.	July, 2000	
Recombination dynamics due to polaron state of electrons in In <sub>0.08</sub> Ga <sub>0.92</sub> N epitaxial layers	H. Kudo, T. Tanabe, H. Ishibashi, R. Zheng, Y. Yamada, and T. Taguchi	Proceedings of 25 <sup>th</sup> International Conference on the Physics of Semiconductors, in press.	Sept., 2000	
Growth and Characterization of GaN Epilayer on Sapphire Substrate by Ammonia Gas Source MBE	S. Kurai, S. Kubo, T. Okazaki, T. Taguchi, M. Rosamond, J. Van Hove, and P. Chow	Proceedings of International Workshop on Nitride Semiconductors 2000, pp. 213-216	Sept., 2000	
Role of Nanostructures in the Radiative Recombination Process in InGaN-based Light-Emitting Diodes	R. Zheng, and T. Taguchi	Proceedings of International Workshop on Nitride Semiconductors 2000, pp. 860-863.	Sept., 2000	
Effects of AlN buffer layer on GaN thin film growth by RF-MBE (in Japanese)	S. Kurai, T. Okazaki, Y. Nanba, T. Tanabe, S. Kubo, S. Manabe, and T. Taguchi	Proceedings of 8 <sup>th</sup> Symposium of Society for Applied Plasma Research, 2000 "Plasma applications and composite functional materials," Vol. 10, pp. 83-84		

Semiconductor Lighting – Light for the 21 <sup>st</sup> Century based on LEDs (in Japanese)	T. Taguchi	Japan Society for the Promotion of Science, Committee No. 125 Symposium (invited)	May 25, 2000	
Behavior of excited electrons and defects in InGaN-based liquid crystal semiconductors (in Japanese)	T. Taguchi	The Japan Society of Applied Physics, Chugoku Branch Symposium “Crystal Defects Control using Electron Excitation” (invited)	May 26, 2000	
GaN growth by ammonia source MBE and evaluation of crystal properties (in Japanese)	S. Kurai, S. Kubo, T. Okazaki, T. Taguchi, and P. Chow	31 <sup>st</sup> Conference on Crystal Growth	July 26~28, 2000	
Radiative recombination mechanisms in InGaN/AlGaIn single-quantum-well LED revealed by time-resolved photoluminescence spectra under external electric fields	H. Kudo, T. Tanabe, H. Ishibashi, R. Zheng, Y. Yamada, and T. Taguchi	Photonics, Taiwan	July 26-28, 2000	
Effect of pre-treatment of GaN substrate for homoepitaxial growth by rf MBE	S. Kubo, T. Okazaki, S. Manabe, S. Kurai, and T. Taguchi	Photonics, Taiwan	July 26-28, 2000	
Characteristics of high-efficiency InGaN-based white LED Lighting	Y. Uchida, T. Setomoto, and T. Taguchi	Photonics, Taiwan	July 26-28, 2000	
White illumination characteristics of ZnS-based phosphor materials excited by InGaN-based ultraviolet Light-emitting diode	K. Murakami, T. Taguchi, and M. Yoshino	Photonics, Taiwan	July 26-28, 2000	
Homoepitaxial GaN thin film growth by RF-MBE with shutter control (in Japanese)	Y. Nanba, T. Okazaki, S. Manabe, S. Kubo, S. Kurai, and T. Taguchi	Preprints of Regular Meeting of The Physical Society of Japan, Chugoku/Shikoku Branch and The Japan Society of Applied Physics, Chugoku Branch	July 29, 2000	
Exciton-based emission characteristics of ELO GaN with	Y. Yoshida,	Preprints of Regular Conference of The	July 29, 2000	

W-mask (in Japanese)	Y. Yamada, T. Taguchi, K. Hiramatsu	Physical Society of Japan, Chugoku/Shikoku Branch and The Japan Society of Applied Physics, Chugoku Branch		
In doping effects on GaN thin film growth by RF MBE (in Japanese)	T. Okazaki, Y. Nanba, S. Manabe, S. Kubo, S. Kurai, and T. Taguchi	Preprints of Regular Conference of The Physical Society of Japan, Chugoku/Shikoku Branch and The Japan Society of Applied Physics, Chugoku Branch	July 29, 2000	
Temperature dependence of PL spectra of $\text{In}_{0.08}\text{Ga}_{0.92}\text{N}$ mixed crystal thin films (in Japanese)	H. Ishibashi, T. Tanabe, H. Kudo, Y. Yamada, and T. Taguchi	Preprints of Regular Conference of The Physical Society of Japan, Chugoku/Shikoku Branch and The Japan Society of Applied Physics, Chugoku Branch	July 29, 2000	
Reverse bias dependence of PL spectra of $\text{In}_{0.2}\text{Ga}_{0.8}\text{N}$ SQW Blue LED (in Japanese)	T. Tanabe, H. Ishibashi, H. Kudo, Y. Yamada, and T. Taguchi	Preprints of Regular Conference of The Physical Society of Japan, Chugoku/Shikoku Branch and The Japan Society of Applied Physics, Chugoku Branch	July 29, 2000	
Excitation wavelength dependence of emission spectra of $\text{In}_x\text{Ga}_{1-x}\text{N}/\text{GaN}$ multiple quantum well structures (in Japanese)	C. Sasaki, M. Iwata, Y. Yamada, T. Taguchi, S. Watanabe, M. S. Minsky, T. Takeuchi, N. Yamada, R. Schneider	Preprints of Regular Conference of The Physical Society of Japan, Chugoku/Shikoku Branch and The Japan Society of Applied Physics, Chugoku Branch	July 29, 2000	
In composition dependence of room temperature emission characteristics in $\text{In}_x\text{Ga}_{1-x}\text{N}/\text{GaN}$ multiple quantum well structures (in Japanese)	M. Iwata, C. Sasaki, Y. Yamada, T. Taguchi, S. Watanabe, M. S. Minsky, T. Takeuchi, N. Yamada,	Preprints of Regular Conference of The Physical Society of Japan, Chugoku/Shikoku Branch and The Japan Society of Applied Physics, Chugoku Branch	July 29, 2000	

	R. Schneider			
Emission mechanism and emission efficiency improvement strategy for GaN-based blue and ultraviolet LEDs (in Japanese)	T. Taguchi	33 <sup>rd</sup> All-Japan Conference of The Institute of Illuminating Engineers of Japan	August 24-25, 2000	
Design of white LED illumination devices using multiple point light source illuminance calculation technique (in Japanese)	Y. Uchida, T. Taguchi	33 <sup>rd</sup> All-Japan Conference of The Institute of Illuminating Engineers of Japan	August 24-25, 2000	
Emission characteristics of Y, Sr, ZnS-based white fluorescent materials excited by In <sub>x</sub> Ga <sub>1-x</sub> N ultraviolet LEDs (in Japanese)	K. Murakami, T. Taguchi, Y. Yoshida	33 <sup>rd</sup> All-Japan Conference of The Institute of Illuminating Engineers of Japan	August 24-25, 2000	
Development of solar power-based illumination systems utilizing white LEDs (in Japanese)	T. Setomoto, T. Taguchi	33 <sup>rd</sup> All-Japan Conference of The Institute of Illuminating Engineers of Japan	August 24-25, 2000	
Homoepitaxial GaN thin film growth by ammonia gas source MBE (in Japanese)	S. Kubo, T. Okazaki, S. Manabe, Y. Nanba, S. Kurai, and T. T. Taguchi	Preprints of 61 <sup>st</sup> Scientific Symposium of The Japan Society of Applied Physics, Vol. No. 1	Sept. 3-7, 2000	
External electric field dependence of PL spectra in In <sub>0.2</sub> Ga <sub>0.8</sub> N SWQ blue LEDs (in Japanese)	H. Kudo, T. Tanabe, H. Ishibashi, Y. Yamada, and T. Taguchi	Preprints of 61 <sup>st</sup> Scientific Symposium of The Japan Society of Applied Physics, Vol. No. 1	Sept. 3-7, 2000	
Excitation wavelength dependence of emission characteristics of In <sub>x</sub> Ga <sub>1-x</sub> N/GaN multiple quantum well structures (in Japanese)	C. Sasaki, M. Iwata, Y. Yamada, T. Taguchi, S. Watanabe, M. S. Minsky, T. Takeuchi, N. Yamada, R. Schneider	Preprints of 61 <sup>st</sup> Scientific Symposium of The Japan Society of Applied Physics, Vol. No. 3	Sept. 3-7, 2000	
Fundamental physical properties of InN quantum lines in In <sub>x</sub> Ga <sub>1-x</sub> N epitaxial thin films (in Japanese)	R. Zheng, T. Taguchi	Preprints of 61 <sup>st</sup> Scientific Symposium of The Japan Society of Applied Physics, Vol. No. 1	Sept. 3-7, 2000	
Evaluation of characteristics of white LED illumination light sources using multiple point light source illuminance calculation technique (in Japanese)	Y. Uchida, T. Taguchi	2000 Combined Conference of Fundamental/Materials Sections of The Institute of Electrical	Sept. 7-8, 2000	

		Engineers of Japan		
Recombination dynamics due to polaron state of electrons in $\text{In}_{0.08}\text{Ga}_{0.92}\text{N}$	H. Kudo, T. Tanabe, H. Ishibashi, R. Zheng, Y. Yamada, and T. Taguchi	25 <sup>th</sup> International Conference on the Physics of Semiconductors	Sept. 17-22, 2000	
Growth and Characterization of GaN Epilayer on Sapphire Substrate by Ammonia Gas Source MBE	S. Kurai, S. Kubo, T. Okazaki, T. Taguchi, M. Rosamond, J. Van Hove, and P. Chow	International Workshop on Nitride Semiconductors, 2000	Sept. 24-27, 2000	
Role of Nanostructures in the Radiative Recombination Process in InGaN-based Light-Emitting Diodes	R. Zheng, and T. Taguchi	International Workshop on Nitride Semiconductors, 2000	Sept. 24-27, 2000	
Strategy of the Compound Semiconductor-based "Lighting for the 21 <sup>st</sup> Century" National Project and Future Prospects (in Japanese)	T. Taguchi	Ministry of Education, Sports, Science, and Technology Special Area Development Symposium (special invitation)	October 6, 2000	
Compound Semiconductor Lighting Based on InGaN Ultraviolet LED and Phosphor System	T. Taguchi, and K. Murakami	27 <sup>th</sup> International Symposium on Compound Semiconductors	October 2-6, 2000	
Effects of AlN buffer layer on GaN thin film growth by RF-MBE (in Japanese)	S. Kurai, T. Okazaki, Y. Nanba, T. Tanabe, S. Kubo, S. Manabe, and T. Taguchi	8 <sup>th</sup> Symposium of Society for Applied Plasma Research	March 16-17, 2001	
White LEDs using ZnS-, Y-, and Sr-based phosphor materials and $\text{In}_x\text{Ga}_{1-x}\text{N}$ ultraviolet LEDs (in Japanese)	K. Murakami, H. Kudo, T. Taguchi, and M. Yoshino	Preprints of The 48 <sup>th</sup> Combined Conference on Applied Physics, Vol. No. 1	March 28-31, 2001	
Implementation of energy-saving street lighting systems based on special emission mechanisms of InGaN-based LEDs (in Japanese)	T. Taguchi	Preprints of The 48 <sup>th</sup> Combined Conference on Applied Physics, Vol. No. 1	March 28-31, 2001	

GaN homoepitaxial thin film growth on GaN single crystal substrates by RF-MBE (in Japanese)	T. Tanabe, Y. Nanba, S. Manabe, S. Kubo, S. Kurai, T. Taguchi, T. Inoue, H. Kurita	Preprints of The 48 <sup>th</sup> Combined Conference on Applied Physics, Vol. No. 1	March 28-31, 2001	
Excitation levels of In <sub>0.08</sub> Ga <sub>0.92</sub> N mixed crystal thin films (in Japanese)	H. Kudo, K. Murakami, S. Kubo, S. Kurai, T. Taguchi, T. Inoue, H. Kurita	Preprints of The 48 <sup>th</sup> Combined Conference on Applied Physics, Vol. No. 1	March 28-31, 2001	
Time-resolved non-linear emission in exciton-based optical transition process in ELO-GaN (in Japanese)	Y. Yoshida, H. Kugimiya, Y. Yamada, T. Taguchi, H. Miyake, K. Hiramatsu, Y. Iyechika, T. Maeda	Preprints of The 48 <sup>th</sup> Combined Conference on Applied Physics, Vol. No. 1	March 28-31, 2001	
Well layer thickness dependence of optical characteristics in InGaN multiple quantum well structures (in Japanese)	H. Kudo, K. Murakami, H. Ishibashi, Y. Yamada, T. Taguchi, T. Tsunekawa, Y. Ouchi, H. Okagawa, K. Tadatomo, Y. Imada	Preprints of The 48 <sup>th</sup> Combined Conference on Applied Physics, Vol. No. 1	March 28-31, 2001	
Room temperature emission characteristics of In <sub>x</sub> Ga <sub>1-x</sub> N/GaN multiple quantum well structures (in Japanese)	M. Iwata, C. Sasaki, Y. Yamada, T. Taguchi, S. Watanabe, M. S. Minsky, T. Takeuchi, S. Y. Yamada, R. Schneider	Preprints of The 48 <sup>th</sup> Combined Conference on Applied Physics, Vol. No. 1	March 28-31, 2001	

Excitation spectra of In <sub>x</sub> Ga <sub>1-x</sub> N/GaN multiple quantum well structures (in Japanese)	C. Sasaki, M. Iwata, Y. Yamada, T. Taguchi, S. Watanabe, M. S. Minsky, T. Takeuchi, S. Y. Yamada, R. Schneider	Preprints of The 48 <sup>th</sup> Combined Conference on Applied Physics, Vol. No. 1	March 28-31, 2001	
Study of initial stage processes in GaN thin film growth by ammonia source MBE (in Japanese)	S. Kubo, S. Onishi, T. Okazaki, S. Kurai, and T. Taguchi	Preprints of The 48 <sup>th</sup> Combined Conference on Applied Physics, Vol. No. 1	March 28-31, 2001	
Temperature Dependent Carrier Dynamics in GaInN/GaN Multiple Quantum Well with Varying In Composition	S. Watanabe, M. S. Minsky, N. Y. Yamada, T. Takeuchi, R. Schneider, C. Sasaki, M. Iwata, Y. Yamada, T. Taguchi	International Workshop on Nitride Semiconductors, 2000	2000	
High Temperature Time Resolved Photoluminescence of InGaN/GaN Multi Quantum Well LEDs	M. S. Minsky, S. Watanabe, R. Schneider, N. Yamada, C. Sasaki, M. Iwata, Y. Yamada, and T. Taguchi	61 <sup>st</sup> Scientific Symposium of The Japan Society of Applied Physics	Sept. 6, 2000	
Emission efficiency and emission lifetime characteristics of GaInN/GaN-based multiple quantum well LEDs (in Japanese)	S. Watanabe, Milan Minsky, T. Takeuchi, N. Y. Yamada, C. Sasaki, M. Iwata, Y. Yamada, and T. Taguchi	62 <sup>nd</sup> Scientific Symposium of The Japan Society of Applied Physics	2001	

Photoluminescence peak shift in GaInN/GaN multi-quantum wells with Si doped barriers	M. S. Minsky, S. Watanabe, T. Takeuchi, N. Yamada, W. Goetz, N. Gardner, S. Stockman, and M. Krames	61 <sup>nd</sup> Scientific Symposium of The Japan Society of Applied Physics	2001	
Carrier Recombination Processes in GaInN/GaN Multiple Quantum Well LED with varying In Composition	S. Watanabe, M. S. Minsky, N. Yamada, and T. Takeuchi	Submitted to PIERS2001	2001	
GaN bulk wafer and its applications (in Japanese)	O. Oda	SEMI Japan-sponsored Workshop on Compound Semiconductors “Technological Strategy for Compound Semiconductor Materials and Devices”	June 1, 2000	
Growth of Bulk GaN Single Crystals by the Pressure-Controlled Solution Growth Method	T. Inoue, Y. Seki, O. Oda, S. Kurai, Y. Yamada, and T. Taguchi	The 1 <sup>st</sup> Asian Conference on Crystal Growth and Crystal Technology (CGCT-1), T-B-12	August 31, 2000	
Pressure-Controlled Solution Growth of Bulk GaN Crystals under High Pressure (invited)	T. Inoue, Y. Seki, O. Oda, S. Kurai, Y. Yamada, and T. Taguchi	9 <sup>th</sup> Conference on High Pressure Semiconductor Physics (HPSP9), 25C1	Sept. 25, 2000	
Growth of Bulk GaN Single Crystals By Pressure-Controlled Solution Growth Method (II) (in Japanese)	T. Inoue, H. Kurita, S. Kurai, Y. Yamada, and T. Taguchi	48 <sup>th</sup> Combined Conference on Applied Physics	March 30, 2001	
Evaluation of Bulk GaN Single Crystals Grown By Pressure-Controlled Solution Growth Method (in Japanese)	T. Inoue, H. Kurita, S. Kurai,	48 <sup>th</sup> Combined Conference on Applied Physics	March 30, 2001	

	Y. Yamada, and T. Taguchi			
Growth of Bulk GaN Single Crystals by the Pressure-Controlled Solution Growth Method	T. Inoue, Y. Seki, O. Oda, S. Kurai, Y. Yamada, and T. Taguchi	Jpn. J. Appl. Phys. 39, 2394-2398.	2000	
Development of GaN Bulk Substrates for GaN Based LEDs and LDs	O. Oda, T. Inoue, Y. Seki, A. Wakahara, A. Yoshida, S. Kurai, Y. Yamada, and T. Taguchi	IEICE Trans. Electron E83-C, 639-646	2000	
GaN Bulk Substrates for GaN Based LEDs and LDs	O. Oda, T. Inoue, Y. Seki, K. Kainosho, S. Yaegashi, A. Wakahara, A. Yoshida, S. Kurai, Y. Yamada, and T. Taguchi	Phys. Stat. Sol. 180, 51- 58	2000	
Growth of Bulk GaN Single Crystals by Pressure-Controlled Solution Growth Method (in Japanese)	T. Inoue, Y. Seki, O. Oda, S. Kurai, Y. Yamada, and T. Taguchi	J. of Jpn. Association of Crystal Growth 27, 54-59	2000	
Pressure-Controlled Solution Growth of Bulk GaN Crystals under High Pressure (Editor's Choice)	T. Inoue, Y. Seki, O. Oda, S. Kurai, Y. Yamada, and	Phys. Stat. Sol. (b) 223, 15-27.	2001	

	T. Taguchi			
GaN <sub>P</sub> growth by Photo-assisted MOCVD (in Japanese)	Y. Yoshida, Y. Itoh, J. Kikawa	Japanese Association of Crystal Growth	July 26, 2000	
Nitride rich GaN <sub>1-x</sub> P <sub>x</sub> growth by photo-assisted MOCVD and Int'l Workshop on Nitride Semicond.	S. Yoshida, J. J. Kikawa, Y. Itoh	Workshop on Nitride Semicond. IWN2000	Sept. 27, 2000	
Evaluation of GaNP grown by MOCVD (in Japanese)	Y. Itoh, S. Yoshida, J. J. Kikawa.	61 <sup>st</sup> Scientific Symposium of The Japan Society of Applied Physics	Sept. 5, 2000	
Hexagonal GaNP growth by laser-assisted MOCVD	S. Yoshida, J. Kikawa, Y. Itoh	The 1 <sup>st</sup> Asian Conf. On Crystal Growth and Crystal Tech., Sendai	August 2000	
Organometallic growth of N rich hexagonal and cubic GaNP mixed crystals (in Japanese)	T. Kimura, S. Yoshida, Y. Itoh, N. Chudan, Wu Jun, K. Onabe, J. Kikawa, Y. Shiroki	61 <sup>st</sup> Scientific Symposium of The Japan Society of Applied Physics	Sept. 5, 2000	
Nitride rich GaNP hexagonal growth using MOCVD	S. Yoshida, J. Kikawa, Y. Itoh	2000 MRS Fall Meeting, Boston	Nov. 27, 2000	
Nitride rich GaN <sub>1-x</sub> P <sub>x</sub> growth by photo-assisted MOCVD and its LED property	J. J. Kikawa, S. Yoshida, Y. Itoh	Proc. Int'l Workshop on Nitride Semicon. IPAP Conf. Ser. 1, 429	Dec. 2000	
Hexagonal GaNP growth by laser-assisted MOCVD	J. J. Kikawa, S. Yoshida, Y. Itoh	J. Crystal Growth, in press	May 2001	
Growth of GaNP by photo-assisted MOCVD and its evaluation (in Japanese)	Y. Itoh, S. Yoshida, J. Kikawa	9 <sup>th</sup> Symposium on SiC and related wide bandgap semiconductors	December 13-14, 2000	
Nitride rich GaNP hexagonal GaNP growth using MOCVD	J. J. Kikawa, S. Yoshida, Y. Itoh	To be published in MRS symp. Proc., 2001 (MRS Web site)	Apr., 2001	
GaN <sub>P</sub> LED prototype (in Japanese)	S. Yoshida, Y. Itoh, K. Onabe, Y. Shiroki	48 <sup>th</sup> Conference of The Japan Society of Applied Physics	March 31, 2001	
Evaluation of MOCVD-grown	Y. Itoh,	48 <sup>th</sup> Conference of The Japan Society of	March 30, 2001	

GaN <sub>P</sub> (2) (in Japanese)	S. Yoshida, J. Kikawa, K. Onabe, Y. Shiroki	Applied Physics		
GaN <sub>P</sub> growth by MOCVD (in Japanese)	Y. Itoh, N. Chudan, S. Yoshida, J. Kikawa, K. Onabe, and Y. Shiroki	48 <sup>th</sup> Conference of The Japan Society of Applied Physics	March 31, 2001	
MOVPE growth of lattice-matched quaternary Ga <sub>1-x</sub> In <sub>x</sub> P <sub>1-y</sub> N mixed crystals on GaP substrate (in Japanese)	N. Chudan, T. Kimura, Wu Jun, Y. Itoh, S. Yoshida, J. Kikawa, K. Onabe, and Y. Shiroki	48 <sup>th</sup> Conference of The Japan Society of Applied Physics	March 30, 2001	
Recent progress in selective area growth and ELO of III-nitrides	K. Hiramatsu K. Nishiyama, A. Motogaito H. Miyake, Y. Iyechika, and T. Maeda	The 3 <sup>rd</sup> Int. Conf. On Nitride Semiconductors	July 5, 1999	
Recent progress in selective area growth and Epitaxial Lateral Overgrowth of III-Nitrides: Effects of Reactor Pressure in MOVPE Growth	K. Hiramatsu, K. Nishiyama, A. Motogaito, H. Miyake, Y. Iyechika, and T. Maeda	Phys. Stat. Sol. (a) 176, 535	July 4, 1999	
Optical and crystalline properties of epitaxial lateral overgrown GaN using W-mask by HVPE	H. Sone, S. Nanbu, Y. Kawaguchi, M. Yamaguchi, H. Miyake, Y. Iyechika, T. Maeda, and N. Sawaki	Jpn. J. Appl. Phys. 38, L356	1999	

Crystal orientation fluctuation of epitaxial lateral overgrown GaN with W and SiO <sub>2</sub> mask observed by TEM and X-ray rocking curves	Y. Honda, Y. Iyechika, T. Maeda, H. Miyake, K. Hiramatsu, H. Sone, and N. N. Sawaki	Jpn. J. Appl. Phys. 38, L1299		
Effects of heat treatment on W/n-GaN junction (in Japanese)	S. Nanbu, H. Sone, Y. Kawaguchi, N. Sawaki, U. Mototsune, H. Miyake, K. Hiramatsu, Y. Iyechika, T. Maeda	The 46 <sup>th</sup> Combined Conference on Applied Physics	March 1999	
W buried structure in selective lateral growth and its evaluation (in Japanese)	K. Hiramatsu, S. Nanbu, Y. Kawaguchi, N. Sawaki, M. Haino, U. Mototsune, H. Miyake, Y. Iyechika, T. Maeda	60 <sup>th</sup> Scientific Conference of The Japan Society of Applied Physics, 2p-W- 6	September 1999	
Effects of pressure on GaN grown by selective lateral growth using reduced-pressure MOVPE (in Japanese)	H. Mizuya, M. Haino, K. K. Nishiyama, U. Mototsune, H. Miyake, K. Hiramatsu	60 <sup>th</sup> Scientific Conference of The Japan Society of Applied Physics, 2p-W- 3	September 1999	
MOVPE-GaN selective growth-based fabrication of W buried structures (in Japanese)	S. Nanbu, Y. Kawaguchi, N. Sawaki, U. Mototsune, H. Miyake, K. Hiramatsu, Y. Iyechika, T. Maeda	60 <sup>th</sup> Scientific Conference of The Japan Society of Applied Physics, 2p-W- 6	September 1999	
Evaluation of ELO GaN with W mask by TEM (in Japanese)	Y. Honda, Y. Iyechika,	60 <sup>th</sup> Scientific Conference of The Japan Society of	September 1999	

	T. Maeda, H. Miyake, K. Hiramatsu, H. Sone, N. Sawaki	Applied Physics, 2p-W-6		
Crystalline and optical properties of ELO GaN by HVPE using tungsten mask	K. Hiramatsu, A. Motogaito, H. Miyake, Y. Honda, Y. Iyechika, T. Maeda, F. Bertram, J. Christen, and A. Hoffman	Special Issue on Blue Laser Diodes and related Devices, IEICE Trans. Electron., Vol. E83-C, p. 620.	2000	
Buried tungsten metal structure fabricated by epitaxial-lateral-overgrowth GaN via low-pressure MOVPE	M. Haino, M. Yamaguchi, H. Miyake, A. Motogaito, K. Hiramatsu, Y. Kawaguchi, N. Sawaki, Y. Iyechika, and T. Maeda	Jpn. J. Appl. Phys., 39, L449	2000	
Selective lateral overgrowth (ELO) of GaN using $WN_x$ as a mask and $WN_x/GaN$ electrode characteristics (in Japanese)	H. Miyake, K. Hiramatsu, Y. Iyechika, T. Maeda, et al.	The 47 <sup>th</sup> Combined Conference on Applied Physics	March 2000	
GaN layer structures with buried Tungsten Nitride (WN) using epitaxial lateral overgrowth (ELO) via MOVPE	K. Hiramatsu, H. Miyake, Y. Iyechika, T. Maeda, et al.	European-MRS	May 30, 2000	
Fabrication and evaluation of GaN structures with buried $WN_x$ electrode by ELO (in Japanese)	H. Miyake, K. Hiramatsu, Y. Iyechika, T. Maeda, et al.	The Institute of Electronics, Information, and Communication Engineers	May 2000	
Reduction of dislocations in GaN by FACELO (facet-controlled ELO) (in Japanese)	H. Miyake, K. Hiramatsu,	The Institute of Electronics, Information, and	May 2000	

	Y. Iyechika, T. Maeda et al.	Communication Engineers		
Fabrication and characterization of low defect density GaN using facet controlled epitaxial lateral overgrowth (FACELO)	K. Hiramatsu, H. Miyake, Y. Iyechika, T. Maeda et al.	Int. Conf. On Metal Organic Vapor Phase Epitaxy	June 5, 2000 (invited)	
Evaluation of FACELO (facet-controlled selective lateral overgrowth)-grown GaN crystals (in Japanese)	H. Miyake, K. Hiramatsu, Y. Iyechika, T. Maeda et al.	All-Japan Conference on Crystal Growth	July 7, 2000	
Reduction of dislocation density in GaN by Facet Controlled ELO	H. Miyake, K. Hiramatsu, Y. Iyechika, T. Maeda et al.	IWN 2000	September 24, 2000	
Epitaxial lateral overgrowth of GaN using Tungsten Nitride (WN <sub>x</sub> ) mask via MOVPE and electrical properties of WN <sub>x</sub> /GaN contacts	H. Miyake, K. Hiramatsu, Y. Iyechika, T. Maeda et al.	IWN 2000	September 24, 2000	
Carrier gas dependence of GaN grown using the ELO technique by HVPE (in Japanese)	S. Machimoto, M. Fukui, H. Miyake, K. Hiramatsu, Y. Iyechika, T. Maeda	Preprints of The 48 <sup>th</sup> Combined Conference on Applied Physics, Vol. No. 1	March 28-31, 2001	
Transmission Electron Microscopy Investigation of Dislocations in GaN Layer Grown by Facet-Controlled Epitaxial Lateral Overgrowth	Y. Honda, Y. Iyechika, T. Maeda, H. Miyake, and K. Hiramatsu	Jpn. J. Appl. Phys., 40, L309	2001	
Growth of GaN Single Crystals from Vapor Phase (in Japanese)	M. Tatsumi, T. Hirota, M. Kusao	The 31 <sup>st</sup> All-Japan Conference on Crystal Growth	July 2000	
Growth of GaN Crystals from Vapor Phase	T. Hirota and M. Tatsumi	The 1 <sup>st</sup> Asian Conference on Crystal Growth and Crystal Technology	August 31, 2000	
Growth of low dislocation density GaN by lateral overgrowth on processed substrates (2) (in	H. Okagawa, T. Shiroichi,	Preprints of The 48 <sup>th</sup> Combined Conference on Applied Physics,	March 28-31, 2001	

Japanese)	Y. Ouchi, T. Tsunekawa, K. Tadatomo, Y. Imada	Vol. No. 1		
Study of light source materials combining blue LED with YAG phosphors (in Japanese)	K. Yamada, S. Murai, Y. Imai, K. Ishii	Proc. of All-Japan Conference of The Institute of Illuminating Engineers of Japan, 2000	August 25, 2000	
Study of structure and emission characteristics of phosphor conversion type LED light source devices (in Japanese)	K. Yamada, Y. Imai, K. Ishii	Proc. of Kansai Branch Conference of The Institute of Illuminating Engineers of Japan, 2000	November 26, 2000	

## PATENTS

Title of Invention	Inventor(s)	Application Date	Application No.
GaN Based Light Emitting Element and Method of Its Manufacture	Kiyoteru YOSHIDA	May 11, 2000	Japanese Patent Application No. 2000-138978
Lighting Fixture	Osamu UEDA, Akihito YASUHARA	May 16, 2000	Japanese Patent Application No. 2000-142690
Lighting Lamp	Osamu UEDA, Masaki KOYAMA	May 16, 2000	Japanese Patent Application No. 2000-142691
Lighting Fixture	Kunio SATO, Kin'ichi SUGINO	May 16, 2000	Japanese Patent Application No. 2000-142692
Method for Growing III-V Nitride Semiconductor and Vapor Growth Device	Tatsuhiro Hirota, Masami TATSUMI	May 26, 2000	Japanese Patent Application No. 2000-157036
Group III-V Nitride Semiconductor Growth Method and Growth Apparatus	Tatsuhiro Hirota, Masami TATSUMI	May 26, 2000	Japanese Patent Application No. 2000-157041
Group III-V Nitride Semiconductor Growth Method and Vapor Phase Growth Apparatus	Tatsuhiro Hirota, Masami TATSUMI	June 29, 2000	00113814.8 (Europe)
Group III-V Nitride Semiconductor Growth Method and Vapor Phase Growth Apparatus	Tatsuhiro Hirota, Masami TATSUMI	June 29, 2000	09/605845 (United States)
Group III-V Nitride Semiconductor Growth Method and Vapor Phase	Tatsuhiro Hirota, Masami TATSUMI	June 29, 2000	2313155 (Canada)

Growth Apparatus			
Group III-V Nitride Semiconductor Growth Method and Vapor Phase Growth Apparatus	Tatsu Hirota, Masami TATSUMI	June 29, 2000	36354/00 (South Korea)
Group III-V Nitride Semiconductor Growth Method and Vapor Phase Growth Apparatus	Tatsu Hirota, Masami TATSUMI	June 30, 2000	89112997 (Taiwan)
Group III-V Nitride Semiconductor Growth Method and Vapor Phase Growth Apparatus	Tatsu Hirota, Masami TATSUMI	June 30, 2000	001200164.6 (People's Republic of China)
Lighting fixture	Osamu UEDA, Masaki KOYAMA, Akihito YASUHARA	July 17, 2000	Japanese Patent Application No. 2000-215410
Semiconductor Light Emitting Element	Kazuyuki TADATOMO, Hiroaki OKAGAWA, Tatsuo SHIROICHI, Yoichiro OUCHI, Takashi TSUNEKAWA	September 5, 2000	Japanese Patent Application No. 2000-268274
Semiconductor Substrate Material	Kazuyuki TADATOMO, Hiroaki OKAGAWA, Yoichiro OUCHI, Takashi TSUNEKAWA	September 18, 2000	Japanese Patent Application No. 2000-282047
Group III-V compound semiconductor and method of producing the same	Kazumasa HIRAMATSU, Takayoshi MAEDA, Yasushi IYECHIKA	September 22, 2000	Japanese Patent Application No. 2000-288259
Semiconductor Light Emitting Element	Kazuyuki TADATOMO, Hiroaki OKAGAWA, Tatsuo SHIROICHI, Yoichiro OUCHI, Takashi TSUNEKAWA	November 24, 2000	Japanese Patent Application No. 2000-357026
Semiconductor Element	Kazuyuki TADATOMO, Hiroaki OKAGAWA, Yoichiro OUCHI, Takashi TSUNEKAWA	December 25, 2000	Japanese Patent Application No. 2000-393229
Emission Spectrum Measurement Apparatus and Measurement Method	Satoshi WATANABE, M. S. MINSKY	January 19, 2001	Japanese Patent Application No. 2001-011214
Color Temperature Variable LED Light Source Module	Yasuo IMAI, Ken'ichi ISHII, Ken'ichi Y. Yamada	March 14, 2001	Japanese Patent Application No. 2001-071940
Semiconductor Light	Kiyoteru Y. Yoshida	March 21, 2001	Japanese Patent Application No. 2001-

Emitting Element			080739
Nitride Semiconductor Light Emitting Element	Kiyoteru Y. Yoshida	March 21, 2001	Japanese Patent Application No. 2001-080740
Group III-V compound semiconductor and method of producing the same	Kazumasa HIRAMATSU, Hideto MIYAKE, Takayoshi MAEDA, Yasushi IYECHIKA	March 22, 2001	Japanese Patent Application No. 2001-082240
Group III-V compound semiconductor and method of producing the same	Kazumasa HIRAMATSU, Hideto MIYAKE, Takayoshi MAEDA, Yasushi Y. Iyechika	March 20, 2001	90106463 (Taiwan)
Group III-V compound semiconductor and method of producing the same	Kazumasa HIRAMATSU, Hideto MIYAKE, Takayoshi MAEDA, Yasushi Y. Iyechika	March 21, 2001	200101805-0 (Singapore)
Group III-V compound semiconductor and method of producing the same	Kazumasa HIRAMATSU, Hideto MIYAKE, Takayoshi MAEDA, Yasushi Y. Iyechika	March 22, 2001	101 14 029.0 (Germany)
Group III-V compound semiconductor and method of producing the same	Kazumasa HIRAMATSU, Hideto MIYAKE, Takayoshi MAEDA, Yasushi Y. Iyechika	March 23, 2001	09/814,875 (United States)
Group III-V compound semiconductor and method of producing the same	Kazumasa HIRAMATSU, Hideto MIYAKE, Takayoshi MAEDA, Yasushi IYECHIKA	March 23, 2001	10-2001-0015251 (South Korea)
Semiconductor Element	Kazuyuki TADATOMO	March 27, 2001	Japanese Patent Application No. 2001-091129
Semiconductor Light Emitting Element	Kazuyuki TADATOMO	March 27, 2001	Japanese Patent Application No. 2001-091141
LED Light Source Device Used for Illumination and Lighting Fixture	Ken'ichi YAMADA, Ken'ichi ISHII, Yasuo IMAI	March 29, 2001	Japanese Patent Application No. 2001-096197
LED Light Source Fixture	Ken'ichi ISHII, Yasuo IMAI, Ken'ichi YAMADA	March 29, 2001	Japanese Patent Application No. 2001-096198
Reflection Type LED Light Source	Ken'ichi YAMADA, Ken'ichi ISHII, Yasuo IMAI	March 29, 2001	Japanese Patent Application No. 2001-096541

LED Light Source Device and Lighting Fixture	Ken'ichi ISHII, Yasuo IMAI, Ken'ichi YAMADA, Chiyoharu MAKIHARA	March 29, 2001	Japanese Patent Application No. 2001- 097222
Semiconductor Light Emitting Element	Kazuyuki TADATOMO	April 20, 2001	Japanese Patent Application No. 2001- 123345
GaN-based Light Emitting Element	Kiyoteru YOSHIDA	April 26, 2001	Japanese Patent Application No. 2001- 129492